

***FY 2015 Status Report:
CIRFT Testing of High-Burnup
Used Nuclear Fuel Rods from
Pressurized Water Reactor and
Boiling Water Reactor
Environments***

Fuel Cycle Research & Development

***Prepared for
US Department of Energy
Used Fuel Disposition Campaign***

***J.-A. Wang, H. Wang, H. Jiang, Y. Yan,
and B. B. Bevard
Oak Ridge National Laboratory***

***September 4, 2015
M2-FCRD-UFD-2015-000101***



DISCLAIMER

This information was prepared as an account of work sponsored by an agency of the U.S. Government. Neither the U.S. Government nor any agency thereof, nor any of their employees, makes any warranty, expressed or implied, or assumes any legal liability or responsibility for the accuracy, completeness, or usefulness, of any information, apparatus, product, or process disclosed, or represents that its use would not infringe privately owned rights. References herein to any specific commercial product, process, or service by trade name, trade mark, manufacturer, or otherwise, does not necessarily constitute or imply its endorsement, recommendation, or favoring by the U.S. Government or any agency thereof. The views and opinions of authors expressed herein do not necessarily state or reflect those of the U.S. Government or any agency thereof.

Materials Science and Technology Division

**FY 2015 Status Report: CIRFT Testing of High-Burnup Used Nuclear Fuel
Rods from Pressurized Water Reactor and Boiling Water Reactor
Environments**

Jy-An John Wang, Hong Wang, Hao Jiang, and Y. Yan

Program Manager
Bruce Bevard

Date Published: September 4, 2015

Prepared by
OAK RIDGE NATIONAL LABORATORY
Oak Ridge, TN 37831-6283
managed by
UT-BATTELLE, LLC
for the
US DEPARTMENT OF ENERGY
under contract DE-AC05-00OR22725

This page intentionally left blank.

CONTENTS

FIGURES.....	v
TABLES	xiii
ABBREVIATIONS	xv
SUMMARY	xvii
1. INTRODUCTION	1
2. SPECIMEN PREPARATION.....	2
2.1 Limerick (LMK) Rods	2
2.2 North Anna (NA) and Catawba (MOX) Rods	4
3. DATA PROCESSING	7
4. TEST RESULTS FOR LMK SPECIMENS.....	9
4.1 Tuning and Testing Using LMK01/574D-A	9
4.2 MK02/575D-A, ± 12.7 N·m, 5 Hz.....	12
4.3 LMK03/575B-A, ± 10.16 N·m, 5 Hz.....	15
4.4 LMK05/574D-B, ± 8.64 N·m, 5 Hz.....	19
4.5 LMK06/574D-E, ± 7.62 N·m, 5 Hz.....	21
4.6 LMK07/575C-A, ± 15.24 N·m, 5 Hz.....	23
4.7 LMK08/575B-D, ± 7.62 N·m, 5 Hz.....	27
4.8 LMK09/574D-D, ± 10.16 N·m, 5 Hz	29
4.9 LMK10/575B-E, ± 20.32 N·m, 5 Hz.....	33
4.10 LMK11/575B-D, ± 8.64 N·m, 5 Hz	35
4.11 LMK12/575B-A, ± 7.11 N·m, 5 Hz	39
4.12 LMK13/575C-D, ± 25.40 N·m, 5 Hz.....	41
4.13 LMK14/575C-B, ± 10.16 N·m, 5 Hz.....	41
4.14 LMK15/575C-C, ± 10.16 N·m, 5 Hz.....	41
5. TESTING RESULTS ON H. B. ROBINSON SPENT NUCLEAR FUEL	42
5.1 D13/R3/606B3E at ± 13.72 N·m, 5 Hz	42
5.2 D14/R4/606B3D at ± 8.89 N·m, 5 Hz.....	44
5.3 D15/R5/606B3C at ± 7.62 N·m, 5 Hz.....	46
6. TESTING OF NORTH ANNA M5	48
6.1 NA3/651D3	48
6.2 NA1/651C5 at 12.70 N·m, 5 Hz.....	50
6.3 NA2/651C5 at 10.16 N·m, 5 Hz.....	56
6.4 NA4/652B1B at 7.62 N·m, 5 Hz	59
6.5 NA5/652B2 at 5.08 N·m, 5 Hz.....	61
6.6 NA6/652D1 at 5.08 N·m, 5 Hz.....	61
6.7 NA7/652D2 at 15.24 N·m, 5 Hz.....	61
7. TESTING RESULTS ON MOX	62
7.1 MOX1/MOX-A-11	62
7.2 MOX3/MOX-A-13	64
7.3 MOX2/MOX-A-12 at 10.16 N·m, 5 Hz.....	65
7.4 MOX4/MOX-B-05 at 5.08 N·m, 5 Hz.....	70
7.5 MOX5/MOX-B-06 at 6.10 N·m, 5 Hz.....	72
7.6 MOX6/MOX-B-07 at 5.08 N·m, 5 Hz.....	74
7.7 MOX7/MOX-C-06 at 15.24 N·m, 5 Hz.....	77

7.8	MOX8/MOX-C-07 at 12.7 N·m, 5 Hz.....	77
7.9	MOX9/MOX-C-08 at 7.62 N·m, 5 Hz.....	77
7.10	MOX10/ MOX-K-09 at 10.16 N·m, 5 Hz.....	77
7.11	MOX11/MOX-K-10 at 10.16 N·m, 5 Hz.....	77
7.12	MOX12/MOX-K-11 at 10.16 N·m, 5 Hz.....	78
8.	FRACTOGRAPHY FOR HBR, NA, AND MOX SNF.....	79
9.	DISCUSSIONS	83
9.1	Static Response of SNF.....	83
9.2	Effect of Probe Contact on Large Curvature Measurements	84
9.2.1	The Adjusted Stress-Strain and Moment-Curvature Profiles.....	84
9.3	M-N Curve of Limerick Rods	87
9.4	Comparison of SNF Cyclic Fatigue Lifetimes	88
9.4.1	M-N Curve and e-N Curve	92
9.4.2	S-N Curve Based on Equivalent Stress	93
9.4.3	S-N Curve Based on Young’s Modulus	94
9.4.4	The Impact of Transient Shock on SNF Vibration Fatigue Life.....	96
10.	FINITE-ELEMENT ANALYSIS OF LMK BWR CLAD MATERIAL	99
10.1	Introduction	99
10.2	Interface Bonding Efficiency Analysis of BWR Fuel Rod	99
10.2.1	Good Interface Bonding and No Fuel Rod System Fracture	100
10.2.2	Debonding at Pellet-Pellet Interfaces and Bonding at Pellet-Clad Interfaces.....	107
10.2.3	Debonded Pellet-Clad and Pellet-Pellet Interfaces.....	118
10.2.4	Comparison of Flexural Rigidity with Different Fuel Young’s Modulus Cases.....	127
10.3	Discussion	131
11.	HYDRIDE REORIENTATION TESTING ON HBR FUEL.....	134
11.1	Background	134
11.2	Materials, Equipment, and Test Methods.....	135
11.2.1	Description of Cladding Material and High-Burn-Up Fuel Segments	135
11.2.2	Equipment for Sample Preparation	137
11.2.3	Hydride Reorientation System	139
11.3	Materials Hydriding and Characterization	141
11.4	Out-Of-Cell Hydride Reorientation Testing.....	142
11.4.1	HR-HBR #1, 145 MPa at 400°C, 1 cycle	142
11.4.2	HR-HBR #2, 145-150 MPa at 400°C, 5 cycles.....	145
11.4.3	HR-HBR #3, 100 MPa at 400°C, 5 cycles.....	148
11.4.4	HR-HBR #4, 120 MPa at 400°C, 5 cycles.....	151
11.5	DISCUSSION.....	154
12.	CONCLUSIONS	157
13.	ACKNOWLEDGMENTS.....	159
14.	REFERENCES	160
	APPENDIX A: CIRFT TEST RESULTS ON HIGH BURN-UP HBR SNF.....	A1
	APPENDIX B: FINITE ELEMENT ANALYSIS ON HBR PWR SNF MATERIAL	B1

FIGURES

Fig. 1. Cutting plan of BWR Limerick SNF rods for CIRFT testing.	2
Fig. 2. Determination of the bending curvature of the rod by use of deflections measured at three points.....	7
Fig. 3. Grip design of CIRFT with one end-block removed.	8
Fig. 4. Moment-curvature curves in (a) the first loading cycles and (b) the second and third cycles for the LMK01/574D-A rod.	10
Fig. 5. Fracture segments for the LMK01/574D-A rod that survived two cycles of loading to relative displacement of 24.0 mm with a maximum moment of around 85 N·m in the initial cycle. A follow-up dynamic test was carried out at ± 25.4 N·m, 5 Hz; $N_f = 9.4 \times 10^3$ cycles.....	11
Fig. 6. Fracture segments for LMK01/574D-A. (a) and (d) show the specimen ID side of the segment on end caps A and B; (b) and (e) show the mating fracture surface; and (c) and (f) show the opposite specimen ID side of the segment on end caps A and B.	11
Fig. 7. (a) Moment-curvature range and (b) flexural rigidity-curvature range at various numbers of cycles for LMK02/575D-A.	12
Fig. 8. Variations in (a) curvature range, (b) moment range, and (c) flexural rigidity as a function of the number of cycles for LMK02/575D-A. Measurements were made with 0.2 and 0.4 mm relative displacements; $N_f = 1.71 \times 10^5$ cycles at ± 12.70 N·m, 5 Hz.	13
Fig. 9. Variations in (a) curvature range, (b) applied moment range, (c) flexural rigidity, (d) maximum and minimum values of curvature, and (e) maximum and minimum values of moment as a function of the number of cycles for LMK02/575D-A; $N_f = 1.71 \times 10^5$ cycles at ± 12.70 N·m, 5 Hz.	14
Fig. 10. Fracture segments for LMK02/575D-A; $N_f = 1.71 \times 10^5$ cycles at ± 12.70 N·m, 5 Hz.....	15
Fig. 11. Variations in (a) curvature range, (b) moment range, and (c) flexural rigidity as a function of the number of cycles for LMK03/575B-A; $N_f = 4.92 \times 10^5$ cycles at ± 10.16 N·m, 5 Hz.....	16
Fig. 12. Variations in (a) curvature range, (b) applied moment range, (c) flexural rigidity, (d) maximum and minimum values of curvature, and (e) maximum and minimum values of moment as a function of the number of cycles for LMK03/575B-A; $N_f = 4.92 \times 10^5$ cycles at ± 10.16 N·m, 5 Hz.	17
Fig. 13. Fracture segments for LMK03/575B-A $N_f = 4.92 \times 10^5$ cycles at ± 10.16 N·m, 5 Hz.....	18
Fig. 14. Fracture segments for LMK03/575B-A. (a) and (d) show the specimen ID side of the segment on end caps A and B; (b) and (e) show the mating fracture surface; and (c) and (f) show the opposite specimen ID side of the segment on end caps A and B.	18
Fig. 15. Variations in (a) curvature range, (b) moment range, and (c) flexural rigidity as a function of the number of cycles for LMK05/574D-B; $N_f = 2.49 \times 10^5$ cycles at ± 8.64 N·m, 5 Hz.....	19
Fig. 16. Variations in (a) curvature range, (b) applied moment range, (c) flexural rigidity, (d) maximum and minimum values of curvature, and (e) maximum and minimum values of moment as a function of the number of cycles for LMK05/574D-B; $N_f = 2.49 \times 10^5$ cycles at ± 8.64 N·m, 5 Hz.	20
Fig. 17. Variations in (a) curvature range, (b) moment range, and (c) flexural rigidity as a function of the number of cycles for LMK06/575D-E; $N_f = 1.79 \times 10^6$ cycles at ± 7.62 N·m, 5 Hz.....	21
Fig. 18. Variations in (a) curvature range, (b) applied moment range, (c) flexural rigidity, (d) maximum and minimum values of curvature, and (e) maximum and minimum values of moment as a function of the number of cycles for LMK06/575D-E; $N_f = 1.79 \times 10^6$ cycles at ± 7.62 N·m, 5 Hz.	22
Fig. 19. Variations in (a) curvature range, (b) moment range, and (c) flexural rigidity as a function of the number of cycles for LMK07/575C-A; $N_f = 1.22 \times 10^5$ cycles at ± 15.24 N·m, 5 Hz.....	24
Fig. 20. Variations in (a) curvature range, (b) applied moment range, (c) flexural rigidity, (d) maximum and minimum values of curvature, and (e) maximum and minimum values	

of moment as a function of the number of cycles for LMK07/575C-A; $N_f = 1.22 \times 10^5$ cycles at $\pm 15.24 \text{ N}\cdot\text{m}$, 5 Hz.	25
Fig. 21. Fracture segments for LMK07/575C-A. (a) and (d) show the specimen ID side of the segments on end caps A and B; (b) and (e) show the mating fracture surface; and (c) and (f) show the opposite specimen ID side of the segment on end caps A and B.	26
Fig. 22. Variations in (a) curvature range, (b) moment range, and (c) flexural rigidity as a function of the number of cycles for LMK08/575B-D. Measurements were made with 0.2 and 0.35 mm relative displacements; $N_f = 4.70 \times 10^6$ cycles at $\pm 7.62 \text{ N}\cdot\text{m}$, 5 Hz.	27
Fig. 23. Variations in (a) curvature range, (b) applied moment range, (c) flexural rigidity, (d) maximum and minimum values of curvature, and (e) maximum and minimum values of moment as a function of the number of cycles for LMK08/575B-D; $N_f = 4.70 \times 10^6$ cycles at $\pm 7.62 \text{ N}\cdot\text{m}$, 5 Hz.	28
Fig. 24. Fracture segments for LMK08/575B-D; $N_f = 4.70 \times 10^6$ cycles at $\pm 7.62 \text{ N}\cdot\text{m}$, 5 Hz.	29
Fig. 25. Variations in (a) curvature range, (b) moment range, (c) flexural rigidity as a function of the number of cycles for LMK09/574D-D. Measurements were made with 0.2 and 0.4 mm relative displacements; $N_f = 7.31 \times 10^5$ cycles at $\pm 10.16 \text{ N}\cdot\text{m}$, 5 Hz.	30
Fig. 26. Variations in (a) curvature range, (b) applied moment range, (c) flexural rigidity, (d) maximum and minimum values of curvature, and (e) maximum and minimum values of moment as a function of the number of cycles for LMK09/574D-D; $N_f = 7.31 \times 10^5$ cycles at $\pm 10.16 \text{ N}\cdot\text{m}$, 5 Hz.	31
Fig. 27. Fracture segments for LMK09/574D-D; $N_f = 7.31 \times 10^5$ cycles at $\pm 10.16 \text{ N}\cdot\text{m}$, 5 Hz.	32
Fig. 28. Fracture segments for LMK09/574D-D. (a) and (d) show the specimen ID side of the segment on end caps A and B; (b) and (e) show the mating fracture surface; and (c) and (f) show the opposite specimen ID side of segment on end caps A and B.	32
Fig. 29. Variations in (a) curvature range, (b) moment range, and (c) flexural rigidity as a function of the number of cycles for LMK10/575B-E. Measurements were made with 0.2, and 0.4 mm relative displacements; $N_f = 5.20 \times 10^4$ cycles at $\pm 20.32 \text{ N}\cdot\text{m}$, 5 Hz.	33
Fig. 30. Variations in (a) curvature range, (b) applied moment range, (c) flexural rigidity, (d) maximum and minimum values of curvature, and (e) maximum and minimum values of moment as a function of the number of cycles for LMK10/575B-E; $N_f = 5.20 \times 10^4$ cycles at $\pm 20.32 \text{ N}\cdot\text{m}$, 5 Hz.	34
Fig. 31. Variations in (a) curvature range, (b) moment range, and (c) flexural rigidity as a function of the number of cycles for LMK11/575B-D. Measurements were made with 0.2 and 0.35 mm relative displacements; $N_f = 3.55 \times 10^5$ cycles at $\pm 8.64 \text{ N}\cdot\text{m}$, 5 Hz.	36
Fig. 32. Variations in (a) curvature range, (b) applied moment range, (c) flexural rigidity, (d) maximum and minimum values of curvature, and (e) maximum and minimum values of moment as a function of the number of cycles for LMK11/575B-D; $N_f = 3.55 \times 10^5$ cycles at $\pm 8.64 \text{ N}\cdot\text{m}$, 5 Hz.	37
Fig. 33. Fracture segments for LMK11/574D-D; $N_f = 3.55 \times 10^5$ cycles at $\pm 8.64 \text{ N}\cdot\text{m}$, 5 Hz.	38
Fig. 34. Fracture segments for LMK11/575B-D. (a) and (d) show the specimen ID side of the segment on end caps A and B; (b) and (e) show the mating fracture surface; and (c) and (f) show the opposite specimen ID side of segment on end caps A and B.	38
Fig. 35. Variations in (a) curvature range, (b) moment range, and (c) flexural rigidity as a function of the number of cycles for LMK12/575B-A. Measurements were made with 0.2 and 0.35 mm relative displacements; $N = 7.58 \times 10^6$ cycles at $\pm 7.11 \text{ N}\cdot\text{m}$, 5 Hz.	39
Fig. 36. Variations in (a) curvature range, (b) applied moment range, (c) flexural rigidity, (d) maximum and minimum values of curvature, and (e) maximum and minimum values of moment as a function of the number of cycles for LMK12/575B-A; $N = 7.58 \times 10^6$ cycles at $\pm 7.11 \text{ N}\cdot\text{m}$, 5 Hz.	40
Fig. 37. Failed specimen LMK14 showing that the failure occurred in the gage section.	41

Fig. 38. Variations in (a) curvature range, (b) applied moment range, (c) flexural rigidity, (d) maximum and minimum values of curvature, and (e) maximum and minimum values of moment as a function of the number of cycles for D13/R3 (606B3E); $N_f = 1.29 \times 10^5$ cycles at ± 13.72 N·m, 5 Hz.	43
Fig. 39. Variations in (a) curvature range, (b) applied moment range, and (c) flexural rigidity as a function of the number of cycles for D13/R3 (606B3E); $N_f = 1.29 \times 10^5$ cycles at ± 13.72 N·m, 5 Hz.	43
Fig. 40. Variations in (a) curvature range, (b) applied moment range, (c) flexural rigidity, (d) maximum and minimum values of curvature, and (e) maximum and minimum values of moment as a function of the number of cycles for R4 (606B3D); $N_f = 2.7 \times 10^5$ cycles at ± 8.89 N·m, 5 Hz.	45
Fig. 41. Variations in (a) curvature range, (b) applied moment range, and (c) flexural rigidity as a function of the number of cycles for R4 (606B3D); $N_f = 2.7 \times 10^5$ cycles at ± 8.89 N·m, 5 Hz.	45
Fig. 42. Variations in (a) curvature range, (b) applied moment range, (c) flexural rigidity, (d) maximum and minimum values of curvature, and (e) maximum and minimum values of moment as a function of the number of cycles for R5 (606B3C); $N = 2.23 \times 10^7$ cycles at ± 7.62 N·m, 5 Hz.	47
Fig. 43. Variations in (a) curvature range, (b) applied moment range, and (c) flexural rigidity as a function of the number of cycles for R5 (606B3C); $N = 2.23 \times 10^7$ cycles at ± 7.62 N·m, 5 Hz.	47
Fig. 44. (a) Moment-curvature curves and (b) equivalent stress-strain curves based on the first four loading cycles for specimen NA3 (651D3).	49
Fig. 45. Image of specimen NA3 (651D3) after testing; the rod sustained four cycles of loading to 24.00 mm relative displacement; the maximum moment of 47 N·m was reached during the initial loading cycle.	49
Fig. 46. Moment and curvature as a function of time and moment-curvature loops based on measurements when (a) $N=1$ and (b) $N = 111,000$ cycles for NA1 (651B2). Measurements were made with 1.0, 2.0, and 3.0 mm relative displacements; $N_f = 1.57 \times 10^4$ cycles at ± 12.70 N·m, 5 Hz.	50
Fig. 47. (a) Moment-curvature relation and (b) moment-flexural rigidity relation at various numbers of cycles for NA1 (651B2). Measurements were made with 1.0, 2.0, and 3.0 mm relative displacements; $N_f = 1.57 \times 10^4$ cycles at ± 12.70 N·m, 5 Hz.	51
Fig. 48. Variations in (a) curvature range, (b) moment range, and (c) flexural rigidity as a function of the number of cycles for NA1 (651B2). Measurements were made with 1.0, 2.0, and 3.0 mm relative displacements; $N_f = 1.57 \times 10^4$ cycles at ± 12.70 N·m, 5 Hz.	52
Fig. 49. Variations in (a) curvature range, (b) applied moment range, (c) flexural rigidity, (d) maximum and minimum values of curvature, and (e) maximum and minimum values of moment as a function of the number of cycles for NA1 (651B2); $N_f = 1.57 \times 10^4$ cycles at ± 12.70 N·m, 5 Hz.	53
Fig. 50. Moment and curvature as a function of time and moment-curvature loops at (a) 50 cycles and (b) 1.35×10^4 cycles; results are based on online monitoring of NA1 (651B2).	54
Fig. 51. Fracture segments for NA1 (651B2); $N_f = 1.57 \times 10^4$ cycles at ± 12.70 N·m, 5 Hz.	55
Fig. 52. Variations in (a) curvature range, (b) moment range, and (c) flexural rigidity as a function of the number of cycles for NA2 (651C5). Measurements were made with 1.0 and 2.0 mm relative displacements; $N_f = 2.2 \times 10^4$ cycles at ± 10.16 N·m, 5 Hz.	56
Fig. 53. Variations in (a) curvature range, (b) applied moment range, (c) flexural rigidity, (d) maximum and minimum values of curvature, and (e) maximum and minimum values of moment as a function of the number of cycles for NA2 (651C5); $N_f = 2.2 \times 10^4$ cycles at ± 10.16 N·m, 5 Hz.	57
Fig. 54. Fracture location of NA2 (651C5), $N_f = 2.2 \times 10^4$ cycles at ± 10.16 N·m, 5 Hz.	58

Fig. 55. Variations in (a) curvature range, (b) moment range, and (c) flexural rigidity as a function of the number of cycles for NA4 (652B1B). Measurements were made with 1.0 and 2.0 mm relative displacements; $N_f = 6.1 \times 10^4$ cycles at ± 7.62 N·m, 5 Hz.	59
Fig. 56. Variations in (a) curvature range, (b) applied moment range, (c) flexural rigidity, (d) maximum and minimum values of curvature, and (e) maximum and minimum values of moment as a function of the number of cycles for NA4 (652B1B); $N_f = 6.1 \times 10^4$ cycles at ± 7.62 N·m, 5 Hz.	60
Fig. 57. (a) Moment-curvature curves and (b) equivalent stress-strain curves based on the first four loading cycles for MOX1 (specimen MOX-A-11).	63
Fig. 58. Fracture segments for MOX1 (specimen MOX-A-11); the rod survived two cycles of loading to a relative displacement of 24.00 mm with a maximum moment of 47 N·m in the initial cycle. A follow-up dynamic test was carried out at ± 15.24 N·m, 5 Hz; $N_f = 4.0 \times 10^3$ cycles.	63
Fig. 59 (a) Moment-curvature curves and (b) equivalent stress-strain curves based on the first four loading cycles for MOX3 (MOX-A-13).	64
Fig. 60. Moment and curvature as a function of time and moment-curvature loops based on measurements when (a) $N=1$ and (b) $N = 111,000$ cycles for MOX2 (MOX-A-12). Measurements were made with 0.8 and 1.6 mm relative displacements; $N_f = 3.7 \times 10^4$ cycles at ± 10.16 N·m, 5 Hz.	66
Fig. 61 (a) Moment-curvature relation and (b) moment-flexural-rigidity relation at various numbers of cycles for MOX (MOX-A-12). Measurements were made with 0.8 and 1.6 mm relative displacements; $N_f = 3.7 \times 10^4$ cycles at ± 10.16 N·m, 5 Hz.	67
Fig. 62. Variations in (a) curvature range, (b) moment range, and (c) flexural rigidity as a function of the number of cycles for MOX (MOX-A-12). Measurements were made with 0.8 and 1.6 mm relative displacements; $N_f = 3.7 \times 10^4$ cycles at ± 10.16 N·m, 5 Hz.	67
Fig. 63. Variations in (a) curvature range, (b) applied moment range, (c) flexural rigidity, (d) maximum and minimum values of curvature, and (e) maximum and minimum values of moment as a function of the number of cycles for MOX2 (MOX-A-12); $N_f = 3.7 \times 10^4$ cycles at ± 10.16 N·m, 5 Hz.	68
Fig. 64. Moment and curvature as a function of time and moment-curvature loops at (a) 50 cycles and (b) 3.6×10^4 cycles; results are based on online monitoring of MOX2 (MOX-A-12); $N_f = 3.7 \times 10^4$ cycles at ± 10.16 N·m, 5 Hz.	69
Fig. 65. Variations in (a) curvature range, (b) moment range, and (c) flexural rigidity as a function of the number of cycles for MOX4 (MOX-B-05). Measurements were made with 0.4 and 0.7 mm relative displacements; $N_f = 2.15 \times 10^6$ cycles at ± 5.08 N·m, 5 Hz.	70
Fig. 66. Variations in (a) curvature range, (b) applied moment range, (c) flexural rigidity, (d) maximum and minimum values of curvature, and (e) maximum and minimum values of moment as a function of the number of cycles for MOX4 (MOX-B-05); $N_f = 2.15 \times 10^6$ cycles at ± 5.08 N·m, 5 Hz.	71
Fig. 67. Variations in (a) curvature range, (b) moment range, and (c) flexural rigidity as a function of the number of cycles for MOX5 (MOX-B-06). Measurements were made with 0.4 and 0.7 mm relative displacements; $N_f = 4.49 \times 10^5$ cycles at ± 6.10 N·m, 5 Hz.	72
Fig. 68. Variations in (a) curvature range, (b) applied moment range, (c) flexural rigidity, (d) maximum and minimum values of curvature, and (e) maximum and minimum values of moment as a function of the number of cycles for MOX5 (MOX-B-06); $N_f = 4.49 \times 10^5$ cycles at ± 6.10 N·m, 5 Hz.	73
Fig. 69. Variations in (a) curvature range, (b) moment range, and (c) flexural rigidity as a function of the number of cycles for MOX6 (MOX-B-07). Measurements were made with 0.4 and 0.7 mm relative displacements; $N_f = 5.42 \times 10^5$ cycles at ± 5.08 N·m, 5 Hz.	75
Fig. 70. Variations in (a) curvature range, (b) applied moment range, (c) flexural rigidity, (d) maximum and minimum values of curvature, and (e) maximum and minimum values	

	of moment as a function of the number of cycles for MOX6 (MOX-B-07); $N_f = 5.42 \times 10^5$ cycles at $\pm 5.08 \text{ N}\cdot\text{m}$, 5 Hz.	76
Fig. 71	(a) Lateral or front view, (b) transverse view, and (c) back view of fracture surface for HBR R4 tested at $\pm 8.89 \text{ N}\cdot\text{m}$, 5 Hz, $N_f = 2.7 \times 10^5$ cycles.	79
Fig. 72	(a) Lateral or front view, (b) transverse view, and (c) back view of fracture surface for NA1 tested at $\pm 12.7 \text{ N}\cdot\text{m}$, 5 Hz, $N_f = 1.57 \times 10^4$ cycles.	80
Fig. 73	(a) Lateral or front view, (b) transverse view, and (c) back view of fracture surface for NA2 tested at $\pm 10.16 \text{ N}\cdot\text{m}$, 5 Hz, $N_f = 2.20 \times 10^4$ cycles.	80
Fig. 74	(a) Lateral or front view, (b) transverse view, and (c) back view of fracture surface for NA4 tested at $\pm 7.62 \text{ N}\cdot\text{m}$, 5 Hz, $N_f = 6.10 \times 10^4$ cycles.	81
Fig. 75	(a) Lateral or front view, (b) transverse view, and (c) back view of fracture surface for MOX1 tested first to 47 N·m for two cycles and then dynamic loading at $\pm 15.24 \text{ N}\cdot\text{m}$, 5 Hz, $N_f = 4.0 \times 10^3$ cycles.....	81
Fig. 76	(a) Lateral or front view, (b) transverse view, and (c) back view of fracture surface for MOX2 tested at dynamic loading $\pm 10.16 \text{ N}\cdot\text{m}$, 5 Hz, $N_f = 3.70 \times 10^4$ cycles.....	82
Fig. 77	(a) Stress-strain curves based on static testing results for HBR, NA, and MOX SNF. Relative displacement was 24.00 mm; the loading/unloading rate at each point was 0.1/0.2 mm/s.	84
Fig. 78	(a) Three curvature LVDTs being held against the rod; (b) LVDT clamp open to show (b) flat probe and (c) chisel probe.	84
Fig. 79	Moment-curvature curves based on stainless steel aluminum pellet (SSAP) rod testing in which the rod is bent with respect to three LVDTs; (a) concave and (b) convex.	85
Fig. 80	Moment-curvature curves as a function of sensor spacing adjustment in which a rod is bent with respect to three LVDTs: (a) concavely and (b) convexly.	85
Fig. 81	Updated stress-strain profiles based on adjustment factor \square/h of 2.9 mm.	86
Fig. 82	Moment-curvature plots based on bending tests and comparison with PNNL data with sensing spacing correction; no pellets were involved in PNNL's moment evaluation. Due to dimension and material variability of the tested SNF, the variability in CIRFT bending resistance was also observed.	86
Fig. 83	Applied moment amplitude as a function of cycles to failure or cycles completed. The data point of pre-statically tested is based on a follow-up dynamic test of LMK01.	87
Fig. 84	Curvature amplitude as a function of cycles to failure or cycles completed. The data point of pretested is based on a follow-up dynamic test of LMK01. Three LMK fatigue data points are pending further analyses and are not included here.	88
Fig. 85	Moment amplitudes as a function of number of cycles; results are based on CIRFT testing of various used fuels at 5 Hz. The power function was obtained from curve fitting based on the HBR data set.	92
Fig. 86	Strain amplitudes as a function of number of cycles; results are based on CIRFT testing of various used fuels at 5 Hz. The power function was obtained from curve fitting based on the HBR data set.	93
Fig. 87	Stress amplitudes as a function of number of cycles; results are based on CIRFT testing of various used fuels at 5 Hz. The power function was obtained from curve fitting based on the HBR data set.	94
Fig. 88	E-based stress amplitudes as a function of number of cycles; results are based on CIRFT testing of various used fuels at 5 Hz. The power function was obtained from curve fitting based on the HBR data set.	95
Fig. 89	Equivalent stress vs. life curves based on CIRFT testing results for HBR, NA, and MOX SNF. The equivalent stress is based on Eq. (3) with modified moment of inertia, $I = I_c + 0.5 \cdot I_p$	96
Fig. 90	Typical load-time history on a transport cask with the acceleration-time history showing discrete shock signals superimposed on continuous vibration signals.	97

Fig. 91. Pilot transient shocks simulation study on MOX and LMK SNF. The reduction in lifetime of CIRFT-tested SNF samples was observed from combining the harmonic vibration loading and drop-induced transient shock load. LMK CIRFT results also reveal that the CIRFT sample from the spacer grid region (B section) has the lowest lifetime compared to samples from locations A, C, and D.	98
Fig. 92. Geometry of horizontal U-frame bending fatigue testing system with a coplanar rod configuration.....	100
Fig. 93. FEA model of BWR pellet.....	101
Fig. 94. Geometry of clad-pellet 2 in. section model of BWR fuel rod with six pellets.....	101
Fig. 95. Detail area from Fig. 94 for the perfect bond cases.....	102
Fig. 96. Normal stress distribution and curvature results for clad-pellet 2 in. section model of BWR fuel rod with perfect bonding.....	104
Fig. 97. Shear stress distribution at the clad for the clad-pellet 2 in. section model of BWR fuel rod with perfect bonding.	105
Fig. 98. ORNL hot-cell CIRFT test data of PWR HBR fuel rod, flexural rigidity, and curvature. ¹⁸	107
Fig. 99. Transportation-induced reversal bending stress fields in an SNF system.....	109
Fig. 100. Detail from Fig. 94 for the case of empty gaps at debonded pellet-pellet interfaces.....	109
Fig. 101. Normal stress distribution and curvature results for the clad-pellet 2 in. section model of BWR fuel rod with debonded pellet-pellet interfaces with gaps and bonded pellet-clad interfaces.	111
Fig. 102. Shear stress distribution at the clad of the clad-pellet 2 in. section model of BWR fuel rod with debonded pellet-pellet interfaces with gaps and bonded pellet-clad interfaces.	113
Fig. 103. Detail from Fig. 94 for the case of no gaps at debonded pellet-pellet interfaces.....	113
Fig. 104. Normal stress distribution and curvature results for clad-pellet 2 in. section model of BWR fuel rod with debonded pellet-pellet interfaces without gaps and bonded pellet-clad interfaces.	115
Fig. 105. Shear stress distribution at the clad of the clad-pellet 2 in. section model of BWR fuel rod with debonded pellet-pellet interfaces without gaps and bonded pellet-clad interfaces.	117
Fig. 106. Detail area from Fig. 94 for the cases of empty gaps at debonded pellet-pellet interfaces and a thin Zircaloy-4 film filled at the debonded pellet-clad interfaces.....	119
Fig. 107. Normal stress distribution and curvature results for clad-pellet 2 in. section model of BWR fuel rod with empty gaps at debonded pellet-pellet interfaces and a Zircaloy-4 film at debonded pellet-clad interfaces.....	120
Fig. 108. Shear stress distribution at the clad of the clad-pellet 2 in. section model of the BWR fuel rod with empty gaps at debonded pellet-pellet interfaces and a Zircaloy-4 film at the debonded pellet-clad interfaces.	122
Fig. 109. Detail area from Fig. 94 for the case with no gaps at debonded pellet-pellet interfaces and a thin Zircaloy-4 film at debonded pellet-clad interfaces.	123
Fig. 110. Normal stress distribution and curvature results for the clad-pellet 2 in. section model of a BWR fuel rod without gaps at debonded pellet-pellet interfaces and with a Zircaloy-4 film at debonded pellet-clad interfaces.	124
Fig. 111. Shear stress distribution and curvature results for the clad-pellet 2 in. section model of BWR fuel rod without gaps at debonded pellet-pellet interfaces and with a Zircaloy-4 film at debonded pellet-clad interfaces.	126
Fig. 112. ORNL hot-cell CIRFT test data of BWR fuel rod flexural rigidity and curvature.....	127
Fig. 113. Stress distribution at the clad for the fuel Young's modulus $\frac{1}{4}$ of the original with gaps at debonded pellet-pellet interfaces and with a Zircaloy-4 film at bonded pellet-clad interfaces.	129
Fig. 114. Stress distribution at the clad for the fuel Young's modulus $\frac{1}{2}$ of the original without gaps at debonded pellet-pellet interfaces and with a Zircaloy-4 film at debonded pellet-clad interfaces.	130

Fig. 115. High-burnup HBR fuel morphology for Sample 607D4A.	137
Fig. 116. Hydrogen charging apparatus.	138
Fig. 117. A typical pressure and temperature profile of hydrogen charging process.	138
Fig. 118. Astro Arc Polysoude tubing welder.	139
Fig. 119. (a) Schematic of the hydride reorientation system.	140
Fig. 119. (b) Hydride reorientation system.	140
Fig. 120. Micrographs showing typical circumferential hydride distributions in hydrogen charged Zircaloy-4.	141
Fig. 121. Time vs pressure and temperature for Test HR-HBR#1.	143
Fig. 122. High magnification micrograph showing radial hydrides of Sample HR-HBR#1 with hydrogen content $H \approx 274$ ppm. The specimen was sectioned at the mid-plane of a 6"-long sample.	143
Fig. 123. Radial hydride distribution shown in eight areas in different circumferential directions of Sample HR-HBR#1. The specimen was sectioned at the mid-plane of a 6"-long sample.	144
Fig. 124. Time vs pressure and temperature for Test HR-HBR#2.	145
Fig. 125. High magnification micrograph showing radial hydrides of Sample HR-HBR#2 with hydrogen content $H \approx 286$ ppm. The specimen was sectioned at the mid-plane of a 6"-long sample.	146
Fig. 126. Radial hydride distribution shown in eight areas in different circumferential directions of Sample HR-HBR#2. The specimen was sectioned at the mid-plane of a 6"-long sample.	147
Fig. 127. Time vs pressure and temperature for Test HR-HBR#3.	148
Fig. 128. High magnification micrograph showing radial hydrides of Sample HR-HBR#3 with hydrogen content $H \approx 310$ ppm. The specimen was sectioned at the mid-plane of a 6"-long sample.	149
Fig. 129. Radial hydride distribution shown in eight areas in different circumferential directions of Sample HR-HBR#3. The specimen was sectioned at the mid-plane of a 6"-long sample.	150
Fig. 130. Time vs pressure and temperature for Test HR-HBR#4.	151
Fig. 131. High magnification micrograph showing radial hydrides of Sample HR-HBR#4 with hydrogen content $H \approx 312$ ppm. The specimen was sectioned at the mid-plane of a 6"-long sample.	152
Fig. 132. Radial hydride distribution shown in eight areas in different circumferential directions of Sample HR-HBR#4. The specimen was sectioned at the mid-plane of a 6"-long sample.	153
Fig. 133. Schematic diagram and basal pole figure showing the grain orientation in stress-relieved Zircaloy-4.	154
Fig. 134. Terminal solid solubility for dissolution of hydrogen in Zircaloy.	155
Fig. 135. SEM images of fracture D10 specimen shows non-uniform hydride ring along the outer diameter of the clad wall.	156

This page intentionally left blank.

TABLES

Table 1. Segment identification of Limerick SNF rod ¹⁰	3
Table 2. Outer diameters (ODs) of Limerick SNF rod segments (in.)	4
Table 3. CIRFT test number and segment labels of Limerick SNF rod	4
Table 4. Specimen labels used for NA M5 SNF	5
Table 5. Specimen labels used for MOX SNF	5
Table 6. Outside diameters of NA M5 SNF segments (in.)* ¹²	6
Table 7. Tuning parameters based on LMK01	9
Table 8. Summary of CIRFT testing of HBR rods	89
Table 9. Summary of CIRFT testing of NA/MOX fuels	90
Table 10. Summary of CIRFT testing of LMK fuels	91
Table 11. Cross section geometric size, Young's Modulus and yield stress 903 of SNF rods	93
Table 12. Mechanical properties of the fuel rod	99
Table 13. The curvature, flexural rigidity, and bending moment comparison for the perfect interface bonding simulation	106
Table 14. Comparison of curvature, flexural rigidity, and bending moment for the bonded pellet-clad and debonded pellet-pellet cases	117
Table 15. The curvature, flexural rigidity, and bending moment comparison for debonded pellet-clad and pellet-pellet interfaces	127
Table 16. The flexural rigidity comparison of the different fuel Young's modulus cases	128
Table 17. Comparison of max stress at cladding between different fuel Young's modulus cases	129
Table 18. The flexural rigidity comparison between the different bonding and debonding cases	132
Table 19. The flexural rigidity comparison between BWR and PWR HBR fuel rods for different interface bonding conditions	133
Table 20. Dimensions and Chemistry of HBR Archive Zircaloy-4 Used in the ORNL Test Program (the "<" sign means below the detection limit)	135
Table 21. Characteristics of High-burnup HBR Fuel Rods for the ORNL Hydride Reorientation Test. Burnup values are rod averaged	136

This page intentionally left blank.

ABBREVIATIONS

AP	alumina pellets
BWR	boiling water reactor
CIRFT	Cyclic Integrated Reversible-Bending Fatigue Tester
DOE	Department of Energy
FCRD	Fuel Cycle Research & Development
FEA	finite-element analysis
FY	fiscal year
GWd/MTU	gigawatt-days per metric ton of uranium
HBR	H. B. Robinson Nuclear Power Station
HBU	high burn-up
ID	identification numbers
LMK	Limerick Nuclear Power Station
LVDT	linear variable differential transformer
MOX	mixed uranium-plutonium oxide
NA	North Anna Power Station
NCT	normal conditions of transport
NRC	US Nuclear Regulatory Commission
NUREG	Nuclear Regulatory Commission technical report
NUREG/CR	NUREG Contractor Report
OD	outer diameter
ORNL	Oak Ridge National Laboratory
PCI	peripheral component interconnect
PIE	post-irradiation examination
PNNL	Pacific Northwest National Laboratory
PPI	pellet-to-pellet interface
PWR	pressurized water reactor
RT	room temperature
SNF	spent nuclear fuel
SS	stainless steel
SSAP	stainless steel alumina pellets
UFDC	Used Fuel Disposition Campaign
SNF	used nuclear fuel

This page intentionally left blank.

SUMMARY

High burn-up spent nuclear fuel (SNF) cladding has a significant amount of microcracks and hydrides, which will reduce the stress intensity required for crack growth. The potential linking of microcracks during vibration loading could also reduce the fatigue threshold/incubation period significantly, accelerating fatigue failure. In addition to cladding damage, the microstructure of fuel pellets and the characteristics of the interfaces between fuel pellets and between fuel pellets and cladding are likely to be dramatically changed after high burn-up. These modifications can have a direct impact on the structural integrity and vibration response of SNF rods in transportation.

As a result, vibration has been included as one of the mandatory testing conditions in the structural evaluation of packages used by the US Nuclear Regulation Commission (NRC) in transporting SNF (10 CFR §71.71). Prior to this program development, no current system was available to test the SNF and evaluate the performance of fuel rods during spent fuel transportation. The objective of this research is to develop a system that can appropriately test the response of high-burnup SNF rods in a simulated loading condition.

SNF rods lie horizontally and are supported by the assembly guide tubes and spacer grids inside specially designed transportation casks. During normal conditions of transport, these fuel rods are subjected to oscillatory bending due to inertial effects. This oscillatory bending is the major vibrational load of SNF rods as discussed in 10 CFR §71.71. Besides the change in composite structure of fuel pellets and cladding that occurs during irradiation, the SNF rods typically have burnup induced damage (pores and microcracks), oxide and hydride layers, residual stresses, altered interfaces, and trapped fission products. Understanding the impact these changes may have on the strength of the SNF fuel/cladding system is required to accurately simulate the performance of SNF rods during transport.

Also, the predominance of the hydride platelets that do exist in the cladding after the fuel is discharged from reactors are oriented in the circumferential direction. At elevated temperatures during drying-transfer, some of the hydrogen may go into solution (up to 200 wppm at 400°C). The pressure-induced cladding tensile hoop stress during drying-transfer operations is high relative to in-reactor and pool-storage conditions. During cooling under tensile hoop stress, some of the dissolved hydrogen will precipitate in the radial direction across the cladding wall. Further cooling during storage may result in radial-hydride-induced embrittlement.

Vibration integrity of high-burnup SNF while being transported continues to be a critical issue for the US nuclear waste management system. Structural evaluation of spent fuel packaged for transportation will need to reveal whether the contents or spent fuel is in a subcritical condition. However, such a system for testing and characterizing spent fuel is still lacking, mainly due to complications associated with testing radioactive specimens in a hot cell environment. The current state of the art in spent fuel research and development cannot provide reliable mechanical property data for evaluating spent fuels in transport packaging.

Initially, under the sponsorship of NRC, Oak Ridge National Laboratory (ORNL) accepted the challenge of developing a robust testing system for spent fuel in a hot cell. An extensive literature survey showed that a variety of bending fatigue testing methods have been developed, including cantilever beam bending, three- and four-point bending, pure bending, and their variants, to take into account environmental factors, particularly temperature. Bending fatigue testing, both nonrotating and rotating, has evolved over more than a half century, based on whether the rotation is introduced to carry out the reverse bending. However, the vibration of SNF rods usually shows deflection instead of rotation during transportation, and the dominant frequencies involved with these dynamical events are generally less than 100 Hz. Therefore, the nonrotating reverse bending by a universal material testing machine or its equivalents has been pursued in this project.

Currently, cyclic bending fatigue tests are being used to test and characterize various engineering materials and their components, including concrete, composites, ceramics, metal alloys, metallic glasses, etc. This includes nonreversible unipolar mode and fully reversible bipolar mode. Mechanical support and contact techniques to enable the designed beam bending boundary condition have advanced significantly. However, most of the bending fatigue tests are application based.

A bending fatigue system has been developed at ORNL to test high-burnup SNF rods. Pure bending was adopted as the bending mode of the testing system. Using a pure bending method in which a uniform bending moment is exerted on the gage length of the specimen apparently eliminates the effect of shear. The latter can eventually lead to a failure mode that is not relevant to the fatigue failure of concern. The main features of the system are summarized as follows.

- Rigid sleeves are introduced to reinforce the specimen and to enable the conversion of external force couples to the bending moments.
- Bending moments are applied through two horizontal rigid arms of a U-frame structure. The arms are equipped with two co-axial holes that accommodate the rod to be tested.
- Roller bearings or equivalent bearing sets in the arms of the U-frame allow the release of any axial load related to the loading of a specimen and at the same time transfer the bending moments from the rigid arms to the specimen.
- The initial setup of a specimen in testing can be accomplished by simply inserting the specimen into the holes, which is advantageous in a hot cell environment because most of the operations available can be adapted to the current testing system.
- The U-frame is comprised of fewer components, which results in a system with enhanced reliability and controllability.
- Versatile designs in the loading member and joints or corners of the U-frame provide wide options for different experimental studies.

This report provides a detailed description of test results based on the latest Cyclic Integrated Reversible-Bending Fatigue Tester (CIRFT) used to determine the vibration integrity of a spent fuel rod under normal transportation conditions. The CIRFT consists mainly of a U-frame testing setup and a real-time curvature measurement method. The three-component U-frame setup of the CIRFT has two rigid arms and linkages to a universal testing machine. The curvature of rod bending is obtained through a three-point deflection measurement method. Three linear variable differential transformers (LVDTs) are used and clamped to the side connecting plates of the U-frame to capture the deformation of the rod.

Unique features of the system include the following.

1. The setup enables the rod to simply be inserted using linear bearings incorporated with rigid sleeves.
2. The reverse cyclic bending test can be carried out effectively and efficiently by push and pull at the loading point of the setup. Any test machine with a linear motion function can be used to drive the setup.
3. The embedded and preloaded linear roller bearings eliminate the backlash that occurs in conventional reverse bending.
4. A minimal number of linkages to the universal machine are used. Only two linkages are needed at the two loading points of a U-frame setup, while a conventional four/three point bending demands four linkages.
5. The curvature measurement is immune to the effects from compliant layers and rigid body motion of the machine. The LVDT technique is proven to be robust in a hot cell environment and is free from the restraints related to noncontact measurements.

6. The test protocol for cyclic reversible bending test has been developed and has been used in a hot cell since September 2013.

The objective of this project is to perform a systematic study of spent nuclear fuel (SNF), also known as “used nuclear fuel” [SNF]) integrity under simulated transportation environments using CIRFT hot-cell testing technology developed at ORNL in August 2013. Under NRC sponsorship, ORNL completed four benchmark tests, four static tests, and 12 dynamic or cycle tests on H. B. Robinson (HBR) high-burnup (HBU) fuel. The cladding of the HBR fuels was made of Zircaloy-4. Testing was continued in fiscal year (FY) 2014 using Department of Energy (DOE) funds. Additional CIRFT testing was conducted on three HBR rods; two specimens failed, and one specimen was tested to over 2.23×10^7 cycles without failing. The data analysis on all the HBR SNF rods demonstrated that it is necessary to characterize the fatigue life of the SNF rods in terms of (1) the curvature amplitude and (2) the maximum absolute of curvature extremes. The maximum extremes are significant because they signify the maximum tensile stress for the outer fiber of the bending rod. CIRFT testing also addressed a large variation in hydrogen content of the HBR rods. While the load amplitude is the dominant factor that controls the fatigue life of bending rods, the hydrogen content also has an important effect on the lifetime attained at each load range tested.

In FY 2015, 14 SNF rod segments from the Limerick (LMK) boiling water reactor (BWR) were tested using the ORNL CIRFT equipment—one test under static conditions and 13 tests under dynamic loading conditions. Under static unidirectional loading, a moment of 85 N·m was obtained at a maximum curvature of 4.0 m^{-1} . The specimen did not show any sign of failure during three repeated loading cycles to a similar maximum curvature. Thirteen cyclic tests were conducted with load amplitudes varying from 25.4 to 7.1 N·m. Failure was observed in 12 of the tested rod specimens. The cycles-to-failure ranged from 2.14×10^4 to 4.70×10^6 . One cycled to 7.58×10^6 without failure, and the test was stopped. The measurements taken once the test was stopped indicated a range of flexural rigidity from 30 to 50 N·m². The online monitoring revealed that the flexural rigidity was slightly lower due to the higher loading, from 25 to 42 N·m². This level of rigidity was a little lower than that of the PWR HBR specimens at 39 to 51 N·m². While the two claddings were based on Zircaloy-2 and Zircaloy-4, respectively, it is interesting to note that the geometrical sizes contribute more to the observed difference, where HBR rods had a relative smaller cladding outer diameter (OD) and pellet diameters compared to those of the Limerick BWR. Thus, the observed higher rigidity of HBR pressurized water reactor (PWR) SNF may primarily be due to the higher strength of Zircaloy-4 cladding and higher pellet-clad interface bonding of the PWR pressurized environment. A BWR has about half the coolant pressure of a PWR.

In general, no substantial change of rigidity was observed based on the online monitoring during the cyclic fatigue testing process. Overall, the decreasing trend in lifetime with the increasing load amplitude is well defined.

Additional CIRFT tests were performed on three North Anna (NA) spent fuel rods and six mixed oxide (MOX) rods in a hot cell in FY15. A total of six dynamic tests were completed on NA rods in the hot cell. Applied moment amplitudes were varied from ± 5.08 to ± 15.24 N·m. Five specimens failed with fatigue lives ranging from 1.26×10^4 to 4.27×10^5 cycles. One specimen cycled to 5.11×10^6 without failure. Ten dynamic tests were also conducted on MOX spent fuel rods with amplitudes ranging from 5.08 to 15.24 N·m, and the specimens failed between 1.29×10^4 and 2.15×10^6 cycles. Online monitoring indicated a variation in rigidity of 21 to 28 N·m² for this group of spent fuel rods that had a similar cladding OD. Apparently, the range of flexural rigidity is much lower than that of HBR and LMK rods mainly due to the smaller size cross section of the rods.

The use of equivalent strain and equivalent stress obviously reduced the cladding/pellet size effect to a certain extent, and data points can be consolidated more to the HBR curve. More investigation is required to understand the performance of SNF fatigue life in terms of these quantities, including cladding materials, pellets, cladding-to-pellet and pellet-to-pellet interface bonding, and cladding oxide and hydrides.

Out-of-cell testing continues to support the ongoing ORNL hot cell testing. A number of important issues have been identified as a result of both the test system and the fuel rod itself. Research in a hot cell of some of these issues is prohibitive due to high cost and limited access. Therefore, the out-of-cell CIRFT system is being used for these studies.

Due to the inhomogeneous composite structure of the SNF system, finite-element analyses (FEAs) are needed to translate the global moment-curvature measurement into local stress-strain profiles for further investigation. Furthermore, the detailed mechanisms of the pellet-pellet and pellet-clad interactions and the stress concentration effects at the pellet-pellet interface cannot be readily obtained from a CIRFT system measurement. Therefore, detailed FEAs will be necessary for further interpretation of the global test response.

The FEA simulation focused on the BWR fuel rods and the results were compared with that of the PWR HBR fuel rods, which were validated and benchmarked using data from CIRFT. This report provides analysis and conclusions concerning the pellet-pellet and pellet-clad interactions of SNF vibration performance, including (1) the distribution of moment-carrying capacity between pellets and clad and (2) the impact of clad material on the flexural rigidity of the fuel rod system. The immediate consequences of interface debonding are a shift in the load-carrying capacity from the fuel pellets to the clad and a reduction in the flexural rigidity of the composite rod system. Therefore, the flexural rigidity of the fuel rod and the bending moment resistance capacity between the clad and fuel pellets are highly dependent on the interface bonding efficiency at the pellet-pellet and pellet-clad interfaces. Furthermore, the curvature and associated flexural rigidity estimates based on tests conducted on the CIRFT system are very different from the localized clad data at the pellet-pellet interface region as estimated by FEA, where the local tensile clad curvature is approximately three to four times that of the global curvature at the tension side of the clad.

The initial comparison of bending flexural rigidity variation at different bonding efficiencies between PWR and BWR is summarized below.

Flexural rigidity comparison of LMK BWR Zircaloy-2 clad and PWR HBR Zircaloy-4 clad

Interface bonding conditions	BWR flexural rigidity EI (N·m²)	PWR HBR flexural rigidity EI (N·m²)	Difference from BWR to PWR HBR (%)
Perfect bond	99	77	22
Pellet-pellet interface with gap debond, pellet-clad interface bonded	76	39	49
Pellet-pellet interface with gap debond, pellet-clad interface debonded	35	29	17
Pellet-pellet interface without gap debond, pellet-clad interface bonded	84	53	37
Pellet-pellet interface without gap debond, pellet-clad interface debonded	54	43	20

CIRFT test results indicate that the FEA-simulated BWR flexural rigidity was significantly overestimated, for perfect bond or partial debonding cases. This is because of the original UO₂ fuel property used in the BWR FEA study as well as the assumption made regarding the similar interface bonding efficiency between BWR and PWR environments. However, post-irradiation investigation (PIE) indicates that the BWR fuel pellet has more fracture intensity than that of the PWR fuel pellet;

furthermore, PWR SNF should have a higher interface bonding efficiency than that of BWR fuel due to higher radial compressive residual stress induced by higher coolant pressure. Thus, the combined effect of BWR-degraded spent fuel and interface bonding deficiency was taken into consideration in follow-on FEA simulations by reducing the Young’s modulus to 25% and 50% to quantify the interface bonding conditions that result in similar estimated rigidity to CIRFT SNF testing results, at pellet-pellet interface debond and pellet-clad interface bond conditions. The final BWR rod FEA simulation results are shown below, which indicate that updated FEA results, with consideration given to fuel module reductions, are more appropriate and consistent with those of CIRFT test results.

Flexural rigidity comparison of BWR Zr-2 clad with fuel properties reduction consideration

Interface bonding conditions	Fuel UO₂ full E Flexural rigidity, EI (N·m²)	Fuel UO₂ ½ E Flexural rigidity, EI (N·m²)	Fuel UO₂ ¼ E Flexural rigidity, EI (N·m²)
Perfect bond	99	68	52
Pellet-pellet interface with gap debond, pellet-clad interface bonded	76	57	47
Pellet-pellet interface with gap debond, pellet-clad interface debonded	35	35	35
Pellet-pellet interface without gap debond, pellet-clad interface bonded	84	62	49
Pellet-pellet interface without gap debond, pellet-clad interface debonded	54	47	42

The impact of the interface bonding efficiency on SNF vibration integrity on M5™ clad is discussed below. As the Young’s modulus of the interface material increases, the fuel rod system’s stiffness increases accordingly. As debonding of the pellet-clad interface advances, the impact of the interface material property change is limited. The immediate consequences of interface debonding are (1) a shift in load-carrying capacity from the fuel pellets to the clad and (2) a reduction in composite rod system flexural rigidity. Therefore, the flexural rigidity of the fuel rod and the bending moment resistance capacity between the clad and fuel pellets are highly dependent on the interface bonding efficiency at the pellet-pellet and pellet-clad interfaces. The majority of bonding strength is from the clad radial compressive residual stress, induced from the pellet-clad mechanical interaction during reactor operation. The detailed FEA results of interface bonding efficiency of M5 clad are shown in the table below.

The flexural rigidity comparison between the different bonding and debonding cases for M5 clad

Interface bonding conditions	Flexural rigidity EI (N·m²)	Reduction from perfect bond (%)	Reduction from only pellet-pellet debond to further pellet-clad debond (%)	Increase from with gaps to without gaps (%)
Perfect bond	44			
Pellet-pellet interface with gap debond, pellet-clad interface bonded	32	27		
Pellet-pellet interface without gap debond, pellet-clad interface bonded	40	9		20
Pellet-pellet interface with gap debond, pellet-clad interface debonded	16.5	62.5	48	
Pellet-pellet interface without gap debond, pellet-clad interface debonded	26.5	40	34	38

CIRFT test data provide new insights into SNF dynamic behavior. The CIRFT approach also successfully demonstrates the controllable fatigue fracture on HBU SNF in a normal vibration mode, which enables us to examine the underlying mechanism of SNF system dynamic performance, including the following.

- SNF system interface bonding efficiency
- Fuel structural support to the SNF system
- Significant variation in stress and curvature during SNF fatigue cycles due to segment pellets and clad interaction
- Clad hydride system microstructure dynamic evolution
- SNF system S-N limit related to clad fracture threshold
- SNF failure initiated at pellet-pellet-clad interface region which appears to be spontaneous failure

Lessons learned from CIRFT testing on SNF vibration integrity are summarized as follows.

- Fuel contribution to clad stiffness during random vibration
- Stress concentration effects on clad at pellet-pellet interfaces
- Relationship of flexural deformation mechanism to SNF rod aging history
- Potential hydrogen effects on SNF vibration integrity
- Pellet-clad bonding efficiency on SNF mechanical properties
- Finite element analysis is needed to translate CIRFT data into local stress-strain profiles
- Failure mechanisms of HBU SNF rods
- Potential impact of combined loading modes and loading rates

USED FUEL DISPOSITION CAMPAIGN

FY 2015 Status Report: CIRFT Testing of High-Burnup Used Nuclear Fuel Rods from Pressurized Water Reactor and Boiling Water Reactor Environments

1. INTRODUCTION

The objective of this research is to collect experimental data on spent nuclear fuel (SNF) from pressurized water reactors (PWRs), including H. B. Robinson (HBR) and North Anna (NA) Zircaloy-4 cladding and NA and Catawba M5 cladding, and the Limerick Generating Station boiling water reactor (BWR) under simulated transportation environments using the Cyclic Integrated Reversible-Bending Fatigue Tester (CIRFT), an enabling hot-cell testing technology developed at Oak Ridge National Laboratory^{1,2,3,4,5} (ORNL). This data will be used to support ongoing spent fuel modeling activities, in addition to addressing licensing issues associated with SNF transport.

Testing on SNF rods from PWRs—HBR and NA Zircaloy-4 cladding and Catawba M5 cladding^{6,7,8}—demonstrated that the cyclic fatigue lifetime of SNF rods generally depends on the amplitude of applied moment when a 5 Hz waveform is used. It was also demonstrated that the lifetime of SNF is related to the degree of damage to cladding and fuel pellets resulting from irradiation after a long term of service inside a reactor, as well as the loading amplitude and loading rate of applied moment, due to different fatigue damage mechanisms triggered by the intensity of pellet-clad mechanical interaction. The FY15 study extends the vibration data collected to include Zircaloy-2 data from a BWR environment. An S-N trend similar to that of the PWR data was also observed in the BWR data. Detailed high-burnup (HBU) HBR CIRFT test results are published in NUREG/CR-7198⁹ and are provided in Appendix A. Furthermore, the accumulated damage from the combination of low-amplitude CIRFT cyclic bending plus transient shocks (high-amplitude bending load) indicates an accelerated aging effect compared to that of low-amplitude cyclic bend loading alone.

CIRFT enables examination of the underlying mechanisms of SNF system dynamic performance. The major findings of CIRFT tests on the HBU SNF are as follows:

- SNF system interface bonding plays an important role in SNF vibration performance.
- Fuel structure contributes to the SNF system stiffness.
- There are significant variations in the stress and curvature of SNF systems during vibration cycles resulting from pellets and clad interaction.
- SNF failure initiates at the pellet-pellet interface region and appears to be spontaneous.

Due to the inhomogeneous composite structure of the SNF system, finite-element analyses (FEA) are needed to translate the global moment-curvature measurement into local stress-strain profiles for further investigation. Furthermore, the detailed mechanisms of the pellet-pellet and pellet-clad interactions and the stress concentration effects at the pellet-pellet interface cannot be readily obtained from a CIRFT system measurement. Therefore, detailed FEA will be necessary to obtain further interpretation of the global test response.

The FEA protocols developed for this activity provide powerful tools to quantify the CIRFT system biases and the associated uncertainties on the HBU SNF under CIRFT testing.

This report also provides the FEA methodology used to evaluate the effects of pellet-pellet and pellet-clad interactions. The methodology is a road map for further protocol development with respect to the effective lifetime prediction of the SNF system under normal transportation vibration.

This study provides detailed explanations of the effects of pellet-pellet and pellet-clad interactions—including pellet fracture and pellet-clad bonding efficiency—on the clad performance reliability. The FEA simulation results will also be calibrated and benchmarked with fatigue aging data obtained from ORNL reversible-bending fatigue testing.

2. SPECIMEN PREPARATION

2.1 Limerick (LMK) Rods

Twenty CIRFT testing segments were prepared as 6 in. segments from four parent Limerick rods. The cutting plan is shown in Fig. 1, and the corresponding segment identification numbers (IDs) are given in Table 1. The outer diameters (ODs) were measured to be 0.44971 in. and 0.44663 in. for two segments, as shown in Table 2.

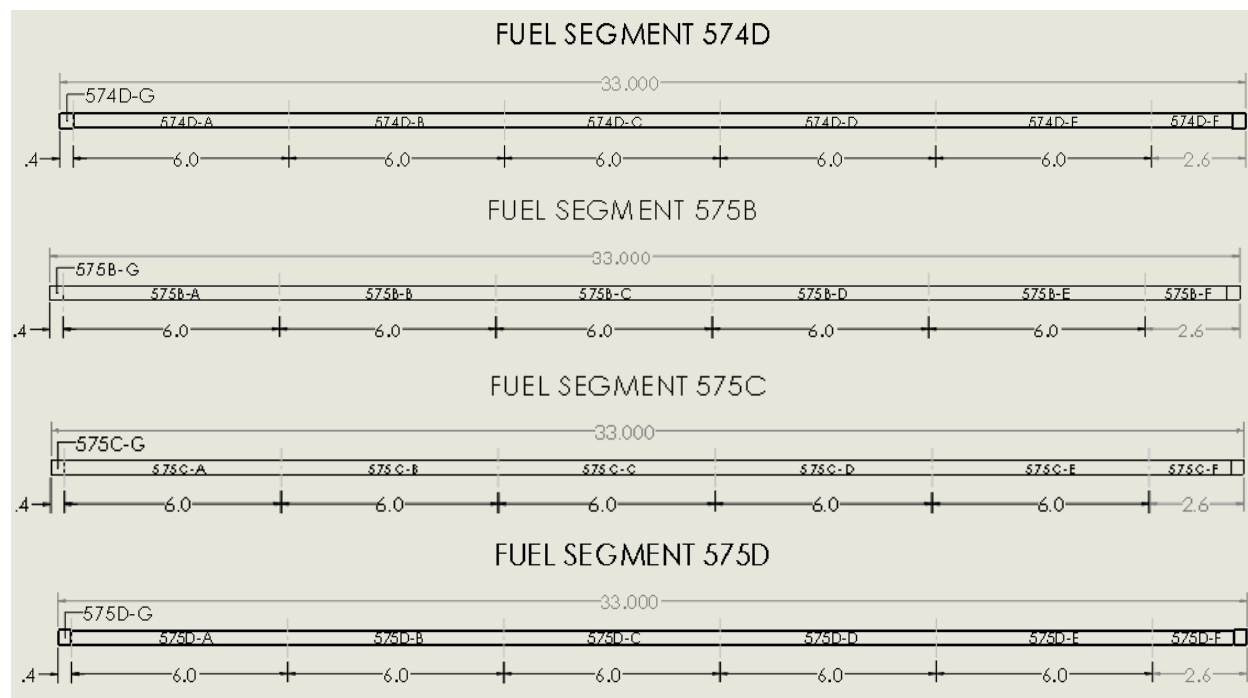


Fig. 1. Cutting plan of BWR Limerick SNF rods for CIRFT testing.¹⁰

Table 1. Segment identification of Limerick SNF rod¹⁰

Parent segment	Segment ID	Fuel length (in.)	Notes
574D	574D-G	0.38	Bottom end cap (indicated by scratches on fuel rod)
	574D-A	6.00	
	574D-B	6.00	
	574D-C	6.00	
	574D-D	6.00	
	574D-E	6.00	
	574D-F	3.00	
575B	575B-G	0.38	Bottom end cap (indicated by scratches on fuel rod)
	575B-A	6.00	
	575B-B	6.00	
	575B-C	6.00	
	575B-D	6.00	
	575B-E	6.00	
	575B-F	3.00	
575C	575C-G	0.38	Bottom end cap (indicated by scratches on fuel rod)
	575C-A	6.00	
	575C-B	6.00	
	575C-C	6.00	
	575C-D	6.00	
	575C-E	6.00	
	575C-F	3.00	
575D	575D-G	0.38	Bottom end cap (indicated by scratches on fuel rod)
	575D-A	6.00	
	575D-B	6.00	
	575D-C	6.00	
	575D-D	6.00	
	575D-E	6.00	
	575D-F	3.00	

Table 2. Outer diameters (ODs) of Limerick SNF rod segments (in.)

	Orientation	Distance (in.) from left end (Fig. 1)			Mean
		2.5	3.0	3.5	
574D-A	A (0°)	0.45274	0.45210	0.45072	0.45185
	B (90°)	0.44852	0.44764	0.44652	0.44756
	Average				0.44971
575D-A	A (0°)	0.44824	0.44284	0.44664	0.44591
	B (90°)	0.44828	0.44758	0.44620	0.44735
	Average				0.44663

Each 6 in. rod segment was assembled using two end caps. This was done using the developed vise mold designed for BWR SNF rods with larger ODs. The end cap labels and segment IDs are provided in Table 3.

Table 3. CIRFT test number and segment labels of Limerick SNF rod

Test number	End cap A*	End cap B*	Segment ID	Note
LMK01	LM1A	LM1B	574D-A	
LMK02	LM2A	LM2B	575D-A	
LMK03	LM3A	LM3B	575B-A	
LMK04	LM4A	LM4B	575B-C	Two end caps misaligned. Test was not performed on this specimen.
LMK05	LM5A	LM5B	574D-B	
LMK06	LM6A	LM6B	574D-E	
LMK07	LM7A	LM7B	575C-A	
LMK08	LM8A	LM8B	575B-D	
LMK09	LM9A	LM9B	574D-D	
LMK10	LM10A	LM10B	575B-E	
LMK11	LM11A	LM11B	575B-D	
LKM12	LM11A	LM11B	575B-A	
LKM13	LM13A	LM13B	575C-D	
LKM14	LM14A	LM14B	575C-B	
LKM15	LM15A	LM15B	575C-C	
LKM16	LM16A	LM16B	575D-E	Not tested yet
LKM17	LM17A	LM17B	575C-E	Not tested yet

*Rod specimen is loaded into testing machine such that end caps A and B are on motor 2 and motor 1 sides, respectively.

2.2 North Anna (NA) and Catawba (MOX) Rods

Labels were applied on the end caps for NA and Catawba mixed oxide (MOX) SNF using laser engraving to ensure test sample identification. The label systems for NA and MOX fuel specimens are given in Table 4 and

Table 5, respectively. An inventory was made of the NA M5 SNF, and the outside diameters of the fuel segments were measured. The results are given in Table 6.^{11,12}

Table 4. Specimen labels used for NA M5 SNF

Fuel segment ID	CIRFT label	End-cap A	End-cap B
651B2	NA1	NA-1A	NA-1B
651C5	NA2	NA-2A	NA-2B
651D3	NA3	NA-3A	NA-3B
652B1B	NA4	NA-4A	NA-4B
652B2	NA5	NA-5A	NA-5B
652D1	NA6	NA-6A	NA-6B
652D2	NA7	NA-7A	NA-7B

Table 5. Specimen labels used for MOX SNF

Segment ID	CIRFT label	End-cap A	End-cap B
MOX-A-11	MOX1	MOX-1A	MOX-1B
MOX-A-12	MOX2	MOX-2A	MOX-2B
MOX-A-13	MOX3	MOX-3A	MOX-3B
MOX-B-05	MOX4	MOX-4A	MOX-4B
MOX-B-06	MOX5	MOX-5A	MOX-5B
MOX-B-07	MOX6	MOX-6A	MOX-6B
MOX-C-06	MOX7	MOX-7A	MOX-7B
MOX-C-07	MOX8	MOX-8A	MOX-8B
MOX-C-08	MOX9	MOX-9A	MOX-9B
MOX-K-09	MOX10	MOX-10A	MOX-10B
MOX-K-10	MOX11	MOX-11A	MOX-11B
MOX-K-11	MOX12	MOX-12A	MOX-12B
MOX-K-13	MOX13	MOX-13A	MOX-13B
MOX-K-14	MOX14	MOX-14A	MOX-14B
MOX-K-15	MOX15	MOX-15A	MOX-15B

Table 6. Outside diameters of NA M5 SNF segments (in.)*,¹²

Fuel Segment	A			B			Mean
	1	2	3	1	2	3	
651B2	0.37942	0.37872	0.37732	0.37998	0.37918	0.37798	0.3788
651C5	0.37710	0.37660	0.37632	0.37774	0.37720	0.37682	0.3770
651D3	0.38032	0.37934	0.38020	0.38198	0.38220	0.38300	0.3812
652B1B	0.37964	0.37890	0.37767	0.37954	0.37860	0.37784	0.3787
652B2	0.38012	0.37990	0.37924	0.37860	0.37796	0.37714	0.3788
652D1	0.37966	0.37894	0.37802	0.37904	0.37888	0.37760	0.3787
652D2	0.37998	0.38008	0.38020	0.37924	0.37994	0.38022	0.3799

*The measurements were made at the top (A, 0°) and the side (B, 90°) at three locations (1, 2, 3) in the middle of the rod segment. These measurement points were 0.5 in. apart.

3. DATA PROCESSING

Measurement data are converted into the applied moment and curvature, based on the load channel (load1 and load2) information, the loading arm length (101.60 mm), and linear variable differential transformer (LVDT) data (LVDT1, 2, and 3). The moment was estimated by

$$M = F \times L, \quad (1)$$

where F is the averaged value of applied loads (load1 and load2) from the Bose dual motors, and L is the loading arm length (101.60 mm).

Theoretically, the bending radius and maximum strain of a rod can be estimated on the basis of the traveling displacement at the loading points of the rigid arm. The displacement measured, however, contains the contribution of the compliant layers, depending on the materials used in the compliant layers and the level of loading. To address this issue, direct measurement of the specimen displacement at three adjacent points along the rod method was adopted and has been implemented to evaluate the curvature of a bending rod in this study.

Given the deflections from three LVDTs, d_1 , d_2 , and d_3 , as shown in Fig. 2, the curvature κ of the bending rod can be evaluated as follows:

$$\kappa = [(x_0 - d_2)^2 + y_0^2]^{-1/2}, \quad (2)$$

$$x_0 = \frac{-2m_a m_b h - m_a (d_2 + d_3) + m_b (d_1 + d_2)}{2(m_b - m_a)}, \quad y_0 = -\frac{1}{m_a} \left(x_0 - \frac{d_1 + d_2}{2} \right) - \frac{h}{2},$$

where

$$m_a = \frac{h}{d_2 - d_1}, \quad m_b = \frac{h}{d_3 - d_2},$$

and h is the sensor distance (12 mm).

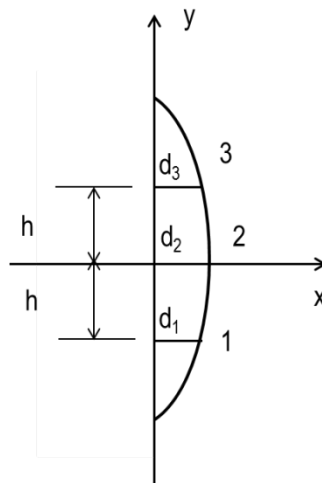


Fig. 2. Determination of the bending curvature of the rod by use of deflections measured at three points.

The arrangement of the three LVDTs and their installation in the setup are shown in Fig. 3.

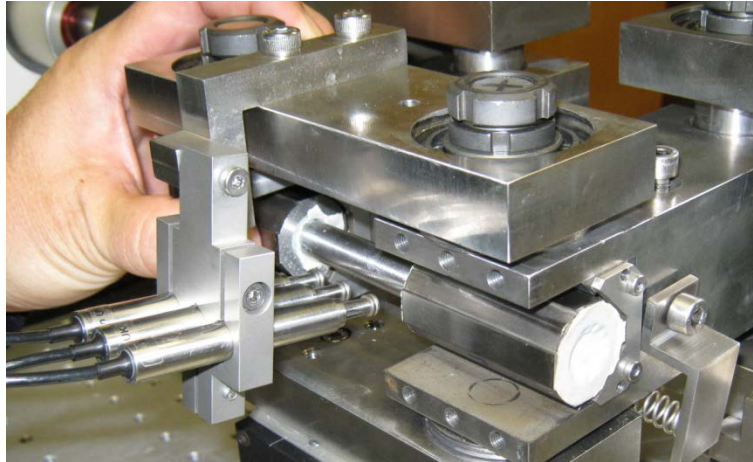


Fig. 3. Grip design of CIRFT with one end-block removed.

An equivalent stress-strain curve can be obtained under the assumption that the SNF rod can be idealized as a linear elastic homogeneous material without consideration of the effects induced by pellet-clad interaction. The equivalent stress was calculated using

$$\sigma = M \times y_{max} / I, \quad (3)$$

where I is the moment of inertia, $I = I_c + I_p$, I_c , and I_p are moments of inertia of cladding and pellet, respectively, and y_{max} is the maximum distance to the neutral axis of the test rod of the section and is measured by the radius of the cladding. The calculation of stress disregards the difference in elastic moduli between clad and pellets.

The equivalent strain is then

$$\epsilon = \kappa \times y_{max}. \quad (4)$$

4. TEST RESULTS FOR LMK SPECIMENS

Fourteen specimens were prepared and tested in hot cell. The first specimen was used for tuning and a static test and rest for dynamic tests. These dynamic tests were conducted with moment amplitudes ranging from 7.62 to 25.40 N·m. Twelve specimens failed with lifetimes from 2.14×10^4 to 4.70×10^6 cycles. One cycled 7.58×10^6 times without failing and was stopped.

4.1 Tuning and Testing Using LMK01/574D-A

The testing machine was tuned with specimen LMK01 under displacement control, ± 1.0 mm, 5Hz. The tuning parameters were recorded and are shown in Table 7.

Table 7. Tuning parameters based on LMK01

Axial 1		Axial 2	
TuneIQ1	2.080890	TuneIQ1	1.749211
TuneIQ2	0.021591	TuneIQ2	0.017062
TuneIQ3	-10.596725	TuneIQ3	-9.816423

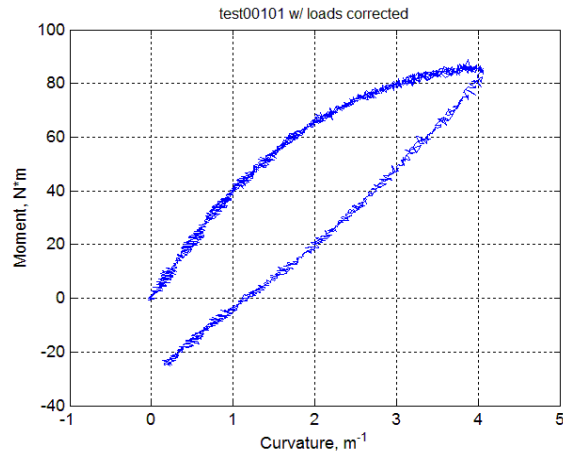
The static test was conducted on LMK01/574D-A under a displacement control mode using the following test procedure.

1. Initial ramp-up to 12.00 mm at a rate of 0.1 mm/s at each loading point or each Bose motor
2. Back to 0.0 mm at 0.2 mm/s
3. If the rod specimen does not fail during testing, repeat steps (1) and (2) two more times

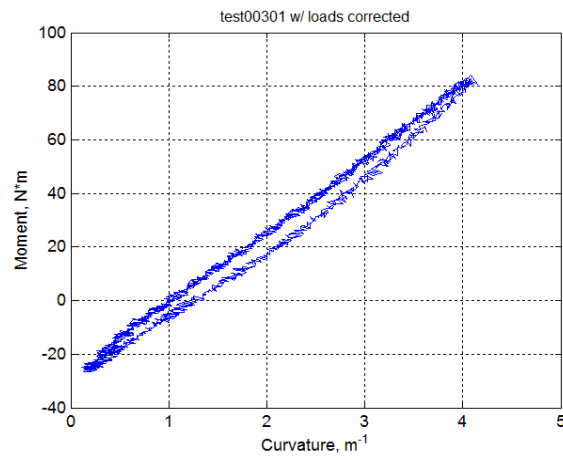
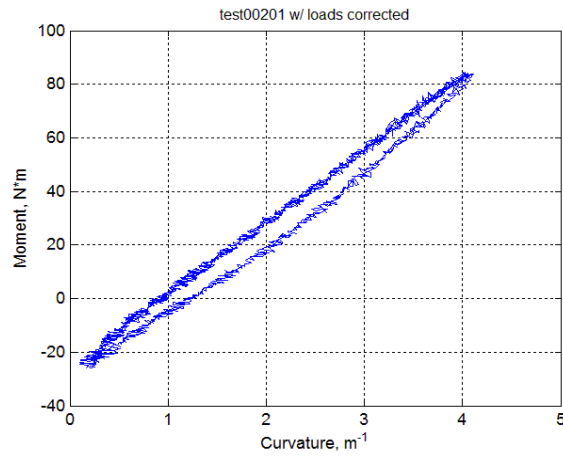
Sample LMK01 survived three loading cycles without any sign of failure. The moment-curvature curves are shown in Fig. 4. There was a significant nonlinear deformation after 35 N·m, and the maximum moment at a level of 85 N·m was attained during the initial loading cycle. The subsequent loading cycles did not produce additional deformation, but they introduced a closed hysteresis loop. The maximum curvature under a relative displacement of 24.0 mm at loading points of U-frame (i.e., 12.0 mm at each motor) was approximately 4 m^{-1} .

In order to observe the failure mode of the sample, a dynamic test was carried out at ± 25.4 N·m, 5 Hz. The lifetime of the rod (N_f) equaled 9.43×10^5 cycles. The rod ultimately failed in the gage section, as shown in Fig. 5.

The segments of tested rod specimens were observed under the hot cell stereomicroscope,¹³ and images were taken, as shown in Fig. 6. The fracture apparently occurred on the pellet-to-pellet interface. The pellets themselves fractured also, which is believed to be due to irradiation. Scratches can be seen as well, particularly along the longitudinal axis. However, the surface integrity of cladding appears to be generally maintained.



(a)



(b)

Fig. 4. Moment-curvature curves in (a) the first loading cycles and (b) the second and third cycles for the LMK01/574D-A rod.



Fig. 5. Fracture segments for the LMK01/574D-A rod that survived two cycles of loading to relative displacement of 24.0 mm with a maximum moment of around 85 N·m in the initial cycle. A follow-up dynamic test was carried out at ± 25.4 N·m, 5 Hz; $N_f = 9.4 \times 10^3$ cycles.

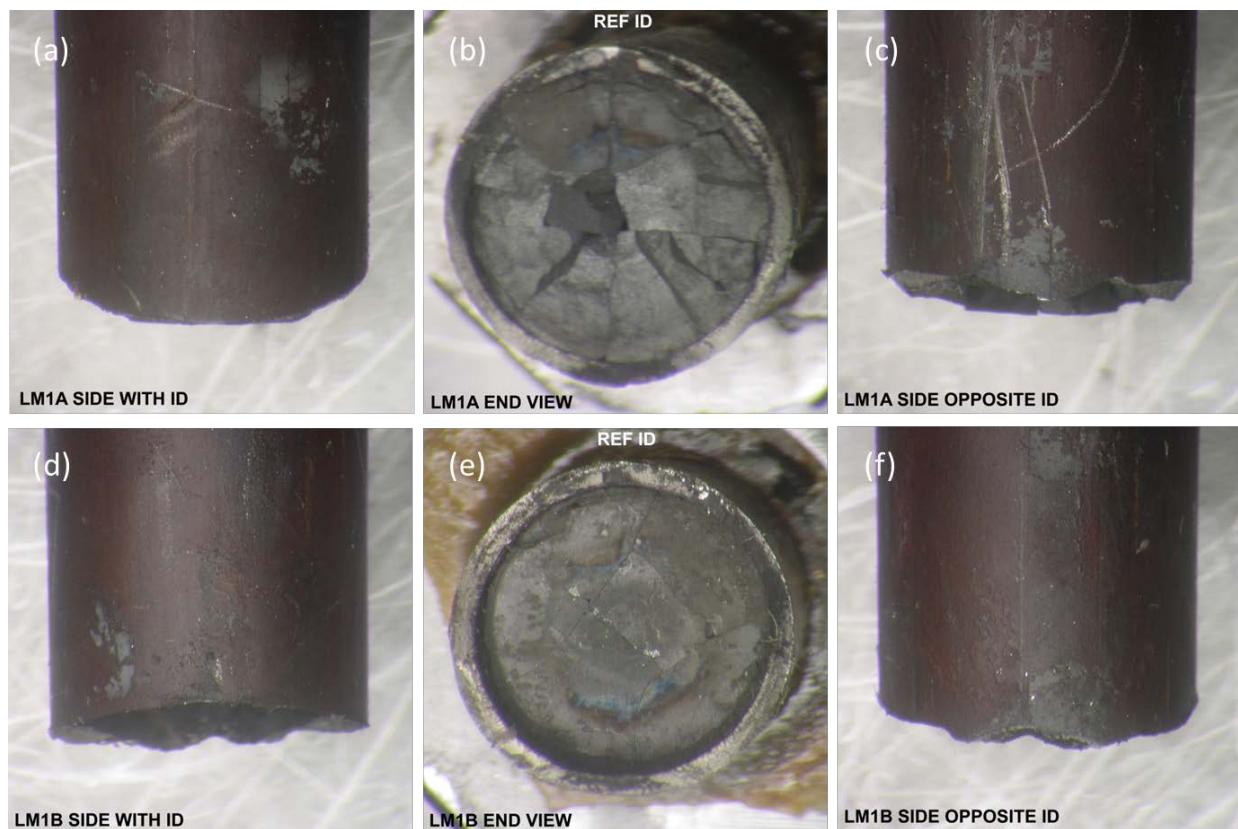


Fig. 6. Fracture segments for LMK01/574D-A. (a) and (d) show the specimen ID side of the segment on end caps A and B; (b) and (e) show the mating fracture surface; and (c) and (f) show the opposite specimen ID side of the segment on end caps A and B.

4.2 MK02/575D-A, ±12.7 N·m, 5 Hz.

The test on LMK02/575D-A was conducted at ±12.70 N·m, 5 Hz. A lifetime of 1.71×10^5 cycles was obtained. Periodic quasistatic measurements of rod deformation were conducted using two relative displacement levels (0.2 and 0.4 mm) at the selected target number of cycles. The curvature range–moment range and flexural rigidity are illustrated in Fig. 7. The variations in these quantities as a function of number of cycles are further given in Fig. 8. The initial rigidity of the measurements at the two displacements was 47 to 50 N·m². The rigidity dropped a little near 10^3 cycles and stayed quite constant after that.

The curvature, moment, and flexural rigidity based on online monitoring data are presented in Fig. 9. The online monitoring showed a flexural rigidity of about 42 N·m², a little lower than that observed in measurements. This is believed to be because different loading conditions were used in measurement and cycling. A sudden drop of flexural rigidity was observed. Overall, a quite stable response was seen before the final failure. The peak and valley of curvature and moment waveforms were also monitored, as shown in the same figure, and it can be seen that there was no significant offset of curvature during whole fatigue testing.

The failure was observed in the gage section again, as shown in Fig. 10. The feature of fracture surface is not quite clearly observed at this level of resolution.

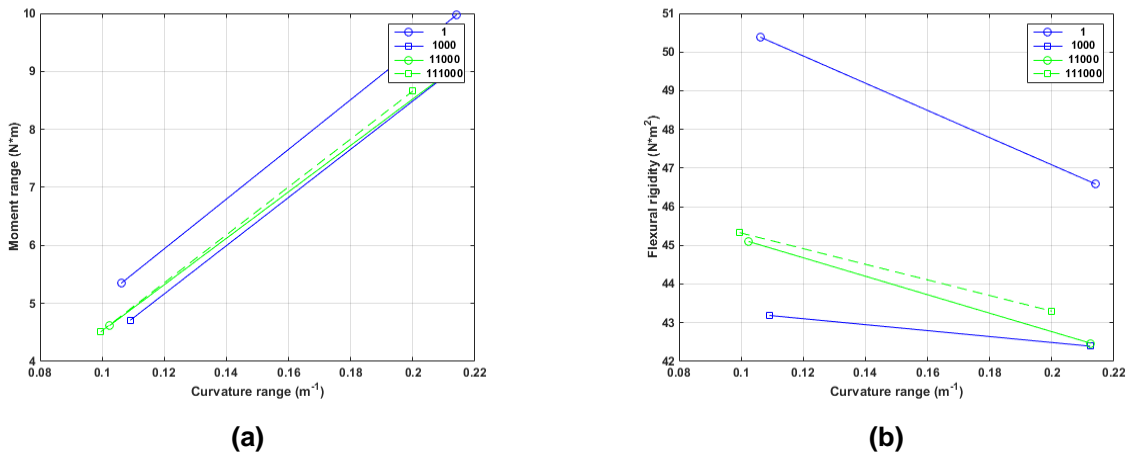
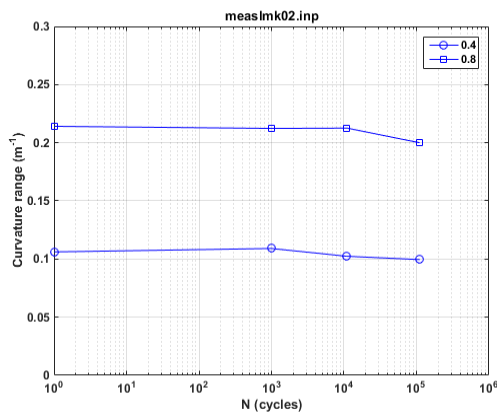
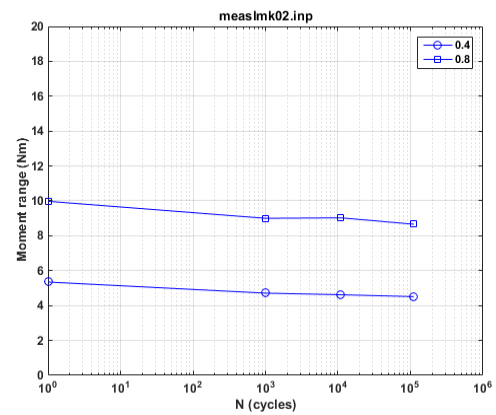


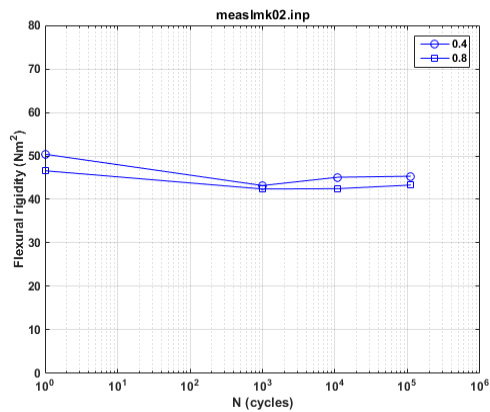
Fig. 7. (a) Moment-curvature range and (b) flexural rigidity-curvature range at various numbers of cycles for LMK02/575D-A. Measurements were made with 0.2 and 0.4 mm relative displacements; $N_f = 1.71 \times 10^5$ cycles at ±12.70 N·m, 5 Hz.



(a)



(b)



(c)

Fig. 8. Variations in (a) curvature range, (b) moment range, and (c) flexural rigidity as a function of the number of cycles for LMK02/575D-A. Measurements were made with 0.2 and 0.4 mm relative displacements; $N_f = 1.71 \times 10^5$ cycles at ± 12.70 N·m, 5 Hz.

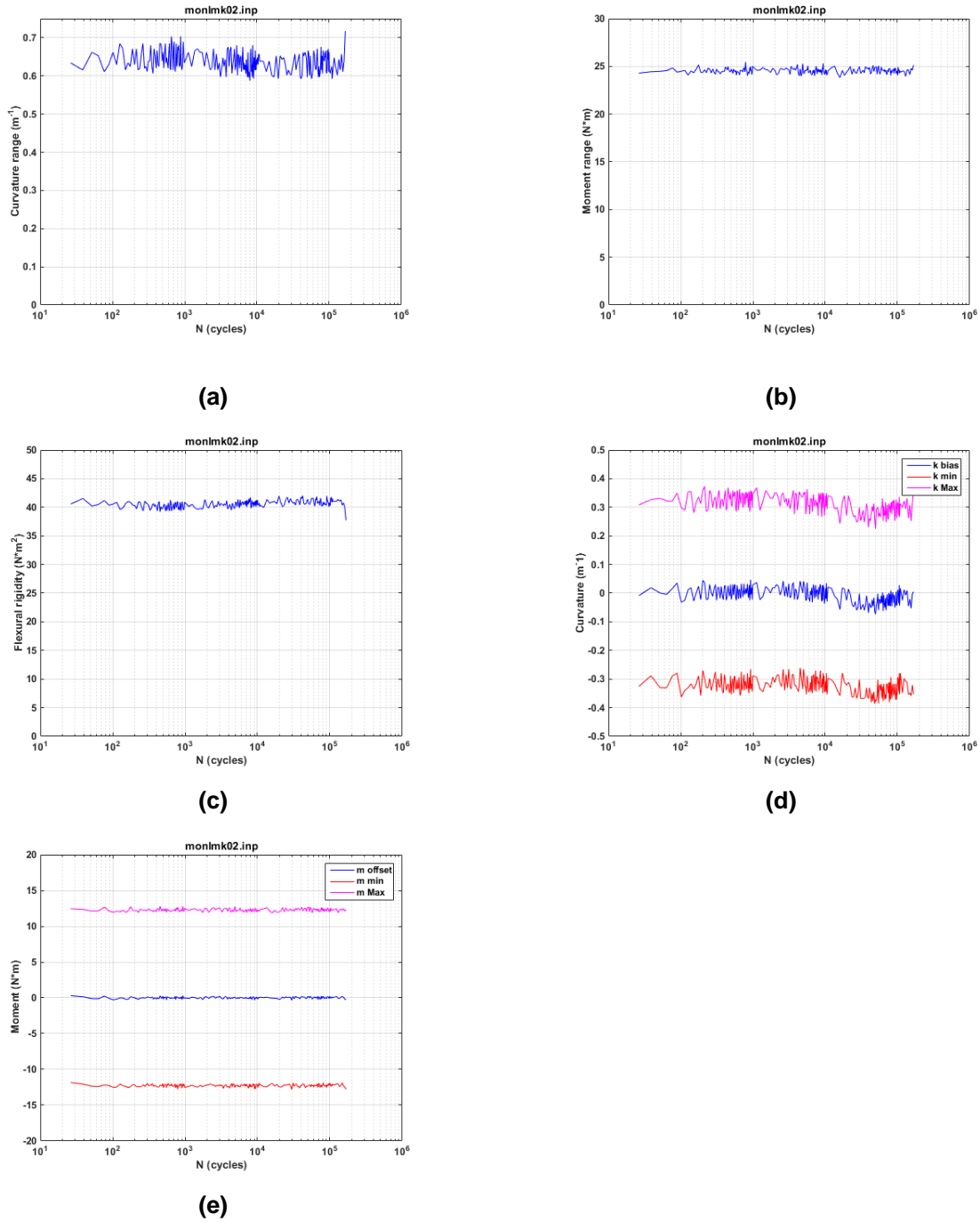


Fig. 9. Variations in (a) curvature range, (b) applied moment range, (c) flexural rigidity, (d) maximum and minimum values of curvature, and (e) maximum and minimum values of moment as a function of the number of cycles for LMK02/575D-A; $N_t = 1.71 \times 10^5$ cycles at ± 12.70 N·m, 5 Hz.



Fig. 10. Fracture segments for LMK02/575D-A; $N_f = 1.71 \times 10^5$ cycles at ± 12.70 N·m, 5 Hz.

4.3 LMK03/575B-A, ± 10.16 N·m, 5 Hz

The test on LMK03/575B-A was conducted at ± 10.16 N·m, 5 Hz. The applied moment was higher than that of LMK02, and the lifetime of the specimen was accordingly longer at 4.92×10^5 cycles.

Periodic quasistatic measurements of rod deformation were conducted using two relative displacement levels (0.2 and 0.4 mm) at the selected target number of cycles. The variations in curvature range, moment range, and flexural rigidity as a function of number of cycles are given in Fig. 11. The rigidity of the measurements at the two displacements started with 44 to 48 N·m², dropped to less than 40 N·m² around 10^3 cycles, and remained nearly at a constant level afterwards.

The curvature, moment, and flexural rigidity based on online monitoring data are presented in Fig. 12. The online monitoring showed a flexural rigidity of about 35 N·m², a little lower than that observed in measurements. Again, an abrupt decrease in flexural rigidity was seen before the final failure.

The failure occurred in the gage section again as shown in Fig. 13. The failed specimen was manually broken into two pieces for fractographic study. The images of lateral surface and fracture surfaces are presented in Fig. 14. Again, the fracture occurred on the pellet-to-pellet interface. Cracks developed in pellets, and pellets fractured into several large size fragments that were held in place. No apparent gap can be seen between the pellet and cladding. On the specimen ID side, a gray area can be seen. At this magnification level, it cannot be determined if the gray area is a damage area.

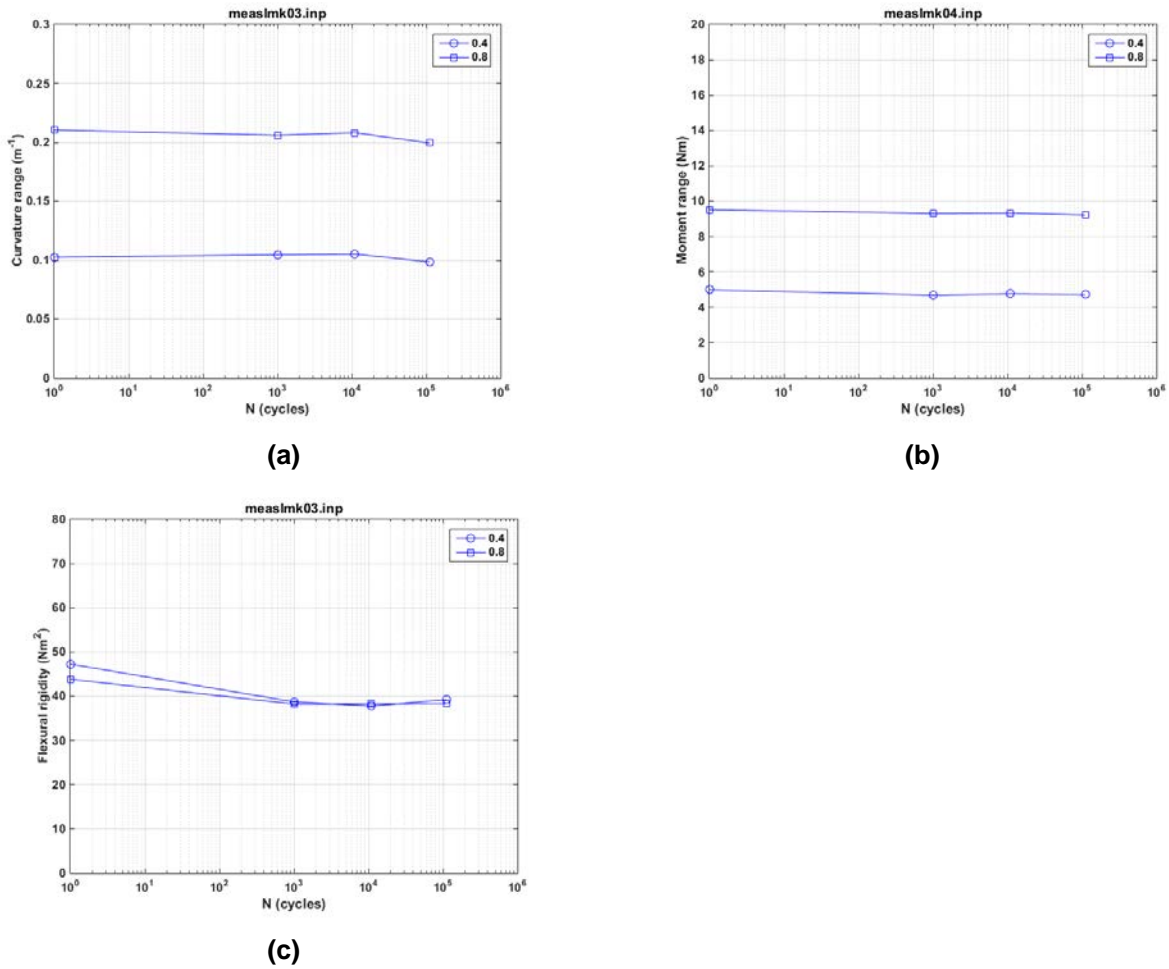


Fig. 11. Variations in (a) curvature range, (b) moment range, and (c) flexural rigidity as a function of the number of cycles for LMK03/575B-A; $N_f = 4.92 \times 10^5$ cycles at ± 10.16 N·m, 5 Hz.

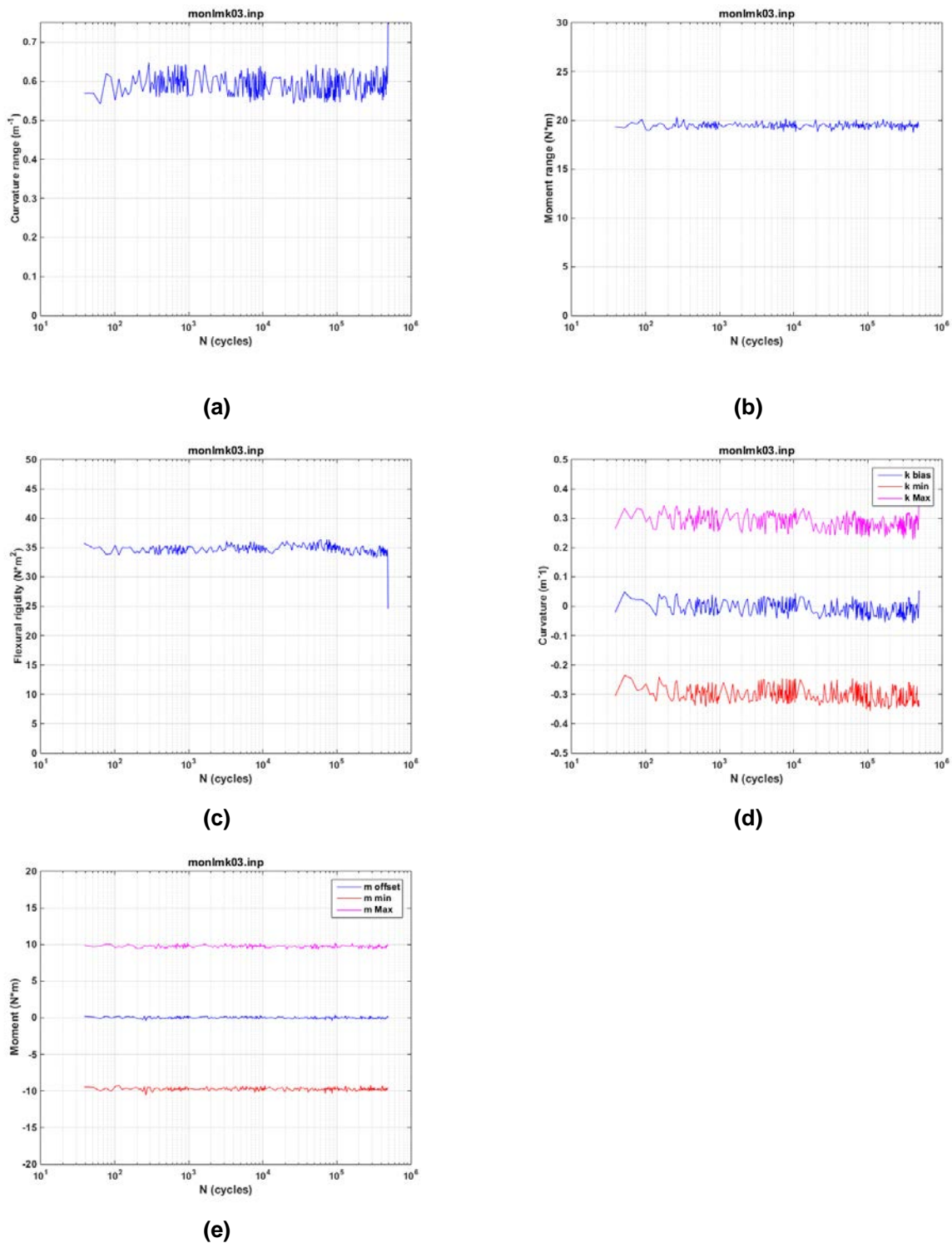


Fig. 12. Variations in (a) curvature range, (b) applied moment range, (c) flexural rigidity, (d) maximum and minimum values of curvature, and (e) maximum and minimum values of moment as a function of the number of cycles for LMK03/575B-A; $N_f = 4.92 \times 10^5$ cycles at ± 10.16 N·m, 5 Hz.



Fig. 13. Fracture segments for LMK03/575B-A $N_f = 4.92 \times 10^5$ cycles at ± 10.16 N·m, 5 Hz.

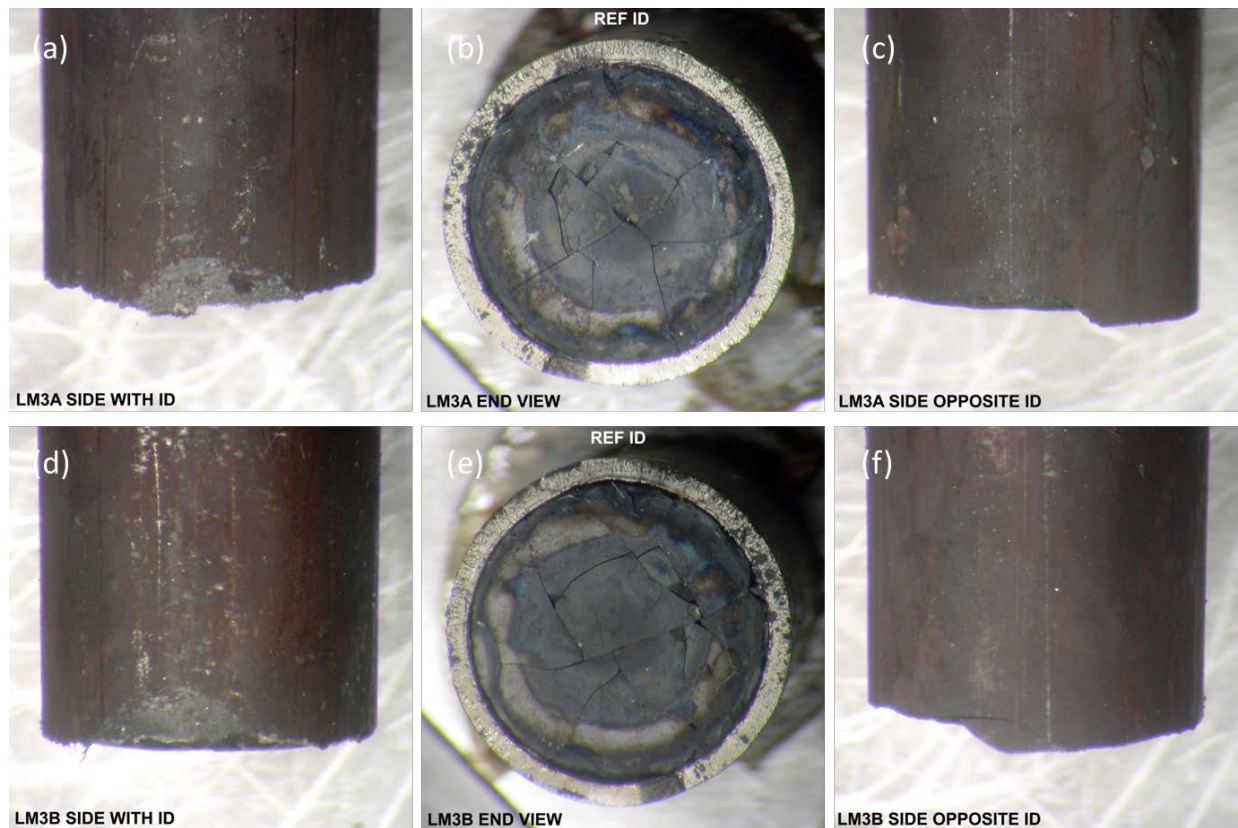


Fig. 14. Fracture segments for LMK03/575B-A. (a) and (d) show the specimen ID side of the segment on end caps A and B; (b) and (e) show the mating fracture surface; and (c) and (f) show the opposite specimen ID side of the segment on end caps A and B.

4.4 LMK05/574D-B, ± 8.64 N·m, 5 Hz

The test on the LMK05/574D-B rod was conducted at ± 8.64 N·m, 5 Hz. The lifetime of the specimen was 2.49×10^5 cycles. Periodic quasistatic measurements of rod deformation were conducted using two relative displacement levels (0.2 and 0.4 mm) at the selected target number of cycles. The variations in curvature range, moment range, and flexural rigidity as a function of number of cycles are given in Fig. 15. With an initial level of $45 \text{ N}\cdot\text{m}^2$, the rigidity of the measurements at the two displacements stayed almost at a constant level over the entire fatigue testing process.

The curvature, moment, and flexural rigidity based on online monitoring data are presented in Fig. 16. The online monitoring showed a flexural rigidity of about $37.5 \text{ N}\cdot\text{m}^2$ in most of the testing. An abrupt drop was observed again before the final failure of the specimen. In addition, curvature waveform demonstrated a negative curvature offset of about -0.075 m^{-1} and drifting at 10^5 cycles. The drift may be related to the tightening of bolts in specimen grips. Compared to LMK03, a shorter lifetime was obtained even though a lower moment amplitude was used. Whether the uncertainty of the testing result is caused by variation in the initial condition of the segment remains to be investigated.

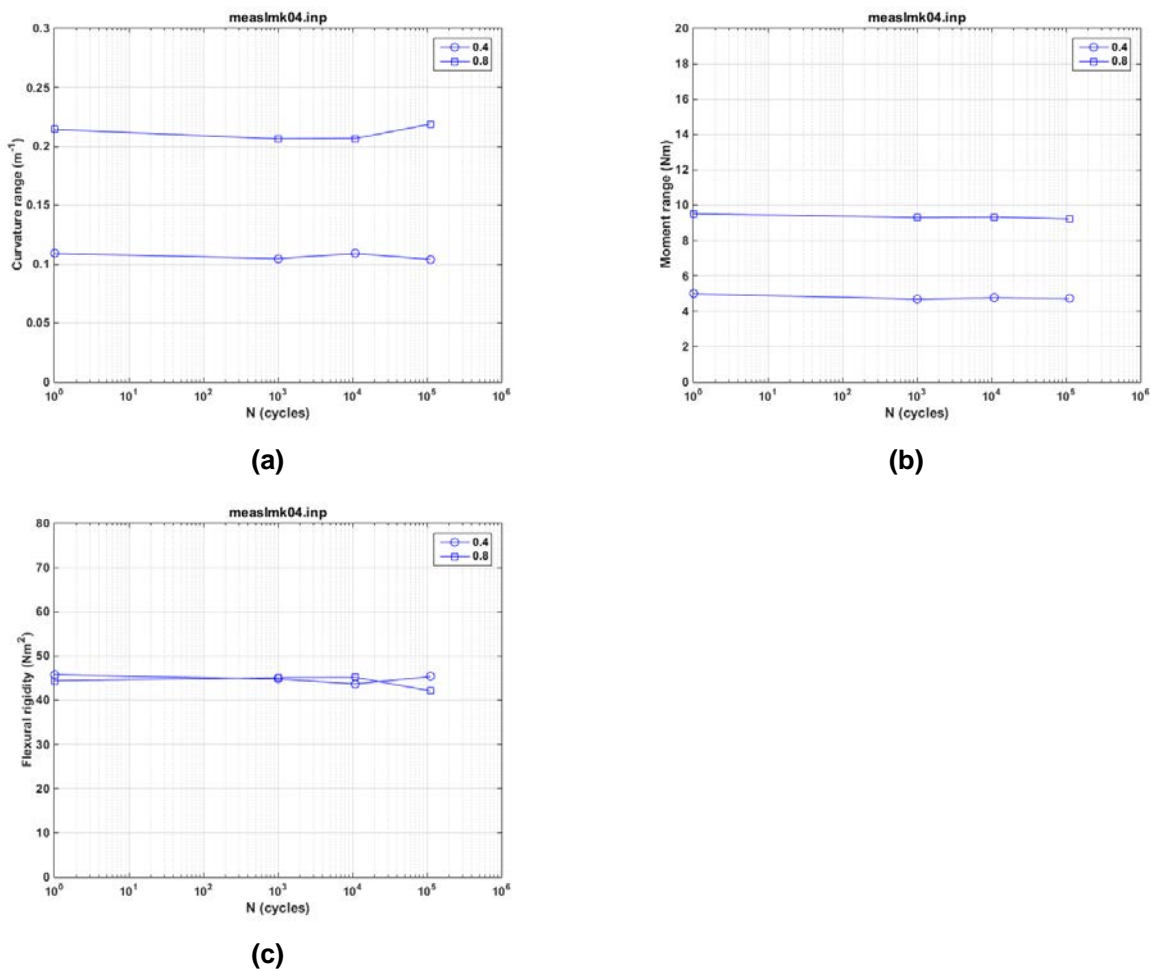


Fig. 15. Variations in (a) curvature range, (b) moment range, and (c) flexural rigidity as a function of the number of cycles for LMK05/574D-B; $N_f = 2.49 \times 10^5$ cycles at ± 8.64 N·m, 5 Hz.

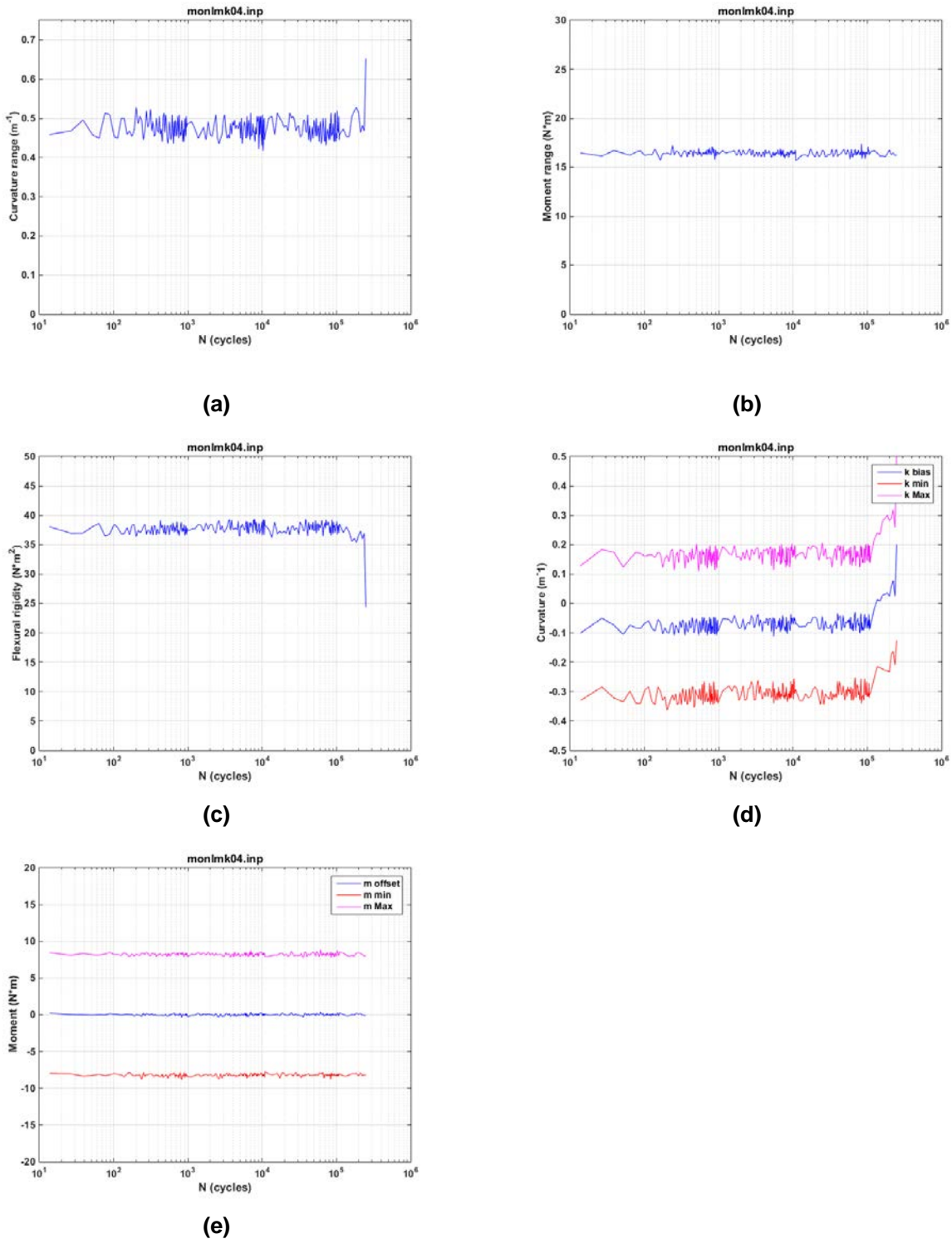


Fig. 16. Variations in (a) curvature range, (b) applied moment range, (c) flexural rigidity, (d) maximum and minimum values of curvature, and (e) maximum and minimum values of moment as a function of the number of cycles for LMK05/574D-B; $N_f = 2.49 \times 10^5$ cycles at $\pm 8.64 N \cdot m$, 5 Hz.

4.5 LMK06/574D-E, ± 7.62 N·m, 5 Hz

The test on the LMK06/575D-E rod was conducted at ± 7.62 N·m, 5 Hz. The lifetime of the specimen was 1.79×10^6 cycles. Periodic quasistatic measurements of rod deformation were conducted using two relative displacement levels (0.2 and 0.35 mm) at the selected target number of cycles. The variations in curvature range, moment range, and flexural rigidity as a function of the number of cycles are given in Fig. 17. The rigidity of the measurements was observed to fluctuate slightly, but it essentially stayed around 42 N·m² during the cyclic testing.

The curvature, moment, and flexural rigidity based on online monitoring data are presented in Fig. 18. The online monitoring showed a flexural rigidity of about 33 N·m², slightly lower than that observed in measurements. Overall, a quite stable rod response was exhibited before the final failure. At the same time, a negative curvature offset of approximately -0.075 m⁻¹ was observed from the peak and valley monitoring of waveform.

The examination of the tested specimen indicated that the failure is located inside of one end cap. It is not certain if out-of-gage section failure is related to the structural flaw or the epoxy casting of the end cap. Nevertheless, among all the dynamic tests that were completed (LMK02, 03, 05 and 06), a longer lifetime was obtained with LMK06 when a lower moment amplitude was used.

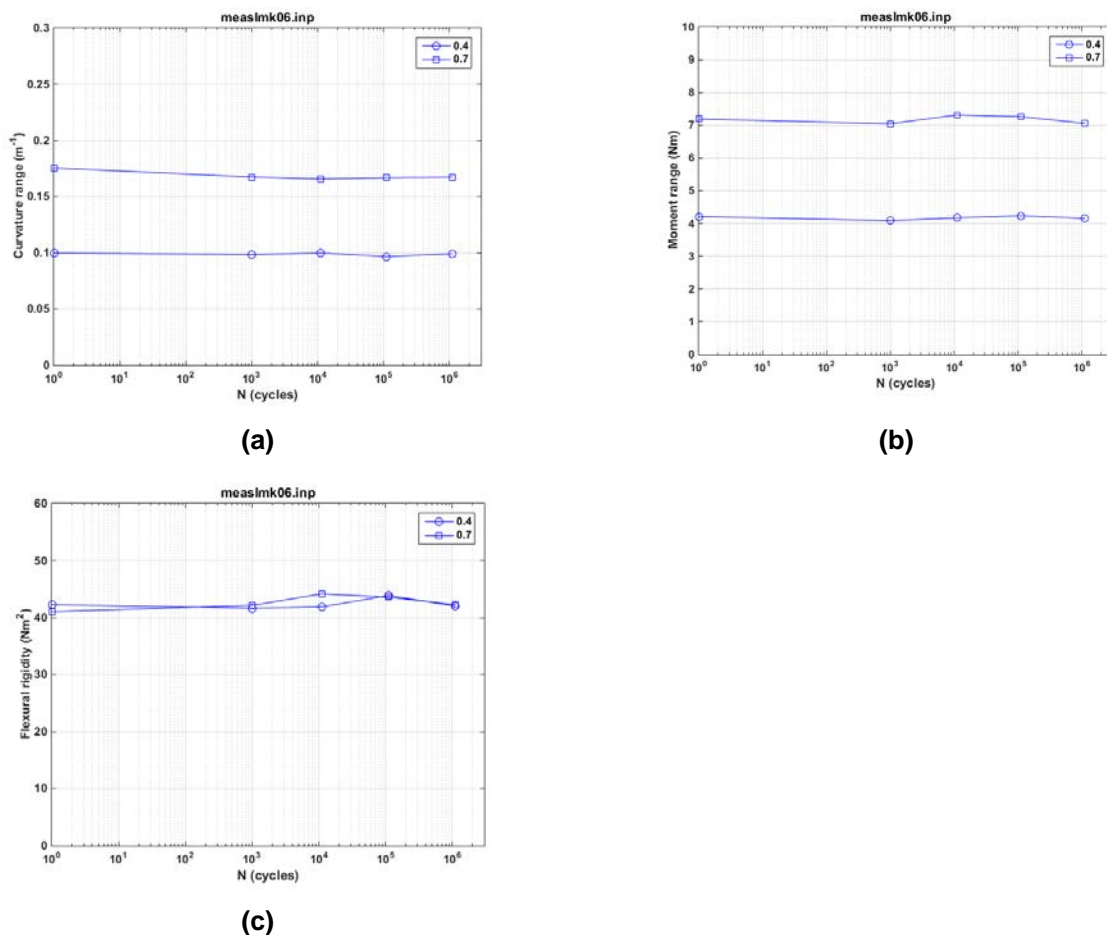
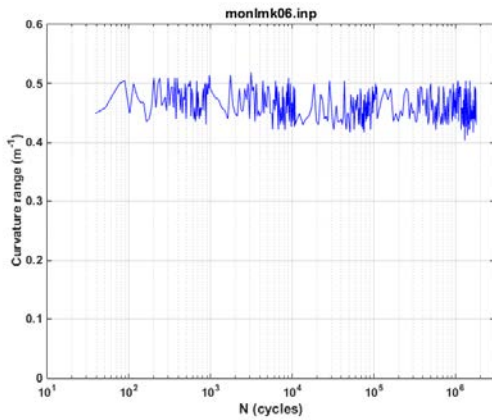
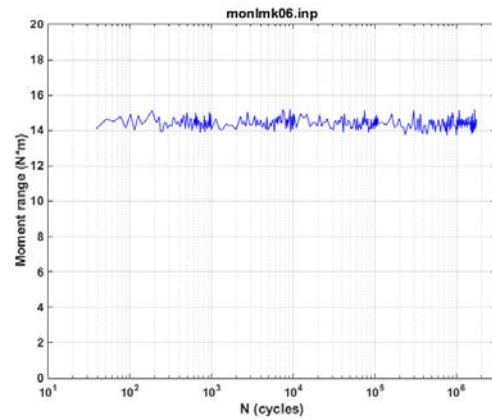


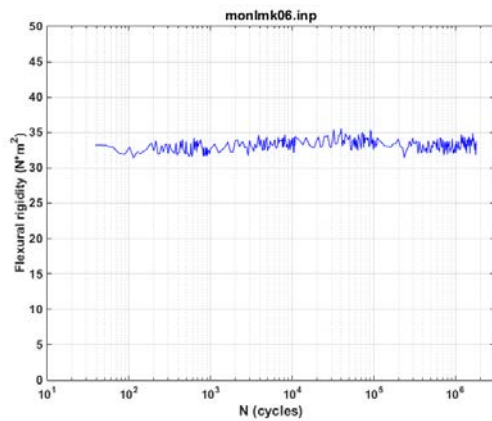
Fig. 17. Variations in (a) curvature range, (b) moment range, and (c) flexural rigidity as a function of the number of cycles for LMK06/575D-E; $N_f = 1.79 \times 10^6$ cycles at ± 7.62 N·m, 5 Hz.



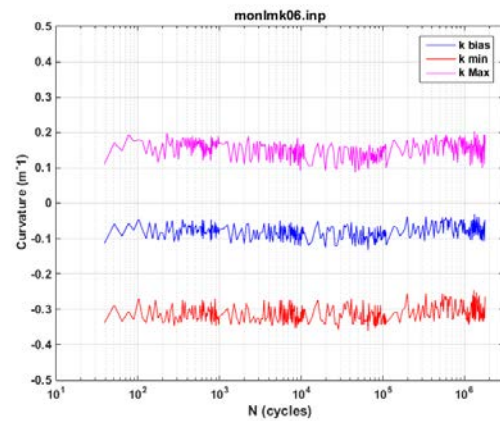
(a)



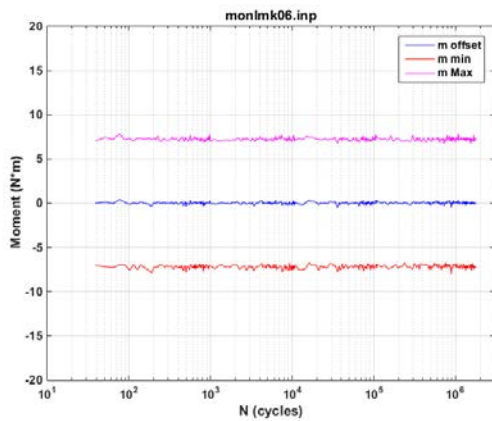
(b)



(c)



(d)



(e)

Fig. 18. Variations in (a) curvature range, (b) applied moment range, (c) flexural rigidity, (d) maximum and minimum values of curvature, and (e) maximum and minimum values of moment as a function of the number of cycles for LMK06/575D-E; $N_f = 1.79 \times 10^6$ cycles at ± 7.62 N·m, 5 Hz.

4.6 LMK07/575C-A, ± 15.24 N·m, 5 Hz

The test on the LMK07/575C-A rod was conducted at ± 15.24 N·m, 5 Hz. The lifetime of the specimen was 1.22×10^5 cycles. Periodic quasistatic measurements of rod deformation were conducted using two relative displacement levels (0.2 and 0.4 mm) at the selected target number of cycles. The variations in curvature range, moment range, and flexural rigidity as a function of number of cycles are given in Fig. 19. As can be seen, there was a significant decrease in rigidity near 10^5 cycles from 45–50 to ~ 40 N·m², corresponding to the high moment cycling.

The curvature, moment, and flexural rigidity based on online monitoring data are presented in Fig. 20. The online monitoring showed a flexural rigidity of about 38 N·m², a little lower than that observed in measurements. Essentially, no significant change can be observed with the monitored flexural rigidity over the cyclic testing process, except a slight downward bend of the curve near 7×10^4 cycles. At the same time, a little negative curvature offset (-0.05 m⁻¹) was observed.

The images of lateral surface and fracture surfaces are presented in Fig. 21. The feature of fracture surface is quite similar to that observed in LMK03. Again, the fracture occurred on the pellet-to-pellet interface. The pellets developed cracks and fractured into several large size fragments, but they held in place. There appeared to be filling at the pellet-to-cladding interface, but this cannot be confirmed at this level of magnification.

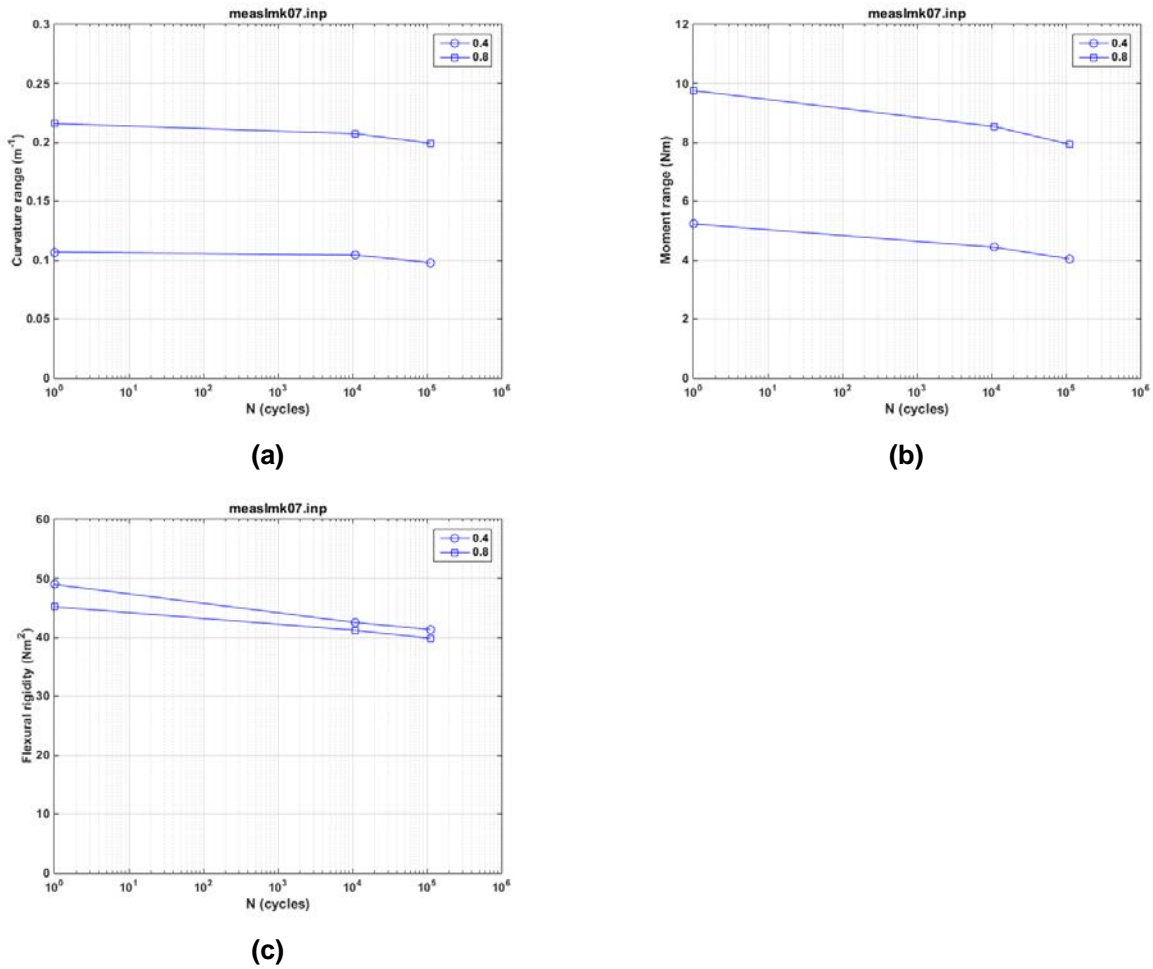
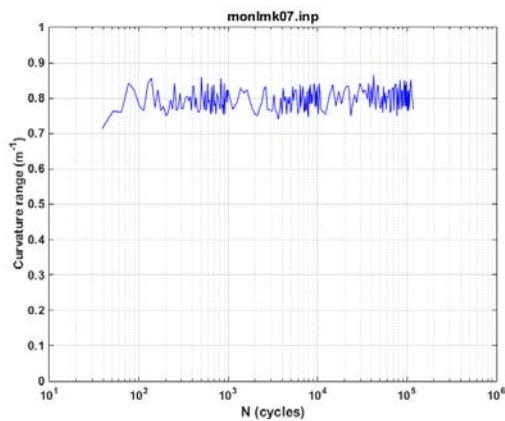
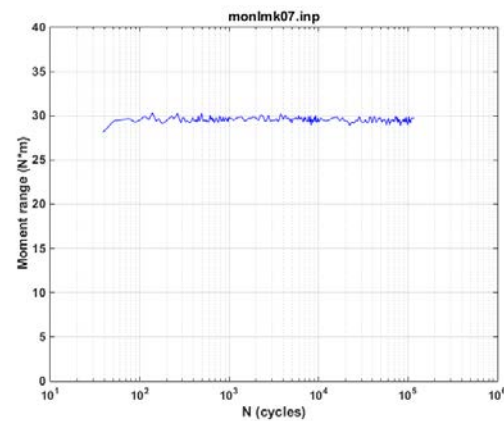


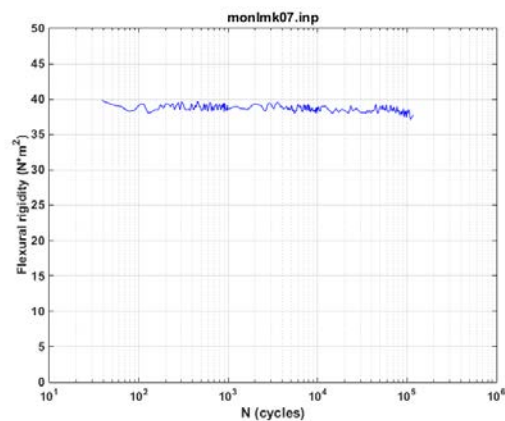
Fig. 19. Variations in (a) curvature, (b) moment, and (c) flexural rigidity as a function of the number of cycles for LMK07/575C-A; $N_f = 1.22 \times 10^5$ cycles at ± 15.24 N·m, 5 Hz.



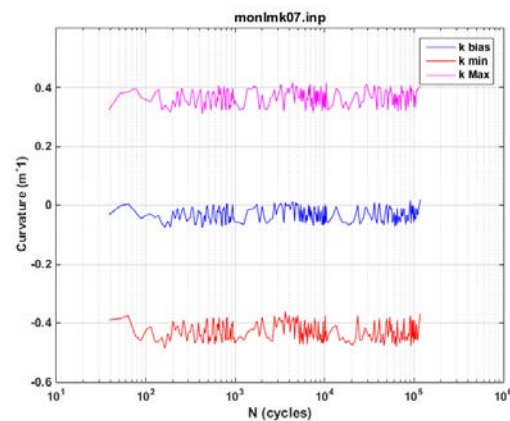
(a)



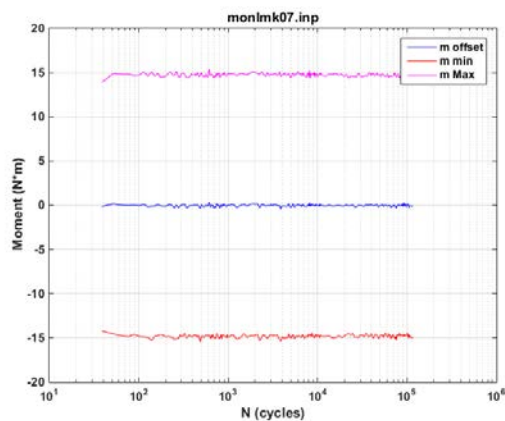
(b)



(c)



(d)



(e)

Fig. 20. Variations in (a) curvature range, (b) applied moment range, (c) flexural rigidity, (d) maximum and minimum values of curvature, and (e) maximum and minimum values of moment as a function of the number of cycles for LMK07/575C-A; $N_f = 1.22 \times 10^5$ cycles at ± 15.24 N·m, 5 Hz.

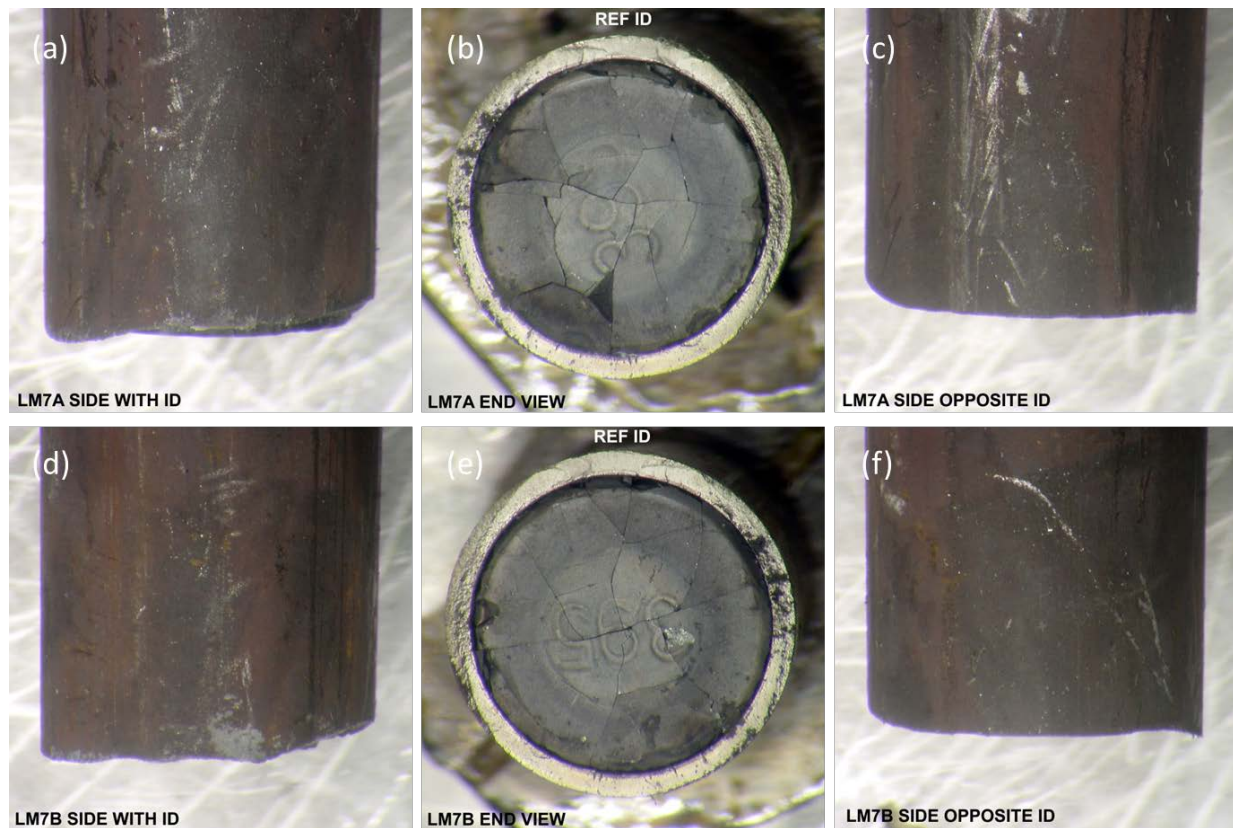


Fig. 21. Fracture segments for LMK07/575C-A. (a) and (d) show the specimen ID side of the segments on end caps A and B; (b) and (e) show the mating fracture surface; and (c) and (f) show the opposite specimen ID side of the segment on end caps A and B.

4.7 LMK08/575B-D, ± 7.62 N·m, 5 Hz

The test on the LMK08/575B-D rod was conducted at ± 7.62 N·m, 5 Hz. The specimen failed at 4.70×10^6 cycles. Periodic quasistatic measurements of rod deformation were conducted using two relative displacement levels (0.2 and 0.35 mm) at the selected target number of cycles. The variations in curvature range, moment range, and flexural rigidity as a function of the number of cycles are given in Fig. 22. The rigidity of the measurements at two displacements started with 43 to 47 $\text{N}\cdot\text{m}^2$ and demonstrated a slight decreasing trend.

The curvature, moment, and flexural rigidity based on online monitoring data are presented in Fig. 23. The online monitoring showed a flexural rigidity of about 36.5 $\text{N}\cdot\text{m}^2$, slightly lower than that observed in the measurements. This was mainly because different loading conditions were used in the measurement and cycling. Overall, a quite steady response was exhibited over the entire cyclic testing period. Meanwhile, a positive curvature offset of 0.1 m^{-1} was seen during the cyclic fatigue process.

Failure of the specimen occurred in the gage section, as shown in Fig. 24.

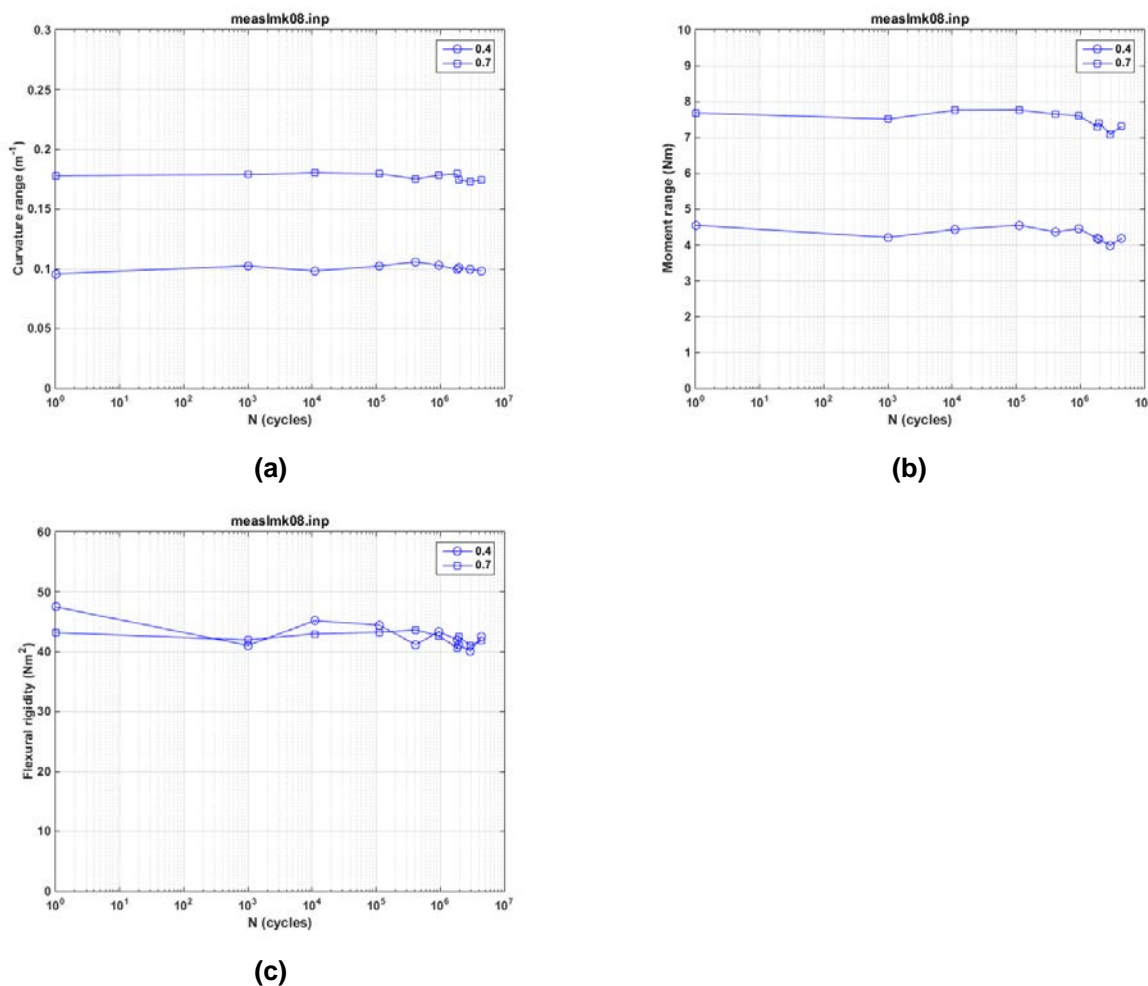
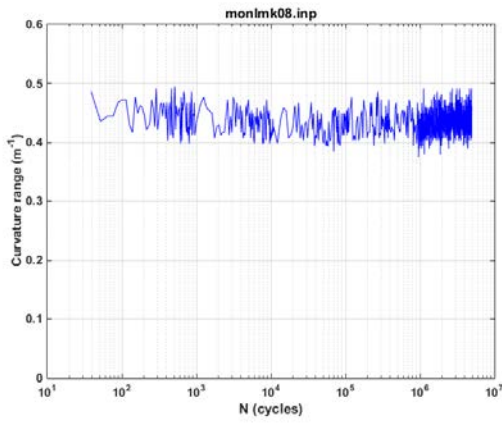
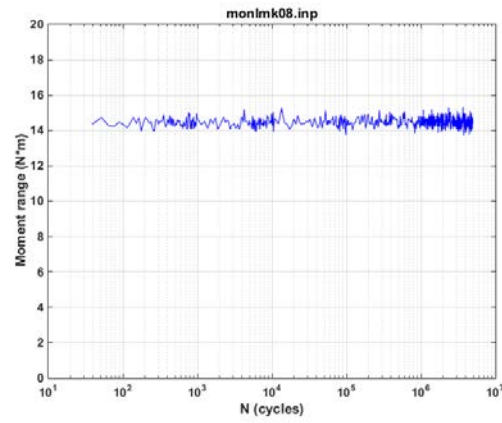


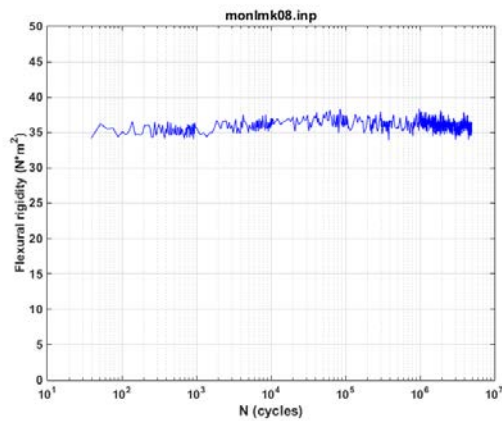
Fig. 22. Variations in (a) curvature range, (b) moment range, and (c) flexural rigidity as a function of the number of cycles for LMK08/575B-D. Measurements were made with 0.2 and 0.35 mm relative displacements; $N_f = 4.70 \times 10^6$ cycles at ± 7.62 N·m, 5 Hz.



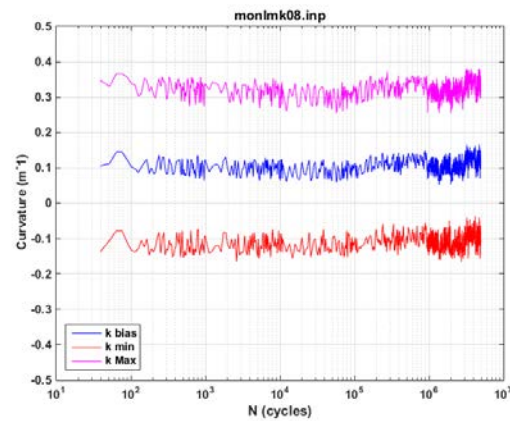
(a)



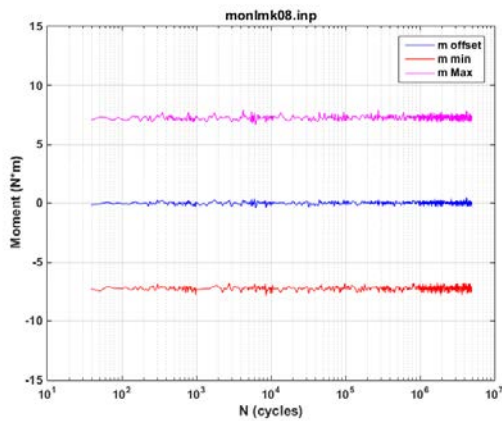
(b)



(c)



(d)



(e)

Fig. 23. Variations in (a) curvature range, (b) applied moment range, (c) flexural rigidity, (d) maximum and minimum values of curvature, and (e) maximum and minimum values of moment as a function of the number of cycles for LMK08/575B-D; $N_f = 4.70 \times 10^6$ cycles at ± 7.62 N·m, 5 Hz.

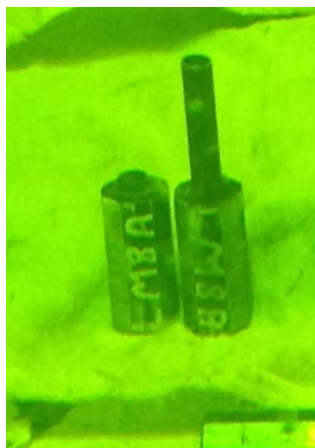


Fig. 24. Fracture segments for LMK08/575B-D; $N_f = 4.70 \times 10^6$ cycles at ± 7.62 N·m, 5 Hz.

4.8 LMK09/574D-D, ± 10.16 N·m, 5 Hz

The test on the LMK09/574D-D rod was conducted at ± 10.16 N·m, 5 Hz. The specimen failed at 7.31×10^5 cycles. Periodic quasistatic measurements of rod deformation were conducted using two relative displacement levels (0.2 and 0.4 mm) at the selected target number of cycles. The variations in curvature range, moment range, and flexural rigidity as a function of the number of cycles are given in Fig. 25. The rigidity of the measurements at two displacements started with 45 to 47 N·m² and demonstrated a slight decreasing trend.

The curvature, moment, and flexural rigidity based on online monitoring data are presented in Fig. 26. The online monitoring showed a flexural rigidity of about 39 N·m², slightly lower than that observed in measurements. This is believed to be because different loading conditions were used in measurement and cycling. Overall, a quite steady response was exhibited over the entire cyclic testing period. Meanwhile, a positive curvature offset of 0.02 m⁻¹ was seen during the cyclic fatigue process.

The failure occurred again in the middle of gage section of the specimen, as shown in Fig. 27. A fractographic study was conducted using a stereo-optical microscope. Images of the lateral surface and fracture surfaces are presented in Fig. 28. Overall surface integrity was maintained to a certain extent. Again, the fracture clearly occurred at the pellet-to-pellet interface. The pellets developed cracks and fractured into several large size of fragments, and they held in place. No apparent gap can be seen between the pellet and cladding.

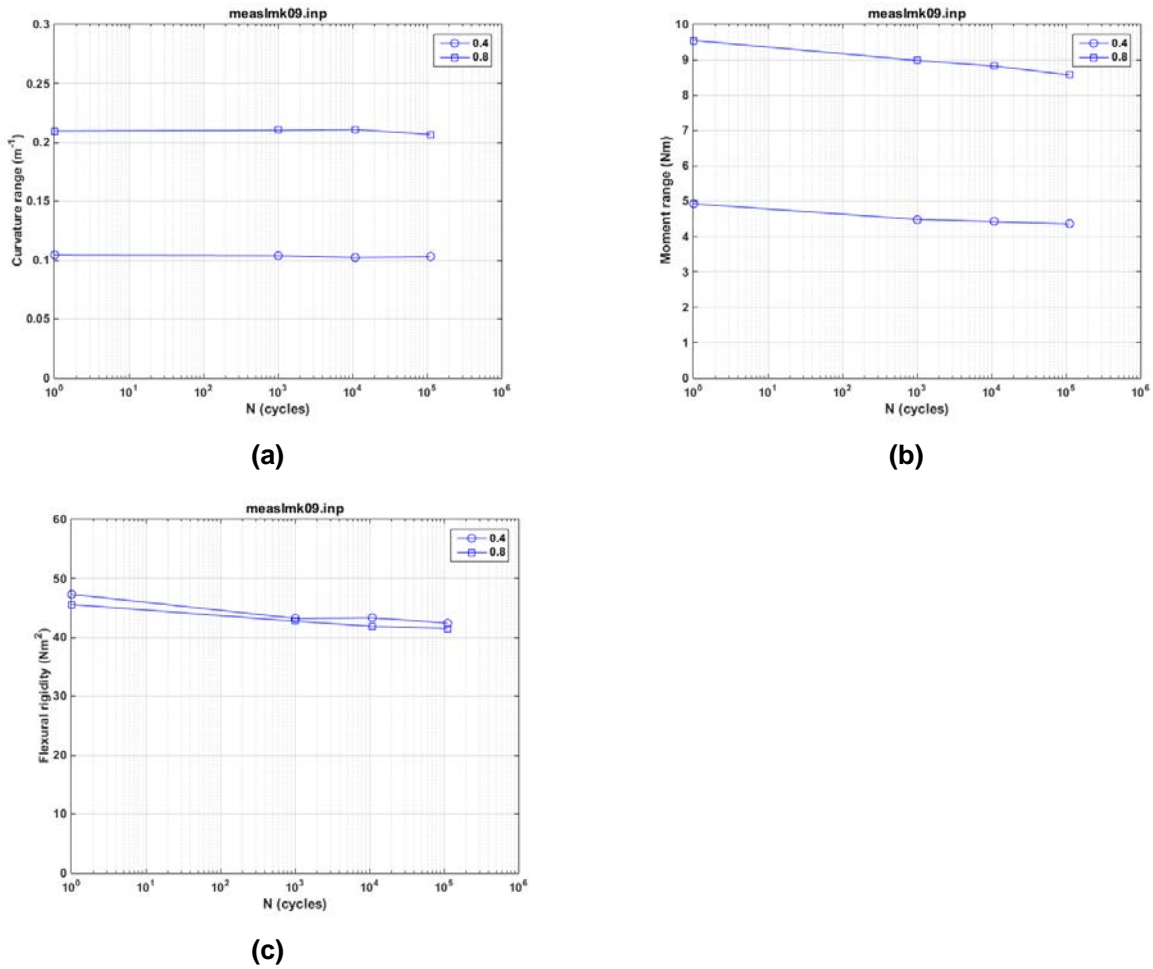


Fig. 25. Variations in (a) curvature range, (b) moment range, (c) flexural rigidity as a function of the number of cycles for LMK09/574D-D. Measurements were made with 0.2 and 0.4 mm relative displacements; $N_f = 7.31 \times 10^5$ cycles at ± 10.16 N·m, 5 Hz.

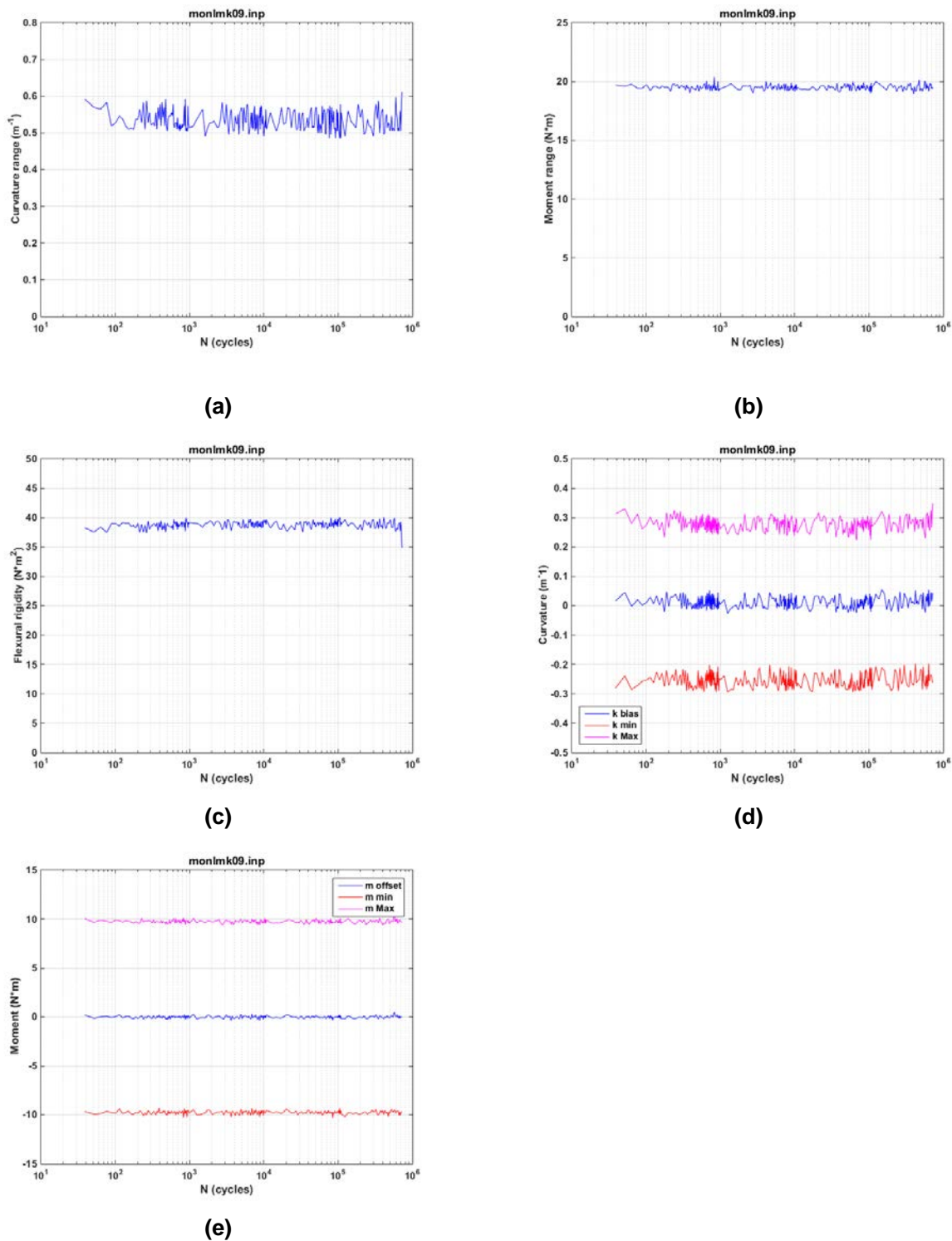


Fig. 26. Variations in (a) curvature range, (b) applied moment range, (c) flexural rigidity, (d) maximum and minimum values of curvature, and (e) maximum and minimum values of moment as a function of the number of cycles for LMK09/574D-D; $N_f = 7.31 \times 10^5$ cycles at ± 10.16 $N \cdot m$, 5 Hz.

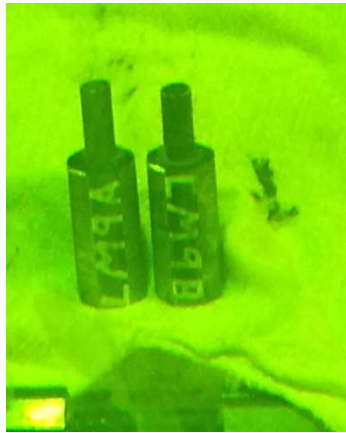


Fig. 27. Fracture segments for LMK09/574D-D; $N_f = 7.31 \times 10^5$ cycles at ± 10.16 N·m, 5 Hz.

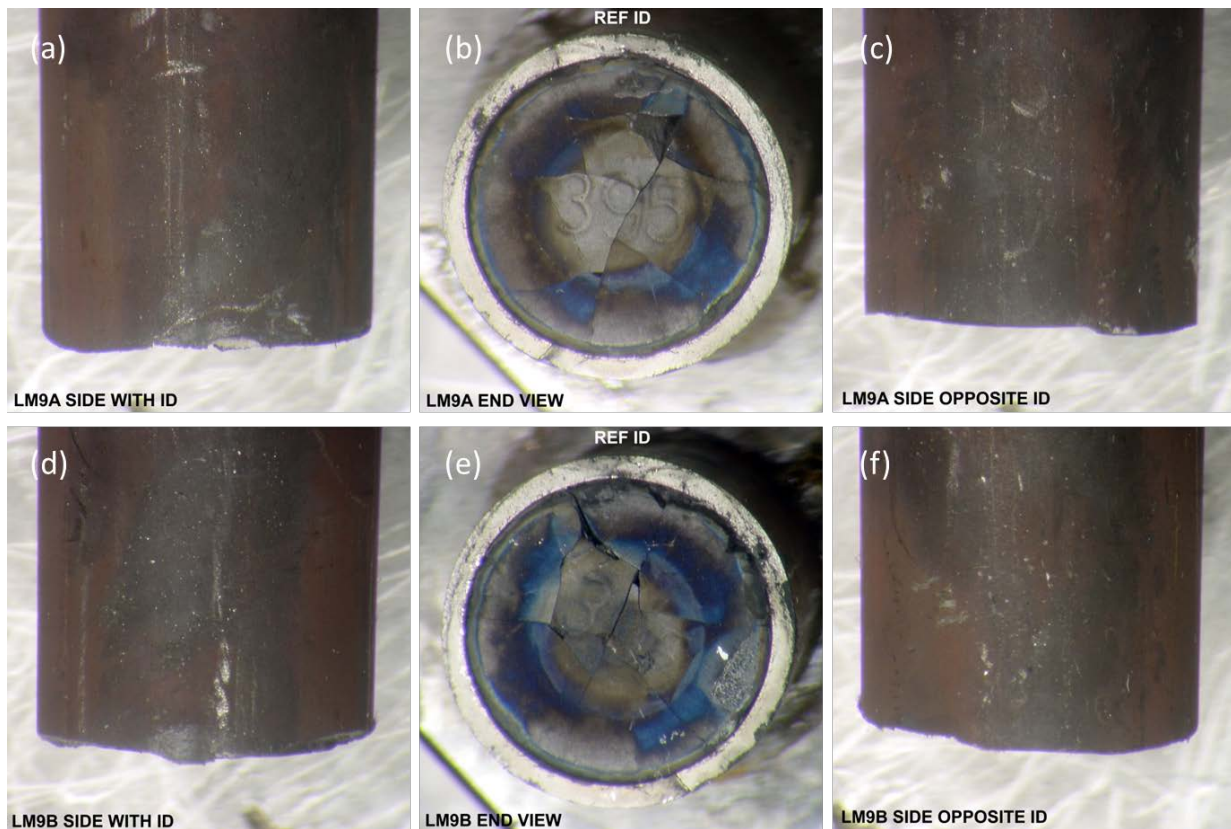


Fig. 28. Fracture segments for LMK09/574D-D. (a) and (d) show the specimen ID side of the segment on end caps A and B; (b) and (e) show the mating fracture surface; and (c) and (f) show the opposite specimen ID side of segment on end caps A and B.

4.9 LMK10/575B-E, ± 20.32 N·m, 5 Hz

The test on the LMK10/575B-E rod was conducted at ± 20.32 N·m, 5 Hz. The specimen failed at 5.20×10^4 cycles. Periodic quasistatic measurements of rod deformation were conducted using two relative displacement levels (0.2 and 0.4 mm) at the selected target number of cycles. The variations in curvature range, moment range, and flexural rigidity as a function of number of cycles are given in Fig. 29. The rigidity of the measurements at two displacements started with 45 to 50 N·m² and demonstrated a clear decreasing trend.

The curvature, moment, and flexural rigidity based on online monitoring data are presented in Fig. 30. The online monitoring showed a flexural rigidity of about 38 N·m², slightly lower than that observed in the measurements. This is mainly because different loading conditions were used in measurement and cycling. Overall, a quite steady response was exhibited over the entire cyclic testing period. Meanwhile, a positive curvature offset of 0.05 m⁻¹ was seen during the cyclic fatigue process.

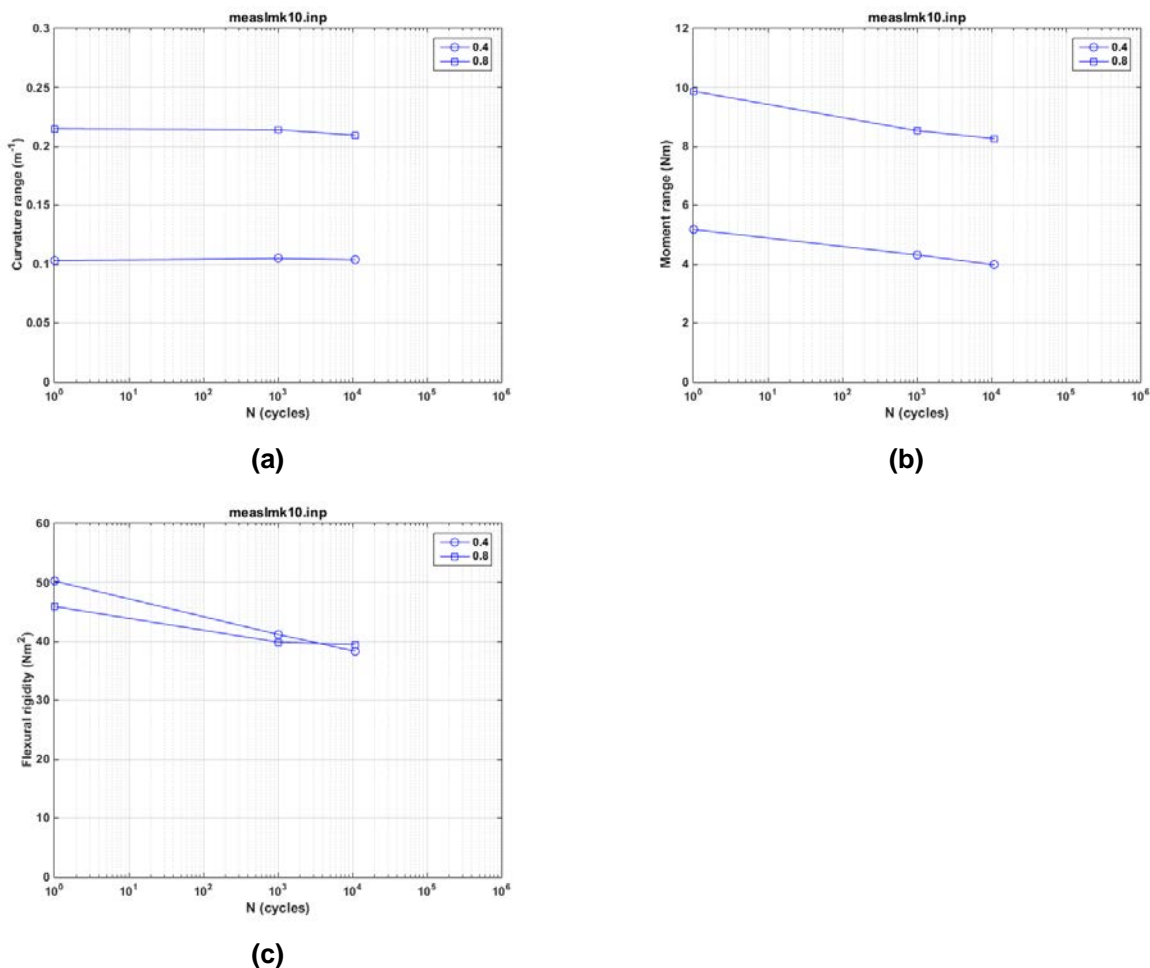


Fig. 29. Variations in (a) curvature range, (b) moment range, and (c) flexural rigidity as a function of the number of cycles for LMK10/575B-E. Measurements were made with 0.2, and 0.4 mm relative displacements; $N_f = 5.20 \times 10^4$ cycles at ± 20.32 N·m, 5 Hz.

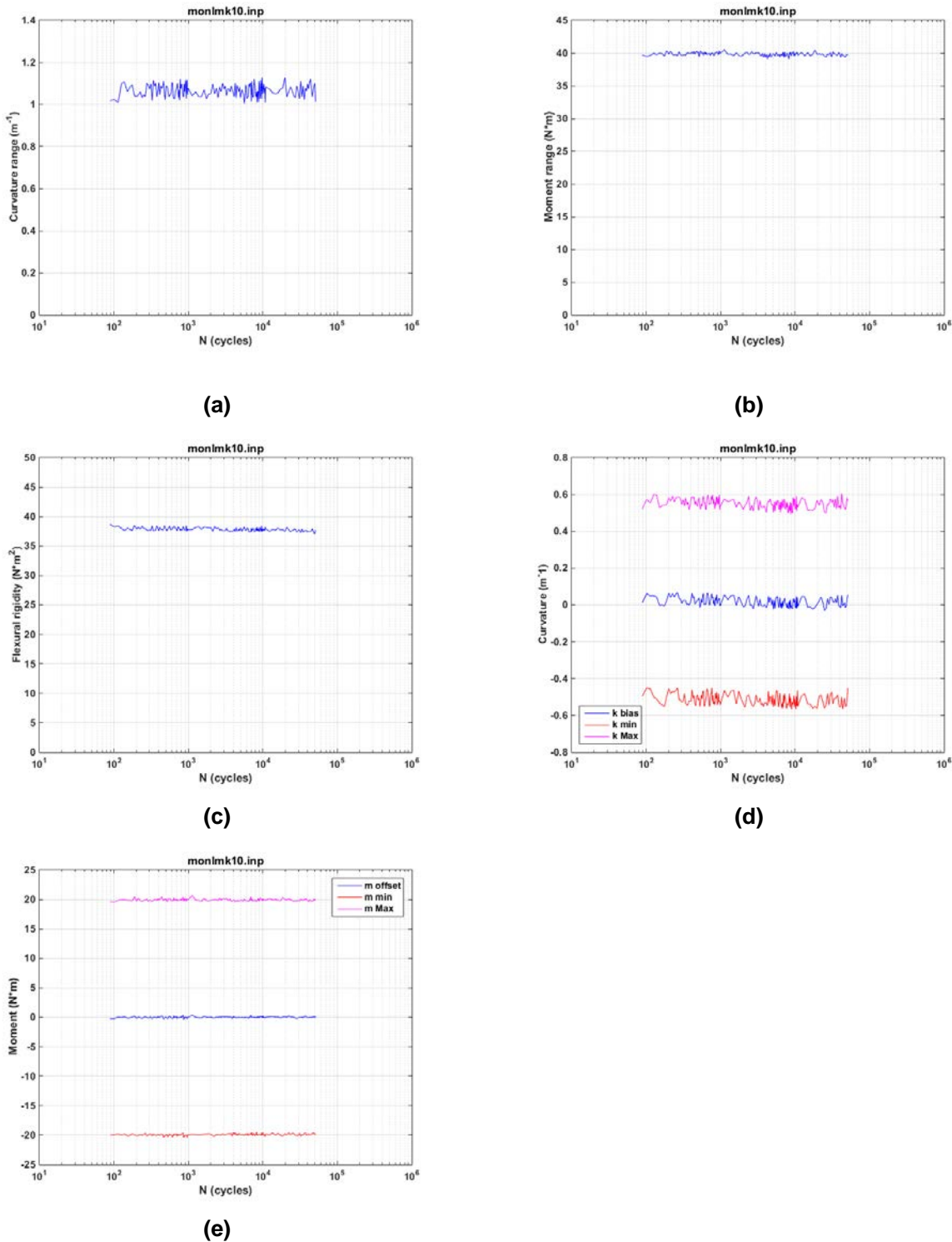


Fig. 30. Variations in (a) curvature range, (b) applied moment range, (c) flexural rigidity, (d) maximum and minimum values of curvature, and (e) maximum and minimum values of moment as a function of the number of cycles for LMK10/575B-E; $N_f = 5.20 \times 10^4$ cycles at ± 20.32 N·m, 5 Hz.

4.10 LMK11/575B-D, $\pm 8.64\text{N}\cdot\text{m}$, 5 Hz

The test on the LMK11/575B-D rod was conducted at $\pm 8.64\text{ N}\cdot\text{m}$, 5 Hz. The specimen failed at 3.55×10^5 cycles. Periodic quasistatic measurements of rod deformation were conducted using two relative displacement levels (0.2 and 0.35 mm) at the selected target number of cycles. The variations in curvature range, moment range, and flexural rigidity as a function of number of cycles are given in Fig. 31. The rigidity of the measurements at two displacements started with 48 to $50\text{ N}\cdot\text{m}^2$ and demonstrated slight fluctuations during the cycling.

The curvature, moment, and flexural rigidity based on online monitoring data are presented in Fig. 32. The online monitoring showed a flexural rigidity of about $39\text{ N}\cdot\text{m}^2$, slightly lower than that observed in the measurements. This is mainly because different loading conditions were used in the measurements and cycling. Overall, a steady response was exhibited over the entire cyclic testing period. Meanwhile, a negative curvature offset, -0.06 m^{-1} , was seen during the cyclic fatigue process.

Fig. 33 illustrates the failure position of the specimen. A fractographic study was conducted using a stereo-optical microscope. The images of the lateral surface and fracture surfaces are presented in Fig. 34. Although some scratches are seen over the lateral surface, overall surface integrity was maintained to a certain extent. The fracture clearly occurred on the pellet-to-pellet interface. Mosaic cracks developed in the pellets. No apparent gap can be seen between the pellet and cladding.

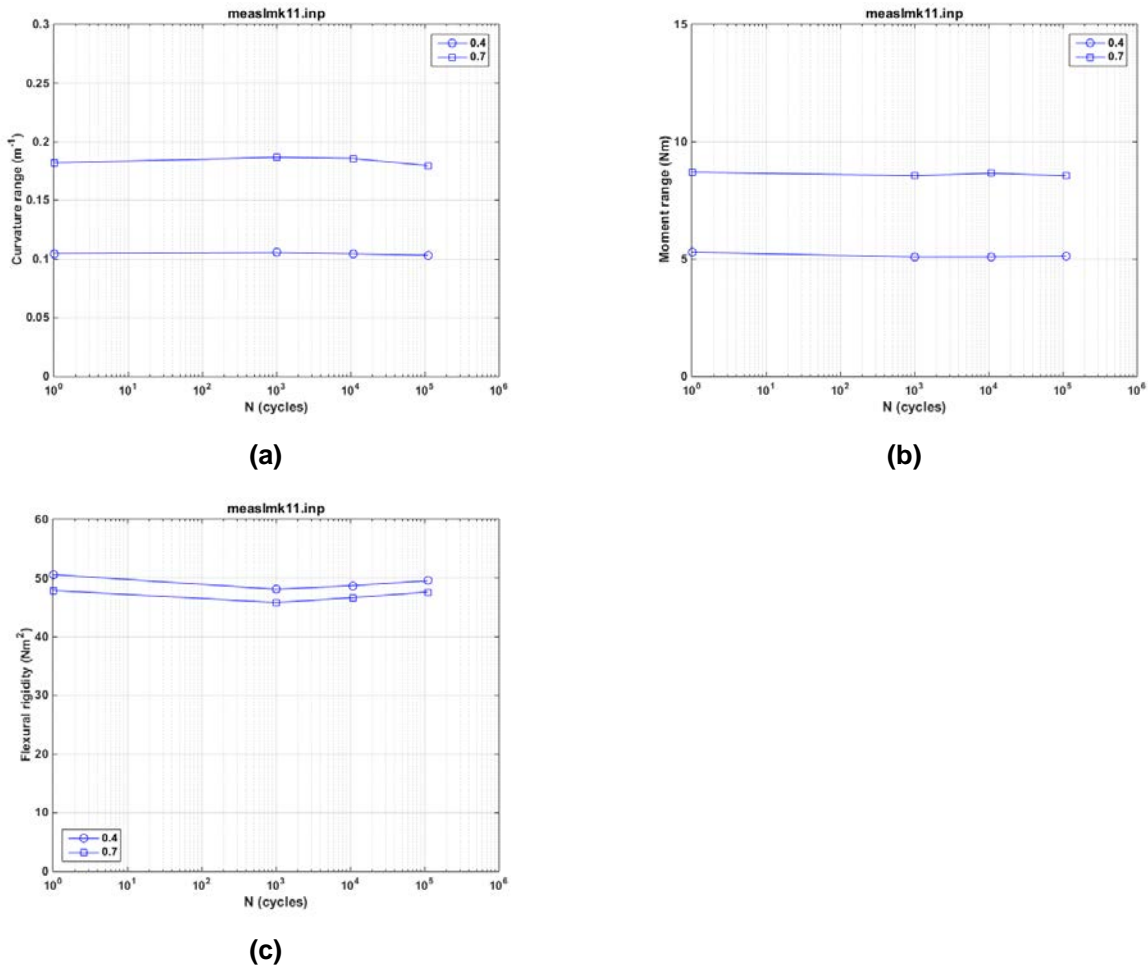


Fig. 31. Variations in (a) curvature range, (b) moment range, and (c) flexural rigidity as a function of the number of cycles for LMK11/575B-D. Measurements were made with 0.2 and 0.35 mm relative displacements; $N_f = 3.55 \times 10^5$ cycles at ± 8.64 N·m, 5 Hz.

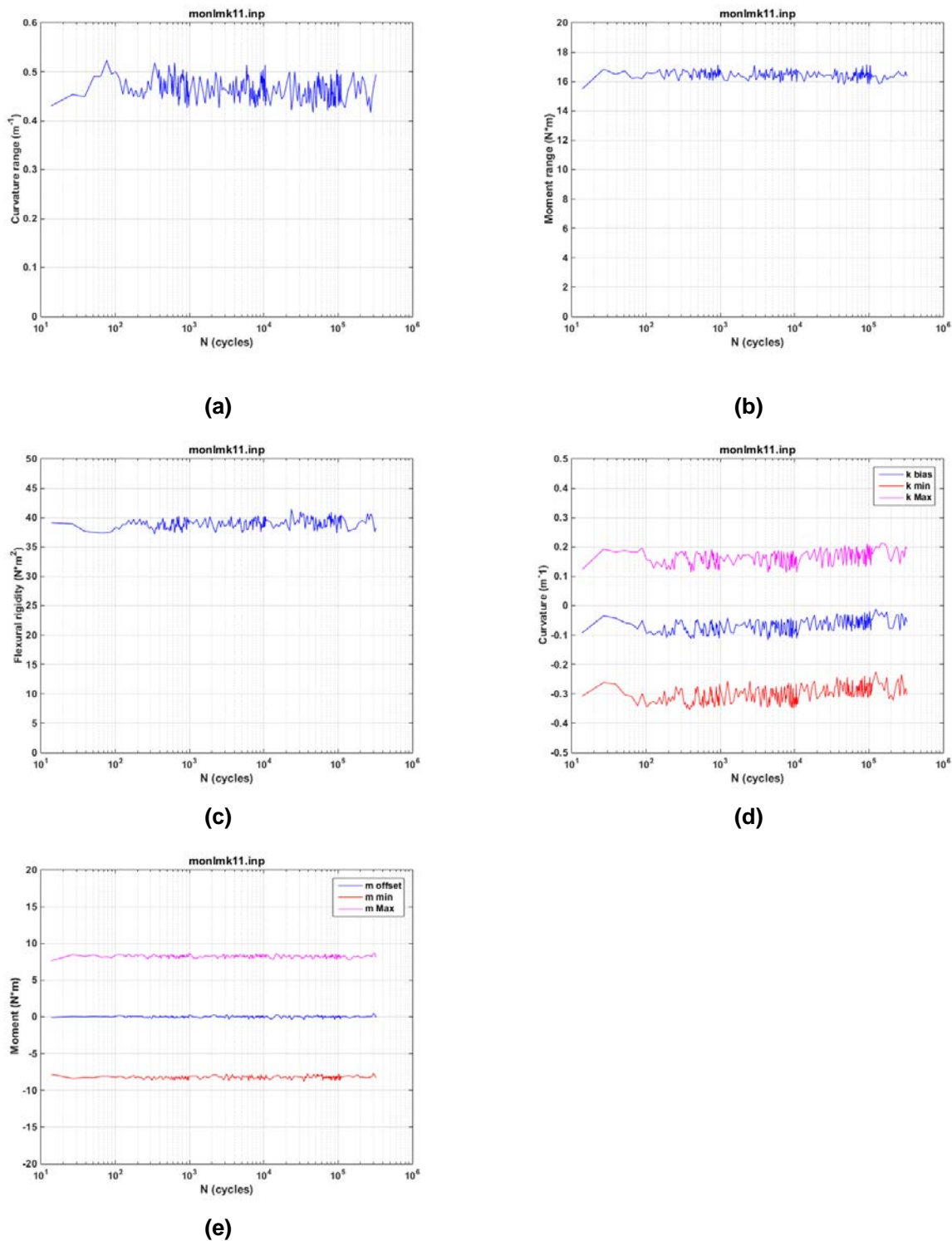


Fig. 32. Variations in (a) curvature range, (b) applied moment range, (c) flexural rigidity, (d) maximum and minimum values of curvature, and (e) maximum and minimum values of moment as a function of the number of cycles for LMK11/575B-D; $N_f = 3.55 \times 10^5$ cycles at ± 8.64 N·m, 5 Hz.

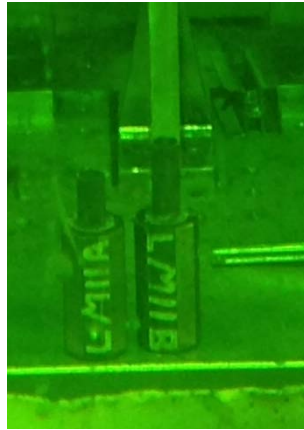


Fig. 33. Fracture segments for LMK11/574D-D; $N_f = 3.55 \times 10^5$ cycles at ± 8.64 N·m, 5 Hz.

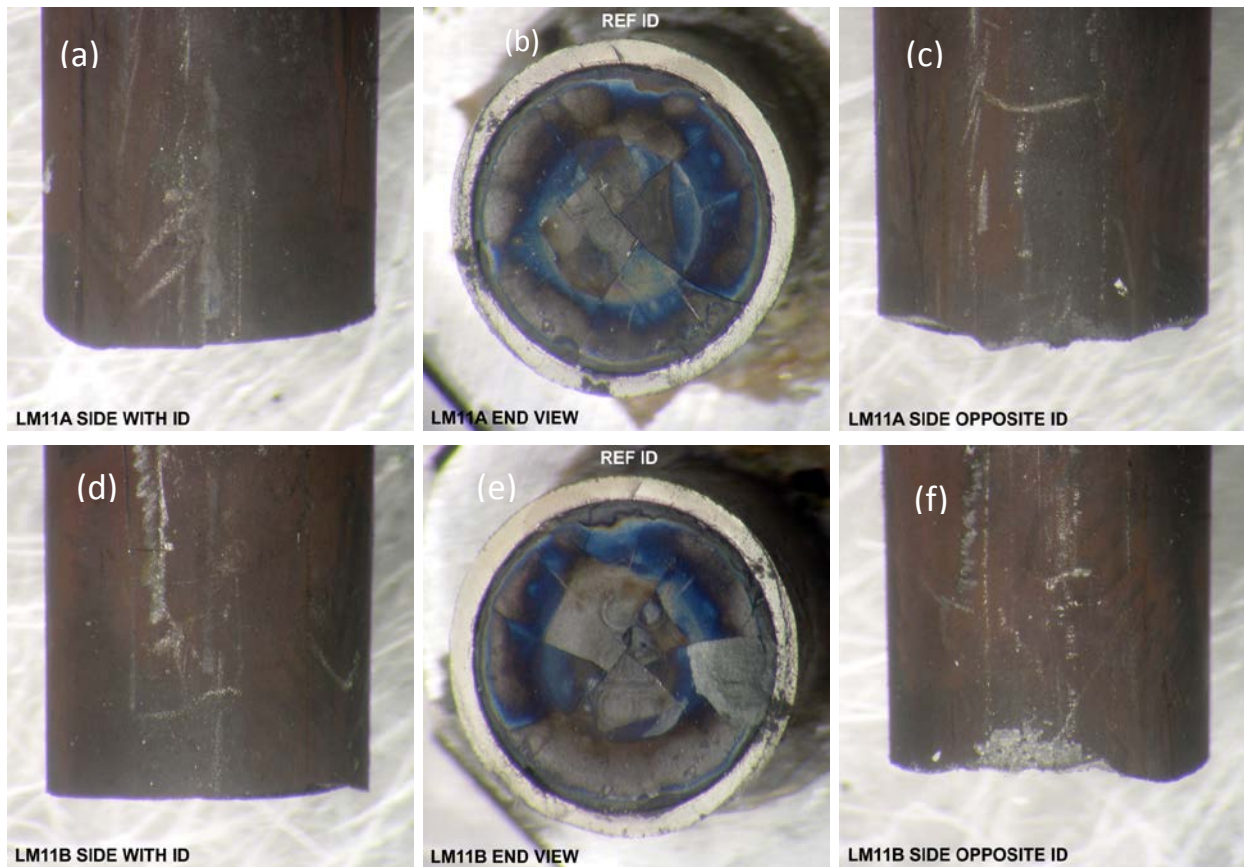


Fig. 34. Fracture segments for LMK11/575B-D. (a) and (d) show the specimen ID side of the segment on end caps A and B; (b) and (e) show the mating fracture surface; and (c) and (f) show the opposite specimen ID side of segment on end caps A and B.

4.11 LMK12/575B-A, ± 7.11 N·m, 5 Hz

The test on the LMK12/575B-A rod was conducted at ± 7.11 N·m, 5 Hz and stopped at the cycle number 7.58×10^6 . The quasistatic measurements were conducted using two relative displacement levels (0.2 and 0.35 mm) at the selected number of cycles, and results are illustrated in Fig. 35. A small fluctuation occurred near 4 to 6×10^6 cycles. The reason for such fluctuation is not clear. However, the overall rigidity stayed around 30 to 38 N·m².

The curvature, moment, and flexural rigidity based on online monitoring data are presented in Fig. 36. The online monitoring showed a flexural rigidity variation of 24 to 29 N·m². At the same time, the curvature exhibited a slight upward drift at the end of cycling of around 0.05 m⁻¹. The rigidity of this rod specimen is relatively lower compared to other LMK rods.

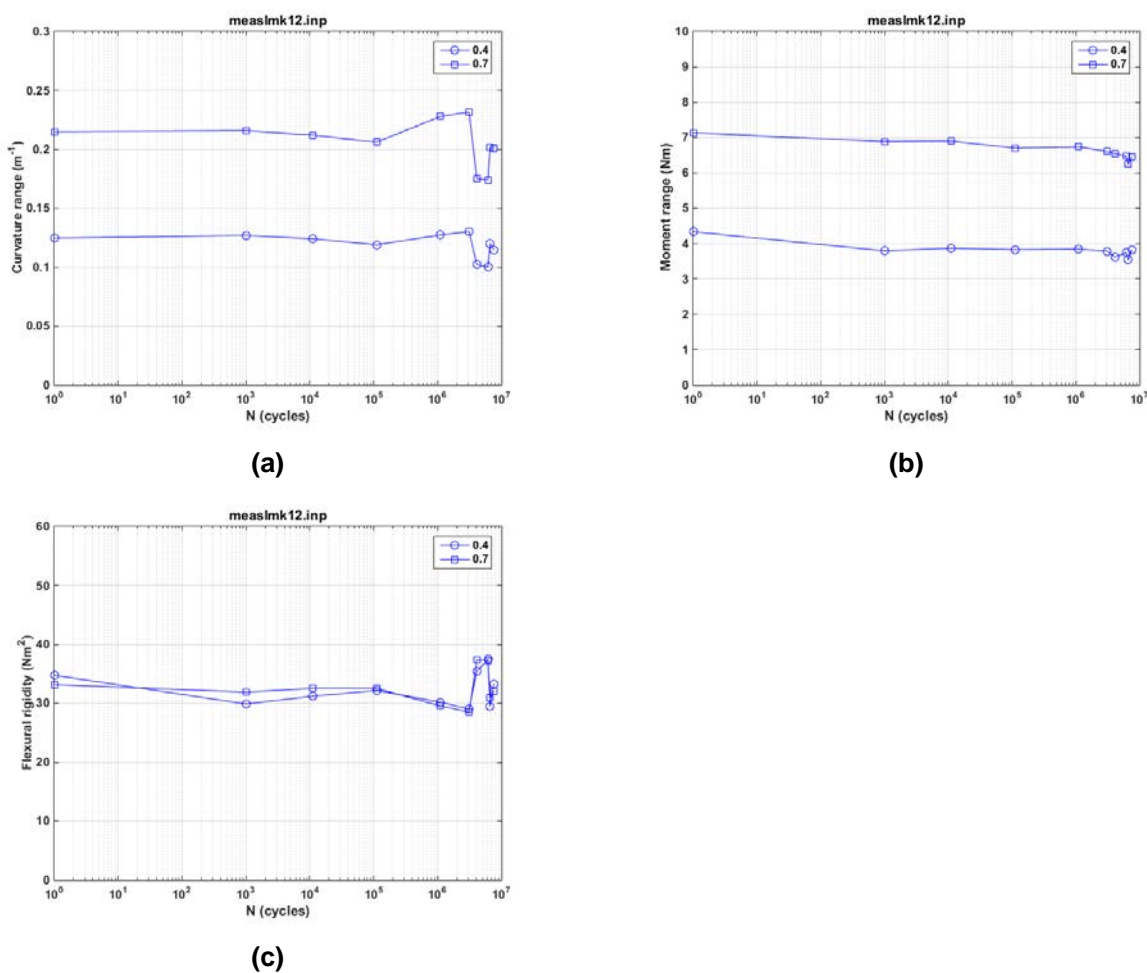
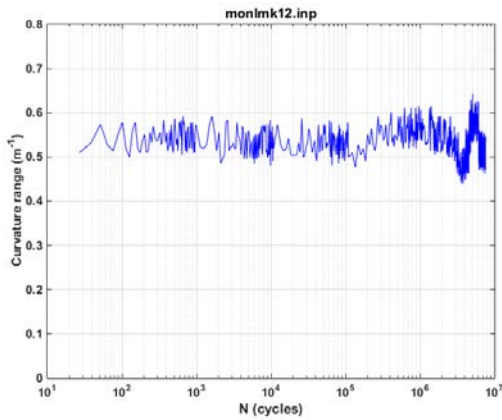
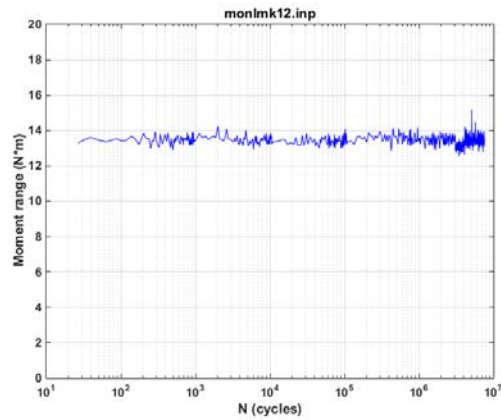


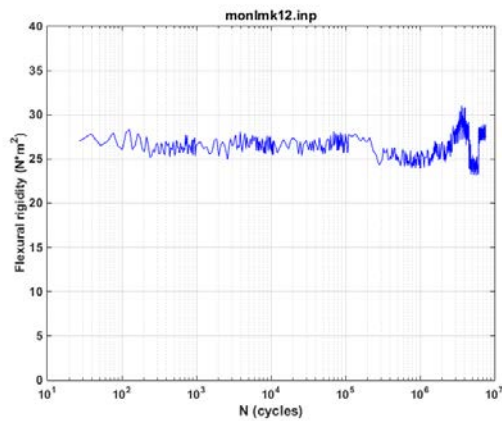
Fig. 35. Variations in (a) curvature range, (b) moment range, and (c) flexural rigidity as a function of the number of cycles for LMK12/575B-A. Measurements were made with 0.2 and 0.35 mm relative displacements; $N = 7.58 \times 10^6$ cycles at ± 7.11 N·m, 5 Hz.



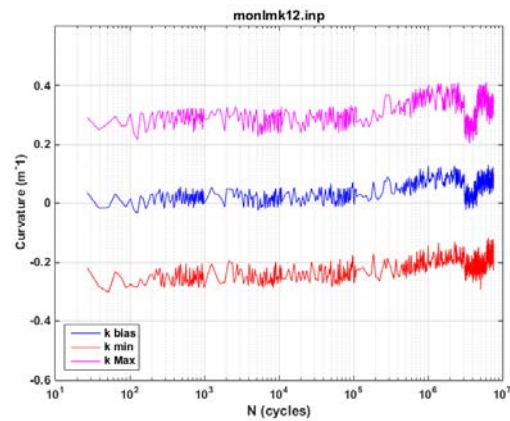
(a)



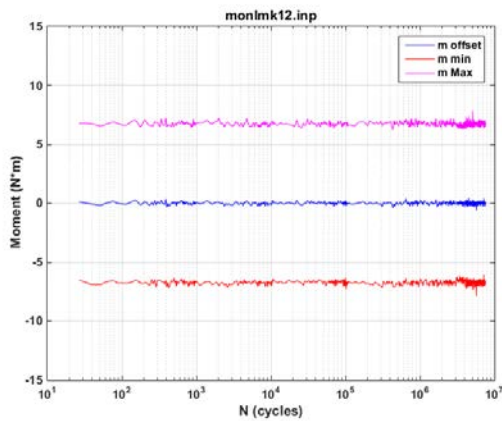
(b)



(c)



(d)



(e)

Fig. 36. Variations in (a) curvature range, (b) applied moment range, (c) flexural rigidity, (d) maximum and minimum values of curvature, and (e) maximum and minimum values of moment as a function of the number of cycles for LMK12/575B-A; $N = 7.58 \times 10^6$ cycles at ± 7.11 N·m, 5 Hz.

4.12 LMK13/575C-D, ± 25.40 N·m, 5 Hz

The test on LMK13/575C-D was conducted at ± 25.40 N·m, 5 Hz. The number of cycles to failure of the specimen was 2.1×10^4 . The quasi-static measurements were conducted using relative displacement levels of 0.4 and 0.8 mm at the selected number of cycles. Further data analyses are to be performed in the next report cycle.

4.13 LMK14/575C-B, ± 10.16 N·m, 5 Hz

The test on LMK14/575C-B was conducted at ± 10.16 N·m, 5 Hz. The amplitude applied in this test was the same as that for LMK09/574D-D. The failure cycle number (3.90×10^5) of LMK14/575C-B appeared to be slightly lower than that of LMK09/574D-D. The quasistatic measurements were conducted using relative displacement levels of 0.4 and 0.8 mm at the selected number of cycles. Further data analyses are to be performed in the next report cycle.

The failure was determined to be located within the gage section, as shown in Fig. 37.

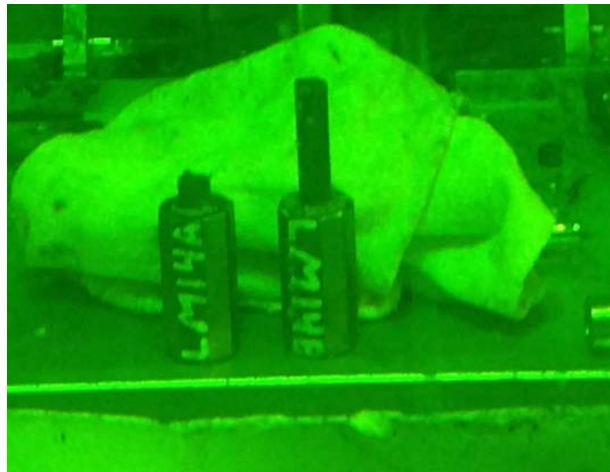


Fig. 37. Failed specimen LMK14 showing that the failure occurred in the gage section.

4.14 LMK15/575C-C, ± 10.16 N·m, 5 Hz

The test on LMK15/575C-C was conducted at ± 10.16 N·m, 5 Hz. The amplitude applied in this test again is the same as that for LMK09/574D-D and LMK14. The specimen was dropped three times from a height of about 2 ft. before the test was conducted in order to explore the effect on the fatigue response of the material. The number of cycles to failure (4.41×10^5) of LMK15 appeared to be slightly lower than that of LMK09/574D-D, but higher than that of LMK14/575C-B. Thus, the effect of dropping before cyclic testing cannot be evaluated with the data at hand, considering the uncertainty regarding the preexisting condition of the specimen. The quasistatic measurements were conducted using relative displacement levels of 0.4 and 0.8 mm at the selected number of cycles. Further data analyses are to be performed in next report cycle.

5. TESTING RESULTS ON H. B. ROBINSON SPENT NUCLEAR FUEL

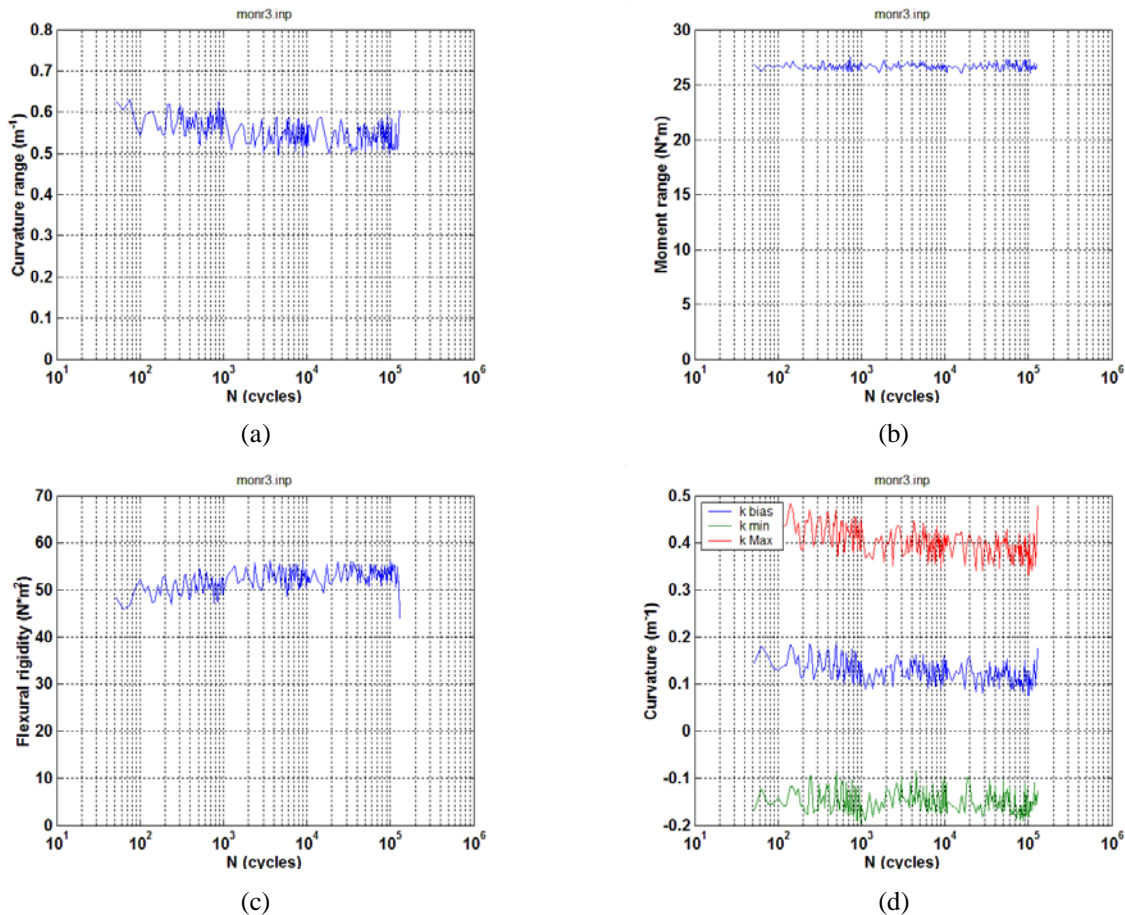
Under DOE sponsorship, ORNL conducted the CIRFT tests on rod specimens R3, R4, and R5. Brief descriptions of these tests are given below. Detailed information on the all the test data based on HBR SNF are provided in Appendix A, as cited from NUREG/CR-7198 report⁹.

5.1 D13/R3/606B3E at ± 13.72 N·m, 5 Hz

The cycle test on sample D13/R3 (606B3E, 66.5 gigawatt-days per megaton of uranium (GWd/MTU) burnup, 100–110 μm oxide layer, 750 ppm hydrogen content) was conducted at ± 13.72 N·m at 5 Hz. Rod specimen R3 failed at approximately 1.29×10^5 cycles within the gage section.

Online monitoring showed that rigidity increased prior to the final rigidity drop at failure, as shown in Fig. 38. The peak and valley of curvature data reflect the decreased curvature range as seen by the drop in the peak value shown in Fig. 38d.

The possible causes of the single-side change in curvature waveform during the cyclic test are unknown, but decreased rigidity was seen in the measurement shown in Fig. 39.



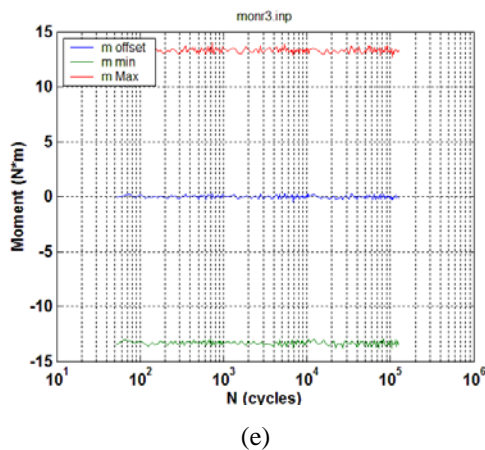


Fig. 38. Variations in (a) curvature range, (b) applied moment range, (c) flexural rigidity, (d) maximum and minimum values of curvature, and (e) maximum and minimum values of moment as a function of the number of cycles for D13/R3 (606B3E); $N_f = 1.29 \times 10^5$ cycles at ± 13.72 N·m, 5 Hz.

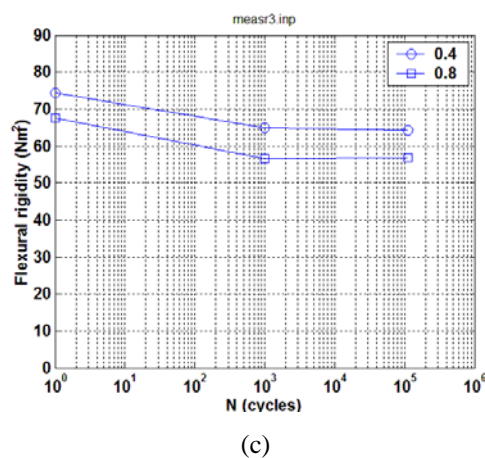
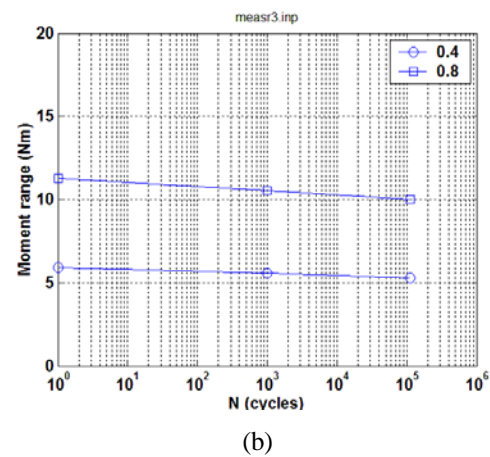
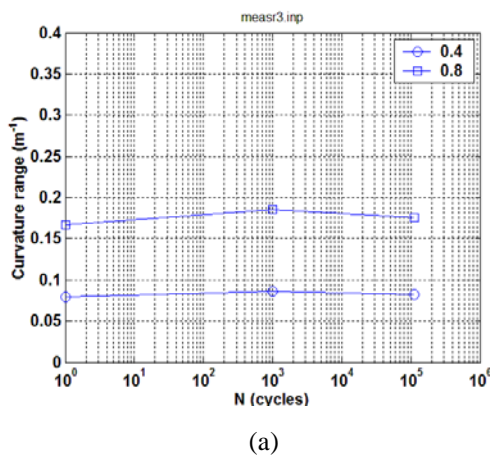
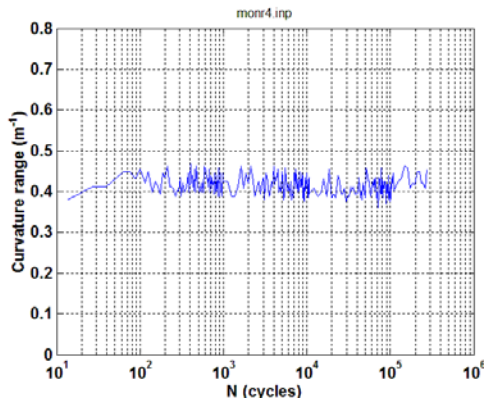


Fig. 39. Variations in (a) curvature range, (b) applied moment range, and (c) flexural rigidity as a function of the number of cycles for D13/R3 (606B3E); $N_f = 1.29 \times 10^5$ cycles at ± 13.72 N·m, 5 Hz.

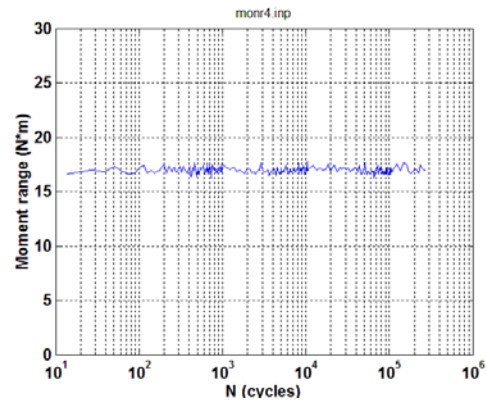
5.2 D14/R4/606B3D at ± 8.89 N·m, 5 Hz

The cycle test on sample D14/R4 (606B3D, 66.5 GWd/MTU burnup, 100–110 μm oxide layer, 750 ppm hydrogen content) was conducted at ± 8.89 N·m at 5 Hz. This test condition was the same as that for sample DM3, see Appendix A. The test on rod specimen R4 was used to generate an additional observation with the same testing conditions as those used on sample DM3. Rod specimen R4 exhibited a relatively short fatigue life with 2.7×10^5 cycles to failure. The short fatigue life may have been due to a preexisting condition in the specimen; it had a higher estimated hydrogen content. The hydrogen content of rod specimen R4 was approximately 750 ppm; the estimated hydrogen content of DM3 was approximately 550 ppm.

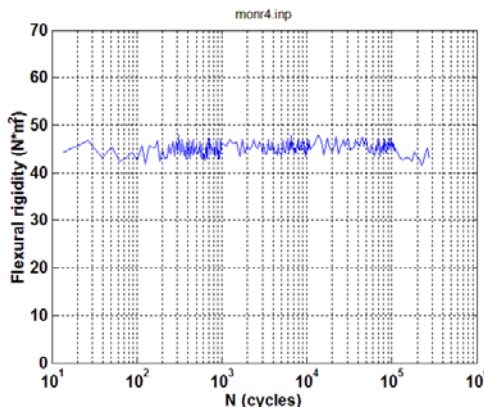
Online monitoring demonstrated a flat rigidity response with a slight rigidity drop prior to failure (Fig. 40). The measurement showed that rigidity increased slightly (Fig. 41).



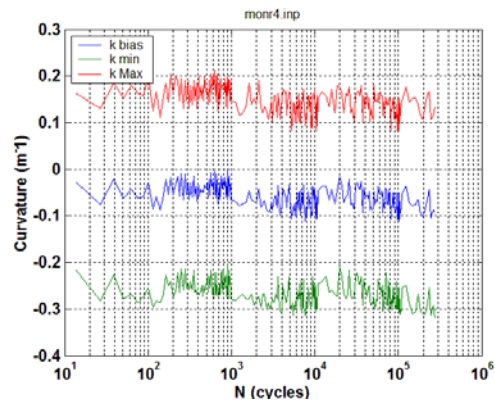
(a)



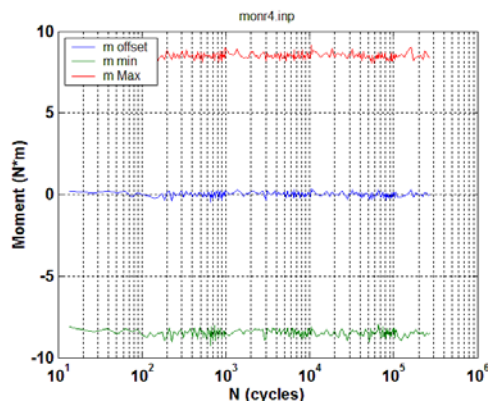
(b)



(c)

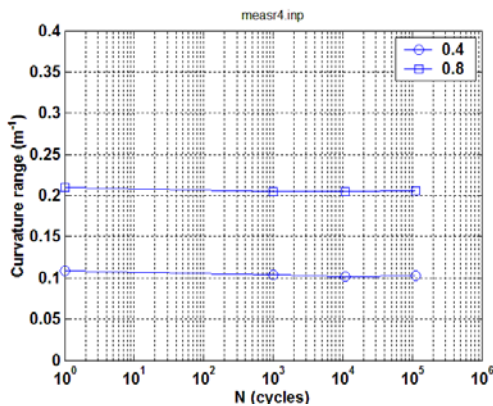


(d)

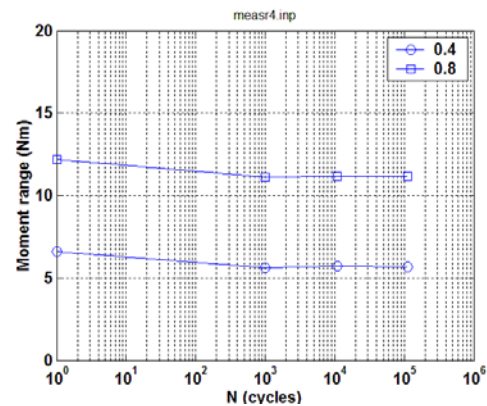


(e)

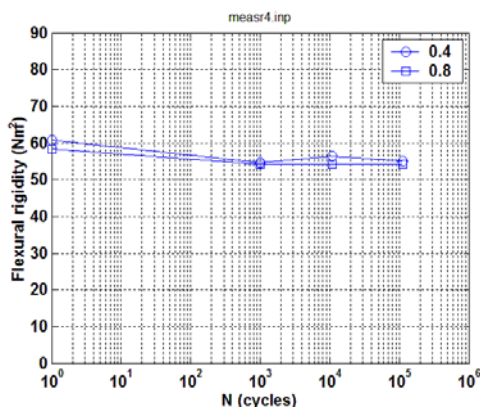
Fig. 40. Variations in (a) curvature range, (b) applied moment range, (c) flexural rigidity, (d) maximum and minimum values of curvature, and (e) maximum and minimum values of moment as a function of the number of cycles for R4 (606B3D); $N_f = 2.7 \times 10^5$ cycles at ± 8.89 N·m, 5 Hz.



(a)



(b)



(c)

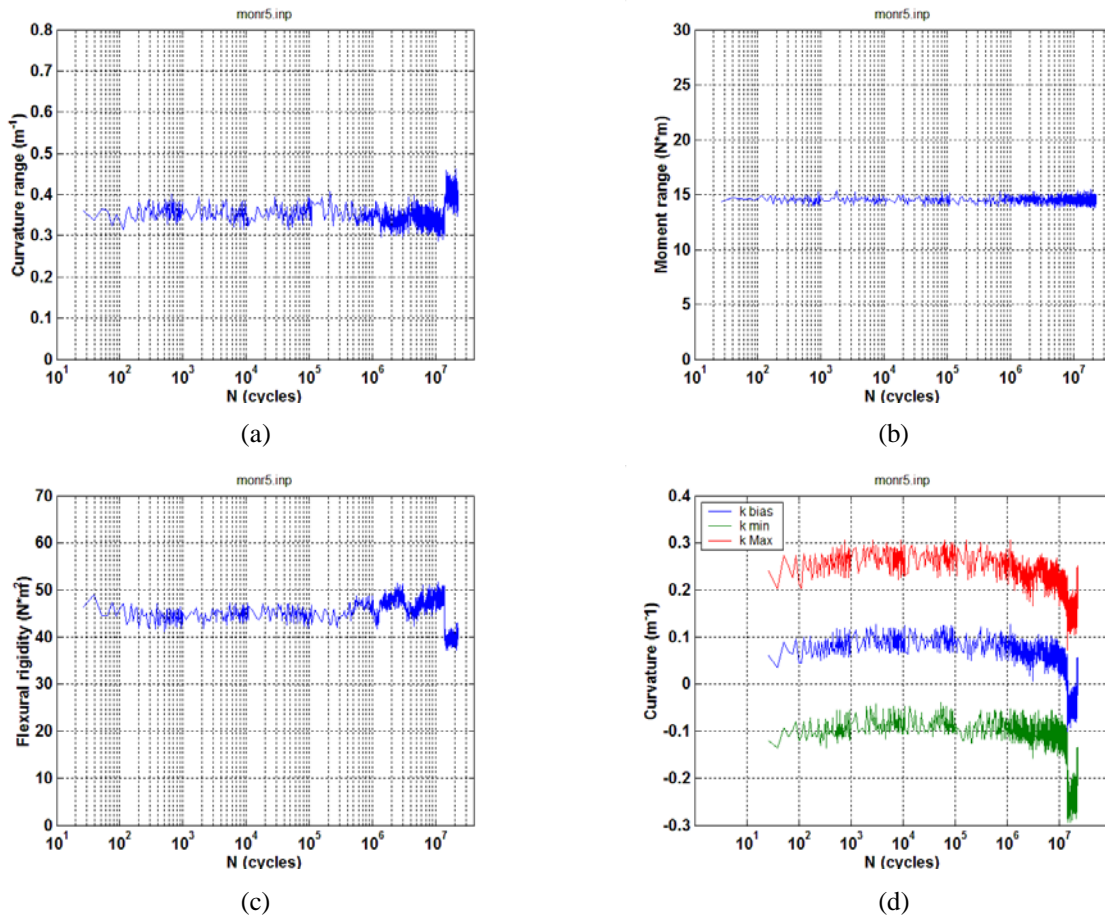
Fig. 41. Variations in (a) curvature range, (b) applied moment range, and (c) flexural rigidity as a function of the number of cycles for R4 (606B3D); $N_f = 2.7 \times 10^5$ cycles at ± 8.89 N·m, 5 Hz.

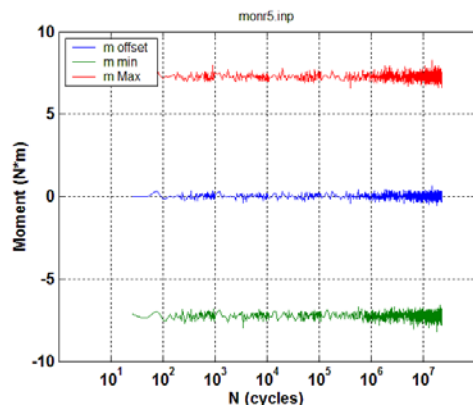
5.3 D15/R5/606B3C at ± 7.62 N·m, 5 Hz

The cycle test on sample R5 (606B3C, 66.5 GWd/MTU burnup, 100–110 μm oxide layer, 750 ppm hydrogen content) was conducted at ± 7.62 N·m, 5 Hz. The moment range used for rod specimen R5 was the same as that used in DM1. The test on sample R5 provided the opportunity to examine the variation in fatigue response between different rods. The test on sample R5 was stopped after 2.23×10^7 cycles because it showed no sign of failure.

Analysis based on the monitoring data indicated that the flexural rigidity was fairly stable and limited to a range of 40 to 50 N·m². A drop in flexural rigidity was observed after the rod was taken off and remounted to the testing machine. The reason for this change is not clear; however, the rod appeared to be quite stable in the subsequent cycling process.

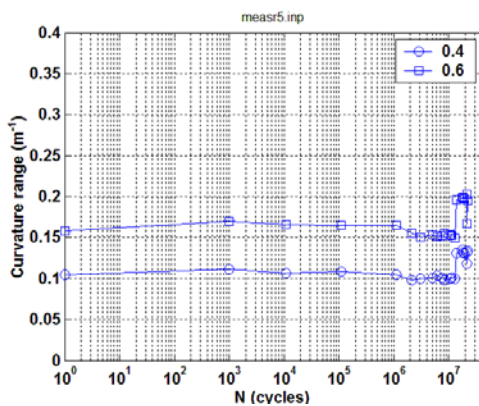
The online monitoring and measurement data are given in Fig. 42 and Fig. 43, respectively.



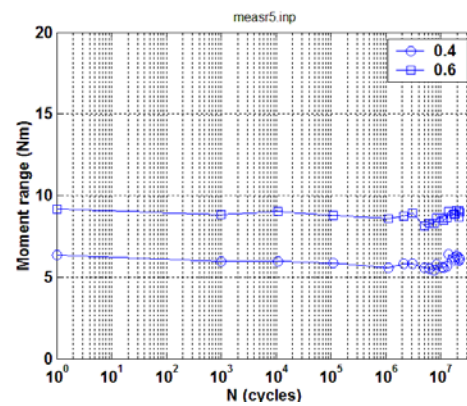


(e)

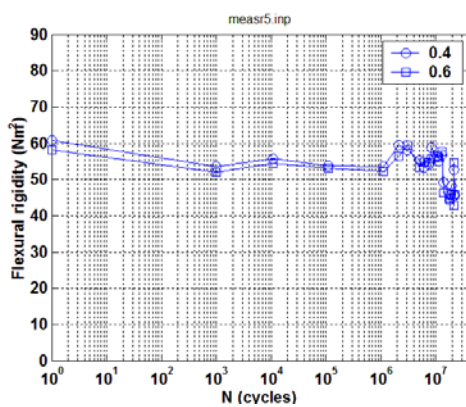
Fig. 42. Variations in (a) curvature range, (b) applied moment range, (c) flexural rigidity, (d) maximum and minimum values of curvature, and (e) maximum and minimum values of moment as a function of the number of cycles for R5 (606B3C); $N = 2.23 \times 10^7$ cycles at $\pm 7.62 \text{ N}\cdot\text{m}$, 5 Hz.



(a)



(b)



(c)

Fig. 43. Variations in (a) curvature range, (b) applied moment range, and (c) flexural rigidity as a function of the number of cycles for R5 (606B3C); $N = 2.23 \times 10^7$ cycles at $\pm 7.62 \text{ N}\cdot\text{m}$, 5 Hz.

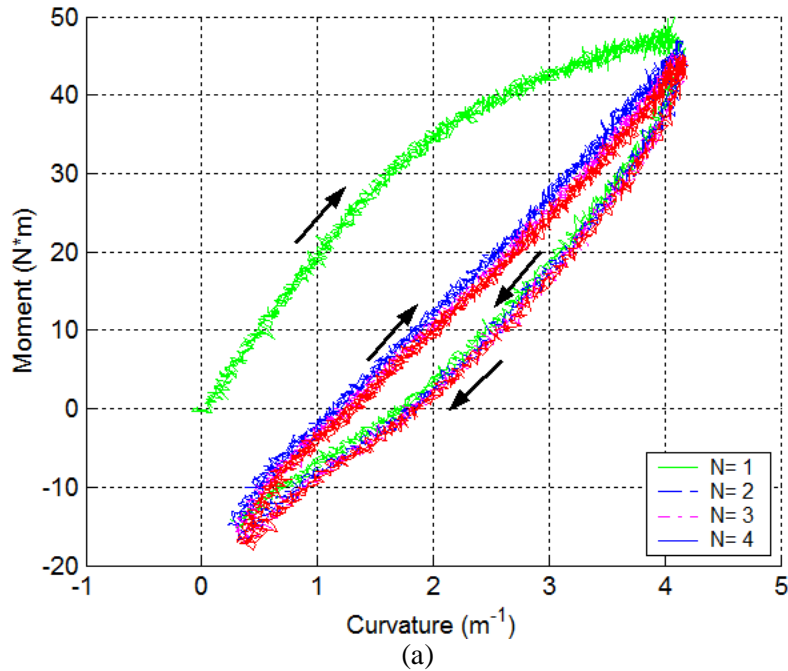
6. TESTING OF NORTH ANNA M5

6.1 NA3/651D3

The static test was conducted on the specimen with the CIRFT label NA3 (fuel segment 651D3) at a displacement control mode using the following test procedure.

1. Ramp up to 12.00 mm at 0.1 mm/s rate at each loading point or each Bose motor.
2. Return to 0.0 mm at 0.2 mm/s.
3. If the rod specimen does not fail, repeat steps 1 and 2 four times.

Specimen NA3 survived four loading cycles without any sign of failure. The moment-curvature curves and equivalent stress-strain curves are shown in Fig. 44. In the estimates of equivalent stress and strain, inside and outside diameters of 8.293 and 9.683 mm were used, respectively. There was a significant nonlinear deformation after 30 N·m; the maximum moment of 47 N·m was attained during the initial loading cycle. A deflection point appeared at approximately 8 N·m in the initial loading cycle. Subsequent loading cycles did not produce additional deformation, but they did introduce a closed hysteresis loop. The maximum curvature at a relative displacement of 24.00 mm at the loading points of the U-frame (i.e., 12.00 mm at each motor) was 4.1 m^{-1} . The maximum equivalent stress and strain obtained were 522 MPa and 2%, respectively. The rod appeared to be bent with significant plastic deformation after the static tests, as shown in Fig. 45.



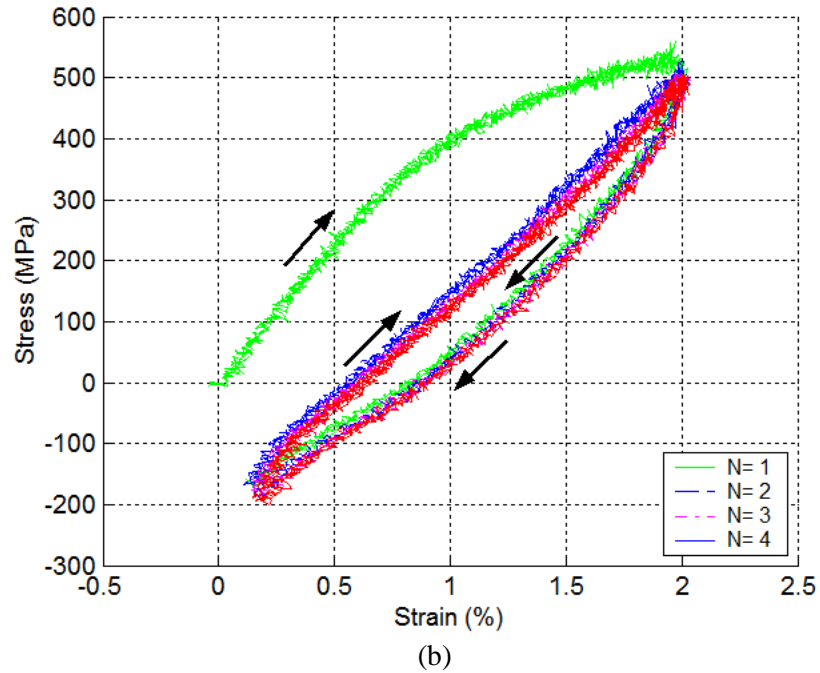


Fig. 44. (a) Moment-curvature curves and (b) equivalent stress-strain curves based on the first four loading cycles for specimen NA3 (651D3).

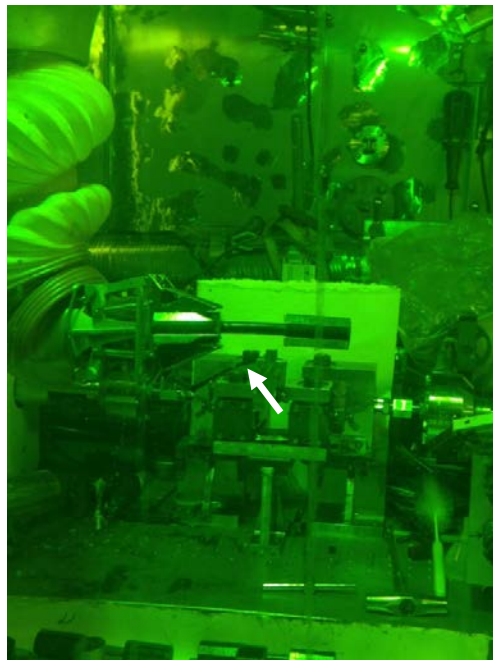


Fig. 45. Image of specimen NA3 (651D3) after testing; the rod sustained four cycles of loading to 24.00 mm relative displacement; the maximum moment of 47 N·m was reached during the initial loading cycle.

6.2 NA1/651C5 at 12.70 N·m, 5 Hz

The test on specimen NA1/651C5/ was conducted at ± 12.70 N·m, 5 Hz. A fatigue life of 1.57×10^4 cycles was obtained. Periodic quasistatic measurements of rod deformation were conducted using three relative displacement levels—1.0, 2.0, and 3.0 mm—at the selected target number of cycles as described in Wang and Wang.⁹ Time histories of moment and curvature and curvature-moment loops obtained at the first cycle and 11,000 cycles are shown in Fig. 46. The curvature-moment loops are quite twisted, without the regular elliptical shape seen before in HBR rods.⁹ The twisted loops may have been associated with the lowered sampling rate used in the curvature measurement. Nevertheless, the curvature ranges were still captured.

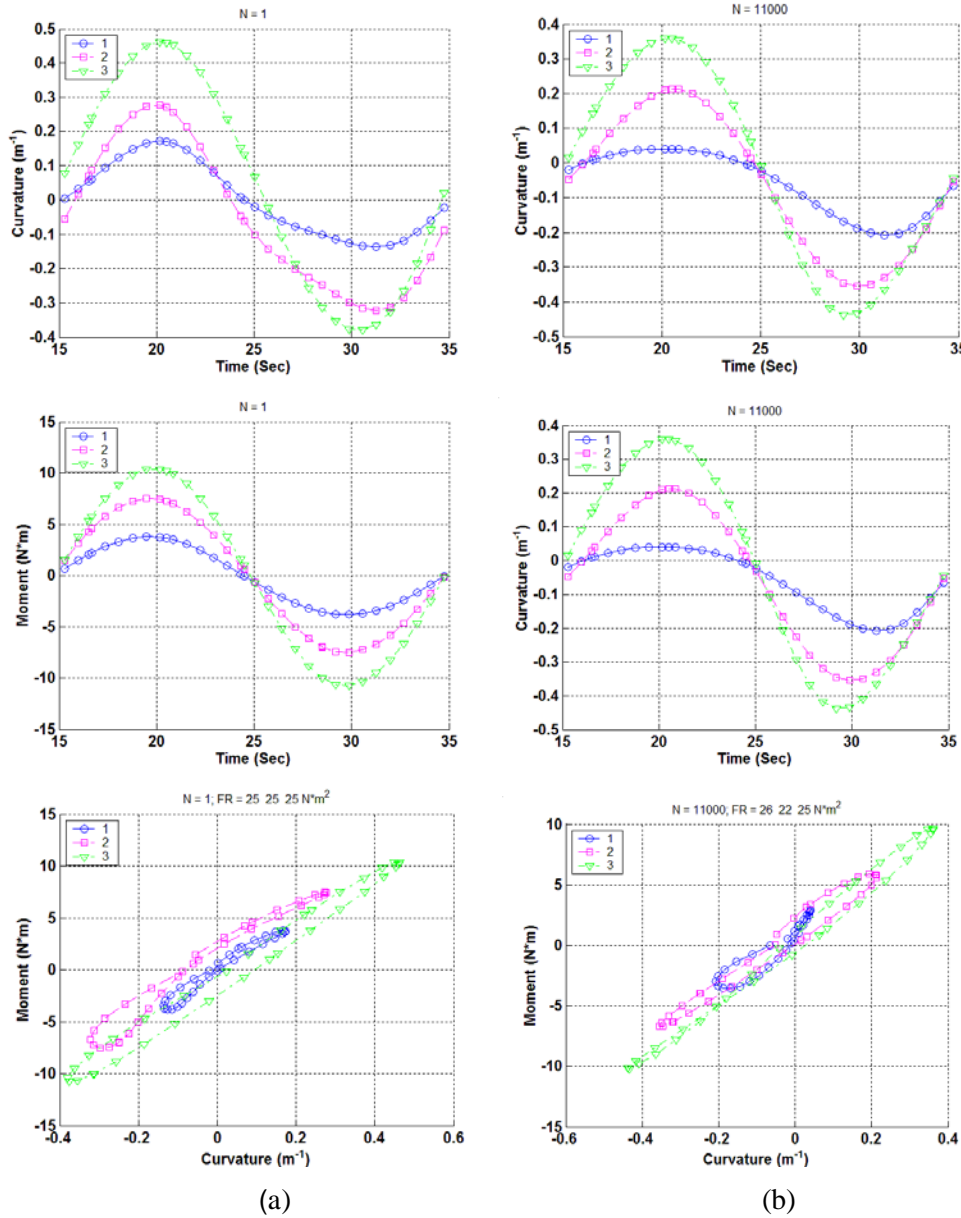


Fig. 46. Moment and curvature as a function of time and moment-curvature loops based on measurements when (a) $N=1$ and (b) $N = 111,000$ cycles for NA1 (651B2). Measurements were made with 1.0, 2.0, and 3.0 mm relative displacements; $N_f = 1.57 \times 10^4$ cycles at ± 12.70 N·m, 5 Hz.

The curvature range-moment range and flexural rigidity are illustrated in Fig. 47. The variations in these quantities as a function of the number of cycles are given in Fig. 48. The rigidity of the measurements at three displacements started with 25 N·m² and then dropped. The curvature, moment, and flexural rigidity based on online monitoring data are presented in Fig. 49. Online monitoring showed a flexural rigidity of about 24 N·m², slightly lower than the periodic measurement data. This discrepancy is because different loading conditions were used in measurement and cycling. Overall, a quite stable rod response was exhibited before the final failure. Moment and curvature time history and moment-curvature loops based on online monitoring at early and late stages of dynamic testing are shown in Fig. 50. The moment-curvature loops based on online monitoring were well defined. Except for slightly drifting toward the left, no significant change can be observed between loops measured in two points of the cycle process. The failure was observed in the gage section, as seen in Fig. 51. The fracture surface is not clearly visible at this level of resolution.

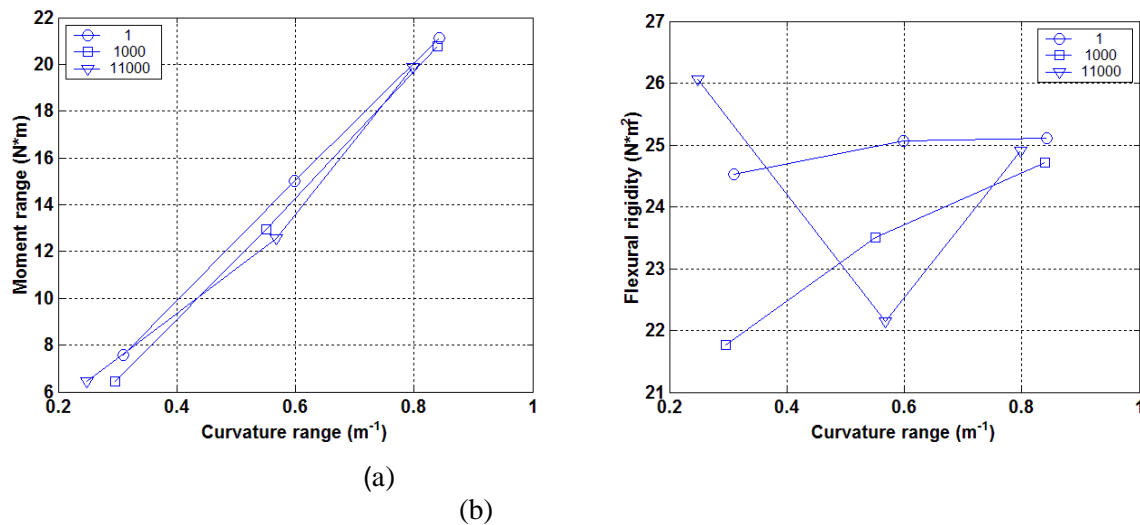


Fig. 47. (a) Moment-curvature relation and (b) moment-flexural rigidity relation at various numbers of cycles for NA1 (651B2). Measurements were made with 1.0, 2.0, and 3.0 mm relative displacements; $N_f = 1.57 \times 10^4$ cycles at ± 12.70 N·m, 5 Hz.

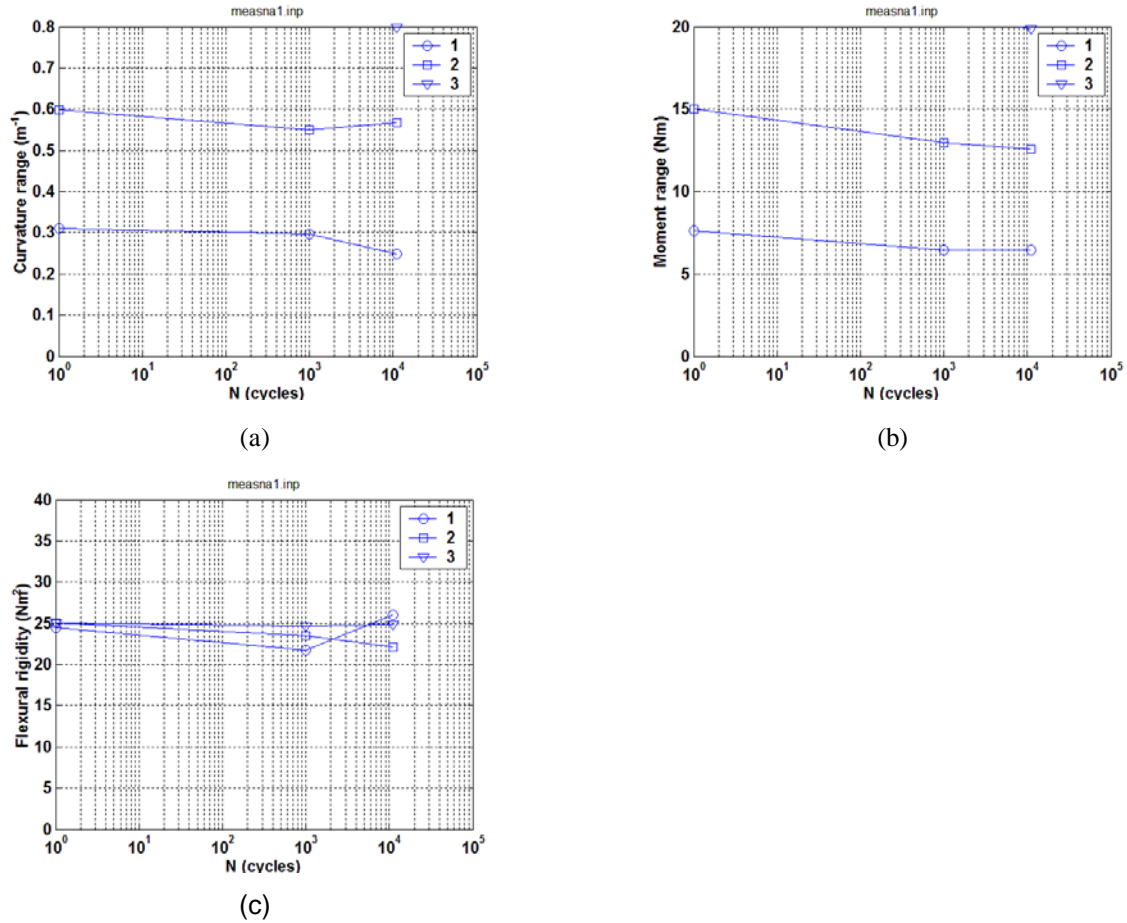


Fig. 48. Variations in (a) curvature range, (b) moment range, and (c) flexural rigidity as a function of the number of cycles for NA1 (651B2). Measurements were made with 1.0, 2.0, and 3.0 mm relative displacements; $N_f = 1.57 \times 10^4$ cycles at ± 12.70 N·m, 5 Hz.

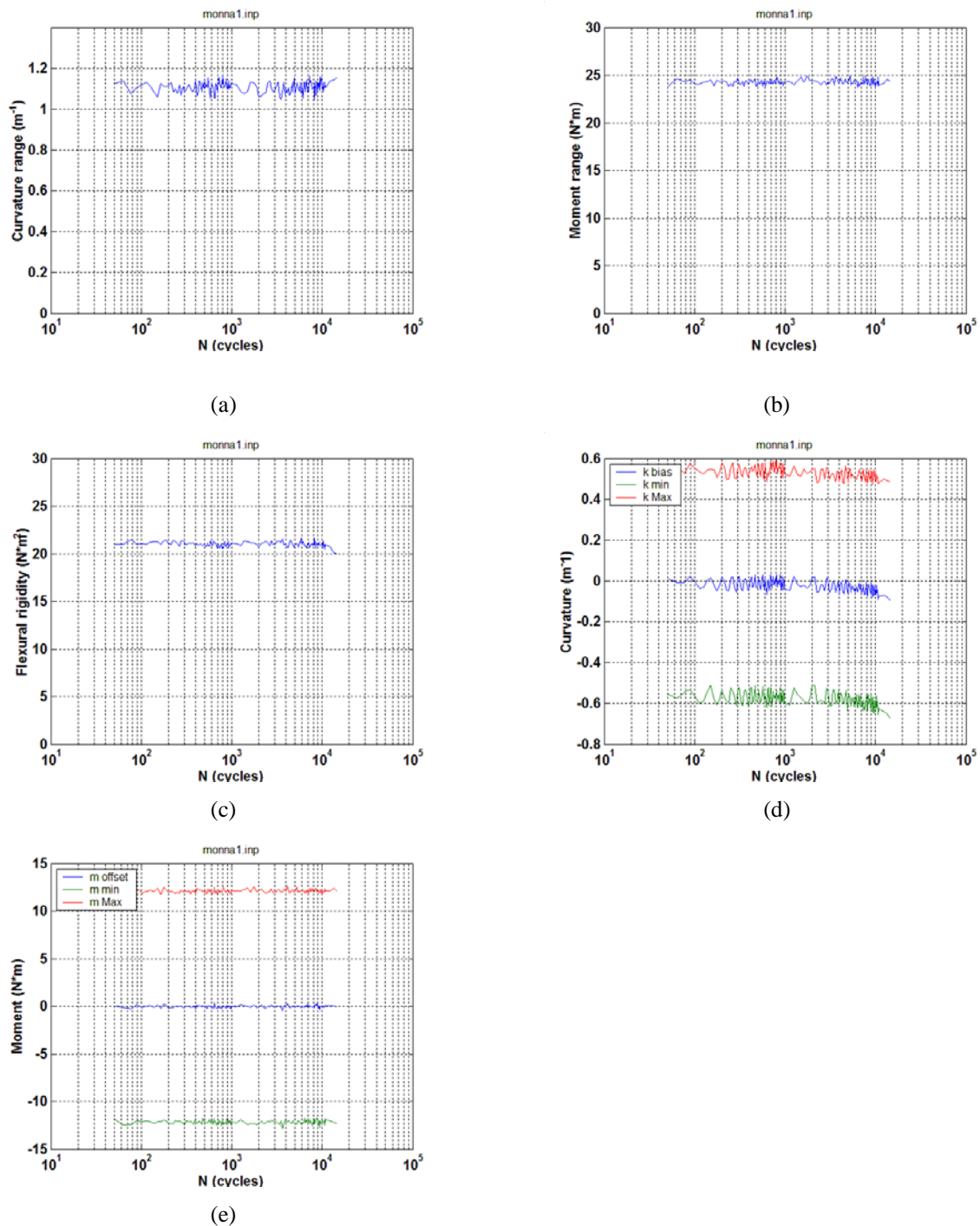


Fig. 49. Variations in (a) curvature range, (b) applied moment range, (c) flexural rigidity, (d) maximum and minimum values of curvature, and (e) maximum and minimum values of moment as a function of the number of cycles for NA1 (651B2); $N_f = 1.57 \times 10^4$ cycles at ± 12.70 N·m, 5 Hz.

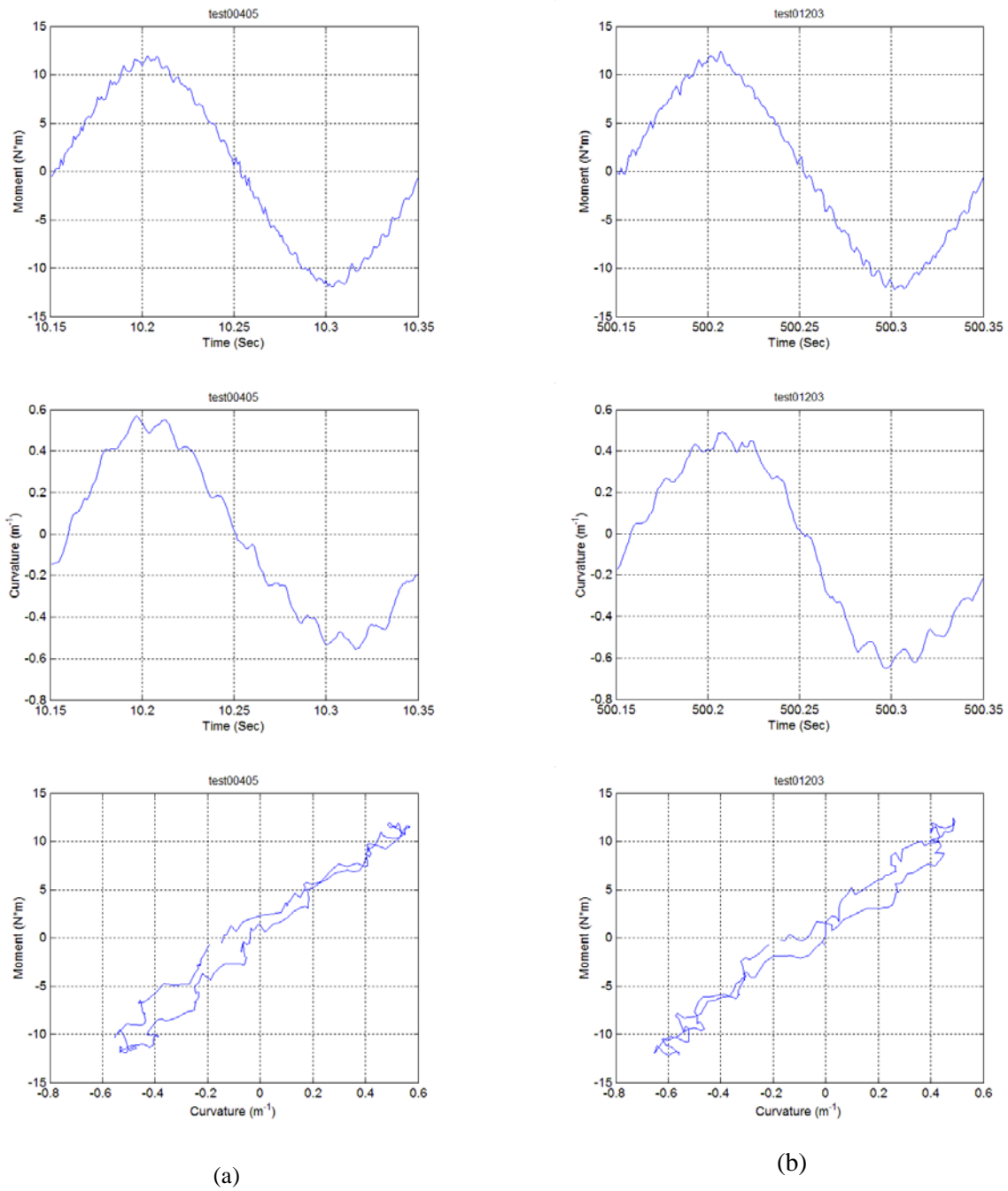


Fig. 50. Moment and curvature as a function of time and moment-curvature loops at (a) 50 cycles and (b) 1.35×10^4 cycles; results are based on online monitoring of NA1 (651B2).

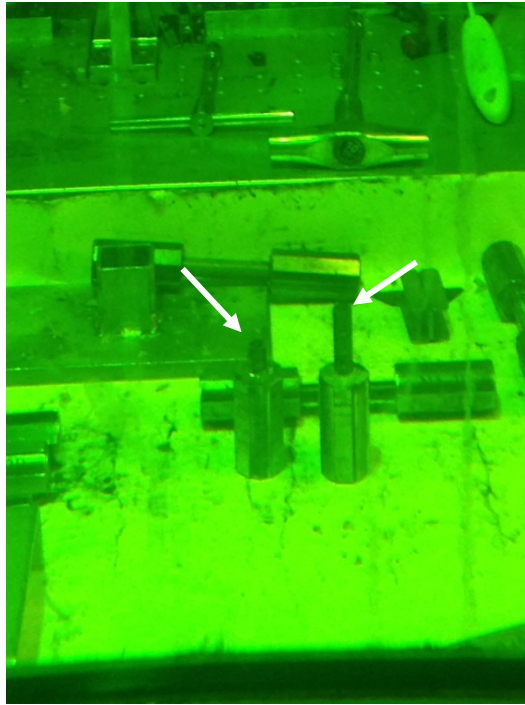


Fig. 51. Fracture segments for NA1 (651B2); $N_f = 1.57 \times 10^4$ cycles at ± 12.70 N·m, 5 Hz.

6.3 NA2/651C5 at 10.16 N·m, 5 Hz

The test on NA2 (651C5) was conducted at ± 10.16 N·m, 5 Hz. A fatigue life of 2.2×10^4 cycles was obtained.

Periodic quasistatic measurements of rod deformation were conducted using two relative displacement levels—1.0 and 2.0 mm—at the target intervals as described in Wang and Wang.⁹ Variations in the curvature, moment, and flexural rigidity as a function of the number of cycles are given in Fig. 52. The flexural rigidity of the rod stayed between 22 and 25 N·m² during most of the cycle testing period. This value of rigidity is slightly lower than but still close to that of NA2. The results from online monitoring are given in Fig. 53, and the image showing the failure location of the rod specimen is given in Fig. 54.

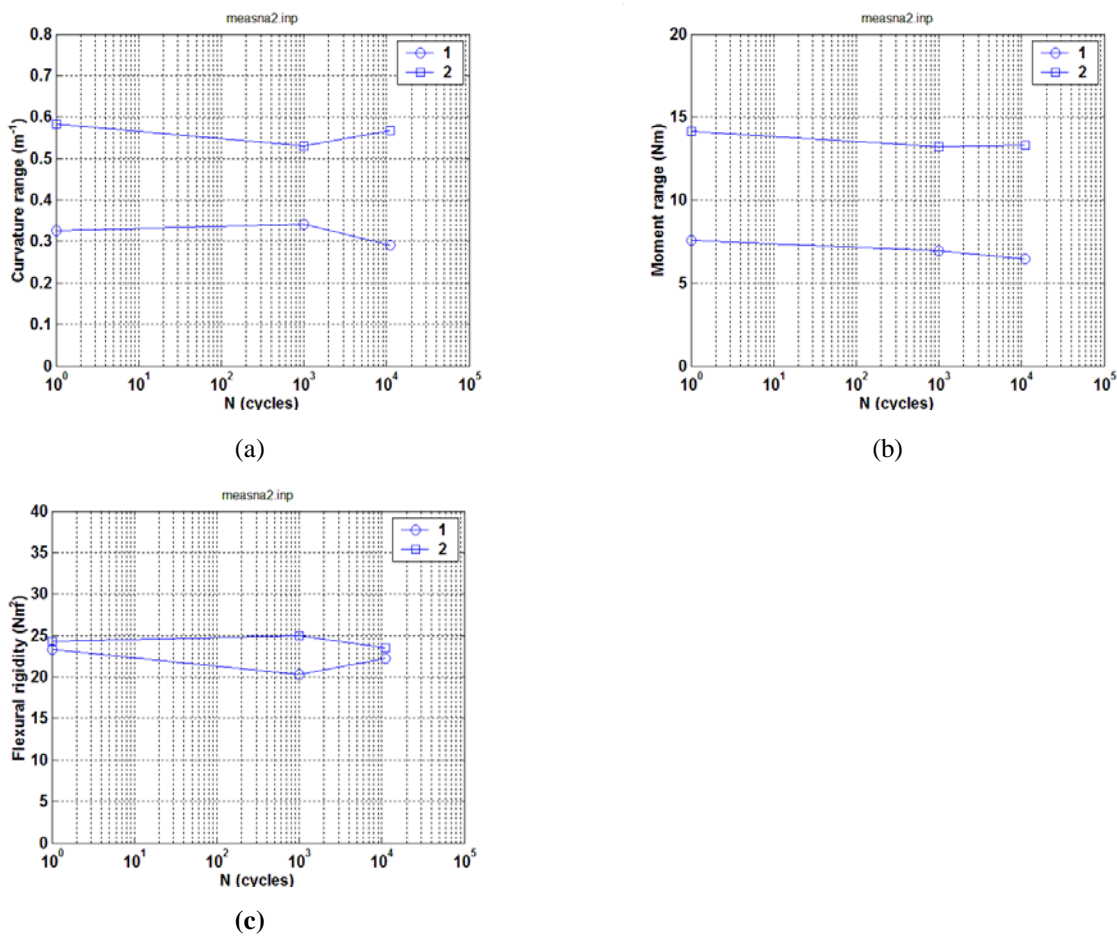


Fig. 52. Variations in (a) curvature range, (b) moment range, and (c) flexural rigidity as a function of the number of cycles for NA2 (651C5). Measurements were made with 1.0 and 2.0 mm relative displacements; $N_f = 2.2 \times 10^4$ cycles at ± 10.16 N·m, 5 Hz.

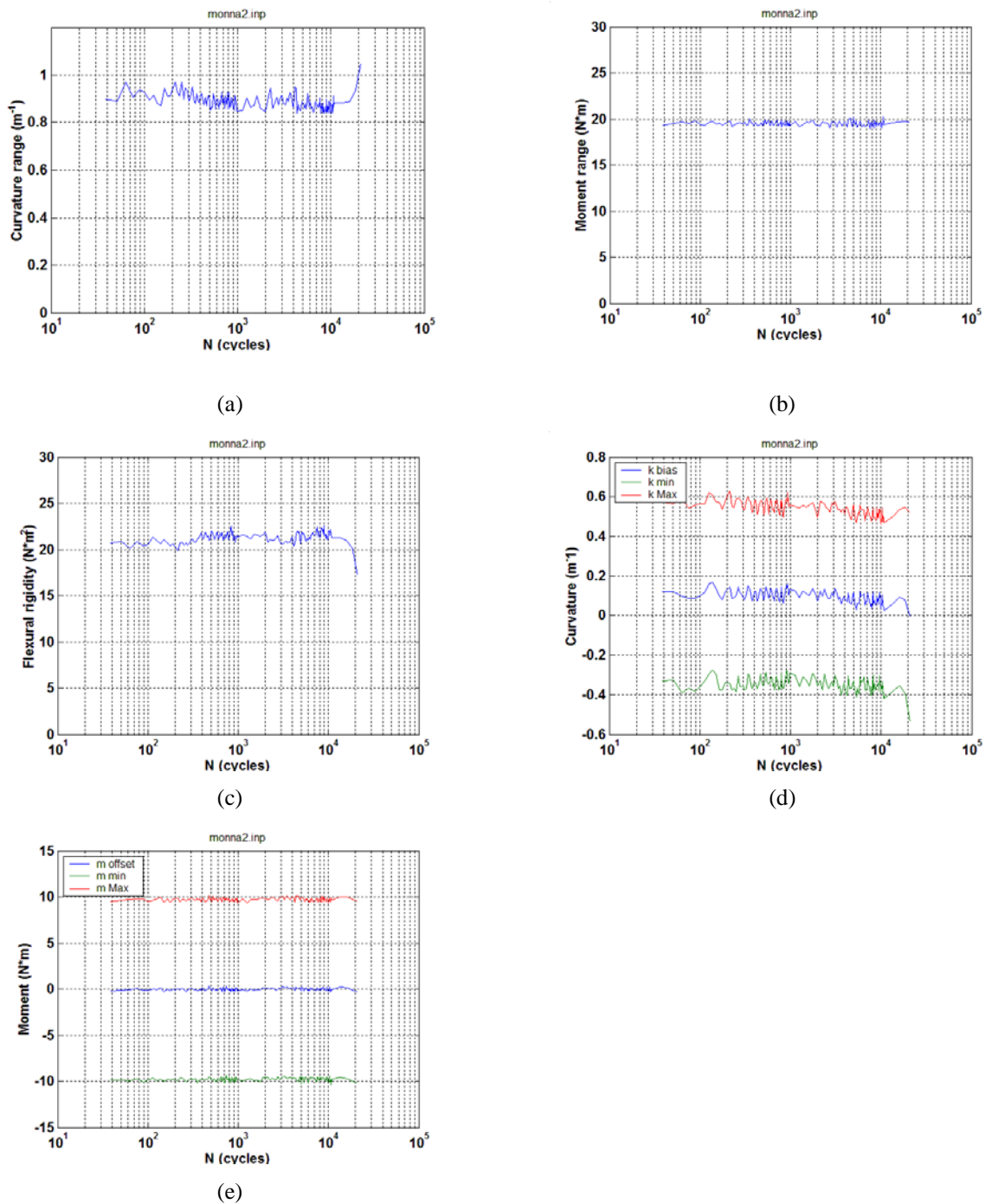


Fig. 53. Variations in (a) curvature range, (b) applied moment range, (c) flexural rigidity, (d) maximum and minimum values of curvature, and (e) maximum and minimum values of moment as a function of the number of cycles for NA2 (651C5); $N_f = 2.2 \times 10^4$ cycles at $\pm 10.16 N \cdot m$, 5 Hz.

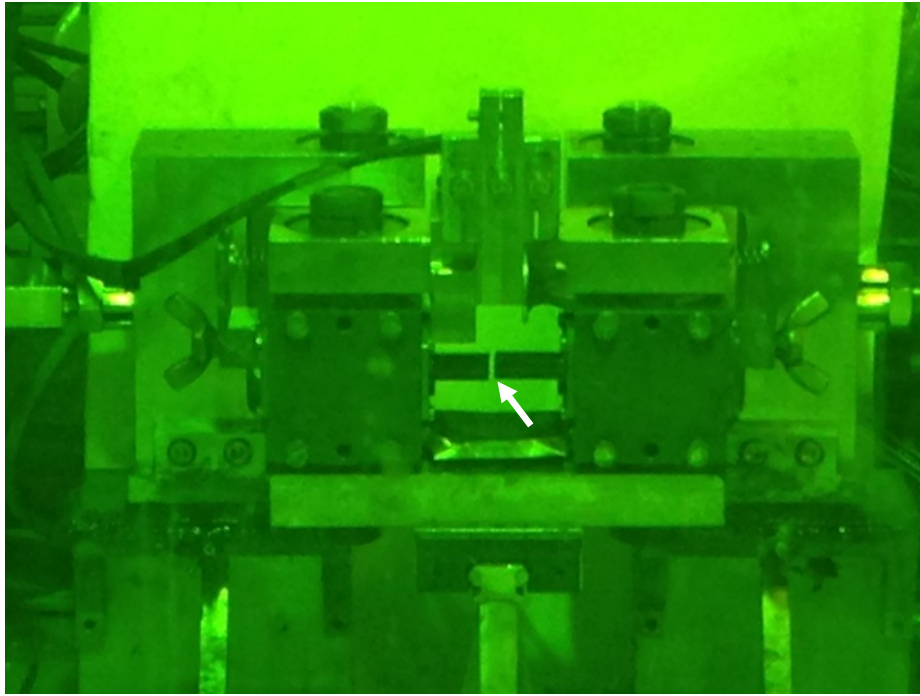


Fig. 54. Fracture location of NA2 (651C5), $N_f = 2.2 \times 10^4$ cycles at ± 10.16 N·m, 5 Hz.

6.4 NA4/652B1B at 7.62 N·m, 5 Hz

The test on NA4 (652B1B) was conducted at ± 7.62 N·m, 5 Hz. A fatigue life of 6.1×10^4 cycles was obtained.

Again, periodic quasistatic measurements of rod deformation were conducted using two relative displacement levels—0.8 and 1.6 mm—at the target intervals. Variations in the curvature, moment, and flexural rigidity as a function of the number of cycles are given in Fig. 55. The initial values of flexural rigidity ranged between 24.5 and 28 N·m². The level of rigidity is apparently close to the values observed for NA1 and NA2. The flexural rigidity of NA4 exhibited an increasing trend during the period of the test cycle, especially in the case of the 0.8 mm measurement. This increasing trend was also observed in the variation in flexural rigidity (Fig. 56). At the same time, a positive offset of curvature was found for the rod under reverse bending. The mean value of curvature was around 0.05 m⁻¹.

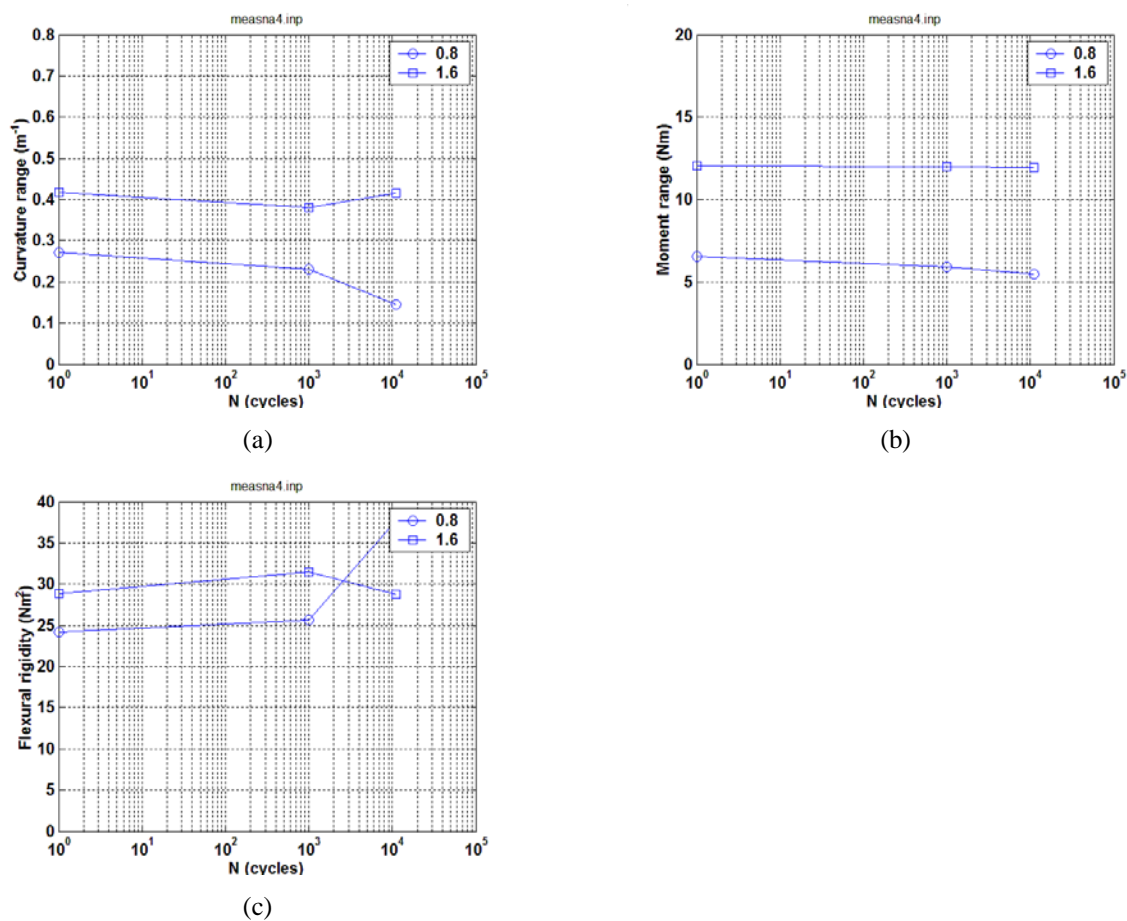


Fig. 55. Variations in (a) curvature range, (b) moment range, and (c) flexural rigidity as a function of the number of cycles for NA4 (652B1B). Measurements were made with 1.0 and 2.0 mm relative displacements; $N_f = 6.1 \times 10^4$ cycles at ± 7.62 N·m, 5 Hz.

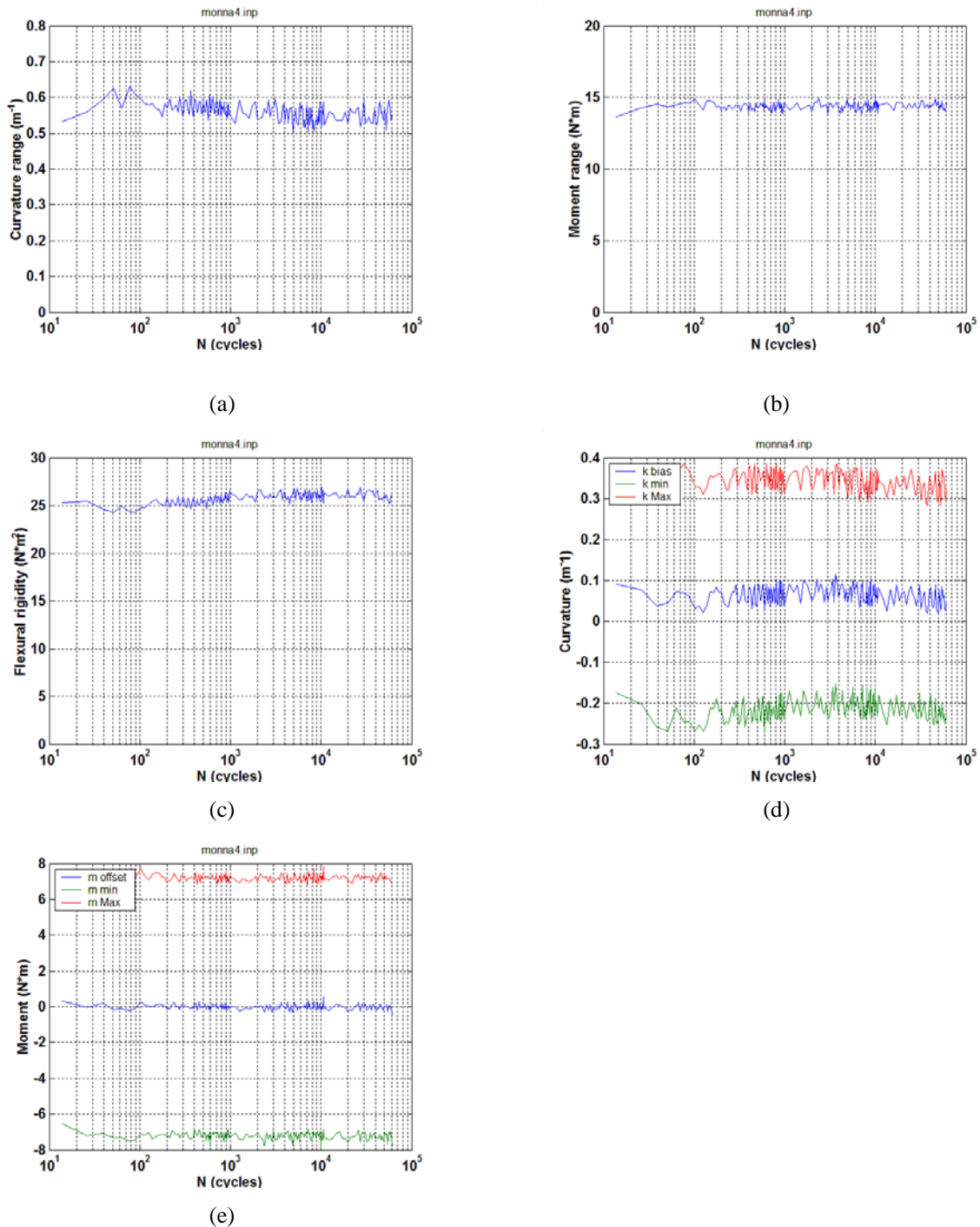


Fig. 56. Variations in (a) curvature range, (b) applied moment range, (c) flexural rigidity, (d) maximum and minimum values of curvature, and (e) maximum and minimum values of moment as a function of the number of cycles for NA4 (652B1B); $N_f = 6.1 \times 10^4$ cycles at ± 7.62 N·m, 5 Hz.

6.5 NA5/652B2 at 5.08 N·m, 5 Hz

The test on NA5 (652B2) was conducted at ± 5.08 N·m, 5 Hz. The specimen sustained 5.11×10^6 total cycles and did not show any sign of failure, so the test was stopped.

Periodic quasistatic measurements of rod deformation were conducted using two relative displacement levels—0.4 and 0.8 mm—at the target intervals.

Further data analyses will be performed in the next report cycle.

6.6 NA6/652D1 at 5.08 N·m, 5 Hz

The test on NA6 (652D1) was conducted at ± 5.08 N·m, 5 Hz. A fatigue life of 4.27×10^5 cycles was obtained.

Periodic quasistatic measurements of rod deformation were conducted using two measurement displacements on the loading frame.

Further data analyses will be performed in the next report cycle.

6.7 NA7/652D2 at 15.24 N·m, 5 Hz

The test on NA7 (652D2) was conducted at ± 15.24 N·m, 5 Hz. A fatigue life of 1.26×10^4 cycles was obtained.

Periodic quasistatic measurements of rod deformation were conducted using two displacements, 0.4 and 0.8 mm, on the U-frame.

Further data analyses will be performed in the next report cycle.

7. TESTING RESULTS ON MOX

7.1 MOX1/MOX-A-11

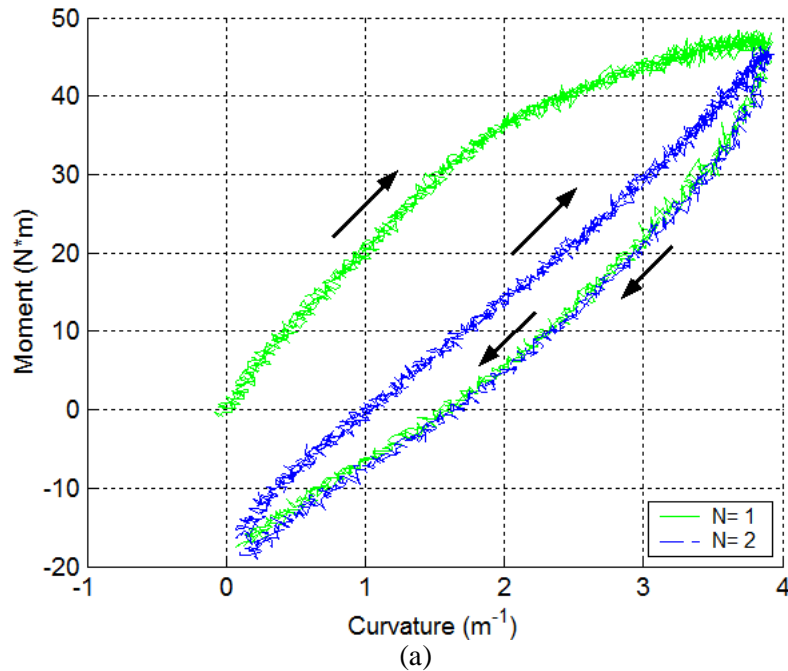
The first static test was conducted on MOX1 SNF (specimen MOX-A-11) under a displacement control mode using the following test procedure.

1. Ramp up to 12.00 mm at 0.1 mm/s rate at each loading point or each Bose motor.
2. Return to 0.0 mm at 0.2 mm/s.
3. If the rod specimen does not fail, repeat steps 1 and 2 four times.

No hot-cell measurement data are available on the MOX SNF segment. The inside and outside diameters of the NA fuel rod segment (8.293 and 9.683 mm, respectively) are used as a reference in the analysis below. The MOX1 specimen survived two loading cycles without any sign of failure.

The moment-curvature curves and equivalent stress-strain curves based on the first four loading cycles for MOX1 (specimen MOX-A-11) are shown in Fig. 57. There was a significant nonlinear deformation after 30 N·m; the maximum moment of 47 N·m was reached during the initial loading cycle. A deflection point appeared at approximately 8 N·m in the initial loading cycle. Subsequent loading cycles did not produce additional deformation, but loadings generated a closed hysteresis loop. The maximum curvature under a relative displacement of 24.00 mm at the loading points of the U-frame (i.e., 12.00 mm at each motor) was 3.85 m^{-1} . The maximum equivalent stress and strain were 520 MPa and 1.8%, respectively.

A dynamic test was carried out at $\pm 15.24 \text{ N}\cdot\text{m}$, 5 Hz to observe the failure mode of the rod. The fatigue life of the rod was $N_f = 4.0 \times 10^3$ cycles. The rod finally failed in the gage section, as shown in Fig. 58.



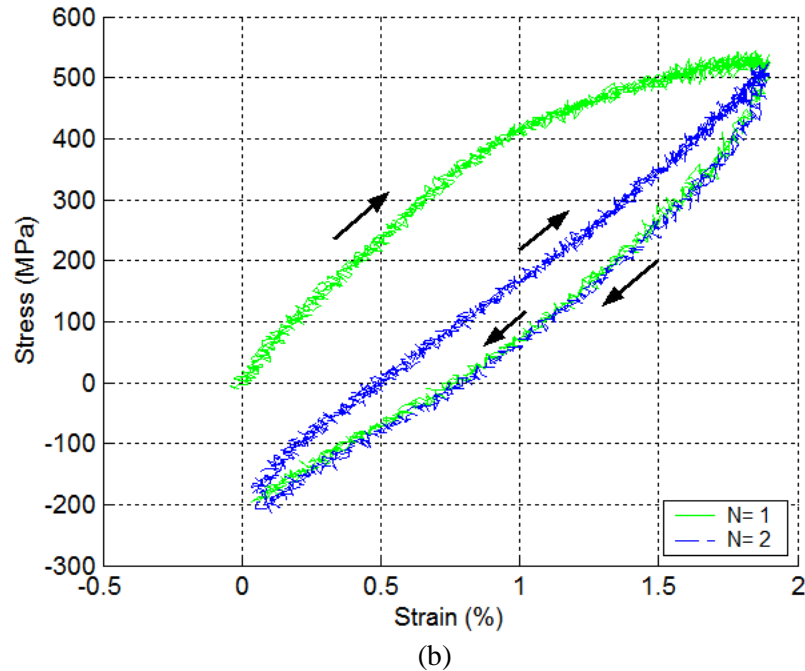


Fig. 57. (a) Moment-curvature curves and (b) equivalent stress-strain curves based on the first four loading cycles for MOX1 (specimen MOX-A-11).

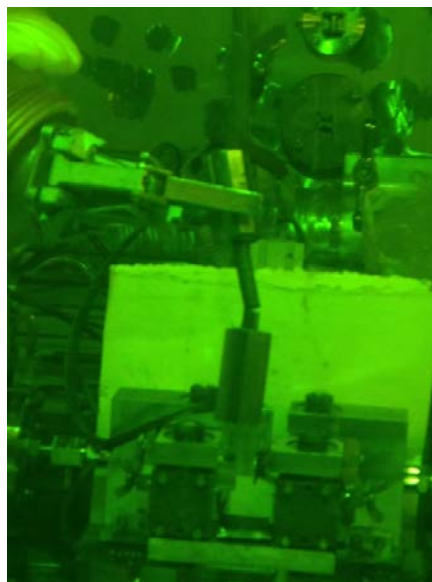


Fig. 58. Fracture segments for MOX1 (specimen MOX-A-11); the rod survived two cycles of loading to a relative displacement of 24.00 mm with a maximum moment of 47 N·m in the initial cycle. A follow-up dynamic test was carried out at ± 15.24 N·m, 5 Hz; $N_f = 4.0 \times 10^3$ cycles.

7.2 MOX3/MOX-A-13

The MOX3 (specimen MOX-A-13) was tested using the same procedure as that of MOX1, but only the first two steps were executed.

The moment-curvature curves and equivalent stress-strain curves are shown in Fig. 59. The second stage as seen in MOX1 and other HBR fuel specimens is hard to identify because the moment-curvature curve turned out to be nonlinear starting at approximately 9 N·m. The maximum moment was 45 N·m. The maximum curvature under a relative displacement of 24.00 mm at the loading points of the U-frame (i.e., 12.00 mm at each motor) was 3.53 m^{-1} . The maximum equivalent stress and strain were 510 MPa and 1.7%, respectively.

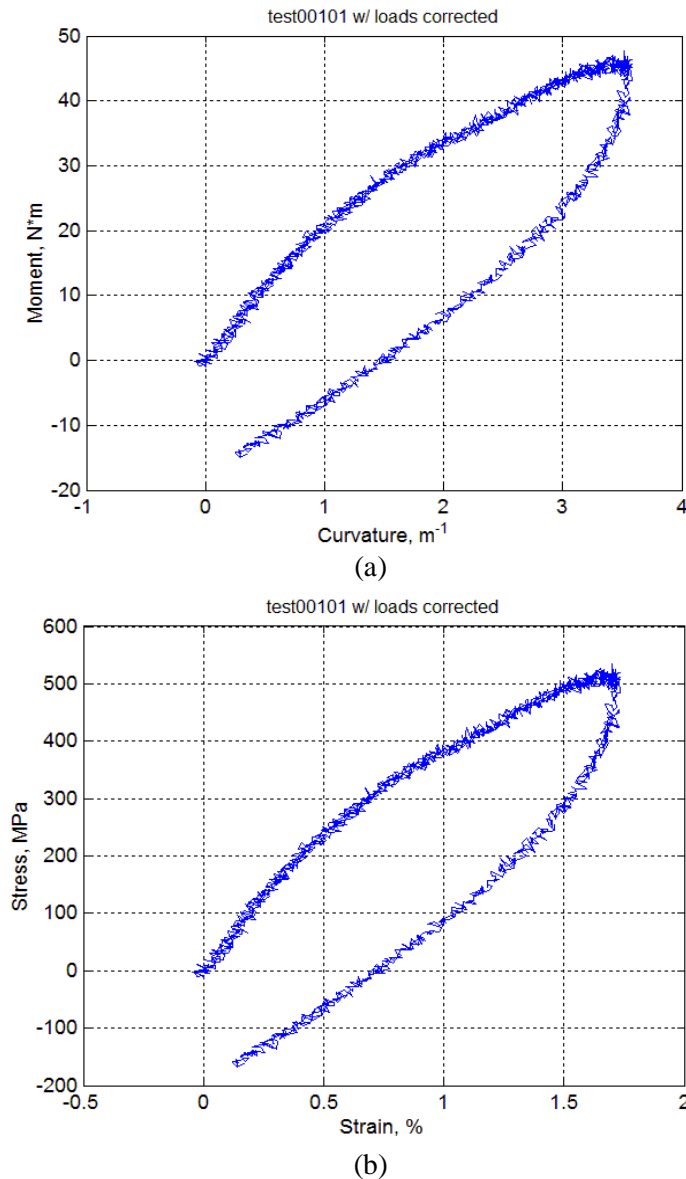


Fig. 59 (a) Moment-curvature curves and (b) equivalent stress-strain curves based on the first four loading cycles for MOX3 (MOX-A-13).

7.3 MOX2/MOX-A-12 at 10.16 N·m, 5 Hz

The test on MOX2/MOX-A-12 was conducted at ± 10.16 N·m, 5 Hz. A fatigue life of 3.70×10^4 cycles was obtained.

Periodic quasistatic measurements of rod deformation were conducted using two relative displacement levels—0.8 and 1.6 mm—at the selected target number of cycles, as described above. Investigation into the distorted moment-curvature loop indicated that the distortion may result from a reduced sample rate. Therefore, the sampling rate was adjusted to that used for dynamic tests of HBR fuel. Time histories of moment and curvature and curvature-moment loops obtained at the first cycle and 11,000 cycles are shown in Fig. 60. The regular curvature-moment loops were obtained with the modified data acquisition setting.

The curvature range–moment range and flexural rigidity are illustrated in Fig. 61. The variations in these quantities as a function of the number of cycles are given in Fig. 62. The rigidity of the measurements clearly showed a decreasing trend starting with $24 \text{ N}\cdot\text{m}^2$ and then dropping to $20 \text{ N}\cdot\text{m}^2$ at 1.1×10^4 cycles.

The curvature range, moment range, and flexural rigidity based on online monitoring data are presented in Fig. 63, along with the maxima and minima. Online monitoring showed that flexural rigidity was essentially stable with a small amount of decrease (19 to $18 \text{ N}\cdot\text{m}^2$) prior to the failure. The degree of decrease is lower than the value seen in the measurement. At the same time, the positive offset of curvature with an initial level of 0.1 m^{-1} tended to decrease during the cycle test. Moment and curvature time history and moment-curvature loops based on online monitoring at early and late stages of dynamic testing are illustrated in Fig. 64. It can be seen that moment-curvature loops based on online monitoring were actually well defined. Except for slightly drifting toward the left, no significant change can be observed between loops measured in the two points of the cycle process.

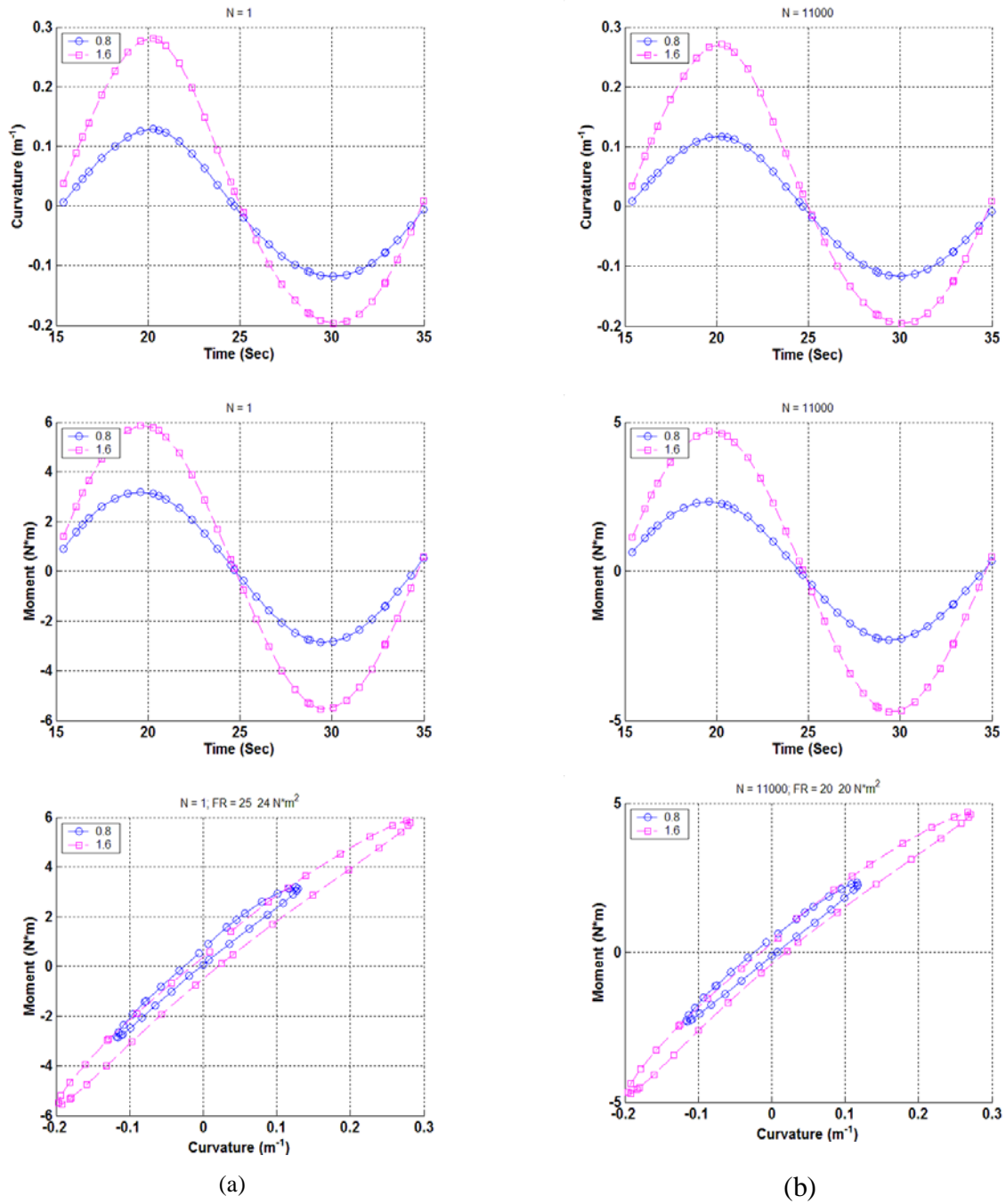


Fig. 60. Moment and curvature as a function of time and moment-curvature loops based on measurements when (a) N=1 and (b) N = 111,000 cycles for MOX2 (MOX-A-12). Measurements were made with 0.8 and 1.6 mm relative displacements; $N_f = 3.7 \times 10^4$ cycles at ± 10.16 N·m, 5 Hz.

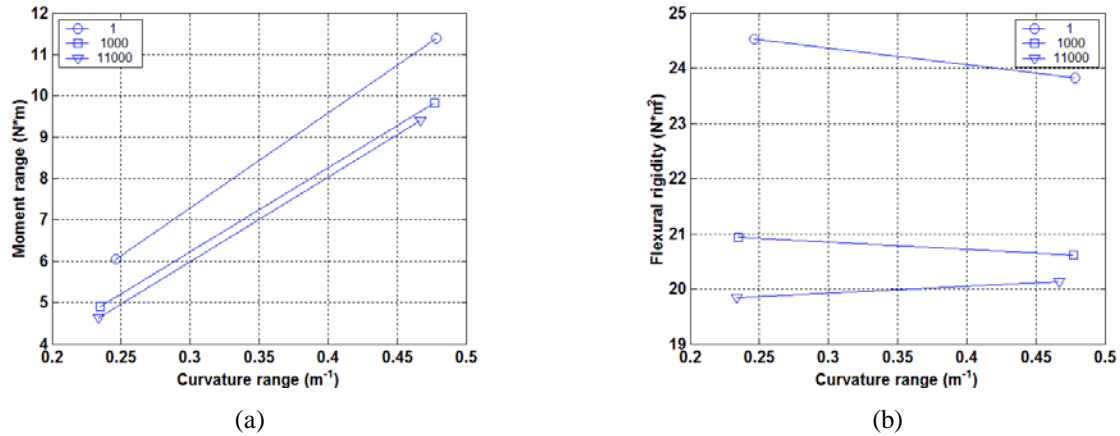


Fig. 61 (a) Moment-curvature relation and (b) moment-flexural-rigidity relation at various numbers of cycles for MOX (MOX-A-12). Measurements were made with 0.8 and 1.6 mm relative displacements; $N_f = 3.7 \times 10^4$ cycles at ± 10.16 N·m, 5 Hz.

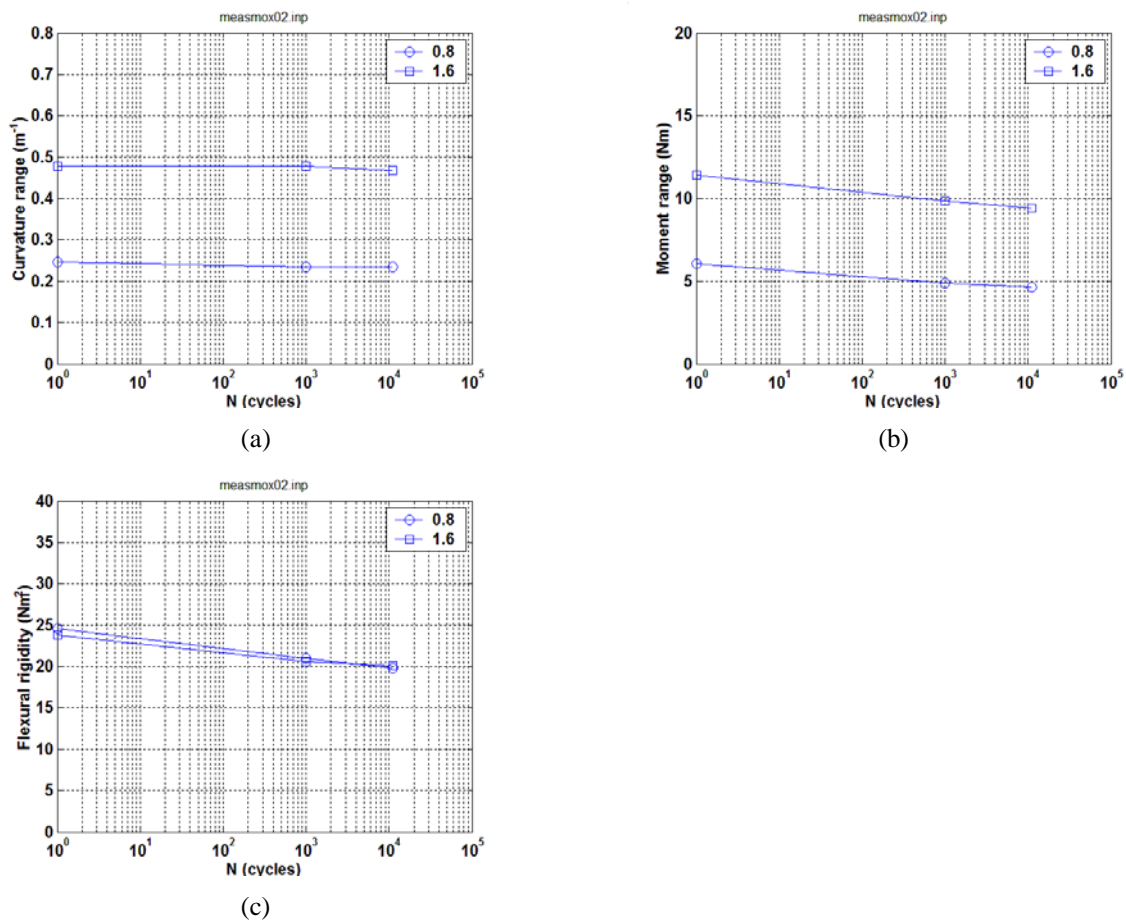


Fig. 62. Variations in (a) curvature range, (b) moment range, and (c) flexural rigidity as a function of the number of cycles for MOX (MOX-A-12). Measurements were made with 0.8 and 1.6 mm relative displacements; $N_f = 3.7 \times 10^4$ cycles at ± 10.16 N·m, 5 Hz.

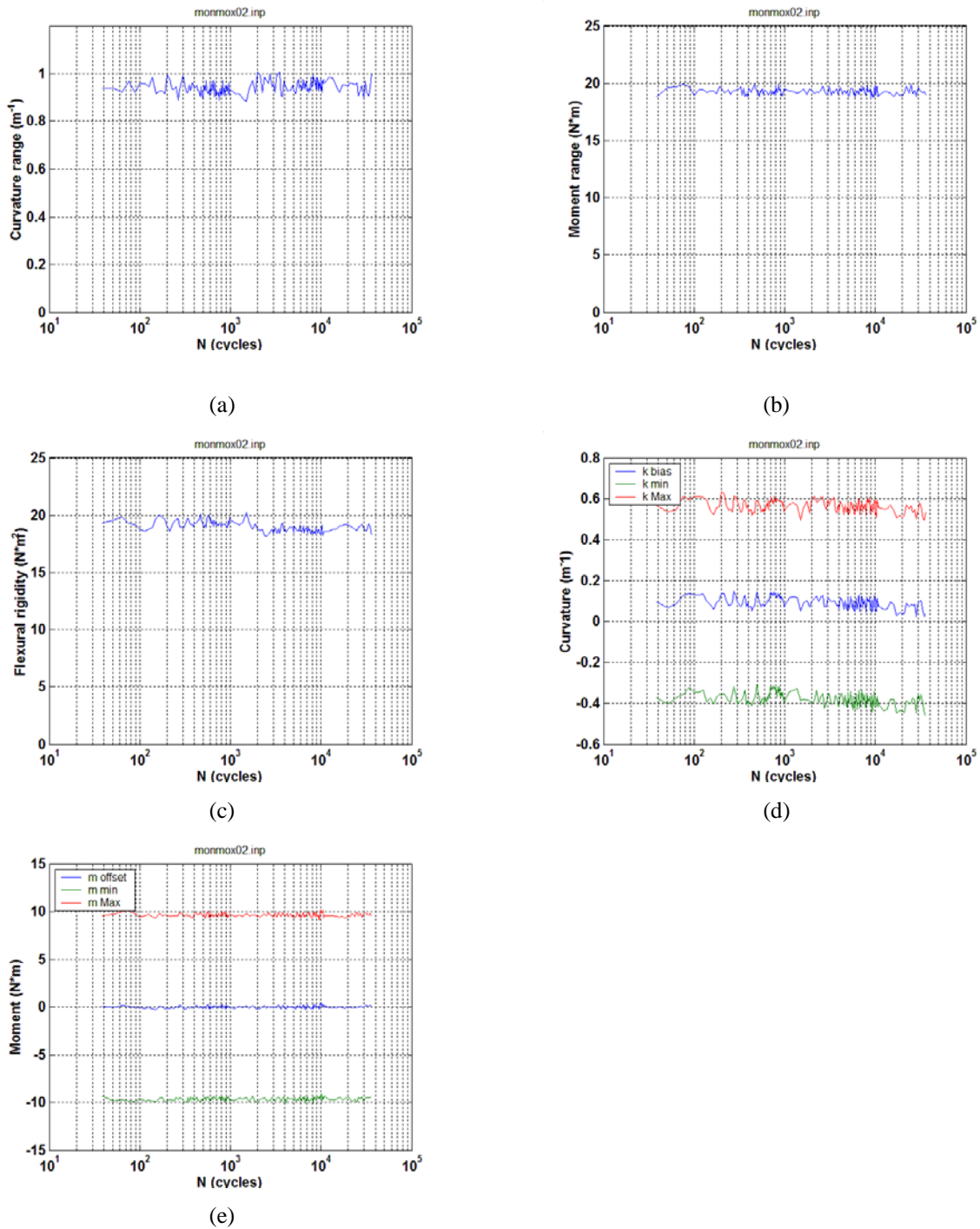


Fig. 63. Variations in (a) curvature range, (b) applied moment range, (c) flexural rigidity, (d) maximum and minimum values of curvature, and (e) maximum and minimum values of moment as a function of the number of cycles for MOX2 (MOX-A-12); $N_f = 3.7 \times 10^4$ cycles at ± 10.16 N·m, 5 Hz.

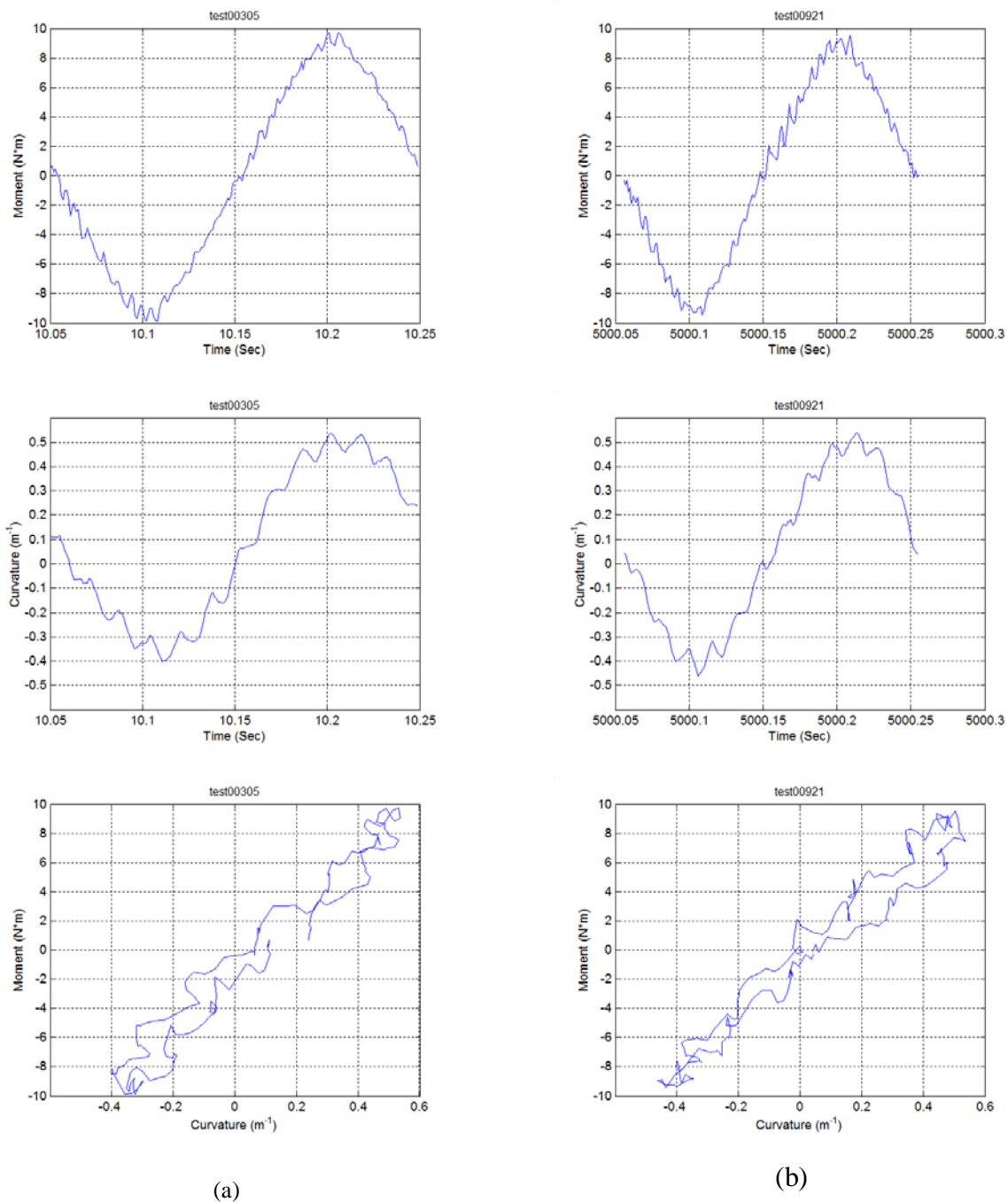


Fig. 64. Moment and curvature as a function of time and moment-curvature loops at (a) 50 cycles and (b) 3.6×10^4 cycles; results are based on online monitoring of MOX2 (MOX-A-12); $N_f = 3.7 \times 10^4$ cycles at ± 10.16 N·m, 5 Hz.

7.4 MOX4/MOX-B-05 at 5.08 N·m, 5 Hz

The test on MOX4/MOX-B-05 was conducted at ± 5.08 N·m, 5 Hz. A fatigue life of 2.15×10^6 cycles was obtained.

Periodic quasistatic measurements of rod deformation were conducted using two relative displacement levels—0.4 and 0.7 mm—at the selected target number of cycles as described above, and results are given in Fig. 65. The moment range exhibited a decreasing trend, and flexural rigidity showed a similar decrease. The effect of measurement displacement on the rigidity response was seen at the beginning, but it became diminished at the later stage of the test. The initial level of rigidity was slightly higher than that of MOX2, perhaps due to the smaller displacement used in the measurement of this specimen. The overall decrease in rigidity was about 20%.

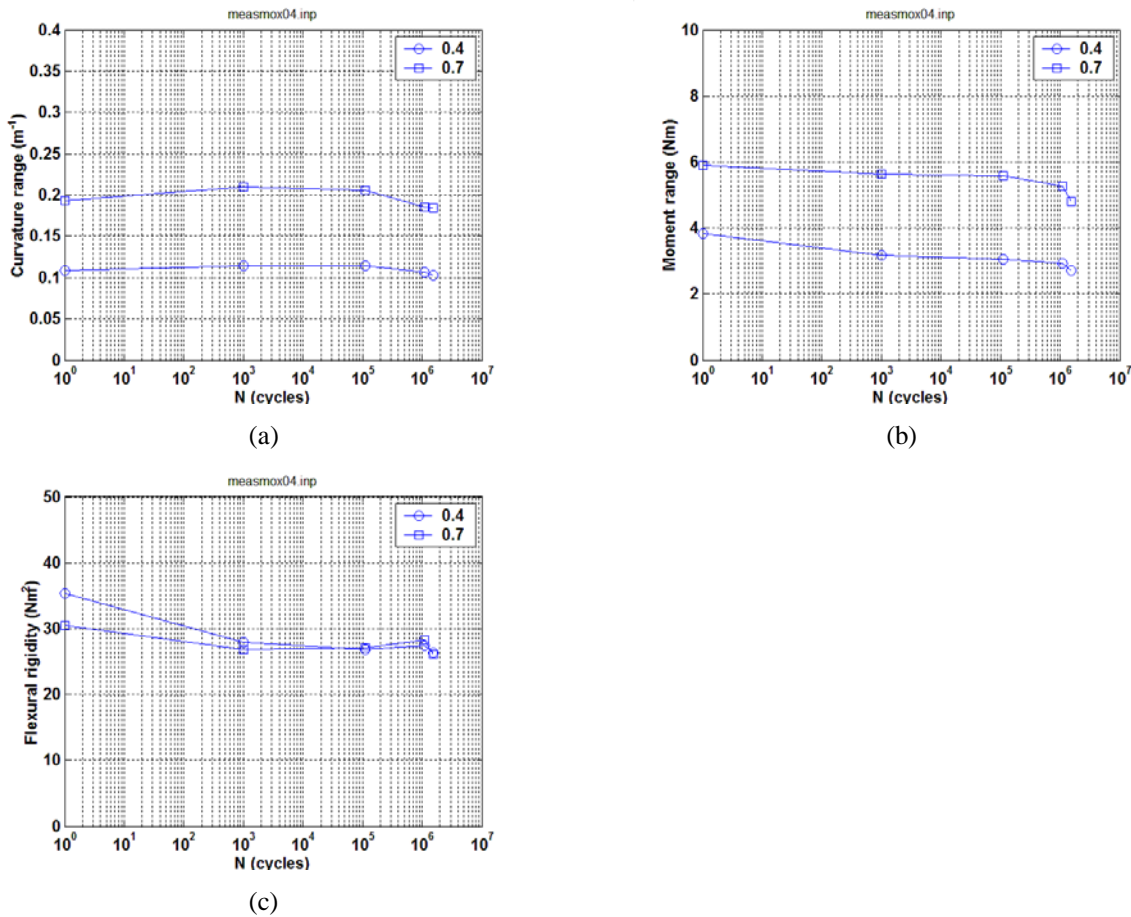


Fig. 65. Variations in (a) curvature range, (b) moment range, and (c) flexural rigidity as a function of the number of cycles for MOX4 (MOX-B-05). Measurements were made with 0.4 and 0.7 mm relative displacements; $N_f = 2.15 \times 10^6$ cycles at ± 5.08 N·m, 5 Hz.

Flexural rigidity from online monitoring exhibited a rise-and-fall trend during the cycle test, as shown in Fig. 66. The rigidity started with 22.5, increased to 24.5, and dropped to 23 N·m² prior to the failure. Detailed examination showed that the moment-curvature loop drifted downward along with the accumulated number of cycles, as can be seen from the parallel curvature fatigue curves. The fatigue failure seemed related to the single-side fracture development.

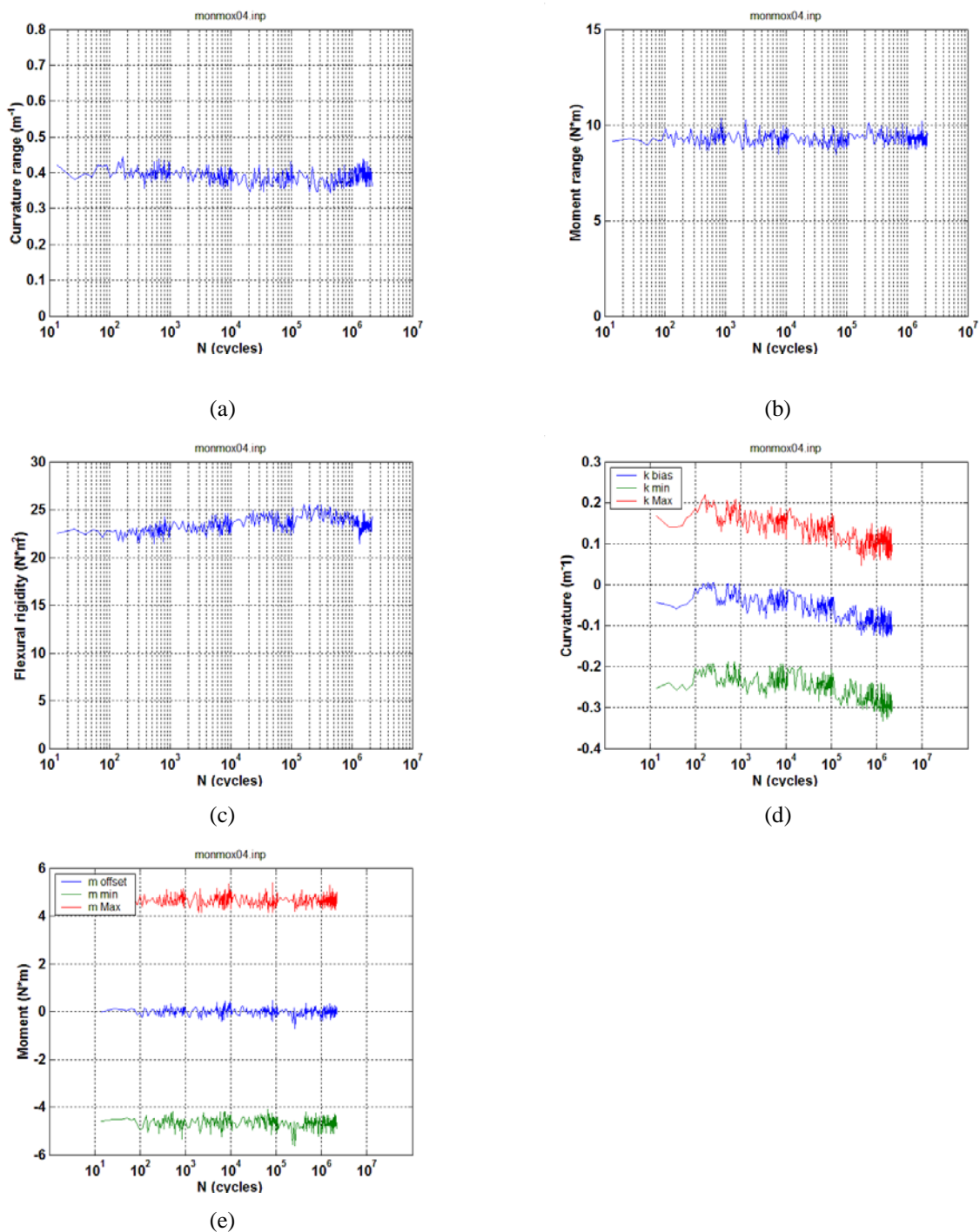


Fig. 66. Variations in (a) curvature range, (b) applied moment range, (c) flexural rigidity, (d) maximum and minimum values of curvature, and (e) maximum and minimum values of moment as a function of the number of cycles for MOX4 (MOX-B-05); $N_f = 2.15 \times 10^6$ cycles at ± 5.08 N·m, 5 Hz.

7.5 MOX5/MOX-B-06 at 6.10 N·m, 5 Hz

The test on MOX5/MOX-B-06 was conducted at ± 6.10 N·m, 5 Hz. The applied moment amplitude was between those of MOX2 and MOX4, and a fatigue life between those was also observed (4.49×10^5).

Periodic quasistatic measurements of rod deformation were conducted using relative displacement levels of 0.4 and 0.7 mm at the selected target number of cycles as described above, and results are given in Fig. 67. The prefatigue rigidity was about 30 N·m², which was slightly lower than that of MOX4, even though the measurement displacements were the same. This was reflected in the difference in the mechanical response of various rods under deflection. As can be seen, the flexural rigidity showed a decrease with about 13% drop at the later stage of fatigue.

Online monitoring (Fig. 68) showed a well-defined decreasing trend on flexural rigidity with the same percentage of decrease as in the measurement. Downward drifting similar to that in MOX4 was seen, along with the accumulated number of cycles. The fatigue failure appeared to be related to the single-side fracture development.

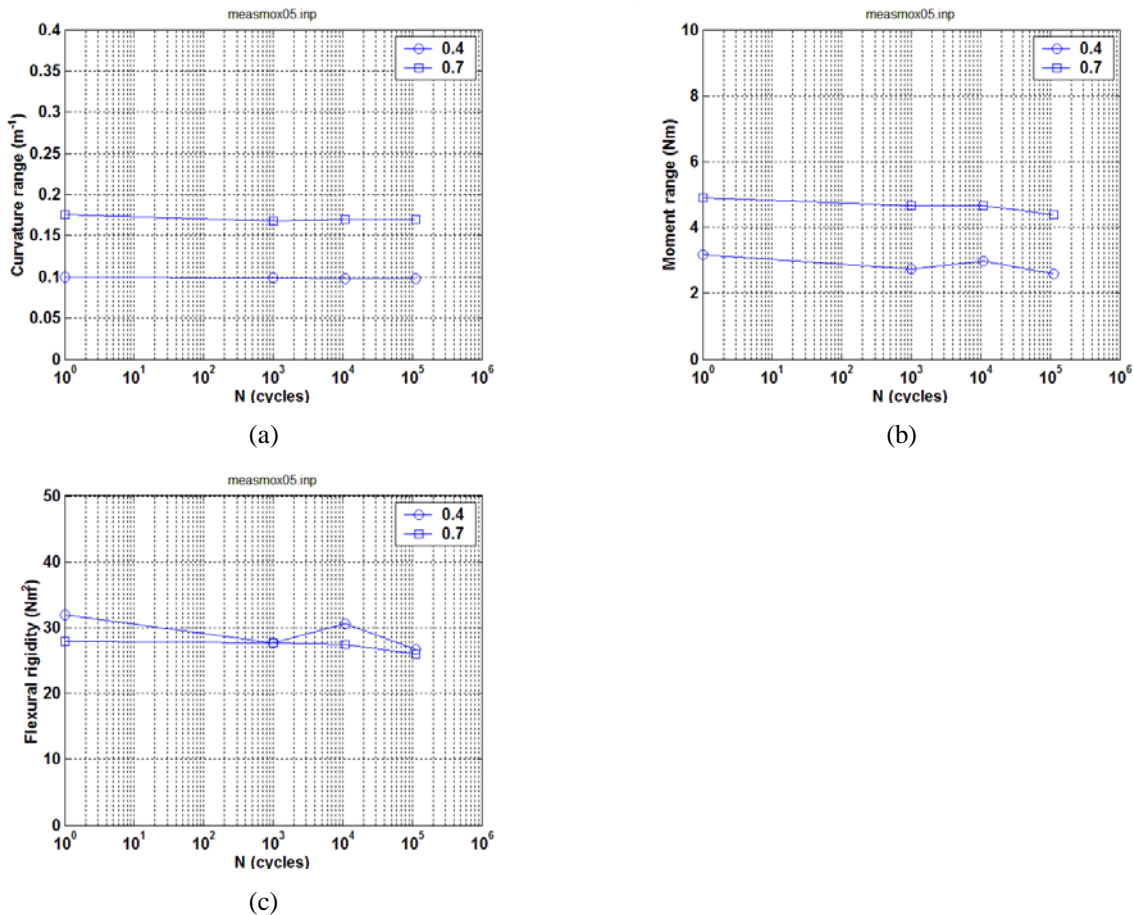


Fig. 67. Variations in (a) curvature range, (b) moment range, and (c) flexural rigidity as a function of the number of cycles for MOX5 (MOX-B-06). Measurements were made with 0.4 and 0.7 mm relative displacements; $N_f = 4.49 \times 10^5$ cycles at ± 6.10 N·m, 5 Hz.

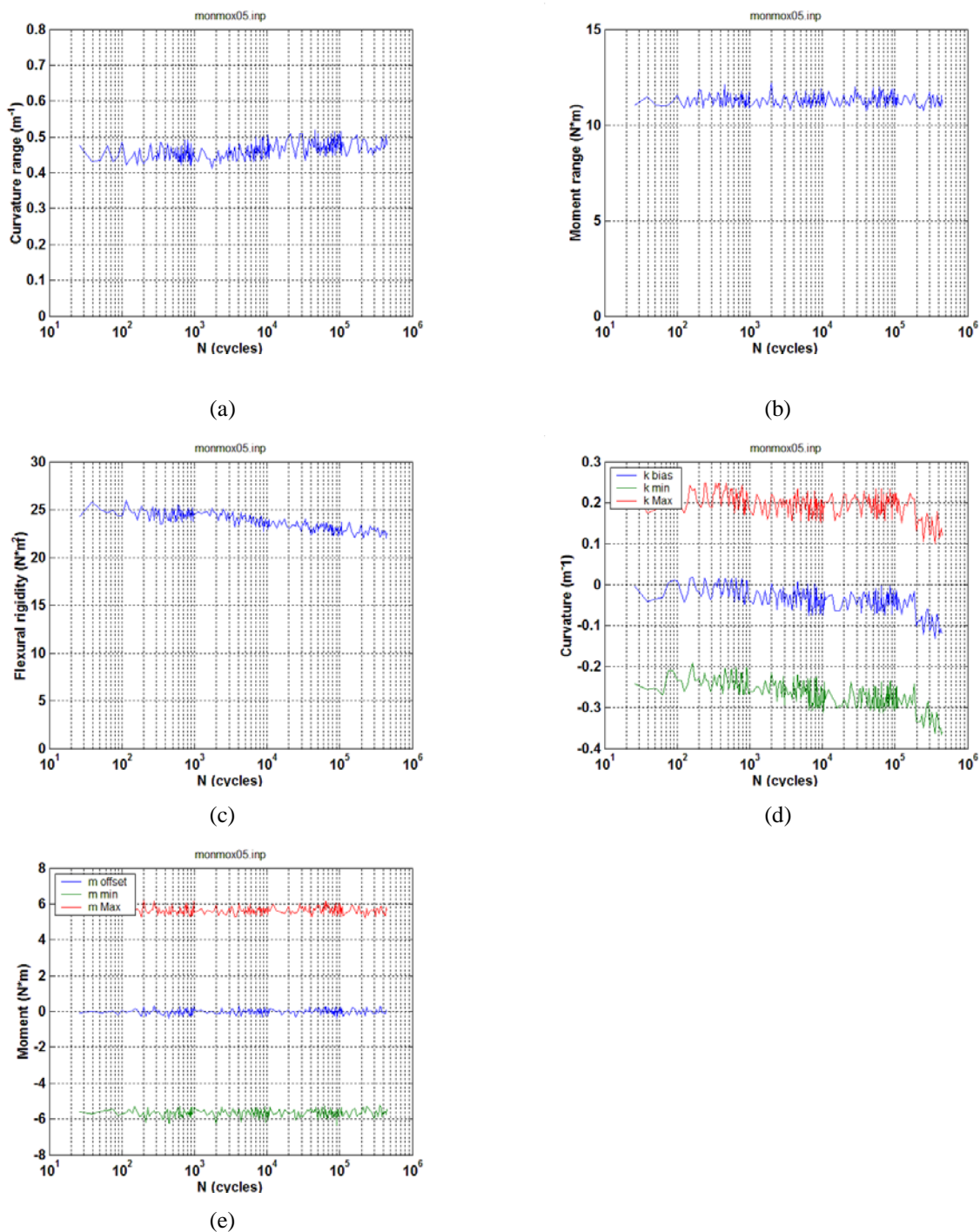


Fig. 68. Variations in (a) curvature range, (b) applied moment range, (c) flexural rigidity, (d) maximum and minimum values of curvature, and (e) maximum and minimum values of moment as a function of the number of cycles for MOX5 (MOX-B-06); $N_f = 4.49 \times 10^5$ cycles at ± 6.10 N·m, 5 Hz.

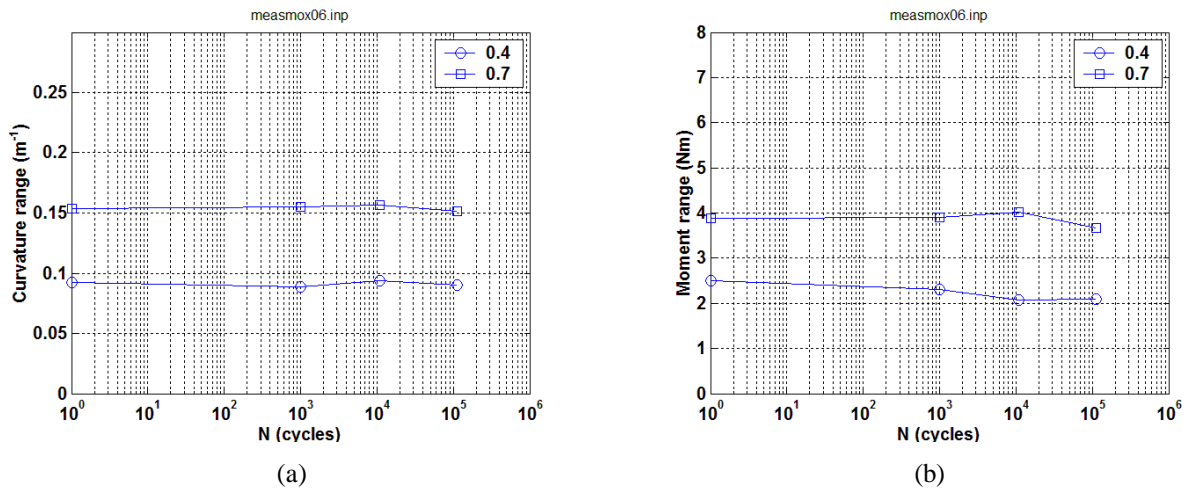
7.6 MOX6/MOX-B-07 at 5.08 N·m, 5 Hz

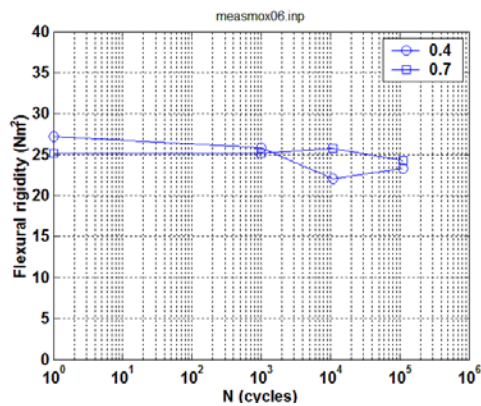
The test on MOX6/MOX-B-07 was conducted at ± 5.08 N·m, 5 Hz with the same amplitude as that of MOX4. In order to test the impact of a handling drop or transient shock under normal conditions of transport (NCT) on the fatigue life of SNF, after the two end caps were put on, the MOX6 specimen was dropped twice from a height of approximately 2 ft in a horizontal position. The test was conducted using the same procedure as those used in all other dynamic tests.¹¹ The MOX6 sample failed at 5.42×10^5 cycles, which was much shorter than that of MOX4 (2.15×10^6 cycles).

At 0.4 and 0.7 mm, the initial rigidity of MOX6 was between 25 and 27 N·m². For the same relative displacements, the level of rigidity of MOX6 was obviously lower than that of MOX 4 and 5. This result indicates that the drop from 2 ft may have induced additional damage to the rod and thus may have caused the reduced fatigue life that was observed.

Periodic quasistatic measurements of rod deformation were conducted routinely using two relative displacement levels—0.4 and 0.7 mm—at the selected target number of cycles as described above, and results are given in Fig. 69. As can be seen, the flexural rigidity showed a certain amount of decrease, with the largest drop at about 15% occurring at 0.4 mm.

As with MOX4, online monitoring of MOX6 (Fig. 70) showed a rise-and-fall pattern for the variation in flexural rigidity. However, the overall rigidity of MOX6 (20 N·m²) was lower than that of MOX4. Therefore, reduced rigidity was exhibited in both the periodic measurement process and in online monitoring. This is an important indication that dropping or transient shocks during NCT can have an accelerated aging effect on the fatigue performance of HBU SNF. The observation and related mechanisms warrant further investigation to confirm such phenomenon.





(c)

Fig. 69. Variations in (a) curvature range, (b) moment range, and (c) flexural rigidity as a function of the number of cycles for MOX6 (MOX-B-07). Measurements were made with 0.4 and 0.7 mm relative displacements; $N_f = 5.42 \times 10^5$ cycles at ± 5.08 N·m, 5 Hz.

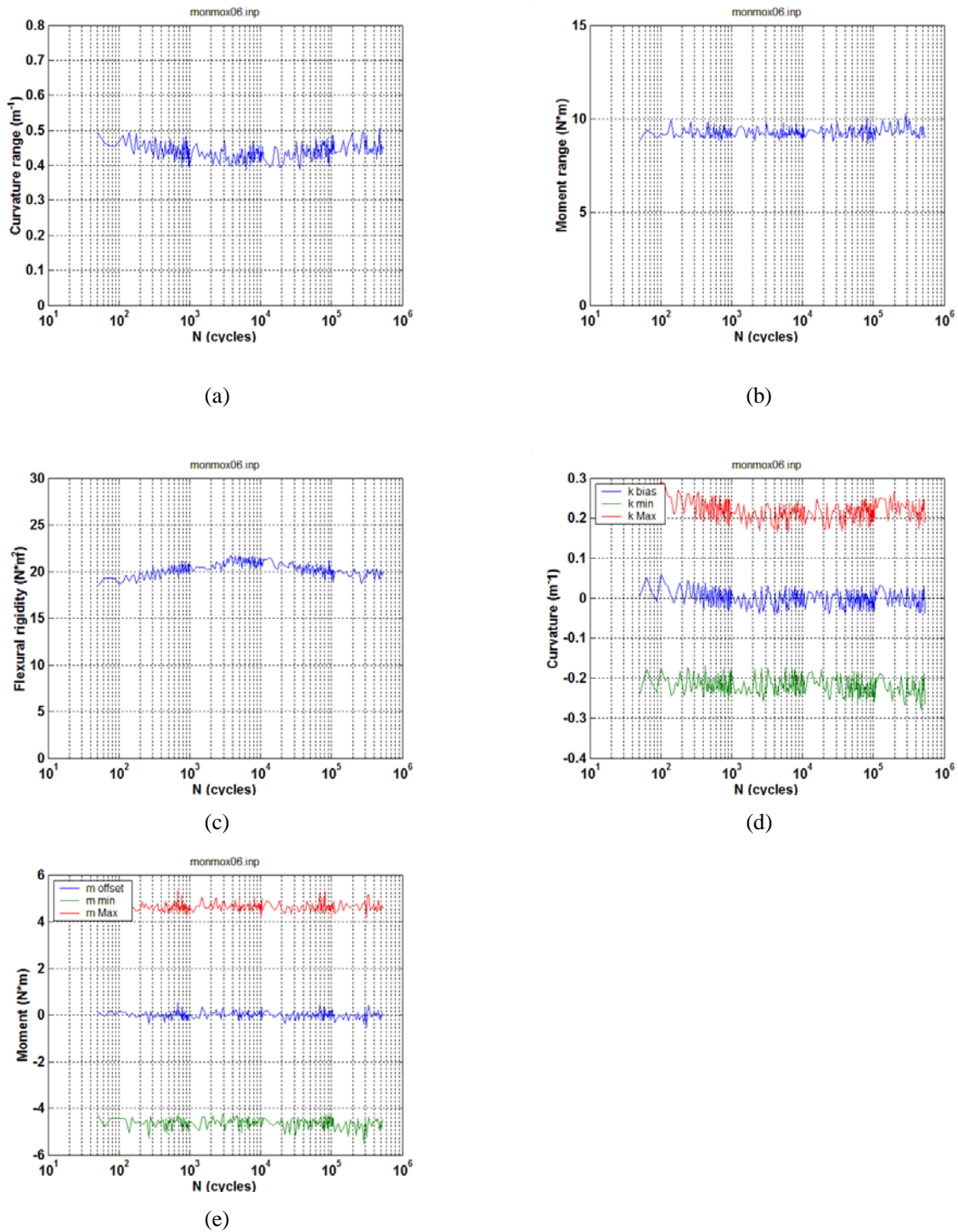


Fig. 70. Variations in (a) curvature range, (b) applied moment range, (c) flexural rigidity, (d) maximum and minimum values of curvature, and (e) maximum and minimum values of moment as a function of the number of cycles for MOX6 (MOX-B-07); $N_f = 5.42 \times 10^5$ cycles at ± 5.08 N·m, 5 Hz.

7.7 MOX7/MOX-C-06 at 15.24 N·m, 5 Hz

The test on MOX7/MOX-C-06 was conducted at ± 15.24 N·m, 5 Hz, and the sample failed at 1.55×10^4 cycles.

Measurements were made in different stages of cyclic testing using 0.4 and 0.8 mm at individual loading points of the U-frame.

Further data analyses will be performed in the next report cycle.

7.8 MOX8/MOX-C-07 at 12.7 N·m, 5 Hz

The test on MOX8/MOX-C-07 was conducted at ± 12.7 N·m, 5 Hz with the number of cycles to failure at 1.29×10^4 cycles. The failure occurred within the gage section.

The measurements were conducted at various stages of cyclic testing using 0.4 and 0.8 mm amplitude.

Further data analyses will be performed in the next report cycle.

7.9 MOX9/MOX-C-08 at 7.62 N·m, 5 Hz

The test on MOX9/MOX-C-08 was conducted at ± 7.62 N·m, 5 Hz with the number of cycles to failure at 8.98×10^4 cycles, and the failure position was located within the gage section of specimen.

The measurements were conducted at various stages of cyclic testing using 0.4 and 0.8 mm measurement amplitude.

Further data analyses will be performed in the next report cycle.

7.10 MOX10/ MOX-K-09 at 10.16 N·m, 5 Hz

The test on MOX10/MOX-K-09 was conducted at ± 10.16 N·m, 5 Hz. Specimen MOX10 failed at 3.85×10^4 cycles. Again, the failure took place within the gage section of the specimen.

The measurements were conducted at various stages of cyclic testing using 0.4 and 0.8 mm measurement amplitude.

Further data analyses will be performed in the next report cycle.

7.11 MOX11/MOX-K-10 at 10.16 N·m, 5 Hz

The test on MOX11/MOX-K-10 was conducted at ± 10.16 N·m, 5 Hz with the same amplitude as that of MOX2 and MOX10. The MOX11 sample lasted a little longer than MOX2 and MOX10, namely, 4.23×10^4 cycles. The failure of MOX11 occurred within the gage section.

The measurements were conducted at various stages of cyclic testing using 0.4 and 0.8 mm measurement amplitude.

Further data analyses will be performed in the next report cycle.

7.12 MOX12/MOX-K-11 at 10.16 N·m, 5 Hz

The test on MOX12/MOX-K-11 was conducted at ± 10.16 N·m, 5 Hz again with the same amplitude as that of MOX2 and MOX10.

The specimen was dropped from a height of about 2 ft three times before the test in order to explore the effect of dropping on the fatigue response of the material. The number of cycles to failure of the MOX12 sample was the same as that of MOX11, namely, 4.23×10^4 cycles.

The measurements were conducted at various stages of cyclic testing using 0.4 and 0.8 mm measurement amplitude.

Further data analyses will be performed in the next report cycle.

8. FRACTOGRAPHY FOR HBR, NA, AND MOX SNF

A PIE study was performed by using an optical microscope in an ORNL hot cell on the fractured/failed CIRFT specimens, including HBR R4, NA1, NA2, NA4, MOX1 and MOX2.¹⁷ The failed specimens were tested under pure dynamic loading, except for MOX1, in which the dynamic loading followed the static loading cycles discussed in Section 4.6.1. The fracture surfaces for these specimens are presented in Fig. 71–Fig. 76.

The fracture topography observed in HBR R4 indicated that the failure mode includes fractured fuel pellets. The stressed surface of the tested rod revealed equally spaced circumferential cracks, as reported in Ref. 9. These cracks apparently are related to the oxide layers of cladding.

No obvious circumferential cracks were seen on the stressed surface of NA and MOX fuels, partly due to low image resolution and the appearance of dark grease on the tested rod surface. The failure of NA fuels mostly occurred at the pellet-to-pellet interface. The failure of the two MOX specimens seemingly took place within a fuel pellet where no identifiable mark of pellet ends can be seen from the matching halves of fracture surfaces. The underlying failure mechanism for these MOX fuels remains to be explored.

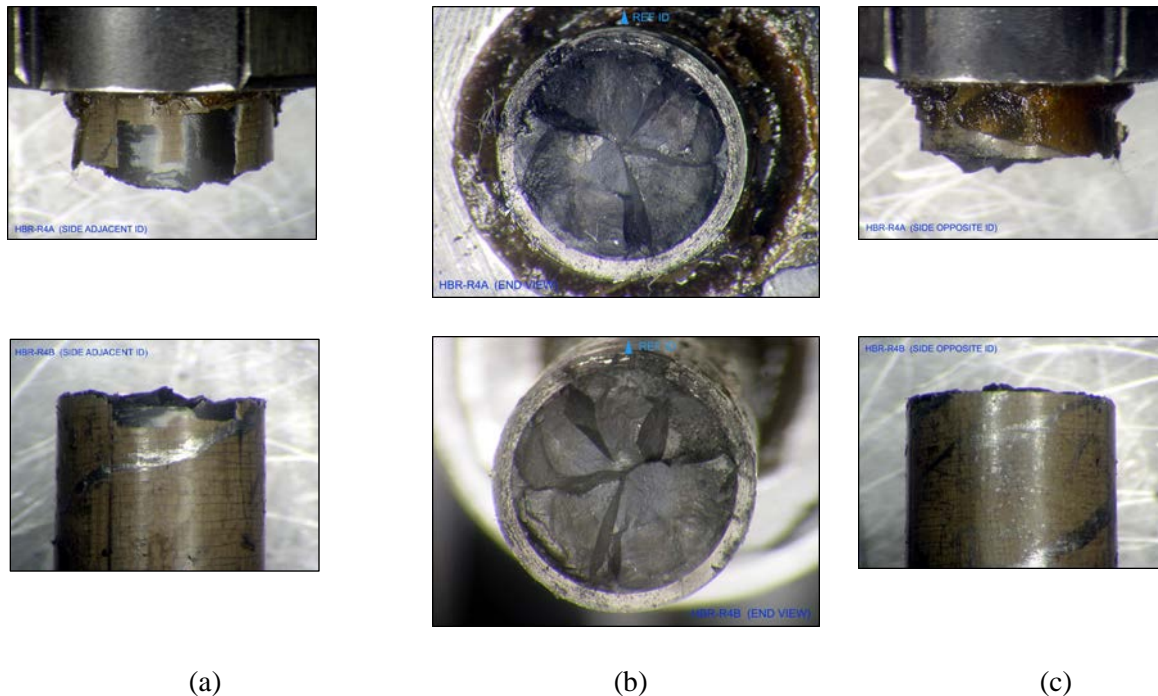


Fig. 71 (a) Lateral or front view, (b) transverse view, and (c) back view of fracture surface for HBR R4 tested at $\pm 8.89 \text{ N}\cdot\text{m}$, 5 Hz, $N_f = 2.7 \times 10^5$ cycles.

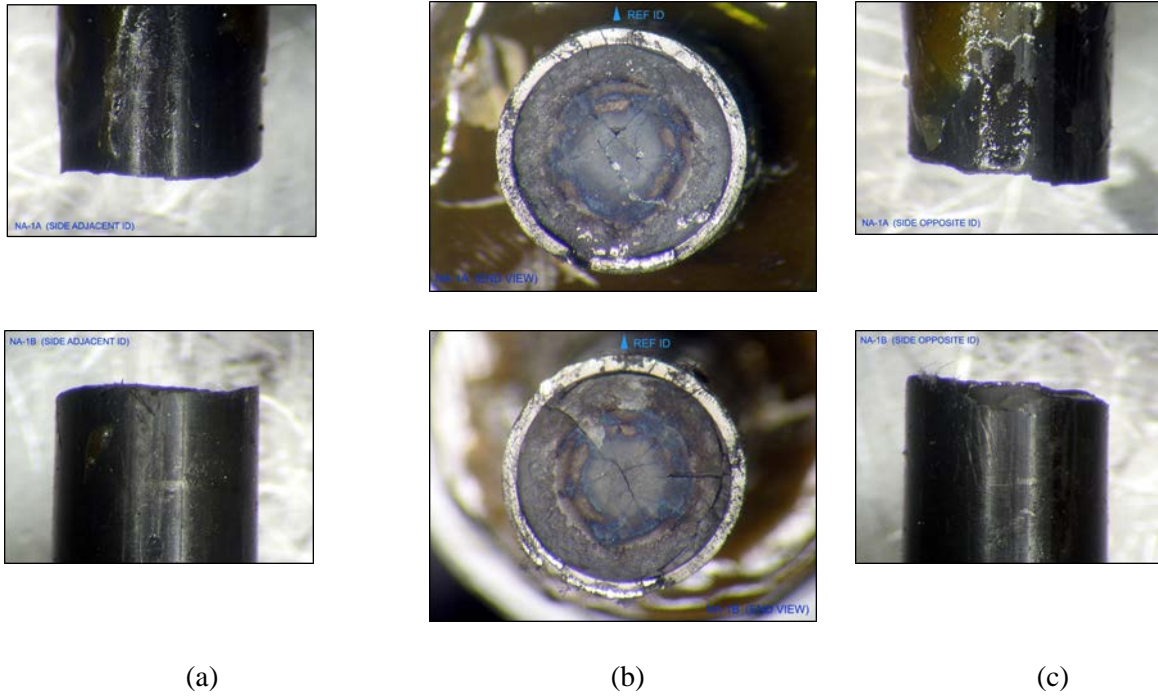


Fig. 72 (a) Lateral or front view, (b) transverse view, and (c) back view of fracture surface for NA1 tested at $\pm 12.7 \text{ N}\cdot\text{m}$, 5 Hz, $N_f = 1.57 \times 10^4$ cycles.

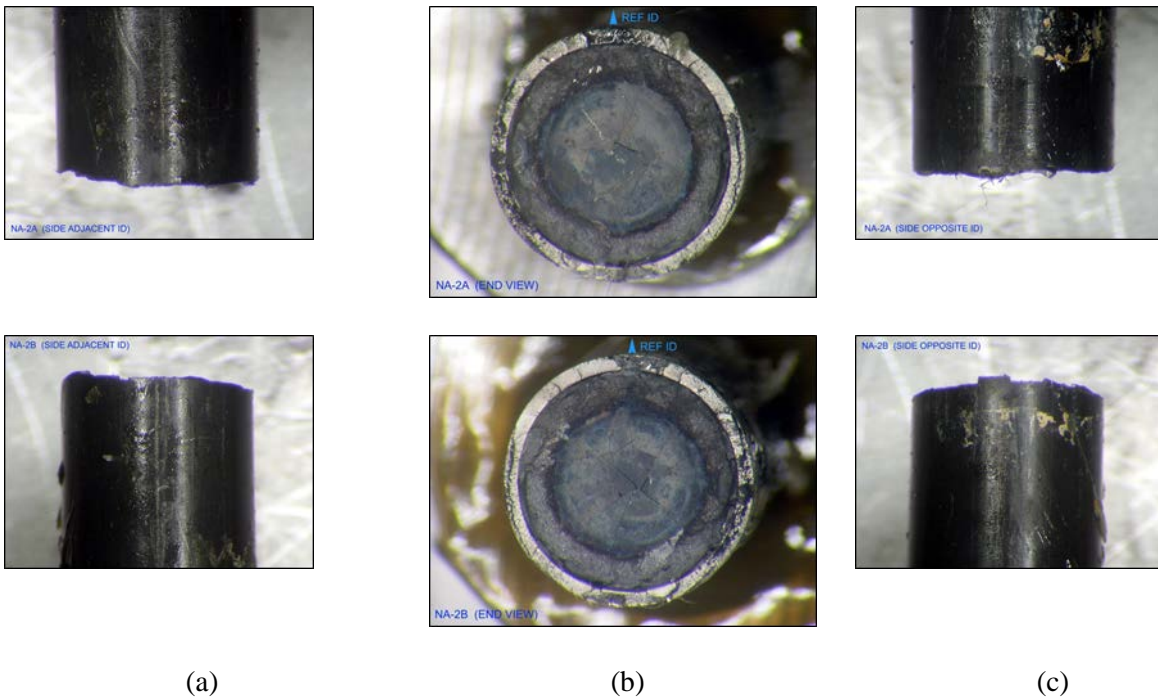


Fig. 73 (a) Lateral or front view, (b) transverse view, and (c) back view of fracture surface for NA2 tested at $\pm 10.16 \text{ N}\cdot\text{m}$, 5 Hz, $N_f = 2.20 \times 10^4$ cycles.

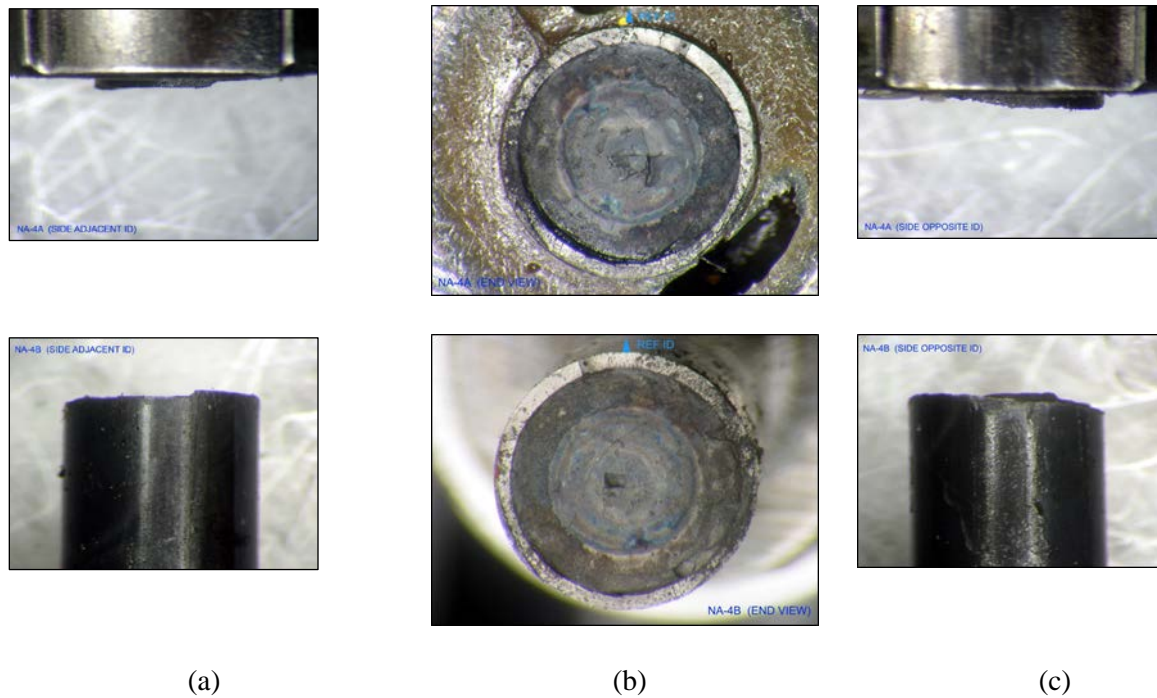


Fig. 74 (a) Lateral or front view, (b) transverse view, and (c) back view of fracture surface for NA4 tested at $\pm 7.62 \text{ N}\cdot\text{m}$, 5 Hz, $N_f = 6.10 \times 10^4$ cycles.

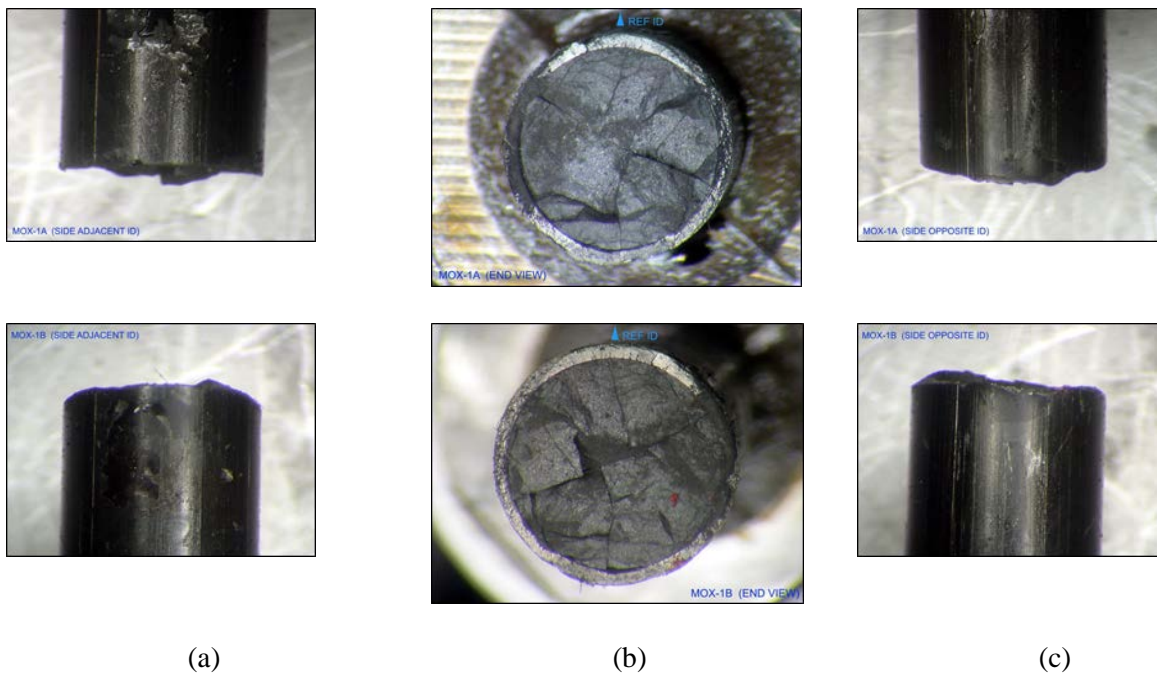


Fig. 75 (a) Lateral or front view, (b) transverse view, and (c) back view of fracture surface for MOX1 tested first to 47 N·m for two cycles and then dynamic loading at $\pm 15.24 \text{ N}\cdot\text{m}$, 5 Hz, $N_f = 4.0 \times 10^3$ cycles.

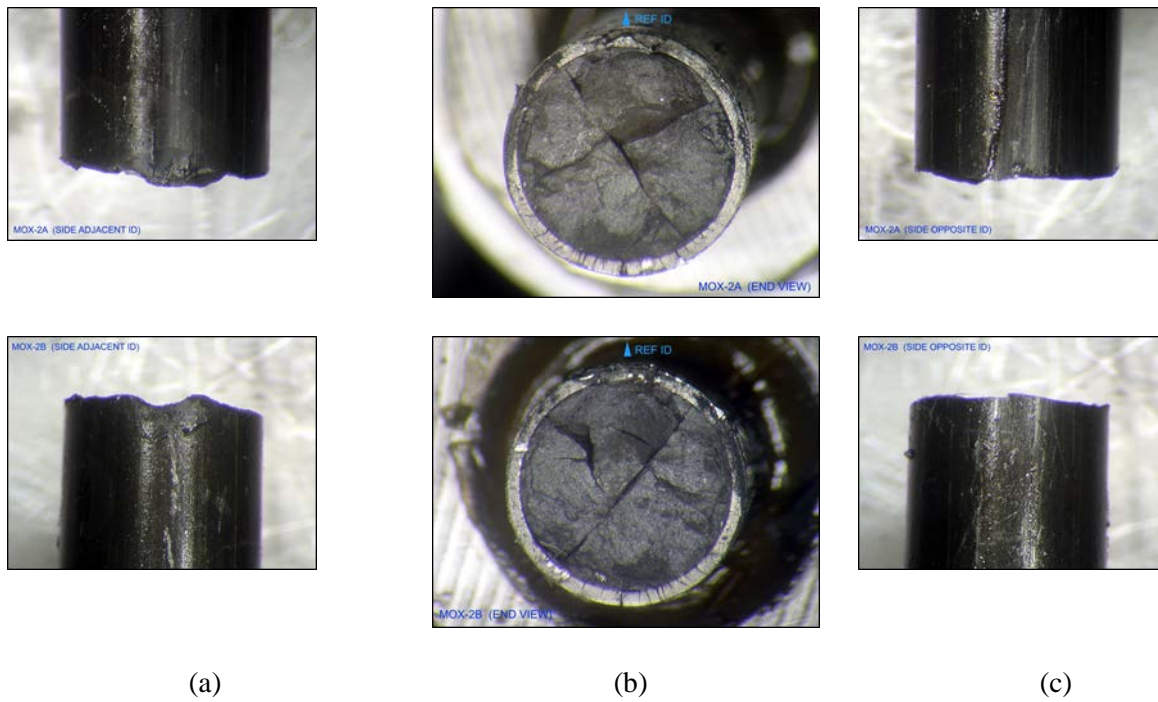


Fig. 76 (a) Lateral or front view, (b) transverse view, and (c) back view of fracture surface for MOX2 tested at dynamic loading $\pm 10.16 \text{ N}\cdot\text{m}$, 5 Hz, $N_f = 3.70 \times 10^4$ cycles.

9. DISCUSSIONS

9.1 Static Response of SNF

Fig. 77 summarizes the equivalent stress and strain results from static testing on all SNF rods (HBR, NA M5TM, and MOX M5TM). The static responses of NA M5TM and MOX M5TM specimens were quite consistent. The three stages of the curve (Fig. 77) can be identified with the first and second deflection points (approximately 90 and 300 MPa, respectively). The curves of NA and MOX fuels were obviously well below those of HBR fuels, due to the lower yield stress of M5 cladding compared to Zircaloy-4 cladding. The maximum stress of HBR fuels at the same relative displacement (24.00 mm) was between 733 and 748 MPa, while that of NA and MOX were between 510 and 530 MPa. The maximum strains among the three tested fuels were close in value, ranging from 1.67 to 1.98%. The stress level at the first deflection for NA/MOX M5TM fuels was located near 100 MPa, and the second was between 300 and 400 MPa. These stress levels are lower than those of the HBR fuel.⁹ It is interesting to note that the behavior of BWR LMK is similar to that of M5, except with slightly higher maximum stress and strain levels.

A comparison revealed a large discrepancy between the curves of CIRFT static results and the Pacific Northwest National Laboratory (PNNL) data for Zircaloy-4 cladding, where the HBR CIRFT equivalent stress level appears to be lower and HBR strain level appears to be higher than that of the PNNL data. Regarding the stress level, this could be due to an overestimation of the SNF moment of inertia used in the equivalent stress evaluation or the residual stress in a CIRFT-tested SNF samples. It is emphasized that the concept of reduced pellet moment of inertia and Eqs. (2) and (3) were used to demonstrate the relative stress levels between different SNFs. More modeling is needed to understand the deformation mechanisms and to predict the response of the SNF rod under the corresponding loading condition.

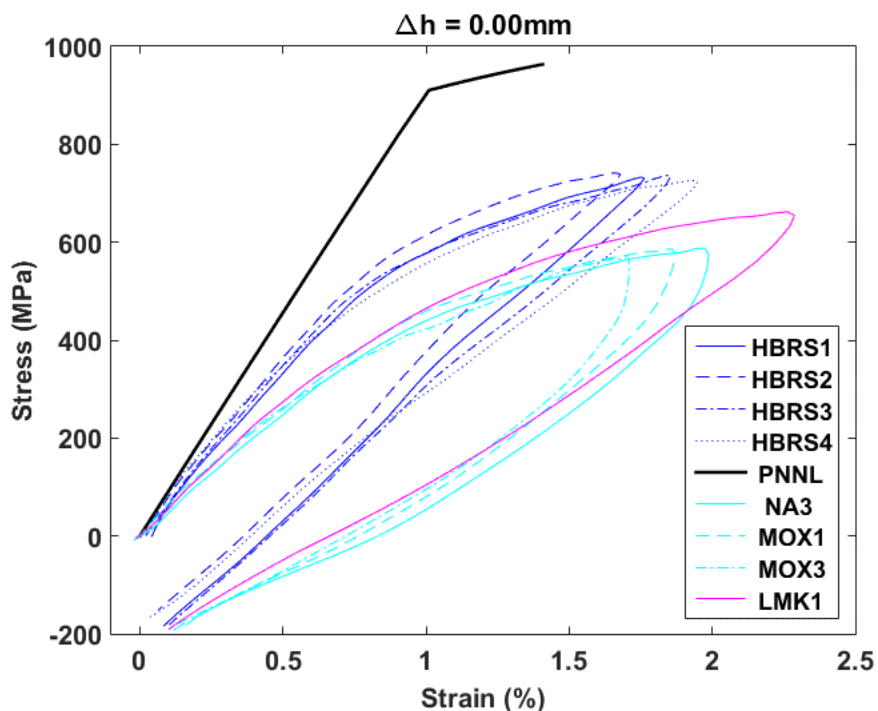


Fig. 77 (a) Stress-strain curves based on static testing results for HBR, NA, and MOX SNF. Relative displacement was 24.00 mm; the loading/unloading rate at each point was 0.1/0.2 mm/s.

9.2 Effect of Probe Contact on Large Curvature Measurements

The effect of the LVDT probe in contact with the test specimen when taking curvature measurements may be an important factor when the curvature becomes large and bending is reversed.

An experimental study was performed using two surrogate rods made of the same materials and using same configuration (stainless steel [SS] tube and ten alumina pellets [AP], or SSAP). The same flat probe was used, as seen in Fig. 78.

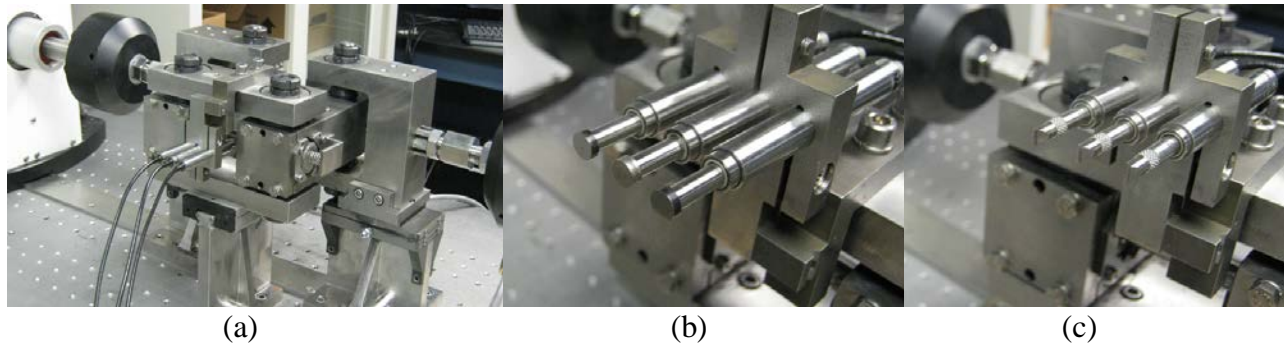


Fig. 78 (a) Three curvature LVDTs being held against the rod; (b) LVDT clamp open to show (b) flat probe and (c) chisel probe.

In order to study the effect of reverse bending on curvature measurement, the rod was subjected to both positive (concave) and negative (convex) bending of the three LVDTs. In the case of convex bending, the rod was bent toward the three LVDTs. Three RDP brand D5/200AG-337 LVDTs with a stroke of ± 5 mm were used in the testing.

As shown in Fig. 79, at a similar level of applied moment, the maximum curvature obtained is significantly larger when a rod is bending concavely with respect to the LVDTs than when a rod is bending convexly. The discrepancy can be corrected by adjusting sensor spacing h , as illustrated in Fig. 80. The moment-curvature curves in both cases converge if a sensor spacing adjustment Δh of 2.5 mm is used (21% of sensor spacing h and a little less than the contact radius of 3.0 mm). Of course, the actual sensor spacing adjustment can be calibrated, while the study demonstrated that the curvature based on flat-probe contact can be corrected if necessary.

9.2.1 The Adjusted Stress-Strain and Moment-Curvature Profiles

Additional stainless steel aluminum pellet (SSAP) surrogate specimens were used to optimize the sensor spacing adjustment factor, where Δh of 2.9 mm was selected. Based on the adjustment sensing factor Δh of 2.9 mm, updated stress-strain profiles were developed, as shown in Fig. 81, where the updated strain level of CIRFT HBR data is very similar to that of PNNL data. The associated CIRFT bending load vs. curvature data and PNNL bending resistance without pellets are shown in Fig. 82; due to pellet contribution, HBR and LMK has much higher bending resistance compared to PNNL data with the same clad dimension as that of HBR. Further evaluation of the probe sensing adjustment in dynamic CIRFT testing will be pursued in the next report cycle.

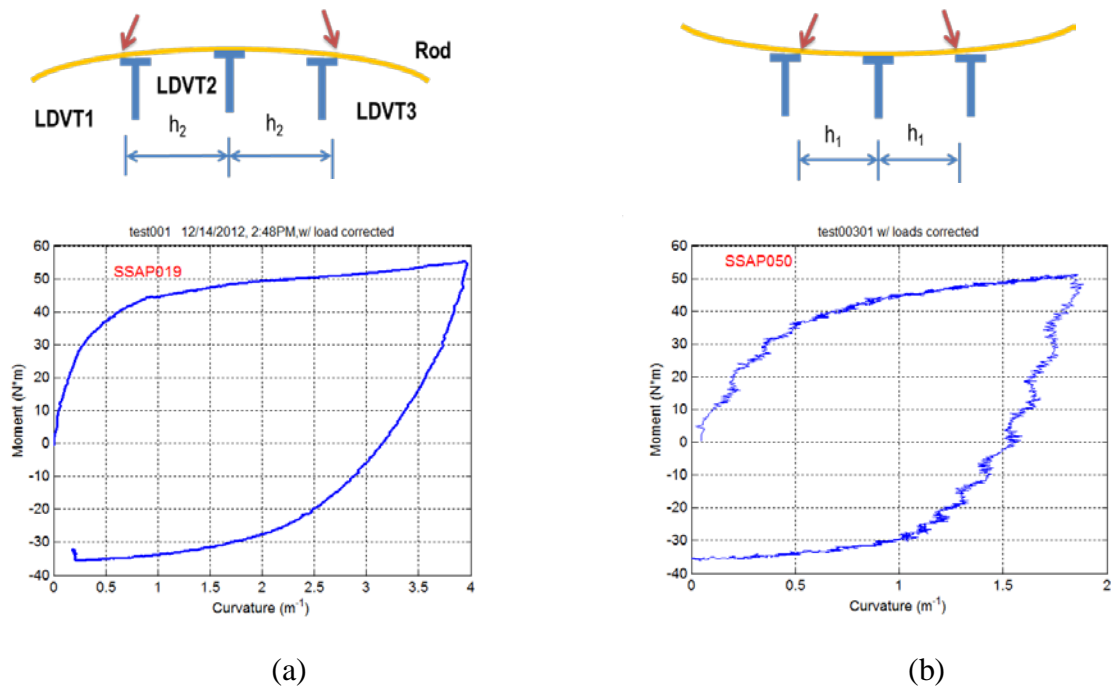


Fig. 79. Moment-curvature curves based on stainless steel aluminum pellet (SSAP) rod testing in which the rod is bent with respect to three LVDTs; (a) concave and (b) convex.

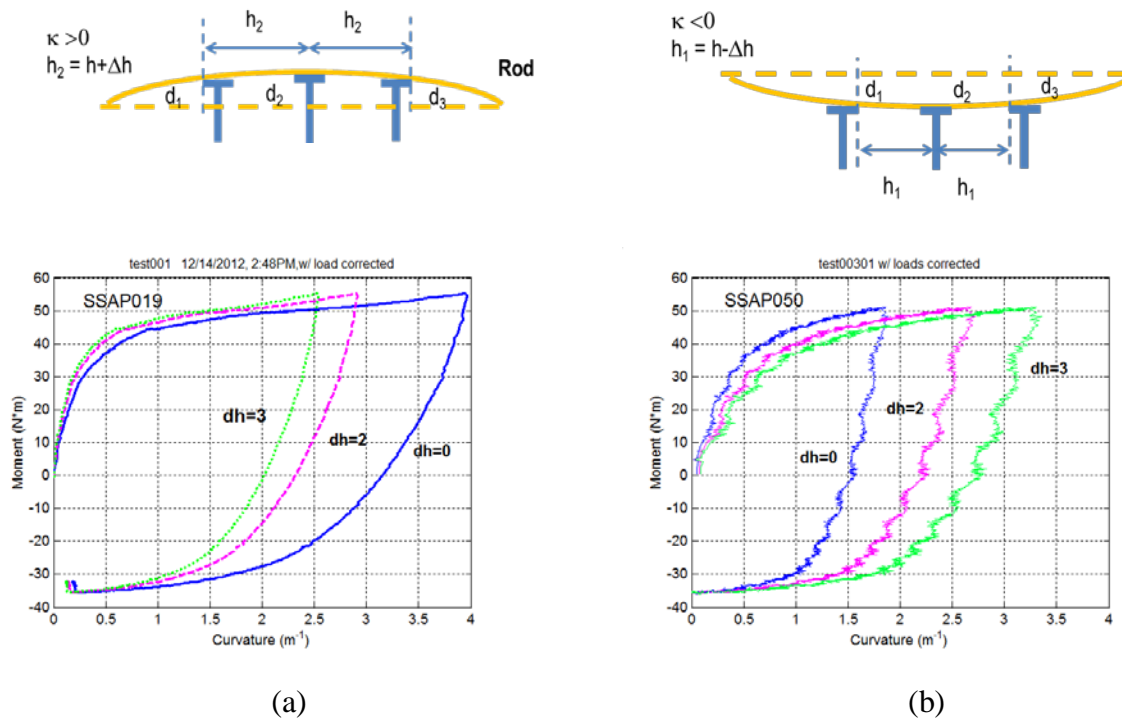


Fig. 80. Moment-curvature curves as a function of sensor spacing adjustment in which a rod is bent with respect to three LVDTs: (a) concavely and (b) convexly.

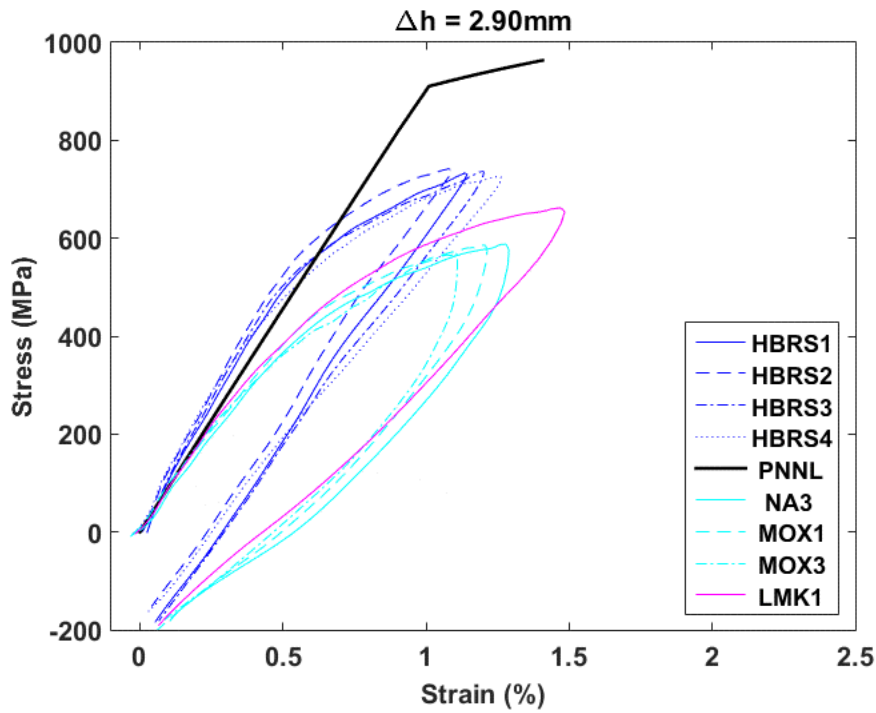


Fig. 81. Updated stress-strain profiles based on adjustment factor Δh of 2.9 mm.

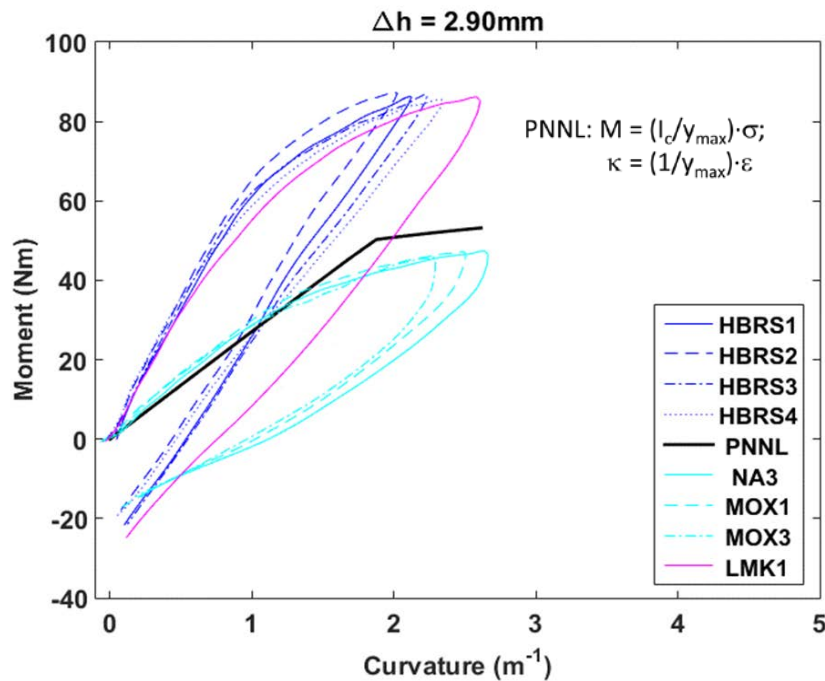


Fig. 82. Moment-curvature plots based on bending tests and comparison with PNNL data with sensing spacing correction; no pellets were involved in PNNL's moment evaluation. Due to dimension and material variability of the tested SNF, the variability in CIRFT bending resistance was also observed.

9.3 M-N Curve of Limerick Rods

Fourteen SNF rod segments from the Limerick BWR were tested using the ORNL CIRFT, with one segment tested under static loading conditions and 10 segments under dynamic loading conditions.

Under static unidirectional loading, a moment of 85 N·m was obtained at maximum curvature 4.0 m^{-1} . The specimen did not show any failure in three repeated loading cycles to nearly similar maximum curvature values.

Failure was observed when the SNF rod segments were cycled to various applied moments. The cycles to failure ranged from 1.22×10^5 to 4.70×10^6 when the amplitude varied from 15.2 to 7.6 N·m. The measurements upon interruption indicated a range of flexural rigidity from 30 to 50 N·m². The online monitoring revealed that the flexural rigidity was a little lower due to the high level of loading, from 25 to 42 N·m². Generally, no substantial change of rigidity was observed based on online monitoring during the cyclic fatigue testing process.

The CIRFT dynamic testing results are summarized in Fig. 83 and Fig. 84. Overall, the decreasing trend in test specimen lifetime with the increasing amplitude is well defined.

The fatigue curves of the Limerick rods were compared with those of HB Robinson, North Anna, and Catawba MOX SNF in terms of amplitude of moment and strain, and the results are given in Fig. 85 and Fig. 86.

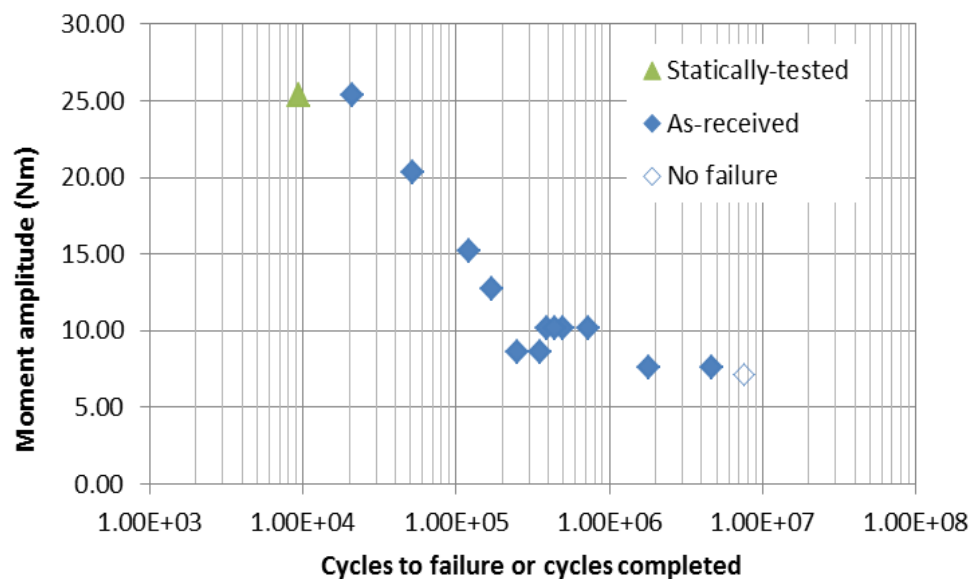


Fig. 83. Applied moment amplitude as a function of cycles to failure or cycles completed. The data point of pre-statically tested is based on a follow-up dynamic test of LMK01.

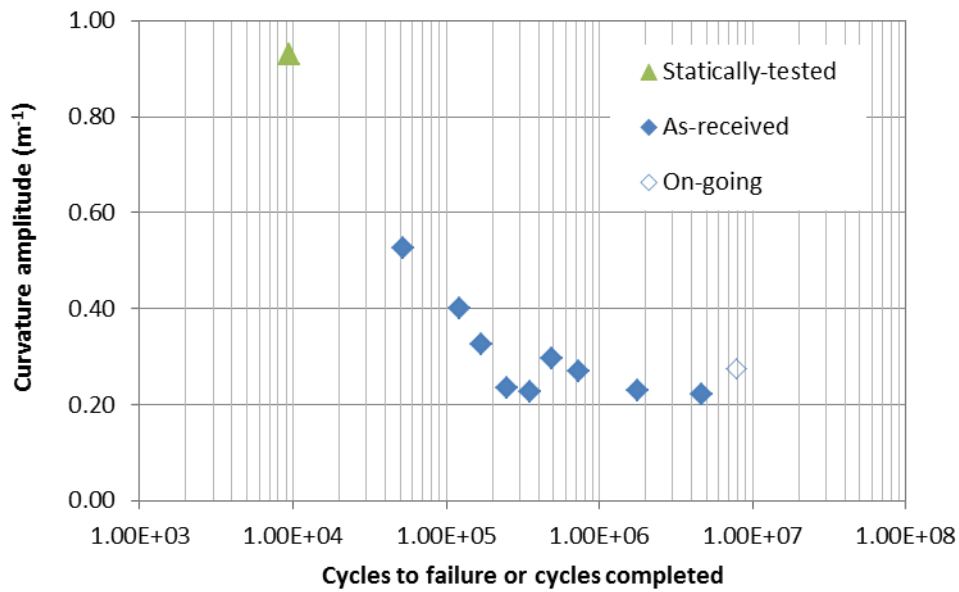


Fig. 84. Curvature amplitude as a function of cycles to failure or cycles completed. The data point of pretested is based on a follow-up dynamic test of LMK01. Three LMK fatigue data points are pending further analyses and are not included here.

9.4 Comparison of SNF Cyclic Fatigue Lifetimes

The CIRFT testing data for the high-burnup spent fuel rods are summarized in Tables 8-10. Data are presented in terms of various loading intensities and fuel dimensions.

Table 8. Summary of CIRFT testing of HBR rods

TN	Label	Seg. ID	ID*	OD	Pellet*	Load	$\Delta M/2$	N_f	Failure	$\Delta \kappa/2$	$\Delta \varepsilon/2$	E**	$\Delta \sigma_{E/2}$	$\Delta \sigma/2$
			in.	in.	in.	N	N·m			m ⁻¹	%	GPa	MPa	MPa
18	DH3	609C7	0.364	0.423	0.357	350	35.56	7.10E+03	1	0.907	0.487	91.01	443.327	306.111
20	R1	607C4A	0.364	0.427	0.357	300	30.48	5.50E+03	1	0.656	0.355	91.01	323.259	255.017
3	S3	605D1F	0.364	0.423	0.357	250	25.4	2.50E+04	1	0.571	0.307	91.01	279.310	217.993
16	DH2	609C3	0.364	0.424	0.357	200	20.32	6.50E+04	1	0.485	0.261	91.01	237.681	172.830
9	DL1	607C4B	0.364	0.427	0.357	150	15.24	1.10E+05	1	0.317	0.172	91.01	156.416	127.509
22	R3	606B3E	0.364	0.424	0.357	135	13.716	1.29E+05	1	0.271	0.146	91.01	132.722	117.099
19	S5	606C3A	0.364	0.424	0.357	125	12.7	1.80E+05	1	0.303	0.163	91.01	148.131	108.588
15	DH1	609C4	0.364	0.423	0.357	125	12.7	2.50E+05	1	0.302	0.162	91.01	147.736	108.997
21	R2	608C4A	0.364	0.426	0.357	110	11.176	3.86E+05	1	0.244	0.132	91.01	119.944	93.856
12	DL3	605C10A	0.364	0.424	0.357	100	10.16	1.00E+06	1	0.223	0.120	91.01	109.558	86.480
14	DM2	605D1B	0.364	0.424	0.357	90	9.144	2.30E+06	1	0.204	0.110	91.01	100.219	77.890
23	R4	606B3D	0.364	0.424	0.357	87.5	8.89	2.74E+05	1	0.210	0.113	91.01	102.842	75.897
17	DM3	606C3E	0.364	0.423	0.357	87.5	8.89	1.28E+07	0	0.198	0.106	91.01	96.710	76.470
13	DM1	605D1C	0.364	0.423	0.357	75	7.62	1.10E+07	0	0.179	0.096	91.01	87.606	65.349
24	R5	606B3C	0.364	0.424	0.357	75	7.62	2.24E+07	0	0.172	0.093	91.01	84.321	65.006
10	DL2	608C4B	0.364	0.425	0.357	50	5.08	6.40E+06	0	0.131	0.071	91.01	64.422	43.143

*EPRI data¹⁴

**PNNL data¹⁵

Table 9. Summary of CIRFT testing of NA/MOX fuels

TN	Label	Seg. ID	ID*	OD	OD_P*	$\Delta P/2$	$\Delta M/2$	Nf	Failure	$\Delta k/2$	$\Delta \epsilon/2$	E	$\Delta \sigma_E/2$	$\Delta \sigma/2$
			in.	in.	in.	N	N·m			m ⁻¹	%	GPa	MPa	MPa
NA1	NA1	651B2	0.334	0.379	0.323	125	12.70	1.57E+04	1	0.550	0.265	100.67	266.357	157.577
NA2	NA2	651C5	0.332	0.377	0.323	100	10.16	2.20E+04	1	0.450	0.215	100.67	216.893	126.279
NA4	NA4	652B1B	0.334	0.379	0.323	75	7.62	6.10E+04	1	0.275	0.132	100.67	133.143	94.556
NA5	NA5	652B2	0.334	0.379	0.323	50	5.08	5.11E+06	0					
NA6	NA6	652D1	0.334	0.379	0.323	50	5.08	4.27E+05	1					
NA7	NA7	652D2	0.335	0.380	0.323	150	15.24	1.26E+04	1					
MOX2	MOX2	MOX-A-12	0.333	0.378	0.323	100	10.16	3.70E+04	1	0.470	0.226	100.67	227.233	126.139
MOX4	MOX4	MOX-B-05	0.333	0.378	0.323	50	5.08	2.15E+06	1	0.200	0.096	100.67	96.695	63.069
MOX5	MOX5	MOX-B-06	0.333	0.378	0.323	60	6.10	4.49E+05	1	0.225	0.108	100.67	108.782	75.683
MOX6	MOX6	MOX-B-07	0.333	0.378	0.323	50	5.08	5.42E+05	1	0.223	0.107	100.67	107.573	63.069
MOX7	MOX7	MOX-C-06	0.333	0.378	0.323	150	15.24	1.55E+04	1					
MOX8	MOX8	MOX-C-07	0.333	0.378	0.323	125	12.7	1.29E+04	1					
MOX9	MOX9	MOX-C-08	0.333	0.378	0.323	75	7.62	8.98E+04	1					
MOX10	MOX10	MOX-K-09	0.333	0.378	0.323	100	10.16	3.85E+04	1					
MOX11	MOX11	MOX-K-10	0.333	0.378	0.323	100	10.16	4.23E+04	1					
MOX12	MOX12	MOX-K-11	0.333	0.378	0.323	100	10.16	4.23E+04	1					

*Based on THK 0.57mm, ANL¹⁶

Blank fields indicate further data analyses to be conducted in the next report period.

Table 10. Summary of CIRFT testing of LMK fuels

TN	Label	Seg. ID	ID*	OD	OD_P	$\Delta P/2$	$\Delta M/2$	N_f	Failure	$\Delta k/2$	$\Delta \epsilon/2$	E**	$\Delta \sigma_{E/2}$	$\Delta \sigma/2$
			in.	in.	in.	N	N·m	Cycles		m ⁻¹	%	GPa	MPa	MPa
LMK02	LM2	575D-A	0.391	0.447	0.374	125	12.70	1.71E+05	1	0.325	0.184	113.078	208.441	97.691
LMK03	LM3	575B-A	0.392	0.448	0.374	100	10.16	4.92E+05	1	0.295	0.168	113.078	189.878	78.024
LMK05	LM5	574D-B	0.392	0.448	0.374	85	8.64	2.49E+05	1	0.235	0.134	113.078	151.259	66.320
LMK06	LM6	574D-E	0.392	0.448	0.374	75	7.62	1.79E+06	1	0.230	0.131	113.078	148.041	58.518
LMK07	LM7	575C-A	0.392	0.448	0.374	150	15.24	1.22E+05	1	0.400	0.228	113.078	257.462	117.035
LMK08	LM8	575B-D	0.392	0.448	0.374	75	7.62	4.70E+06	1	0.220	0.125	113.078	141.604	58.518
LMK09	LM9	574D-D	0.392	0.448	0.374	100	10.16	7.31E+05	1	0.270	0.154	113.078	173.787	78.024
LMK10	LM10	575B-E	0.392	0.448	0.374	200	20.32	5.20E+04	1	0.525	0.299	113.078	337.919	156.047
LMK11	LM11	575B-D	0.392	0.448	0.374	85	8.64	3.55E+05	1	0.228	0.129	113.078	146.432	66.320
LMK13	LM13	575C-D	0.392	0.448	0.374	250	25.40	2.10E+04	1	0.625	0.356	113.078	402.285	195.059
LMK14	LM14	575C-B	0.392	0.448	0.374	100	10.16	3.90E+05	1	0.265	0.151	113.078	170.569	78.024
LMK15	LM15	575C-C	0.392	0.448	0.374	100	10.16	4.41E+05	1					
LMK12	LM12	575B-A	0.392	0.448	0.374	70	7.11	7.58E+06	0					

*Based on THK 0.71mm, ANL¹⁶

**PNNL data¹⁵

Blank fields indicate further data analyses to be conducted in the next report period.

9.4.1 M-N Curve and e-N Curve

The fatigue curves of Limerick rods were compared with those of HBR, NA, and MOX fuels in terms of amplitude of moment and strain, and results are given in Fig. 85 and Fig. 86. The strain amplitudes were obtained according to Eq. (4).

The data points for NA and MOX fuels are generally below the curve of moment amplitude versus N_f (cycles-to-failure, M-N curve) of HBR fuel, mainly due to the smaller cladding diameters of these fuels, as shown in Table 11. Using strain amplitudes as a function of cycles will filter out some variability in SNF's dimensions and makes the data points from NA and MOX come close to M-N curve of HBR rods. Furthermore, due to the relatively lower rigidity of LMK compared to that of HBR, the LMK strain amplitude profile appeared to be above the HBR trend curve.

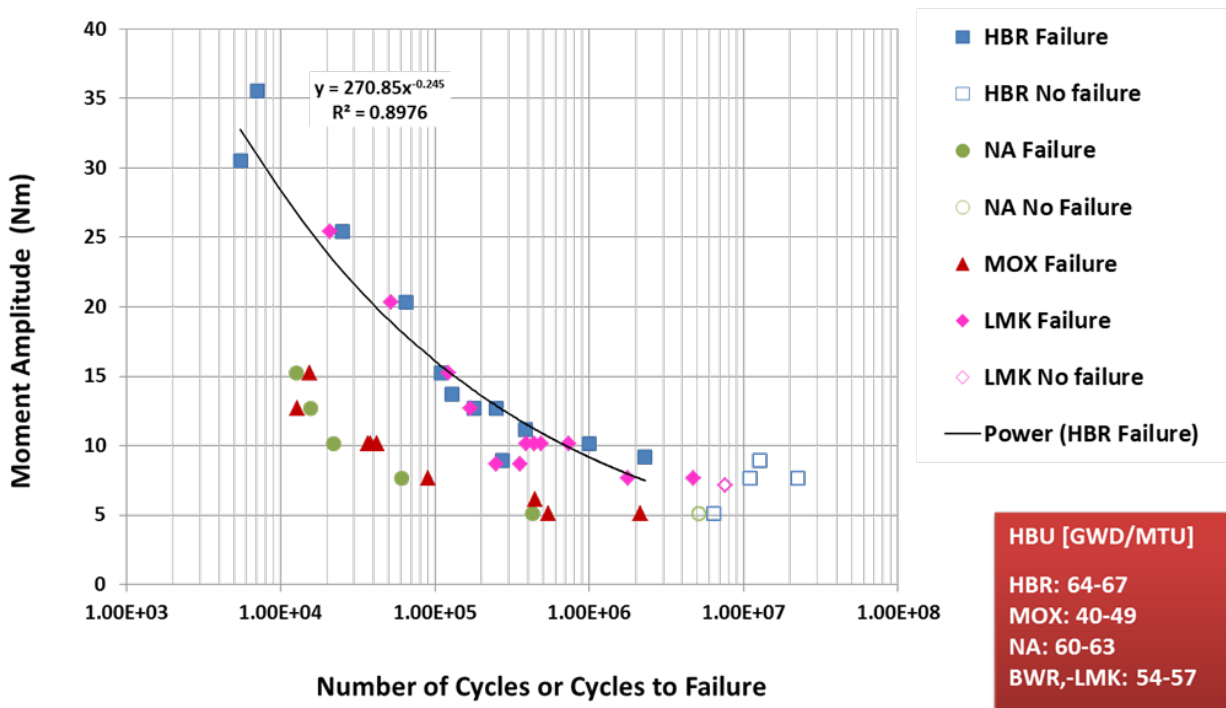


Fig. 85. Moment amplitudes as a function of number of cycles; results are based on CIRFT testing of various used fuels at 5 Hz. The power function was obtained from curve fitting based on the HBR data set.

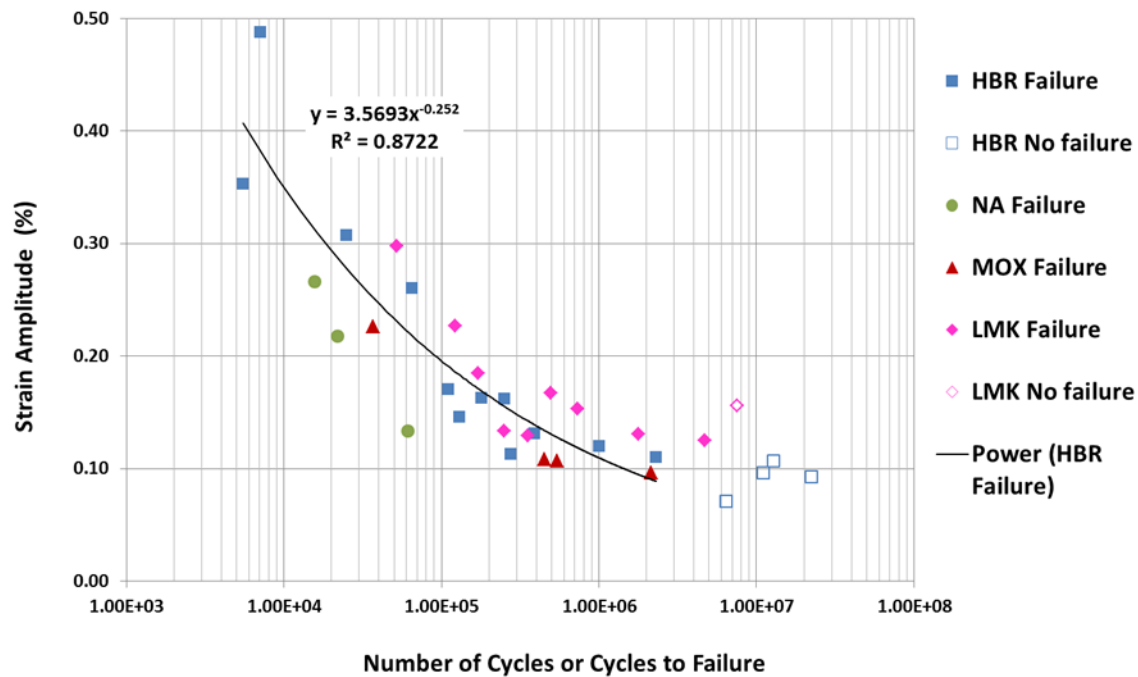


Fig. 86. Strain amplitudes as a function of number of cycles; results are based on CIRFT testing of various used fuels at 5 Hz. The power function was obtained from curve fitting based on the HBR data set.

Table 11. Cross section geometric size, Young’s Modulus and yield stress 903 of SNF rods

SNF	Cladding material	ID (mm)	OD (mm)	Pellet diameter (mm)	Cladding Young's modulus (GPa)	Cladding yield stress (MPa)
HBR	Zircaloy-4	9.246	10.770	6.91	91	900
NA	M5	8.466	9.606	11.05	91	680
MOX	M5	8.466	9.606	11.05	91	680
Limerick	Zircaloy-2	9.964	11.384	10.57	91	920

9.4.2 S-N Curve Based on Equivalent Stress

The equivalent stress can be estimated based on Eq. (3), and the results are shown in Fig. 87. The estimated stress profile of LMK data is now below the HBR stress profile.

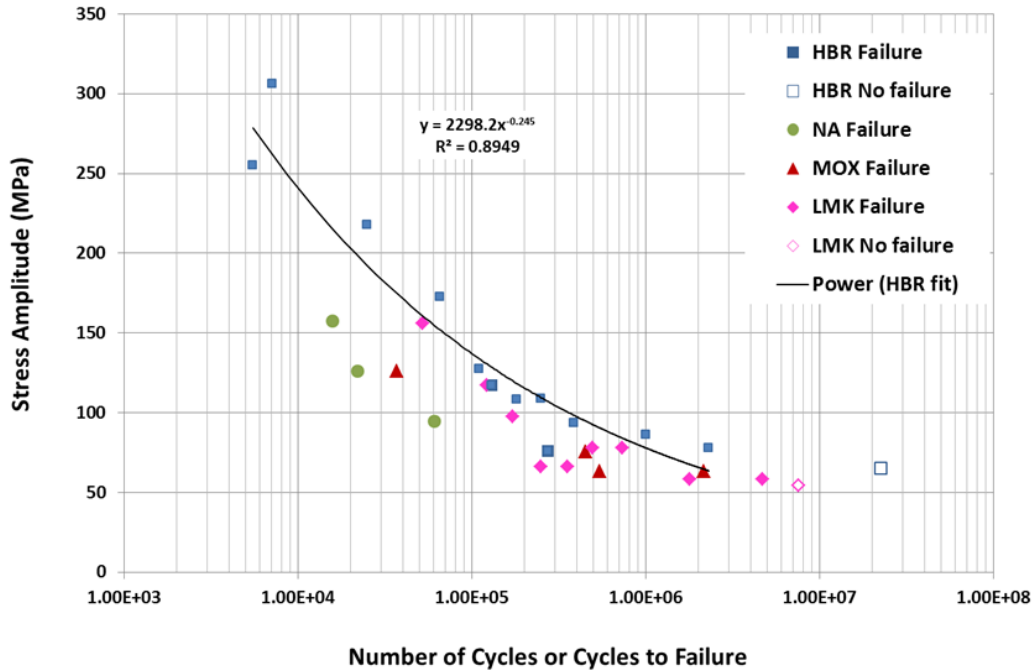


Fig. 87. Stress amplitudes as a function of number of cycles; results are based on CIRFT testing of various used fuels at 5 Hz. The power function was obtained from curve fitting based on the HBR data set.

9.4.3 S-N Curve Based on Young’s Modulus

If Young’s modulus can be estimated with confidence for HBU SSNFNF clads, the lifetime curve can be expressed in terms of stress amplitude at the outer fiber of the cladding. The stress amplitude can be obtained by multiplying the strain amplitude with Young’s modulus provided in Table 11. Based on the limited data collected, there is no difference in Young’s modulus among the listed SNF clad materials.

$$\sigma = E \cdot \varepsilon \tag{5}$$

The results are shown in Fig. 88, although the relative positions of the data points in four SNFs are similar to those expressed by strain amplitude, as shown in Fig. 86. A comparison of the stress estimates of CIRFT-tested samples revealed a large discrepancy between equivalent stress-based and Young’s modulus-based (E-based) approaches. This could be due to the potentially large variances/uncertainties in the clad mechanical properties of HBU SNF systems or due to the simplified SNF system properties assumed in the equivalence stress evaluation. For example, the flexural rigidity (EI) of an ideal SNF system can be written as follows.

Flexural Rigidity: $EI = M/k$

$$EI = E_P I_P + E_C I_C, \text{ for a perfect interface bonding case} \tag{6}$$

$$EI = E_P I_P + E_C I_C - IBE \text{ (Penalty) for interface bonding deficiency case}$$

At fresh fuel state, E_P is typically twice that of E_C . The effective I (calibrated with clad property) in a perfect bond condition can be expressed as $I = I_C + (E_P/E_C) I_P$. The equivalent strain approach is $I = I_C + I_P$, which implies a 50% reduction in Young's modulus of fresh fuel to take into account the SNF system bonding deficiency and aging fuel property degradation.

If SNF Young's modulus for cladding is available and representative (shown in Table 11), then the E-base stress evaluation would be genuine and credible. Further study was done to reconcile the difference between E-based stress and equivalent stress evaluations, where the E-based stress level is much higher than that of the equivalent stress-based profile. A preliminary investigation showed that a reduction in pellet inertia by 50% (due to the porosity and an increase in crack density of irradiated pellets), i.e., $I = I_C + 0.5 I_P$, could actually bring the CIRFT HBR static testing curve up enough to close the gap between the PNNL data and HBR data. The same procedure was applied to processing HBR, LMK, NA, and MOX data, and the results are given in Fig. 89. Including reduced pellet inertia in the calculation of equivalent stress raised the stress as expected. Note that the concept of reduced pellet inertia of moment and the use of Eqs. (2) and (3) were made to demonstrate the relative stress levels between different SNFs and that more modeling is needed to understand the deformation mechanisms and to predict the response of the SNF rod under the corresponding loading condition.

Furthermore, by utilizing and combining E-based and equivalent stress-based evaluation protocols, one can qualitatively estimate the SNF system properties, such as fuel degradation and fuel-clad interface bonding efficiency, if the irradiated clad mechanical properties are available from other means. Also note that the equivalent stress-based profile approach from a global SNF system response point seems to be more representative with regards to SNF composite system properties as well as the interaction potential of SNF system pellet-clad components. Therefore, the E-based stress approach is directly related to clad properties only, instead of a SNF system performance evaluation index.

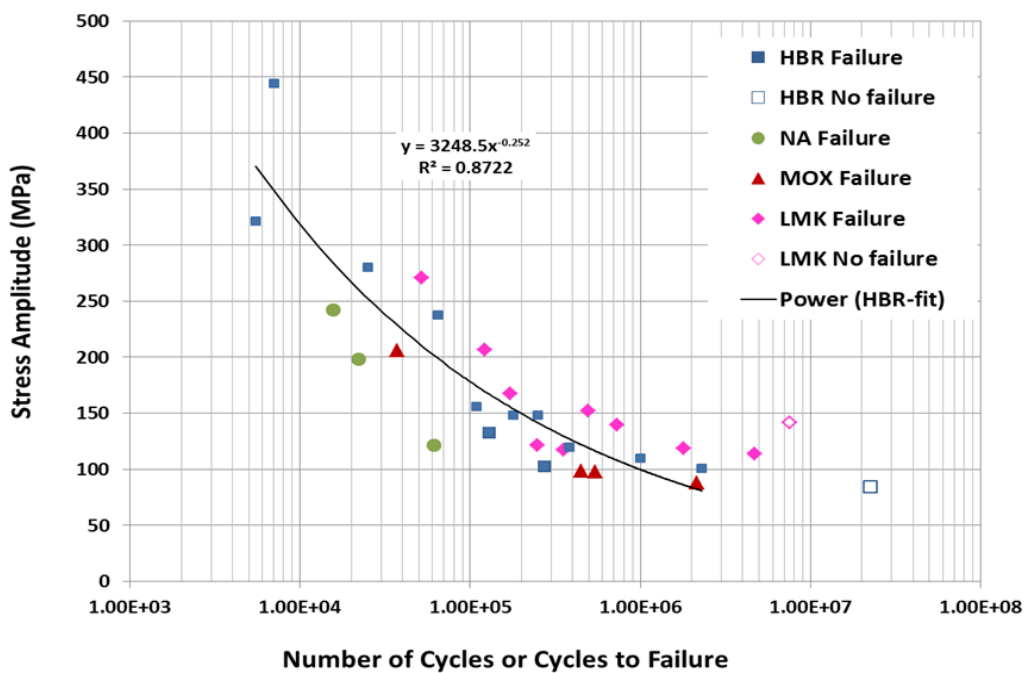


Fig. 88. E-based stress amplitudes as a function of number of cycles; results are based on CIRFT testing of various used fuels at 5 Hz. The power function was obtained from curve fitting based on the HBR data set.

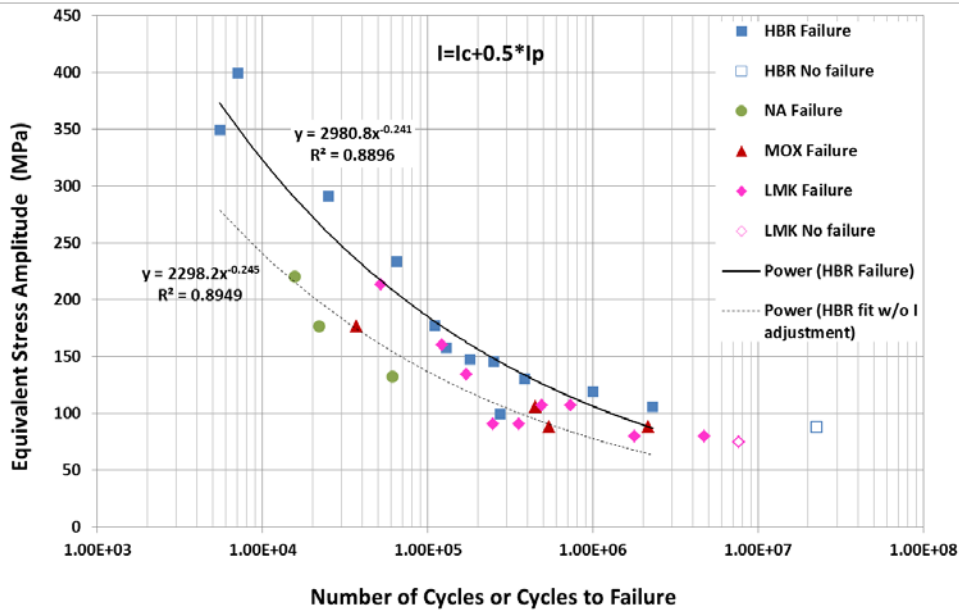


Fig. 89. Equivalent stress vs. life curves based on CIRFT testing results for HBR, NA, and MOX SNF. The equivalent stress is based on Eq. (3) with modified moment of inertia, $I = I_c + 0.5 * I_p$.

9.4.4 The Impact of Transient Shock on SNF Vibration Fatigue Life

In general, hydrides reduce cladding fracture toughness, impact strength, and ductility, especially at a high strain rate loading, i.e., transient shocks under NCT of SNF transport. The degree of embrittlement critically depends on the hydride orientation relative to the applied stress. Factors such as cladding composition, fabrication, and irradiation history, including temperature, chemical, cooling rate, and clad residual stress levels, will influence hydride characteristics that can dictate SNF dynamic performance and its associated fatigue lifetime.

A fuel assembly skeleton, formed by guide tubes and spacer grids, is typically designed to constrain the fuel assembly in a reactor operation. However, due to the SNF horizontal installation for fuel transport, guide tubes and spacer grids are now becoming load-bearing members for fuel assembly dead and dynamic loads. Therefore, spacer grids and guide tubes are responsible for the load transferring/linking mechanism within the fuel assembly during transport. Thus, the integrity of guide tubes and spacer grids will critically affect the vibration modes and the vibration intensity/amplitude of a fuel assembly during transport. The typical load-time history registered by an accelerometer on a transport cask is shown in Fig. 90, which consists of continuous excitation and periodic transient shock loading.

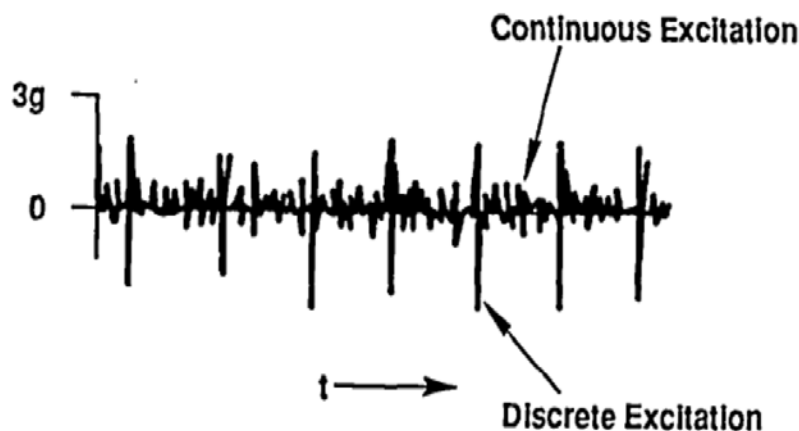


Fig. 90. Typical load-time history on a transport cask with the acceleration-time history showing discrete shock signals superimposed on continuous vibration signals.

The above mentioned cask random vibration history provides the external loading driver to SNF assembly. Regarding the cask internal, another form of transient shocks driver existed from the dynamic contacts interactions of the fuel assembly components, such as canister basket wall, fuel rods, and spacer grids dynamic contact impacts, during normal conditions of SNF transport. This internal transient shock event was demonstrated in SNL truck test results,¹⁷ where significant acceleration of 20 g was registered/observed at spacer grip while the surrogate rods show insignificant strain deformation in axial orientation.

In order to further quantify or estimate the damage potential of the transient shock to the SNF vibration lifetime, a pilot study was carried out on MOX and LMK SNF. The CIRFT specimens were dropped two to three times from heights ranging from 1 to 2 ft to simulate the transient shock prior to initiating the CIRFT bending cycling test at a frequency of 5 Hz. The accelerated aging effects of the tested MOX and LMK CIRFT samples that had been dropped are shown in Fig. 91. The details of samples' locations in the as-received LMK rods are also identified in Fig. 91 on the right. The LMK CIRFT rods that were dropped 1 ft at 10 N-m load show a 50% reduction in fatigue life. MOX CIRFT rods that were dropped 2 ft at 5 N-m load show a 73% reduction in fatigue life. Noted that one MOX rod at a 10 N-m loading level that had been dropped 2 ft does not show any accelerated aging. Due to variability of SNF rods and their inherent defect intensity, a more controlled CIRFT testing protocol needs to be included in the follow-on CIRFT high-rate testing program development.

All the LMK rods that were received are from the bottom portion of the parent SNF rods. It is interesting to note that the CIRFT sample taken from spacer grid region (*B* location shown in Fig. 91) shows the lowest life compared to CIRFT samples from other locations under the same bending amplitude vibration, even with drop loads. This could be due to higher fretting damage potential at spacer grid regions. Moreover, LMK samples taken from the bottom of the fuel rod, which has higher mechanical constraint in a SNF system under reactor operation, also show accelerated aging compared to that of samples from A and B sections.

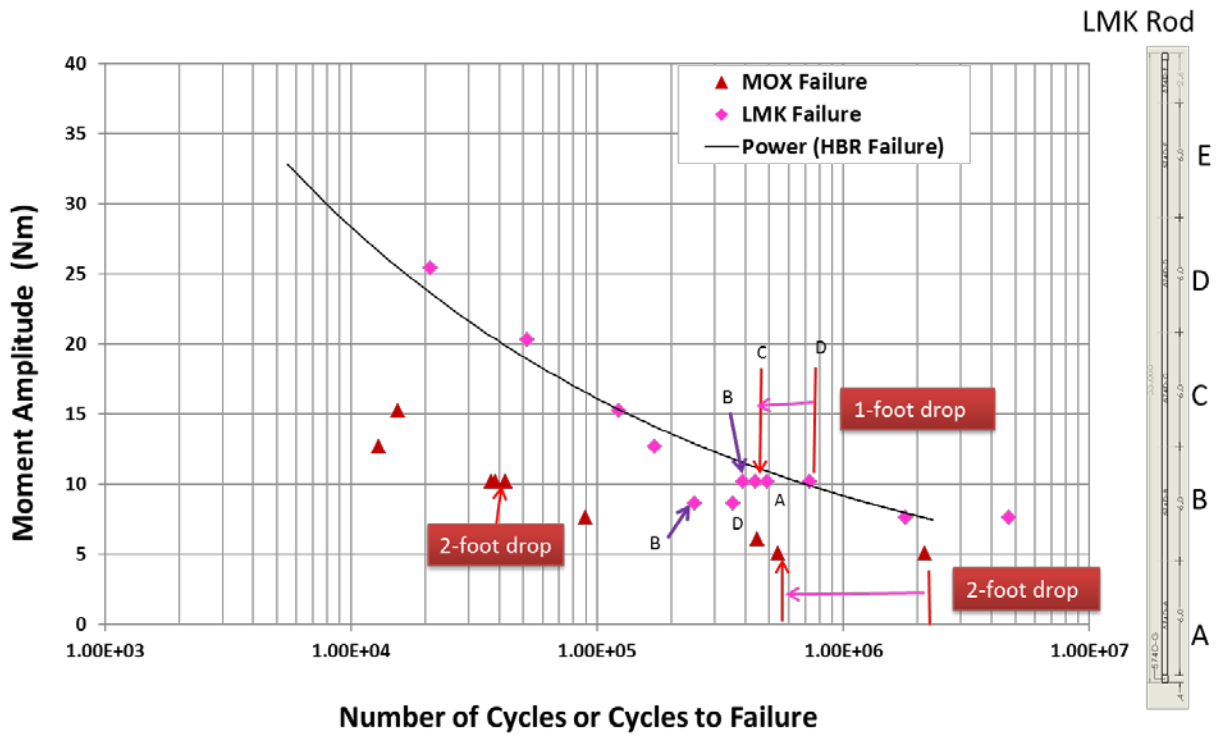


Fig. 91. Pilot transient shocks simulation study on MOX and LMK SNF. The reduction in lifetime of CIRFT-tested SNF samples was observed from combining the harmonic vibration loading and drop-induced transient shock load. LMK CIRFT results also reveal that the CIRFT sample from the spacer grid region (B section) has the lowest lifetime compared to samples from locations A, C, and D.

10. FINITE-ELEMENT ANALYSIS OF LMK BWR CLAD MATERIAL

10.1 Introduction

The finite-element analysis (FEA) model of an LMK fuel rod system is formed by UO₂ pellets and Zircaloy-2 cladding. It incorporates appropriate boundary conditions including the bonding layer at clad/pellet interfaces. The model consists of a fuel rod with a three-dimensional (3D) representation of fuel pellets, clad, and possible combinations of gaps at the pellet-pellet and pellet-clad interfaces. The ABAQUS code was used, and the fuel rod was represented by a beam element with the associated effective stiffness. This approach was used to obtain the effective properties of the beam elements for use as input for further development of the detailed SNF assembly model. The approach is also designed to estimate the damping properties of the beam elements due to frictional resistance between the clad and the embedded pellets. This pellet-clad interaction modeling uses a “contact element” algorithm and can be further implemented into other embedded boundary conditions such as internal pressure and residual stress.

This study provides detailed explanations of the effects of pellet-pellet and pellet-clad interactions—including pellet fracture and pellet-clad bonding efficiency—on cladding performance reliability. The FEA simulation results were also calibrated and benchmarked with CIRFT LMK data.

10.2 Interface Bonding Efficiency Analysis of BWR Fuel Rod

Following the method described in Refs. 18 and 19, ABAQUS was used in a structural analysis and interfacial bonding evaluation of BWR fuel rods. Simulation results were closely compared with those of PWR HBR fuel rods. The BWR fuel rods and PWR HBR fuel rods were both tested in a hot cell environment with the CIRFT tester developed at ORNL.^{3,20,21} To validate the simulation results, the same fuel rod materials were used in the hot cell tests and the FEA. The pellet material was UO₂, and the clad material was Zircaloy-2 for BWR and Zircaloy-4 for PWR. An epoxy was used as an interface bonding material to simulate fused areas for PWR. The interface material for BWR was Zircaloy-4. Table 12 lists the material properties of the fuel rod.

Table 12. Mechanical properties of the fuel rod

	Material	Young’s modulus (psi)	Poisson’s ratio	Yield strength (psi)	Density (lb/in. ³)
Pellet	UO ₂ *	2.92e7	0.32	3.11e5	0.396
BWR Clad	Zircaloy-2**	1.32e7	0.37	1.33e5	0.237
PWR Clad	Zircaloy-4*	1.32e7	0.33	1.31e5	0.237
PWR Interface	Epoxy*	5.07e5	0.37	10007.6	0.0452
BWR Interface	Zircaloy-4*	1.32e7	0.33	1.31e5	0.237

*Ref. 3

**Ref. 14

10.2.1 Good Interface Bonding and No Fuel Rod System Fracture

In this section, the simulation case for the BWR fuel rod with good interface bonding and without inserted rod fracture was studied. The pellet-clad interfaces were tied together with a thin Zircaloy-4 film.

Fig. 92 shows the geometry of a U-frame bending fatigue testing system with a coplanar configuration for the fuel rod. The 2 in. gage section is highlighted in black. A finite-element model was established to represent the 2 in. gage section of the test specimen. The model is referred to as the “clad-pellet two inch section model.”

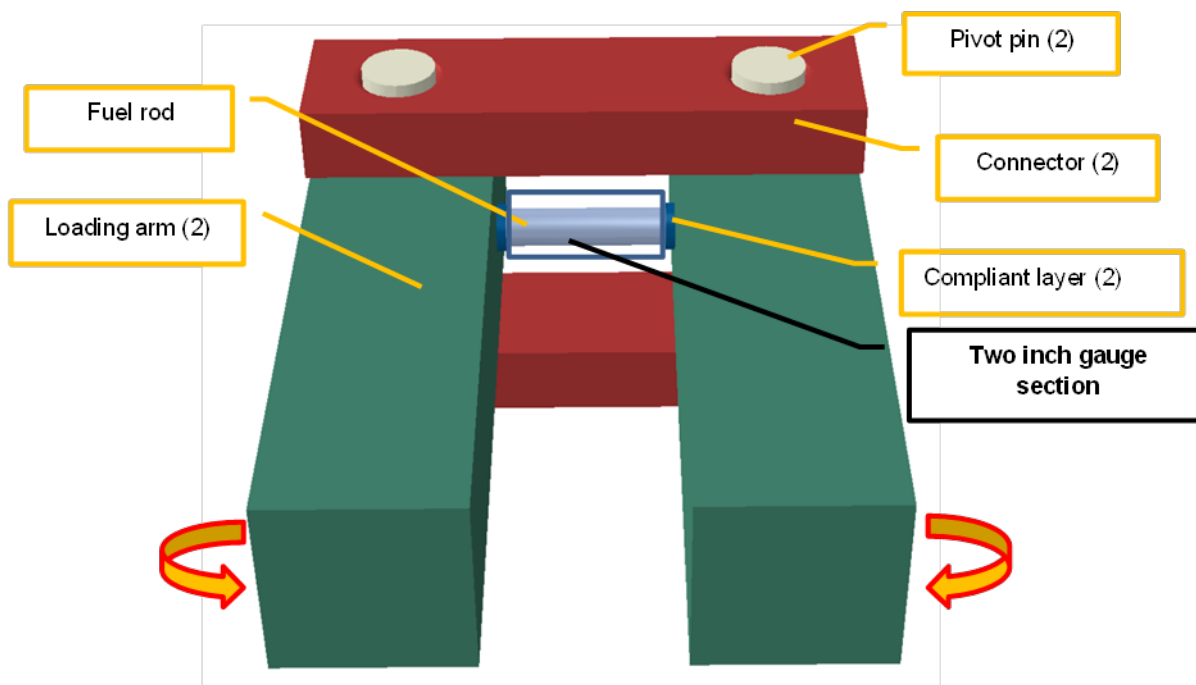


Fig. 92. Geometry of horizontal U-frame bending fatigue testing system with a coplanar rod configuration.

The outer diameter (OD) of the BWR cladding is 0.4402 in. The cladding thickness is 0.028 in., so the inner diameter (ID) is 0.3842 in. The BWR pellet length is 0.4162 in., which is longer than the 0.273 in. length of the PWR HBR rod in a previous report.²² The pellet OD is 0.3742 in. The pellet ends dish-in to reduce pellet surface clinging. As shown in Fig. 93, both ends of the pellet were constructed with a dip diameter of 0.28 in. and a depth of 0.001 in., so that the end surfaces would not touch at the dished-in area.

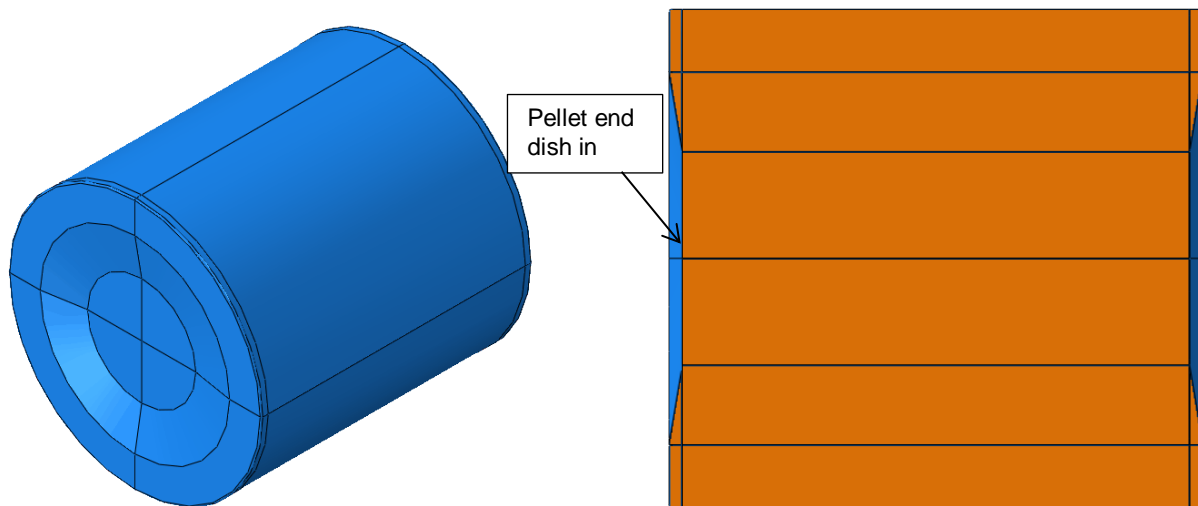


Fig. 93. FEA model of BWR pellet.

Fig. 94 illustrates the clad-pellet 2 in. section model of BWR fuel rod with six pellets. In the 2 in. gage section, four full-length and two partial-length pellets were modeled. There is a Zircaloy-4 film between the clad and pellet interface with a thickness of 0.005 in. To simulate “good interface bonding” at the pellet-pellet interface and an unfractured rod system, the pellet-pellet and pellet-clad interfaces were all tied. Bending moments were applied on both ends of the fuel rod rotating along the X axis as shown in Fig. 94 (b). The bending moment M_x was 7.6 N·m, the same as that used in the tests of the BWR fuel rod. Both loading surfaces of the fuel rod were constrained with rotation along the Y and Z axes and translation along the X direction. In the following finite-element models, the global mesh is 0.02 in., and some local meshes are as small as 0.0025 in. The quasistatic procedure is used in the FEA from ABAQUS.

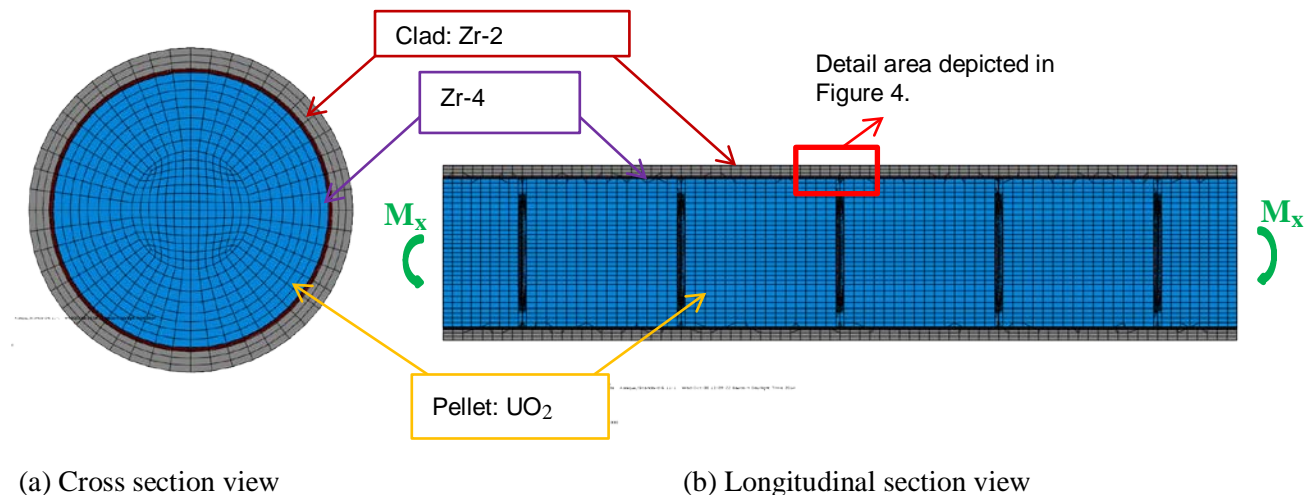


Fig. 94. Geometry of clad-pellet 2 in. section model of BWR fuel rod with six pellets.

Fig. 95 shows the configuration of the detail area from Fig. 94. The pellets were modeled with rounding of 0.002 in. on the end surfaces, and the end surfaces were dished at both ends to avoid pellet clinging. The dished areas of the pellet end surfaces do not come into contact during bending. Thin Zircaloy-4 film is tied to the surfaces of the pellet-clad interfaces. At the pellet-pellet interfaces, epoxy is filled in the gap to simulate the perfect bond at the interfaces. The epoxy layers at the pellet-pellet interfaces in the model are 0.0014 inch thick.

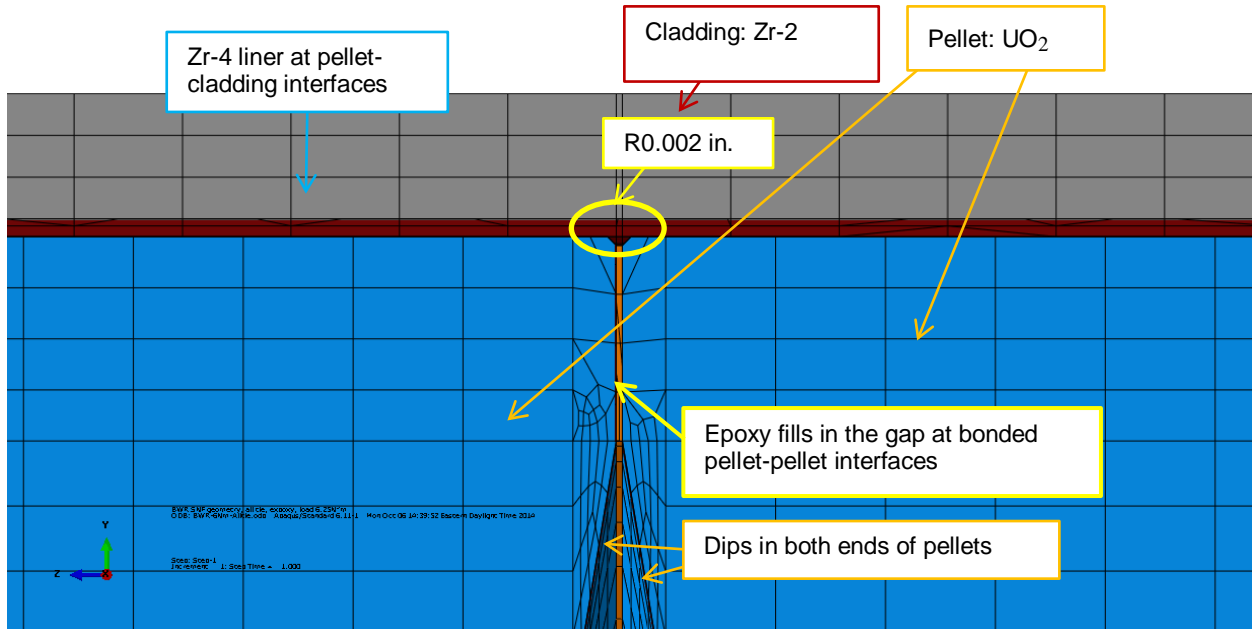
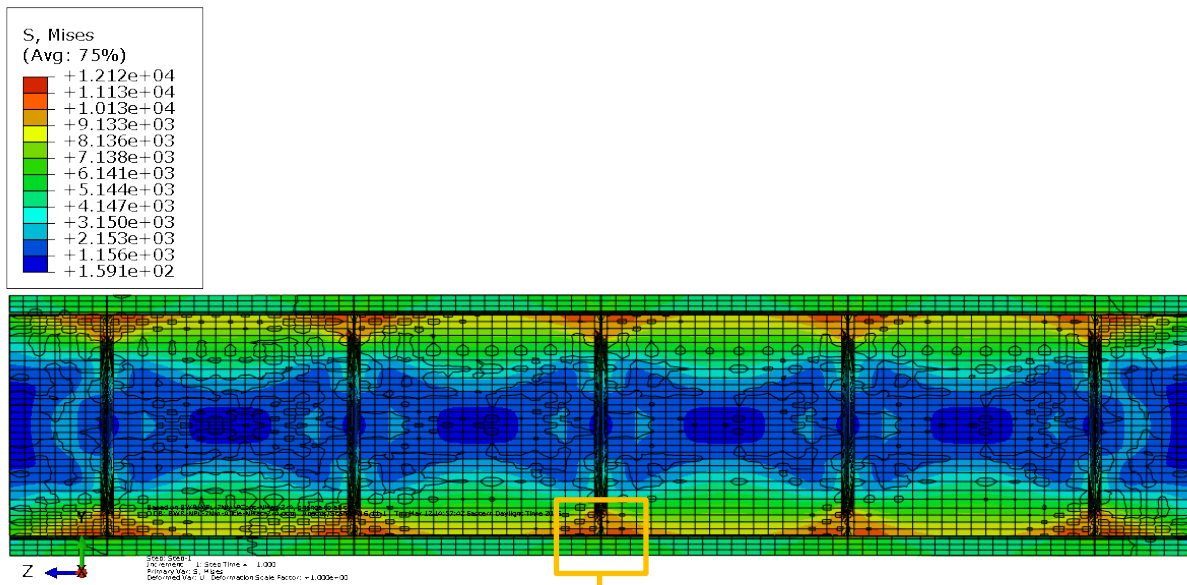
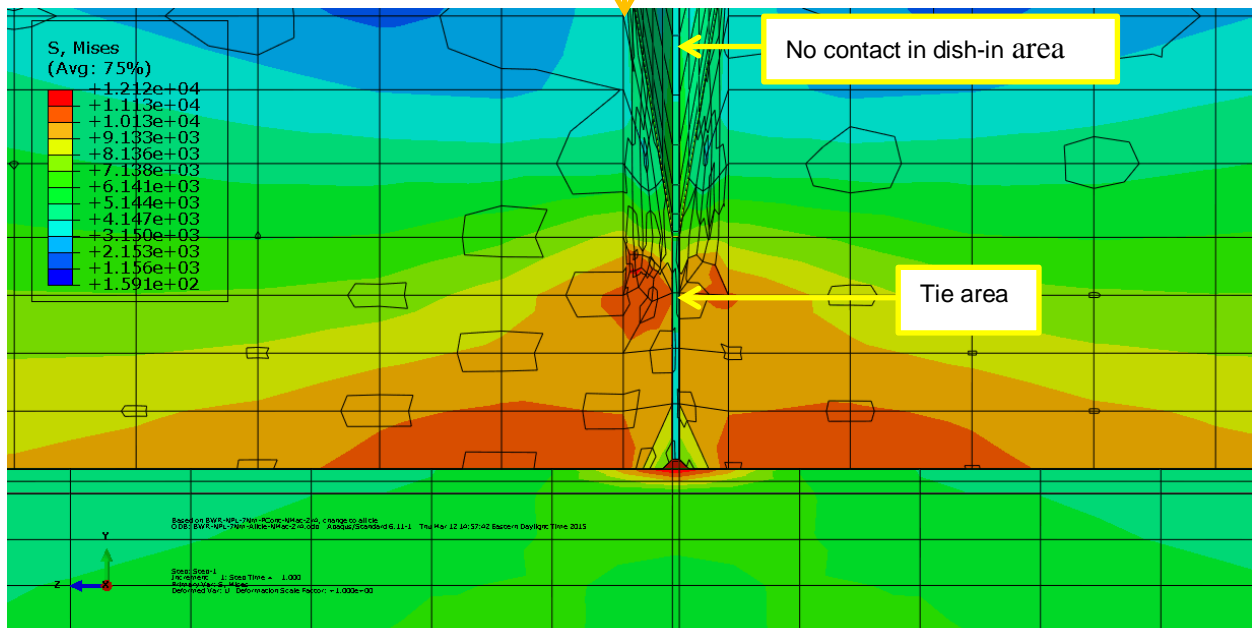


Fig. 95. Detail area from Fig. 94 for the perfect bond cases.

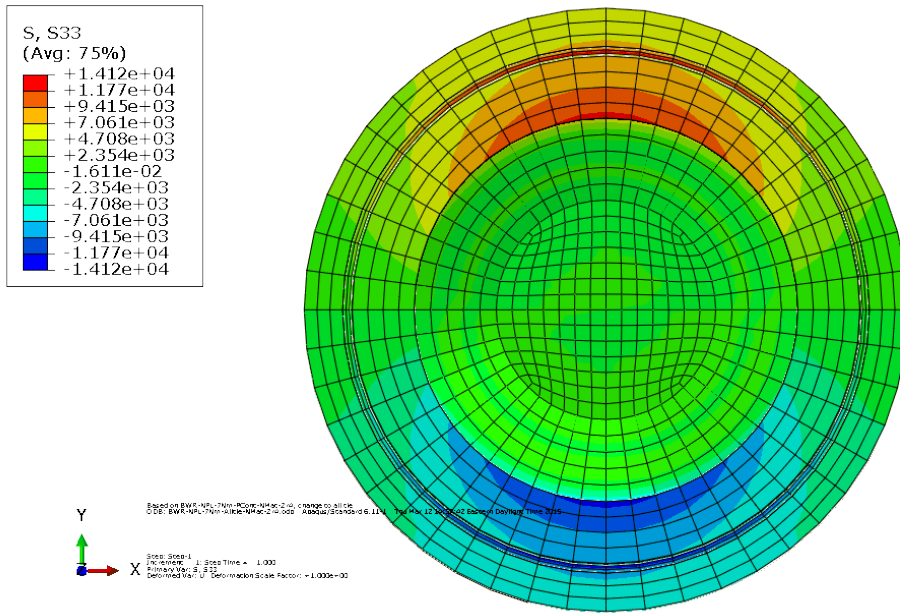
The resulting normal stress distribution and the curvature under the bending moment 7.6 N·m are shown in Fig. 96. The resultant curvature is 0.077 m^{-1} , which is too small to be noticeable. Based on the stress distribution shown in Fig. 96 (a), the maximum stress occurs at the pellets, which indicates that the perfectly bonded pellets carry a larger portion of the moment resistance than the clad. From the detail view shown in Fig. 96 (b), the maximum stress is observed at the pellet-pellet interface tie area. The perfect bond assigned at the interface tie area is carrying most of the bending moment resistance. The stress in the clad is under the yield point of 133 ksi. Therefore, the clad has not yielded under the 7.6 N·m bending moment, nor has the pellet, which has much higher yield strength than the clad. This indicates that the BWR fuel rod with a perfect bonding condition will remain within the linear elastic range under the target loading. The resultant σ_{zz} at the pellet-pellet interface in Fig. 96 (c) shows the maximum stress concentrated on the limited tie areas. This occurs because the dips in the ends of the pellets cause the contact surfaces to be confined to a limited area.



(a) Longitudinal section view of curvature and von Mises stress



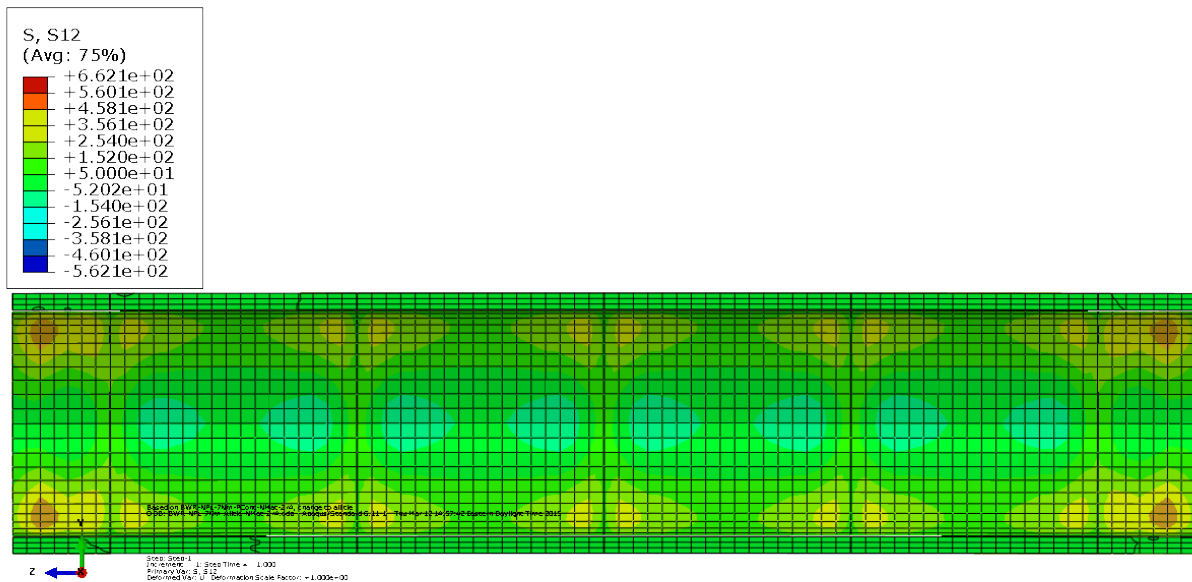
(b) Detail area view



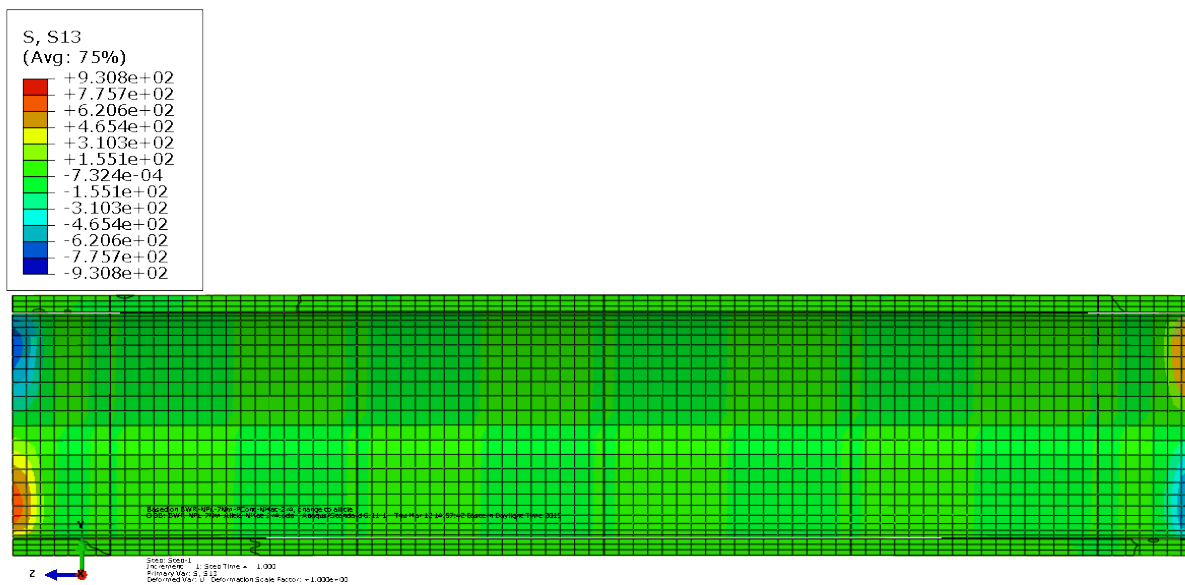
(c) Cross section view of σ_{zz} at a pellet-pellet interface

Fig. 96. Normal stress distribution and curvature results for clad-pellet 2 in. section model of BWR fuel rod with perfect bonding.

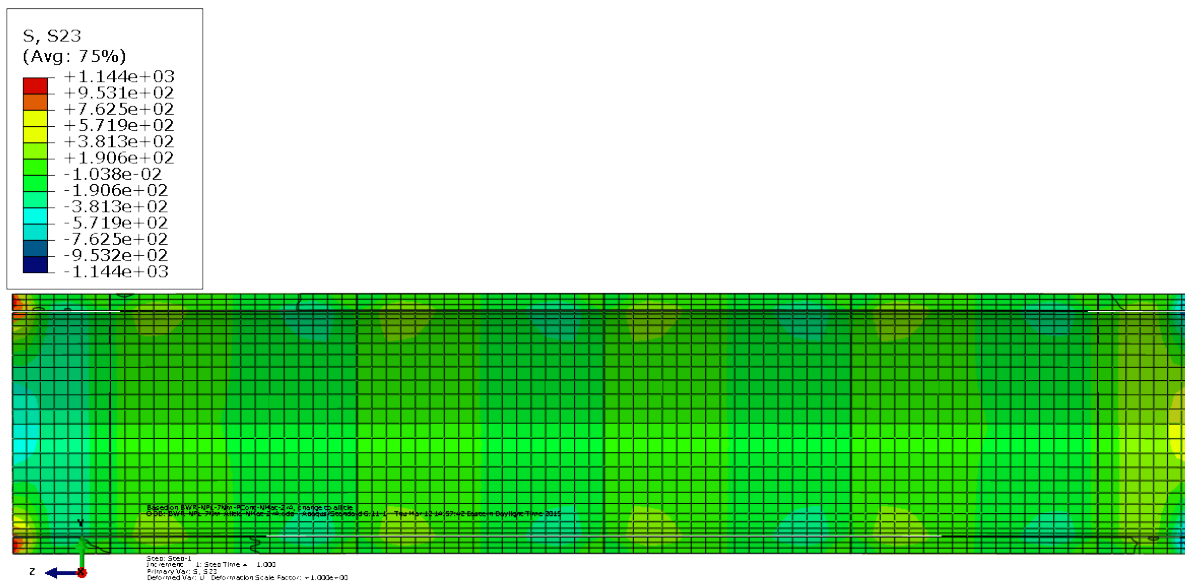
Fig. 97 shows the shear stress distribution under the bending moment of 7.6 N·m at the cladding. Shear stresses at the cladding are minimal. As a result of the perfect bonding, the pellets and the cladding work as a whole. There is no shear stress concentration inside the gage section. The stress concentration occurs at the boundary as a result of composite material mismatch under flexural deformation.



(a) Shear stress σ_{xy}



(b) Shear stress σ_{xz}



(c) Shear stress σ_{yz}

Fig. 97. Shear stress distribution at the clad for the clad-pellet 2 in. section model of BWR fuel rod with perfect bonding.

The curvature and flexure rigidity for this case is summarized in Table 13. A load control procedure was used. The bending moment M was applied to both ends of the fuel rod, and the bending curvature κ was estimated from the FEA results within the gage section. The flexural rigidity EI (the product of the Young’s modulus E and the moment of inertia I) of a fuel rod can be estimated using the applied moment M and the resultant curvature κ , as described in Eq. (6).

$$EI = M/\kappa. \tag{6}$$

Based on the resulting σ_{zz} , shown in Fig. 96 (c), the bending moment was calculated for the cladding and pellets, respectively. The total resultant bending moment should be equal to the bending load M_x , 7.6 N·m for BWR and 6.25 N·m for PWR. Estimated bending moments for the cladding and pellets are also summarized to directly compare the load carrying capacity of the different system components. In order to directly compare with PWR fuel rods with HBR pellets, the simulation results of PWR fuel rods with HBR pellets for the perfect bond case are also summarized in Table 13.

Table 13. The curvature, flexural rigidity, and bending moment comparison for the perfect interface bonding simulation

		Curvature $\kappa(1/m)$	Flexural rigidity EI (N·m ²)	Clad bending moment M (N·m)	Pellet bending moment M (N·m)	Total bending moment M (N·m)
Perfect bond	BWR	0.077	99	2.79	4.81	7.6
	PWR HBR	0.082	77	2.45	3.80	6.25

Table 13 shows that the flexural rigidity for a perfect bonding condition is 99 N·m² for the BWR fuel rod and 77 N·m² for the PWR HBR fuel rod. The flexural rigidity of BWR is 22% higher than PWR rod. When the two systems are compared, the differences are pellet length and the material at the pellet-clad interface. For a perfect bonding condition, pellet length will not be the cause of the difference, while pellet-clad interface material will be a major factor. As shown in Table 12, Zircaloy-4 has a much higher Young’s modulus than epoxy, which causes much higher stiffness of the BWR system. Based on the load-carrying capacity, the perfectly bonded pellets take over more of the bending moment than the cladding for both cases. Bending moment distributions among pellet and cladding are similar for both cases.

The condition of the ORNL HBR fuel rod hot-cell testing specimens resembles that of the clad-pellet 2 in. section model with epoxy-filled gaps at the pellet-pellet interfaces. The HBR fuel specimen was tested at a 6.25 N·m bending moment. Fig. 98 shows the ORNL hot-cell CIRFT test data. The flexural rigidity based on the hot-cell test data was observed to be between 60 and 70 N·m², and the curvature was around 0.09 m⁻¹. The initial (first cycle) test data usually have the highest flexural rigidity, since the pellet-clad and pellet-pellet interface bonds should maintain the best status before bending fatigue damage. The flexural rigidity in the first test data was a little lower than the FEA estimate, which indicates this testing sample probably has interfacial debonding, rather than perfect bonding, at the initial test stage.

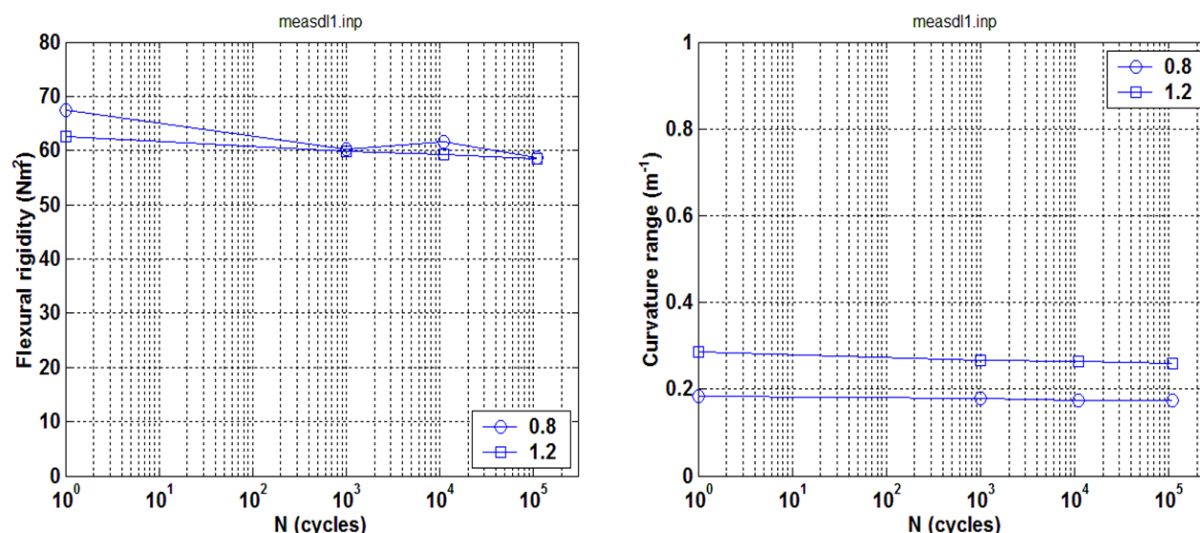


Fig. 98. ORNL hot-cell CIRFT test data of PWR HBR fuel rod, flexural rigidity, and curvature.¹⁸

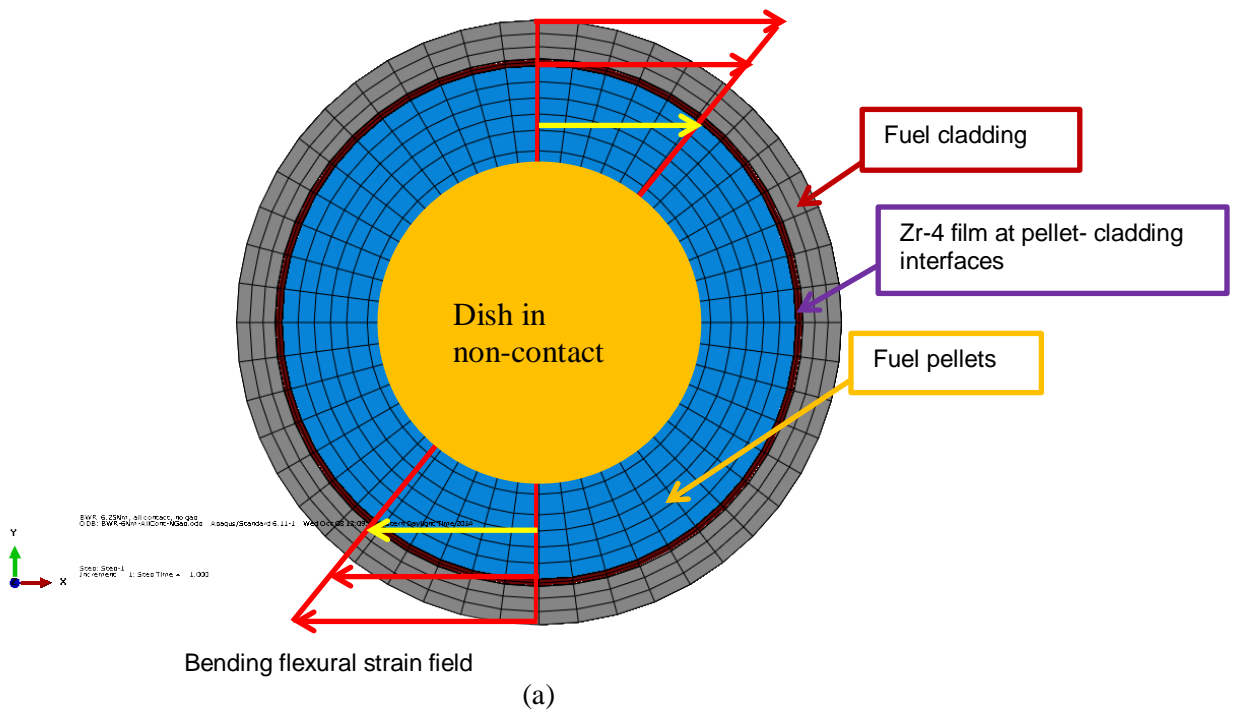
With good interface bonding and without fuel rod fracture, the fuel rod can carry most of the bending moment under normal transportation vibration as a result of the higher Young’s modulus of the fuel pellet compared with the clad—in addition to a much higher yield stress, as shown in Table 12. ORNL fuel data validate that inserted pellets can carry more moment resistance than the cladding because of their higher stiffness, if the pellet-clad and pellet-pellet interface bonds remain intact. Because of the high yield strength of the pellets, the fuel rod responds to the bending moment within the linear elastic range. The high flexural rigidity estimated from FEA agrees well with that estimated from bending fatigue testing data. Furthermore, under cyclic loading, it is expected that the interface bond will be progressively degraded, as is demonstrated in Fig. 98, with decreasing flexural rigidity under increased loading cycles.

10.2.2 Debonding at Pellet-Pellet Interfaces and Bonding at Pellet-Clad Interfaces

Before high-burnup SNF is transported, there are inherent stress fields in the SNF system. For example, there may be axial tensile stress and tangential tensile stress due to pellet-clad mechanical interaction or oxide volume expansion, radial compressive stress due to hydride compaction, and tangential shear stress due to hydride volume expansion. Vibration during transportation will induce reversal bending in an SNF assembly. Repeated expansion and contraction in both the axial and tangential directions of the SNF rod due to reversal bending flexural deformation, combined with stress concentration, can degrade the interface bonding at the fuel pellet-clad and pellet-pellet interfaces (Fig. 99). Although the shear stress is small relative to the normal stress due to bending, that does not mean that it can be neglected. In

composite rods or SNF rods in particular, excessive shear due to material mismatch can be a cause of interfacial bonding failure.

At pellet-pellet interfaces, interfacial bonding failure is caused mostly by normal stress due to reversal bending flexural deformation combined with relatively smaller shear stress (see Fig. 99). At pellet-clad interfaces, localized high shear stress will also arise to compensate for the material mismatch under flexural deformation. As mentioned earlier, the shear stress is small relative to the normal stress; therefore, it is likely that interfacial bonding failure at pellet-pellet interfaces will begin before debonding occurs at pellet-clad interfaces. In addition, the pellets have dished noncontact areas at both end surfaces, so the bonding area at the pellet-pellet interface is limited to a relatively small area, making it easier for the pellet-pellet interfaces to debond. Observations of an ORNL reversal bending fatigue surrogate stainless steel rod with alumina pellets verified this hypothesis. The clad-epoxy-pellet model with six pellets was used to investigate the BWR fuel rod bending response with perfect bonding at pellet-clad interfaces and debonding at pellet-pellet interfaces. The material properties, geometry, loading and boundary conditions were the same as those used in the previous FEA simulation. The simulation results were compared with those of PWR HBR fuel rod under the same bonding conditions.



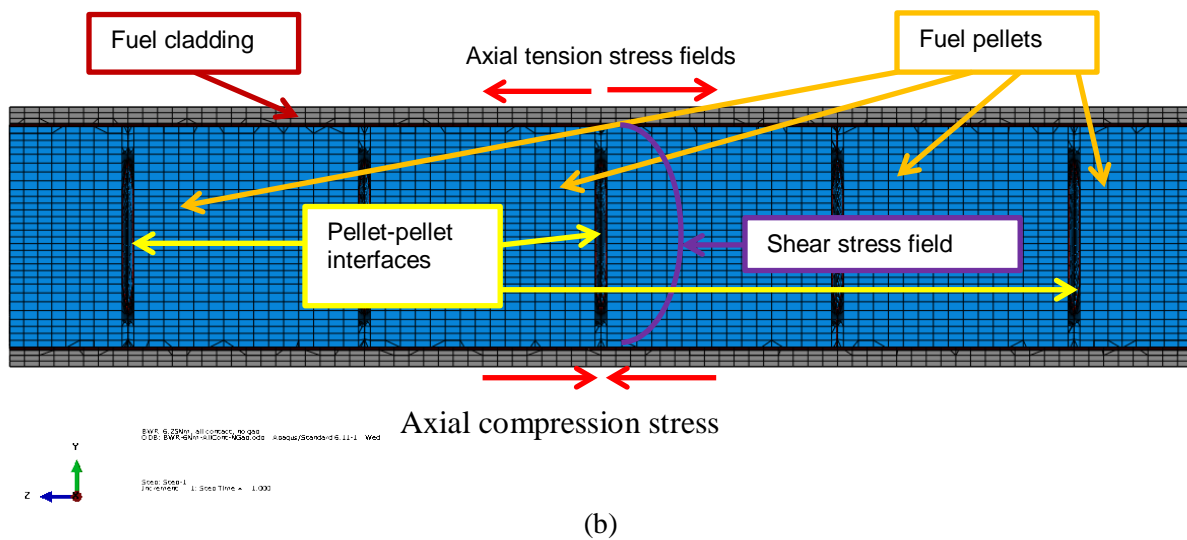


Fig. 99. Transportation-induced reversal bending stress fields in an SNF system.

10.2.2.1 Debonded Pellet-Pellet Interfaces with Empty Gaps

In the BWR rod, there was a thin Zircaloy-4 film at pellet-clad interfaces, so a Zircaloy-4 film was modeled as a bonding layer tied to the surfaces at the pellet-clad interfaces. In this section, the case study was designed to simulate the response with a debonded pellet-pellet interface. There are empty gaps at the pellet-pellet interfaces (Fig. 100), and during bending flexural deformation, the pellets overcome the gaps and then contact one another at the interfaces. The pellets have dips and end surfaces with a rounding of 0.002 in.

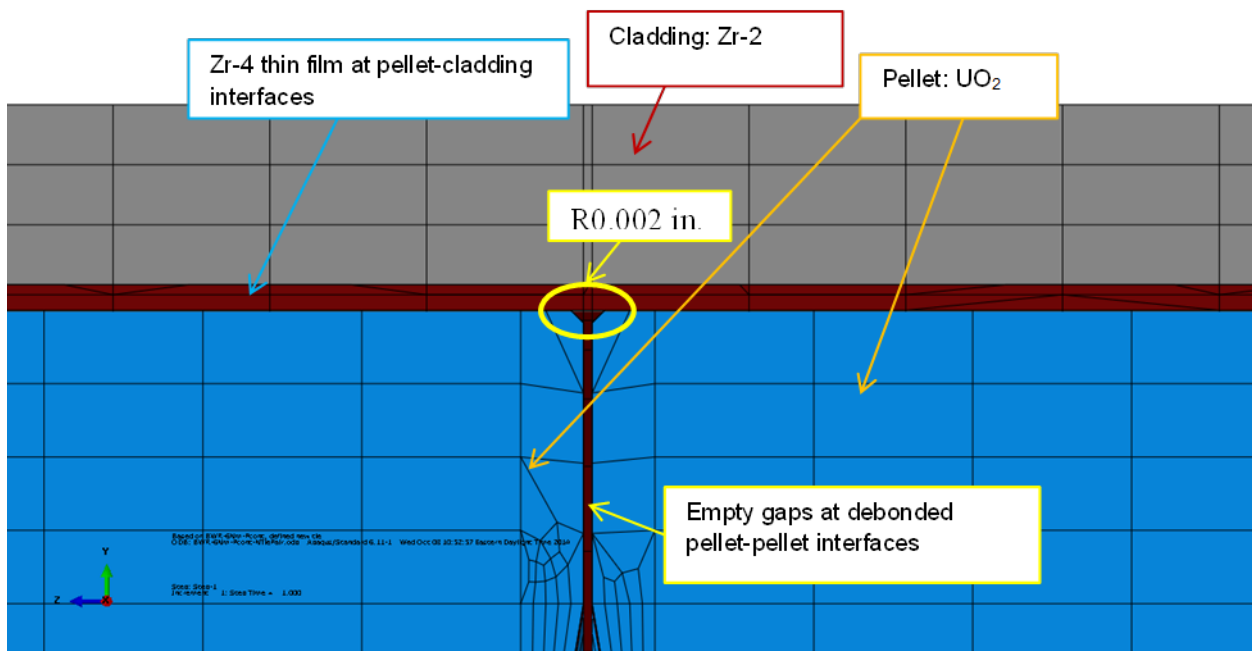
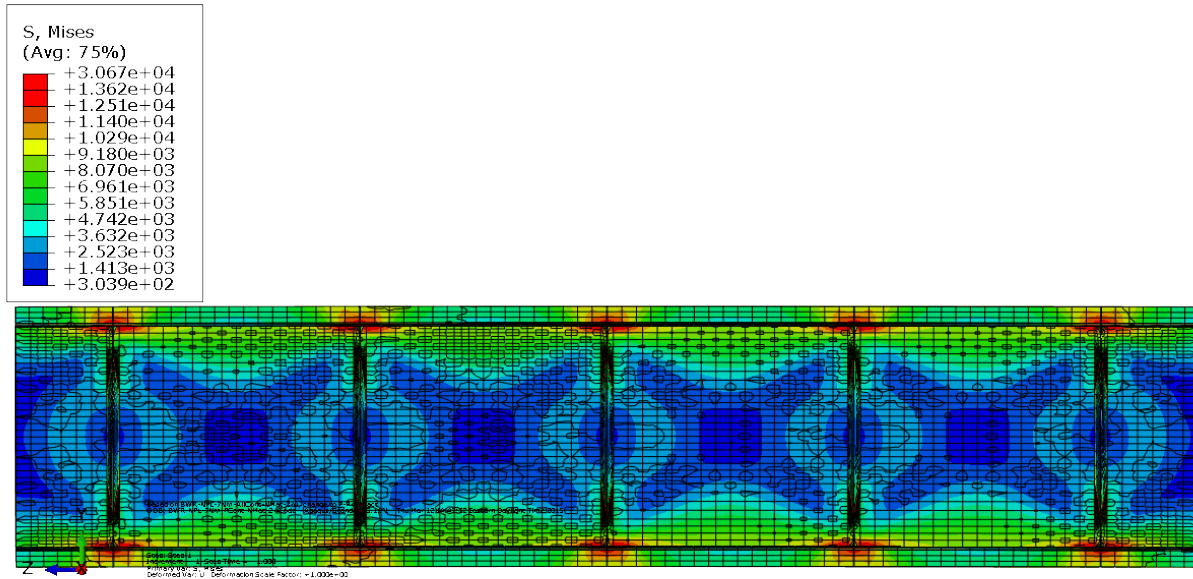


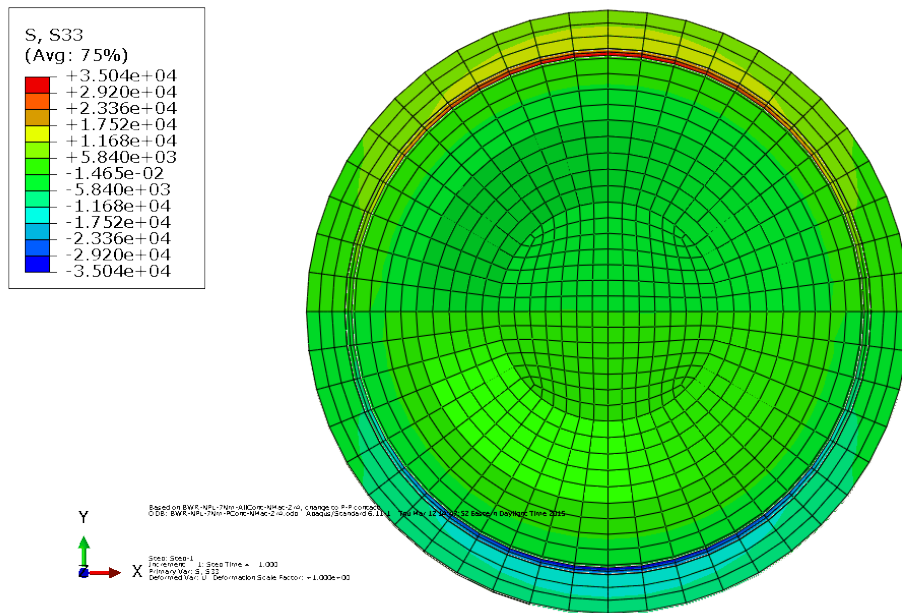
Fig. 100. Detail from Fig. 94 for the case of empty gaps at debonded pellet-pellet interfaces.

The normal stress and curvature responding to the bending moment are illustrated in Fig. 101. Compared with the results shown in Fig. 96, there are significant differences in the stress distribution between the pellet-pellet interface bonding case and the pellet-pellet interface debonding case; the pellet-clad interface remains perfectly bonded in both cases. For instance, at the pellet-pellet interface in the debonding case, the maximum stress occurs at the clad and the Zircaloy-4 film and is located at the top and bottom portions of the pellet-pellet interface regions. As a result of the small bending moment, the maximum stress at the clad is lower than the yield strength of Zircaloy-2, as shown in Table 12, so the Zircaloy-2 clad does not yield. In most of the clad, the stress is much lower than the maximum because the perfect pellet-clad bonding provides good support to the clad. Since there are gaps between pellet-pellet interfaces, the clad deforms continuously until the gaps are reduced by direct contact of the pellet-pellet surfaces. The resulting σ_{zz} clearly indicates that the clad takes over more of the bending moment resistance than the pellets at the debonded pellet-pellet interfaces.

At the debonded pellet-pellet interfaces, the pellets can transfer load only via hard contact, so the load-carrying capacity shifts significantly from the pellets to the clad. When the Zircaloy-2 clad starts to carry most of the bending moment at the pellet-pellet interface region, the result is maximum stress concentration at the Zircaloy-2 clad. However, in most of the gage section, the pellets still provide sufficient internal support to the clad because of good cohesive bonding at the pellet-clad interfaces, and they will carry most of the bending load. Therefore, there is much lower stress in most regions of the Zircaloy-2 clad.



(a) Longitudinal section view of resultant curvature and von Mises stress

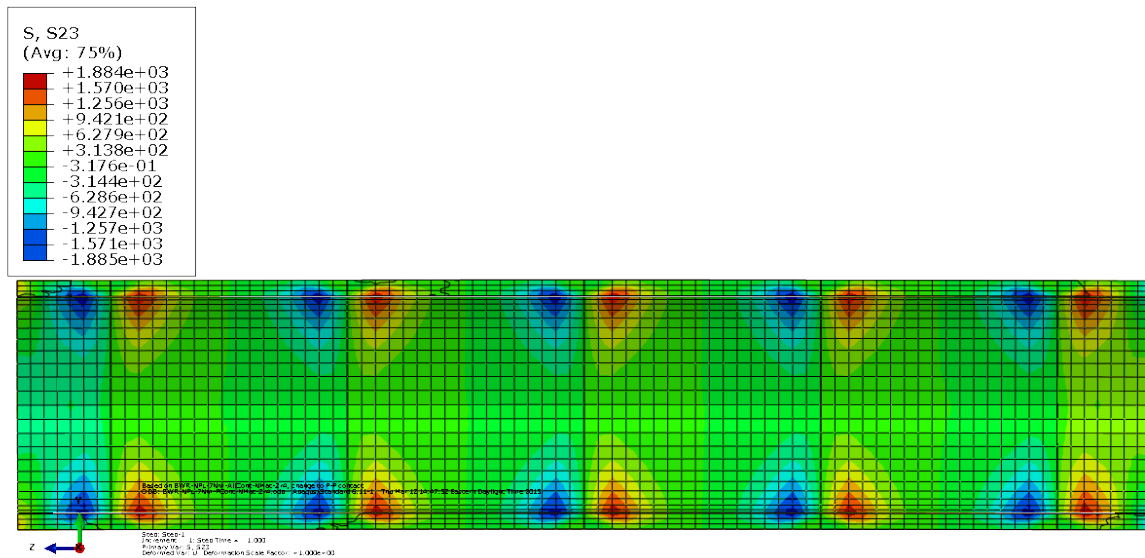


(b) Cross section view of resultant σ_{zz} at a pellet-pellet interface

Fig. 101. Normal stress distribution and curvature results for the clad-pellet 2 in. section model of BWR fuel rod with debonded pellet-pellet interfaces with gaps and bonded pellet-clad interfaces.

In Fig. 96, the results of the perfect bond case show that the pellets carry significant bending moment resistance; the maximum stress resides on the pellets, and there is no yielding at either the pellets or the clad. It is also interesting to note that the von Mises stress distribution in debonded pellets appears to be different from the results of the bonded pellet-pellet interface case. The third discrepancy lies in the induced curvature. In the debonding case, the curvature is 0.10 m^{-1} , 23% higher than that of the perfect bond case shown in Fig. 96.

In Fig. 102, the difference from the results in Fig. 97 for the perfect bond case is apparent. With the pellet-pellet interfaces debonded, the shear stresses surge near the pellet-pellet interface debonding region inside the cladding. The reason might be an increase in shear stress due to a composite material mismatch at the debonded pellet-pellet interface boundary under bending flexural deformation. With good cohesive bonding at pellet-clad interfaces, the clad transfers some shear load at the debonding region. If there are small gaps at the pellet-pellet interfaces, the shear stress concentration occurs at both the top tension and bottom compression regions of the clad. Maximum stress levels are higher than in perfect bond cases; however, the shear stresses are still one order of magnitude lower than the normal stress in the same simulation case.



(c) Shear stress σ_{yz}

Fig. 102. Shear stress distribution at the clad of the clad-pellet 2 in. section model of BWR fuel rod with debonded pellet-pellet interfaces with gaps and bonded pellet-clad interfaces.

10.2.2.2 Debonded Pellet-Pellet Interfaces without Gaps

Fig. 103 illustrates the simulations of debonded pellet-pellet interface and bonded pellet-clad interface. There are no gaps at the pellet-pellet interfaces before bending loading is applied. Similar to the previous cases, a thin Zircaloy-4 film is tied to the surfaces at the pellet-clad interfaces. Except for elimination of the gaps at the pellet-pellet interfaces, the geometry, materials, loading and boundary conditions are all the same as in the previous simulations.

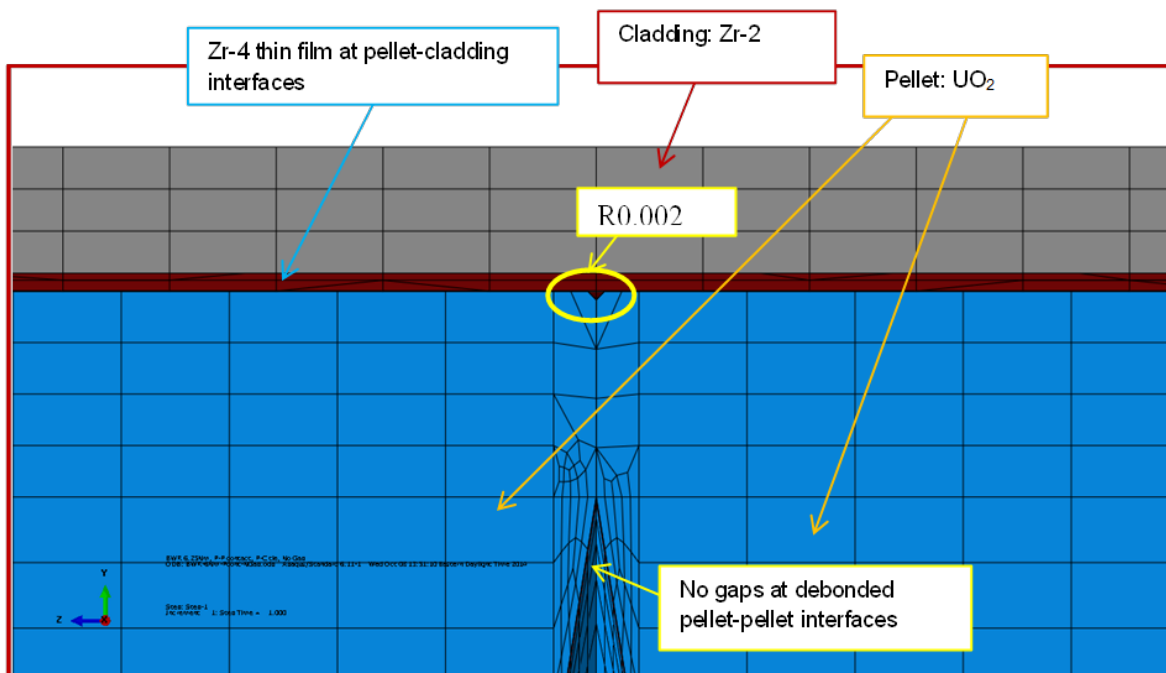
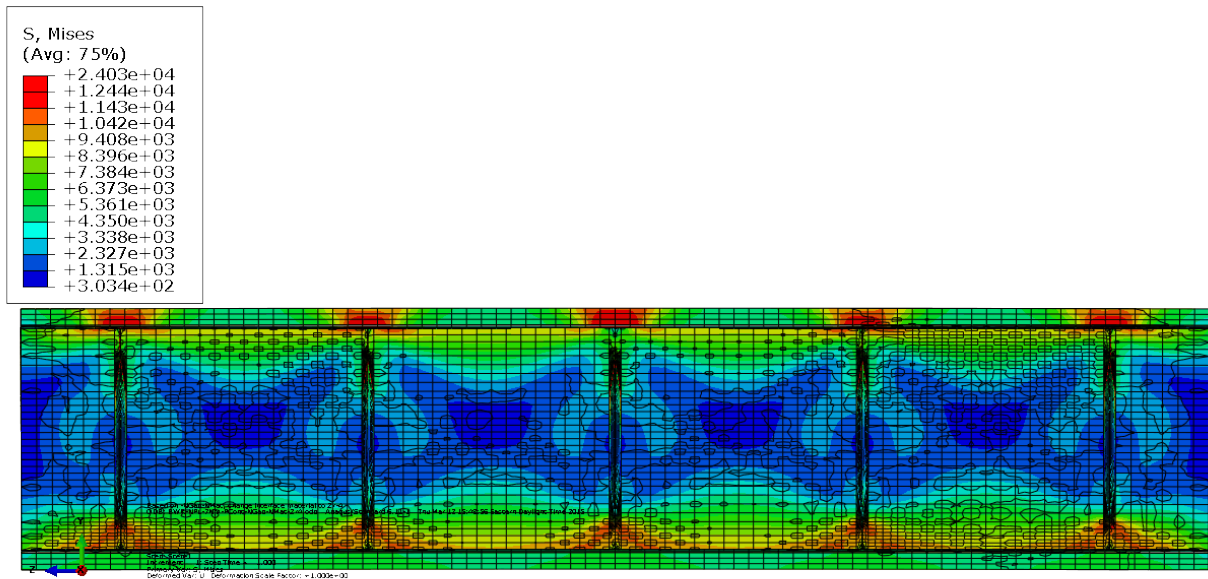
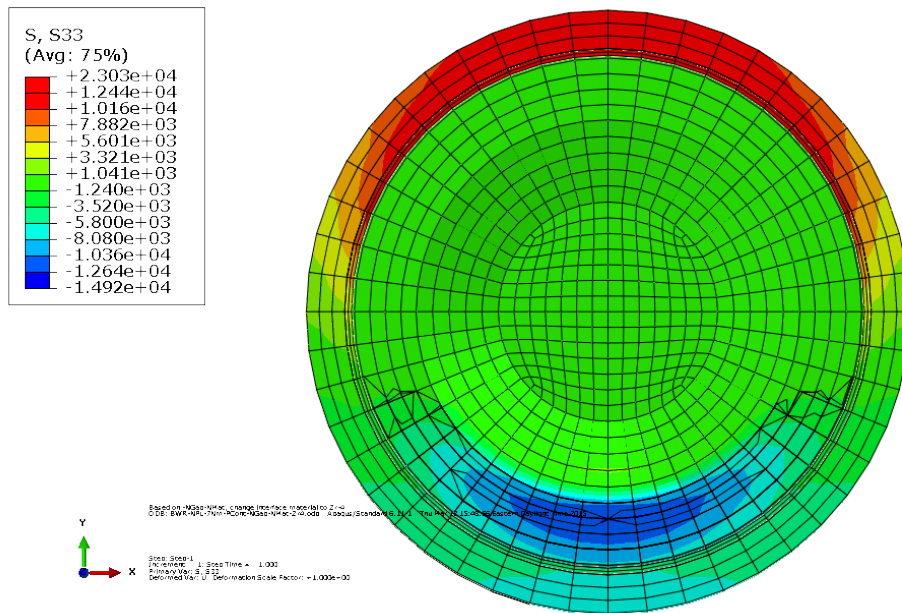


Fig. 103. Detail from Fig. 94 for the case of no gaps at debonded pellet-pellet interfaces.

As illustrated in Fig. 104, the normal stress distribution of this case appears to be different from that of debonded pellet-pellet interface case with empty gaps shown in Fig. 101. The maximum stress occurs at the top of the clad at pellet-pellet interface regions; however, at the compression side, interface stress concentrations occur at the pellets instead of at the clad. This is because there are no gaps at the pellet-pellet-clad interface region. Thus the contact pellets provide good internal support to the clad tubing structure. Furthermore, the pellets seem to carry a significant portion of the bending moment resistance via pellet-pellet interaction (pinching at pellet corners), which significantly mitigates the stress level of the clad at the bottom (compression) region. Because of the high yield strength of the pellet and clad materials, as well as the small bending load, the pellets and the clad are all under the linear elastic range at the maximum stress level. The pellet stress profiles do not have a perfect symmetric dog-bone shape because of the asymmetric contact between the tension and compression sides at the debonded pellet-pellet interfaces. The resultant σ_{zz} profile without gaps at the pellet-pellet interface indicates that the pellets can carry more bending moment resistance than the pellets with gaps shown in Fig. 101.



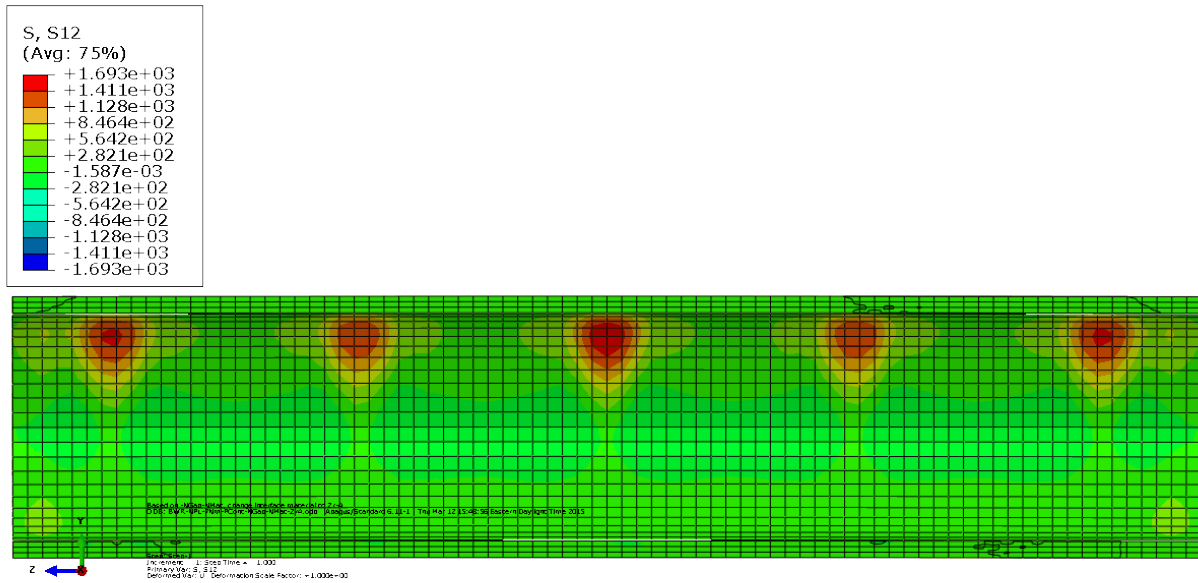
(a) Longitudinal section view of resultant curvature and von Mises stress



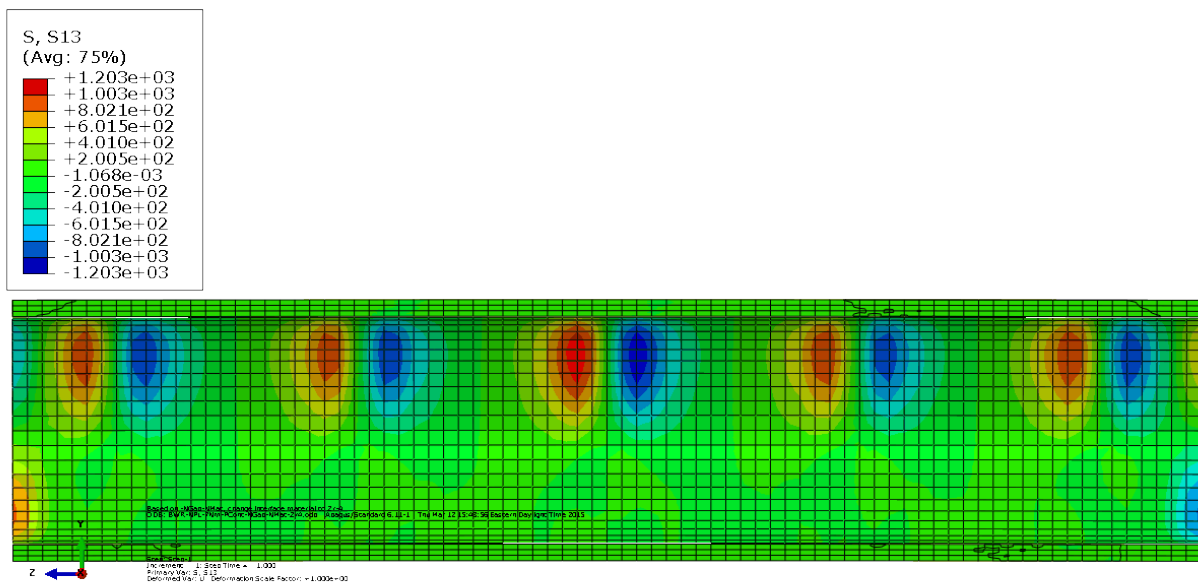
(b) Cross section view of σ_{zz} at a pellet-pellet interface

Fig. 104. Normal stress distribution and curvature results for clad-pellet 2 in. section model of BWR fuel rod with debonded pellet-pellet interfaces without gaps and bonded pellet-clad interfaces.

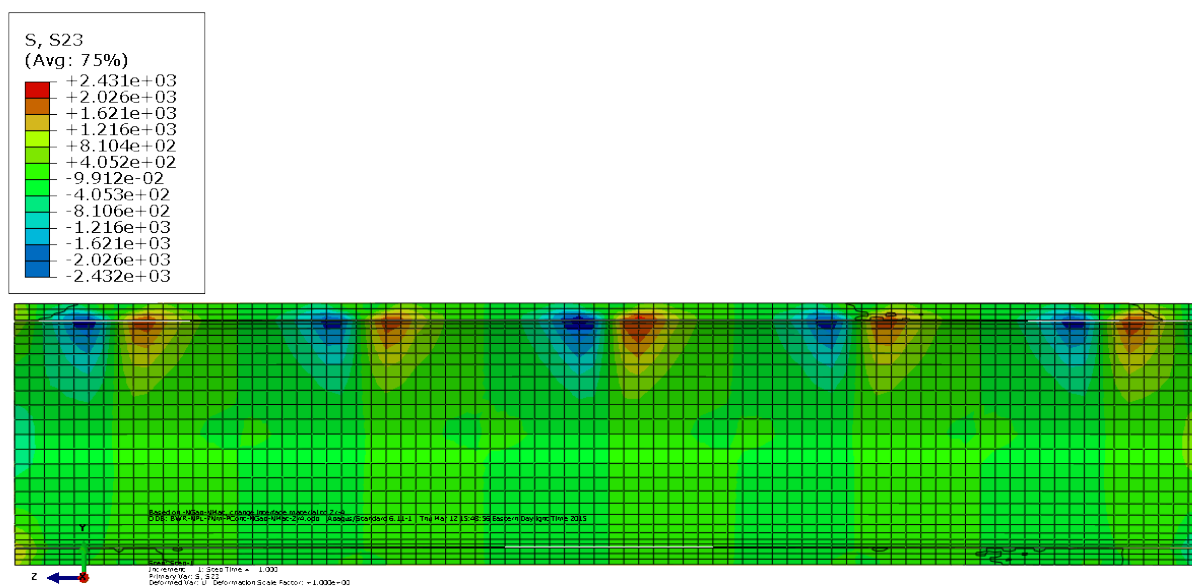
Fig. 105 shows the shear stress distribution at the clad for this case. The shear stress concentration occurs only at the top tension side, unlike in the case for pellet-pellet interface debonding with small gaps. The maximum stress concentration level is close to the results in Fig. 102. At the bottom compression side, the shear stress level is low. The reason is the same as for the normal stress results: when the gaps are eliminated, pellet-to-pellet direct pinning helps lower the stress on the clad at the bottom region.



(a) Shear stress σ_{xy}



(b) Shear stress σ_{xz}



(c) Shear stress σ_{yz}

Fig. 105. Shear stress distribution at the clad of the clad-pellet 2 in. section model of BWR fuel rod with debonded pellet-pellet interfaces without gaps and bonded pellet-clad interfaces.

Table 14 summarizes the estimate curvature, flexural rigidity, and component load-carrying capacity from the two FEA simulation cases discussed in this section, as well as the same cases of PWR HBR fuel rod simulation. The bending load of 7.6 N·m for BWR and 6.25 N·m for PWR were used in the FEA simulations. The curvature and the flexural rigidity listed in Table 14 indicate that for interface bonding simulation, the immediate consequence of debonding at the pellet-pellet interface is a significant increase in curvature, which results in a large reduction in the estimated flexural rigidity. This phenomenon is primarily due to a shift in load-carrying capacity from the pellets to the clad.

Table 14. Comparison of curvature, flexural rigidity, and bending moment for the bonded pellet-clad and debonded pellet-pellet cases

		Curvature κ (1/m)	Flexural rigidity EI (N·m ²)	Clad bending moment M (N·m)	Pellet bending moment M (N·m)	Total bending moment M (N·m)
Pellet-pellet interface with gap debonded; pellet-clad interface bonded	BWR	0.10	76	5.40	2.20	7.6
	PWR HBR	0.160	39	5.73	0.52	6.25
Pellet-pellet interface without gap debonded, pellet-clad interface bonded	BWR	0.091	84	4.36	3.24	7.6
	PWR HBR	0.119	53	3.99	2.26	6.25

The induced curvature of 0.10 m^{-1} for debonded pellet-pellet interfaces with gaps and a pellet-clad interface bonded with Zircaloy-4 film is an increase of 23% compared with the curvature value of 0.077 m^{-1} for the case of perfect bonding. The estimated flexural rigidity of $76 \text{ N}\cdot\text{m}^2$ for the case of a debonded pellet-pellet interface is a reduction of 23% compared with of $99 \text{ N}\cdot\text{m}^2$ for perfect interfacial bonding. The induced curvature for the debonded pellet-pellet interfaces with empty gaps and a pellet-clad interface bonded is 1.1 times that of the debonded pellet-pellet interfaces without gaps. The result is about a 10% reduction in flexural rigidity, from $84 \text{ N}\cdot\text{m}^2$ for the case with no gaps to $76 \text{ N}\cdot\text{m}^2$ for the case with empty gaps.

Table 14 shows that there is 37.5% decrease in induced curvatures from 0.160 m^{-1} of PWR HBR to 0.10 m^{-1} of BWR fuel rods for the pellet-pellet interface debonding cases with gaps. The flexural rigidity increases by the same percentages as the curvature decreases. As shown in Table 12, the Young's modulus of BWR clad material Zircaloy-2 is 24% higher than that of PWR HBR clad material Zircaloy-4. Hence the comparison results indicate that the 36% difference in the flexural rigidity comes from the combination effect of material property differences and gaps. However, for the case without gaps, the difference between the BWR and PWR HBR fuel rods is only 24%. Gaps at the pellet-pellet interfaces play a critical role in estimating the flexural rigidity. With gaps eliminated, the difference in the flexural rigidity mainly results from the material difference. In Table 13, the perfectly bonded pellets carry more bending moment than the clad. In Table 14 the data clearly show a significant shift in bending moment resistance from the pellets to the clad as a result of debonding at pellet-pellet interfaces. The clad carries 71% bending moment at the pellet-pellet interface debonding region. When the pellets directly contact one another without gaps, the bending moment on the clad drops by around 20% compared with the pellets with empty gaps. The bending moments distributed among the clad and pellets are similar for the BWR and PWR HBR fuel rods. The clad of the PWR HBR fuel rod carries a greater percentage of bending moment than the clad of the BWR fuel rod.

These results indicate that the gap-induced stress concentration and large deformations of the clad at the pellet-pellet interface region can lead to a significant reduction in the bending stiffness, i.e., flexural rigidity (EI), of the fuel rod system. If there are no gaps at the pellet-pellet interfaces, the pellets can carry a significant portion of the bending moment resistance via direct pellet-pellet contact (interaction) to mitigate the stress concentration and potential yielding at the clad.

10.2.3 Debonded Pellet-Clad and Pellet-Pellet Interfaces

Under flexural deformation, high shear stress will arise at the pellet-clad interfaces to compensate for the material mismatch and the flexural shear stress in the SNF system. Thus under reversal bending loading during normal transportation, both cyclic normal stress and shear stress can further degrade the interface bonding at pellet-clad interfaces. In this section, debonded pellet-clad interfaces and debonded pellet-pellet interfaces are investigated using the clad-pellet 2 in. section model of the BWR fuel rod with six pellets.

10.2.3.1 Debonded Pellet-Clad Interfaces and Debonded Pellet-Pellet Interfaces with Empty Gaps

As illustrated in Fig. 106, simulations of interfacial debonding at both pellet-clad and pellet-pellet interfaces initially focus on the case with empty gaps at debonded pellet-pellet interfaces and a thin Zircaloy-4 film at debonded pellet-clad interfaces. At pellet-clad interfaces, the outer pellet surfaces contact the inner surface of the thin Zircaloy-4 film, and the outer surface of the thin Zircaloy-4 film contacts the inner surface of the clad. Pellets have dips at both end surfaces with rounding of 0.002 in. A

BWR fuel rod consisting of Zircaloy-2 clad and UO₂ pellet inserts is used to study the system response to the bending moment with debonded interfaces. Loading and boundary conditions are the same as those assumed in the previous cases, and the bending moment is assigned at 7.6 N·m.

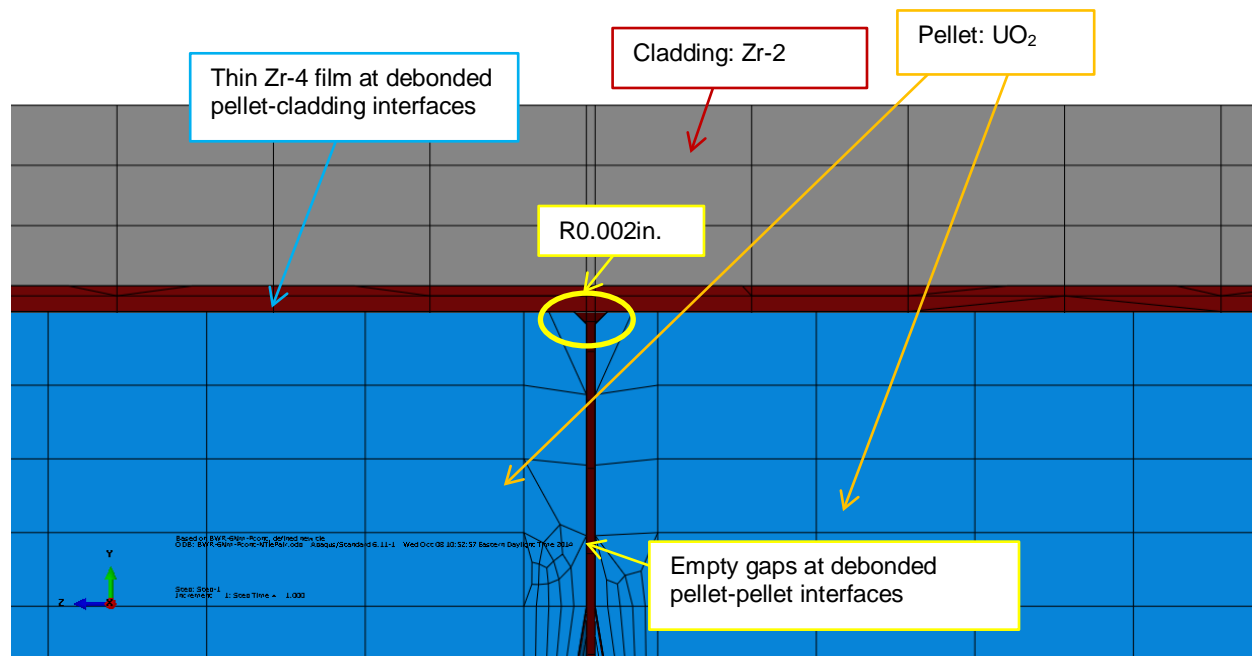
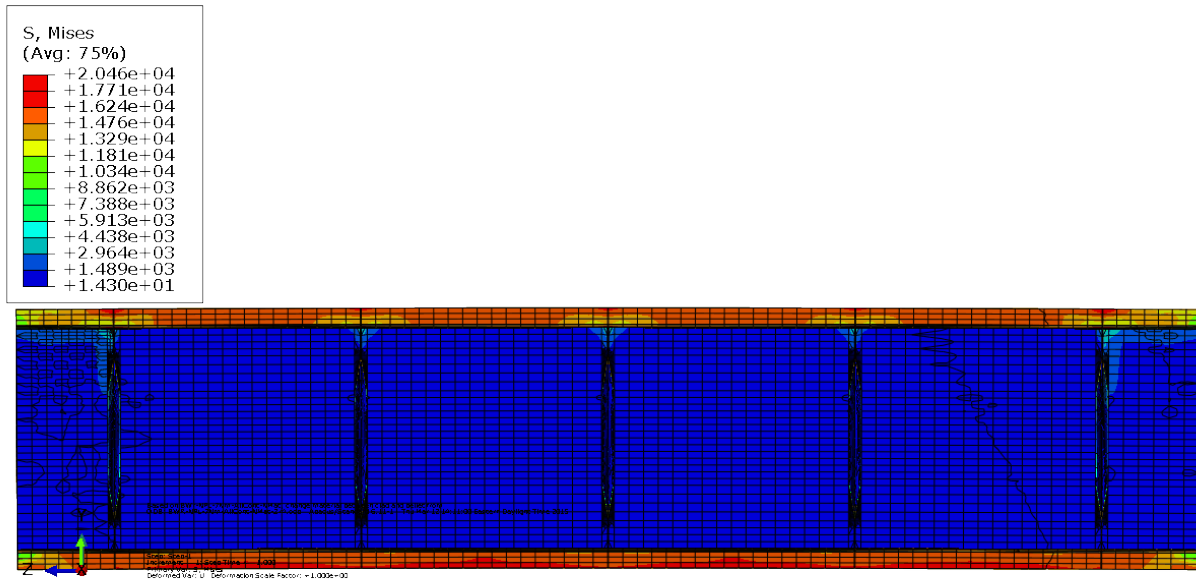
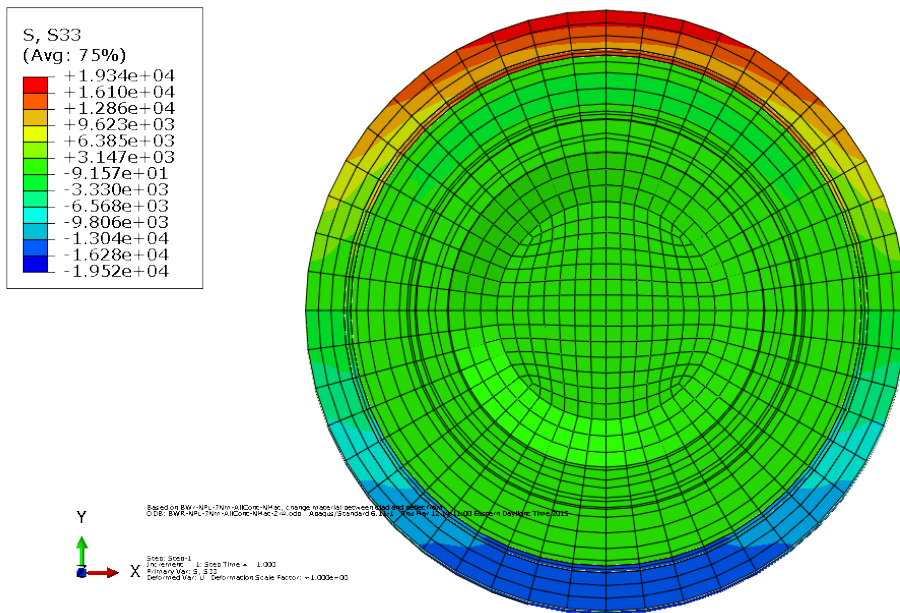


Fig. 106. Detail area from Fig. 94 for the cases of empty gaps at debonded pellet-pellet interfaces and a thin Zircaloy-4 film filled at the debonded pellet-clad interfaces.

The resulting normal stress distribution shown in Fig. 107 indicates that the clad reached maximum stress throughout the whole gage section when interfacial debonding occurred at both pellet-clad and pellet-pellet interfaces. This result is in strong contrast to the results shown in Fig. 101, in which the Zircaloy-2 clad shows stress concentrations only locally at pellet-pellet interface regions. Because of the small bending load and the high material yield strength, the clad did not yield at the maximum stress. The pellets were all below the yielding stress as well. The induced curvature of 0.218m^{-1} is almost triple that of the perfect bond case. This suggests that, as a result of the interface debonding at both the pellet-clad and pellet-pellet interfaces, the pellets and the clad can contact (or pin) only at the pellet-pellet-clad interface region, and pellets cannot provide direct internal support to the clad. Therefore, the load-carrying capacity shifts significantly from the pellets to the clad at the entire gage section. The results also indicate that the Zircaloy-2 clad carries most of the bending moment resistance. The bending deformation in the debonded pellet-clad region is likely to result in further pinning action at pellet-clad interfaces, which may also result in accelerated aging of the clad tubing.



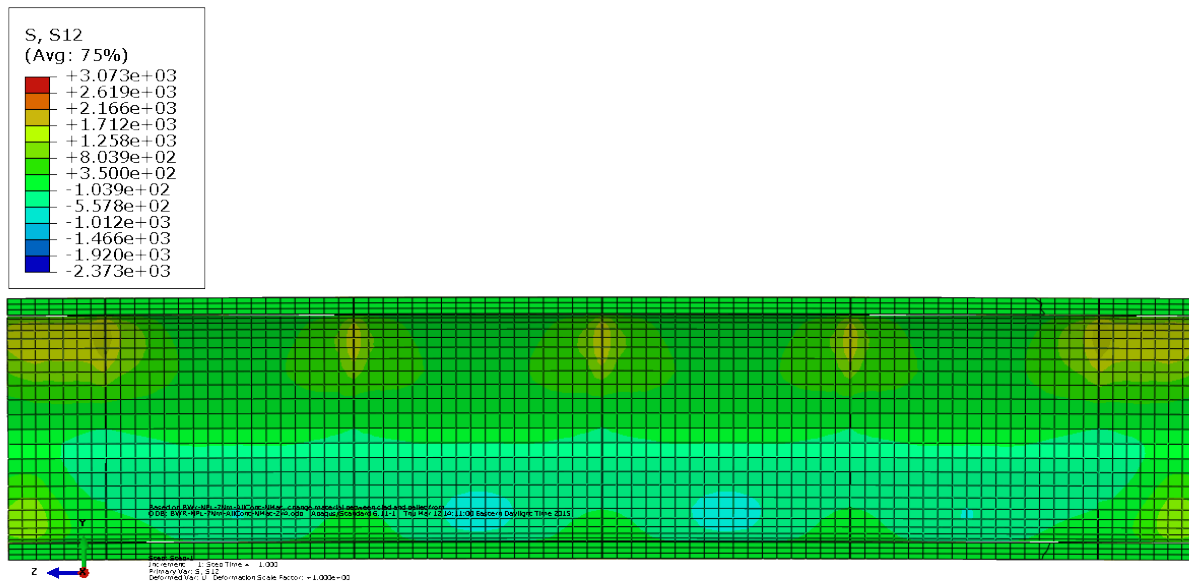
(a) Longitudinal section view of resultant curvature and von Mises stress



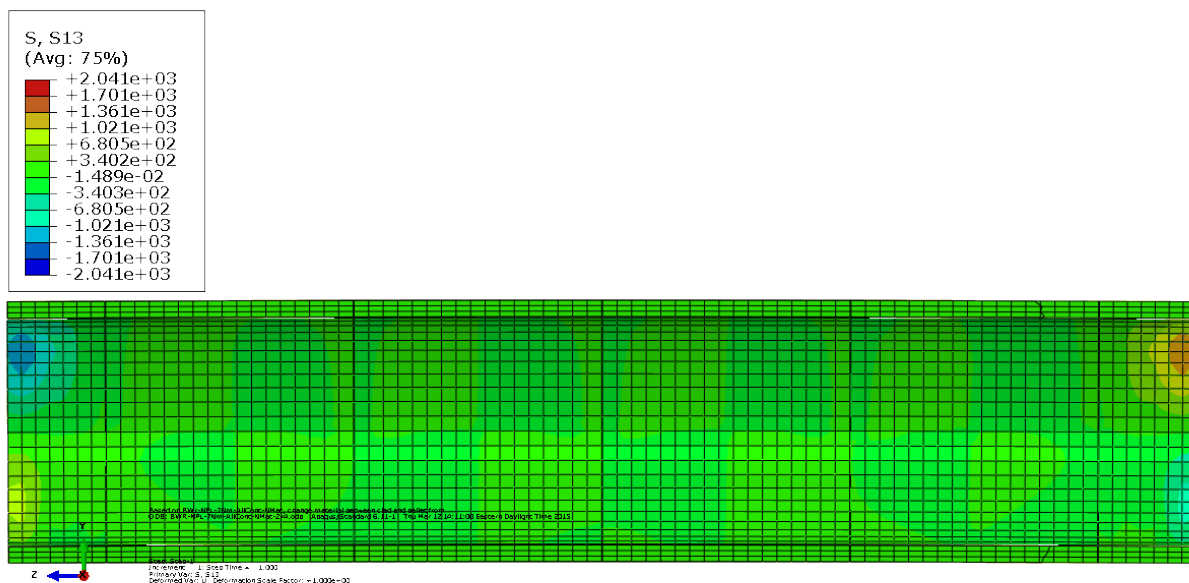
(b) Cross section view of σ_{zz} at a pellet-pellet interface

Fig. 107. Normal stress distribution and curvature results for clad-pellet 2 in. section model of BWR fuel rod with empty gaps at debonded pellet-pellet interfaces and a Zircaloy-4 film at debonded pellet-clad interfaces.

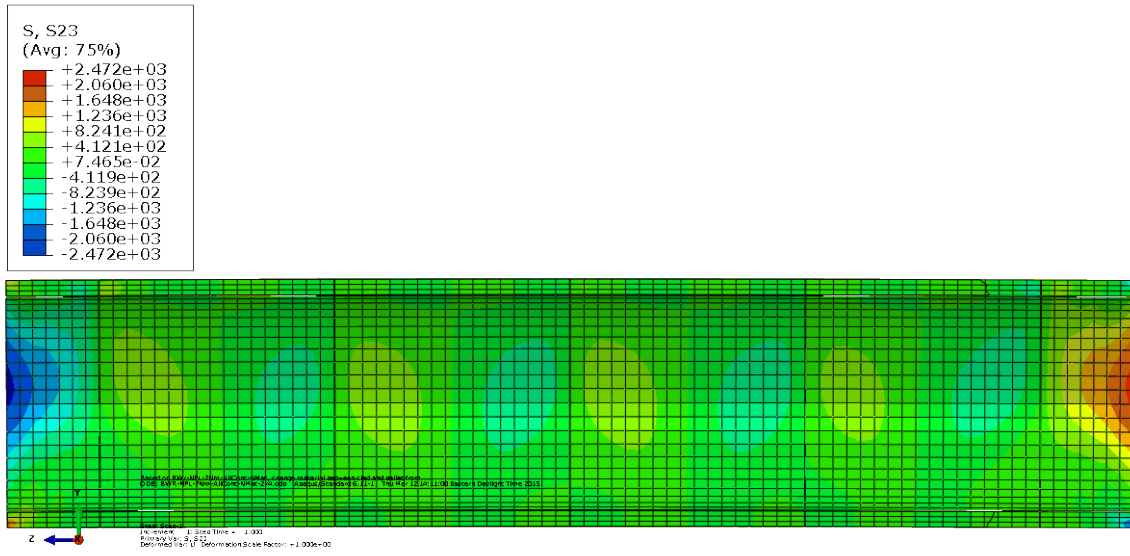
Fig. 108 illustrates the shear stress results for this simulation case. The stress pattern appears to be similar to the perfect bond case. There are no shear stress surges inside the gage section of the cladding as a result of further pellet-clad interface debonding. Because the pellets and the clad can make contact only at the interfaces, the clad cannot directly transfer the shear stress within the gage section. However, there are some stress concentrations at the boundary as a result of component contact.



(a) Shear stress σ_{xy}



(b) Shear stress σ_{xz}



(c) Shear stress σ_{yz}

Fig. 108. Shear stress distribution at the clad of the clad-pellet 2 in. section model of the BWR fuel rod with empty gaps at debonded pellet-pellet interfaces and a Zircaloy-4 film at the debonded pellet-clad interfaces.

10.2.3.2 Debonded Pellet-Clad Interfaces and Debonded Pellet-Pellet Interfaces without Gaps

The simulation cases for debonded pellet-pellet interfaces without gaps are shown in Fig. 109, where a thin Zircaloy-4 film is filled at debonded pellet-clad interfaces, and the pellets are all in direct contact with one another without gaps at the pellet-pellet interfaces. The loading and boundary conditions and the material properties are the same as in the previous cases. In this case, there are still six pellets with rounding of 0.002 in.

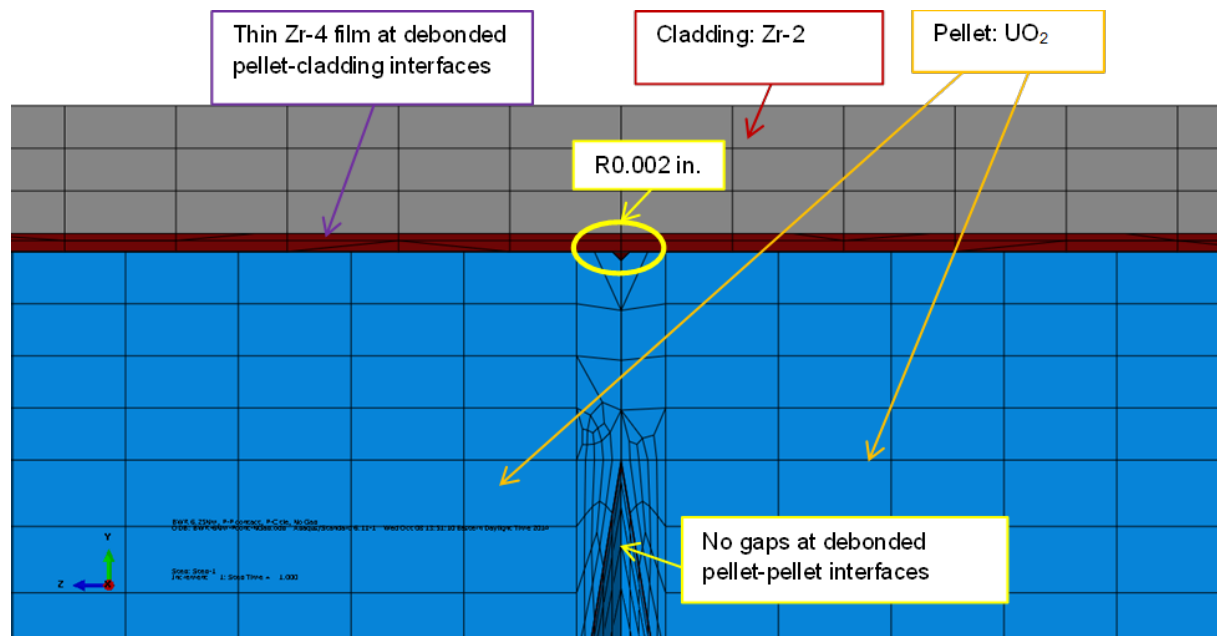
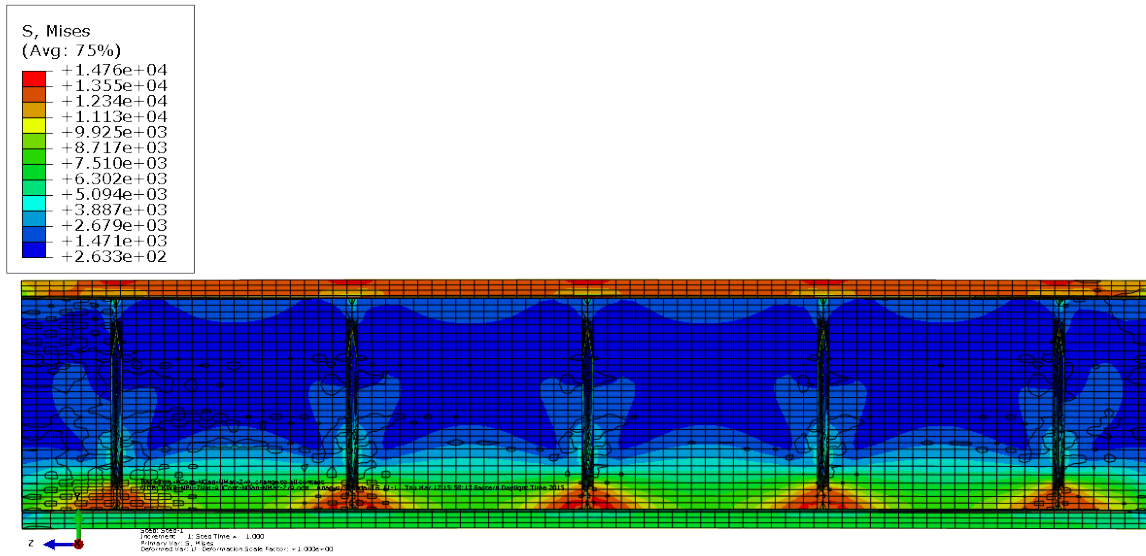
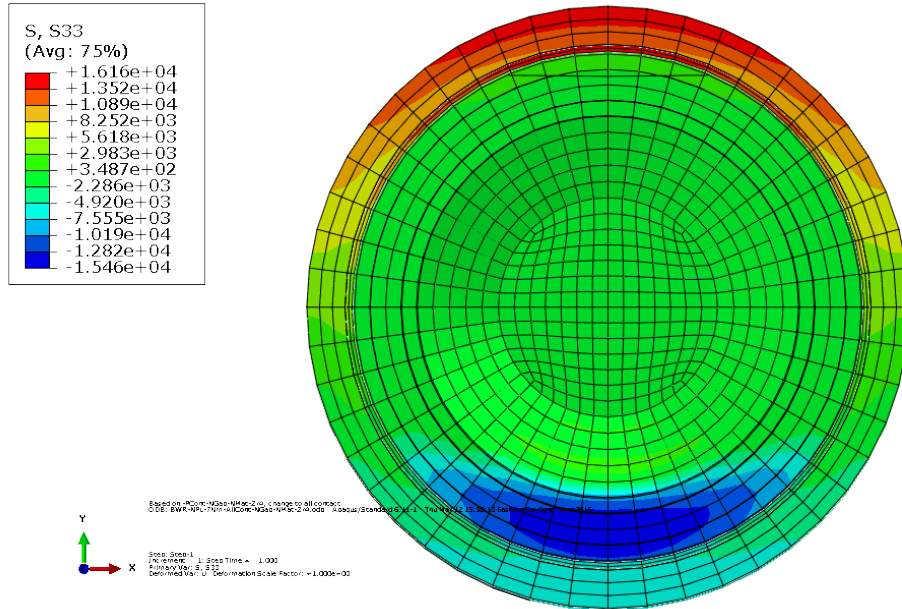


Fig. 109. Detail area from Fig. 94 for the case with no gaps at debonded pellet-pellet interfaces and a thin Zircaloy-4 film at debonded pellet-clad interfaces.

Fig. 110 illustrates the BWR fuel rod responses to the bending moment in this simulation. The longitudinal section view shows a stress concentration at the top (tension) region of the Zircaloy-2 clad throughout the gage section, but the rod did not yield. In the bottom (compression) region, the stress level is low at the clad. The maximum stress occurred at the tension side of the clad. Fig. 110 shows interfacial results similar to those observed in Fig. 104 for the bonded pellet-clad interfaces and debonded pellet-pellet interfaces without gaps. The pellets carry a large portion of the bending moment resistance via the pinching pellet corners, and they reduce the stress intensity at the bottom (compression) portion of the clad. The major difference shown in Fig. 110 is an extensive stress concentration observed at the top region of the clad throughout the entire gage section, which is in contrast to the localized area observed at the interface region as depicted in Fig. 104. The clad assumes most of the bending moment resistance because there is no direct mechanism for transferring the load from the pellet to the clad or vice versa due to the debonded pellet-clad interfaces.



(a) Longitudinal section view of curvature and von Mises stress results

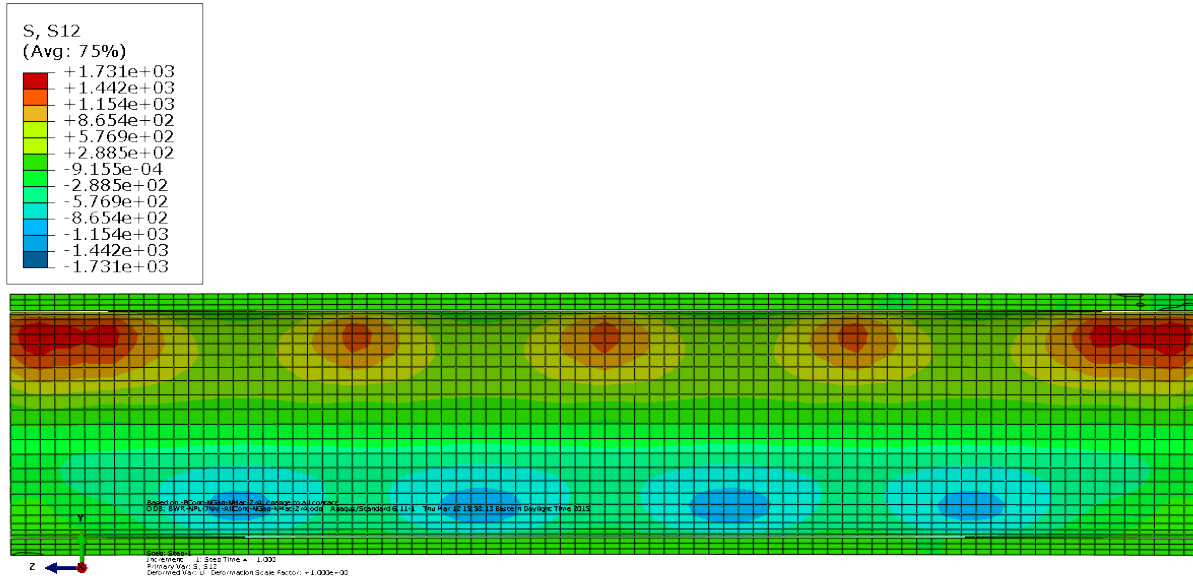


(b) Cross section view of the normal stress, σ_{zz} , results at a pellet-pellet interface

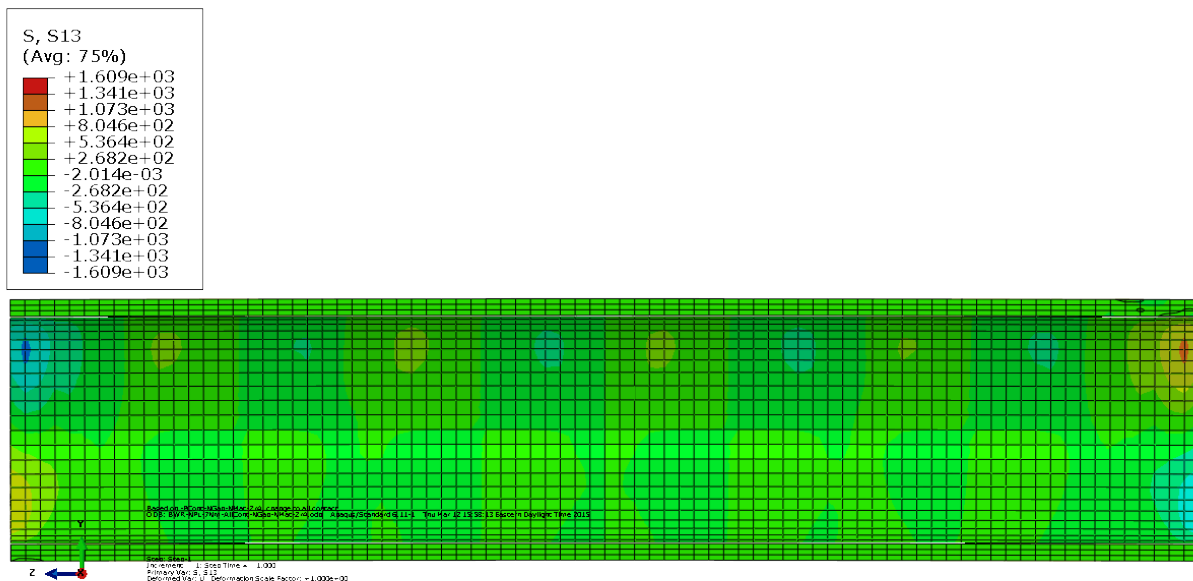
Fig. 110. Normal stress distribution and curvature results for the clad-pellet 2 in. section model of a BWR fuel rod without gaps at debonded pellet-pellet interfaces and with a Zircaloy-4 film at debonded pellet-clad interfaces.

In Fig. 111 (a), the shear stress in radial direction σ_{xy} shows different stress levels at the top tension side and bottom compression side at the clad. Similar to the normal stress distribution, the shear stress at the bottom side of the clad is significantly lowered by pellet-pellet direct pinching at the compression side. The shear stresses σ_{xz} and σ_{yz} show no stress concentration inside the clad, which appears to be a stress pattern similar to that for interface debonding with

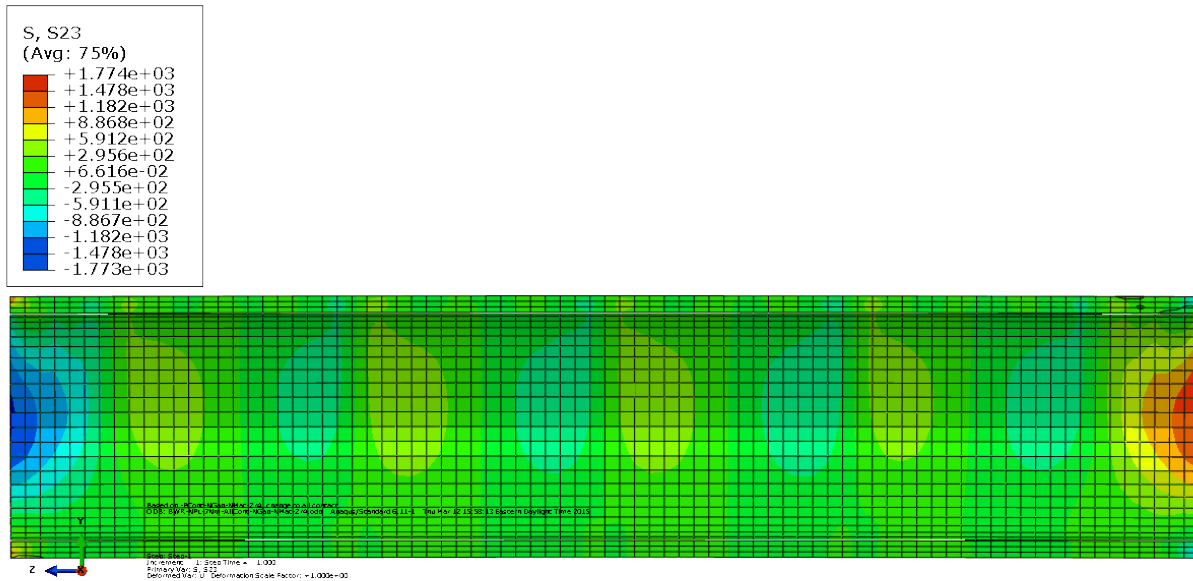
gaps. However, the maximum stress levels are lower than those for cases with gaps. The pellets assume a large portion of the bending load when the gaps are eliminated.



(a) Shear stress σ_{xy}



(b) Shear stress σ_{xz}



(c) Shear stress σ_{yz}

Fig. 111. Shear stress distribution and curvature results for the clad-pellet 2 in. section model of BWR fuel rod without gaps at debonded pellet-pellet interfaces and with a Zircaloy-4 film at debonded pellet-clad interfaces.

Table 15 shows the curvature, flexural rigidity, and bending moment comparison for debonded pellet-clad and pellet-pellet interfaces of the BWR and PWR HBR fuel rods with or without gaps. With pellet-clad interface further debonding, the flexural rigidity further decreases. Compared to the flexural rigidity in Table 14, the further decrease in the flexural rigidity of the BWR fuel rod with gaps and all the interface debonded is up to 54%. The total reduction in the flexural rigidity of the BWR fuel rod for the same bonding condition from the perfect bond result in Table 13 is as high as 65%. The gaps play an important role in flexural rigidity estimation. In Table 15, the flexural rigidity of the cases without gaps at pellet-pellet interfaces are 1.5 times those of the cases with gaps for both the BWR fuel rod and PWR HBR fuel rod. In Table 14 the ratios of the flexural rigidity are 1.1 and 1.4 for the BWR fuel rod and PWR HBR fuel rod, respectively, for the same comparison. The reason for the large increase in flexural rigidity is the direct pellet contact at the pellet-pellet interfaces at the compression side. The direct pellet-pellet contact interaction also provides a significant increase in bending moment resistance; it results in a much smaller curvature deformation, as shown in Table 15.

Table 15 also shows that the bending moment significantly shifts from pellet to clad with all interface debonding, especially when there are gaps at pellet-pellet interfaces. In these cases, the clad carries 87%–99% bending load. When the pellets are in direct contact with one another, the pellets retake a large amount of the bending moment, which helps reduce the bending load on the clad. The bending moments distributed among the clad and pellets are similar for the BWR and PWR HBR fuel rod.

Table 15. The curvature, flexural rigidity, and bending moment comparison for debonded pellet-clad and pellet-pellet interfaces

Interface bonding conditions	Type	Curvature κ (1/m)	Flexural rigidity EI ($N \cdot m^2$)	Clad bending moment M ($N \cdot m$)	Pellet bending moment M ($N \cdot m$)	Total bending moment M ($N \cdot m$)
Pellet-pellet interface with gap debonded; pellet-clad interface debonded	BWR	0.218	35	6.59	1.01	7.6
	PWR HBR	0.218	29	6.23	0.02	6.25
Pellet-pellet interface without gap debonded, pellet-clad interface debonded	BWR	0.141	54	4.21	3.39	7.6
	PWR HBR	0.146	43	4.15	2.10	6.25

10.2.4 Comparison of Flexural Rigidity with Different Fuel Young’s Modulus Cases

Fig. 112 shows ORNL hot-cell CIRFT test data of BWR fuel rod flexural rigidity and curvature. The test on specimen LMK06/575D-E was conducted at 7.6 N·m. The flexural rigidity of the measurement is 42 N·m², as shown in Fig. 112(a). Apparently the flexural rigidity is much lower than that of perfect bond case of 99 N·m². Testing data indicate that the specimen was not in perfect bond condition before testing. There could be several reasons for the flexural rigidity to be low. The first one is the interface debonding, the second is the gaps existing between the interfaces, and the third is the material property change. Based on observation of the cut specimen, there were plentiful cracks in the fuel. The fracture of the fuel rod would cause the reduction in the Young’s modulus.

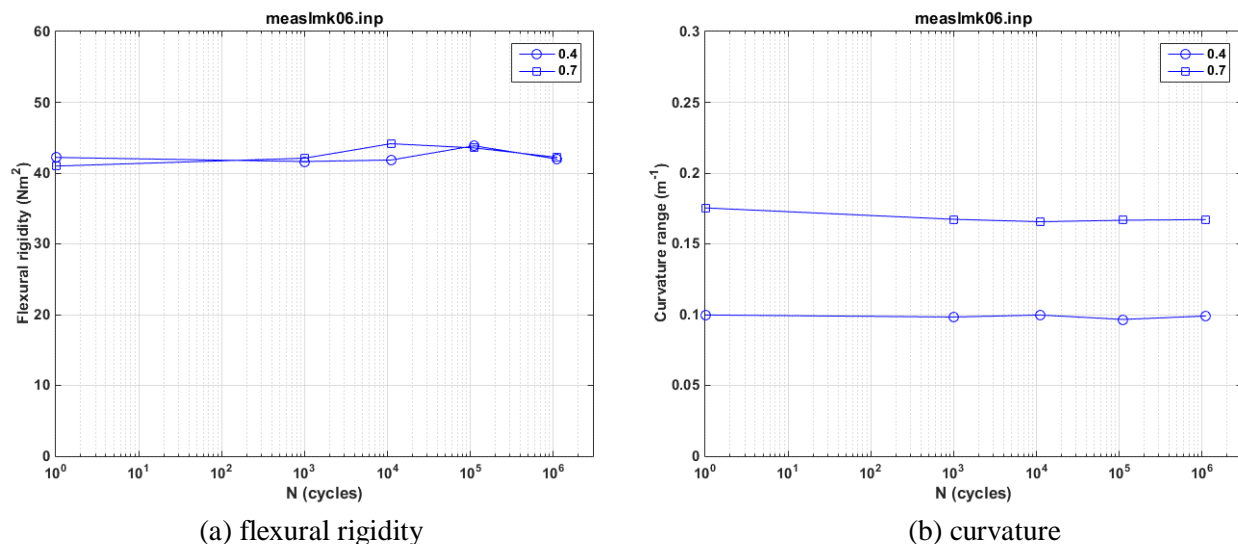


Fig. 112. ORNL hot-cell CIRFT test data of BWR fuel rod flexural rigidity and curvature.

Thus, the similar studies were performed following Sections 2.1 to 2.3 for different interfacial bonding conditions, with the fuel Young’s modulus reduced to half of the original and a quarter of the original. At a bending moment of 7.6 N·m, the resultant flexural rigidities are summarized and compared in Table 16.

Table 16. The flexural rigidity comparison of the different fuel Young’s modulus cases

Interface bonding conditions	Fuel UO ₂ full E Flexural rigidity, EI (N·m ²)	Fuel UO ₂ ½ E Flexural rigidity, EI (N·m ²)	Fuel UO ₂ ¼ E Flexural rigidity, EI (N·m ²)
Perfect bond	99	68	52
Pellet-pellet interface with gap debond, pellet-clad interface bonded	76	57	47
Pellet-pellet interface with gap debond, pellet-clad interface debonded	35	35	35
Pellet-pellet interface without gap debond, pellet-clad interface bonded	84	62	49
Pellet-pellet interface without gap debond, pellet-clad interface debonded	54	47	42

The direct comparison of different fuel Young’s modulus cases in Table 16 clearly shows that the fuel rod system flexural rigidity decreases with a reduction in the fuel Young’s modulus, except for all cases of interfaces debonding with gaps. Due to both pellet-pellet and pellet-clad interface debonding, the majority of the bending load shifts to the cladding within the entire gage section. In addition to this, there are gaps at pellet-pellet interface, and fuel pellets need to overcome the gaps to contact each other, which results in fuel having a very limited contribution on the system stiffness. For this case, the flexural rigidities remain the same for different fuel Young’s modulus cases. For the same fuel Young’s modulus case, the trend of the flexural rigidity change between the different interface bonding conditions is the same.

Compared to the flexural rigidity estimated from test data, the FEA resultant flexural rigidity should be slightly higher because of the ideal condition in simulation. The case of pellet-pellet interface debonded with gap and pellet-clad interface bonded, with fuel Young’s modulus ¼ of the original, and the case of pellet-pellet interface and pellet-clad interface both debond with gap, with fuel Young’s modulus ½ of the original, both have estimated flexural rigidity of 47 N·m² (highlighted in Table 16), which is merely higher than test data of 42 N·m². Thus, these two cases seem to be representative of the specimen material condition.

Table 17 shows the max stress at the cladding for the different fuel Young’s modulus cases under the different interface bonding conditions. For the perfect bond condition, the fuel takes more bending moment than the clad, so the clad stresses are smaller than that of the interface debond condition. With the fuel Young’s modulus reduced, the maximum stresses at the clad increase, which indicates that the bending moment carried by the fuel decreases. Maximum stress at the gap on the clad is higher than the maximum stress not at the gap. The biggest difference is 3.3 times for pellet-pellet interface debond without gap, pellet-clad interface bonded with fuel of the full Young’s modulus case. The smallest difference occurs at pellet-pellet interface debond with gap and pellet-clad interface debond cases. Usually, the bending moment shifts to the clad significantly at the gap regions when interface debonding occurs.

Table 17. Comparison of max stress at cladding between different fuel Young's modulus cases

Interface bonding conditions	Fuel UO ₂ full E		Fuel UO ₂ ½ E		Fuel UO ₂ ¼ E	
	Max stress at gap (psi)	Max stress not at gap (psi)	Max stress at gap (psi)	Max stress not at gap (psi)	Max stress at gap (psi)	Max stress not at gap (psi)
Perfect bond	6061	4945	8333	7589	10801	10380
Pellet-pellet interface with gap debond, pellet-clad interface bonded	13309	5036	14161	7760	14743	10497
Pellet-pellet interface with gap debond, pellet-clad interface debonded	16825	16402	16791	16403	16751	16413
Pellet-pellet interface without gap debond, pellet-clad interface bonded	16402	4917	15965	7582	15782	10388
Pellet-pellet interface without gap debond, pellet-clad interface debonded	14730	13291	15417	14073	15939	14811

As mentioned above, the two cases highlighted in Table 16 were identified as interface bonding conditions close to the testing condition, so the stresses at the clad for these two cases are investigated in detail and compared to the estimation from test data. Fig. 113 shows the stress distribution at the clad for the debonded pellet-pellet interfaces with gap and bonded pellet-clad interfaces case with fuel Young's modulus ¼ of the original. Stress distribution is not uniform, and maximum stress ranges from 14.7 ksi to 10.5 ksi. The average stress in the entire gage section was calculated as 11.5 ksi.

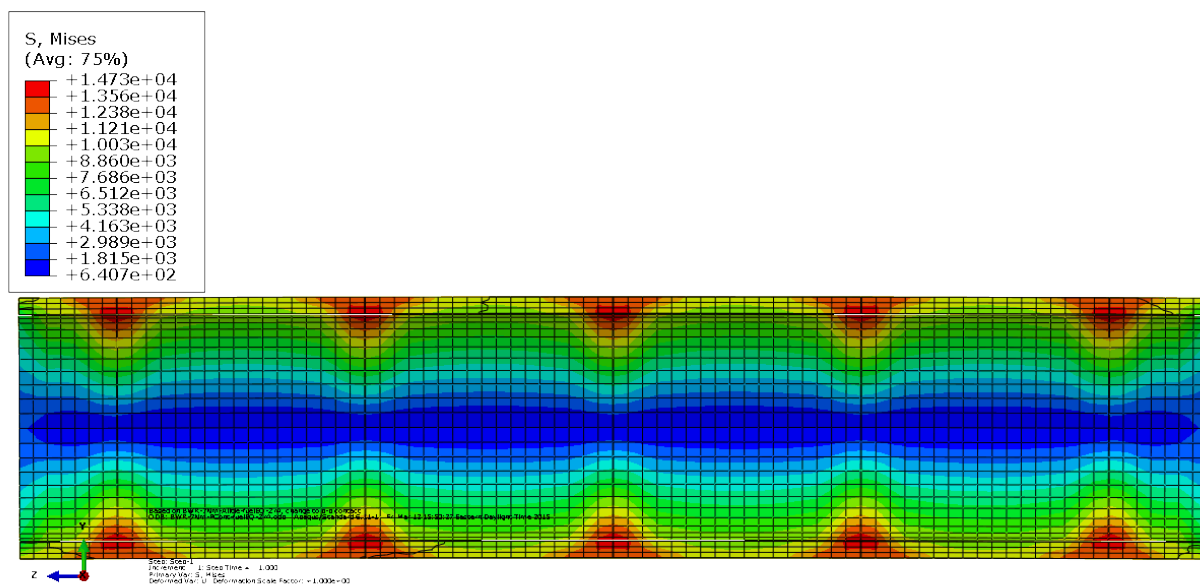


Fig. 113. Stress distribution at the clad for the fuel Young's modulus ¼ of the original with gaps at debonded pellet-pellet interfaces and with a Zircaloy-4 film at bonded pellet-clad interfaces.

Fig. 114 shows the stress distribution at the clad for the debonded pellet-pellet interfaces without gap and the debonded pellet-clad interfaces case with fuel Young’s modulus ½ of the original. Stress distribution is more uniform than that in Fig. 113, and max stress ranges from 15.4 ksi to 14.0 ksi. The average stress in the entire gage section was calculated as 14.1 ksi.

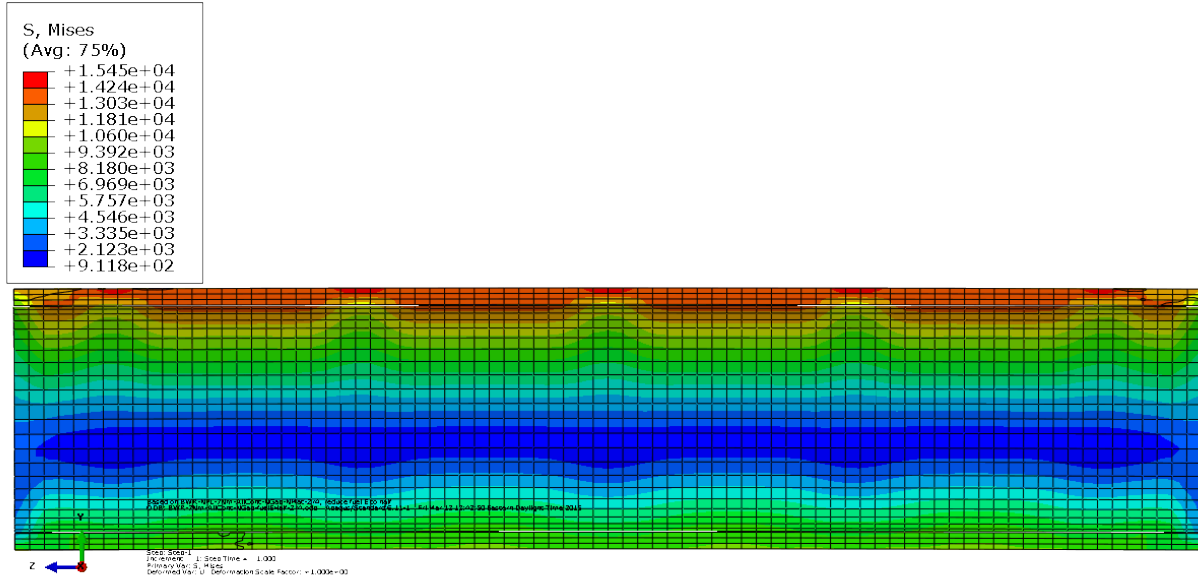


Fig. 114. Stress distribution at the clad for the fuel Young’s modulus ½ of the original without gaps at debonded pellet-pellet interfaces and with a Zircaloy-4 film at debonded pellet-clad interfaces.

Estimate stress at the clad from measurement as the following equations,

$$\epsilon = \kappa * y \tag{3}$$

$$\sigma = \epsilon * E \tag{5}$$

$$\kappa = M / EI \tag{6}$$

- M = bending moment, 7.6N·m
- EI = flexural rigidity from testing, 42 N·m²
- κ = curvature
- y = clad radius
- E = clad Young’s modulus, 1.32e7 psi

The estimated average stress from test data is 13.4 ksi, which is between the estimations from two FEA simulation cases.

10.3 Discussion

Based on the FEA simulation results and a comparison of the BWR fuel rod and the PWR high-burnup HBR rod, the localized system (stress-curvature) biases and uncertainties associated with CIRFT global responses on the SNF rod system performance can be quantified and summarized as discussed below.

First, with good interface bonding and without fuel pellet and clad fracturing, the pellets in the fuel rod will carry more bending moment resistance than the clad under normal transportation vibration. The maximum stress resides in the pellets, and the stresses at the clad and pellet are both below the yield condition; therefore, the system is in a linear elastic state under the target bending loads. There is no shear stress surge inside the cladding.

Upon fuel pellet failure, including debonding at the pellet-pellet interfaces, the load-carrying capacity shifts from the fuel pellets to the clad. The clad starts to carry most of the bending moment at the pellet-pellet interface region, resulting in localized stress concentrations in the clad. However, under the target bending moment, the clad does not yield. With good cohesion bonding at the pellet-clad interfaces, the pellets can continue to support the clad and carry a sufficient portion of the bending moment resistance; therefore, most of the clad at the gage section remains in the linear elastic range. A shear stress surge occurs inside the cladding at the pellet-pellet interface regions.

When further debonding occurs at the pellet-clad interfaces, the embedded pellets can no longer provide effective structural support to the clad and can no longer assist load transfer within the fuel rod system. Thus most of the load-carrying capacity shifts to the clad throughout the entire gage section. The shift leads to maximum stress concentrations in the clad in the entire gage section instead of at localized pellet-pellet interface regions. The clad does not yield because of the high material yield strength and the low bending load. There is no resulting shear stress concentration inside the clad for interface debonding.

When the pellets contact and pinch one another, they seem to take over a significant portion of the bending load resistance, especially where there are no gaps at the pellet-pellet interfaces. This pellet pinning action clearly mitigates and avoids stress concentration and potential yielding at the compression side of the clad.

All of the simulation cases for the BWR fuel rod are summarized in Table 18. The main parameter flexural rigidity EI is compared case by case. The immediate consequence of interface debonding is a shift in the load-carrying capacity from the fuel to the clad, as well as a reduction in flexural rigidity. For example, the flexural rigidity is $99 \text{ N}\cdot\text{m}^2$ when the pellets are perfectly bonded with Zircaloy-4. In the case with gaps at the pellet-pellet interfaces, when there is debonding at the pellet-pellet interfaces alone, the flexural rigidity drops by 23% to $76 \text{ N}\cdot\text{m}^2$. In the case without gaps, it drops by 15%, to $84 \text{ N}\cdot\text{m}^2$. Further debonding at the pellet-clad interfaces causes the flexural rigidity to drop further, by 54% and 36%, respectively, for the cases with gaps and without gaps. Overall, for cases with gaps and without gaps, flexural rigidity drops by about 65% and 45%, respectively, between the perfect bond and the debond cases at all interfaces.

Flexural rigidity is reduced more by debonding at pellet-pellet interfaces than by debonding at pellet-clad interfaces. Table 18 shows a flexural rigidity that is 10–35% higher for the fuel rod without gaps, indicating a significant increase in system stiffness over the case with gaps. Therefore, the gaps at the interfaces of the fuel rod system have a significant impact on system reliability, especially at pellet-pellet interfaces. The flexural rigidity and bending moment resistance capacity of the fuel rod are highly dependent on interface bonding efficiency at pellet-clad and pellet-pellet interfaces. This discovery was

validated by ORNL reversal bending fatigue test results performed on the fuel rod with PWR HBR pellet inserts.

Table 18. The flexural rigidity comparison between the different bonding and debonding cases

Interface bonding conditions	Flexural rigidity EI ($N \cdot m^2$)	Reduction from perfect bond (%)	Reduction from only pellet-pellet debond to further pellet-clad debond (%)	Increase from with gaps to without gaps (%)
Perfect bond	99			
Pellet-pellet interface with gap debond, pellet-clad interface bonded	76	23		
Pellet-pellet interface with gap debond, pellet-clad interface debonded	35	65	54	
Pellet-pellet interface without gap debond, pellet-clad interface bonded	84	15		10
Pellet-pellet interface without gap debond, pellet-clad interface debonded	54	45	36	35

Table 19 directly compares the flexural rigidity between BWR and PWR HBR fuel rods for different interface bonding conditions. Generally, the trends of the flexural rigidity change for different interface bonding conditions are the same between BWR and PWR HBR fuel rods. The flexure rigidity of the BWR fuel rod is 22% higher than the PWR HBR fuel rod for the perfect bond case. For a perfect bonding condition, the major difference between two fuel rod systems is the pellet-clad interface material. For the BWR fuel rod system, the interface material is Zircaloy-4, and for the PWR HBR fuel rod, it is epoxy. As shown in Table 12, Zircaloy-4 has much higher Young’s modulus than epoxy, which causes much higher stiffness of the BWR system. For pellet-pellet interface debonded with gap and pellet-clad interface bonded case, the difference between BWR and PWR HBR fuel rods is 49%, which is much higher than 24%. This big difference might be due to the combined effect of material difference and geometry, including pellet length difference and gaps in the BWR and PWR HBR fuel rods. When the gaps at pellet-pellet interfaces are eliminated, the differences are just 17%. That indicates that for those bonding conditions, material difference again dominates the change in the system flexural rigidity between BWR and PWR HBR fuel rods.

Test results indicate that the specimen was far from the perfect bond condition and the fuel rod was fractured. FEA simulations by reducing the fuel Young’s modulus to 50% and 25% help to identify two interface bonding conditions close to tested specimen condition by comparing the system flexural rigidity. Two interface conditions are referred to (1) the pellet-pellet interface debond with gap and pellet-clad interface bonded case for the fuel Young’s modulus $\frac{1}{4}$ of the original, and (2) the pellet-pellet interface and pellet-clad interface both debonded with gap case for the fuel Young’s modulus $\frac{1}{2}$ of the original. The further stress analysis shows the estimated average stress from test data is between the estimations from two identified FEA simulation cases.

Table 19. The flexural rigidity comparison between BWR and PWR HBR fuel rods for different interface bonding conditions

Interface bonding conditions	BWR Flexural rigidity EI (N·m²)	PWR HBR Flexural rigidity EI (N·m²)	Difference from BWR to PWR HBR
Perfect bond	99	77	22%
Pellet-pellet interface with gap debond, pellet-clad interface bonded	76	39	49%
Pellet-pellet interface with gap debond, pellet-clad interface debonded	35	29	17%
Pellet-pellet interface without gap debond, pellet-clad interface bonded	84	53	37%
Pellet-pellet interface without gap debond, pellet-clad interface debonded	54	43	20%

11. HYDRIDE REORIENTATION TESTING ON HBR FUEL

11.1 Background

Hydrogen embrittlement of zirconium alloys is a growing concern because of the lack of a long-term solution for disposal of SNF in the United States. Normal operation of nuclear fuel in a reactor results in the formation of a waterside corrosion layer (oxide) and the introduction of hydrogen into the zirconium cladding via the reaction $2\text{H}_2\text{O} + \text{Zr} \rightarrow \text{ZrO}_2 + 4\text{H}$. With increasing corrosion, the hydrogen concentration in the cladding will exceed its terminal solid solubility and brittle zirconium hydrides ($\text{Zr} + 2\text{H} \rightarrow \text{ZrH}_2$) may precipitate as cladding cools. The formation of these hydride precipitates cause cladding ductility and failure energy to decrease^{23,24} and increases the likelihood of failure during very long-term storage and/or transportation of SNF. However, failure due to embrittlement is highly dependent upon the microstructural condition, especially the orientation of the zirconium-hydride precipitates.

Under pool-storage conditions after the fuel is discharged from reactors, the precipitated hydride platelets are oriented in the circumferential direction. Circumferential hydrides, in combination with hardening due to irradiation effects, will decrease cladding ductility in response to axial and hoop loads, however, high-burnup cladding usually retains some ductility. At elevated temperatures during drying-transfer operations and the early stage of dry-cask storage, some of the hydrogen may go into solution (up to 200 wppm at 400°C). The pressure-induced cladding tensile hoop stress during drying-transfer operations is high relative to in-reactor and pool-storage conditions. During cooling under tensile hoop stress, some of the dissolved hydrogen will precipitate in the radial direction across the cladding wall when the hoop stress is sufficient. Further cooling during storage may result in radial-hydride-induced embrittlement. This was confirmed by some recent research^{25,26,27,28,29} that featured hydrided Zircaloy-4 cladding and high burnup fueled Zr alloy samples that were exposed to a tensile hoop stress from the internally pressurized cladding at $\approx 400^\circ\text{C}$ —conditions similar to drying operations of the SNF.

The objective of this hydride reorientation study is to collect experimental data on the hydride reorientation testing of HBR high burnup fuels under simulated conditions of drying operations. This report describes a procedure and test results of out-of-cell hydride reorientation tests of hydrided HBR cladding, which will be used as a guideline of in-cell hydride reorientation tests with high burnup fuel segments.

11.2 Materials, Equipment, and Test Methods

11.2.1 Description of Cladding Material and High-Burn-Up Fuel Segments

The out-of-cell experiments were conducted with 15×15 pressurized water reactor (PWR) Zircaloy-4 cladding material provided by AREVA, which has similar dimensions, oxygen content, and mechanical properties as the HBR cladding. After the cladding was received by ORNL, measurements were performed to determine the OD and wall thickness. Table 20 summarizes the dimensions and chemical composition of the unirradiated HBR cladding used in the ORNL test program.

Table 20. Dimensions and Chemistry of HBR Archive Zircaloy-4 Used in the ORNL Test Program (the "<" sign means below the detection limit)

Parameter	15×15 Zircaloy-4 HBR-type Cladding ≈1980 ^a	Nominal Composition of Commercial Zircaloy-4 ^b Cladding Alloys
OD, mm	10.76	---
Wall Thickness, mm	0.76	---
Sn, wt.%	---	1.29±0.1
Nb, wt.%	---	---
O, wt.%	≈0.13	0.120
Fe, wt.%	---	---
Cr, wt.%	---	---
Ni, wppm	---	---
S, wppm	---	---
C, wppm	---	---
Hf, wppm	---	---
Si, wppm	---	---
N, wppm	---	---
H, wppm	≈20	5

^aORNL data based on AREVA lots received in 2014.

^bASTM B811 [3].

Irradiated materials used in the ORNL test program are high-burnup HBR PWR fuel rods received by ORNL in 2008. They were from a 15×15 assembly of HBR Unit 2³⁰ that was operated for seven cycles and reached a rod-average burnup of 67 GWd/MTU (73 GWd/MTU peak pellet). The fuel enrichment is 2.90%. The nominal fuel pellet dimensions are 9.06 mm dia. × 9.93 mm height and the active fuel height is 3.66 m. The cladding is cold-worked/stress-relieved Zircaloy-4, 10.77 mm OD × 9.25 mm inner diameter (ID), with a nominal tin content of 1.42%. The rods were pressurized with helium to 2.0 MPa during fabrication. A detailed description of the as-fabricated cladding, the irradiation history, and the nondestructive testing results (eddy current, profilometry, fission-gas release, etc.) is given by the plant operator and fuel vender³⁰ above.

Irradiated HBR fuel used in the ORNL test program is summarized in Table 21. Detailed characterization was performed to determine the fuel morphology, fuel-cladding bond, corrosion layer, and hydride morphology. Fig. 115 shows a low magnification image of the fuel morphology, which reveals the typical start-up and shut-down cracks.

Table 21. Characteristics of High-burnup HBR Fuel Rods for the ORNL Hydride Reorientation Test. Burnup values are rod averaged

Parameter	H. B. Robinson
Reactor	PWR
Enrichment, wt. %	2.90
Burnup, GWd/MTU	63-67
Discharge Date	1995
Fast Fluence, 10 ²⁵ n/m ²	14
Cladding	15×15 Zircaloy-4
Initial Wall Thickness, mm	0.76
OD Oxide, μm	≤ 100
Hydrogen Pickup, wppm	≤ 800
Fueled	Yes



Fig. 115. High-burnup HBR fuel morphology for Sample 607D4A.

11.2.2 Equipment for Sample Preparation

The hydriding apparatus consists of a closed stainless steel tube that contains zirconium alloy specimens and hydrogen gas, as shown in Fig. 116. The tube is then heated to facilitate hydrogen absorption by the metal. By controlling the initial hydrogen gas pressure in the vessel, the temperature profile hydrogen concentration can be selectively processed. A typical pressure and temperature profile is shown in Fig. 117.



Fig. 116. Hydrogen charging apparatus.

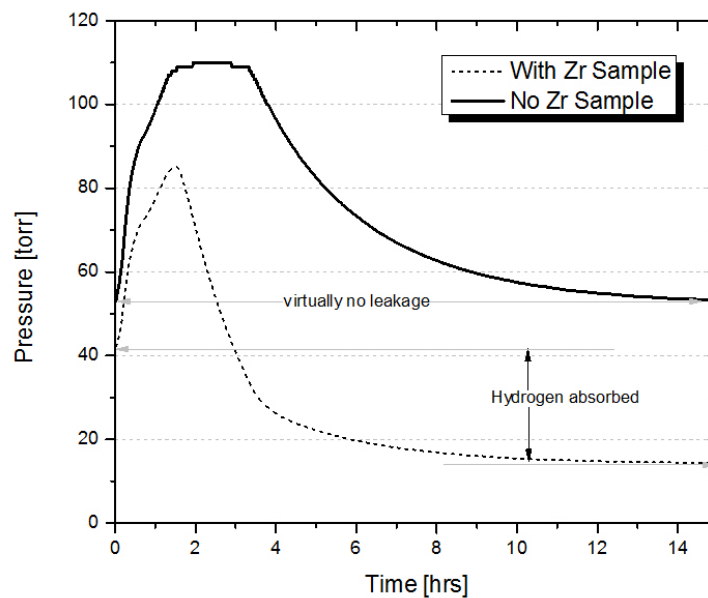


Fig. 117. A typical pressure and temperature profile of hydrogen charging process.

An Astro Arc Polysoude welder (see Fig. 118) was used for automatic orbital welding of the cladding. A circular movement of the welding torch/electrode around fuel cladding, controlled by the welder power source, creates an orbital weld. This welder can be operated remotely with manipulators in hot cell, although practice is required for in-cell welding.



Fig. 118. Astro Arc Polysoude tubing welder.

11.2.3 Hydride Reorientation System

The reorientation system consists of a high pressure piping system and test chamber within a programmable crucible furnace (see Fig. 119a and Fig. 119b). For each experiment, a six-inch-long specimen, (welded with two end plugs with one end sealed and the other opened) was connected to the high pressure piping system within the test chamber. The test chamber was purged with pure argon gas, and then the sample was internally pressurized to cause a hoop stress ranging from zero to $150 \text{ MP}^{\frac{27}{2}}$. Pressurized samples were subjected to a preprogrammed temperature profile for up to five cycles with each cycle being heated to 400°C , held for 2 hours, and slow-cooled/heated ($1^\circ\text{C}/\text{min.}$) to 170°C with the final cycle cooled from 170°C to room temperature (RT). Hoop stress was calculated using values $r = 4.62 \text{ mm}$ for inner radius and $t = 0.76 \text{ mm}$ for the wall thickness of the HBR Zircaloy-4 cladding.

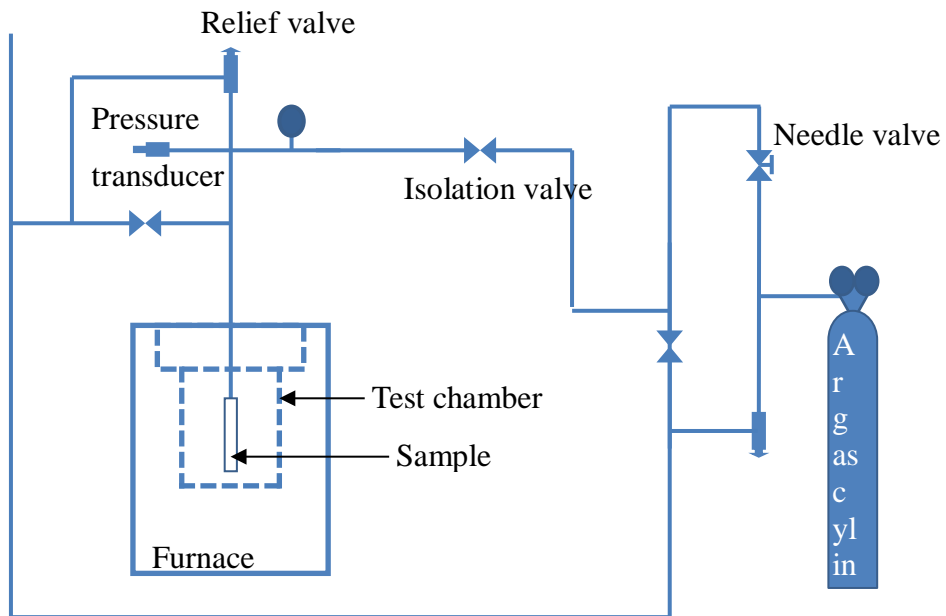


Fig. 119. (a) Schematic of the hydride reorientation system.



Fig. 119. (b) Hydride reorientation system

11.3 Materials Hydridding and Characterization

The Zircaloy-4 cladding samples were hydrogen charged by gaseous method, as described in Section 11.2. Gas charging was conducted under stress free conditions. The target hydrogen concentrations can range from tens of wppm to a few thousands of wppm. The most important ranges for licensing and modeling real reactor fuel are usually less than 1000 wppm. For this work, the Zircaloy-4 was hydrided to a target concentration of 300-400 wppm, which is similar to the hydrogen content of the HBR high burnup cladding to be tested in the hot cell.

Metallographic examinations were performed on hydrided Zircaloy-4 samples. Although axial gradients in hydrogen content are generally observed and reported in hydrided Zircaloy-4 samples, the ORNL hydriding procedure resulted in uniform distributions of circumferential hydrides across the Zircaloy-4 wall. As shown in Fig. 120, the hydride density increases as the hydrogen concentration in the sample increases. The hydrogen measurements indicated the hydrogen content of the specimens shown in Fig. 120 are from 70 to 320 wppm.

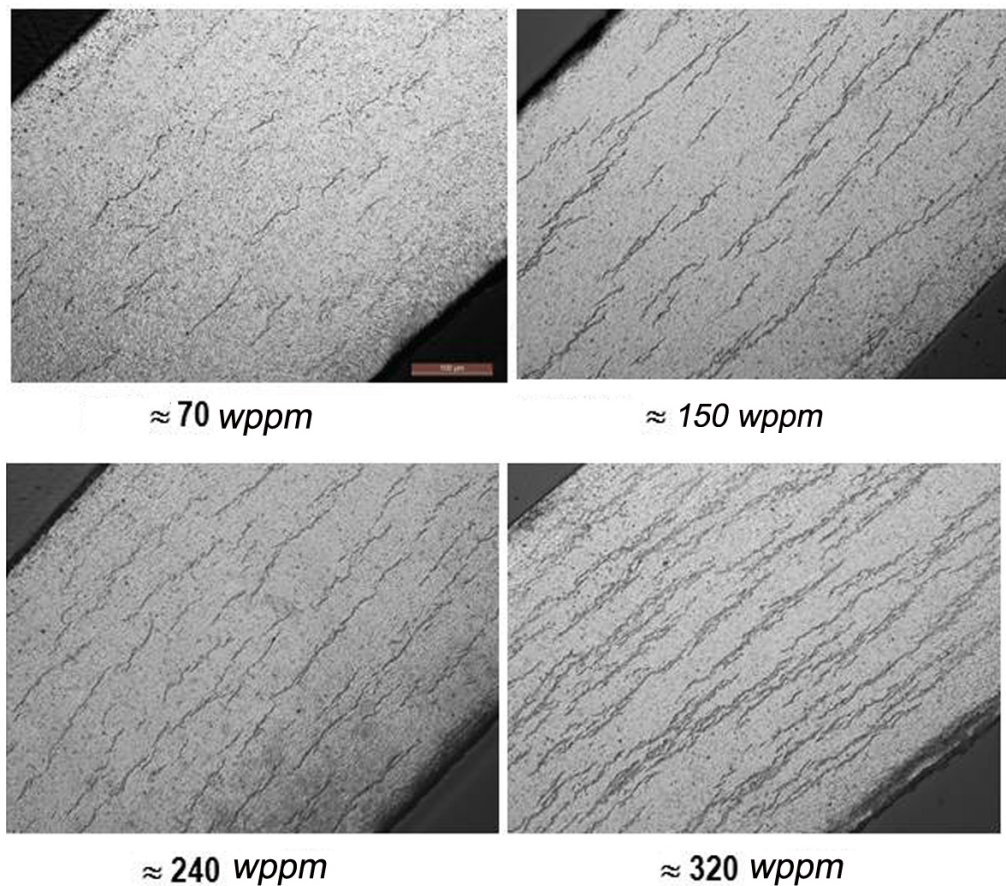


Fig. 120. Micrographs showing typical circumferential hydride distributions in hydrogen charged Zircaloy-4.

11.4 Out-Of-Cell Hydride Reorientation Testing

The objective of the program is to collect experimental data on hydride reorientation testing of the HBR high burnup fuels under simulated drying operations conditions of the SNF. In order to optimize the in-cell test condition, four out-of-cell hydride reorientation tests with hydrided HBR cladding were performed. The out-of-cell test result will provide a guideline to in-cell hydride reorientation tests with high burnup HBR fuel segments.

11.4.1 HR-HBR #1, 145 MPa at 400°C, 1 cycle

Test HR-HBR#1 on a hydrided 15×15 Zircaloy-4 was conducted at the maximum hoop stress of 145 MPa and the hold temperature $T = 400^{\circ}\text{C}$. The total test time was over 72 hours. After fabrication, the specimen was assembled into a holder within the furnace for heating to 400°C , held at 400°C for 2 hours, cooled at $5^{\circ}\text{C}/\text{h}$ to 170°C , then cooled at a faster rate from 170°C to RT. The internal pressure was dynamically monitored with a digital pressure transducer.

Fig. 121 shows the temperature and pressure history for a drying-storage simulation experiment conducted with a 2-h hold time and 1-cycle cooling. The temperature plotted is a thermocouple reading near the specimen surface. The drying-storage simulation mentioned here is also referred to radial hydride treatment in this work.

Fig. 122 shows the hydride morphology of Sample HR-HBR#1 with hydrogen content $H \approx 274$ wppm. The specimen was sectioned at the mid-plane of a 6"-long sample. The radial hydride can be clearly observed. The maximum length of radial hydrides is about 50-60 μm , as they are often terminated when intersecting with circumferential hydrides. Fig. 123 shows the radial hydride distribution in eight areas in different circumferential directions of Sample HR-HBR#1.

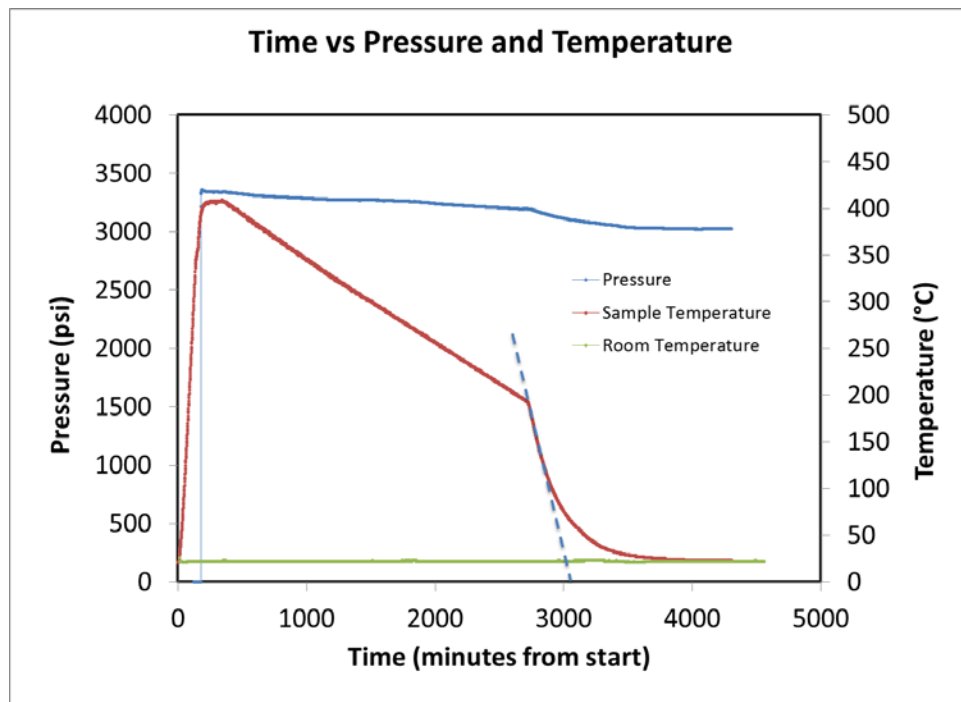


Fig. 121. Time vs pressure and temperature for Test HR-HBR#1.

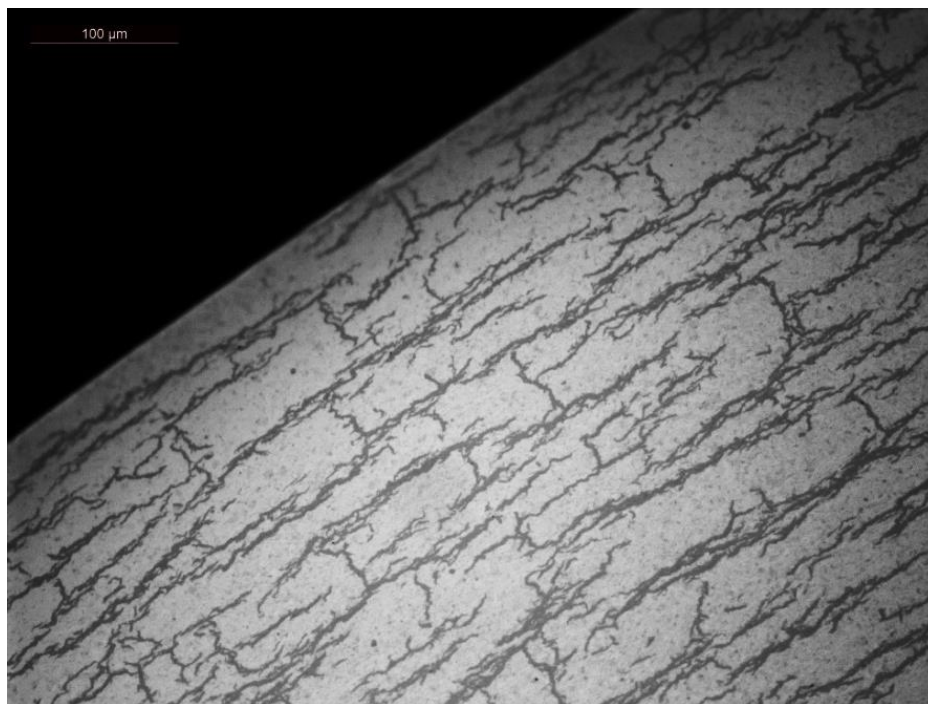


Fig. 122. High magnification micrograph showing radial hydrides of Sample HR-HBR#1 with hydrogen content $H \approx 274$ ppm. The specimen was sectioned at the mid-plane of a 6"-long sample.

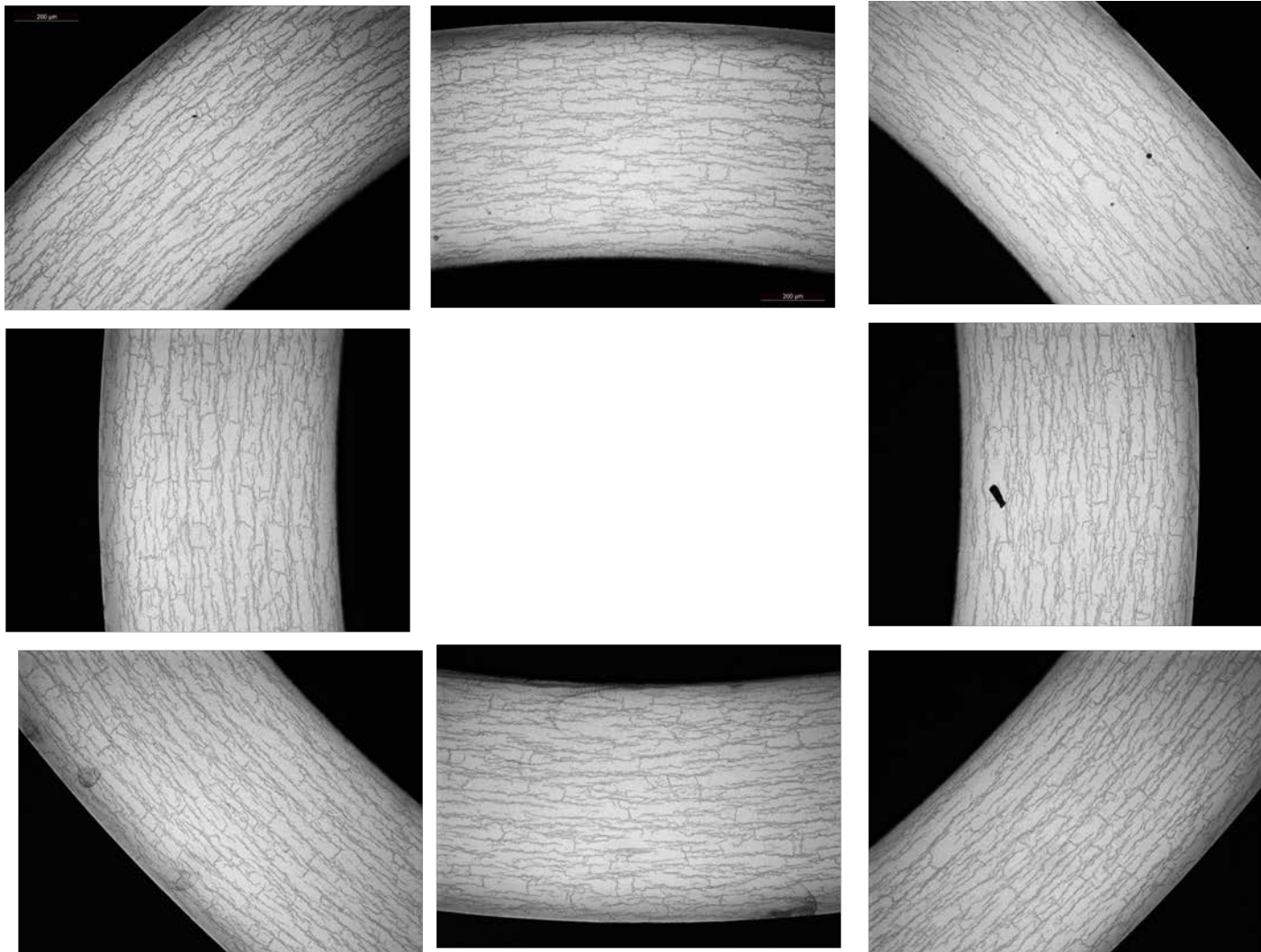


Fig. 123. Radial hydride distribution shown in eight areas in different circumferential directions of Sample HR-HBR#1. The specimen was sectioned at the mid-plane of a 6''-long sample.

11.4.2 HR-HBR #2, 145-150 MPa at 400°C, 5 cycles

Test HR-HBR#2 was conducted on a hydrided 15×15 Zircaloy-4 at the maximum hoop stress of 145 MPa and the target hold temperature $T = 400^{\circ}\text{C}$. However, thermal cycling was performed in order to increase the radial hydrides. After fabrication, the specimen was assembled into a holder within the furnace for heating to target temperature 400°C , held for 2 hours, cooled at $1^{\circ}\text{C}/\text{min}$ to 170°C , and then heated at $1^{\circ}\text{C}/\text{min}$ to target hold temperature 400°C again for 5 cycles. The sample was furnace cooled from 170°C to RT for the last cycle. Fig. 124 shows the temperature and pressure history for HR-HBR#2. The temperature plotted is a thermocouple reading near the specimen surface.

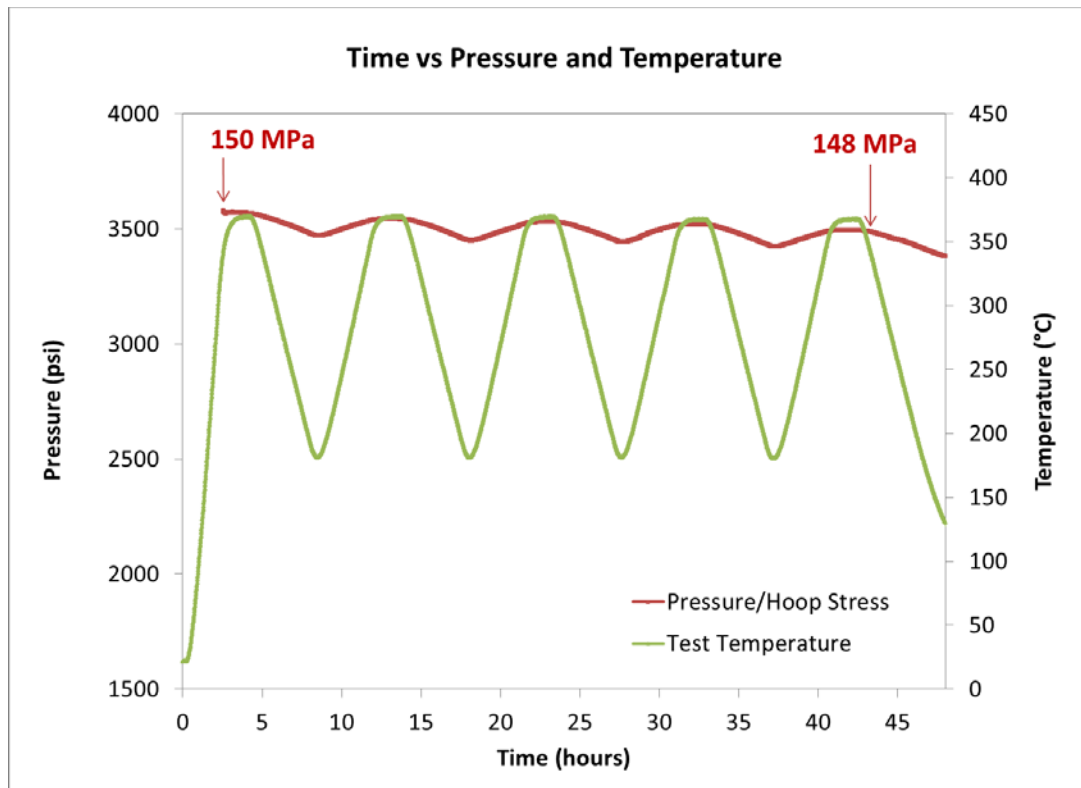


Fig. 124. Time vs pressure and temperature for Test HR-HBR#2.

Fig. 125 shows the hydride morphology of Sample HR-HBR#2 with hydrogen content $H \approx 286$ wppm. The specimen was sectioned at the mid-plane of a 6"-long sample. The radial hydride can be clearly observed. The maximum length of the radial hydride is about $50\text{-}60\ \mu\text{m}$, similar to HR-HBR#2. However, the density of radial hydrides in HR-HBR#2 is much higher than the one in HR-HBR#1, mainly due to multiple thermal cycles. Fig. 126 shows radial hydride distribution in eight areas in different circumferential directions of Sample HR-HBR#2.

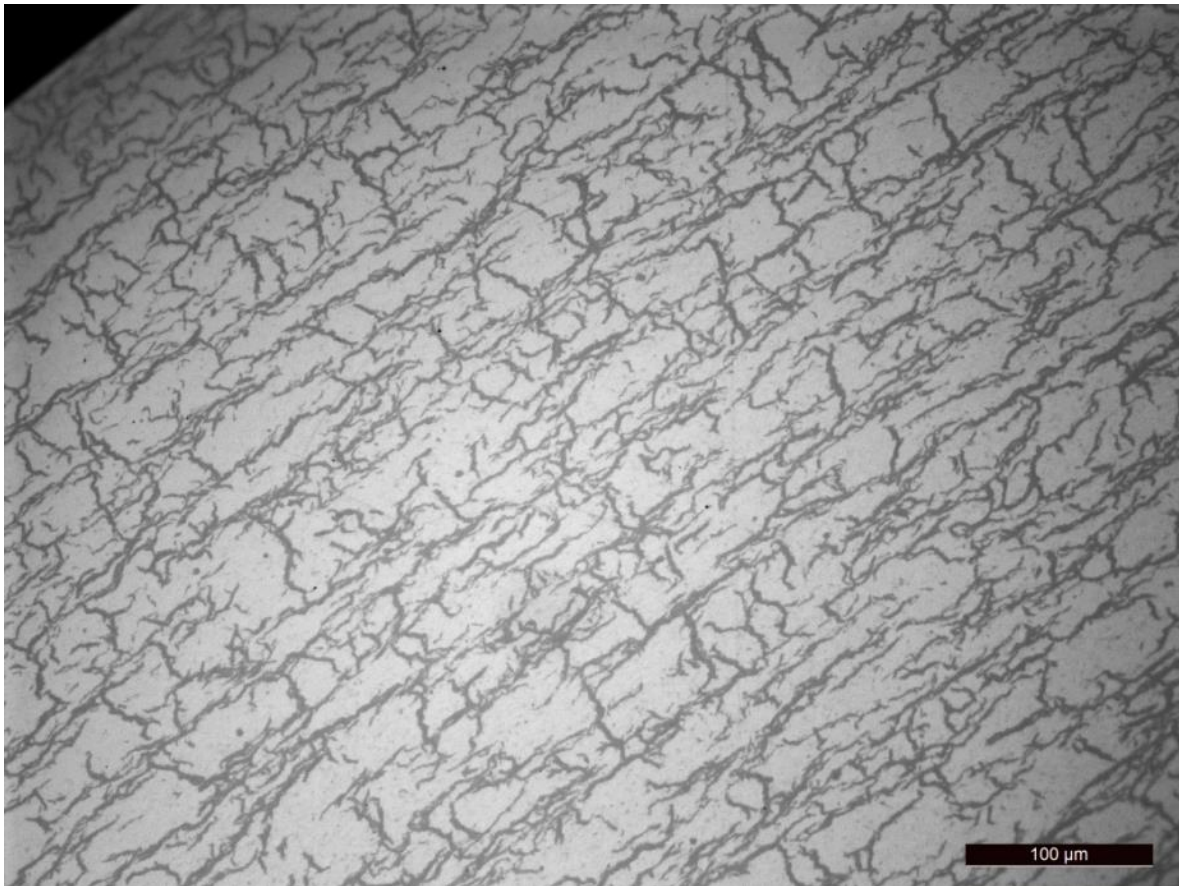


Fig. 125. High magnification micrograph showing radial hydrides of Sample HR-HBR#2 with hydrogen content $H \approx 286$ ppm. The specimen was sectioned at the mid-plane of a 6''-long sample.

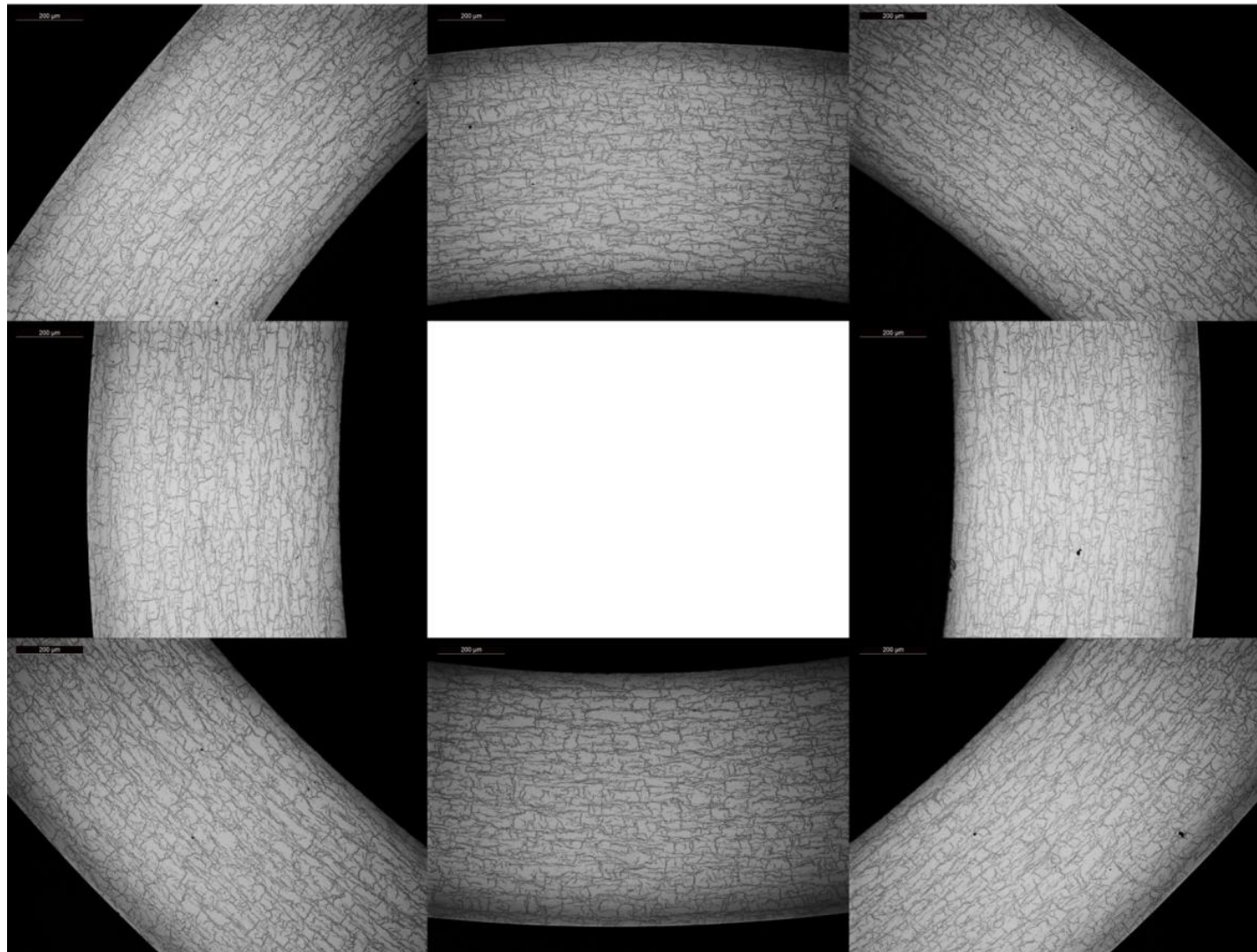


Fig. 126. Radial hydride distribution shown in eight areas in different circumferential directions of Sample HR-HBR#2. The specimen was sectioned at the mid-plane of a 6'-long sample.

11.4.3 HR-HBR #3, 100 MPa at 400°C, 5 cycles

Test HR-HBR#3 was conducted on a hydrided 15×15 Zircaloy-4 at the maximum hoop stress of 100 MPa and the hold temperature $T = 400^{\circ}\text{C}$. After fabrication, the specimen was assembled into a holder within the furnace for heating to 400°C , held at 400°C for 2 hours, cooled at $1^{\circ}\text{C}/\text{min}$ to 170°C , and then heated at $1^{\circ}\text{C}/\text{min}$ to 400°C again for 5 cycles. The sample was furnace cooled from 170°C to RT for the last cycle. Fig. 127 shows the temperature and pressure history for HR-HBR#3. The temperature plotted is a thermocouple reading near the specimen surface.

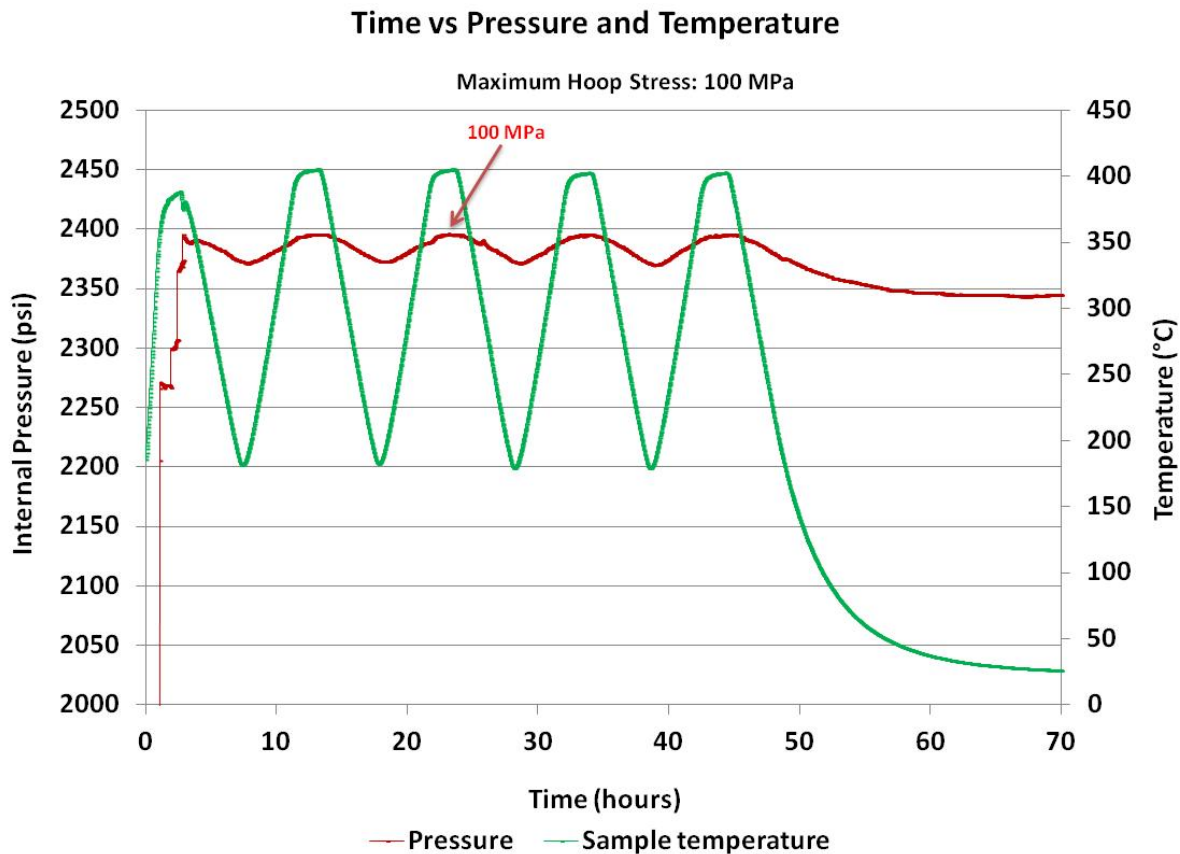


Fig. 127. Time vs pressure and temperature for Test HR-HBR#3.

Fig. 128 shows the hydride morphology of Sample HR-HBR#3 with hydrogen content $H \approx 310$ wppm. The specimen was sectioned at the mid-plane of a 6"-long sample. The radial hydride can be observed. The maximum length of the radial hydride is $< 30 \mu\text{m}$. The radial hydride ratio of HR-HBR#3 also seems lower than HBR#2. Fig. 129 shows radial hydride distribution in eight areas in different circumferential directions of Sample HR-HBR#3.

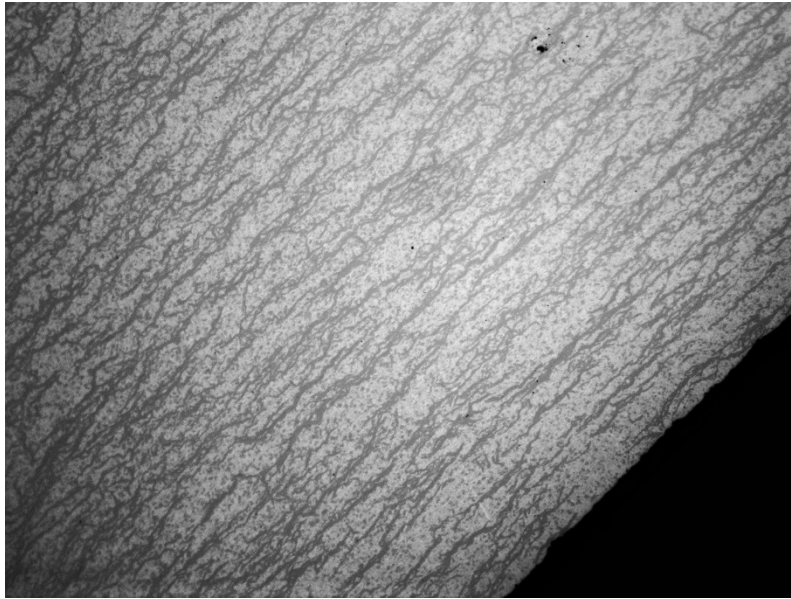


Fig. 128. High magnification micrograph showing radial hydrides of Sample HR-HBR#3 with hydrogen content $H \approx 310$ ppm. The specimen was sectioned at the mid-plane of a 6"-long sample.

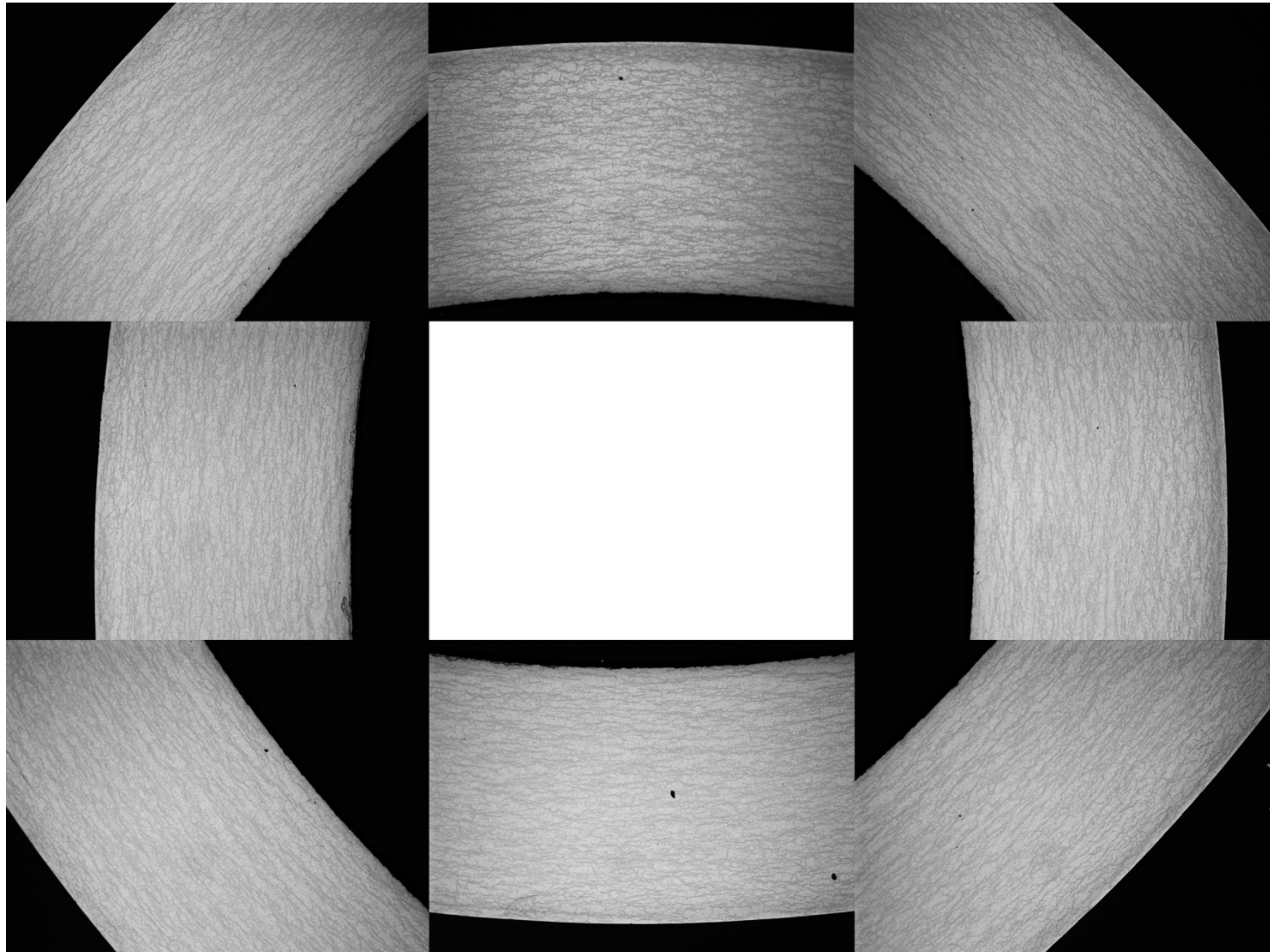


Fig. 129. Radial hydride distribution shown in eight areas in different circumferential directions of Sample HR-HBR#3. The specimen was sectioned at the mid-plane of a 6"-long sample.

11.4.4 HR-HBR #4, 120 MPa at 400°C, 5 cycles

Test HR-HBR#4 was conducted on a hydrided 15×15 Zircaloy-4 at the maximum hoop stress of 120 MPa and the hold temperature $T = 400^{\circ}\text{C}$. After fabrication, the specimen was assembled into a holder within the furnace for heating to 400°C , held at 400°C for 2 hours, cooled at $1^{\circ}\text{C}/\text{min}$ to 170°C , and then heated at $1^{\circ}\text{C}/\text{min}$ to 400°C again for 5 cycles. The sample was furnace cooled from 170°C to RT for the last cycle. Fig. 130 shows the temperature and pressure history for HR-HBR#4. The temperature plotted is a thermocouple reading near the specimen surface.

Fig. 131 shows the hydride morphology of Sample HR-HBR#4 with hydrogen content $H \approx 312$ wppm. The specimen was sectioned at the mid-plane of a 6''-long sample. The radial hydride can be observed. The maximum length of the radial hydride is $< 30 \mu\text{m}$. The radial hydride ratio of HR-HBR#4 is also lower than HBR#2. Fig. 132 shows radial hydride distribution in eight areas in different circumferential directions of Sample HR-HBR#4.

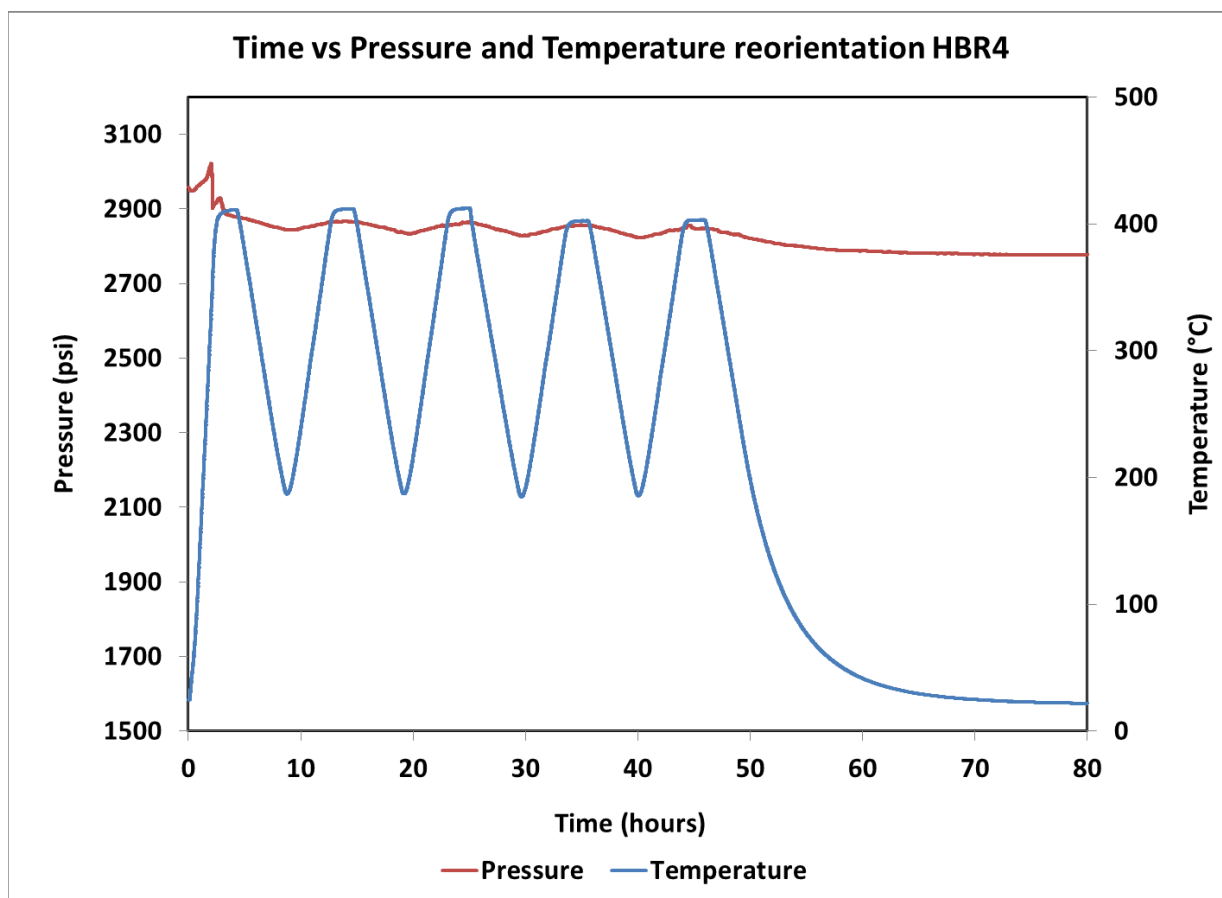


Fig. 130. Time vs pressure and temperature for Test HR-HBR#4.

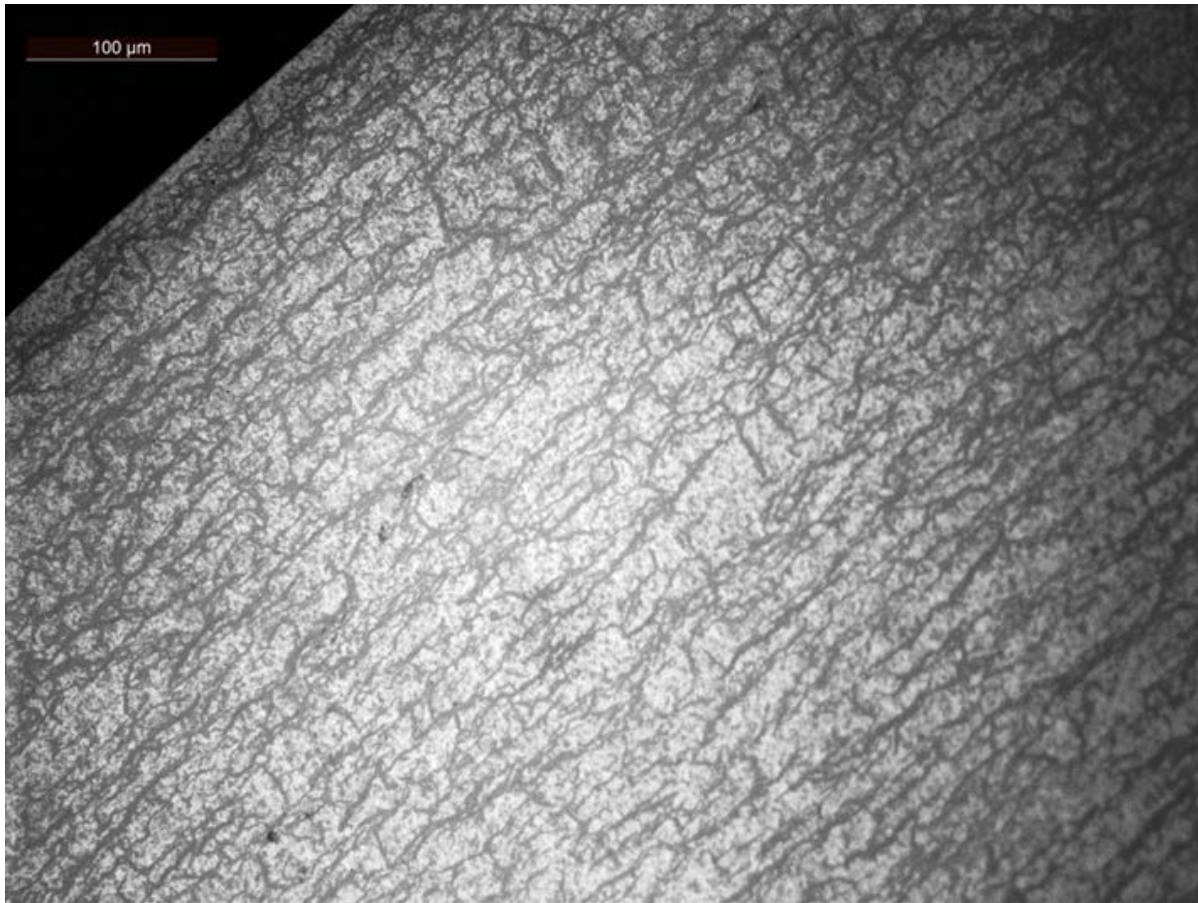


Fig. 131. High magnification micrograph showing radial hydrides of Sample HR-HBR#4 with hydrogen content $H \approx 312$ ppm. The specimen was sectioned at the mid-plane of a 6''-long sample.

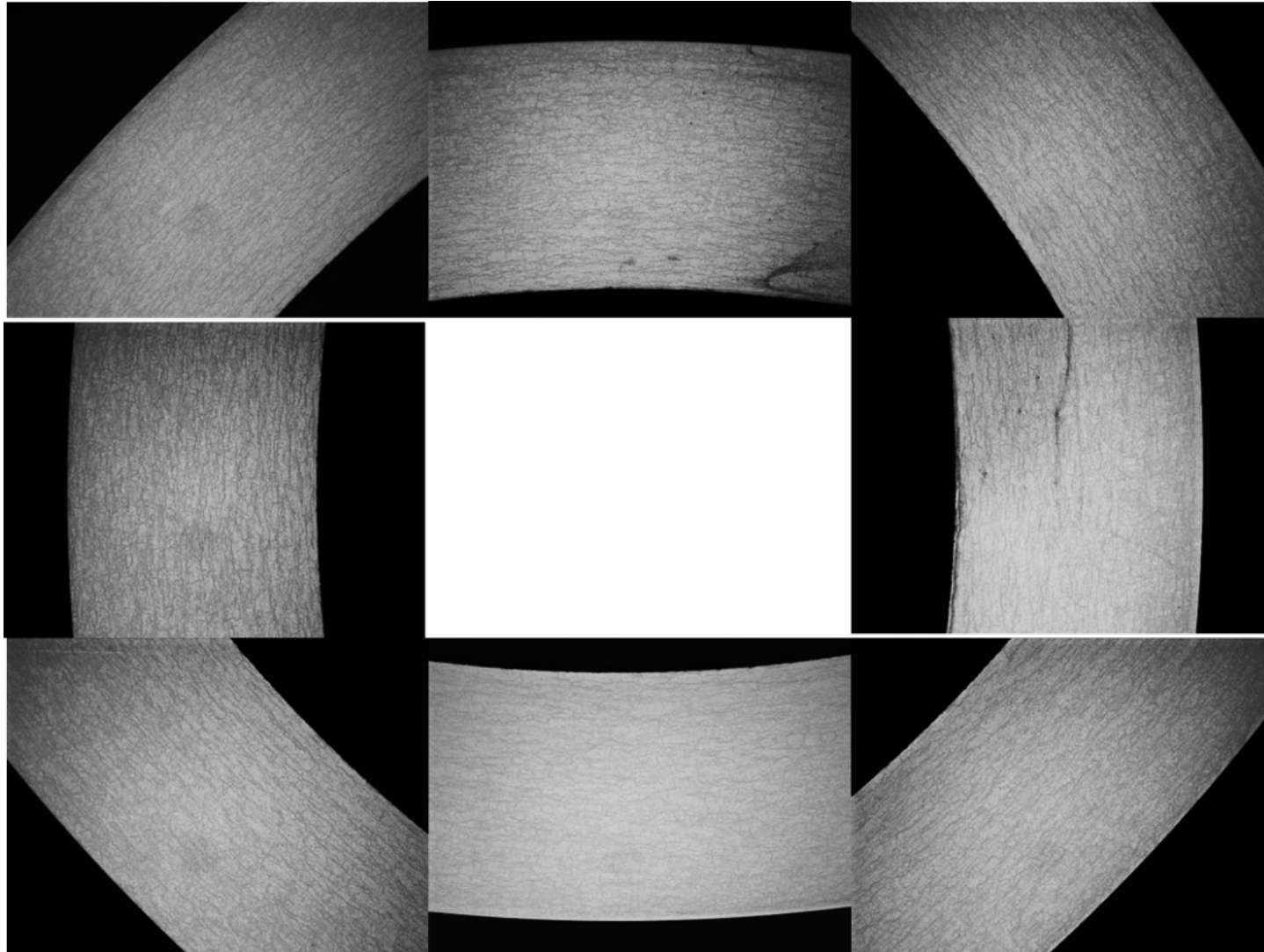


Fig. 132. Radial hydride distribution shown in eight areas in different circumferential directions of Sample HR-HBR#4. The specimen was sectioned at the mid-plane of a 6"-long sample

11.5 DISCUSSION

The microstructure of final Zircaloy-4 cladding consists of elongated grains along the rolling (i.e., longitudinal or axial) direction of the tube. At room temperature, these α -Zr grains exhibit a hexagonal close packed (hcp) lattice with dimensions of $a_o = 0.3232$ nm and $c_o = 0.5147$ nm; the hcp phase is stable up to $\approx 810^\circ\text{C}$ for Zircaloy-4. Hydride morphology from etched hydrided Zircaloy-4 cladding is often used to check the cladding quality. The circumferentially oriented hydride platelets, uniformly distributed across the wall in our hydrided Zircaloy-4 samples are a typical hydride morphology for the Zircaloy-4 cladding³¹, owing to the anisotropy and texture resulting from the material processing history (see Fig. 133).

At reactor temperature, zirconium reacts with water to form zirconia (ZrO_2), and produces hydrogen according to the reaction $\text{Zr} + 2\text{H}_2\text{O} \rightarrow \text{ZrO}_2 + 4\text{H}$. The excess hydrogen can diffuse into the cladding and then precipitate as hydride platelets when it reaches the solubility limit, which is simulated by hydrogen charging in this work. Hydrogen pickup increases with burnup, or more exactly, with the extent of waterside corrosion. A hydride rim has been observed near the outer surface of high burnup cladding^{23,24,25} because the hydride density in high-burnup Zr cladding is greater near the cooler outer surface of the cladding than the hotter middle and inner cladding regions during reactor operation. The hydrogen concentration of the high-burnup HBR cladding to be tested is about 400 wppm. It has a relatively dense hydride rim at the OD surface and a decreased hydride density from below the rim to the cladding inner surface.

The uniformly distributed hydrides in our hydrided samples were obtained by furnace treatment at a homogeneous temperature, which is different from that occurring in-pile in irradiated cladding. In addition, our hydrided samples with $\text{H} \approx 300$ wppm consist of brittle hydrides in a high ductility matrix while high-burnup HBR cladding consists of brittle hydrides in a low ductility matrix. However, for modeling and simulations purposes, we have started working with unirradiated samples, by which we can develop the test procedure to be used for in-cell tests. The out-of-cell result will also provide as a guideline for the irradiated cladding in the future.

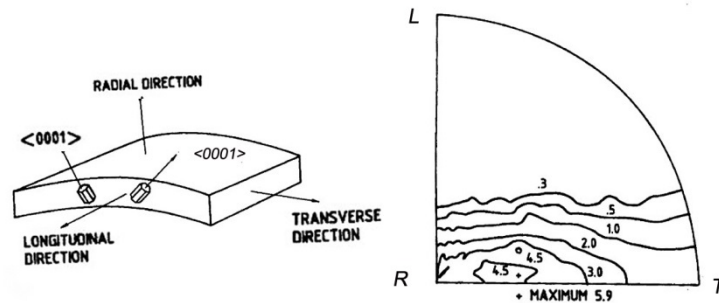


Fig. 133. Schematic diagram and basal pole figure showing the grain orientation in stress-relieved Zircaloy-4³¹.

The terminal solid solubility of hydrogen in Zircaloy is shown in Fig. 134^{32,33}. The solubility limit is very low at room temperature (< 10 wppm is soluble) and ≈ 200 wppm is soluble at 400°C according to the phase diagram for the zirconium-hydrogen binary system^{34,35}. Therefore, when the furnace is cooled from elevated temperature to RT the hydrogen precipitates as a hydride in hydrided cladding samples. In fact, the hydrided Zircaloy-4 is a composite material, which consists of a ductile matrix, α -Zr, and brittle second phase hydrides. It was found that radial hydrides can be formed under a hoop tensile stress when the cladding sample is internally pressurized^{24,25,26,27}.

In this work, the hydrided tubing samples have been internally pressurized to produce a hoop stress up to 150 MPa to form radial hydrides using the hydride reorientation system (see Section 11.4). Tests HR-HBR#1 and HR-HBR#2 indicate that multi-thermal cycling will increase the ratio of radial hydrides under the same maximum temperature and maximum internal pressure. In addition, our test results of Tests HR-HBR#2 to #4 reveal that the ratio of radial hydrides decreases as the internal pressure decreases when the temperature and pressure profiles remain the same. The goal is to investigate the impact of radial hydrides on high burnup fuel cladding ductility and fatigue strength, for which it needs to produce a reasonably high percentage of radial hydrides within the cladding by the hydride reorientation tests. The out-of-cell test result is very important for planning the in-cell hydride reorientation tests, as it establishes a test procedure for in-cell experiments and provides a guideline to in-cell test conditions. Based on the four out-of-cell tests, it was decided to begin the in-cell hydride reorientation test under the same test conditions of Test HR-HBR#2 in order to maximize the radial hydride condition. The hydride reorientation experiments in hot cell are under way, and the results will be reported in the near future.

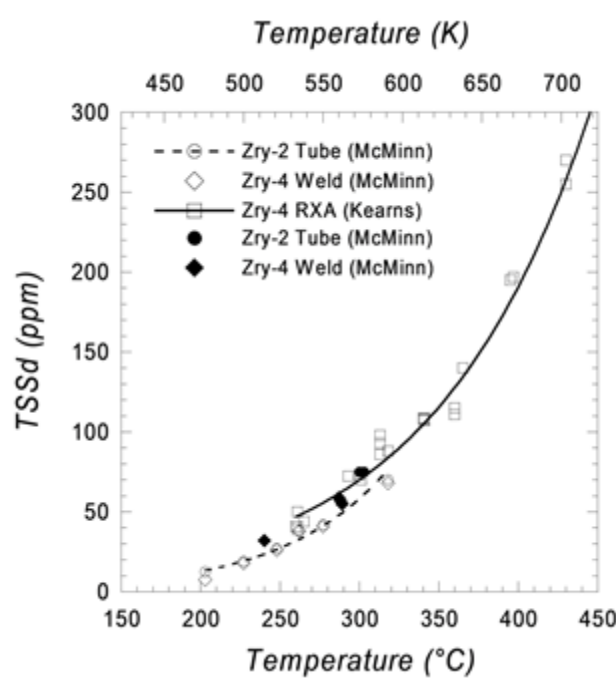


Fig. 134. Terminal solid solubility for dissolution of hydrogen in Zircaloy^{32,33}.

It is also interesting to note that the non-uniform hydride rim was observed in circumferential directions near OD of fatigue fractured CIRFT specimen DL10 of HBU HBR SNF, see Fig. 135.

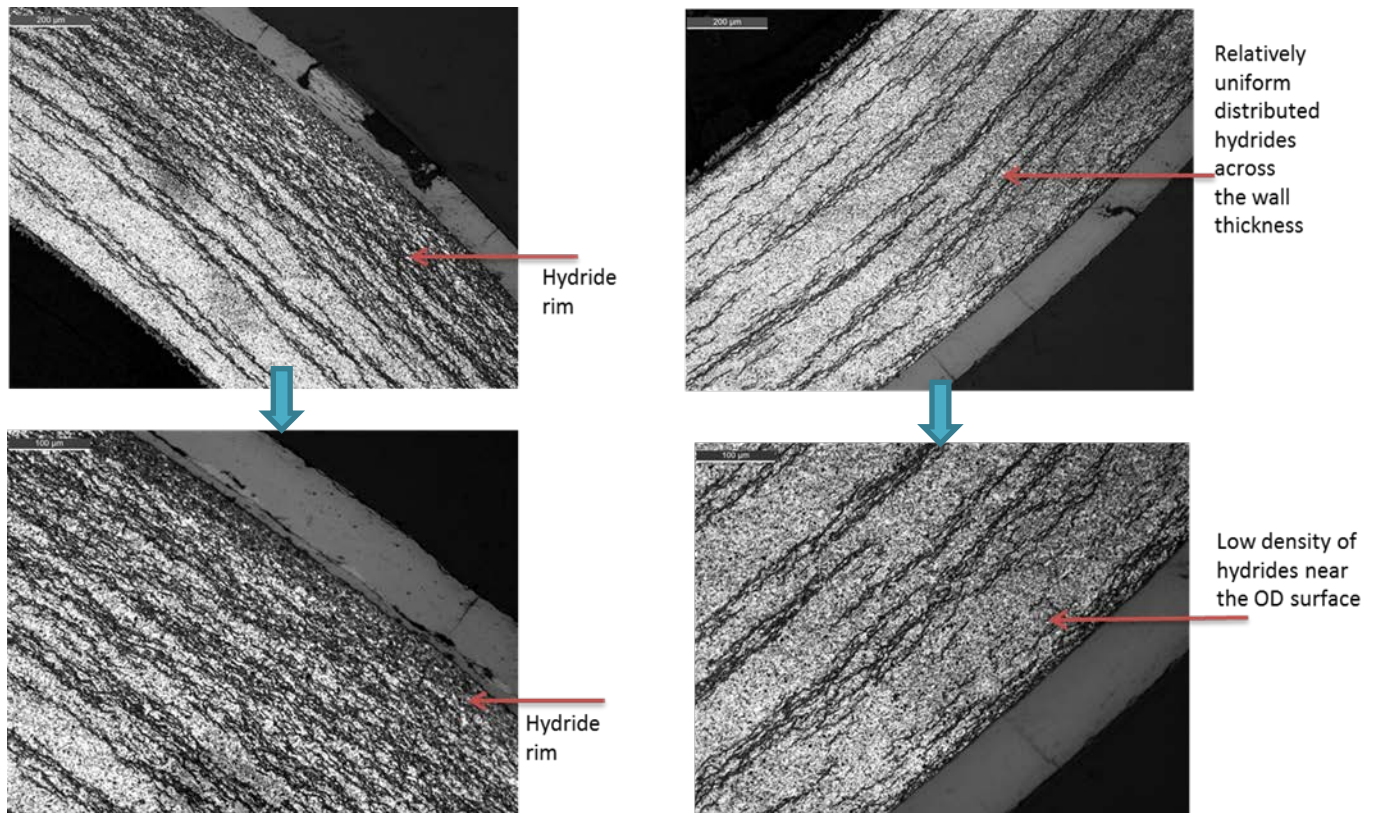


Fig. 135. SEM images of fracture D10 specimen shows non-uniform hydride ring along the outer diameter of the clad wall.

12. CONCLUSIONS

Fourteen BWR LMK specimens were prepared and tested in the hot cell in the reporting period of the project. The first specimen was used for tuning and static testing and the rest were used in dynamic tests. Under static unidirectional loading, a moment of 85 N·m was obtained at maximum curvature 4.0 m^{-1} . The specimen did not show any failure in three repeated loading cycles to almost the same curvature. The dynamic tests were conducted at 5 Hz with a range of moment amplitudes from 7.11 to 25.40 N·m. Twelve specimens failed with lifetimes from 2.14×10^4 to 4.70×10^6 cycles. One (at $\pm 7.11 \text{ N}\cdot\text{m}$) cycled to 7.58×10^6 without failure and stopped. Online monitoring revealed the flexural rigidity was from 25 to 42 $\text{N}\cdot\text{m}^2$. Such level of rigidity was lower than that of PWR HBR specimens, at 39 to 51 $\text{N}\cdot\text{m}^2$. While the two claddings were based on Zircaloy-2 and Zircaloy-4, respectively, the geometrical sizes contributed more to the observed difference. This can be seen from Table 8 and 10, where HBR rods had a relative larger cladding OD and pellet diameter.

Additional CIRFT tests were performed on three NA spent fuel rods and six MOX rods in this reporting period. A total of six dynamic tests were completed on NA rods in the hot cell. Applied moment amplitudes were varied from ± 5.08 to $\pm 15.24 \text{ N}\cdot\text{m}$. Five specimens failed with the fatigue life from 1.26×10^4 to 4.27×10^5 cycles. One specimen was cycled at $\pm 5.08 \text{ N}\cdot\text{m}$ to 5.11×10^6 cycles without failure. On other hand, 10 dynamic tests have been completed on MOX spent fuel rods so far with the same moment amplitude range as that of NA rods, and these specimens failed between 1.29×10^4 and 2.15×10^6 cycles. Online monitoring indicated a variation in rigidity of 21 to 28 $\text{N}\cdot\text{m}^2$ for this group of spent fuel that had a similar cladding OD. Apparently, the range of flexural rigidity is much lower than that of HBR and LMK rods mainly due to the smaller cross section size of the rods.

The use of equivalent strain and equivalent stress obviously reduced the cladding/ pellet size effect to a certain extent, and data points can be consolidated more to the HBR curve. More investigation into the several critical factors is required to understand the performance of SNF fatigue life in terms of these quantities, including cladding materials, pellets, cladding-to-pellet and pellet-to-pellet interface bonding, and cladding oxide and hydrides. SNF is a composite structure of fuel pellet and clad system with multi-scale discontinuities. CIRFT global data needs detailed FEA to translate global moment-curvature to local engineering stress-strain data.

CIRFT test data provide new insights into SNF dynamic behavior. The CIRFT approach successfully demonstrates the controllable fatigue fracture on HBU SNF in a harmonic vibration mode, which enables us to examine the underlying mechanism of SNF system dynamic performance, such as the following.

- SNF system interface bonding efficiency
- Fuel structural support to the SNF system
- Significant variation in local stress-strain profile due to pellet-clad interaction
- Clad hydride system microstructure dynamic evolution
- SNF system S-N limit related to clad fracture threshold
- SNF failure initiated at pellet-pellet-clad interface region and appear to be spontaneous failure

Lessons learned from CIRFT testing on SNF vibration integrity study are summarized below.

- Fuel contribution to clad stiffness during random vibration
- Stress concentration effects on clad at pellet-pellet interfaces
- Flexural deformation mechanism linking to SNF rod aging history
- Potential hydrogen effects on SNF vibration integrity
- Pellet-clad bonding efficiency on SNF mechanical properties
- CIRFT measurements for local stress-strain levels evaluation
- Failure mechanisms of HBU SNF rods
- Potential impact of combined loading modes and loading rates, such as transient shocks

More detailed briefings on CIRFT test lessons learned are outlined below.

SNF vibration integrity study needs to consider the pellet-clad interactions.

- Pellet-clad-interaction, P-C bonding efficiency
- Majority CIRFT test HBU failed at pellet-pellet interface
- Tensile and shear flow surge at pellet-pellet interface region
- Pellet-pellet interface regions have relative lower temperatures and higher hydride contents
- Fuel pellet-clad property quantification, EI, E, yield stress, fracture toughness, S-N trend
- Pellet dimension and clad aging evolution effects

HBU fuel-provided support to clad structure will increase overall SNF system fracture toughness.

- Fuel-clad interface bond enables fuel pellets to carry bending flexural load
- Pellet with sufficient interface bond to clad can also carry shear resistance for SNF system
- Fuel internal support to clad reduce clad local buckling potential
- Fracture toughness of SNF rod provides direct aging and damage index to SNF system
- In transient shock load, fuel support can degrade significantly due to low dynamic toughness, K_D
- Torsional loading mode exists in SNF under normal transportation that warrant mixed-mode (I + III) fracture study of SNF system

The loading modes, types and loading rates can affect SNF vibration integrity.

- Reversible loading effect on hydride composite (tensile and compressive stresses – shear stress)
- Fuel assembly and transport cask interaction, including fuel rod to rod and rod to spacer grid contact impact-induced cask internal transient shock loading under NCT
- Transient shocks and normal vibration synergistic effect on SNF under NCT
- HBU fuel inherited low fracture threshold under transient shocks can trigger a secondary shock back to the clad inner wall upon fuel pin fracture

More data is needed for high-burnup SNF vibration integrity investigation.

- Bending fatigue strength time-dependent data for normal vibration and transient shocks, including PWR and BWR fleets and other advanced clads
- Interfacial bonding (fracture toughness) efficiency at pellet-clad interfaces
- The pellet-clad interaction at pellet-pellet-clad interface, in addition to dynamic contact interactions between spacer grids and fuel rods
- Fracture toughness, K_{IC} , and dynamic (high-rate) fracture toughness data for the SNF rod system
- Mixed-mode fracture toughness (circumferential and radial hydride can trigger mixed-mode fracture)

13. ACKNOWLEDGMENTS

This research was sponsored by the DOE Used Fuel Disposition Campaign (UFDC) and NRC under DOE contract DE-AC05-00OR22725 with UT-Battelle, LLC. The authors thank ORNL program managers Bruce Bevard and Rob Howard for their support and guidance during the project; Chuck Baldwin for post-irradiation examination (PIE), Josh Schmidlin for fuel rod cutting and dimension measurement; Bryan Woody and Scott Thurman for hot-cell operation support; Brian Sparks and Randy Parten for drawing and machining support, and J. Schmidlin, T. Smith, and S. Reid for their support on the hydride reorientation study.

14. REFERENCES

- ¹ J.-A. J. Wang, H. Wang, T. Cox, and Y. Yan, *Progress Letter Report on U-Frame Test Setup and Bending Fatigue Test for Vibration Integrity Study (Out-of-Cell Fatigue Testing Development–Task 2.3)*, ORNL/TM-2012/417, Oak Ridge National Laboratory, Oak Ridge, Tenn., August 2012.
- ² J.-A. J. Wang, H. Wang, and T. Tan, Reversal Bending Fatigue Testing, Pub. No. US 2013/0205911 A1, Aug. 15, 2013; also as US Patent No. US 8,863,585 B2, Oct. 21, 2014.
- ³ H. Wang, J.-A. J. Wang, T. Tan, H. Jiang, T. S. Cox, R. L. Howard, B. B. Bevard, and M. E. Flanagan, “Development of U-frame Bending System for Studying the Vibration Integrity of Spent Nuclear Fuel,” *Journal of Nuclear Materials*, **440**, 201–213 (2013).
- ⁴ J.-A. J. Wang, H. Wang, T. Cox, and C. Baldwin, *Progress Letter Report on Bending Fatigue Test System Development for Spent Nuclear Fuel Vibration Integrity Study (Out-of-Cell Fatigue Testing Development–Task 2.4)*, ORNL/TM-2013/225, Oak Ridge National Laboratory, Oak Ridge, Tenn., July 2013.
- ⁵ J.-A. J. Wang, H. Wang, B. B. Bevard, R. L. Howard, and M. E. Flanagan, *Reversible Bending Fatigue Test System for Investigating Vibration Integrity of Spent Nuclear Fuel During Transportation*, PATRAM 2013, DOE/NRC/DOT, San Francisco, Calif., August 18–23, 2013.
- ⁶ J.-A. J. Wang and H. Wang, *The Development of Reversible Bending Fatigue Tester and Its Application to High Burn-up Spent Nuclear Fuel Integrity Study under Normal Transportation Vibration*, ORNL/TM-2013/573, August 2014. <http://info.ornl.gov/sites/publications/Files/Pub47469.pdf>
- ⁷ J.-A. Wang and H. Wang, *2014 Semi-Annual Progress Letter Report on Used Nuclear Fuel Integrity Study in Transportation Environments*, prepared for US Department of Energy, ORNL/TM-2014/63, April 2014. <http://info.ornl.gov/sites/publications/Files/Pub48652.pdf>
- ⁸ J.-A. J. Wang, H. Wang and H. Jiang, *FY14 Status Report: CIRFT Testing Results on High Burnup UNF*, ORNL/LTR-2014/310, September 2014. <http://info.ornl.gov/sites/publications/Files/Pub51054.pdf>
- ⁹ J.-A. Wang and H. Wang, *Mechanical Fatigue Testing of High-Burnup Fuel for Transportation Applications*, NUREG/CR-7198, ORNL/TM-2014/214, May 2015.
- ¹⁰ J. E. Schmidlin, *Limerick fuel segmenting plan*, Oak Ridge National Laboratory, Nov. 3, 2014.
- ¹¹ C. A. Baldwin, Oak Ridge National Laboratory, Oak Ridge, Tenn., June 2013.
- ¹² J. E. Schmidlin, Information about NA Fuel Segment Measurements, Oak Ridge National Laboratory, Oak Ridge, Tenn., July 2, 2014.
- ¹³ C. A. Baldwin, *Fracture Surface Images of Selected CIRFT Tested Samples*, Oak Ridge National Laboratory, Feb. 27, 2015.
- ¹⁴ E. J. Ruzauskas and K. N. Fardell, *Design, Operation, and Performance Data for High Burnup PWR Fuel from the H.B. Robinson Plant for Use in the NRC Experimental Program at Argonne National Laboratory*, Electric Power Research Institute, Report 1001558. Palo Alto, CA, 2001.
- ¹⁵ K. J. Geelhood, C. E. Beyer, and W. G. Luscher, *PNNL Stress/Strain Correlation for Zircaloy*, PNNL-17700, Pacific Northwest National Laboratory, Richland, Wash., July 2008.
- ¹⁶ M. C. Billone, As-Built Parameters for Commercial Reactor Fuel in AGHCF, Argonne National Laboratory, Aug. 18, 2008.

- ¹⁷ P. McConnell, R. Wauneka, S. Saltzstein, K. Sorenson, “Normal Conditions of Transport Truck Test of a Surrogate Fuel Assembly,” DOE report, FCRD-UFD-2014-000066, Revision 0, August 29, 2014.
- ¹⁸ J.-A.J. Wang, H. Jiang, and H. Wang, *Using Surrogate Rods to Investigate the Impact of Interface Bonding Efficiency on Spent Nuclear Fuel Vibration Integrity*, ORNL/LTR-2014/257, Oak Ridge National Laboratory, Oak Ridge, Tennessee, 2014.
- ¹⁹ H. Jiang, J. J. A. Wang, and H. Wang, “Potential Impact of Interfacial Bonding Efficiency on Used Nuclear Fuel Vibration Integrity during Normal Transportation,” *Proceedings of the ASME 2014 Pressure Vessels and Piping Conference*, PVP2014-29117, Anaheim, California, July 2014.
- ²⁰ J.-A.J. Wang, H. Wang, Y. Yan, R. Howard, and B. Bevard, *High Burn-up Spent Fuel Vibration Integrity Study Progress Letter Report (Out-of-Cell Fatigue Testing Development—Task 2.1)*, ORNL/TM-2010/288, Oak Ridge National Laboratory, Oak Ridge, Tennessee, 2011.
- ²¹ J.-A.J. Wang, H. Wang, T. Tan, H. Jiang, T. Cox, and Y. Yan, *Progress Letter Report on U-frame Test Setup and Bending Fatigue Test for Vibration Integrity Study (Out-of-Cell Fatigue Testing Development—Task 2.2)*, ORNL/TM-2011/531, Oak Ridge National Laboratory, Oak Ridge, Tennessee, 2012.
- ²² J.-A.J. Wang, H. Jiang, *FY 2014 Status Report: Quantification of CIRFT System Biases and Uncertainties When Testing High-Burnup Spent Nuclear Fuel*, ORNL/LTR-2014/288, Oak Ridge National Laboratory, Oak Ridge, Tennessee, 2014.
- ²³ Y. Yan, T. A. Burtseva, and M. C. Billone, “Post-quench Ductility Results for North Anna Highburnup 17×17 ZIRLO Cladding with Intermediate Hydrogen Content,” ANL letter report to NRC, April. 17, 2009; available online as ML091200702 at <http://www.nrc.gov/reading-rm/adams.html>.
- ²⁴ M. C. Billone, Y. Yan, T. Burtseva, R. Daum, “Cladding Embrittlement during Postulated Loss-of-Coolant Accidents,” NUREG/CR-6967 ANL-07/04 (2008).
- ²⁵ M. C. Billone, T. Burtseva, and Y. Yan. “Overview of Spent Nuclear Fuel Program: Test Plan and High Burnup Cladding at ANL,” *NRC Program Review Meeting*, Argonne National Laboratory, Argonne, IL, July 7, 2010.
- ²⁶ R. Daum, H. Tsai, Y. Liu, and M. Billone, “High-Burnup Cladding Mechanical Performance during Cask Storage and Post-Storage Handling and Transportation,” *Nuclear Safety Research Conference*, Washington, D.C., October 25-27, 2004.
- ²⁷ Y. Yan, A. S. Blackwell, L. K. Plummer, B. Radhakrishnan, S. B. Gorti, and K. T. Clarno, “Observation and Mechanism of Hydride in Zircaloy-4 and Local Radial Hydride Induced by High Pressure at High Temperatures,” *2013 International High-Level Radioactive Waste Management*, Albuquerque, NM, April 28 – May 2, 2013.
- ²⁸ Y. Yan, L. K. Plummer, H. Ray, T. Cool, and H. Z. Bilheux, “Ductility Evaluation of As-Hydrated and Hydride Reoriented Zircaloy-4 Cladding under Simulated Dry-Storage Condition”, *2013 MRS Fall Meeting Proceeding*, Boston, MA, December 1-6, 2013.

²⁹ M. C. Billone, T. A. Burtseva, and Y. Yan, "Ductile-to-Brittle Transition Temperature for High-Burnup Zircaloy-4 and ZIRLO™ Cladding Alloys Exposed to Simulated Drying-Storage Conditions", ANL-13/13, ANL letter report to NRC, September 28, 2013, available online as ML12181A238.

³⁰ E.J. Ruzauska and K. N. Fardell, "Design, Operation, and Performance Data for High Burnup PWR Fuel from the H.B. Robinson Plant for Use in the NRC Experimental Program at Argonne National Laboratory," EPRI report 1001558, May 2001.

³¹ M. Griffiths, J. F. Mecke, and J. E. Winegar, "Evolution of Microstructure in Zirconium Alloys During Irradiation," *Zirconium in the Nuclear Industry: Eleventh International Symposium*, ASTM STP 1295, pp. 580-602 (1996).

³² J. J. Kearns, "Terminal Solubility and Partitioning of Hydrogen in the Alpha Phase of Zirconium, Zircaloy-2 and Zircaloy-4," *J. Nucl. Mater.* **22**, 292 (1967).

³³ A. McMinn, E. C. Darby, and J. S. Schofield, "The Terminal Solid Solubility of Hydrogen in Zirconium Alloys," *Zirconium in the Nuclear Industry: Twelfth International Symposium*, ASTM STP 1354, p. 173-195 (2000).

³⁴ D. O. Northwood and U. Kosasih, "Hydrides and Delayed Hydrogen Cracking in Zirconium and its Alloys," *International Metals Review*, **28(2)**, 92 (1983).

³⁵ S. Mishra, K. S. Sivaramakrishnan, and M. K. Asundi, "Formation of the Gamma Phase by a Peritectoid Reaction in the Zirconium-Hydrogen System," *J. Nucl. Mater.* **45**, 235 (1972).

APPENDIX A. CIRFT TEST RESULTS ON HIGH BURN-UP HBR SNF

This page intentionally left blank.

CONTENTS

APPENDIX A. CIRFT TEST RESULTS ON HIGH BURN-UP HBR SNF	A-1
LIST OF FIGURES	A-5
LIST OF TABLES	A-7
1. INTRODUCTION	A-9
2. EXPERIMENTAL METHOD	A-10
2.1 The U-Frame Setup	A-10
2.2 Grip Design	A-13
2.3 LVDT Measurements and Curvature Calculation	A-16
2.4 Test Segments	A-19
2.5 Test Protocol	A-21
2.5.1 Static Testing	A-21
2.5.2 Dynamic Testing	A-21
2.6 Data Processing	A-22
2.6.1 HBU SNF Characteristics	A-23
3. STATIC TESTING	A-27
3.1 Results	A-27
3.2 Discussion	A-33
3.2.1 Characteristics of Moment-Curvature Curve	A-33
3.2.2 Comparison of Static Results with PNNL Cladding Data	A-36
3.2.3 Effect of LVDT Probe Contact on Large Curvature Measurement	A-38
4. DYNAMIC TESTING	A-40
4.1 Results	A-40
4.2 Discussion	A-54
4.2.1 κ -N Curve	A-54
4.2.2 Post-Irradiation Examination (PIE)	A-58
5. CONCLUSIONS	A-62
6. REFERENCES	A-63

This page intentionally left blank.

LIST OF FIGURES

Figure	Page
Figure 1. (a) Horizontal layout of ORNL U-frame setup; (b) rod specimen under test and three LVDTs for curvature measurement (operator is facing the three LVDTs); and (c) front view of CIRFT installed in ORNL hot cell.	A-12
Figure 2. Schematic drawings of U-frame setup for reversal bending when rigid arms are (a) closing, (b) neutral, and (c) opening.	A-12
Figure 3. Assembled grip (left) and two views (right) of detached grip body.	A-13
Figure 4. Image showing the grip design of CIRFT with one end-block removed.	A-14
Figure 5. (a) Vise mold for assembling octagonal rigid sleeves into a rod; (b) rod (Demo1, 606B2) to be inserted; (c) one pin was turned away and a rigid sleeve loaded with epoxy inserted into the lower chamber.	A-15
Figure 6. Determination of the bending curvature of the rod by use of deflections measured at three points.	A-16
Figure 7. (a) Diagrams showing the effect of the LVDT probe with disk shape on curvature measurement, where the contact points are shifted.	A-18
Figure 8. Segment 608C4B for DL2 taken from rod G10, with the storage tube.	A-19
Figure 9. Flowchart for cyclic testing of spent fuel rod.	A-22
Figure 10. Moment, curvature time series, and moment-curvature hysteresis loop for rod D1.	A-23
Figure 11. “Empty-run” conducted on HBR S1, for which the load and displacement were plotted.	A-26
Figure 12. (a) Curve of moment versus curvature, and (b) equivalent strain–stress curve for S1 (606C3C).	A-28
Figure 13. Mating fracture surfaces (a) and (b); lateral sides near the neutral axis of the bending rod for S1 (606C3C) (c) and (d).	A-29
Figure 14. Moment-curvature curves measurements in static tests (Corresponding stress and strain displayed on right and top axes, respectively).	A-30
Figure 15. Characteristic points of moment-curvature curve.	A-34
Figure 16. Comparison of CIRFT global data with PNNL moment-curvature curve converted from PNNL cladding stress-strain data.	A-37
Figure 17. Moment-curvature curves based on stainless steel alumina pellet (SSAP) rod testing when rod is bending with respect to three LVDTs (a) concavely and (b) convexly.	A-39
Figure 18. Moment-curvature curves as a function of sensor spacing adjustment when rod is bending with respect to three LVDTs (a) concavely and (b) convexly.	A-39
Figure 19. Moment and curvature as a function of time and moment-curvature loops based on measurements when (a) $N = 1$ and (b) $N = 111,000$ cycles for D1 (607C4B).	A-41
Figure 20. (a) Moment-curvature relation and (b) moment-flexural rigidity relation at various numbers of cycles for D1 (607C4B); $N_f = 1.1 \times 10^5$ cycles under ± 15.24 N·m, 5 Hz. Fuel particles collected < 1.0 g.	A-42
Figure 21. Variations of (a) curvature range, (b) moment range, (c) flexural rigidity as a function of number of cycles for D1 (607C4B); $N_f = 1.1 \times 10^5$ cycles under ± 15.24 N·m, 5 Hz. Fuel particles collected < 1.0 g.	A-42
Figure 22. Variations of (a) curvature range, (b) applied moment range, (c) flexural rigidity, (d) maximum and minimum values of curvature, (e) maximum and minimum values of moment, and (f) flexural hysteresis as a function of number of cycles for D1 (607C4B); $N_f = 1.1 \times 10^5$ cycles under ± 15.24 N·m, 5 Hz. Fuel particles collected < 1.0 g.	A-43
Figure 23. Moment and curvature as a function of time and moment-curvature loops at (a) 26 and (b) 1.10×10^5 cycles; results are based on online monitoring.	A-45

Figure 24. (a) and (b) Mating fracture surfaces, (c) frontal, and (d) back sides for D1 (607C4B), $N_f = 1.1 \times 10^5$ cycles under $\pm 15.24 \text{ N}\cdot\text{m}$, 5 Hz. Fuel particles collected $< 1.0 \text{ g}$ A-46

Figure 25. Equivalent strain amplitudes ($\Delta\varepsilon/2$) as a function of number of cycles. A-47

Figure 26. Equivalent strain amplitudes ($\Delta\varepsilon/2$) as a function of number of cycles with curve fitting extended to include the data points without failure..... A-53

Figure 27. (a) Maxima of absolute curvature extremes and curvature amplitudes as a function of number of cycles, (b) Maxima of absolute strain extremes and strain amplitudes as a function of number of cycles. A-55

Figure 28. (a) Curvature amplitudes, (b) maxima of absolute curvature extremes, and (c) maxima of absolute strain extreme as a function of number of cycles with curve-fitting extended to include the no-failure data points. A-58

Figure 29. Optical images of untested segment 605D for (a) overall axial cross section and (b) enlarged area A. A-59

Figure 30. (a) Axial cross section of S2/ 605D1E, (b) fracture surface near back side of rod and an enlarged area, and (c) fracture surface near front side of rod and an enlarged area. A–delamination, B–cracking of oxide layer. A-60

LIST OF TABLES

Table	Page
Table 1. Physical and mechanical properties of related materials.....	A-14
Table 2. Specifications of specimens used in hot-cell testing.....	A-20
Table 3. Summary of static tests	A-31
Table 4. Characteristic points and quantities based on curvature-moment curves.....	A-35
Table 5. Characteristic points and quantities based on equivalent stress-strain curves.....	A-35
Table 6. Comparison of flexural rigidity results between CIRFT testing and PNNL data.....	A-37
Table 7. Summary of dynamic test results.....	A-48
Table 8. Failure modes of rods from dynamic tests	A-49

This page intentionally left blank.

1. INTRODUCTION

This report describes testing designed to determine the ability of high burnup (HBU) (>45 GWd/MTU) spent fuel to maintain its integrity under normal conditions of transportation. An innovative system, Cyclic Integrated Reversible-bending Fatigue Tester (CIRFT), has been developed at Oak Ridge National Laboratory (ORNL) to test and evaluate the mechanical behavior of spent nuclear fuel (SNF) under conditions relevant to storage and transportation. The CIRFT system is composed of a U-frame equipped with load cells for imposing the pure bending loads on the SNF rod test specimen and measuring the in-situ curvature of the fuel rod during bending using a setup with three linear variable differential transformers (LVDTs).

The HBU H.B. Robinson (HBR) nuclear plant SNF rods with Zircaloy-4 (Zry-4) cladding and intact fuel were studied under both static and dynamic (cyclic) bending. The HBR HBU rods survived static unidirectional bending to a maximum curvature of 3.1 to 3.5 m^{-1} , or a maximum moment of 86 to 87 N·m. The maximum longitudinal cladding offset strain before failure or before reaching CIRFT displacement capacity was 1.7 to 1.9%, and the maximum bending stress was 733 to 748 MPa. The 0.2% offset yield stress of the HBU irradiated clad was estimated to be 687 to 727 MPa based on the equivalent stress-strain curves.

In general, the static CIRFT test results indicate a significant increase in flexural rigidity compared to that of the defueled HBU rod specimen. Nevertheless, the segment composite structure of an HBU rod also introduces numerous stress concentration sites into an HBU rod system, ultimately resulting in HBU specimen fractured at the pellet-pellet interface regions under dynamic CIRFT fatigue testing.

The majority of the HBR dynamic test samples failed at or near a pellet-pellet interface. The fatigue life of HBU HBR rods during dynamic testing mainly depended on the level of loading and fuel pellet-clad interaction and the conditions of the rod. Under loading with moments of ± 8.89 to ± 35.56 N·m, resulting in an equivalent strain ϵ of ± 0.07 to $\pm 0.49\%$ strain at 5 Hz, the fatigue life N ranged from 5.5×10^3 to 2.3×10^6 cycles. Considering the complexity and non-uniformity of the HBU HBR fuel cladding system, it was significant to find that the ϵ - N data for the HBU HBR were characterized by a curve that would be expected of standard uniform materials. The ϵ - N curve of the HBU HBR rods can be described by a power function of $y = 3.5693 x^{-0.252}$, where x is the number of cycles to failure, and y is the strain amplitude (%). It was also significant to find that, if an endurance limit is defined by survival of $>10^7$ cycles, then the HBU HBR exhibited an endurance limit. The endurance limit for HBR HBU is likely located at approximately 0.1% strain.

The maxima of the imposed curvature κ during dynamic testing ranged from ± 0.16 to ± 1.19 m^{-1} at 5 Hz. The κ - N curve of the HBU HBR rods can be described by a power function of $y = 8.1941 x^{-0.252}$, where x is the number of cycles to failure, and y is the maxima of clad tensile curvature $|\kappa|_{\text{max}}$ (m^{-1}). An endurance limit is likely located at approximately 0.2 m^{-1} when it is defined at 10^7 cycles.

2. EXPERIMENTAL METHOD

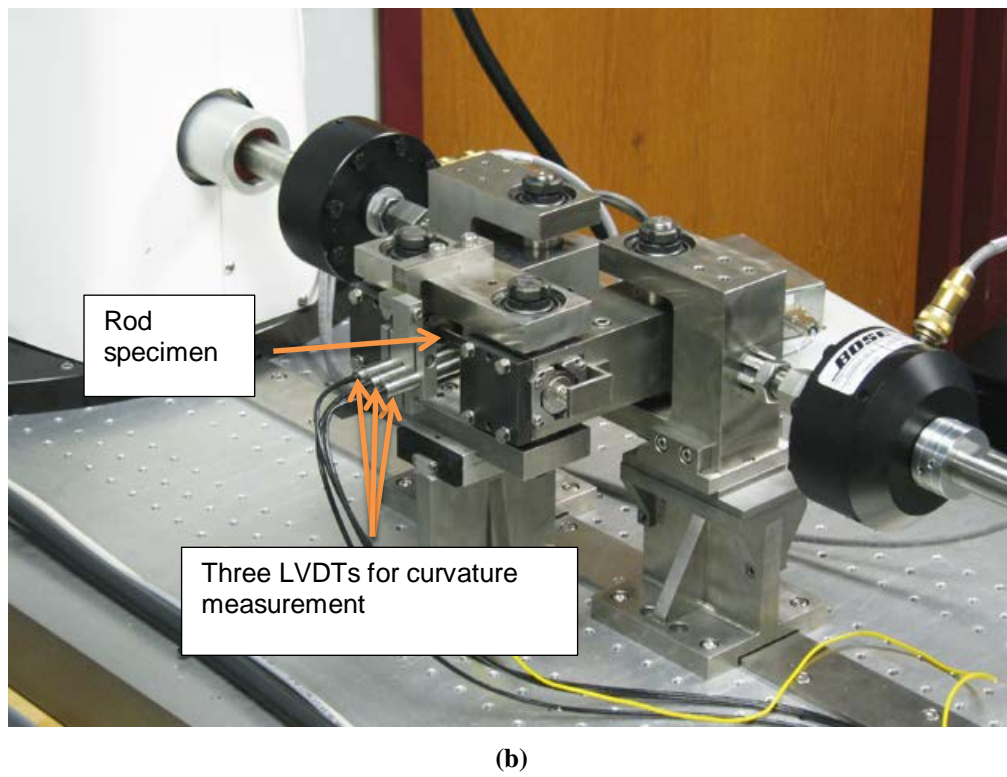
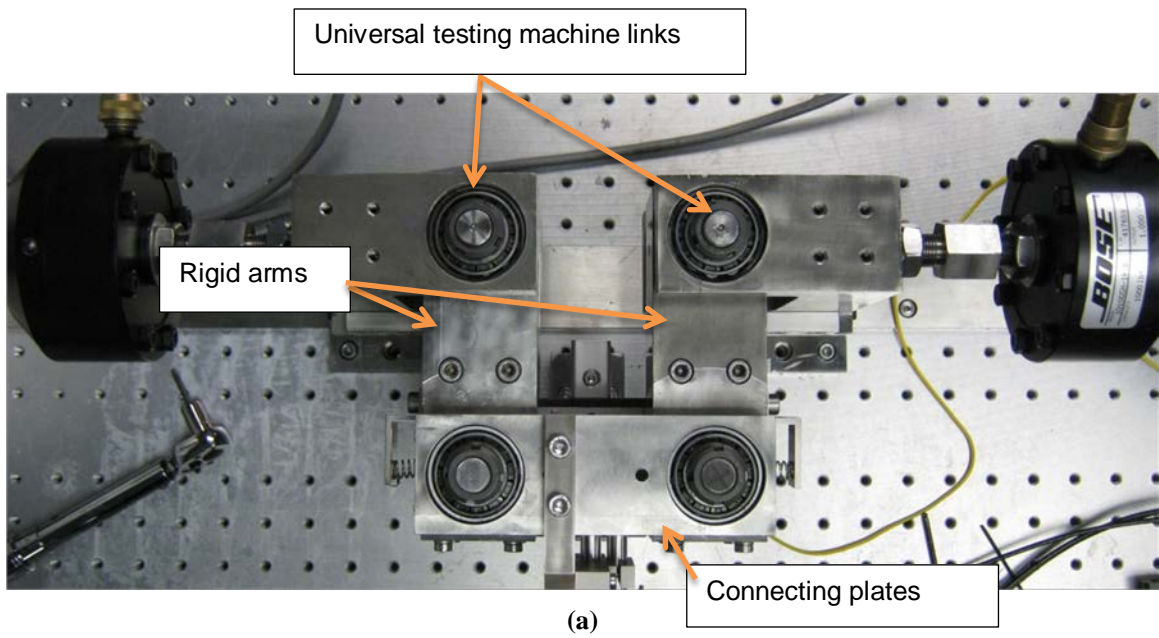
The objective of this testing program is to develop testing protocols to evaluate the bending deformation responses and the associated fatigue mechanical properties for HBU fuel rods relevant to transportation conditions. Thus, the HBU fuel rods would be tested in a condition and geometry as close as possible to normal conditions of transport (NCT). Currently, most of the mechanical testing devices require a specified specimen design, such as a pre-notch or reduced gage section, to prevent failure at the grip location and ensure meaningful data. For this testing program, it was recommended that the test segment not be altered by machining a gage section. Therefore, an innovative U-frame and grip design were developed. Key features of the U-frame and grip design will be discussed in the sections that follow. Cost considerations also had a significant influence on the development of the testing program. Hot-cell space and time are extremely limited and costly, as is testing material. For this testing program, we wanted to use a small test segment, design a compact test device, and develop a test protocol for efficient testing. Important features of the test segments and test protocol will be discussed later in this report. Finally, the curvature response of the test segment needed to be measured with as little interpretation as possible. It was not practical to weld strain gauges onto the segments or use lasers to measure deflection on HBU material in a hot cell. Therefore, three adjacent linear variable differential transformers (LVDTs) were used to measure lateral deflections of the test specimen so that the curvature of the specimen could be calculated without interpretation or assumptions regarding the deformation of various components of the testing system. The important aspects of the three LVDTs and the calculation of specimen curvature are discussed in Section 2.3.

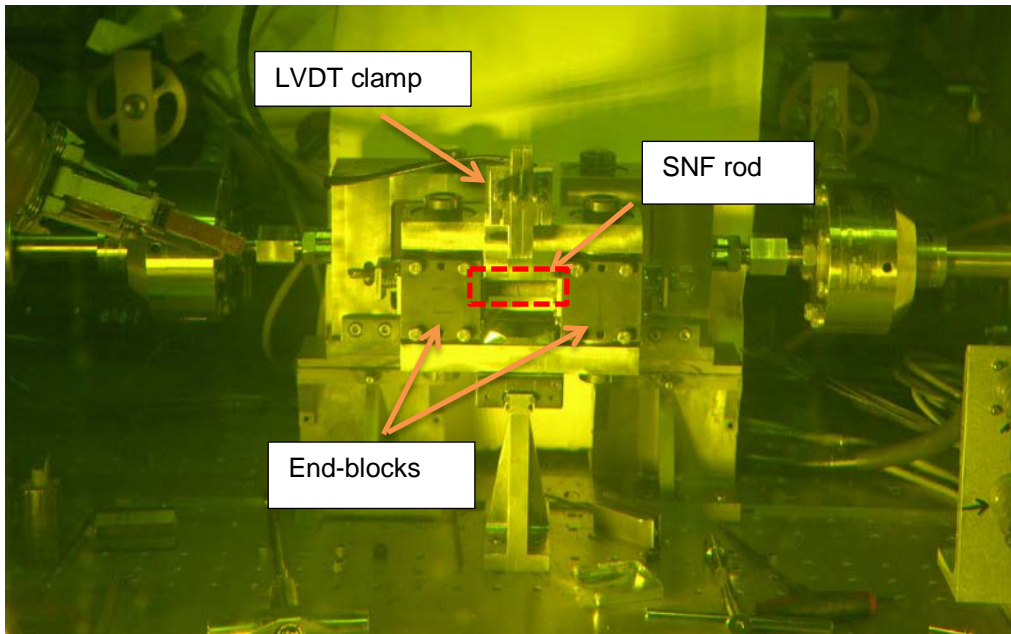
2.1 The U-Frame Setup

Testing of the SNF rod specimen was accomplished using a cyclic integrated reversible-bending fatigue tester (CIRFT) recently developed by ORNL.^{1,2,3,4,5,6,7,8,9} The integrated U-frame is shown in Figure 1.

The U-frame includes two rigid arms, connecting plates, and universal testing machine links. The rod specimen is coupled to the rigid arms through two specially designed grips. The U-frame setup is oriented in a horizontal plane and is driven by electromagnetic-force-based Bose dual linear motors. With help from the coupling, linear motions applied at the loading points of the rigid arms are converted into bending moments exerted on the rod. The dual linear motor (model LM2) test bench has a maximum load capacity of $\pm 3,000$ N and a maximum stroke of ± 25.6 mm.

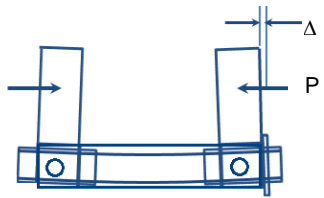
Bending is imposed through a U-frame with dual driving points and a 101.60 mm loading arm. Under a pair of forces or displacements that face outward, the rigid arms are opened, and bending moments force the rod to deflect outward (namely, away from operator, as shown in Figure 2). Under a pair of forces facing each other, the rigid arms are closed, forcing the rod to deflect inward. With the special grips that will be described in Section 2.2, a pure reversible bending condition can be obtained. The CIRFT can deliver dynamic loading to a rod specimen in the load-control mode at 5 to 10 Hz. The current configuration enables the system to test a rod 9.70 to 11.74 mm in diameter, 152.40 mm (6 in.) in length, and 50.80 mm (2 in.) in gage section. Three LVDTs measure rod deflections at three adjacent points within the gage section to determine rod curvature, which is then correlated to the applied moment to characterize the mechanical properties of the bending rod. Online monitoring can capture mechanical property changes to reveal fatigue behavior during testing.



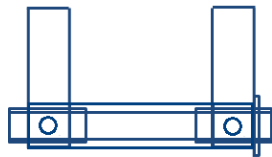


(c)

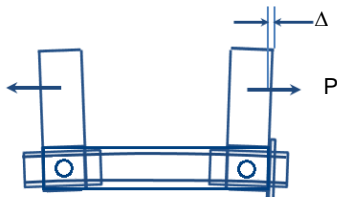
Figure 1. (a) Horizontal layout of ORNL U-frame setup; (b) rod specimen under test and three LVDTs for curvature measurement (operator is facing the three LVDTs); and (c) front view of CIRFT installed in ORNL hot cell.



(a) Rigid arms are closing. The curvature is concave outward and designated with a negative sign.



(b) Rigid arms are in neutral position.



(c) Rigid arms are opening. The curvature concave inward and designated with a positive sign.

Figure 2. Schematic drawings of U-frame setup for reversal bending when rigid arms are (a) closing, (b) neutral, and (c) opening.

2.2 Grip Design

Each grip consists of a V-shaped block integrated into the rigid arm of the U-frame, and a V-shaped end-block (Figure 3). The surfaces of the blocks serve as contacts to the specimen assembly and have been equipped with linear roller bearing sets embedded to ensure the free axial movement of the specimen when the force is being transferred. The rod specimen is secured by opening and closing the end-blocks in two grips.^{2,3,4,5} A partly exposed view on one end of the specimen is shown in Figure 4 with the end-block removed. The specimen has a pair of rigid sleeves on both holding areas. The sleeves protect the specimen from any contact damage through a compliant layer between the specimen and sleeves. The rigid sleeves also enable the specimen to move freely in the axial direction while being set against the embedded linear roller bearing sets. The free axial movement of the specimen is a critical requirement in pure bending, as discussed elsewhere in the literature.¹

**Uniquely designed
Grip-end for free-fixed
boundary condition
and hot-cell
application**



Figure 3. Assembled grip (left) and two views (right) of detached grip body.

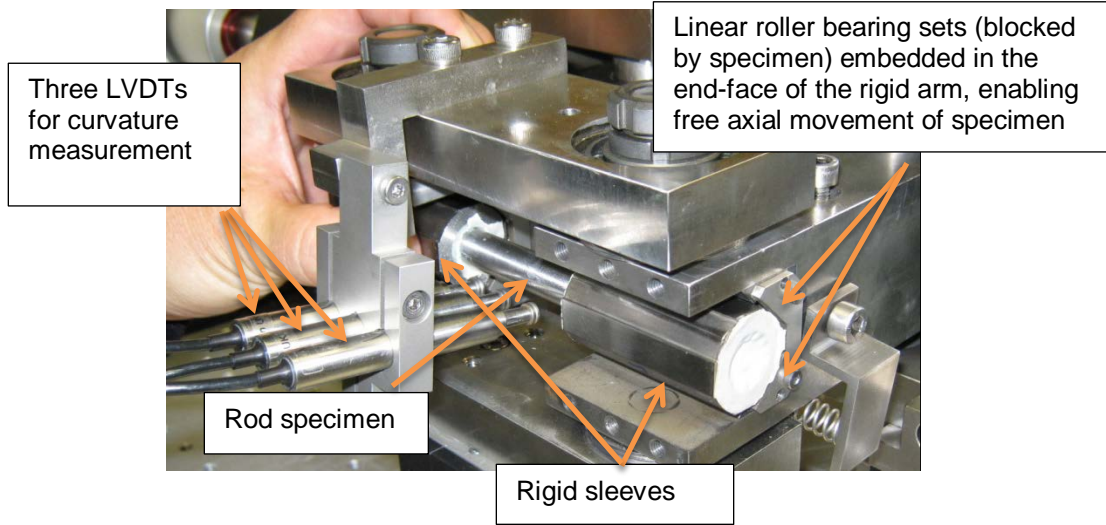


Figure 4. Image showing the grip design of CIRFT with one end-block removed.

The mounting of rigid sleeves onto the rod is achieved using casting epoxy. The cast epoxy, therefore, serves as the compliant layer whose size depends on the dimensions of the rigid sleeve and rod. The current rigid sleeves have an inside diameter (ID) of 15 mm, an outside diameter (OD) of 25 mm, and a length of 50 mm. For fuel rods with an OD of 10.70 mm, taken from the H. B. Robinson Nuclear Plant reactor in South Carolina, the cast epoxy layer would have a thickness of 2.15 mm and the same length of rigid sleeves. Related physical and mechanical properties of the cast epoxy are listed in Table 1, along with those of the stainless steel in the U-frame setup. The use of cast epoxy as a compliant layer has been demonstrated to be effective in meeting requirements for both specimen protection and pure bending boundary conditions.^{2,5}

Table 1. Physical and mechanical properties of related materials

Materials	Density (kg/m ³)	Young's modulus (GPa)	Poisson's ratio	0.2% yield strength (MPa)
Stainless steel	8,030	193	0.30	290
Epoxy	1,200	3.5	0.25	45

Casting of the epoxy has been proven feasible in the hot cell environment. A vise mold has been designed and built for that purpose, and the procedures to cast the epoxy and mount the rigid sleeves into the rod specimen have been developed.^{2,3} Several important modifications were made to adapt the vise mold to hot cell testing.⁷ The images in Figure 5 (a) show different views of the vise mold, and those in Figures 5(b) and 5(c) illustrate the process of epoxy casting in the hot cell. The robust mold design enables two important functionalities for casting the CIRFT specimen in a hot cell environment: (1) the rod ends up in the center every time, and (2) the compliant layer is applied the same way each time so as not to introduce a variable.

The amount of fresh epoxy for each rigid sleeve is determined as needed in the hot cell based on the results from an out-of-cell study. In the case of the HBR rods, 5 g of epoxy can fill the gap properly. The rod released from the vise mold is generally examined visually, and the gap will be refilled if a substantial cavity is observed between the rod and the rigid sleeves.

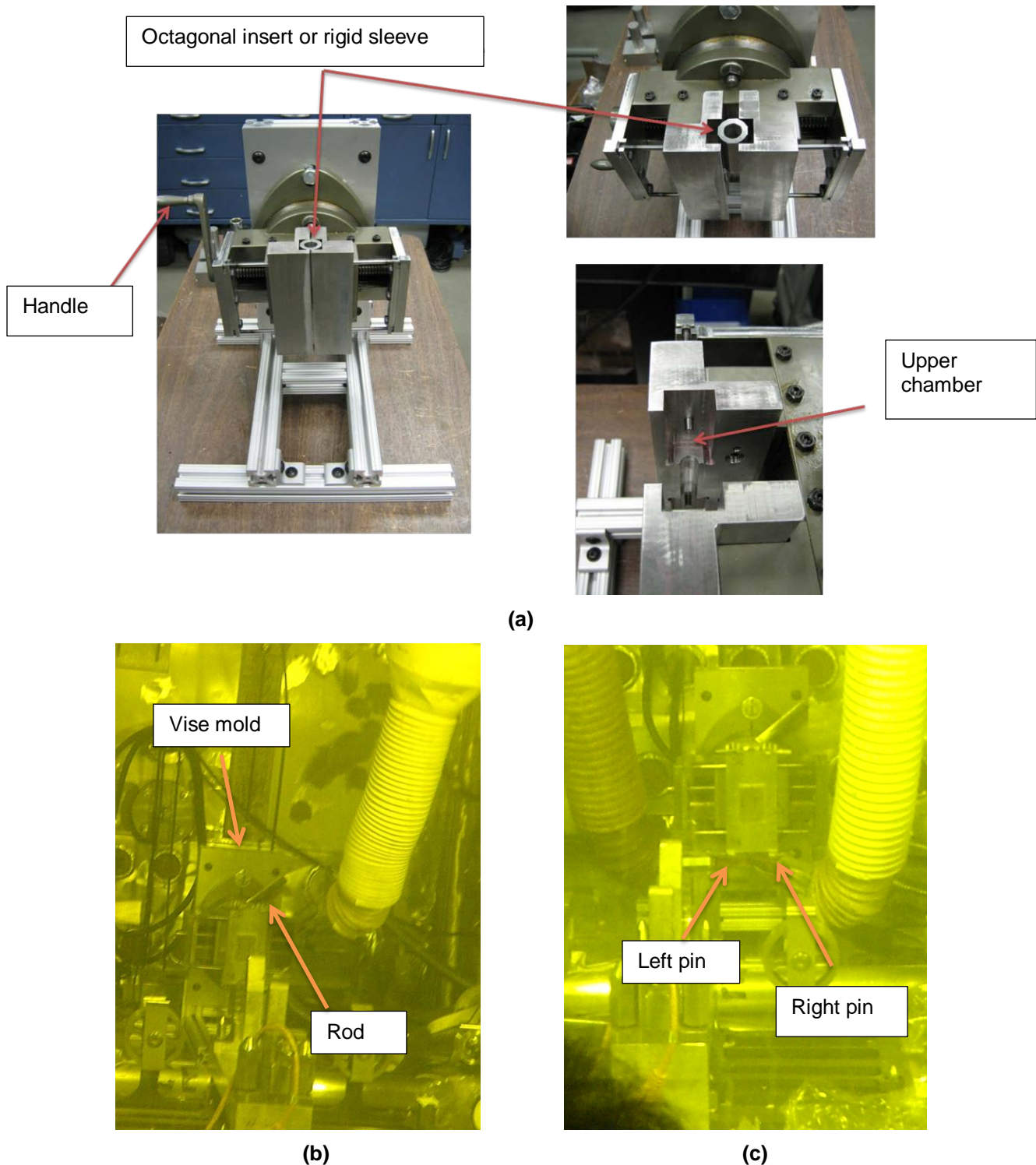


Figure 5. (a) Vise mold for assembling octagonal rigid sleeves into a rod; (b) rod (Demo1, 606B2) to be inserted; (c) one pin was turned away and a rigid sleeve loaded with epoxy inserted into the lower chamber.

2.3 LVDT Measurements and Curvature Calculation

Theoretically, the bending radius and maximum strain of a rod can be estimated on the basis of the traveling displacement at the loading points of the rigid arm. The displacement measured, however, contains the contribution of the compliant layers, depending on the materials used in the compliant layers and the level of loading.

To address this issue, direct measurement of the specimen displacement at three adjacent points along the rod method was proposed¹⁰ and has been implemented to evaluate the curvature of a bending rod in this study.^{2,5}

Given the deflections from three LVDTs, d_1 , d_2 , and d_3 , as shown in Figure 6, the curvature κ of the bending rod can be evaluated as follows:

$$\kappa = [(x_0 - d_2)^2 + y_0^2]^{-1/2}$$

$$x_0 = \frac{-2m_a m_b h - m_a (d_2 + d_3) + m_b (d_1 + d_2)}{2(m_b - m_a)}$$

$$y_0 = -\frac{1}{m_a} \left(x_0 - \frac{d_1 + d_2}{2} \right) - \frac{h}{2}$$
(1)

where

$$m_a = \frac{h}{d_2 - d_1}$$

$$m_b = \frac{h}{d_3 - d_2}$$

and h is the sensor distance, 12 mm.

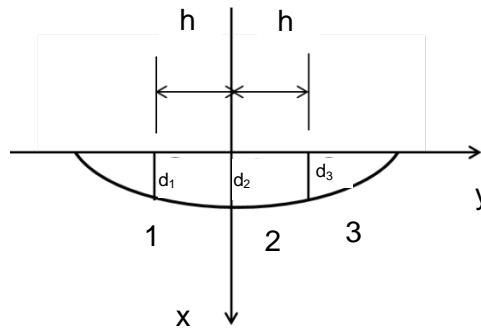


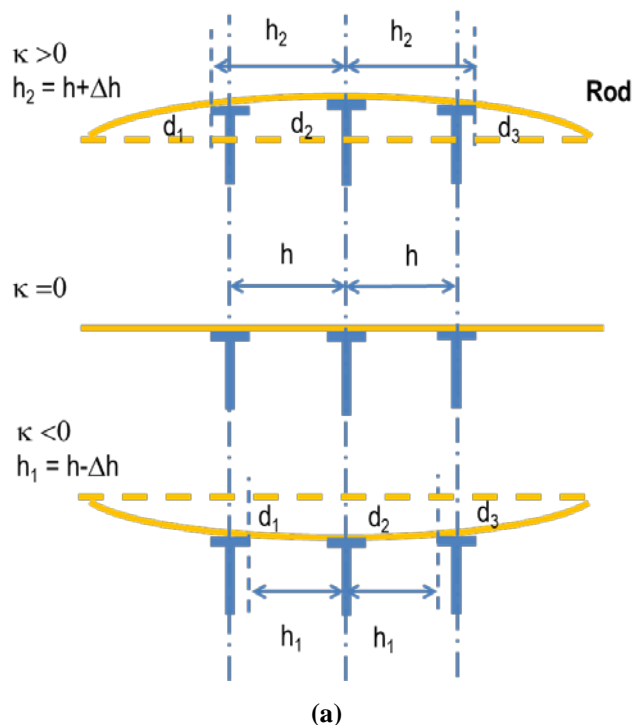
Figure 6. Determination of the bending curvature of the rod by use of deflections measured at three points.

The arrangement of the three LVDTs and their installation in the setup can be seen in Figure 1 and Figure 4. A series of static tests was performed to confirm the measurement method by using a surrogate rod composed of various materials. The curvature obtained by the LVDT measurements has been shown to

correlate well with the calculated flexural rigidity of the specimen based on the estimated moment of inertia and Young’s modulus for various materials.⁵

The effect of contact between the LVDT probe and the rod on the curvature measurement became a concern, especially when loading during the hot-cell testing approached very small levels. The current LVDTs use flat, disk-shaped probes. The sensor spacing h in the curvature calculation would be affected by the contact position of the probes. As shown in the upper view of Figure 7(a), the contacts will be shifted outward and the h increases correspondingly when the rod is concave toward the sensors; in the lower view, the h decreases when the rod is concave away from the sensors.

In an out-of-cell study, the effect of the probe on the curvature measurement in dynamic testing has been investigated by using LVDT probes with a chisel contact.¹¹ The results showed that the effect of probe geometry on the curvature measurement is negligible in dynamic testing within a low load range. Thus, the initial data reduction for the hot-cell testing did not envision the correction needed to account for the effect of the probe’s width. However, CIRFT testing in the hot cell reveals the nonsymmetry curvature measurements for the clad tension and clad compressive loading cycles. This is partly because the SNF rod has a very limited pellet-pellet interface bond as compared to that of epoxied surrogate rod with well-bonded pellet-pellet interface structure. The potential sensor probe contact also has some effect. Thus, the SNF pellet-pellet debond interface–induced stress concentration effect cannot be readily observed or revealed from a surrogated rod tested under low loading amplitude. In order to further clarify the potential sensitivity of curvature measurement with regard to LVDT probe contact, a control experiment with a uniform polycarbonate surrogate rod was conducted, and the test results are illustrated in Figures 7(b) and (c). The test results of LVDTs located at the clad compression site show that the measurement with the disk probe overestimates the curvature by 50% compared to measurements with the chisel head probe. An adjustment factor of $\Delta h = 2.9$ mm was applied to develop consistent results. For LVDTs located at the clad tensile site, the disk probe underestimates curvature by 40%, and a correction factor of $\Delta h = 2.4$ mm is needed.



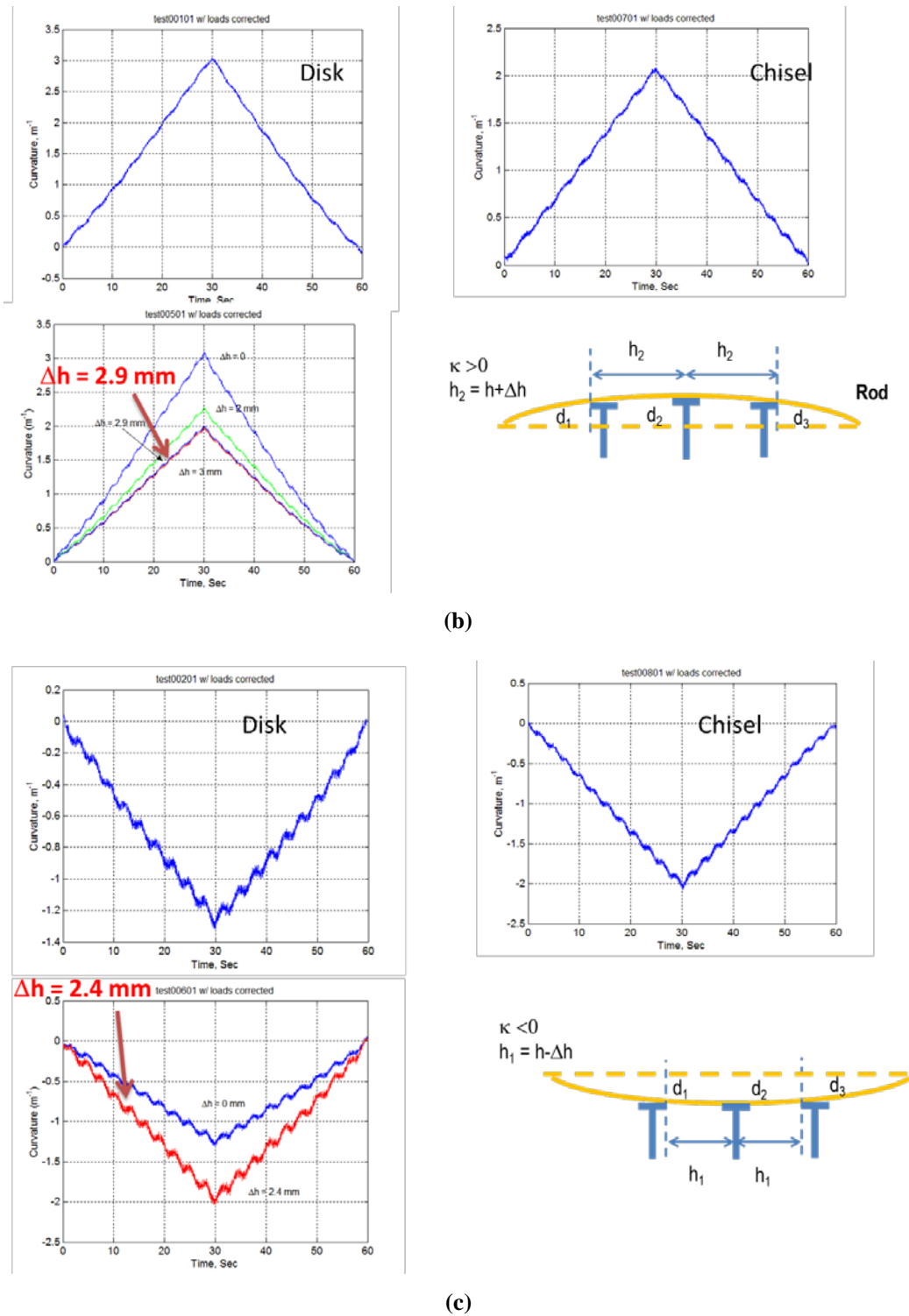


Figure 7. (a) Diagrams showing the effect of the LVDT probe with disk shape on curvature measurement, where the contact points are shifted. Comparisons of curvature measurement between disk and chisel head probe for LVDTs located at clad compression and tension site are shown in (b) and (c), respectively. (c).

The adjustment factors presented above are only applied to a uniform rod system. Further investigation of using the surrogate rod with the debond pellet-pellet interfaces of a nonuniform rod system is needed to take into account the stress concentration effect and the increased curvature resulting from segment pellet structure. This research will help to finalize adjustment factor development.

2.4 Test Segments

The Zry-4 15 × 15 cladding (1.41 wt % Sn, 0.22 Fe, 0.12 Cr, and 0.14 O) tested in this study was irradiated for seven cycles in the HBR Unit 2 pressurized water reactor. The rod-average fuel burnup was 67 GWd/MTU. The test segments were taken from rods at locations E04, E14, F07, G10 and R05 in assembly S-15H. The irradiation history of these rods and details can be found elsewhere.¹

Although the goal of this project was to test static and cyclic bending performance, some rod segments were used for instrumentation demonstration, machine tuning, and benchmarking. The specimen cutting plan and the specimen locations in the father rods can be found in Appendix A.

A summary of specimen information for hot cell testing is provided in Table 2.

According to the plan, 6 in. segments were cut. Figure 8 shows one segment (608C4B) taken from the father rod G10, along with the tube used for specimen storage. The rod diameter of the fuel segments was measured using a dedicated setup in the hot cell.¹² The measurement details are provided in Appendix B. Readings were taken at each half inch from one end of the rod and 3° (0, 120, and 240°) at each reading distance. The mean value and standard deviation of the diameter readings were found to be 10.772 mm (0.4241 in.) and 0.008 mm (0.0003 in.), respectively. It can be seen that the calculated mean value is close to the nominal diameter of the fuel cladding at HBR.¹



Figure 8. Segment 608C4B for DL2 taken from rod G10, with the storage tube.

Table 2. Specifications of specimens used in hot-cell testing

Specimen label	ORNL inventory label ("Seg. ID")	Span	Burnup* (GWd/MTU)	Estimated oxide* (μm)	Estimated hydrogen of span** (wppm)	Estimated local hydrogen (wppm)	Outer diameter (mm)	Wall*** thickness (mm)
Static tests								
S1	606C3C	4	66.8	70–100	550–750	650	10.748	0.751
S2	605D1E	2–3	66.5	40–70	360–550	400	10.746	0.750
S3	609C5	4	66.5	70–100	550–750	550	10.736	0.745
S4	609C6	4	66.5	70–100	550–750	550	10.740	0.747
Dynamic tests								
D0	605D1F	2–3	66.5	40–70	360–550	360	10.746	0.750
D1	607C4B	4	63.8	70–100	550–750	700	10.834	0.794
D2	608C4B	4	63.8	70–100	550–750	700	10.781	0.768
D3	605C10A	4	66.5	70–100	550–750	550	10.774	0.764
D4	605D1C	2–3	66.5	40–70	360–550	500	10.750	0.752
D5	605D1B	2–3	66.5	40–70	360–550	550	10.771	0.763
D6	609C4	4	66.5	70–100	550–750	700	10.748	0.751
D7	609C3	4	66.5	70–100	550–750	750	10.777	0.765
D8	606C3E	4	66.8	70–100	550–750	550	10.739	0.746
D9	609C7	4	66.5	70–100	550–750	550	10.738	0.746
D10	606C3A	4	66.8	70–100	550–750	750	10.759	0.756
D11	607C4A	4	63.8	70–100	550–750	700	10.832	0.793
D12	608C4A	4	63.8	70–100	550–750	700	10.821	0.788
D13	606B3E	5	66.5	100–110	750–800	750	10.765	0.760
D14	606B3D	5	66.5	100–110	750–800	750	10.765	0.760
D15	606B3C	5	66.5	100–110	750–800	750	10.768	0.761

* Reference (1)

** References (13,14)

*** Cladding wall thickness was based on the nominal inner diameter (9.256 mm, 0.364 in.) provided by EPRI (2001) and the outer diameter measured by ORNL.

2.5 Test Protocol

The test system was calibrated under both static and dynamic testing conditions using three surrogate rods consisting of stainless steel cladding with alumina pellets. The system was tuned and benchmarked by testing a number of specimens. The related results can be found in Appendix C.

2.5.1 Static Testing

The purpose of static testing is to generate bending strength data for SNF rods. In particular, the static tests measure the bending strength of *fueled* SNF rods so that the contribution of the fuel to the SNF rod bending strength can be evaluated. The analysis of the static test results also provides a reference yield strength to establish the dynamic testing matrix. Static testing is carried out using displacement control. It involves ramping both loading arms of the U-frame at 0.1 mm/s up to 12 mm, where 12 mm displacement is the machine stroke capacity. The following procedure is followed.

- Perform the standard static bending test beyond SNF rod yielding to failure or up to device displacement or loading capacity.
- If the machine capacity is reached before specimen failure or specimen maximum strength is reached, repeat unidirectional static testing using the same condition for a few more loading/unloading cycles, or to specimen failure, whichever comes first.
- If the SNF rod does not fail after 3–4 loading/unloading cycles, follow a dynamic or cyclic test procedure to fracture the tested specimen to support postmortem examination. Such a dynamic test is called a follow-up test.
- Collect and weigh any fuel fragments that may have become dislodged during the test.

The loading processes to be used after the first loading cycle were suggested because the device might not have sufficient stroke to test these particular specimens to failure.

2.5.2 Dynamic Testing

Dynamic testing consists of two major activities—dynamic real-time online monitoring and periodic quasi-static deformation measurements (see Figure 9). The procedure is as follows:

- Perform the dynamic cyclic test under constant load control using a sine wave input in reverse bending mode.
- Set the cycle frequency at 5 Hz and select the amplitudes for individual cycle tests considering the target cycles to be achieved with each test.
- Monitor the SNF fatigue evolution with defined intervals: Perform static measurements of the rod deformation at the end of each target cycle with a frequency of 0.05 Hz and appropriate amplitude under displacement control.
- Stop the dynamic test when failure/clad fracture is detected or the preselected number of cycles is reached.

- Weigh any fuel fragments that fall out of the fracture.

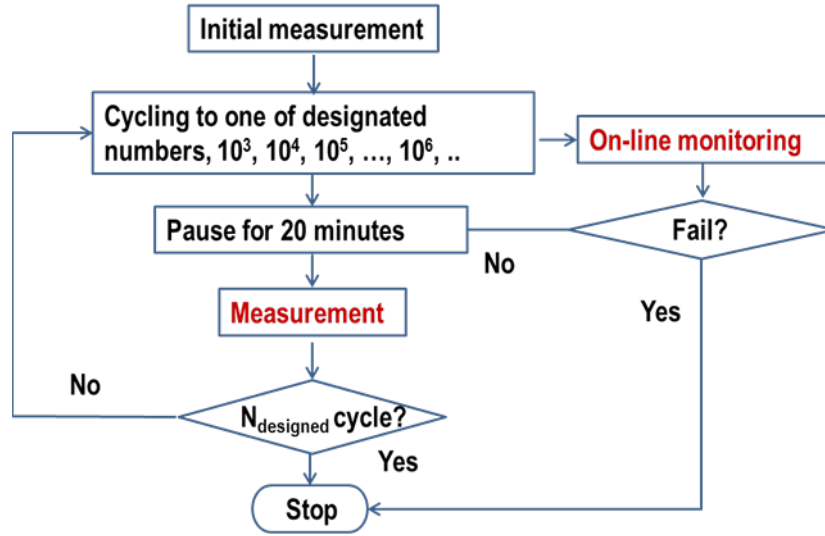


Figure 9. Flowchart for cyclic testing of spent fuel rod.

2.6 Data Processing

Measurement data and online monitoring data are converted into the applied moment and curvature, based on the load channel (load1 and load2) information, the loading arm length (101.60 mm), and LVDT data (LVDT1, 2, and 3). This information is used to generate the time series plots of moment and curvature and the moment-curvature hysteresis loops, such as those illustrated in Figure 10 for D1. The uniform moment applied to the rod is derived simply from the following equation.

$$M = F \times L \tag{2}$$

where F is the averaged value of applied loads (load1 and load2) from the Bose dual motors, and L is the loading arm length, 101.60 mm. The computation of curvature κ is described in Section 2.3.

An equivalent stress-strain curve can be obtained under the assumption that the SNF rod can be idealized as a linear elastic homogeneous material without consideration of the effects induced by pellet-cladding interaction. The equivalent stress was calculated using:

$$\sigma = M \times y_{max} / I \tag{3}$$

where I is the moment of inertia, $I = I_c + I_p$, I_c and I_p are moments of inertia of cladding and pellet, respectively, and y_{max} is the maximum distance to the neutral axis of the test rod section and is set equal to the radius of the cladding. The measured ODs of rod segments are given in Table 2. The calculation of stress disregards the difference of elastic moduli between cladding and pellets.

The equivalent strain is then:

$$\varepsilon = \kappa \times y_{man} \tag{4}$$

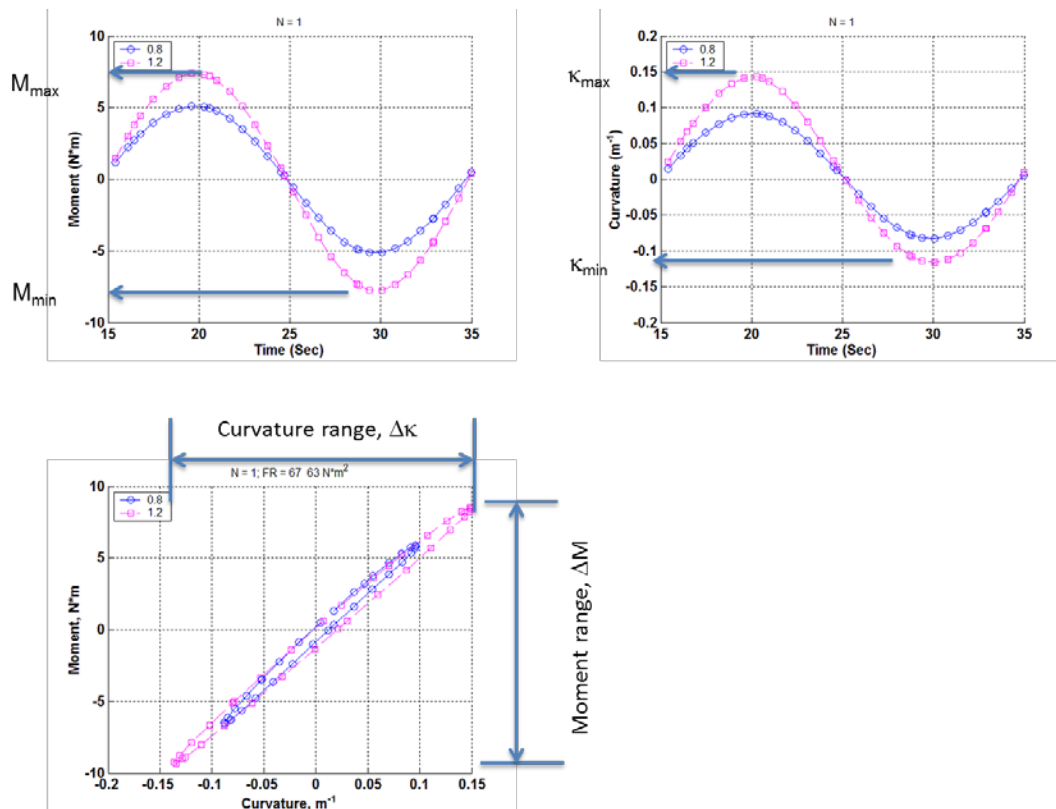


Figure 10. Moment, curvature time series, and moment-curvature hysteresis loop for rod D1. Two measurements are displayed with relative displacement 0.8 and 1.2 mm at the loading points of U-frame.

2.6.1 HBU SNF Characteristics

The SNF system contains multiphase components such as the cladding, pellets, and oxide. Thus, an SNF rod is far from an ideal homogeneous material, especially in HBU fuel, where the irradiated cladding and pellets and the associated interfaces are modified significantly during irradiation. Assuming the HBU rod has a perfect interface bond at pellet-cladding and pellet-pellet interfaces, the associated flexural rigidity EI can be expressed as

$$EI = E_c I_c + E_p I_p, \quad (5)$$

where I_c and I_p are moments of inertia of the cladding and pellet, respectively, and the value of I_p is based on the reference.¹ E_c and E_p are the Young's modulus of the cladding and pellet. The associated stress and strain evaluations of Eqs. (3) and (4) can still be used.

However, because of the imperfect interface cohesive bonding, the effective EI (the slope of moment-curvature) will be less than that of the perfect bonding property, which can be written as

$$EI = E_c I_c + E_p I_p - F(BE, \text{cladding, fuel}), \quad (6)$$

where F is the correction factor, which depends on interface bonding efficiency (BE) and the fuel pellet and cladding aging properties, as well as cyclic loading amplitudes. This hypothesis was further validated in Reference 17.

Based on the static measurements of CIRFT testing, the EI data trend indicates that the cohesive bonding at the pellet-pellet interface is fairly weak. The resulting degradation of flexural rigidity, which is associated with the debonding at the pellet-pellet interface, is reflected by the LVDT measured curvatures evidenced by a significant variation between the cladding tensile stress and cladding compressive stress regions shown in Figure 10. This suggests that the fuel pellet reinforcement for SNF rod flexural deformation at the cladding tensile stress region is no longer available due to pellet-pellet debonding under flexural tensile loading. At the compressive cladding stress region, the fuel reinforcement remains intact in the form of the fuel pellet pinning effect. This results in a shift of neutral axis in an SNF system under reversal bending.

The above mentioned phenomenon was also observed from the CIRFT test online monitoring data, where the tensile cladding stress stage shows a higher curvature reading than the compressive stress stage, as shown in Figure 24 (d). The EI values also change accordingly in each moment reversal cycle, as shown in moment-curvature plot of Figure 10, where the EI in the clad compression cycle is higher than that of clad tension cycle.

Furthermore, a detailed three-dimensional finite element analysis with a 6.25 N·m uniform moment also reveals that the localized stress in the cladding at the pellet-pellet-cladding interface region is about three to four times (depending on the interface cohesive bond parameters)^{15,20} the LVDT measurement for the tensile cladding stress region, and the associated localized stress is about 2.6 times the average tensile cladding stress away from the pellet-pellet interface region. Another complication is that the neutral axis of the SNF rod will no longer reside in the geometric center of the SNF system, and the EI value will shift alternatively around the geometry center under cyclic loading reversals.¹⁷ Therefore, the conventional approach, as stated in Eqs. (3) and (4) from a global $M-\kappa$ consideration, is no longer valid for describing the cladding failure mechanism associated with localized flexural rigidity degradation at the rod pellet-pellet interface. Conducting detailed localized stress-strain evaluation at the pellet-pellet interface translated from global measurements is beyond the current scope of the project. Therefore, only the mechanical response derived from direct measurements (the LVDTs) will be utilized in this study and discussion.

In order to generate the stress-strain relationship associated with $M-\kappa$, a first order approximation approach, commonly used for an isotropic/homogeneous structure, was adopted to translate the global CIRFT $M-\kappa$ data into equivalent stress and strain data of cladding. Where the SNF rod's moment of inertia is written as $I = I_c + c \times I_p$, I_c and I_p are moments of inertia of cladding and pellet, respectively, and $c = E_p/E_c$ (because the baseline Young's modulus of the oxide fuel is twice that of the cladding, c is likely greater than 1). In the proposed equivalent stress and strain approach, c is set to 1, which implies a 50% reduction in pellet Young's modulus, to take into account the radiation induced degradation of the HBU fuel pellet, where the pellets are assumed to be perfectly bonded with the cladding at the pellet-pellet interface. Furthermore, setting $c = 1$ implies the same E properties for the fuel and the cladding, which allows the use of Eqs. (3) and (4) under the homogenous properties hypothesis for an equivalent stress and strain evaluation.

Generally, the moment range (ΔM), curvature range ($\Delta \kappa$), and flexural rigidity EI are used in characterizing the mechanical properties of the fuel rod. These are defined as:

$$\begin{aligned} \Delta M &= M_{max} - M_{min}, \\ \Delta \kappa &= \kappa_{max} - \kappa_{min}, \\ EI &= \Delta M / \Delta \kappa \end{aligned} \tag{7}$$

where the subscripts “max” and “min” represent the maximum and minimum waveforms (Figure 10).

Under a load-controlling mode, the curvature response of a rod is not necessarily symmetric in one cycle of loading as will be discussed in Section 4.1. The offset of the M- κ loop on the κ axis with respect to the origin can be described by a mean value of curvatures, κ_m :

$$\kappa_m = 0.5 \times (\kappa_{max} + \kappa_{min}); \quad (8)$$

and the maximum of absolute curvature extremes, $|\kappa|_{max}$, is

$$|\kappa|_{max} = \max(|\kappa_{max}|, |\kappa_{min}|). \quad (9)$$

For a given specimen, the $|\kappa|_{max}$ given by Eq. (9) corresponds to the curvature that creates the maximum tensile stress in the cladding.

The resistance force of the CIRFT system may be significant, depending on the amplitude of the rigid arm movement. The CIRFT system static resistance force was measured at different displacement levels without a specimen loaded. The net applied load at each displacement level was estimated by subtracting the measured resistance from the applied static test load, shown in Figure 11. The CIRFT system resistance was tested and evaluated by using empty runs in which the specimen was not loaded on the testing machine. This is conducted in the specified period or whenever the calibration is needed.

The effect of CIRFT system resistance on the dynamic loading of the rod was also investigated by using a calibration rod in an out-of-cell study. It was shown that due to low loading amplitude the net effect of system resistance and dynamic inertia on the load applied to the rod is negligible within the tested range. Since the out of cell condition that was evaluated is equivalent to the condition used in hot cell cyclic testing, no correction procedure needs to be applied to the data acquired during dynamic tests.

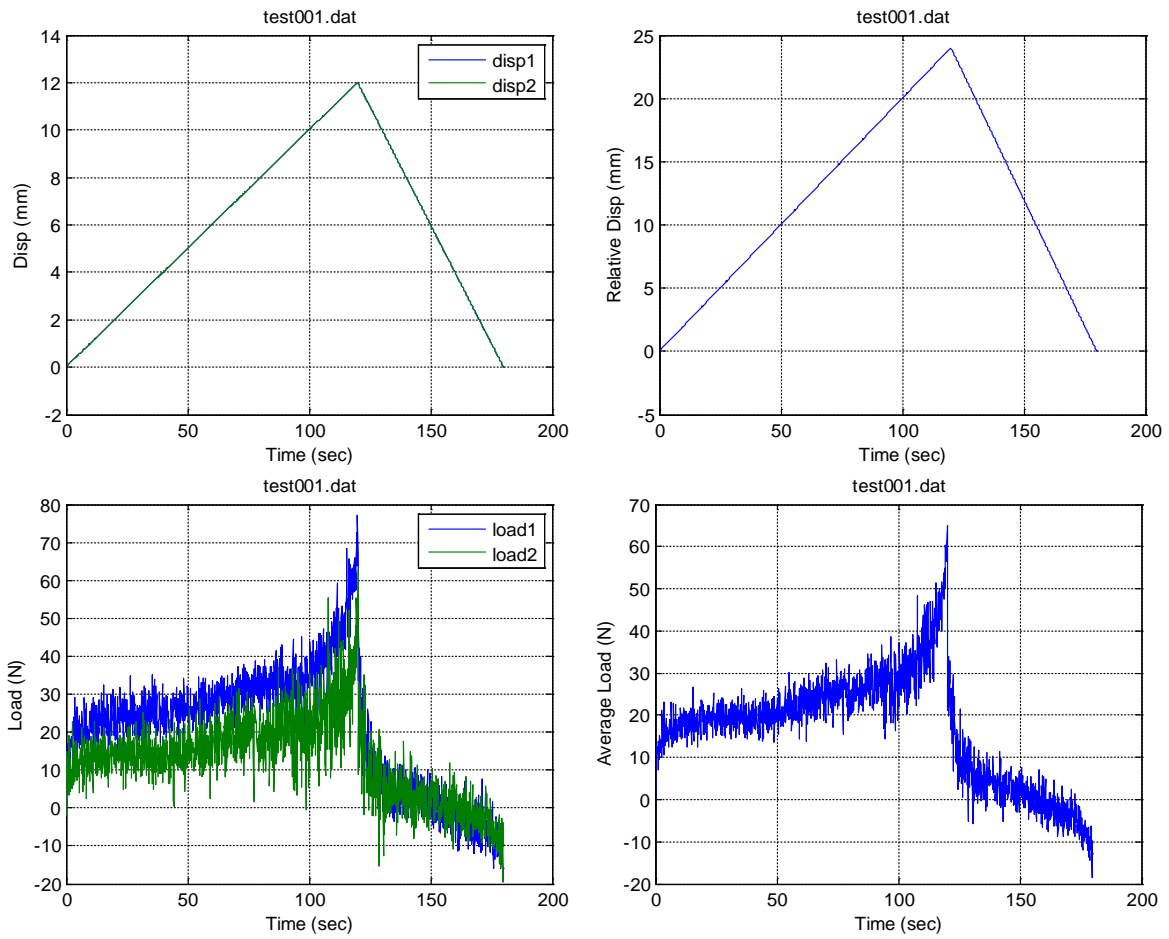


Figure 11. “Empty-run” conducted on HBR S1, for which the load and displacement were plotted.

3. STATIC TESTING

3.1 Results

Three specimens were tested under static loading in the hot cell for test system benchmarking. Four static tests were subsequently conducted. This chapter focuses on these four static tests; refer to Appendix C for the static benchmarking tests.

S1 (606C3C, 66.8 GWd/MTU burnup, 70–100 μm oxide layer) survived four static loading/unloading cycles of unidirectional bending without failure. The moment-curvature curve for the initial cycle is presented in Figure 12(a). (The curves of subsequent cycles overlay one another to a great extent and for clarity are not plotted.) The maximum moment achieved in this test was 85.5 N·m, corresponding to a maximum curvature of 3.2 m^{-1} . The slope changes of the linear portion of moment-curvature curves could be seen approximately near moment levels 12 and 59 N·m, respectively. It is noted here that due to pellet end dish-in design, the pellet-pellet interface bonding strength would be fairly weak, and the pellet-pellet de-bond phenomenon should be observed in the early phase of bending loading. The slope changed points indicate that the flexural rigidity changed in the SNF rod system within the linear elastic range. The changes of slope and associated deflection points are quantified in Section 3.2. The equivalent stress-strain curve based on Eqs. (3) and (4) for the initial cycle is presented in Figure 12(b), where Y_{max} and I are based on the measured clad OD provided in Appendix B.

Since the machine capacity was reached and no failure occurred to the specimen, a follow-up dynamic test was conducted with reversible bending under ± 25.40 to 30.48 N·m at 5 Hz. As mentioned above, the purpose of this procedure was to test the specimen to failure for further postmortem examination. The rod failed after approximately 1.4×10^4 moment reversals. The failure occurred near motor 1 (right side) with a fuel release of 0.9 g. Optical images of the fracture surfaces are shown in Figure 13. The pellet end-face can be identified from the haze zone characterized by a brown-blue color (indicated by the arrow in Figure 13a). This indicates that the rod failure may have initiated at the pellet-to-pellet interface. At the same time, a serrated shear fracture surface of the cladding was observed. The serrated fracture surface was believed to be the end stage of the crack propagation upon the fatigued CIRFT sample fractured. Note that this specimen appears to have been loaded into the test machine at 90° from the specimen ID marks.

The cladding surface [Figure 13(c) and (d)] near the neutral axis of the bending rod is free of visible surface oxide spalling, which is expected since these regions experienced little stress. In contrast, one of the stressed lateral surfaces which experienced the maximum flexural stress is covered with significant visible circumferential surface oxide spalling.

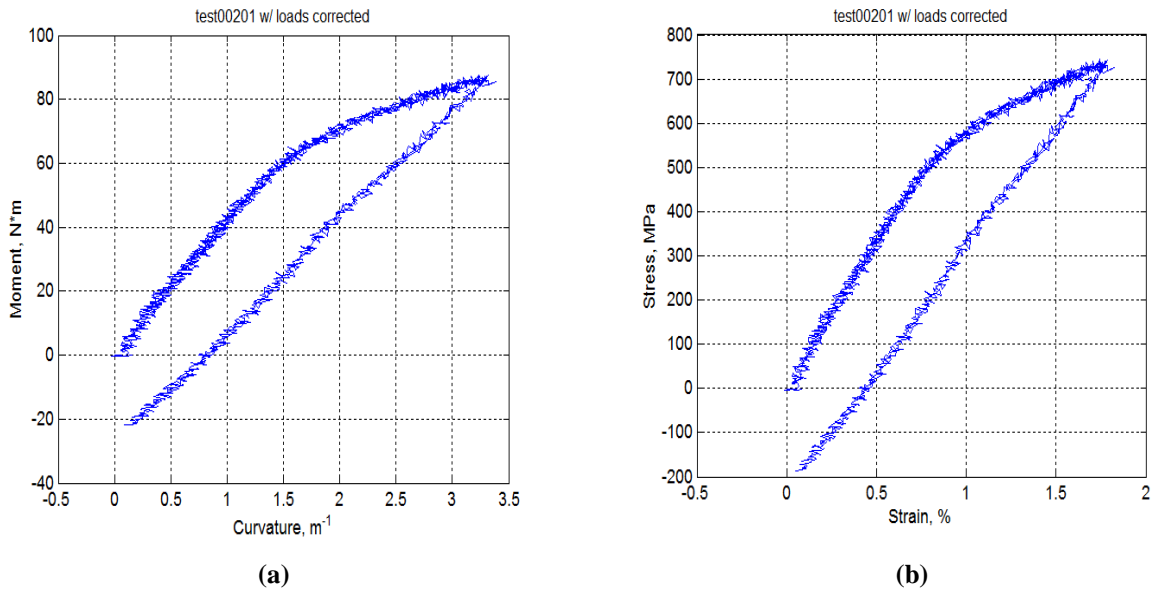
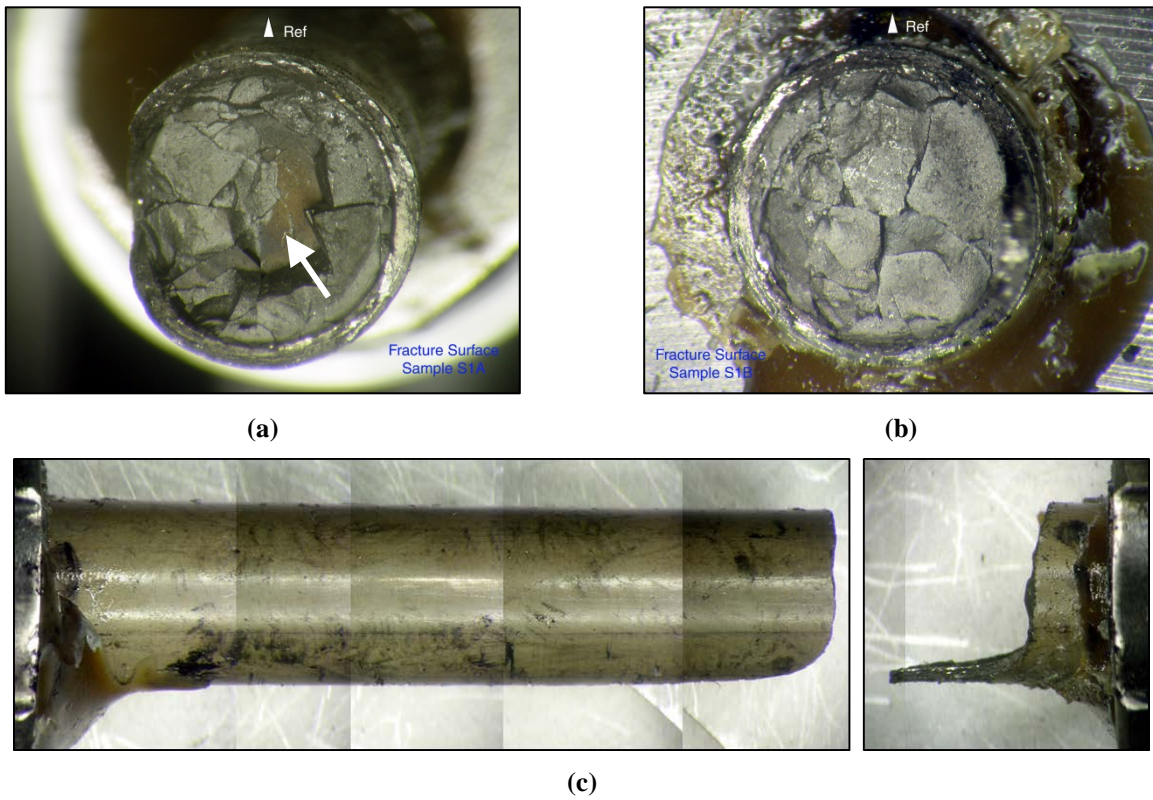
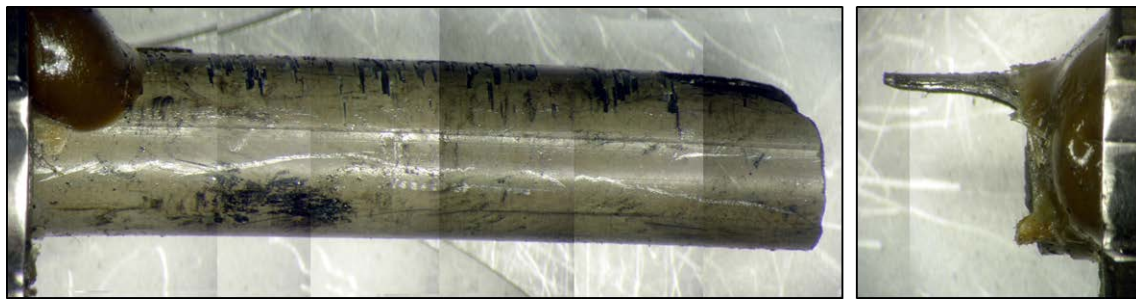


Figure 12. (a) Curve of moment versus curvature, and (b) equivalent strain–stress curve¹ for S1 (606C3C). Based on a static loading cycle in which the maximum relative displacement was 24 mm; rates at the loading points of the U-frame were set at 0.1 and 0.2 mm/s for loading and unloading, respectively.



¹ Based on Eq. (3) and Eq. (4).



(d)

Figure 13. Mating fracture surfaces (a) and (b); lateral sides near the neutral axis of the bending rod for S1 (606C3C) (c) and (d). The rod was subjected to four repeat static cycles to 24 mm maximum relative displacement followed by dynamic cyclic loading ± 25.40 to $30.48 \text{ N}\cdot\text{m}$ at 5 Hz; 1.4×10^4 failure cycles, 0.9 g fuel particles collected. Note: This specimen appears to have been loaded into the test machine at 90° off from the ID marks.

Specimens S2 and S3 were both tested under static condition for three loading/unloading cycles without any sign of failure. They failed in follow-up dynamic tests under $\pm 30.48 \text{ N}\cdot\text{m}$ at 5 Hz. The amplitude of applied moment in the dynamic tests was 35 to 36% of the maximum applied moments used in the respective unidirectional bending process, located in the early second stage of moment-curvature curves. It is noted here that the selection of the applied moment amplitudes was to generate the failure of the tested specimens within a reasonable number of cycles. The bending fatigue response of the as-received fuel rods will be discussed next. Finally, S4 was tested under static conditions for three cycles and failed during the fourth cycle. Details of these static tests can be found in Appendix D.

It should be noted that, in the static tests reported above, loading/unloading cycles did not result in apparent or catastrophic failure of specimens because of the limited stroke of the CIRFT machine. The failure of specimens occurred in the initial loading cycle of two benchmarking tests, Scal1 and Scal2. The peak moments of the two tests were 78.2 and $80.7 \text{ N}\cdot\text{m}$, respectively. Details of these benchmarking tests can be found in Appendix C.

A summary of the moment-curvature curves is shown in Figure 14 for the four static tests. The top and right axes present the scale of the converted maximum strain and stress of the bending specimen according to Eqs. (3) and (4).

Several important observations can be made with respect to the responses of the test specimens during the first loading cycle.

- The static test results of the four specimens prior to the follow-up dynamic testing all show relatively similar elastic behavior.
- The initial moment-curvature response is characterized by a flexural rigidity of 52 to $63 \text{ N}\cdot\text{m}^2$.
- There is a change in the flexural rigidity at the moment of 12 to $21 \text{ N}\cdot\text{m}$. This change will be quantified in Section 3.2.
- After this change, the moment-curvature response is characterized by a degraded flexural rigidity of 37 to $41 \text{ N}\cdot\text{m}^2$.
- Each static test segment experienced 1–2% plastic strain without failure.

- The unloading flexural rigidity is similar to the loading flexural rigidity in the second stage after the moment reaches 12 to 21 N·m.

Overall, the rods failed within the gage sections in all of the tested rods. The majority of the rod fractures involved the pellet-to-pellet interfaces (PPIs). S3 was exceptional in that the failure location seemed away from pellet-pellet interface, as no end face of the pellet can be identified from the fracture surface of the fuel. A summary of static test results is provided in Table 3.

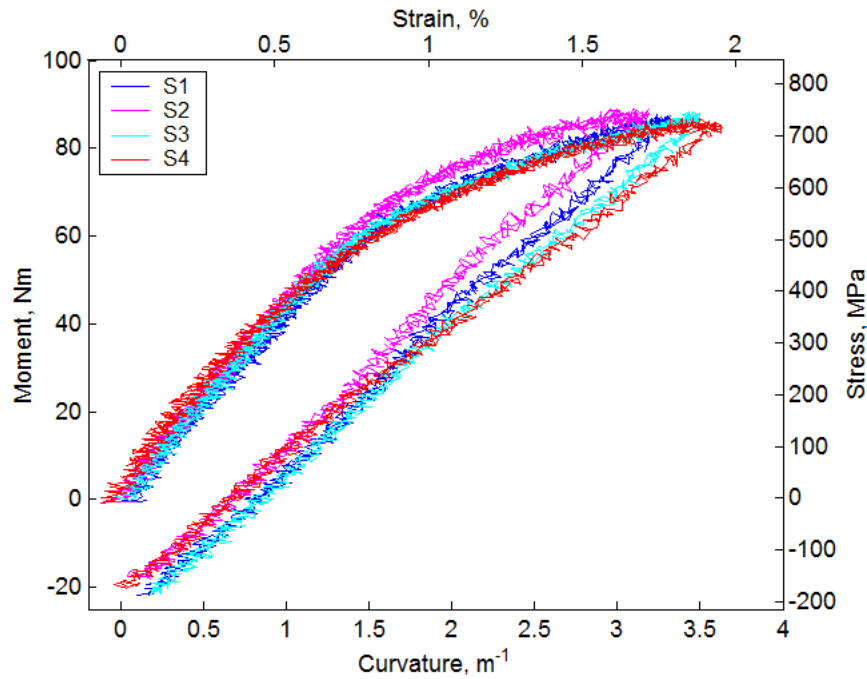


Figure 14. Moment-curvature curves measurements in static tests (Corresponding stress and strain displayed on right and top axes, respectively).

Table 3. Summary of static tests

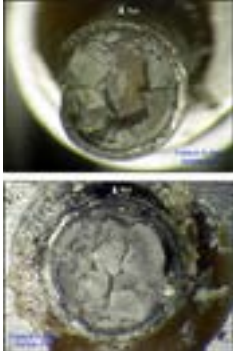
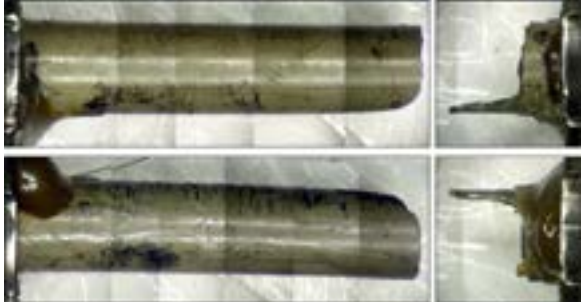

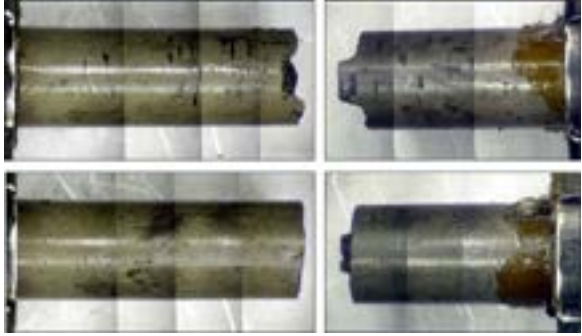
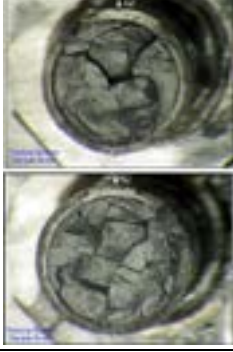
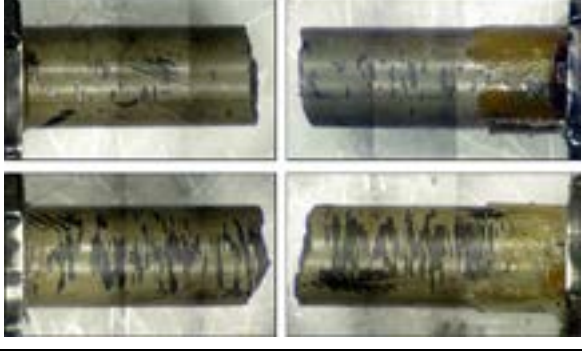
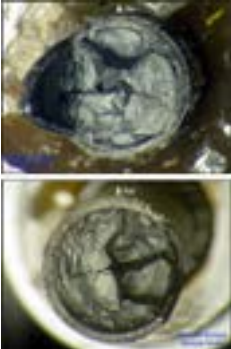
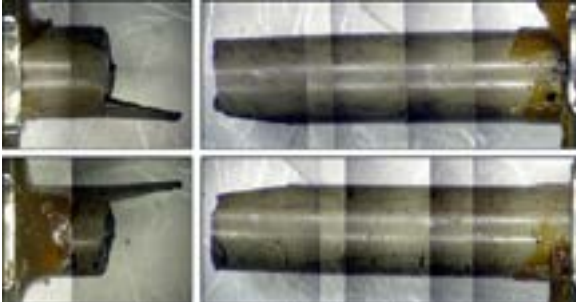
Specimen ID	Specimen burnup	Testing condition and result	Fracture surfaces	Side view of fractured specimens
S1, 606C3C	66.8 GWd/MTU	Four static cycles to 24 mm max. relative displacement, 85.5 N·m max. moment, followed by dynamic loading ± 25.40 to 30.48 N·m, 5 Hz; 1.4×10^4 failure cycles, 0.9 g fuel fragments collected		
S2, 605D1E	66.5 GWd/MTU	Three static cycles to 24 mm max. relative displacement, 87.2 N·m max. moment, followed by dynamic cyclic loading ± 30.48 N·m, 5 Hz; 7.2×10^3 failure cycles, 0.6 g fuel particles collected		
S3, 609C5	66.5 GWd/MTU	Three static cycles to 24 mm max. relative displacement, 85.8 N·m max. moment, followed by dynamic loading: ± 30.48 N·m, 5 Hz; 9.6×10^3 failure cycles, 0.2 g fuel particles collected		

Table 3. Summary of static tests (continued)

Specimen label/ ID	Specimen condition	Testing condition and result	Fracture surfaces	Lateral surfaces of fractured specimens
S4, 609C6	66.5 GWd/MTU	Three repeat static loadings to 24 mm max. relative displacement and failed at 85.5 N·m in the 4th cycle, 1.3 g fuel particles collected		

3.2 Discussion

3.2.1 Characteristics of Moment-Curvature Curve

The moment-curvature responses of all four static test specimens were similar. They are characterized by two linear constituent behavior responses, followed by a nonlinear response during the loading and a linear response upon unloading. It was observed that when reloaded, the rod followed the unloading curve linearly and proceeded with nonlinear response after passing the previously achieved maximum load. Such loading/unloading/reloading responses can be found in many mechanical systems where strain hardening prevails.⁵

An effort was made to characterize the moment-curvature response based on the characteristic points to facilitate understanding test results. The flexural rigidities EI1, EI2, and EI3 were obtained, corresponding to the slopes of the first and second linear segments and of the unloading segment by using curve fitting with the first order polynomial (Figure 15). The characteristic curvatures and moments at the slopes' changed points A and B were then identified. In addition, the moment at point C corresponding to a 0.37 m^{-1} irreversible curvature, or 0.2% equivalent plastic strain, was found by using a line with the same slope as that of unloading and horizontal axis intercept 0.37 m^{-1} . The quantities corresponding to points A, B, and C are designated by κ_A , κ_B , κ_C , and M_A , M_B , and M_C .

The results are summarized in Table 4. For a given specimen, EI1, EI2, and EI3 are generally in decreasing order with a marginal difference between the latter two. The characteristics derived from equivalent stress-strain curves are provided in Table 5. The E1 in the initial stage of the stress-strain curve was 83 to 101 GPa, and the 0.2% yield strength (σ_C) was 687 to 727 MPa. The ranges of the elastic modulus and the 0.2% yield strength appear consistent with the range of HBU HBR cladding.¹⁶ However, the observation should not be overemphasized, for the results observed here reflect a comprehensive global response of fuel rods with both pellets and cladding included. Moreover, substantial simplifications were made with regard to the elasticity and contributions of individual components, where the localized stress riser in cladding at the pellet-pellet interface region was not considered.

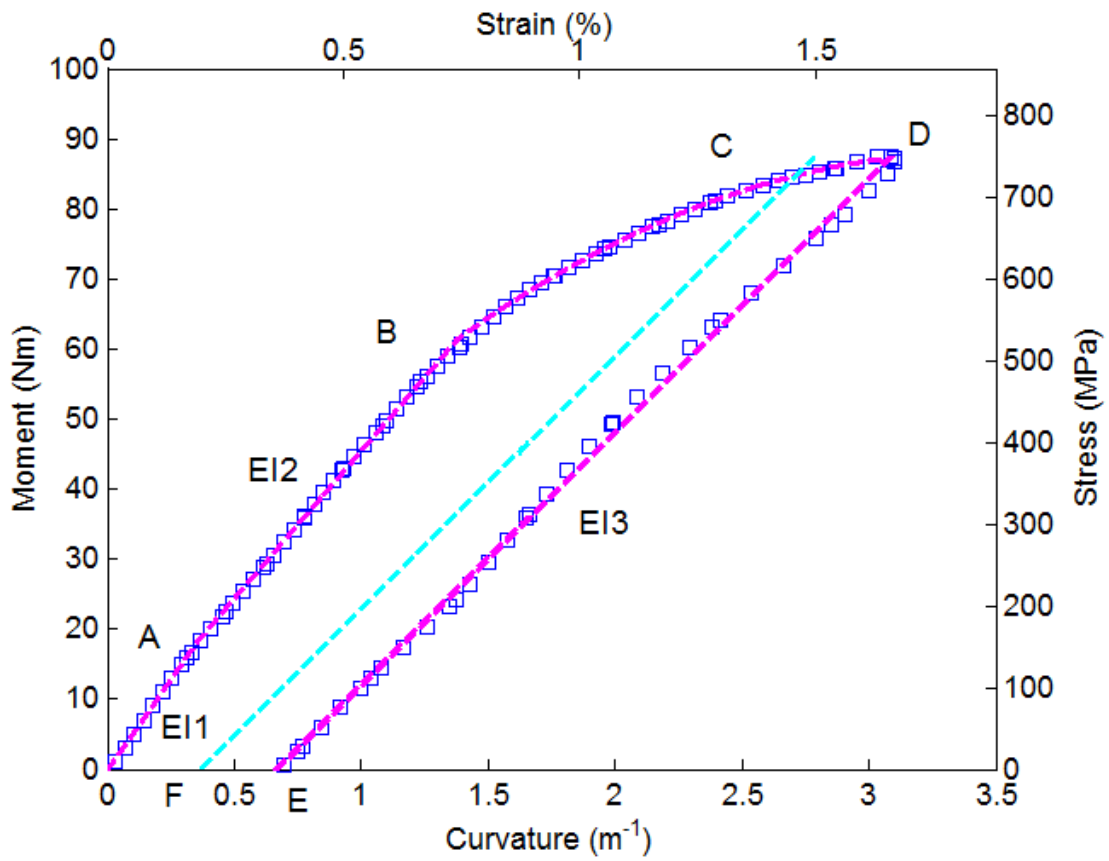


Figure 15. Characteristic points of moment-curvature curve.

Table 4. Characteristic points and quantities based on curvature-moment curves

Spec label	Seg. ID	EI1	EI2	EI3	κ_A	κ_B	κ_C	κ_D	M_A	M_B	M_C	M_D
		N·m ²	N·m ²	N·m ²	m ⁻¹	m ⁻¹	m ⁻¹	m ⁻¹	N·m	N·m	N·m	N·m
S1	606C3C	63.057	40.122	35.016	0.267	1.435	2.659	3.242	12.293	59.142	80.105	85.503
S2	605D1E	52.032	41.462	36.067	0.385	1.419	2.719	3.084	19.651	62.496	84.696	87.155
S3	609C5	51.627	41.457	32.618	0.378	1.373	2.864	3.413	17.684	58.946	81.322	85.843
S4	609C6	52.286	36.736	28.657	0.347	1.146	3.288	3.532	21.306	50.656	83.602	85.515
Avg.		54.751	39.944	33.090	0.344	1.343	2.883	3.318	17.734	57.810	82.431	86.004
Std. Dev.		5.544	2.230	3.289	0.054	0.134	0.284	0.196	3.918	5.040	2.093	0.783

Table 5. Characteristic points and quantities based on equivalent stress-strain curves

Spec label	Seg. ID	E1	E2	E3	ϵ_A	ϵ_B	ϵ_C	ϵ_D	σ_A	σ_B	σ_C	σ_D
		GPa	GPa	GPa	%	%	%	%	MPa	MPa	MPa	MPa
S1	606C3C	100.577	63.995	55.851	0.144	0.771	1.429	1.742	105.388	507.039	686.75	733.032
S2	605D1E	83.121	66.235	57.616	0.207	0.762	1.461	1.657	168.669	536.428	726.971	748.081
S3	609C5	82.796	66.486	52.31	0.203	0.737	1.537	1.832	152.237	507.458	700.088	739.008
S4	609C6	83.721	58.822	45.886	0.187	0.616	1.766	1.896	183.201	435.575	718.86	735.312
Avg.		87.554	63.885	52.916	0.185	0.722	1.548	1.782	152.374	496.625	708.167	738.858
Std. Dev.		8.691	3.556	5.180	0.029	0.072	0.152	0.104	33.781	42.962	18.183	6.623

3.2.2 Comparison of Static Results with PNNL Cladding Data

In order to investigate the contribution of fuel pellets in the fuel rod structure, analysis was performed to compare the measured static results to predicted values considering cladding alone. The cladding properties used for this analysis were obtained from a database maintained by Pacific Northwest National Laboratory (PNNL)¹⁹. The database allows the user to specify the cladding type, temperature, fluence and cold work of the cladding of interest. For this study, the following values were specified:

Cladding – Zry-4
Temperature – 75°F
Fluence – 12×10^{25} n/m²
Cold work – 0.5

Using these values in the PNNL database, the Young’s modulus was given as 9.15×10^{10} Pa, the yield stress 919 MPa, the uniform elongation 0.00393, and ultimate tensile strength 976 MPa. From these values, the engineering stress and strain values can be calculated.

It is noted that the CIRFT LVDTs measured the global rod deformation within the gage section. Thus, the stress-strain estimate is an average evaluation throughout the gage section that covers several pellet lengths with several pellet-pellet interfaces. For the linear response of the cladding region of the rod away from the pellet-pellet interface, evaluation of the stress and strain can be a straightforward composite flexural rigidity formulation due to relatively good bond at the pellet-cladding interface. However, due to the composite structure segmented pellets, the localized stress riser or curvature magnification at the pellet-pellet interface region cannot be estimated directly from the equivalent stress and strain approach; instead, it needs to be evaluated using finite element analysis^{15, 17}.

In order to further quantify the fuel pellet support or reinforcement to the SNF system mechanical property with respect to bending flexural response, the comparison based on CIRFT M-κ data was completed as illustrated below.

For comparison, the PNNL data (σ-ε curve) were converted to a moment-curvature curve by using the following equations, with the consideration of stress distribution that is appropriate for a thin-walled tube under uniform bending,

$$M = \sigma \cdot I/y_{\max}, \quad (10)$$

and

$$\kappa = \varepsilon/y_{\max}, \quad (11)$$

where $I = I_c$, and other quantities have same meanings as in Eqs. (2) and (3). The hypothetical “cladding only” moment-curvature response was plotted together with the moment-curvature response of the high-burnup fuel rod system as shown in Figure 16, where the SNF rod shows much higher bending moment resistance compared to that of PNNL data with cladding alone. A comparison of CIRFT testing results with cladding-only rigidity based on PNNL data is given in Table 6. HBR’s rod used in the flexural rigidity calculation has the following cladding dimension: cladding ID 0.364 in., OD 0.423 in.

In the data comparison above, a distinct difference from that of the four HBU fuel rod systems was observed in the slope of the PNNL data. The slopes of the four HBU fuel rod systems are greater than that of the PNNL data. By focusing on the initial slope, between 0–15 N·m, the slope (flexural rigidity) of

HBU fuel rods was approximately twice that of the PNNL data for cladding alone. The increase in flexural rigidity can be attributed to the presence of fuel. Nevertheless, a detailed analysis is required to determine exactly how the presence of fuel accounts for this increase in flexural rigidity, as well as the net effect of fuel support on SNF rod system fatigue lifetime.

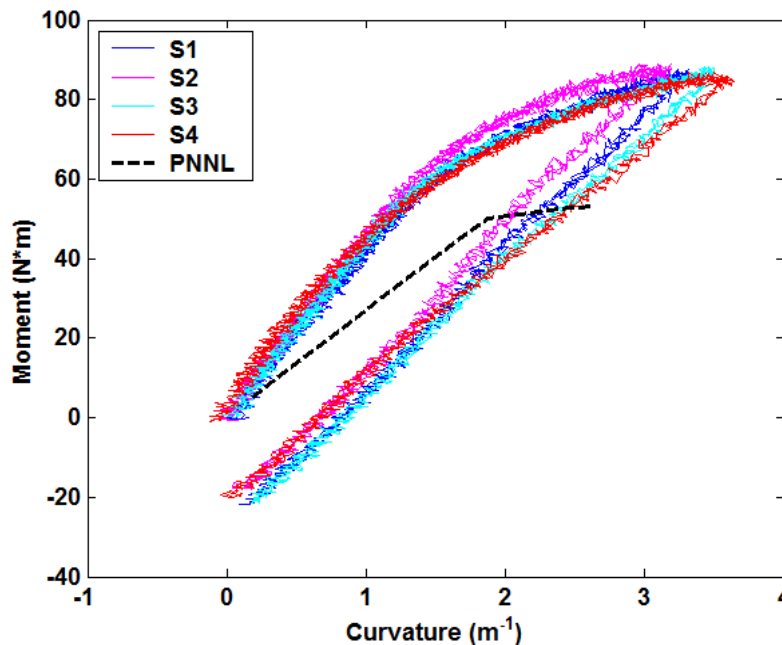


Figure 16. Comparison of CIRFT global data with PNNL moment-curvature curve converted from PNNL cladding stress-strain data.

Table 6. Comparison of flexural rigidity results between CIRFT testing and PNNL data

	EI1 (N·M ²)	EI2 (N·M ²)	EI3 (N·M ²)
CIRFT testing	54.751	39.944	33.090
PNNL data	26.933		

The increase of SNF rod system stiffness is attributed to the fuel’s mechanical properties and fuel’s geometry property of the moment inertia. However, the measured flexural rigidity of a fuel rod system is much less than that estimated from a direct summation of $E_c I_c + E_p I_p$. This is primarily due to interface bonding de-efficiency at fuel-cladding and fuel pellet-pellet interfaces, as well as existing fuel-clad gap potential. All of these factors will affect the degree to which the presence of fuel results in increased rod flexural rigidity. This research effort did not attempt to account for and quantify each of these influences. Thus, the preliminary conclusion based on CIRFT SNF static bending testing is that the flexural rigidity was approximately twice what would be obtained if cladding properties alone were used to predict behavior.

From a flexural rigidity perspective, the fuel pellets indeed increase the SNF rod’s system flexural rigidity; however, due to segmental pellet structure, numerous stress concentration sites within cladding at pellet-pellet interfaces in an SNF rod are created. In general the stress concentration event will cause the structure to experience accelerated aging or reduced lifetime as compared to the very same system without stress concentration sites or discontinuous materials interfaces. The stress concentration effect

due to an HBU rod segment structure was further validated from the dynamic testing where the CIRFT test specimens all failed at pellet-pellet interfaces. Therefore, the pellet and clad mechanical interaction at material discontinuity interface regions seems to reduce the benefit gained from the stiffness increase of an HBU fuel rod system. Moreover, the intensity of the stress concentration or the pellet-clad interaction is strongly dependent on the loading intensity. Thus, at low loading level, cladding alone is still the key that dictates the SNF rod flexural reliability. From CIRFT dynamic testing, it also confirms that as long as the clad fracture threshold was not reached, an SNF system can survive millions of vibration cycles.

3.2.3 Effect of LVDT Probe Contact on Large Curvature Measurement

The LVDT probe contact design with respect to monitoring specimen curvature deformation was found to affect curvature measurement results.

An experimental study was performed using two surrogate rods made of identical materials and configurations [stainless steel (SS) tubes and ten alumina pellets in each surrogate rod]. The same flat disk probe contact was used to test each specimen. The flat disk probe forms a line-contact when the probe initially contacts the rod surface. However, upon loading, the contact will shift from the line-contact to point-contact at one side of the probe disk. As shown in Figure 17, under similar loading levels, the maximum curvature obtained from the LVDT probes located at a cladding compression site is significantly larger than that of probes located at cladding tension sites. The discrepancy due to the probe contact effect can be mitigated or reconciled by adjusting sensor spacing, h , of Eq. (1) as illustrated in Figure 18. It has been shown that under progressive adjustments the moment-curvature curves in both cases seem to converge. The actual sensor spacing adjustment can be calibrated with a chisel head probe that has point contact instead of line contact to the rod, as shown in Section 2.3.

Due to LVDT probes located at cladding compression sites during the static testing, the estimated curvature is expected to be overestimated as demonstrated in Figure 18 of $dh = 0$ mm case. The resultant higher curvature trend seems to be consistent with the observations in Figure 17, where modified equivalence data corresponds to a higher peak tensile strain compared to that of the PNNL data.

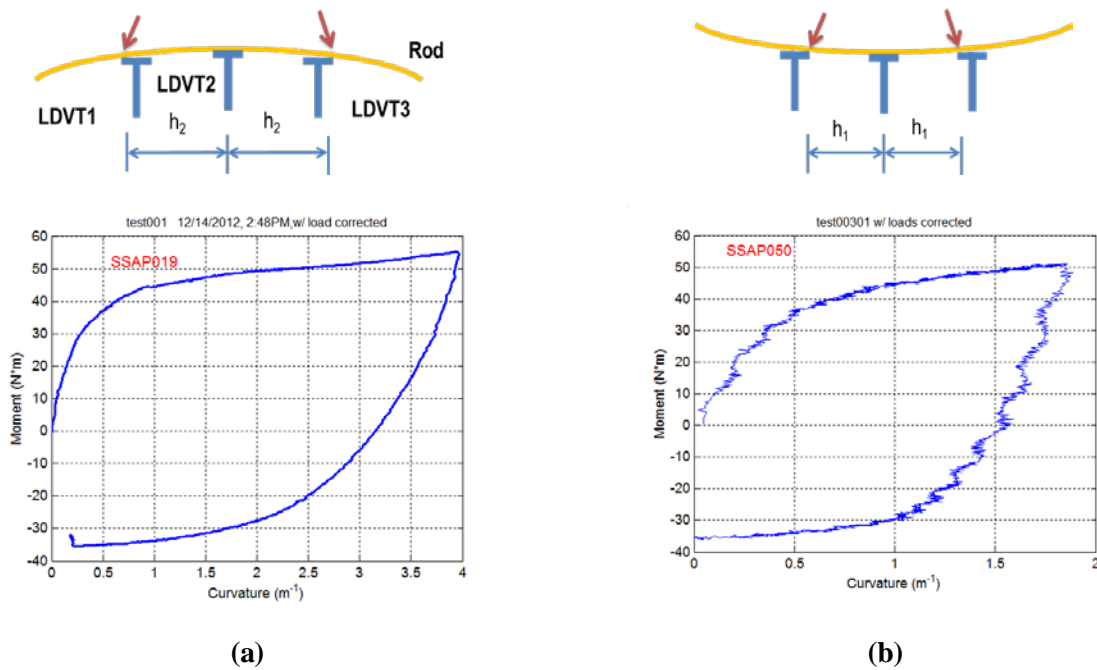


Figure 17. Moment-curvature curves based on stainless steel alumina pellet (SSAP) rod testing when rod is bending with respect to three LVDTs (a) concavely and (b) convexly.

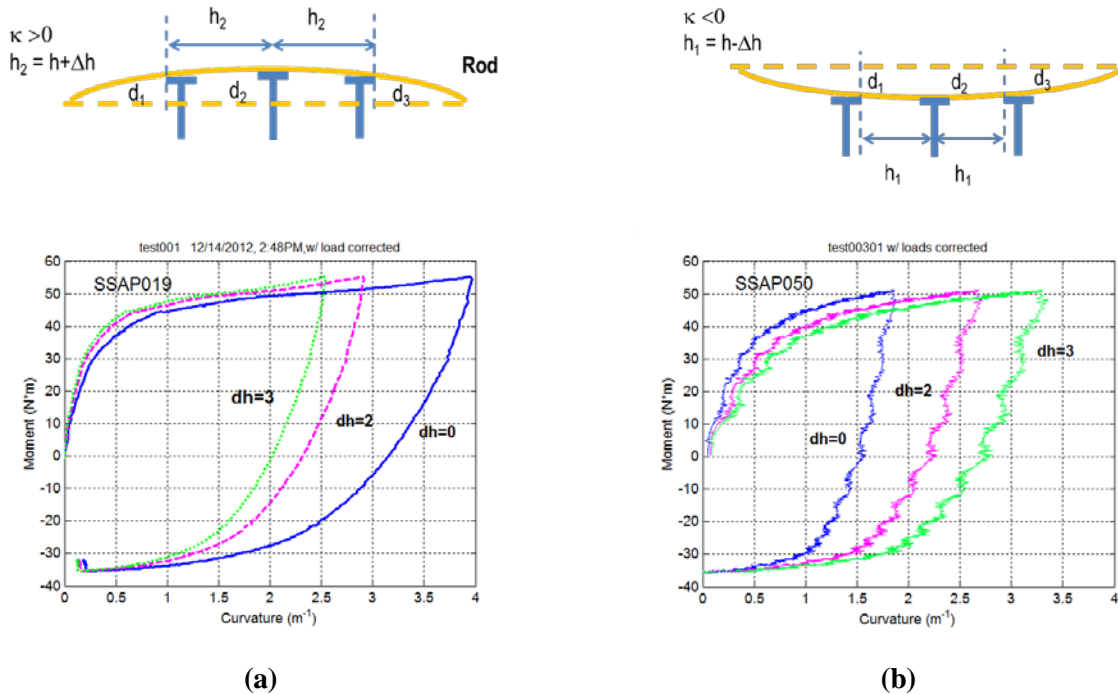


Figure 18. Moment-curvature curves as a function of sensor spacing adjustment when rod is bending with respect to three LVDTs (a) concavely and (b) convexly. The unit of dh is mm.

4. DYNAMIC TESTING

4.1 Results

Sixteen dynamic tests were conducted on the HBU HBR fuel in the hot cell, including one for benchmark testing and fifteen according to the dynamic testing plan. Load amplitudes varied from ± 5.08 to ± 35.56 N·m; 12 tests were completed with specimen failure and four without failure. The fatigue life ranged from 5.5×10^3 to 2.3×10^6 cycles. The tests without failure were conducted under ± 5.08 to ± 8.89 N·m with the accumulated cycles beyond 6.4×10^6 . Details of the dynamic tests can be found in Appendix E; only typical results are described in this section.

The test on D1 (607C4B, 63.8 GWd/MTU burnup, 70–100 μm oxide layer) was conducted under ± 15.24 N·m, 5 Hz. A fatigue life of 1.1×10^5 cycles was obtained, and less than 1 g of fuel fragments was collected at the failure site.

For each cyclic fatigue test, periodic quasi-static measurements of rod deformation were conducted using two relative displacement levels—0.8 and 1.2 mm at the target intervals described in Section 2.5.2. Time series of moment and curvature and moment-curvature loops obtained at the first cycle and after approximately 111,000 cycles are shown in Figure 19. The loops became slender with accumulated cycles, and the amplitude of the loops decreased. The relations of moment-range versus curvature-range and flexural rigidity are illustrated in Figure 20. Most of the rigidity degradation occurred in the first 1,000 cycles. Variations of these quantities as a function of number of cycles are provided in Figure 21. Although the curvature range stayed quite consistent under displacement control, a decrease in moment range was observed. The rigidity of the measurements at two displacements converged before the failure while exhibiting a slightly declining trend.

The curvature, moment, and flexural rigidity based on online monitoring data are presented in Figure 22. The online monitoring showed a flexural rigidity of about $50 \text{ N}\cdot\text{m}^2$, a little lower than that observed in measurements. This occurred because different loading conditions were used in measurement and cycling. A curvature range of less than 0.3 m^{-1} was used in the quasi-static measurement, which is lower than that used in the cyclic test to ensure measurement data did not affect the dynamic cycle data. In general, the flexural rigidity tends to increase with decreasing curvature. This is probably due to a better interface bond at relatively low load resulting in less stiffness reduction. Overall, a stable rod response was exhibited before the final failure. The curvature time history shown in Figure 24(d), it clearly indicated a nonsymmetric deformation under reverse loading, where the cladding tension site has much higher deformation (about 1.6 times) compared to that at the cladding compression site. This phenomenon could be the consequence of debonding at the pellet-pellet interface and the stress concentration occurring at the pellet-pellet interface region at the tension side of the cladding, in addition to sensor probe sensitivity. In general, flexural hysteresis history remains quite uniform throughout the reversal bending test, as shown in Figure 24(f). Under relatively low loading amplitude, the clad or fuel pellet would be mainly under linear elastic behavior, and the root cause of hysteresis energy dissipation under cyclic loading could be the system non-linear response associated with segment pellets' induced stress concentration at interface regions, as well as uncertainly resulting from sensor probe sensitivity.

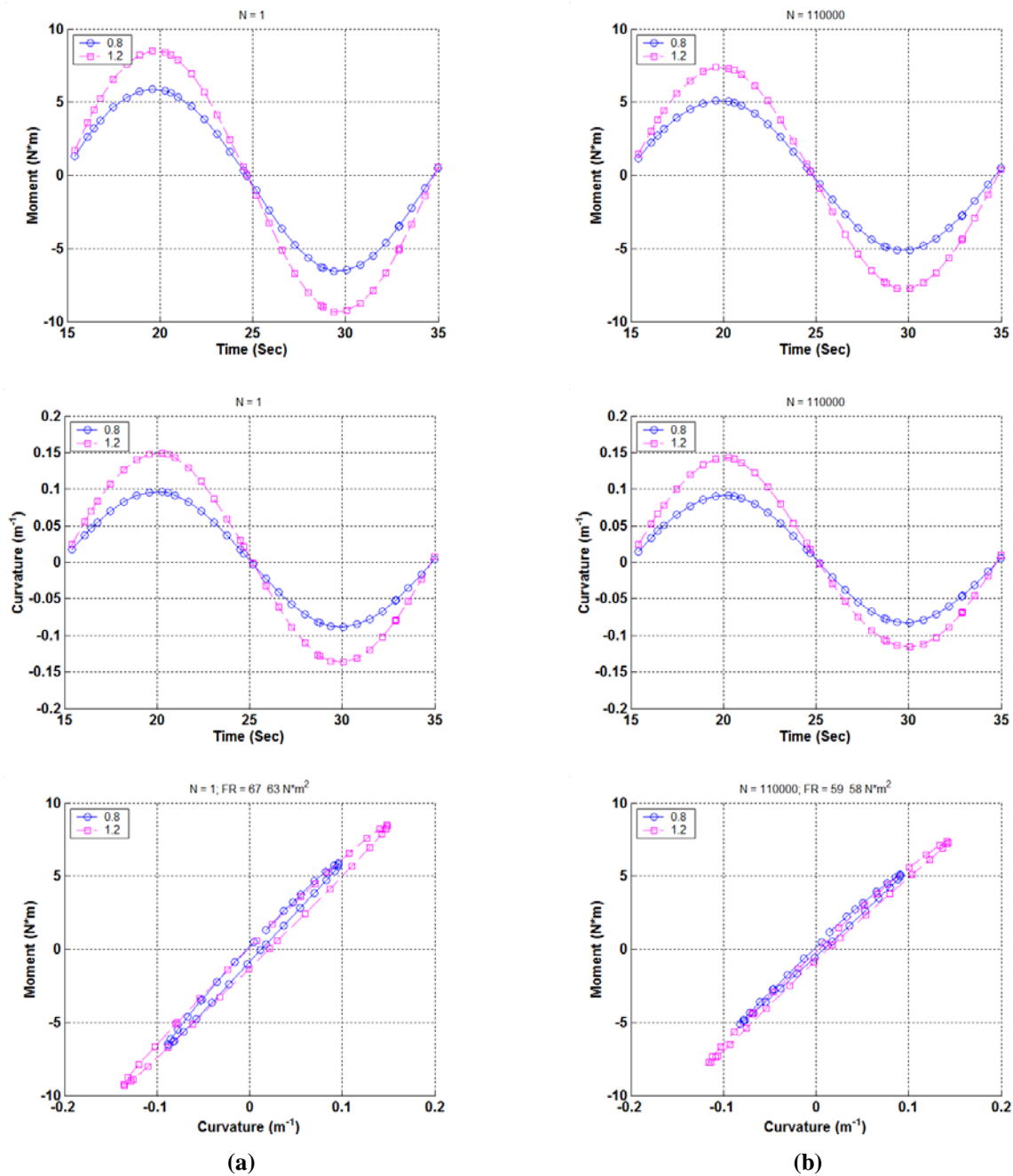


Figure 19. Moment and curvature as a function of time and moment-curvature loops based on measurements when (a) $N = 1$ and (b) $N = 111,000$ cycles for D1 (607C4B). Measurements were made with 0.8 and 1.2 mm relative displacements; $N_f = 1.1 \times 10^5$ cycles under $\pm 15.24 N\cdot m$, 5 Hz. Fuel particles collected $< 1.0 g$.

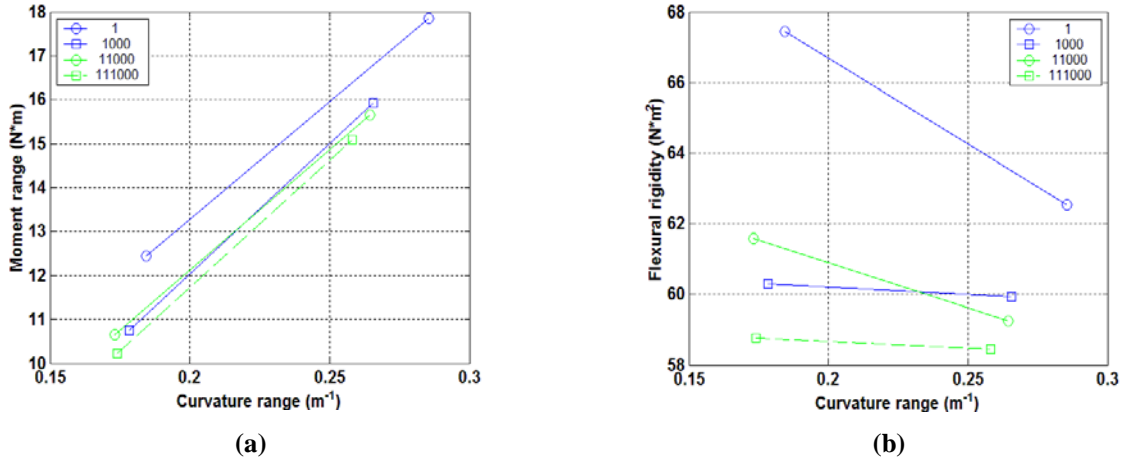


Figure 20. (a) Moment-curvature relation and (b) moment-flexural rigidity relation at various numbers of cycles for D1 (607C4B); $N_f = 1.1 \times 10^5$ cycles under ± 15.24 N·m, 5 Hz. Fuel particles collected <1.0 g.

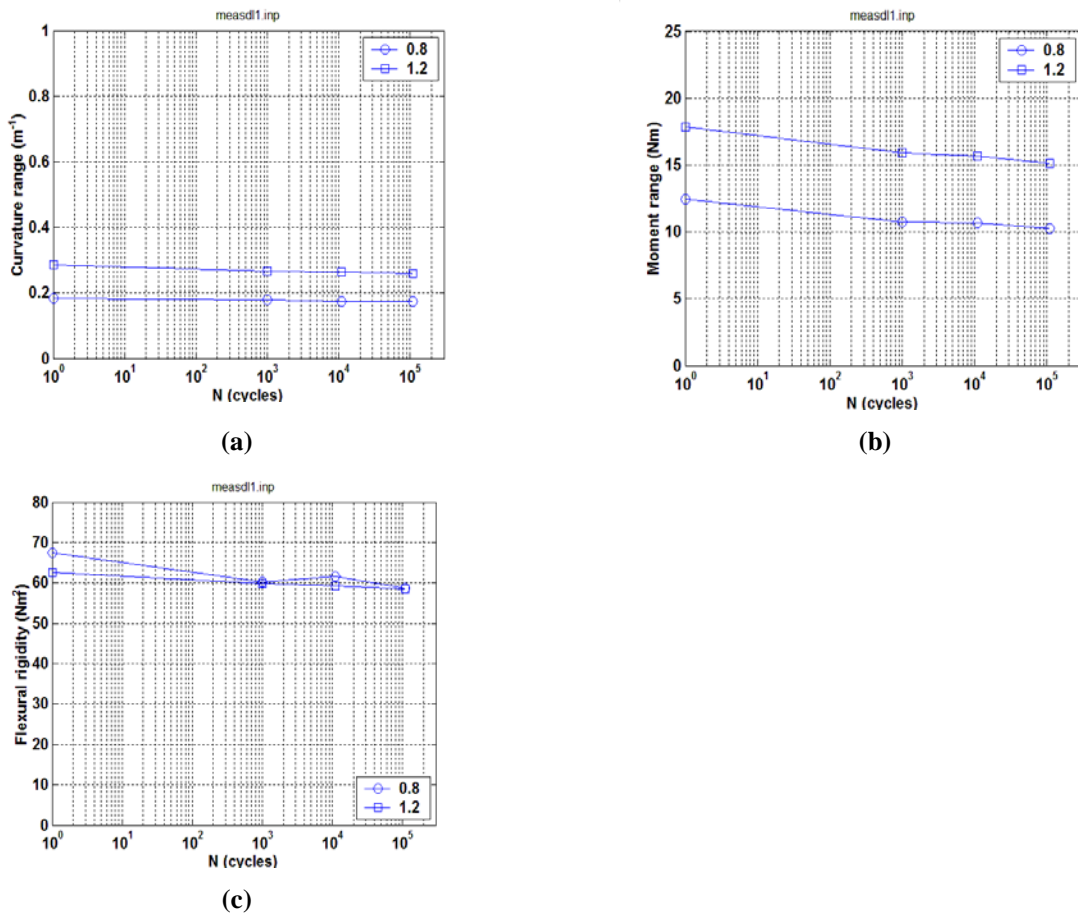


Figure 21. Variations of (a) curvature range, (b) moment range, (c) flexural rigidity as a function of number of cycles for D1 (607C4B); $N_f = 1.1 \times 10^5$ cycles under ± 15.24 N·m, 5 Hz. Fuel particles collected <1.0 g.

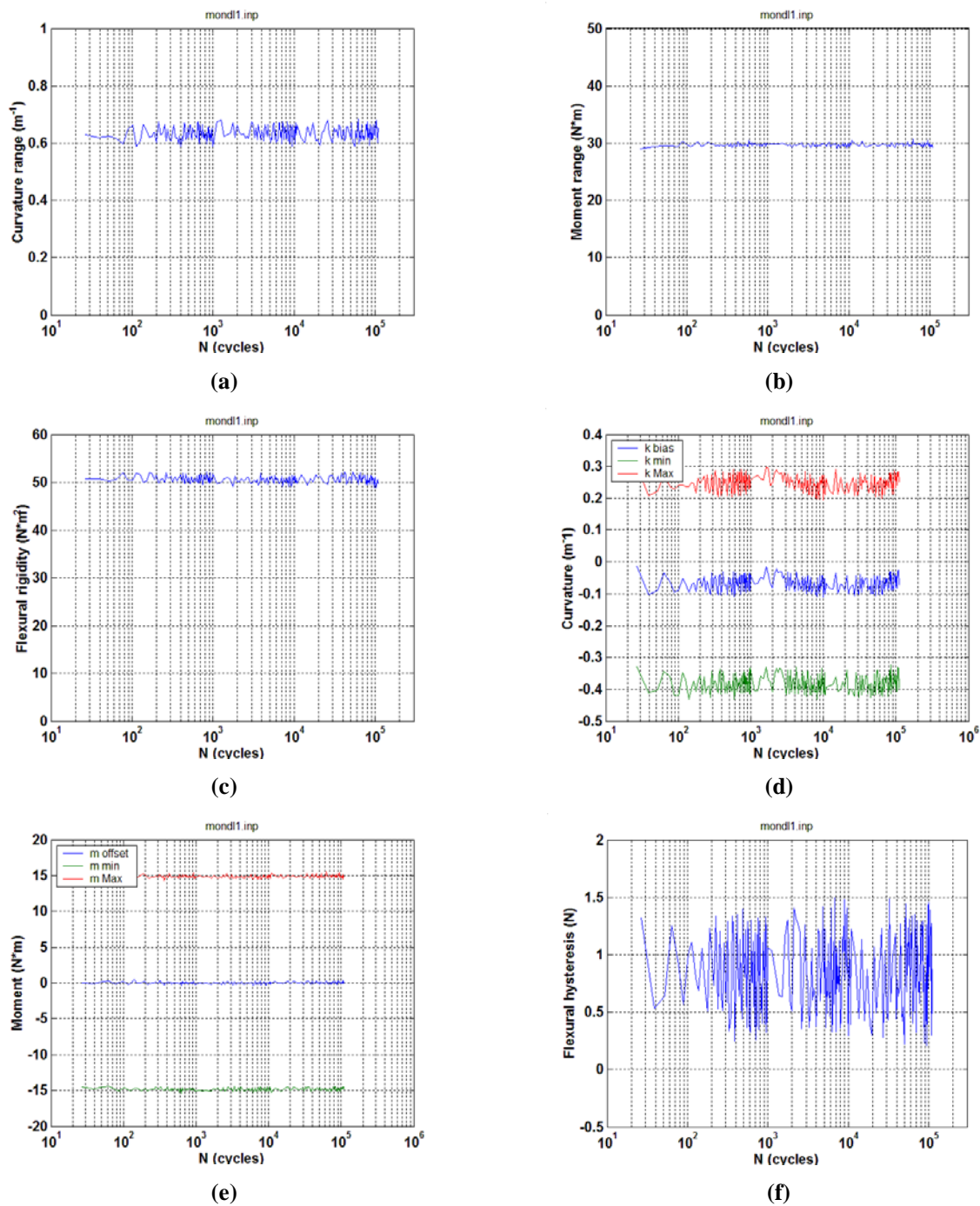


Figure 22. Variations of (a) curvature range, (b) applied moment range, (c) flexural rigidity, (d) maximum and minimum values of curvature, (e) maximum and minimum values of moment, and (f) flexural hysteresis as a function of number of cycles for D1 (607C4B); $N_f = 1.1 \times 10^5$ cycles under ± 15.24 N·m, 5 Hz. Fuel particles collected <1.0 g.

Moment and curvature time history and moment-curvature loops based on online monitoring at 26 and 1.10×10^5 cycles are shown in Figure 23. The curvature data appear to have a much higher noise level compared to that of SSAP out-of-cell test data, as shown in Figure 10. This is primarily due to there being two different calibration ranges for the LVDT setups used in the out-of-cell testing. The large-range setup is designated for static testing due to the large deformation required in that type of test, and the small-range setup which has higher sensitivity is designed for dynamic testing due to its lower test specimen deformation level. In a hot-cell environment, the current CIRFT device is only equipped with the large range calibration LVDT setup, which is used to cover both static and dynamic testing capabilities. Thus, the sensitivity of the small-range setup for the low load dynamic testing was sacrificed, resulting in the higher noise level in the curvature data of Figure 23. It is also noted that the symmetry curvature responses were observed at the beginning of cycles, which may indicate good interface bonds at the beginning of a test cycle, while at higher cycling, the nonsymmetry characteristic of curvatures under clad tension and compression cycles was observed in Figure 25.

The failure in test D1 was observed in the gage section near motor 2 (left side of the U-frame setup). The failure occurred at the pellet-to-pellet interface as illustrated in Figure 24. The end faces of the two neighboring pellets were essentially clean. Both of the stressed cylinder surfaces of the rod were found to have been covered with equally spaced circumferential cracks throughout the gage section. Spalling only occurred on the local area near the fracture. The degree of damage shown on both of the stressed cylinder surfaces of specimen D1 is different from the damage experienced in test specimens undergoing only unidirectional bending. The large deformation arising from the unidirectional bending can produce a greater extent of damage or spalling on one side of the test specimen with much less spalling on the other side of the specimen (for example, see S3 [609C5] in Table 3).

The details of the other dynamic tests can be seen in Appendix E. The dynamic testing results for HBR rods are summarized in Table 7, along with one rod from benchmarking (D0). The result for specimen D0 is considered to be effective in characterizing the cyclic fatigue of rods, as the test followed the dynamic testing procedure. Table 8 shows the failure modes of rods from the dynamic tests.

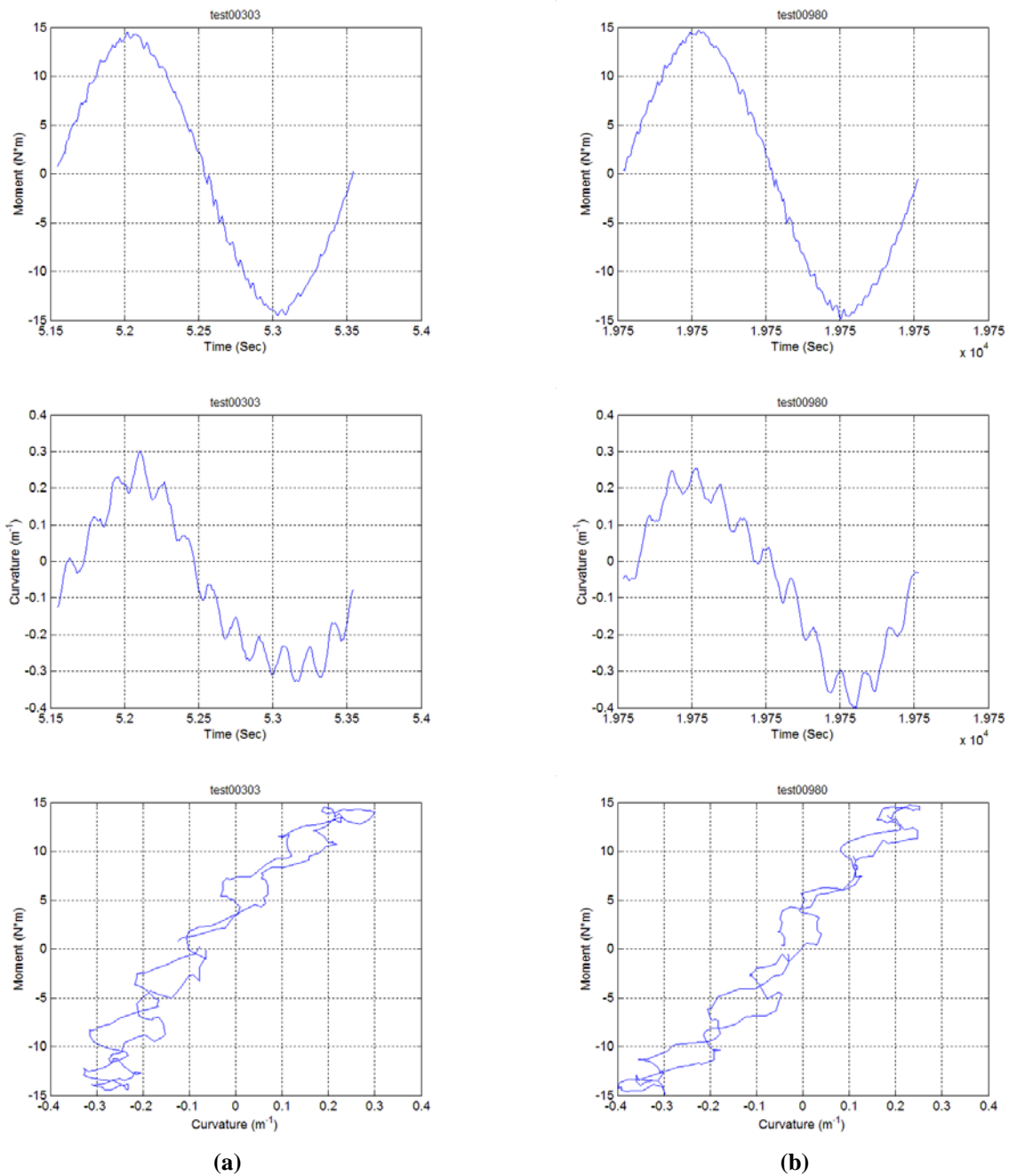


Figure 23. Moment and curvature as a function of time and moment-curvature loops at (a) 26 and (b) 1.10×10^5 cycles; results are based on online monitoring.

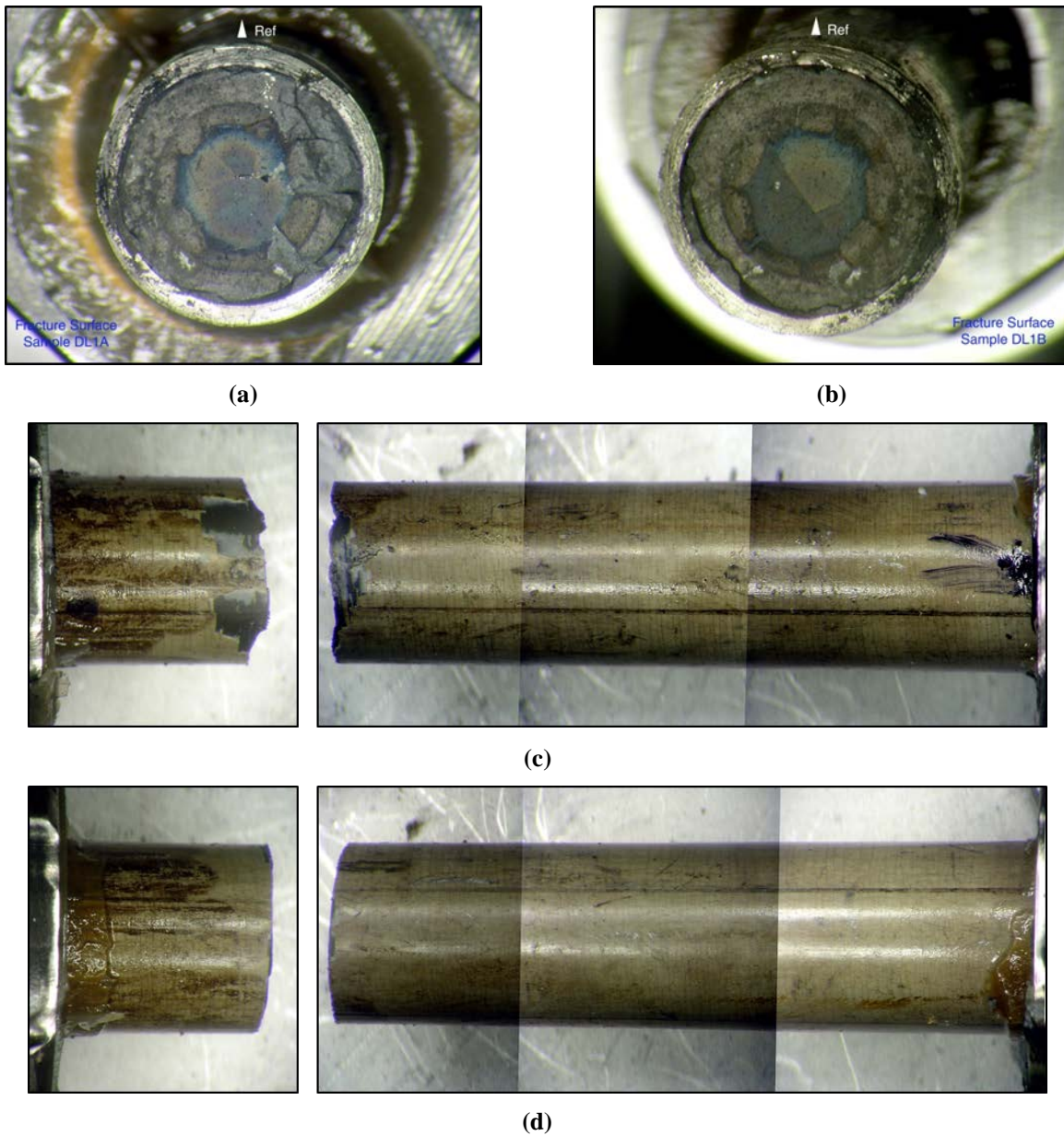


Figure 24. (a) and (b) Mating fracture surfaces, (c) frontal, and (d) back sides for D1 (607C4B), $N_f = 1.1 \times 10^5$ cycles under ± 15.24 N·m, 5 Hz. Fuel particles collected <1.0 g.

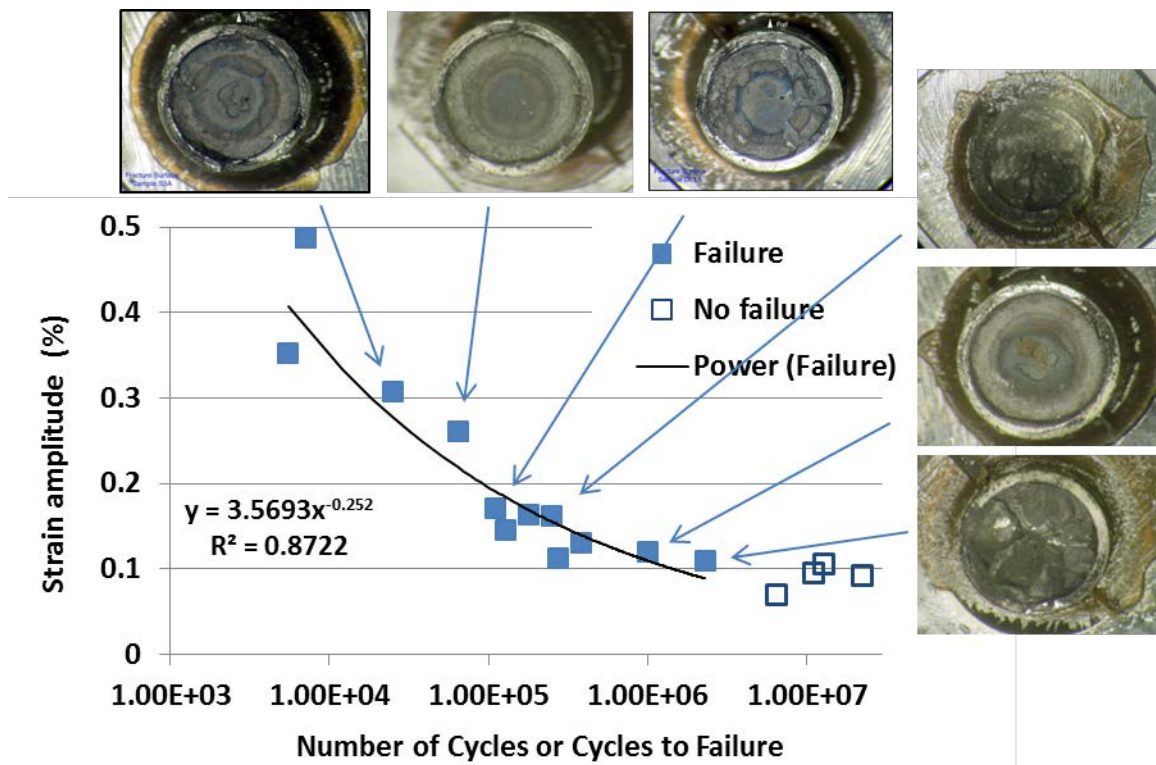


Figure 25. Equivalent strain amplitudes ($\Delta\epsilon/2$) as a function of number of cycles. Solid markers represent tests with specimen's failure; open markers indicate the tests stopped without failure.

Table 7. Summary of dynamic test results

Spec label	Seg. ID	Applied Load	Applied Moment amp.	Number of cycles	Failure **	$\Delta\varepsilon/2$	$\Delta\kappa/2$	$ \kappa _{\max}$	κ_m	κ_{\min}	κ_{\max}
		N	N·m			%	m ⁻¹	m ⁻¹	m ⁻¹	m ⁻¹	m ⁻¹
D0	605D1F	250	25.4	2.50×10 ⁴	1	0.3073	0.5712	0.6169	0.0457	-0.5254	0.6169
D1	607C4B	150	15.24	1.10×10 ⁵	1	0.1707	0.3173	0.3844	-0.0689	-0.3844	0.2465
D2	608C4B	50	5.08	6.40×10 ⁶	0	0.0706	0.1313	0.1629	0.0288	-0.1054	0.1629
D3	605C10A	100	10.16	1.00×10 ⁶	1	0.1202	0.2235	0.3305	-0.0968	-0.3305	0.1369
D4	605D1C	75	7.62	1.10×10 ⁷	0	0.0964	0.1791	0.2312	0.0582	-0.1149	0.2312
D5	605D1B	90	9.144	2.30×10 ⁶	1	0.1100	0.2045	0.2260	-0.0216	-0.2260	0.1829
D6	609C4	125	12.7	2.50×10 ⁵	1	0.1625	0.3021	0.3243	0.0222	-0.2799	0.3243
D7	609C3	200	20.32	6.50×10 ⁴	1	0.2607	0.4847	0.5023	-0.0176	-0.5023	0.4671
D8	606C3E	87.5	8.89	1.28×10 ⁷	0	0.1065	0.1979	0.2125	0.0184	-0.1756	0.2125
D9	609C7	350	35.56	7.10×10 ³	1	0.4882	0.9074	1.1903	0.2829	-0.6245	1.1903
D10	606C3A	125	12.7	1.80×10 ⁵	1	0.1628	0.3026	0.4015	0.0990	-0.2036	0.4015
D11	607C4A	300	30.48	5.50×10 ³	1	0.3528	0.6558	0.8533	0.1975	-0.4582	0.8533
D12	608C4A	110	11.176	3.86×10 ⁵	1	0.1311	0.2436	0.2845	-0.0409	-0.2845	0.2027
D13	606B3E	135	13.716	1.29×10 ⁵	1	0.1458	0.2710	0.3873	0.1164	-0.1546	0.3873
D14	606B3D	87.5	8.89	2.74×10 ⁵	1	0.1130	0.2100	0.2848	-0.0748	-0.2848	0.1351
D15	606B3C	75	7.62	5.11×10 ⁶	0	0.0926	0.1721	0.2445	0.0724	-0.0997	0.2445

** 1-failure, 0-without failure;

Table 8. Failure modes of rods from dynamic tests

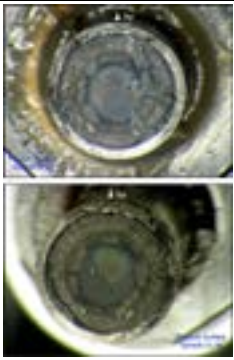
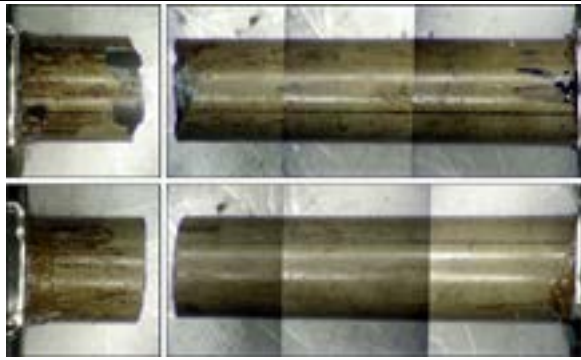

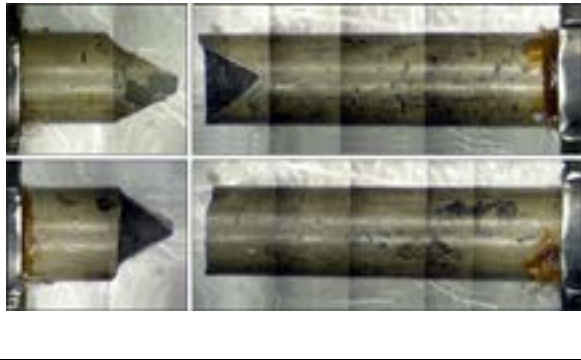
Spec label	Applied Moment amplitude	$\Delta\kappa$	Number of cycles to failure	Cross section	Lateral view
	N·m	m^{-1}			
D1, 607C4B	15.24	0.6346	1.10×10^5		
D2, 608C4B	5.08	0.2626	6.40×10^6 w/o failure; follow-up 35.56 N·m, 5 Hz with 1.8×10^3 cycles to failure		

Table 8. Failure modes of rods from dynamic tests (continued)

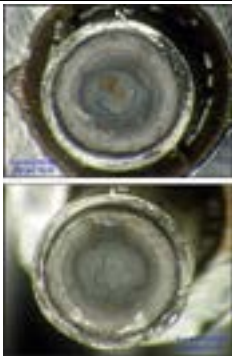
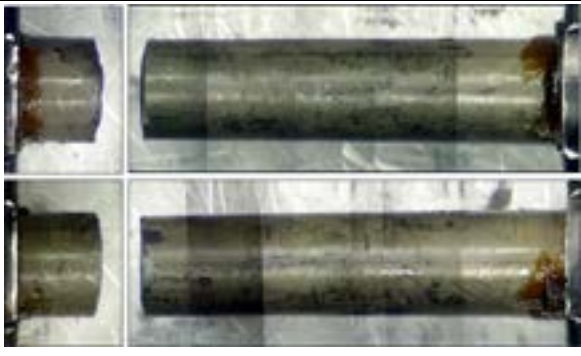

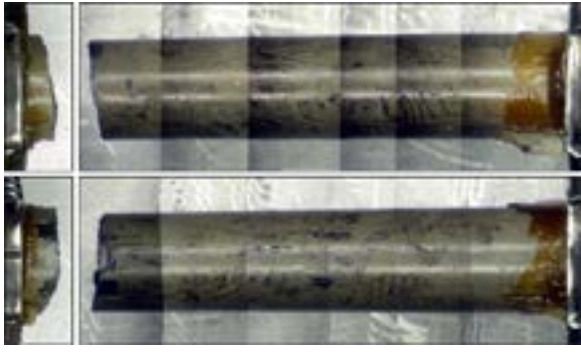
Spec label	Moment amplitude	$\Delta\kappa$	Number of cycles to failure	Cross section	Lateral view
	N·m	m^{-1}			
D3, 605C10A	10.16	0.4469	1.00×10^6		
D5, 605D1B	9.144	0.4089	2.30×10^6		

Table 8. Failure modes of rods from dynamic tests (continued)


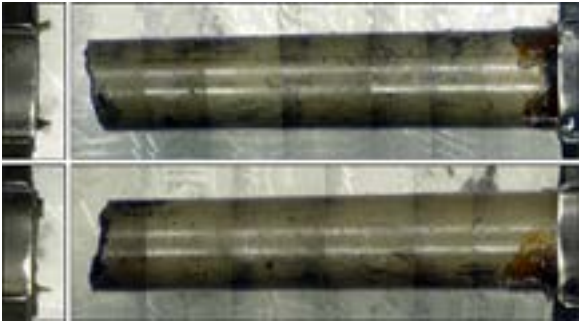
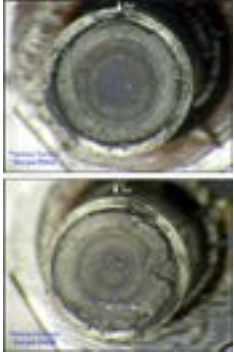
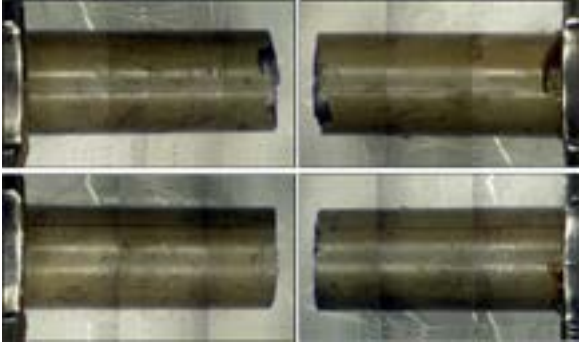
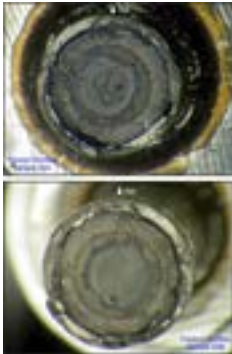
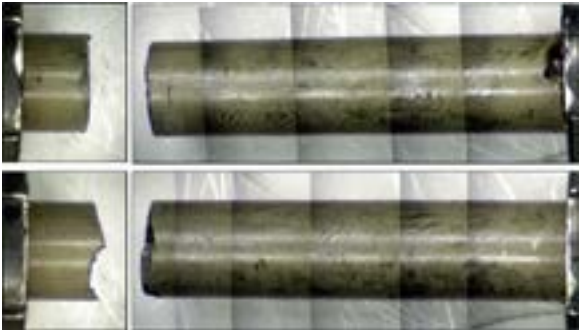
Spec label	Moment amplitude	$\Delta\kappa$	Number of cycles to failure	Cross section	Lateral view
	N·m	m^{-1}			
D6, 609C4	12.7	0.6042	2.50×10^5		
D7, 609C3	20.32	0.9693	6.50×10^4		

Table 8. Failure modes of rods from dynamic tests (continued)

Spec label	Moment amplitude	$\Delta\kappa$	Number of cycles to failure	Cross section	Lateral view
	N·m	m^{-1}			
D16, 605D1F	25.4	1.1423	2.50×10^4		

The equivalent strain amplitudes [ϵ_a , half of strain range $\Delta\epsilon/2$, and equivalent strain ϵ is based on Eq. (4)] as a function of the number of failure cycles are shown in Figure 25.

- For those specimens that failed during testing, the fatigue life decreases with increasing strain amplitude, resulting in a defined ϵ - N curve. The data points can be effectively fit by using the power function $y = 3.5693 x^{-0.252}$ with a correlation coefficient as high as 0.8722, where x is the number of cycles to failure and y is the strain amplitude (%).
- An endurance limit is likely located between 0.106 and 0.110% strains if it is defined at 10^7 cycles. In other words, below 0.1% strain amplitude there appears to be no number of cycles that will cause failure.
- A large variation of hydrogen content existed in the cladding of the test specimens in the dynamic tests. However, the contribution of hydrogen content to the number of cycles to failure appears to be secondary to the effect of imposed loading amplitudes.

The curve fitting to the strain amplitude versus number of cycles was extended to include the data points without failure by using two power functions, as presented in Figure 26. For $N \leq 10^6$, the power function was that based on failure data points, $y = 3.5693 \cdot x^{-0.252}$; for $N > 10^6$, $y = 0.3234 \cdot x^{-0.076}$. It can be seen that the correlation coefficient was quite lower for the second power function. This is because the amplitude is close to the endurance limit, and the number of failure cycles is likely independent of the applied load.

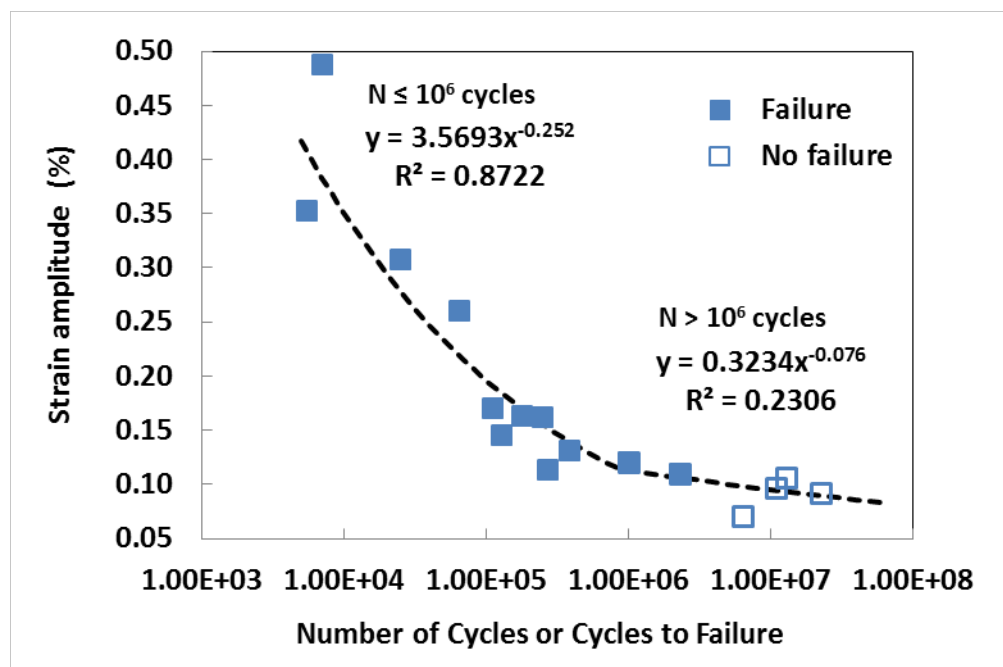


Figure 26. Equivalent strain amplitudes ($\Delta\epsilon/2$) as a function of number of cycles with curve fitting extended to include the data points without failure. Solid markers represent tests with specimen's failure; open markers indicate the tests stopped without failure.

4.2 Discussion

4.2.1 κ -N Curve

The equivalent strain amplitude has been used to describe the loading condition imposed on the rods. The use of equivalent strain provides an expedient means to estimate the global response of the tested rod. However, the more elaborated localized deformation mechanism involved with pellet-pellet interfaces cannot be readily represented by this simplified approach. In order to provide a more accurate representation of a fatigue lifetime estimate (in addition to the curvature range), a new parameter of maximum curvature was defined. Due to dishing on the pellet end and the existence of an oxide contact interface, it is expected that HBU fuel has a fairly weak interface bond at the pellet-pellet interface. This phenomenon was also observed in CIRFT test results where the flexural rigidity dropped off quickly in the initial cycles of testing and where a nonsymmetric curvature response was revealed in the reverse loading cycle. Asymmetrical deformation response is an important signature of the HBU SNF due to pellet-pellet-cladding interaction. The curvature at the cladding tensile stress site has the highest deformation during fatigue cycles, so it was used to develop the maximum curvature plots shown in Figure 27 to serve as another important index for the HBU SNF fatigue life.

The observations based on curvature amplitude (κ_a , half of curvature range $\Delta\kappa/2$) are similar to those of strain amplitude since the conversion simply involved a multiplication factor as shown in Eq. (4).

- The fatigue life decreases with increasing curvature amplitude with a defined κ -N curve. The curve fitting generated a power function $y = 6.6345 \cdot x^{-0.252}$ with a correlation coefficient 0.8722, where x is the number of cycles to failure and y is the curvature amplitude (m^{-1}).
- An endurance limit may be located between 0.198 and 0.204 m^{-1} if it is defined at 10^7 cycles.

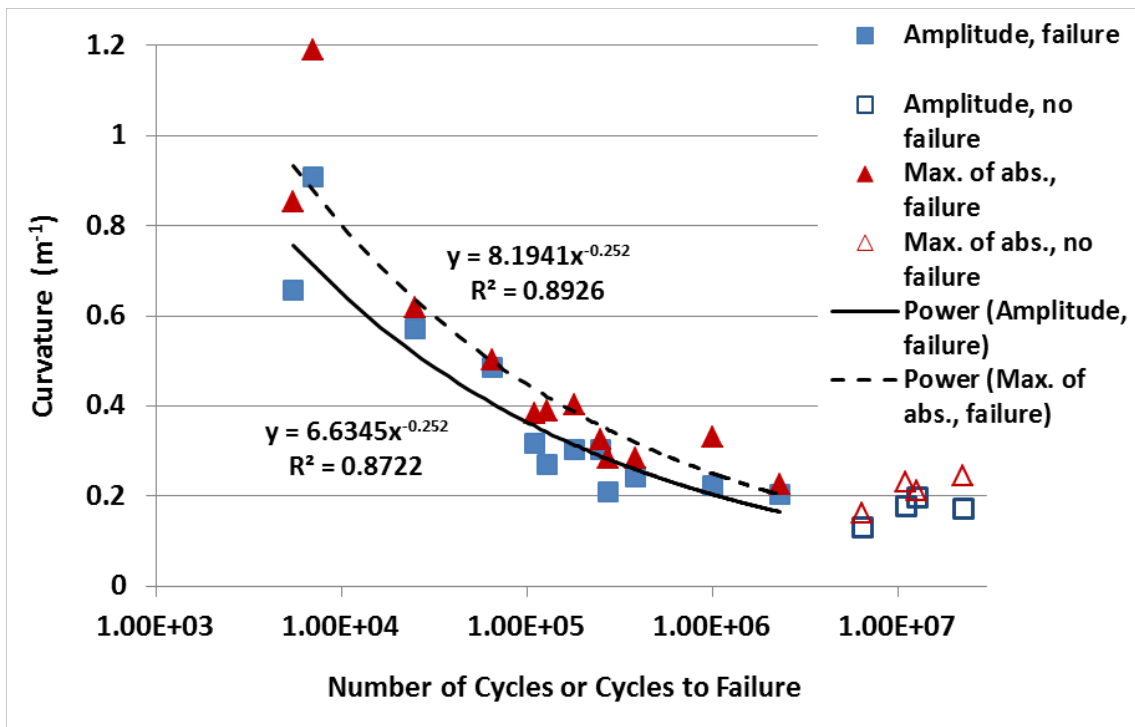
It is worth noting that the dynamic tests were conducted under load control, and the curvature response of the rods was not necessarily symmetric [Figure 22 (d)]. The mean values of the monitored mean curvatures, κ_m , were generally not at the zero level as seen in Table 7.

An investigation of the maxima of absolute values of curvature extremes ($|\kappa|_{max}$, defined in Section 2.6) was pursued as an alternative quantity for describing the loading imposed on fuel. This is significant because the maxima actually reflect the maximum tensile loading levels to which the specimen is subjected during the dynamic testing. The results are shown in Figure 27(a). The κ -N curve has been demonstrated in terms of maxima of cladding curvature $|\kappa|_{max}$ to be similar to that of the curvature amplitude κ_a ; the exponents of the curve-fit power function are in fact the same. The scatter plots based on the two approaches are similar with some changes in the relative positions of points between 1.1 and 3.9×10^5 cycles. Overall, the maxima of absolute curvature are larger than the curvature amplitude, depending on the magnitude of κ_m .

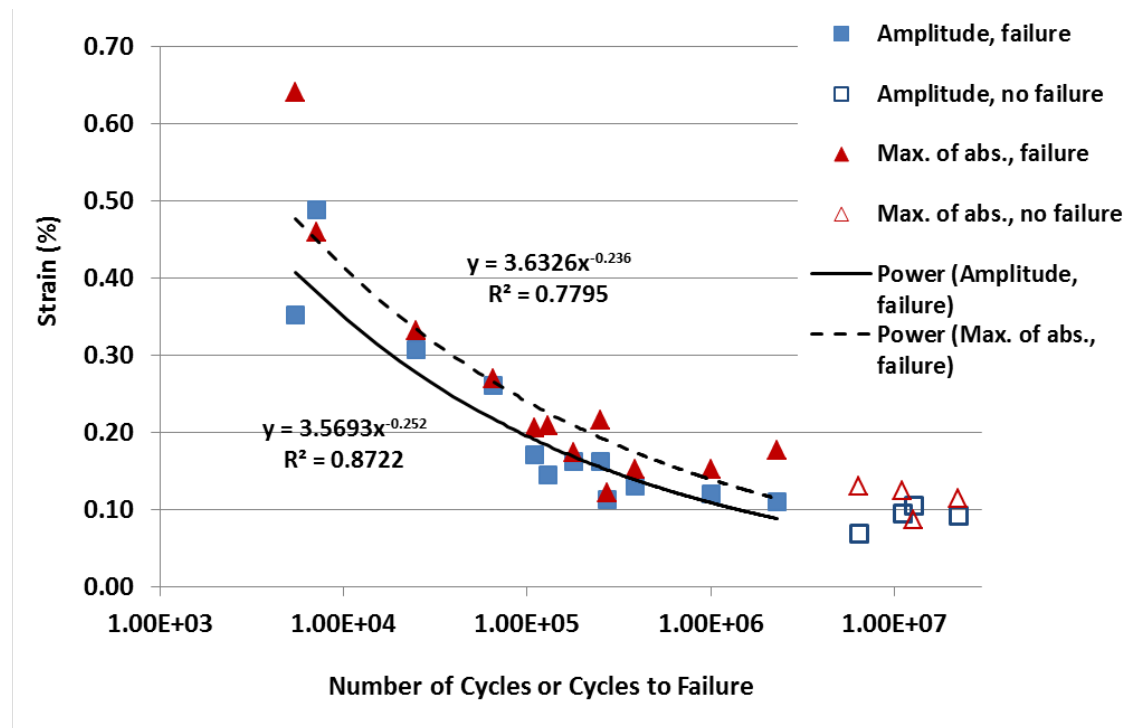
The following observations can be made with regard to curvature maxima:

For those specimens that failed during the tests, the fatigue life decreases with increasing curvature maxima according to a well-defined κ -N curve. The data points can be fit by using the power function $y = 8.1941 \cdot x^{-0.252}$ with a correlation coefficient as high as 0.8926, where x is the number of cycles to failure and y is the curvature maxima (m^{-1}).

A fatigue limit may be located between 0.226 and 0.245 m^{-1} if it is defined at 10^7 cycles.



(a)

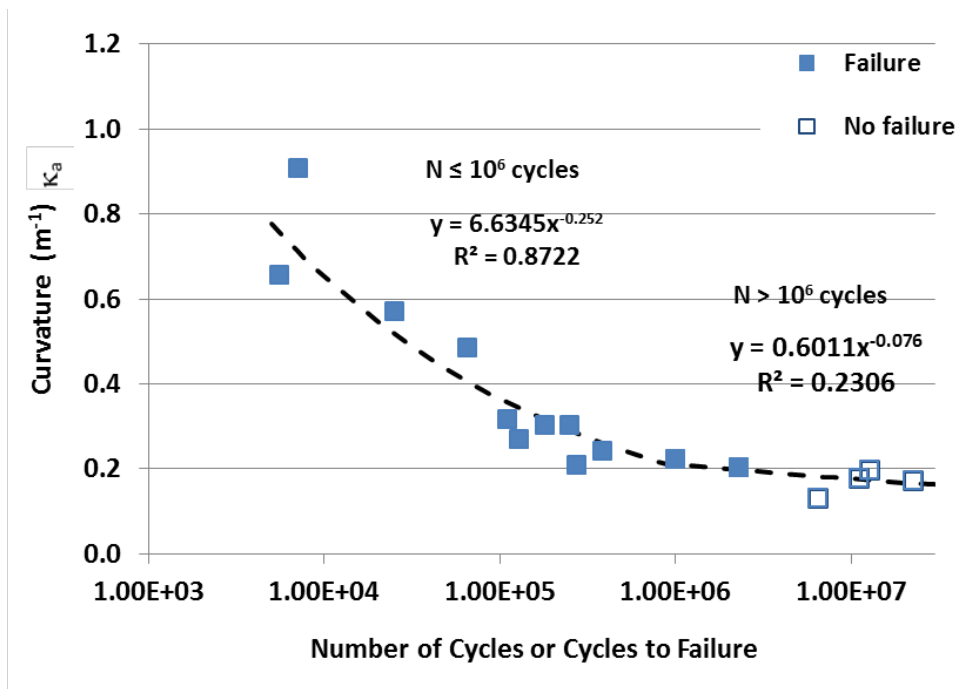


(b)

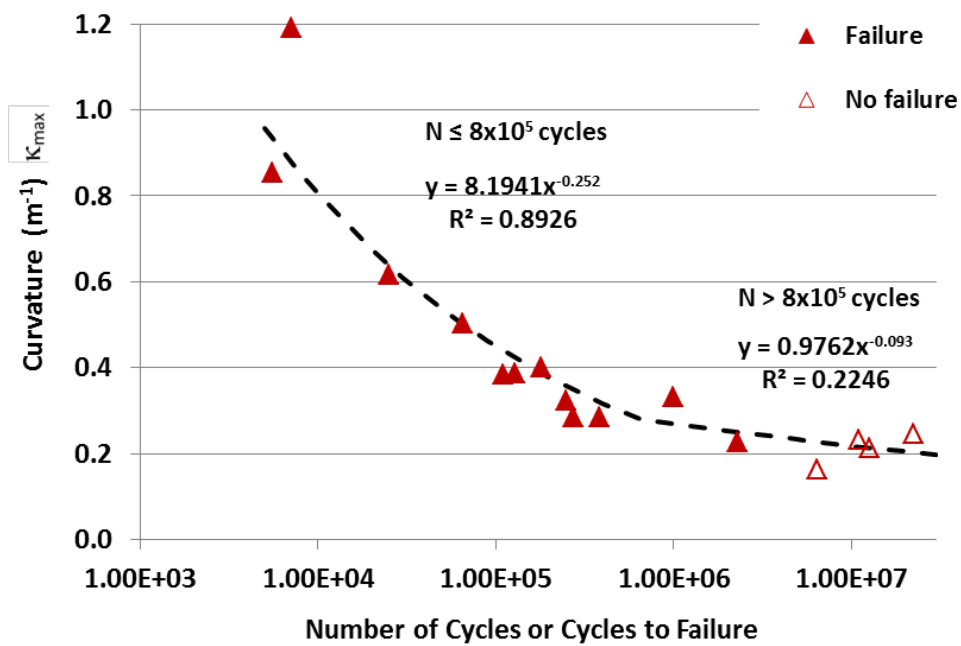
Figure 27. (a) Maxima of absolute curvature extremes and curvature amplitudes as a function of number of cycles, (b) Maxima of absolute strain extremes and strain amplitudes as a function of number of cycles. (Solid markers represent tests with specimen's failure; open markers indicate tests without failure.)

Due to the unsymmetrical deformation nature of HBU SNF under dynamic cycling, the bending neutral axis of the deformed rod is expected to shift away from the cladding tensile stress site. A first order approximation of simplified strain conversion from the curvature was used to derive the strain maxima vs. the number of failure cycles as shown in Figure 27(b).

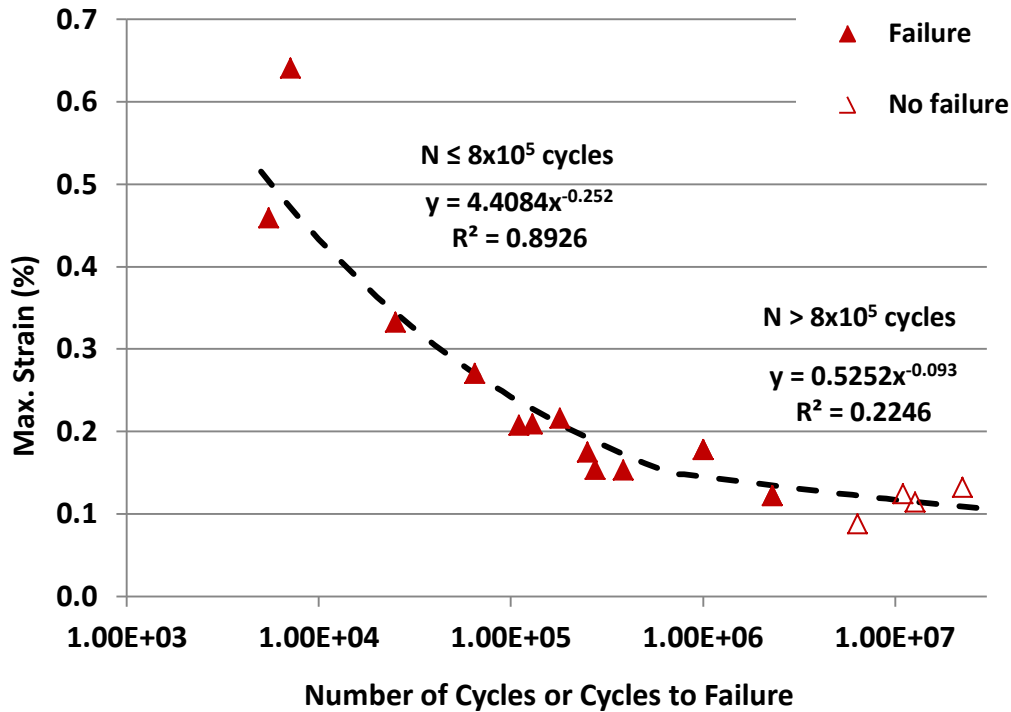
The curve fitting to the fatigue lifetime as a function of curvature amplitudes was extended to include the data points without failure by using two power functions, and the result is presented in Figure 28(a). For $N \leq 10^6$, the power function was that based on failure data points, $y = 6.6345 \cdot x^{-0.252}$; for $N > 10^6$, $y = 0.6011 \cdot x^{-0.076}$. The curve-fitting to the maxima of absolute curvatures resulted in the following power functions shown in Figure 30(b). For $N \leq 8 \times 10^5$, $y = 8.1941 \cdot x^{-0.252}$; for $N > 8 \times 10^5$, $y = 0.9762 \cdot x^{-0.093}$. The curve-fitting to the maxima of absolute strains resulted in the following power functions, shown in Figure 30(c). For $N \leq 8 \times 10^5$, $y = 4.4084 \cdot x^{-0.252}$; for $N > 8 \times 10^5$, $y = 0.5252 \cdot x^{-0.093}$.



(a)



(b)



(c)

Figure 28. (a) Curvature amplitudes, (b) maxima of absolute curvature extremes, and (c) maxima of absolute strain extreme as a function of number of cycles with curve-fitting extended to include the no-failure data points. Solid markers represent tests with specimen's failure; open markers indicate tests without failure.

4.2.2 Post-Irradiation Examination (PIE)

The objective of the PIE is to gather meaningful information to identify underlying failure mechanisms. The primary focuses are:

- To generate information on cladding features such as hydrides and incipient cracks near PPIs and near the mid-pellet.
- To reveal information about the fuel/cladding bond.
- To perform PIE with the fuel pellet intact to ensure that the SNF damage mechanism associated with P-C interaction and fuel failure can be preserved at the PPI region.

PIE was conducted on five fuel segments that were taken from the same father rod (E02-605) but with different mechanical loading histories:

- Untested – 605D1D
- Tested and failed under static loading condition at a PPI – S2/ 605D1E
- Tested but non-failed under dynamic loading condition – D4/ 605D1C
- Tested and failed under dynamic loading at a PPI – D3/ 605C10A
- Tested and failed under dynamic loading but not at PPI – D5/ 605D1B

PIEs were generally conducted on axial sections, while one PIE was carried out on a transverse section. For the tested and failed specimen, the preparation of axial sections mainly involved the following steps: (1) cut a one-inch segment on the fracture end, (2) mount the segment with the bending plane in the horizontal direction and cut the top half away, (3) back-pot the remaining half to keep all the fuel in place, and (4) grind and polish the section to the required finish for metallography. Examinations were then performed on an optical microscope.¹⁶ The section preparation for the other segments/specimens was similar to the above procedure.

PIE on the transverse section was conducted only on D3. The section was prepared using a piece of fuel rod approximately a quarter inch long cut away from the remaining half of specimen D3. The segment was defueled using hot nitric acid. The defueled cladding was removed from the hot cell and cleaned with water and alcohol in an ultrasonic cleaner. The inside and outside surfaces of the cladding were then coated with a thin layer of epoxy. The section was then ground and polished to the required finish for examination using scanning electron microscopy. Observations on the transverse section can be found in Appendix F, and those for the axial sections will be briefly discussed in the following.

An optical image of the axial section for untested segment 605D is shown in Figure 29.

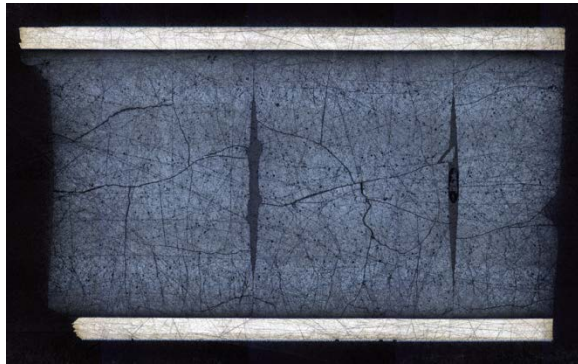
The three dished fuel pellets can be easily identified. Two primary fractures with sizes of pellet length and pellet radius were developed along and normal to the axial direction, respectively. Detailed study showed that the pellet-to-pellet interface near the edge of the dish and the pellet-to-cladding interface were fairly close without any visible gaps. Secondary fractures had developed within pellets near the peripheral area close to the pellet-to-cladding interfaces. A cavity is also observed around some triple boundaries of pellets and cladding. The circumferential hydride layers can be clearly seen over the cladding thickness. The circumferential hydrides are widely spaced in the large middle part of the wall. The density of the hydrides increases significantly toward the outside of the cladding and in the cladding-pellet interface area. The circumferential hydride layers are very sizable and, in the middle of the cladding wall, the layers can run more than 1000 μm . The outside surface of cladding is covered with a continuous thinner oxide layer that measured about 75 μm .



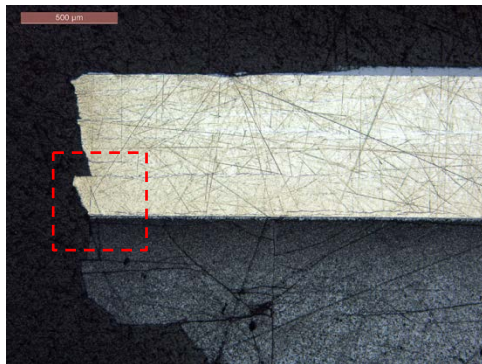
Figure 29. Optical images of untested segment 605D for (a) overall axial cross section and (b) enlarged area A.

Optical images based on the axial section of S2 specimen are shown in Figure 30. Fuel failure occurred at the PPI as seen from the left-side images. Unlike those in the untested fuel segment, the primary axial fractures did not align but tilted toward the axial direction.

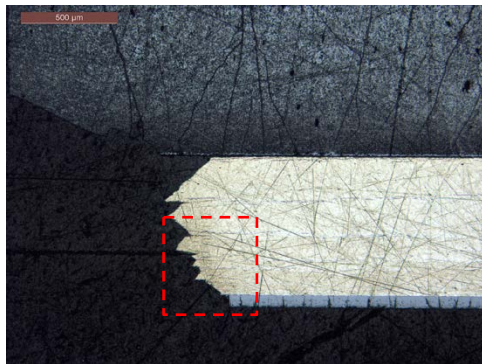
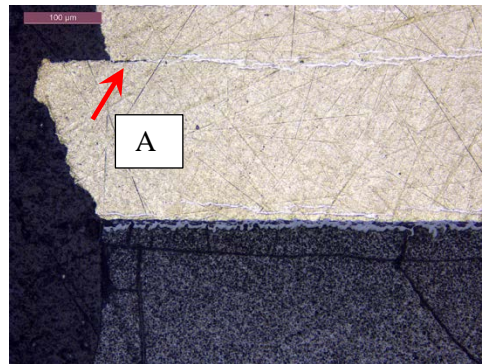
The pellet-to-cladding interface appeared to be in good contact. The fracture surface in the cladding exhibited a zigzag pattern both on the back and front sides of the specimen. The unique pattern resulted from the combination of brittle fracture of hydrides and ductile failure of the metal matrix under tension. Delamination can be seen over the hydride layers near the fracture surface. In addition, spalling and cracking of the surface oxide layer can be seen on the back and front sides.



(a)



(b)



(c)

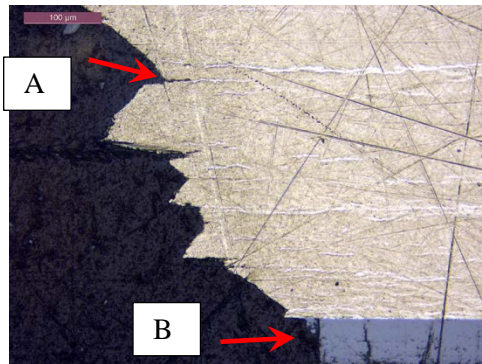


Figure 30. (a) Axial cross section of S2/ 605D1E, (b) fracture surface near back side of rod and an enlarged area, and (c) fracture surface near front side of rod and an enlarged area. A–delamination, B–cracking of oxide layer.

PIEs of the other fuel segments can be found in Appendix F, including five axial sections and one transverse section.

Some technical difficulty was encountered when preparing the PIE polished specimens. The foreign particles from the polished specimen (such as fine fuel particle due to possible micro fracturing of the fuel during dynamic testing) were easily brought into the working surface, introducing scratches.

The following observations were made based on the PIE.

- PPIs and pellet clad interfaces near the edges or peripheral area of pellets appeared to be in good contact. No significant gap or filling was observed in the interfaces.
- The pellets exhibited fracturing that was normal for irradiated fuel. These fractures were observed in both untested and tested fuel segments.
- Specimen failures occurred primarily at PPI.
- The density of the hydride layers increases significantly toward the outside of the cladding wall. The cladding outer wall was covered with an oxide layer of 75 μm thick.

5. CONCLUSIONS

High burnup H. B. Robinson fuel rods were tested and evaluated under both static and dynamic loading conditions using the CIRFT equipment developed at ORNL. The CIRFT system is composed of a U-frame equipped with load cells for imposing the pure bending loads on the spent fuel rod test specimen and measuring the in-situ curvature of the fuel rod during bending using a 3-LVDT setup. In general, the static CIRFT test results indicate a significant increase in flexural rigidity compared to that of the defueled HBU rod specimen. Nevertheless, the segment composite structure of an HBU rod also introduces numerous stress concentration sites into an HBU rod system, ultimately resulting in HBU specimen fractured at the pellet-pellet interface regions under dynamic CIRFT fatigue testing.

The static tests were conducted under displacement control at a rate of 0.1 mm/s to a maximum displacement of 12.0 mm at each loading point. Dynamic tests were conducted under load control of ± 5.08 to ± 35.56 N·m, 5 Hz. PIEs were performed on selected specimens. The following conclusions can be drawn:

- The HBU HBR rods survived static unidirectional bending to a maximum curvature of 3.1 to 3.5 m^{-1} or a maximum moment of 86 to 87 N·m (Table 4). The maximum equivalent strain was 1.7 to 1.9%, corresponding to an equivalent stress of 733 to 748 MPa (Table 5).
- The HBU HBR rods exhibited a multiple-stage constitutive response with two linear stages followed by a nonlinear stage. The flexural rigidity at the initial stage was 52 to 63 N·m², corresponding to an elastic modulus of 83 to 101 GPa (Table 5).
- The equivalent 0.2% yield strength of the HBU cladding was estimated at 687 to 727 MPa (Table 5), depending on the level of hydrogen content or magnitude of oxidation thickness.
- A large majority of the specimen failures of the HBU HBR rods under static unidirectional loading occurred near the PPI as validated by the post-test or PIEs.
- The fatigue life of HBU HBR rods in the cyclic test depended on the level of loading. Under loading with moments of ± 8.89 to ± 35.56 N·m, and strain of ± 0.07 to $\pm 0.49\%$ at 5 Hz (Table 7), the fatigue life ranged from 5.5×10^3 to 2.3×10^6 cycles.
- The ϵ -N curve of the HBU HBR rods can be described by a power function of $y = 3.5693 \cdot x^{-0.252}$, where x is the number of cycles to failure, and y is the strain amplitude (%).
- Based on strain amplitude, a fatigue limit is likely located between 0.106 and 0.110% if it is defined at 10^7 cycles.
- Maxima of the imposed curvature in dynamic tests ranged from ± 0.16 to $\pm 1.19 \text{ m}^{-1}$ at 5 Hz (Table 7). The κ -N curve of the HBU HBR rods can be described by a power function of $y = 8.1941 \cdot x^{-0.252}$, where x is the number of cycles to failure and y is the maxima of cladding tensile curvature $|\kappa|_{\text{max}}$ (m^{-1}). A fatigue limit is likely located between 0.226 and 0.245 m^{-1} if it is defined at 10^7 cycles.
- The failure of HBU HBR rods under cyclic reverse loading was primarily due to pellet-cladding interaction and generally resided at the pellet-to-pellet interface, as validated by the PIE.

6. REFERENCES

- 1 J.-A. J. Wang, H. Wang, Y. Yan, R. Howard, and B. Bevard, *High Burn-up Spent Fuel Vibration Integrity Study Progress Letter Report (Out-of-Cell Fatigue Testing Development–Task 2.1)*, ORNL/TM-2010/288, UT-Battelle, LLC, Oak Ridge National Laboratory, January 2011.
- 2 J.-A. J. Wang, H. Wang, T. Tan, H. Jiang, T. Cox, and Y. Yan, *Progress Letter Report on U Frame Test Setup and Bending Fatigue Test for Vibration Integrity Study (Out-of-Cell Fatigue Testing Development–Task 2.2)*, ORNL/TM-2011/531, UT-Battelle, LLC, Oak Ridge National Laboratory, January 2012.
- 3 J.-A. J. Wang, H. Wang, T. Cox, and Y. Yan, *Progress Letter Report on U-Frame Test Setup and Bending Fatigue Test for Vibration Integrity Study (Out-of-Cell Fatigue Testing Development–Task 2.3)*, ORNL/TM-2012/417, UT-Battelle, LLC, Oak Ridge National Laboratory, August 2012.
- 4 J.-A. J. Wang, H. Wang, and Ting Tan, *An Innovative Dynamic Reversal Bending Fatigue Testing System for Evaluating Spent Nuclear Fuel Rod Vibration Integrity or Other Materials Fatigue Aging Performance*, ORNL Invention Disclosure 201102593, DOE S 124,149, April 8, 2011, Patent in review, 13/396,413, February 14, 2012.
- 5 H. Wang, J.-A. J. Wang, T. Tan, H. Jiang, T. S. Cox, R. L. Howard, B. B. Bevard, and M. E. Flanagan, “Development of U-frame Bending System for Studying the Vibration Integrity of Spent Nuclear Fuel,” *Journal of Nuclear Materials* 440, 201–213 (2013).
- 6 J.-A. J. Wang, H. Wang, B. B. Bevard, R. L. Howard, and M. E. Flanagan, “SNF Test System for Bending Stiffness and Vibration Integrity,” *International High-Level Radioactive Waste Management Conference*, Albuquerque, N.M., April 28–May 2, 2013.
- 7 J.-A. J. Wang, H. Wang, T. Cox, and C. Baldwin, *Progress Letter Report on Bending Fatigue Test System Development for Spent Nuclear Fuel Vibration Integrity Study (Out-of-Cell Fatigue Testing Development–Task 2.4)*, ORNL/TM-2013/225, UT-Battelle, LLC, Oak Ridge National Laboratory, July 2013.
- 8 J.-A. J. Wang, H. Wang, B. B. Bevard, R. L. Howard, and M. E. Flanagan, “Reversible Bending Fatigue Test System for Investigating Vibration Integrity of Spent Nuclear Fuel During Transportation,” *Proceedings of the 17th International Symposium on the Packaging and Transportation of Radioactive Materials PATRAM 2013*, San Francisco, CA, August 18–23, 2013.
- 9 J.-A. J. Wang and H. Wang, *Progress Letter Report on Reversal Bending Fatigue Testing of Zry-4 Surrogate Rod (Out-of-Cell Fatigue Testing Development–Task 2.4)*, ORNL/TM-2013/297, UT-Battelle, LLC, Oak Ridge National Laboratory, August 2013.
- 10 G. Bjorkman, *High Burnup Spent Fuel Testing Program Objectives*, NRC Program Review Meeting, Oak Ridge National Laboratory, August 8, 2011.
- 11 J.-A. J. Wang and H. Wang, *2014 Semi-Annual Progress Letter Report on Used Nuclear Fuel Integrity Study in Transportation Environments*, ORNL/TM-2014/63, UT-Battelle, LLC, Oak Ridge National Laboratory, April 2014
- 12 C. Baldwin, Oak Ridge National Laboratory, Mar. 6, 2013.
- 13 U.S. Nuclear Regulatory Commission, *Cladding Embrittlement during Postulated Loss-of-coolant Accidents*, NUREG/CR-6967/ANL-07/04, Office of Nuclear Regulatory Research, Nuclear Regulatory Commission, July 2008

14 M.C. Billone, T. Burtseva, and Y.Y. Liu, "Baseline Properties and DBTT of High-Burnup PWR Cladding Alloys," *Proceedings of the 17th International Symposium on the Packaging and Transportation of Radioactive Materials*, PATRAM 2013, San Francisco, Calif., August 18–23, 2013.

15 J-A Wang, H. Jiang, *Quantification of CIRFT System Biases and Uncertainties When Testing High-Burnup Spent Nuclear Fuel*, ORNL/TM-2014/288, DOE FCRFD-2014-000604, UT-Battelle, LLC, Oak Ridge National Laboratory, September 2014.

16 R.S. Daum, S. Majundar, and M. C. Billone, "Experimental and analytical investigation of the mechanical behavior of high-burnup Zircaloy-4 fuel cladding," *J. ASTM International*, 5, Paper ID JAI101209.

17 J-A Wang, H. Jiang, and H. Wang, *Using Finite Model Analysis and Out of Hot Cell Surrogate Rod Testing to Analyze High Burnup Used Nuclear Fuel Mechanical Properties*, ORNL/TM-2014/257, DOE FCRD-UFD-2014-000603, UT-Battelle, LLC, Oak Ridge National Laboratory, August 2014.

**APPENDIX B. FINITE ELEMENT ANALYSIS ON HBR PWR SNF
MATERIAL**

This page intentionally left blank.

CONTENTS

APPENDIX B. FINITE ELEMENT ANALYSIS ON HBR PWR SNF MATERIAL	B-1
FIGURES.....	B-5
TABLES	B-7
ACRONYMS.....	B-9
1. INTRODUCTION	B-11
1.1 Background	B-11
1.2 Scope of Current Research	B-11
2. INTERFACE BONDING EFFICIENCY ANALYSIS OF FUEL ROD WITH HBR PELLETS	B-13
2.1 Good Interface Bonding and No HBR Fuel Rod System Fracture	B-13
2.1.1 Epoxy Used as Interfacial Material	B-16
2.1.2 Interfacial Material with $10 \times$ Young's Modulus Material.....	B-19
2.2 Debonding at Pellet-Pellet Interfaces and Bonding at Pellet-Clad Interfaces	B-24
2.2.1 Debonded Pellet-Pellet Interfaces with Empty Gaps.....	B-25
2.2.2 Debonded Pellet-Pellet Interfaces without Gaps.....	B-33
2.3 Debonded Pellet-Clad and Pellet-Pellet Interfaces	B-41
2.3.1 Debonded Pellet-Clad Interfaces and Debonded Pellet-Pellet Interfaces with Empty Gaps.....	B-42
2.3.2 Debonded Pellet-Clad Interfaces and Debonded Pellet-Pellet Interfaces without Gaps	B-48
2.4 Clad Curvature Estimation	B-56
2.4.1 Epoxy Used as Interfacial Material	B-58
2.4.2 Interfacial Material with a $10 \times$ Young's Modulus	B-60
2.5 Clad Stress Investigation and Comparison.....	B-62
2.5.1 Clad Stress Estimation from Conventional Approach Based on Curvature and Flexural Strain.....	B-62
2.5.2 Clad Stress Comparison between Different Interface Bonding Conditions.....	B-65
3. CONCLUSION	B-68
4. REFERENCES	B-71

This page intentionally left blank.

FIGURES

Figure 1. Geometry of horizontal U-frame bending fatigue testing system with a coplanar rod configuration.	B-13
Figure 2. Image of one-inch HBR rod segment from a hot-cell testing sample.	B-14
Figure 3. FEA model of HBR pellet.	B-14
Figure 4. Geometry of clad-epoxy-pellet two inch section model with eight HBR pellets.	B-15
Figure 5. Detail area from Figure 4 for the perfect bond cases.	B-16
Figure 6. Normal stress distribution and curvature results for clad-epoxy-pellet section model of HBR pellets with perfect bonding using epoxy.	B-18
Figure 7. Shear stress distribution at the clad for the clad-epoxy-pellet section model of pellets with perfect bonding using epoxy.	B-19
Figure 8. Normal stress distribution and curvature results for the clad-epoxy-pellet section model of HBR pellets with perfect bonding using a cohesive bonding material with a $10 \times$ Young's modulus material.	B-20
Figure 9. Shear stress distribution at the clad of the clad-epoxy-pellet section model of HBR pellets with perfect bonding using a cohesive bonding material with a $10 \times$ Young's modulus material.	B-22
Figure 10. ORNL hot-cell CIRFT data, flexural rigidity, and curvature [3].	B-23
Figure 11. Transportation-induced reversal bending stress fields in an SNF system.	B-25
Figure 12. Detail from Figure 4 for the case of empty gaps at debonded pellet-pellet interfaces.	B-26
Figure 13. Normal stress distribution and curvature results for the clad-epoxy-pellet section model of HBR pellets with debonded pellet-pellet interfaces with gaps, and bonded pellet-clad interfaces using epoxy.	B-27
Figure 14. Shear stress distribution at the clad of the clad-epoxy-pellet section model of HBR pellets with debonded pellet-pellet interfaces with gaps and bonded pellet-clad interfaces using epoxy.	B-29
Figure 15. Normal stress distribution and curvature results for clad-epoxy-pellet section model of HBR pellets with debonded pellet-pellet interfaces with gaps, and bonded pellet-clad interfaces using a $10 \times$ Young's modulus material.	B-31
Figure 16. Shear stress distribution at the clad of clad-epoxy-pellet section model of HBR pellets with debonded pellet-pellet interfaces with gaps, and bonded pellet-clad interfaces using a $10 \times$ Young's modulus material.	B-33
Figure 17. Detail from Figure 4 for the case of no gaps at debonded pellet-pellet interfaces.	B-34
Figure 18. Normal stress distribution and curvature results for clad-epoxy-pellet section model of HBR pellets with debonded pellet-pellet interfaces without gaps, and bonded pellet-clad interfaces using epoxy.	B-35
Figure 19. Shear stress distribution at the clad of the clad-epoxy-pellet section model of HBR pellets with debonded pellet-pellet interfaces without gaps, and bonded pellet-clad interfaces using epoxy.	B-37
Figure 20. Normal stress distribution and curvature results for clad-epoxy-pellet section model of HBR pellets with debonded pellet-pellet interfaces without gaps, and bonded pellet-clad interfaces using a $10 \times$ Young's modulus material.	B-38
Figure 21. Shear stress distribution results at the clad of the clad-epoxy-pellet section model of HBR pellets with debonded pellet-pellet interfaces without gaps, and bonded pellet-clad interfaces using a $10 \times$ Young's modulus material.	B-40
Figure 22. Detail area from Figure 4 for the cases of empty gaps at debonded pellet-pellet interfaces, and a thin layer filled at the debonded pellet-clad interfaces.	B-42

Figure 23. Normal stress distribution and curvature results for clad-epoxy-pellet section model of HBR pellets with empty gaps at debonded pellet-pellet interfaces, and an epoxy layer at debonded pellet-clad interfaces. B-43

Figure 24. Shear stress distribution at the clad of the clad-epoxy-pellet section model of HBR pellets with empty gaps at debonded pellet-pellet interfaces, and an epoxy layer at debonded pellet-clad interfaces. B-45

Figure 25. Normal stress distribution and curvature results for clad-epoxy-pellet section model of HBR pellets with empty gaps at debonded pellet-pellet interfaces, and a layer with a $10 \times$ Young's modulus material at debonded pellet-clad interfaces. B-46

Figure 26. Shear stress distribution at the clad of clad-epoxy-pellet section model of HBR pellets with empty gaps at debonded pellet-pellet interfaces, and a layer of $10 \times$ Young's modulus material at debonded pellet-clad interfaces. B-48

Figure 27. Detail area from Figure 4 for the case with no gaps at debonded pellet-pellet interfaces and a thin layer at debonded pellet-clad interfaces. B-49

Figure 28. Normal stress distribution and curvature results for the clad-epoxy-pellet section model of HBR pellets without gaps at debonded pellet-pellet interfaces, and with an epoxy layer at debonded pellet-clad interfaces. B-50

Figure 29. Shear stress distribution and curvature results for the clad-epoxy-pellet section model of HBR pellets without gaps at debonded pellet-pellet interfaces, and with an epoxy layer at debonded pellet-clad interfaces. B-52

Figure 30. Normal stress distribution and curvature results for the clad-epoxy-pellet section model of HBR pellets without gaps at debonded pellet-pellet interfaces, and with a layer of $10 \times$ Young's modulus material at debonded pellet-clad interfaces. B-53

Figure 31. Normal stress distribution and curvature of clad-epoxy-pellet section model of HBR pellets without gaps at debonded pellet-pellet interfaces, and with a layer of $10 \times$ Young's modulus material at debonded pellet-clad interfaces. B-55

Figure 32. CIRFT system with horizontal U-frame test setup integrated to Bose dual LM2 TB. B-56

Figure 33. Sketch for curvature calculation. B-57

Figure 34. Curvature estimations from the deflection data at the tension side of the clad for case using epoxy as the interfacial material. B-58

Figure 35. Curvature estimations from the deflection data at the compression side of the clad for the case using epoxy as the interface material. B-59

Figure 36. Curvature estimations from the deflection data at the tension side of the clad for the case using the $10 \times$ Young's modulus material. B-61

Figure 37. Curvature estimations from the deflection data at the compression side of the clad for the $10 \times$ Young's modulus material. B-62

Figure 38. Flexural strain evaluation of a uniform rod. B-63

Figure 39. Clad neutral axis at geometric center line for perfect interface bonding. B-64

Figure 40. Clad neutral axis shifts from geometric center line for pellet-pellet interface debond and pellet-clad interface bond case. B-64

TABLES

Table 1. Mechanical properties of the fuel rod	B-13
Table 2. The curvature, flexural rigidity, and bending moment comparison for the perfect interface bonding simulation.....	B-22
Table 3. Comparison of curvature, flexural rigidity, and bending moment for the bonded pellet-clad and debonded pellet-pellet cases.....	B-40
Table 4. The curvature, flexural rigidity and bending moment comparison for debonded pellet-clad and pellet-pellet interfaces.....	B-55
Table 5. Estimated curvature and flexural rigidity comparison from the tension side of the clad for case using epoxy as the interfacial material.....	B-59
Table 6. Estimated curvature and flexural rigidity comparison from the compression side of the clad for the case using epoxy as the interface material.....	B-60
Table 7. Estimated curvature and flexural rigidity comparison from the tension side of the clad for the interface material with a $10 \times$ Young's modulus.....	B-61
Table 8. Estimated curvature and flexural rigidity comparison from the compression side of the clad for the interface material with a $10 \times$ Young's modulus	B-62
Table 9. Estimated normal stress compared with FEA stress profile	B-65
Table 10. Clad normal stress comparison at tension side for different interface bonding conditions	B-66
Table 11. Clad normal stress comparison at compression side for different interface bonding conditions.....	B-66
Table 12. Clad shear stress comparison at tension side for different interface bonding conditions.....	B-67
Table 13. Clad shear stress comparison at compression side for different interface bonding conditions.....	B-67
Table 14. The flexural rigidity comparison between the different bonding and debonding cases	B-69

This page intentionally left blank.

ACRONYMS

CIRFT	cyclic integrated reversible-bending fatigue tester
DOE	Department of Energy
FEA	finite element analysis
HBR	H.B. Robinson
HBU	high burnup
ID	inner diameter
LVDT	linear variable differential transformers
OD	outer diameter
ORNL	Oak Ridge National Laboratory
RD&D	research, development, and deployment
SNF	spent nuclear fuel

This page intentionally left blank.

1. INTRODUCTION

1.1 Background

The research detailed in this report was conducted to support the Department of Energy (DOE) Used Fuel Disposition Campaign modeling, simulation, and experimental integration research, development, and deployment (RD&D) plan for spent nuclear fuel (SNF) integrity and structural performance under normal conditions of transportation [1].

The Oak Ridge National Laboratory (ORNL) has developed the cyclic integrated reversible-bending fatigue tester (CIRFT) approach to successfully demonstrate the controllable fatigue fracture on high burnup (HBU) SNF in a normal vibration mode. CIRFT enables examination of the underlying mechanisms of SNF system dynamic performance. The major findings of CIRFT on the HBU SNF are as follows:

- SNF system interface bonding plays an important role in SNF vibration performance.
- Fuel structure contributes to the SNF system stiffness.
- There are significant variations in stress and curvature of SNF systems during vibration cycles resulting from segment pellets and clad interaction.
- SNF failure initiates at the pellet-pellet interface region and appears to be spontaneous.

Due to the inhomogeneous composite structure of the SNF system, finite element analysis (FEA) is needed to translate the global moment-curvature measurement into local stress-strain profiles for further investigation. Furthermore, the detailed mechanisms of the pellet-pellet and pellet-clad interactions and the stress concentration effects at the pellet-pellet interface cannot be readily obtained from a CIRFT system measurement. Therefore, detailed FEA will be necessary to obtain further interpretation of the global test response.

The FEA protocols developed for this project provide powerful tools to quantify the CIRFT system biases and the associated uncertainties on the HBU SNF under CIRFT.

This project report also provides the FEA methodology used to evaluate the effects of pellet-pellet and pellet-clad interactions. The methodology is a road map for further protocol development with respect to the effective lifetime prediction of the SNF system under normal transportation vibration.

This study provides detailed explanations of the effects of pellet-pellet and pellet-clad interactions—including pellet fracture and pellet-clad bonding efficiency—on the clad performance reliability. The FEA simulation results were also calibrated and benchmarked with fatigue aging data [2] obtained from ORNL reversal bending fatigue testing.

1.2 Scope of Current Research

The objective of this research is to use the FEA protocols to translate the global response of CIRFT examination to the local stress-strain level and to quantify the CIRFT system biases and associated uncertainties on the HBU SNF under CIRFT.

The FEA simulation results were validated and calibrated by ORNL reversal bending fatigue testing of the H.B. Robinson (HBR) Steam Electric Plant fuel rod.

The FEA models were developed using the ABAQUS FEA software suite. They consist of a two-inch gauge section covering the Zr-4 clad and HBR pellets and interfacial layers that provide chemical cohesive bonding or mechanical radial compressive residual stresses from pellet-clad contact pressure. To estimate fuel rod system responses, including the stress profile and the associated curvature κ , bending moments (M) were applied to both ends of the fuel rod. Based on the FEA results, the flexural rigidity (EI) of the simulation cases was estimated as $EI = M/\kappa$. The detailed discussion of the simulation cases is divided into three sections:

- a section model with good interface bonding and without pellet fracture,
- a section model with good bonding at pellet-clad interfaces and debonding at pellet-pellet interfaces, and
- a section model with debonding at both pellet-clad and pellet-pellet interfaces.

Each section includes a comparison and discussion of the simulation results for (1) an interfacial material using epoxy and (2) an interfacial material with a Young's modulus 10 times that of epoxy (abbreviated hereinafter as "10 × Young's modulus material"). The curvature of a fuel rod system estimated from global and local deflection data for the clad was studied in detail based on the tension and the compression sides of the clad. The fuel composite system neutral axis shift was investigated. Based on the estimated curvature and flexural strain adjusted with the neutral axis shift, the normal stress has been estimated and compared with FEA results for nonuniform distributed stresses. FEA results for normal stress and shear stress for different interface bonding conditions also are compared and discussed.

2. INTERFACE BONDING EFFICIENCY ANALYSIS OF FUEL ROD WITH HBR PELLETS

Following the method described in Refs. 2, 3, and 4, ABAQUS was used for a structural analysis and interfacial bonding evaluation of fuel rods with HBR pellets. The rods were tested in a hot-cell environment in the CIRFT developed by ORNL [5–7]. To validate the simulation results, the same fuel rod materials were used in the hot-cell tests and the FEA. The HBR pellet material was UO_2 , and the clad material was Zr-4. An epoxy was used as an interface bonding material to simulate fused areas. Table 1 lists the material properties of the fuel rod.

Table 1. Mechanical properties of the fuel rod

Material	Young's modulus (psi)	Poisson's ratio	Yield strength (psi)	Density (lb/in. ³)
UO_2^a	2.92e7	0.32	3.11e5	0.396
Zircaloy-4 ^a	1.32e7	0.33	1.31e5	0.237
Epoxy ^a	5.07e5	0.37	10007.6	0.0452

^a Ref. [7]

2.1 Good Interface Bonding and No HBR Fuel Rod System Fracture

Figure 1 shows the geometry of a U-frame bending fatigue testing system with a coplanar configuration for the fuel rod. The two-inch gauge section is highlighted in black. A finite element model was established to represent the two-inch gauge section of the test specimen. The model is referred to as the “clad-epoxy-pellet section model.”

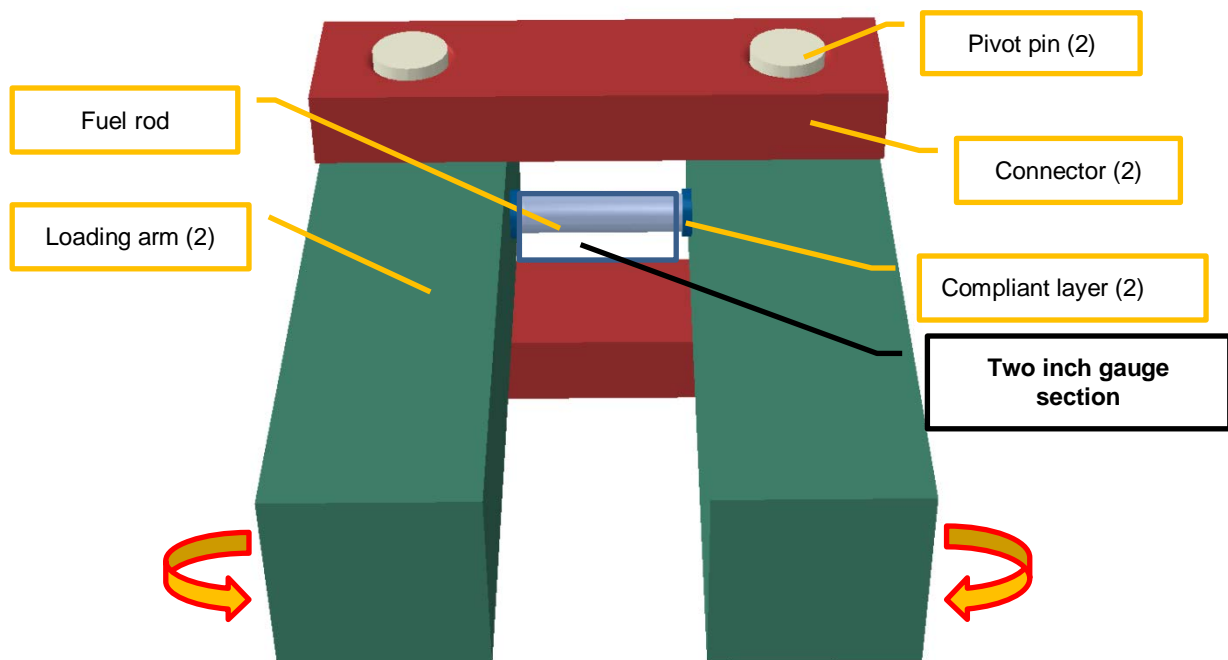


Figure 1. Geometry of horizontal U-frame bending fatigue testing system with a coplanar rod configuration.

Figure 2 shows a one-inch HBR rod segment from a hot-cell testing sample. The measured outer diameter (OD) of the clad is 0.425 in. The cladding thickness is 0.031 in., so the inner diameter (ID) is 0.364 in.

Figure 2 gives a clear view of the HBR pellets. The pellet length is 0.273 in., much less than the 0.6 in. length of the surrogate rod in a previous report [3]. The pellet ends dish in to reduce pellet surface clinging (Figure 2). The pellet OD is 0.354 in. An HBR pellet was modeled by FEA to represent the real testing sample (Figure 3). Both ends of the pellet were constructed with a dip diameter of 0.25 in. and a depth of 0.0006 in. so that the end surfaces would not touch at the dished-in area.



Figure 2. Image of one-inch HBR rod segment from a hot-cell testing sample.

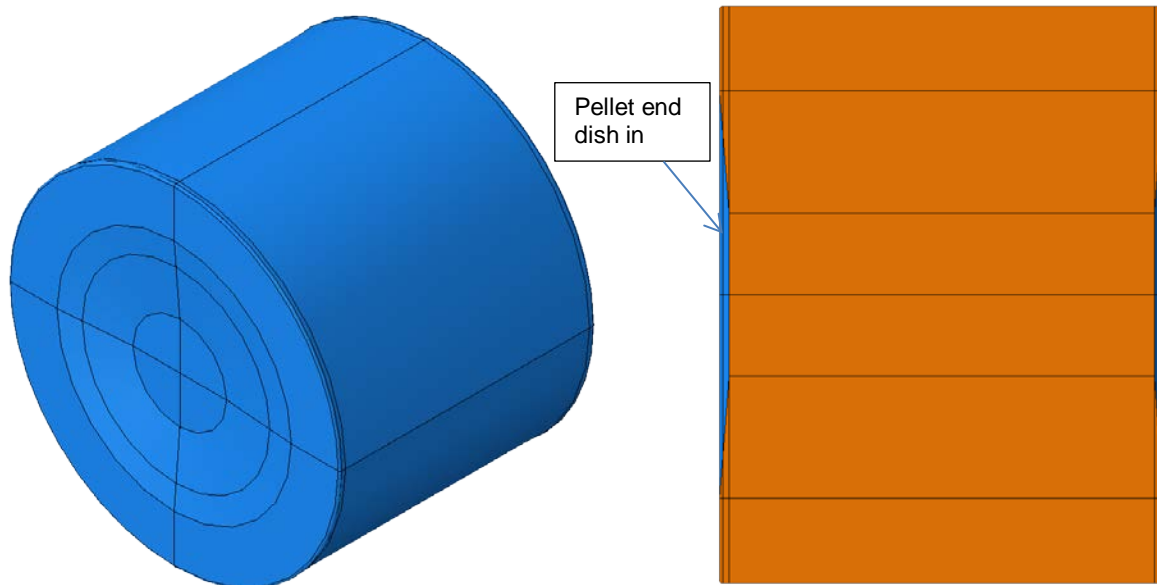


Figure 3. FEA model of HBR pellet.

Figure 4 illustrates the clad-epoxy-pellet section model with HBR pellets. In the two-inch gauge section, six full-length and two partial-length pellets were modeled. The epoxy is 0.005 in. thick. To simulate “good interface bonding” at the pellet-pellet interface and an unfractured rod system, the pellet-pellet and pellet-clad interfaces were all tied. Bending moments were applied on both ends of the fuel rod rotating along the X axis as shown in Figure 4(b). To validate the FEA simulation with the hot-cell testing data, the bending moment M_x was the same as that used in the tests—6.25 N·m. Both loading surfaces of the HBR fuel rod were constrained with rotation along the Y and Z axes and translation along the X direction. In the following finite element models, the global mesh is 0.02 in., and some local meshes are as small as 0.0025 in. The quasistatic procedure is used in the FEA from ABAQUS.

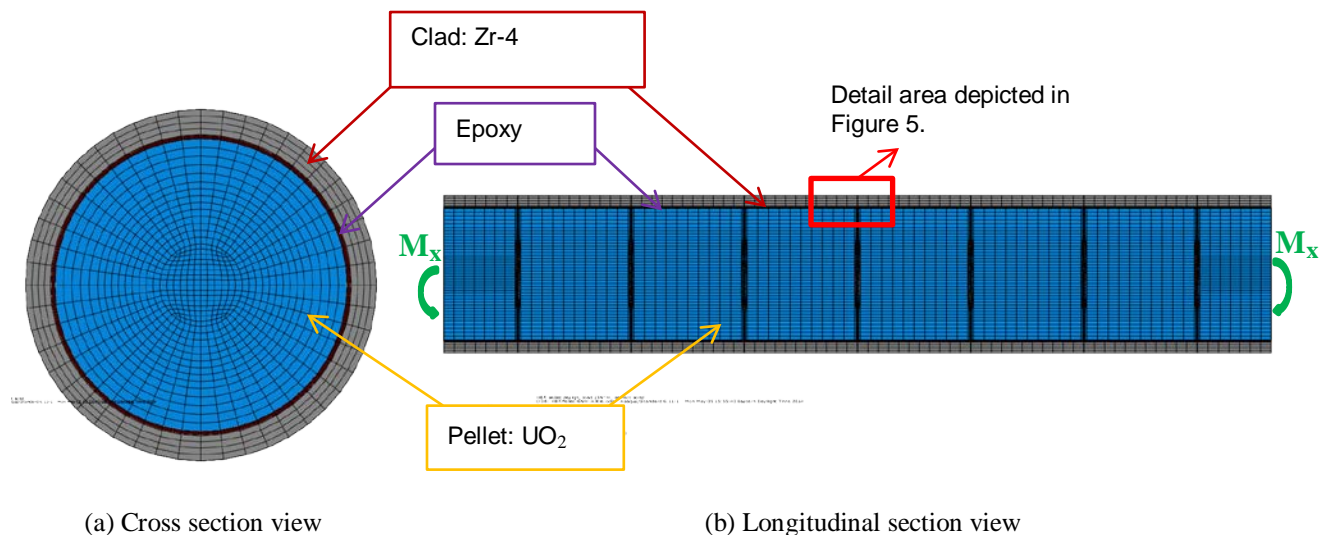


Figure 4. Geometry of clad-epoxy-pellet two inch section model with eight HBR pellets.

Figure 5 shows the configuration of the detail area from Figure 4. The pellets were modeled with rounding of 0.002 in. on the end surfaces, and the end surfaces were dished at both ends to avoid pellet clinging. The dished areas of the pellet end surfaces do not come into contact during bending.

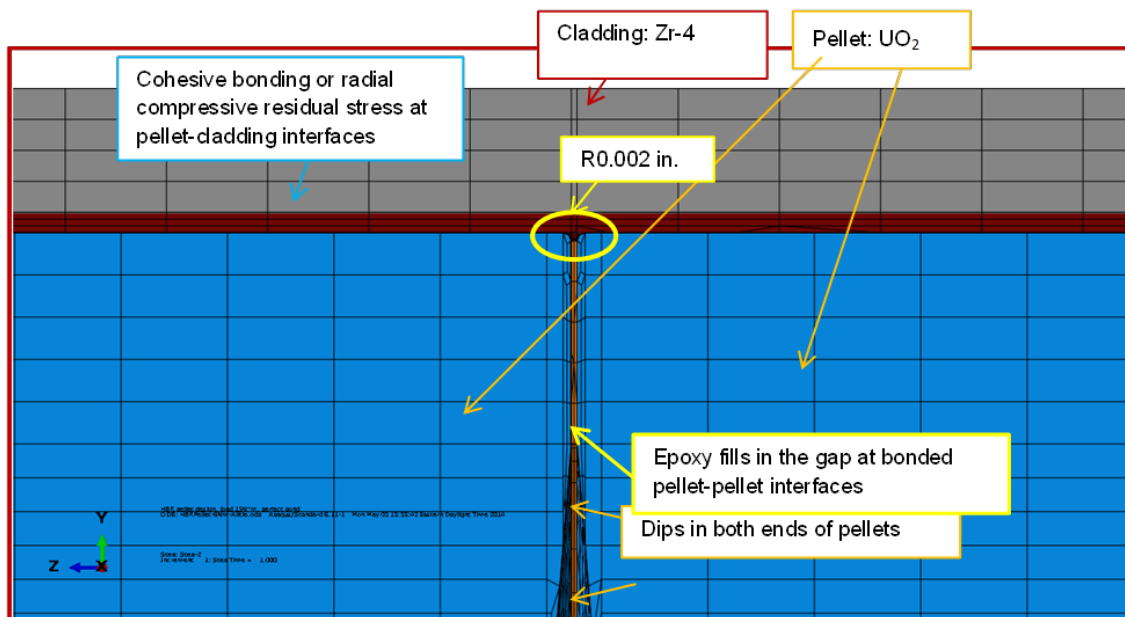
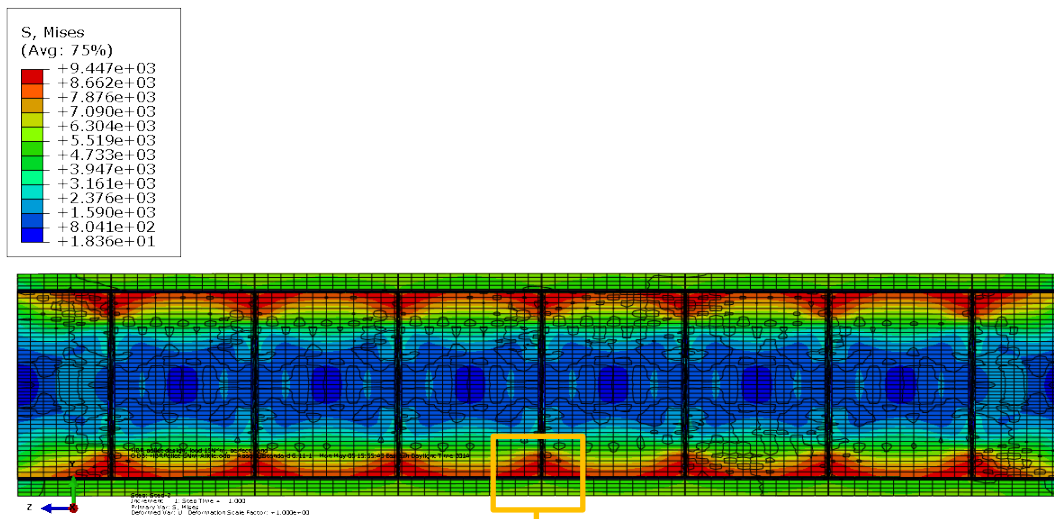


Figure 5. Detail area from Figure 4 for the perfect bond cases.

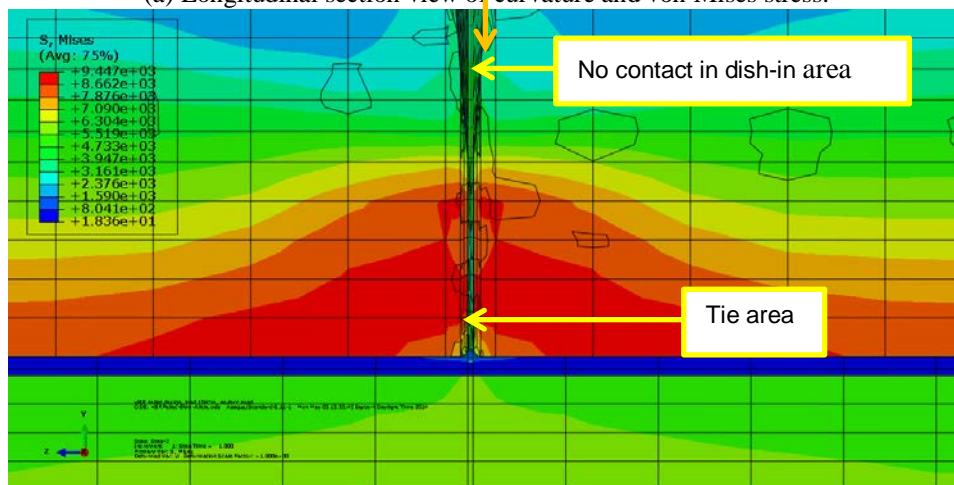
2.1.1 Epoxy Used as Interfacial Material

Thin epoxy layers are tied to the surfaces of the pellet-clad interfaces and the pellet-pellet interfaces to simulate cohesive bonding or radial compressive residual stress. The epoxy layers at the pellet-pellet interfaces in the model are 0.0014 in. thick.

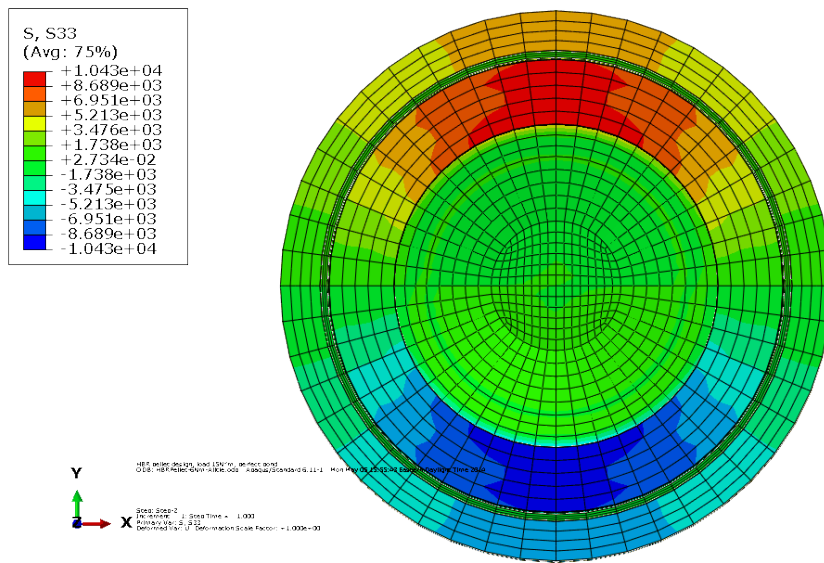
The resulting normal stress distribution and the curvature under the bending moment 6.25 N·m are shown in Figure 6. The resultant curvature is 0.082 m^{-1} , which is too small to be noticeable. Based on the stress distribution shown in Figure 6(a), the maximum stress occurs at the pellets, which indicates that the perfectly bonded HBR pellets carry a larger portion of the moment resistance than the clad. From the detail view shown in Figure 6(b), the maximum stress is observed at the pellet-pellet interface tie area. The perfect bond assigned at the interface tie area is carrying most of the bending moment resistance. The stress in the clad is under the yield point of 131 ksi. Therefore, the clad has not yielded under the 6.25 N m bending moment, nor has the HBR pellet, which has a much higher yield strength than the clad. This indicates that the HBR fuel rod with a perfect bonding condition will remain within the linear elastic range under the target loading. The resultant σ_{zz} at the pellet-pellet interface in Figure 6(c) shows the maximum stress concentrated on the limited tie areas. This occurs because the dips in the ends of the pellets cause the contact surfaces to be confined to a limited area.



(a) Longitudinal section view of curvature and von Mises stress.



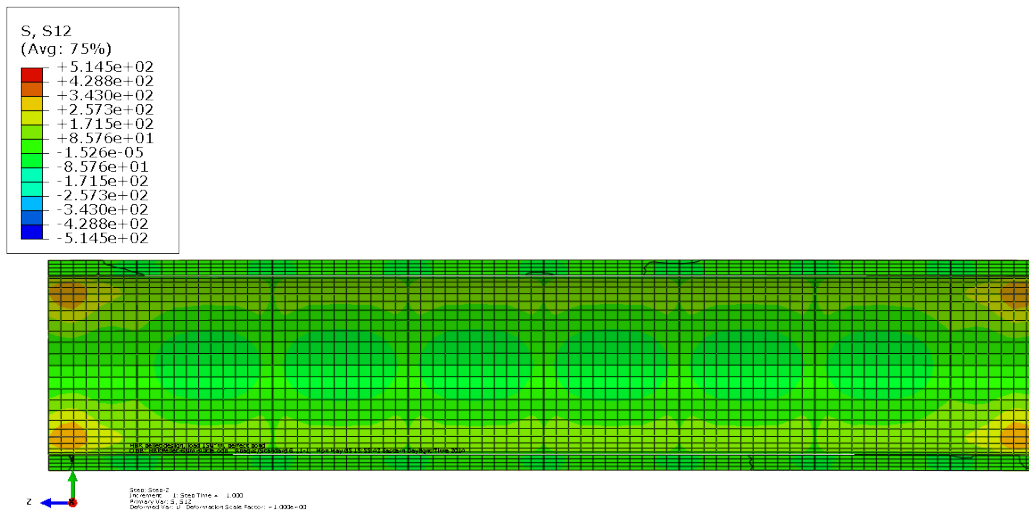
(b) Detail area view.



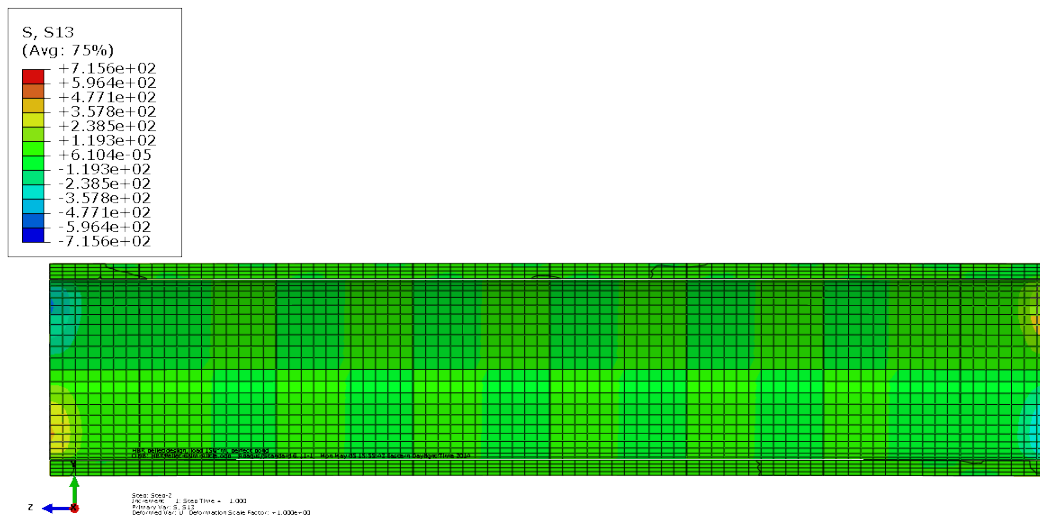
(c) Cross section view of σ_{zz} at a pellet-pellet interface.

Figure 6. Normal stress distribution and curvature results for clad-epoxy-pellet section model of HBR pellets with perfect bonding using epoxy.

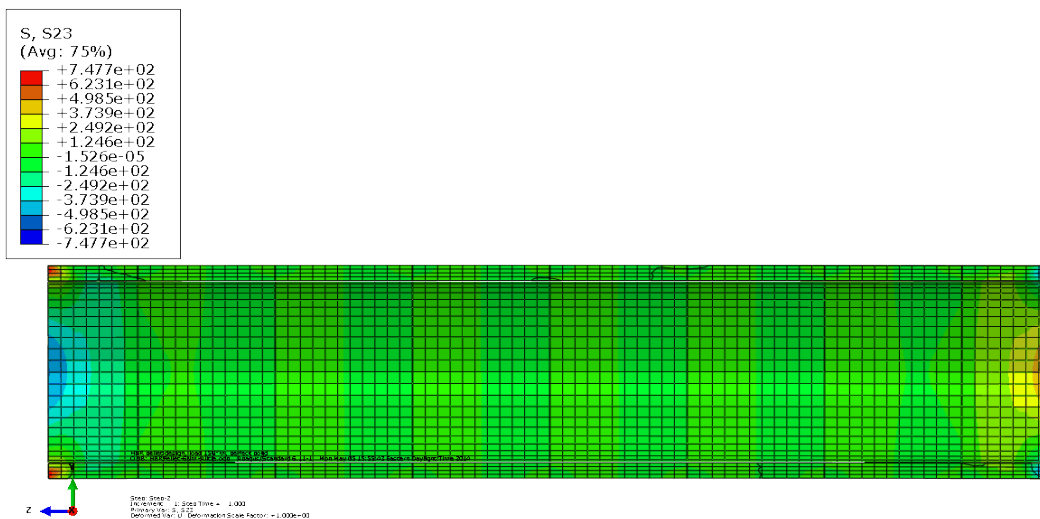
Figure 7 shows the shear stress distribution under the bending moment of 6.25 N·m at the cladding. Shear stresses at the cladding are minimal. As a result of the perfect bonding, the pellets and the cladding work as a whole. There is no shear stress concentration inside the gauge section. The stress concentration occurs at the boundary as a result of composite material mismatch under flexural deformation.



(a) Shear stress σ_{xy} .



(b) Shear stress σ_{xz} .



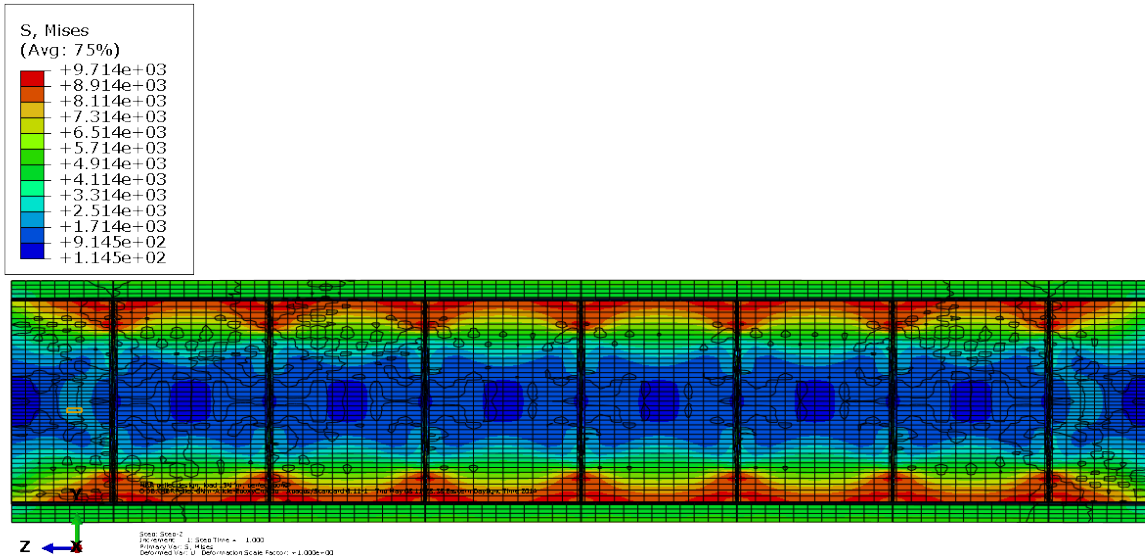
(c) Shear stress σ_{yz} .

Figure 7. Shear stress distribution at the clad for the clad-epoxy-pellet section model of pellets with perfect bonding using epoxy.

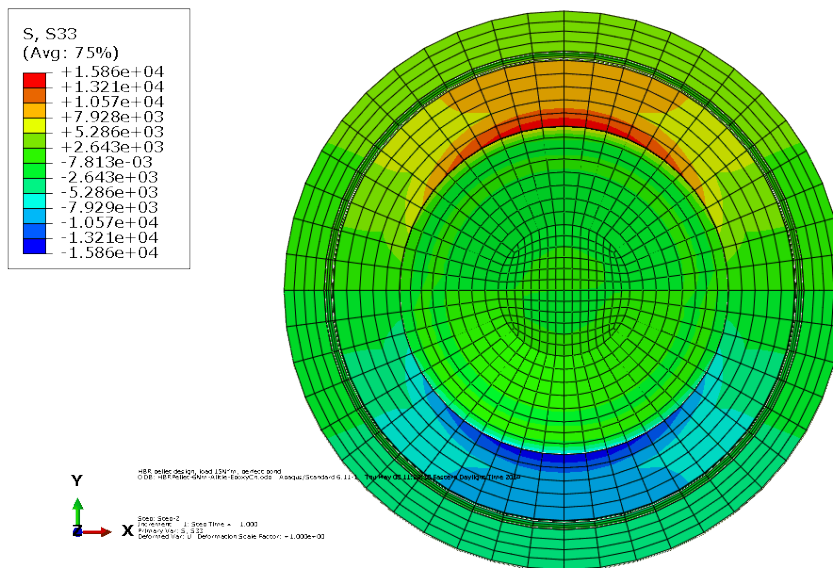
2.1.2 Interfacial Material with $10 \times$ Young's Modulus Material

To investigate the impact of the cohesive bonding material, the Young's modulus of the bonding material was set at an exaggerated level of 10 times the Young's modulus of the epoxy with the material properties shown in Table 1. The second simulation used the same clad-epoxy-pellet section model shown in Figure 4 and Figure 5. Except for the epoxy, all the materials were the same as those used in the previous simulation. The bonding, loading, and boundary conditions were exactly the same as those applied in the first simulation.

Based on the stress distribution seen in Figure 8, the change in the Young's modulus of the cohesive bonding layer does not change the stress distribution. The maximum stress still occurs at the pellet where pellets tie to each other at the pellet-pellet interfaces. The clad and pellets are all under yield stress. However, the maximum stress in this simulation case is higher than that in the first simulation case for the normal epoxy layer, which means that pellets take over more of the bending moment because of stiffer cohesive bonding. The induced curvature is 0.072 m^{-1} , a 12% decrease over that in the first case.



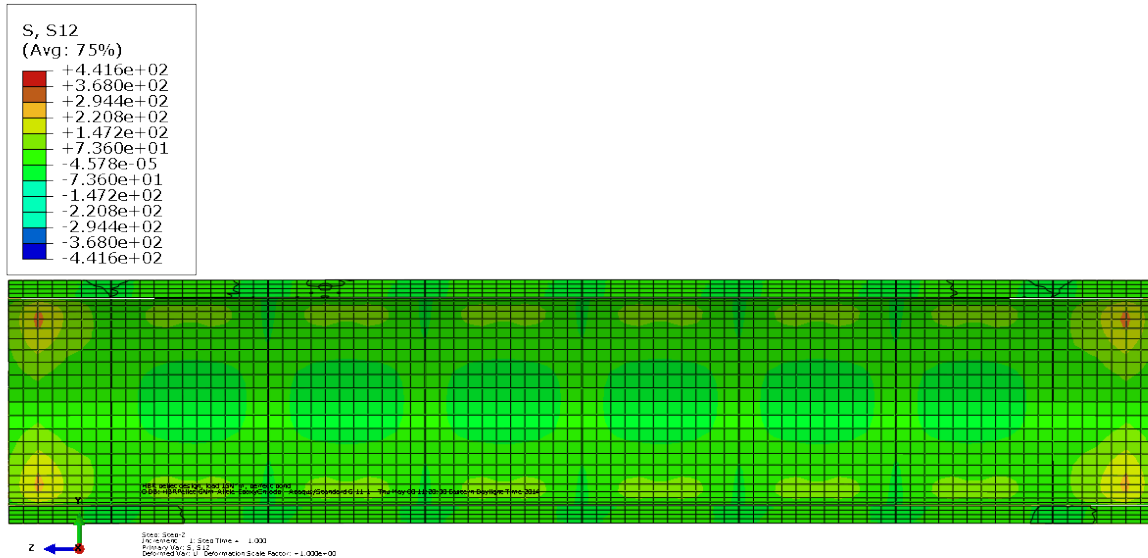
(a) Longitudinal section view of resultant curvature and von Mises stress.



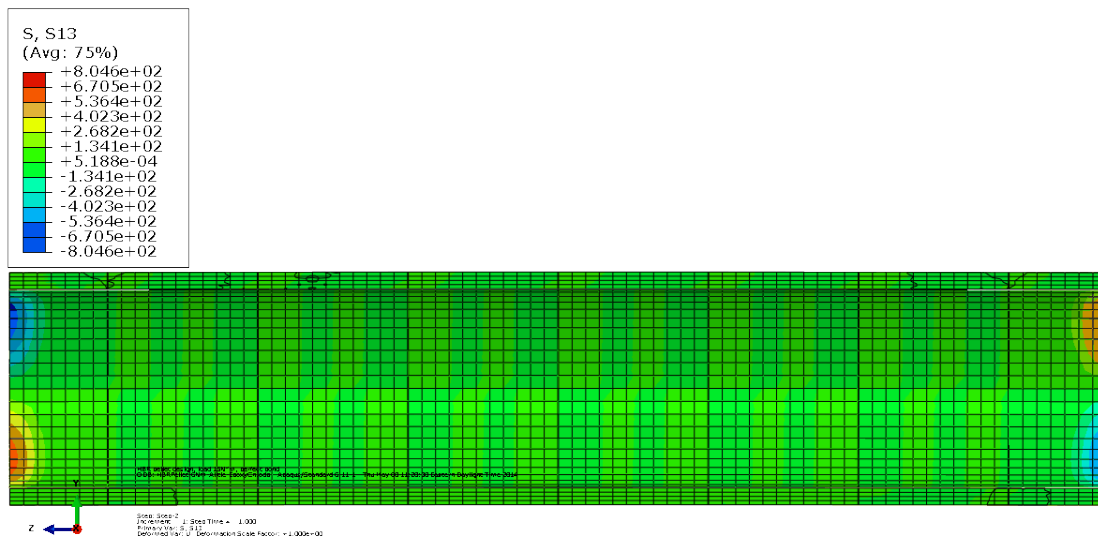
(b) Cross section view of resultant σ_{zz} at a pellet-pellet interface.

Figure 8. Normal stress distribution and curvature results for the clad-epoxy-pellet section model of HBR pellets with perfect bonding using a cohesive bonding material with a $10 \times$ Young's modulus material.

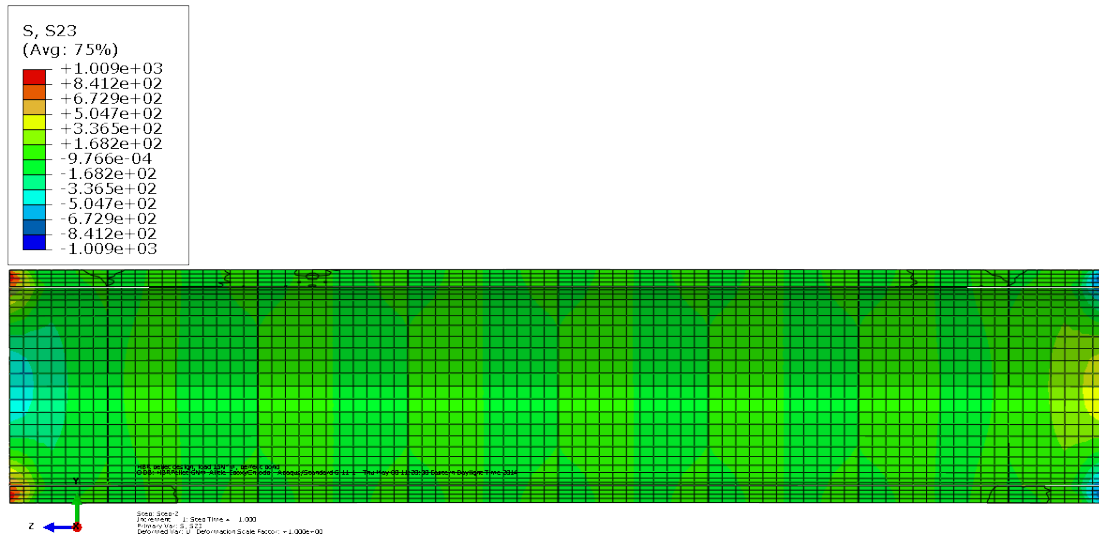
The shear stress distribution in Figure 9 is similar to that in the first case. No shear stress concentration occurs inside the cladding. Shear stresses are small. The change in cohesive bonding material has minimal impact on the shear stress.



(a) Shear stress σ_{xy} .



(b) Shear stress σ_{xz} .



(c) Shear stress σ_{yz} .

Figure 9. Shear stress distribution at the clad of the clad-epoxy-pellet section model of HBR pellets with perfect bonding using a cohesive bonding material with a $10 \times$ Young’s modulus material.

In this section, two simulation cases for the HBR fuel rod—one with good interface bonding and one without inserted rod fracture—were studied. To simulate good cohesive bonding in the FEA, the pellet-clad interfaces were tied together with a thin epoxy layer, while the Young’s modulus of the cohesive bonding material was changed for purposes of the study.

The curvature and flexure rigidity for those cases are summarized in Table 2. A load control procedure was used. The bending moment M was applied to both ends of the fuel rod, and the bending curvature κ was estimated from the FEA results within the gauge section. The flexural rigidity EI (the product of the Young’s modulus E and the moment of inertia I) of a fuel rod can be estimated using the applied moment M and the resultant curvature κ , as described in Eq. (1).

$$EI = M/\kappa \tag{1}$$

Based on the resulting σ_{zz} , shown in Figure 6(c) and Figure 8(b), the bending moment was calculated for the cladding and pellets, respectively. The total resultant bending moment should be equal to the bending load M_x , 6.25 N·m. Estimated bending moments for the cladding and pellets are also summarized to directly compare the load carrying capacity of the different system components.

Table 2. The curvature, flexural rigidity, and bending moment comparison for the perfect interface bonding simulation

	Curvature κ (1/m)	Flexural rigidity EI (N·m ²)	Clad bending moment M (N·m)	Pellet bending moment M (N·m)
Perfect bond with epoxy	0.082	77	2.45	3.8
Perfect bond with $10 \times$ Young’s modulus material	0.072	87	2.06	4.19

Table 2 shows that the flexure rigidity for a perfect bonding condition with epoxy as the cohesive bonding material is $77 \text{ N}\cdot\text{m}^2$ for the HBR pellet fuel rod. The flexure rigidity increases by 11.5% to $87 \text{ N}\cdot\text{m}^2$ as the Young's modulus of the bonding material increases by 10 times. This is a direct result of the fuel rod becoming stiffer. Based on the load-carrying capacity, the perfectly bonded pellets take over more of the bending moment than the cladding for both cases. As the cohesive bonding becomes stiffer, the clad carries less of the bending load.

The condition of the ORNL HBR fuel rod hot-cell testing specimens resembles that of the clad-epoxy-pellet section model with epoxy-filled gaps at the pellet-pellet interfaces. The HBR fuel specimen was tested under a $6.25 \text{ N}\cdot\text{m}$ bending moment. Figure 10 shows ORNL hot-cell CIRFT data. The flexural rigidity based on the hot-cell test data was observed to be between 60 and $70 \text{ N}\cdot\text{m}^2$, and the curvature was around 0.09 m^{-1} . The initial (first cycle) test data usually have the highest flexural rigidity since the pellet-clad and pellet-pellet interface bonds should maintain the best status before bending fatigue damage. The flexural rigidity in the first test data was a little lower than the FEA estimate, which indicates this testing sample probably has interfacial debonding rather than perfect bonding at the initial test stage.

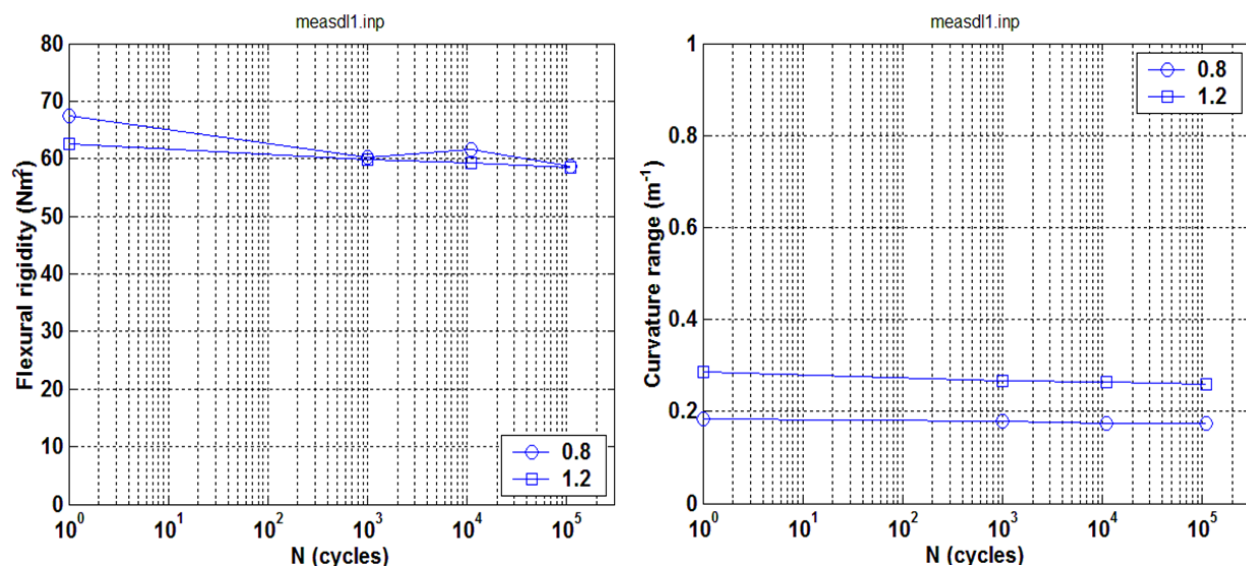


Figure 10. ORNL hot-cell CIRFT data, flexural rigidity, and curvature [3].

With good interface bonding and without fuel rod fracture, the fuel rod can carry most of the bending moment under normal transportation vibration. This is a result of the higher Young's modulus of the fuel pellet compared with the clad, along with a much higher yield stress, as shown in Table 1. ORNL fuel data validate that inserted pellets can carry more moment resistance than the clad because of their higher stiffness if the pellet-clad and pellet-pellet interface bonds remain intact. Because of the high flexural strength of the HBR pellets, the fuel rod responds to the bending moment within the linear elastic range. The high flexural rigidity estimated from FEA agrees well with that estimated from bending fatigue testing data. Furthermore, under cyclic loading, it is expected that the interface bond will be progressively degraded as is demonstrated in Figure 10, with decreasing flexural rigidity under increased loading cycles.

2.2 Debonding at Pellet-Pellet Interfaces and Bonding at Pellet-Clad Interfaces

Before high-burnup SNF is transported, there are inherited stress fields in the SNF system. For example, there may be axial tensile stress and tangential tensile stress due to pellet-clad mechanical interaction or oxide volume expansion, radial compressive stress due to hydride compaction, and tangential shear stress due to hydride volume expansion. Vibration during transportation will induce reversal bending in an SNF assembly. Repeated expansion and contraction in both the axial and tangential directions of the SNF rod due to reversal bending flexural deformation, combined with stress concentration, can degrade the interface bonding at the fuel pellet-clad and pellet-pellet interfaces (Figure 11). Although the shear stress is small relative to the normal stress due to bending, that does not mean that it can be neglected. In composite rods or SNF rods in particular, excessive shear due to material mismatch can be a cause of interfacial bonding failure.

At pellet-pellet interfaces, interfacial bonding failure is caused mostly by normal stress due to reversal bending flexural deformation combined with relatively smaller shear stress (see Figure 11). At pellet-clad interfaces, localized high shear stress will also arise to compensate for the material mismatch under flexural deformation. As mentioned earlier, the shear stress is small relative to the normal stress; therefore, it is likely that interfacial bonding failure at pellet-pellet interfaces will begin before debonding occurs at pellet-clad interfaces. In addition, the HBR pellets have dished noncontact areas at both end surfaces, so the bonding area at the pellet-pellet interface is limited to a relatively small area, making it easier for the pellet-pellet interfaces to debond. Observations of an ORNL reversal bending fatigue surrogate stainless steel rod with alumina pellets verified this hypothesis. In this section, the clad-epoxy-pellet section model with eight pellets was used to investigate the HBR fuel rod bending response with perfect bonding at pellet-clad interfaces and debonding at pellet-pellet interfaces. The material properties, geometry, and loading and boundary conditions were the same as those used in the previous FEA simulation.

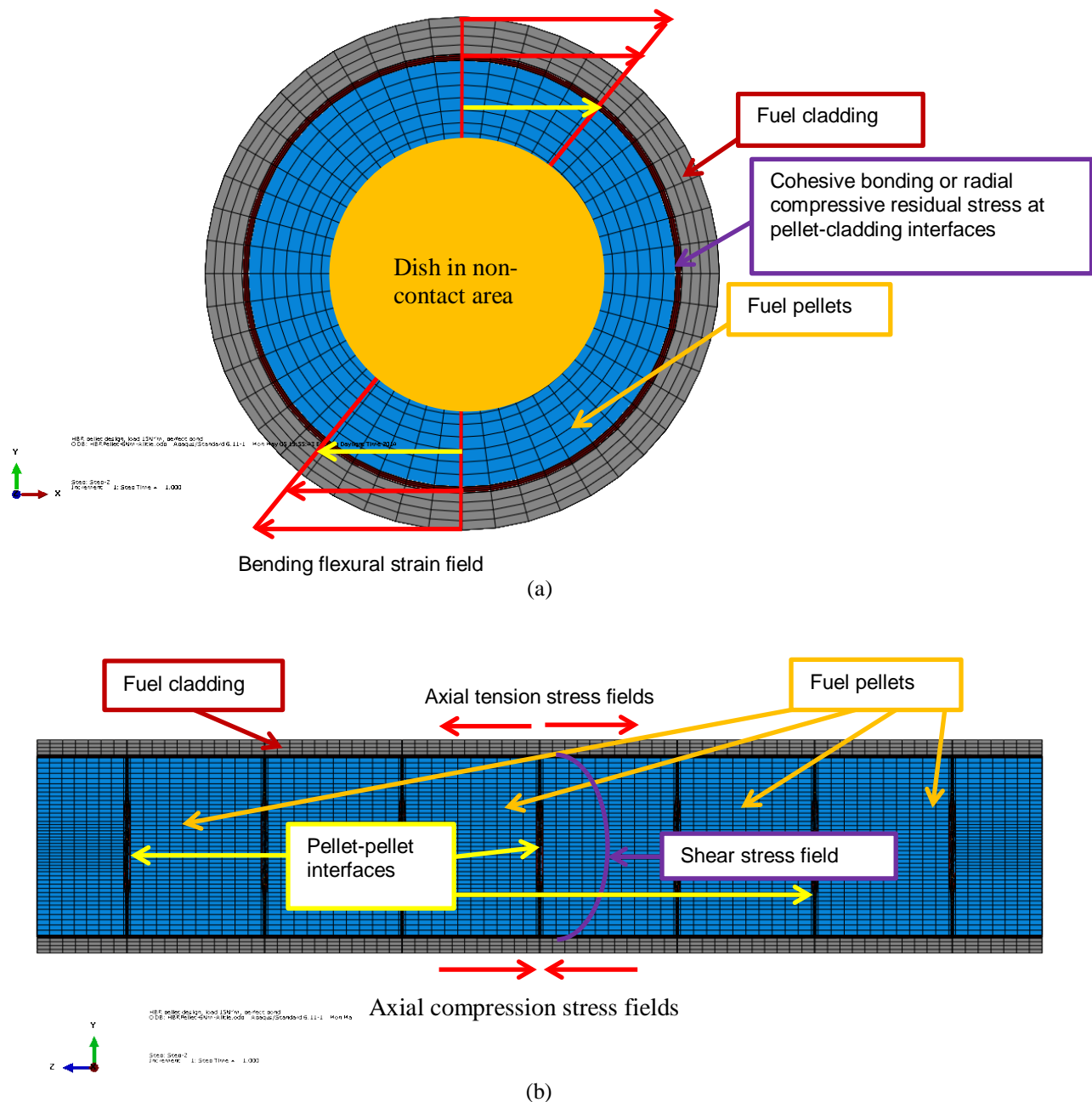


Figure 11. Transportation-induced reversal bending stress fields in an SNF system.

2.2.1 Debonded Pellet-Pellet Interfaces with Empty Gaps

To simulate a good cohesive bond condition or radial compressive residual stress at pellet-clad interfaces, a thin bonding layer was tied to the surfaces at the pellet-clad interfaces. In this section, the case study was designed to simulate the response with a debonded pellet-pellet interface. There are empty gaps at the pellet-pellet interfaces (Figure 12). During bending flexural deformation, the pellets overcome the gaps and then contact one another at the interfaces. The pellets have dips and end surfaces with a rounding of 0.002 in.

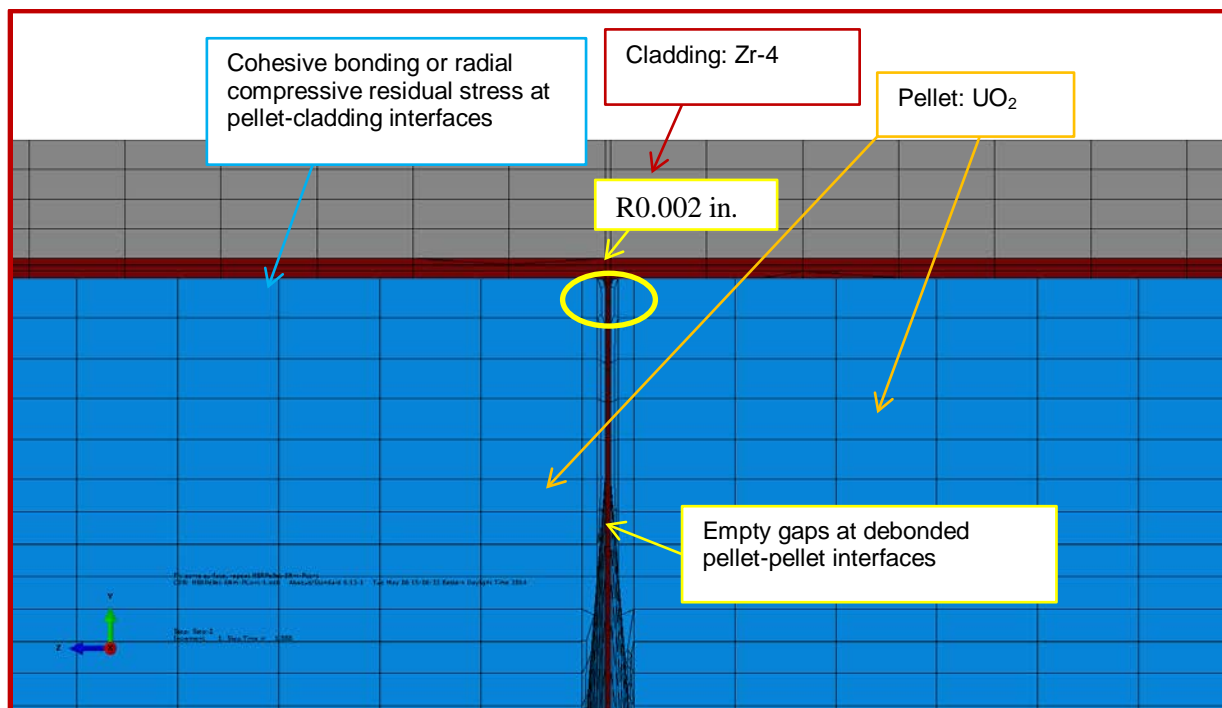


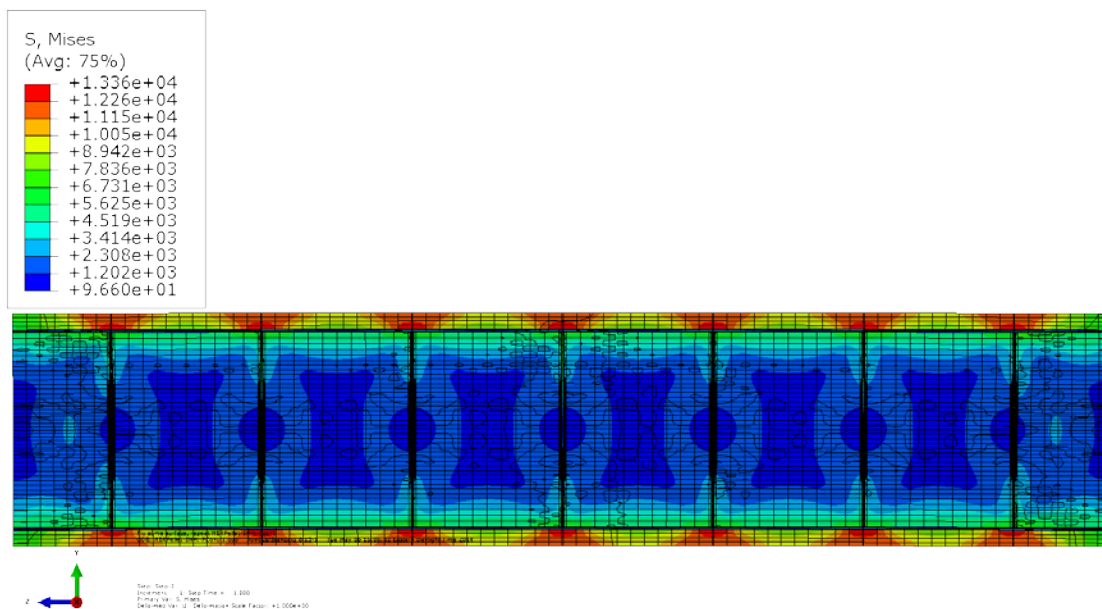
Figure 12. Detail from Figure 4 for the case of empty gaps at debonded pellet-pellet interfaces.

2.2.1.1 Epoxy Used as Interfacial Material

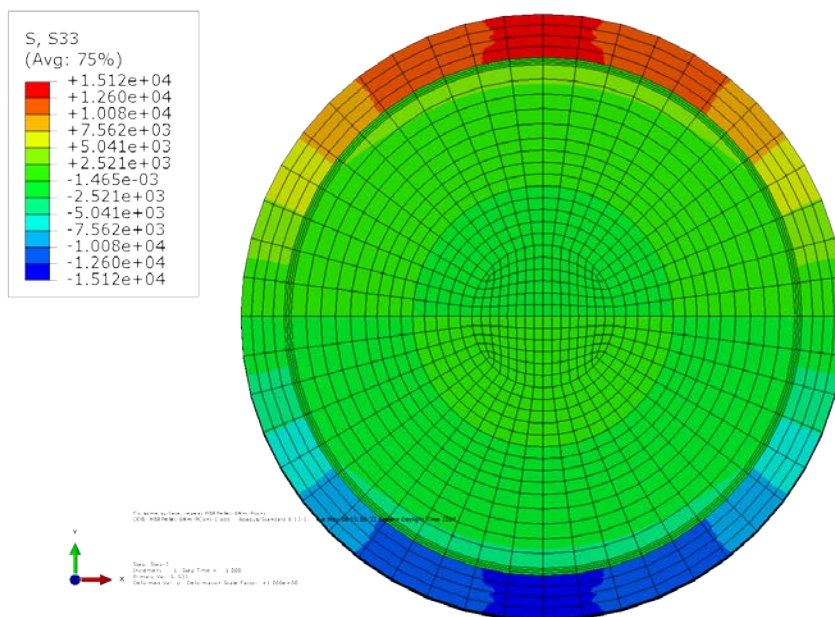
Similar to the perfect bonding case, the first simulation case for pellet-pellet interface debonding with gaps has an epoxy layer tied to the surfaces at the pellet-clad interfaces with the original Young's modulus, as shown in Table 1, to simulate good cohesive bonding at pellet-clad interfaces.

The normal stress and curvature responding to the bending moment are illustrated in Figure 13. Compared with the results shown in Figure 6, there are significant differences in the stress distribution between the pellet-pellet interface bonding case and the pellet-pellet interface debonding case; the pellet-clad interface remains perfectly bonded in both cases. For instance, at the pellet-pellet interface in the debonding case, the maximum stress occurs at the clad and is located at the top and bottom portions of the pellet-pellet interface regions. As a result of the small bending moment, the maximum stress at the clad is 10 times lower than the yield strength of Zr-4, as shown in Table 1, so the Zr-4 clad does not yield. In most of the clad, the stress is much lower than the maximum because the perfect pellet-clad bonding provides good support to the clad. Since there are gaps between pellet-pellet interfaces, the clad deforms continuously until the gaps are reduced by direct contact of the pellet-pellet surfaces. However, no stress concentration is observed at the pellet-pellet contact corners. The resulting σ_{zz} clearly indicates that the clad takes over more of the bending moment resistance than the pellets at the debonded pellet-pellet interfaces.

At the debonded pellet-pellet interfaces, the pellets can transfer load only via hard contact, so the load-carrying capacity shifts significantly from the pellets to the clad. When the Zr-4 clad starts to carry most of the bending moment at the pellet-pellet interface region, the result is maximum stress concentration at the Zr-4 clad. However, in most of the gauge section, the pellets still provide sufficient internal support to the clad because of good cohesive bonding at the pellet-clad interfaces, and they will carry most of the bending load. Therefore, there is much lower stress in most regions of the Zr-4 clad.



(a) Longitudinal section view of resultant curvature and von Mises stress.



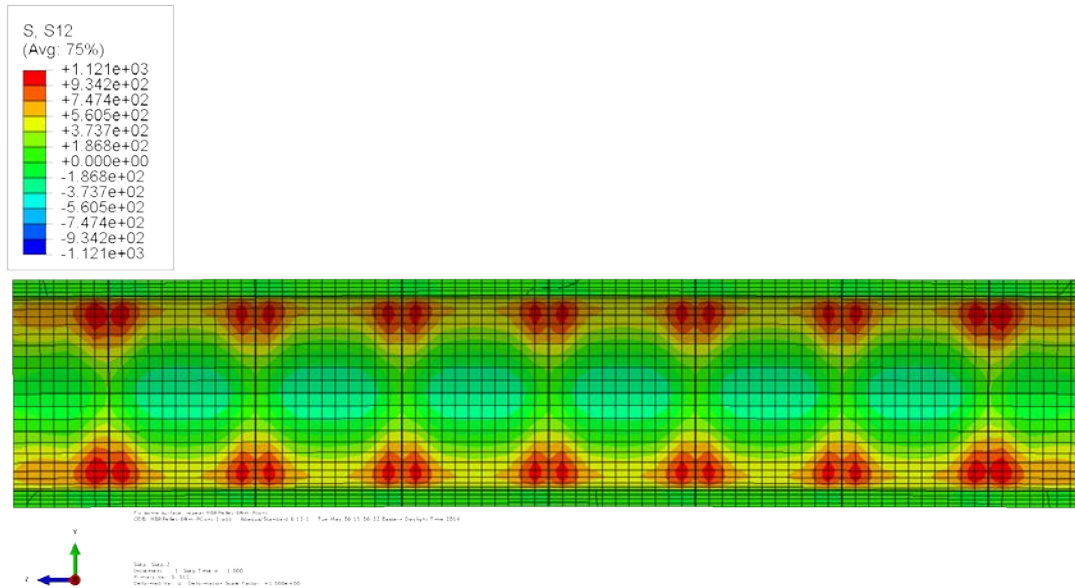
(b) Cross section view of resultant σ_{zz} at a pellet-pellet interface.

Figure 13. Normal stress distribution and curvature results for the clad-epoxy-pellet section model of HBR pellets with debonded pellet-pellet interfaces with gaps, and bonded pellet-clad interfaces using epoxy.

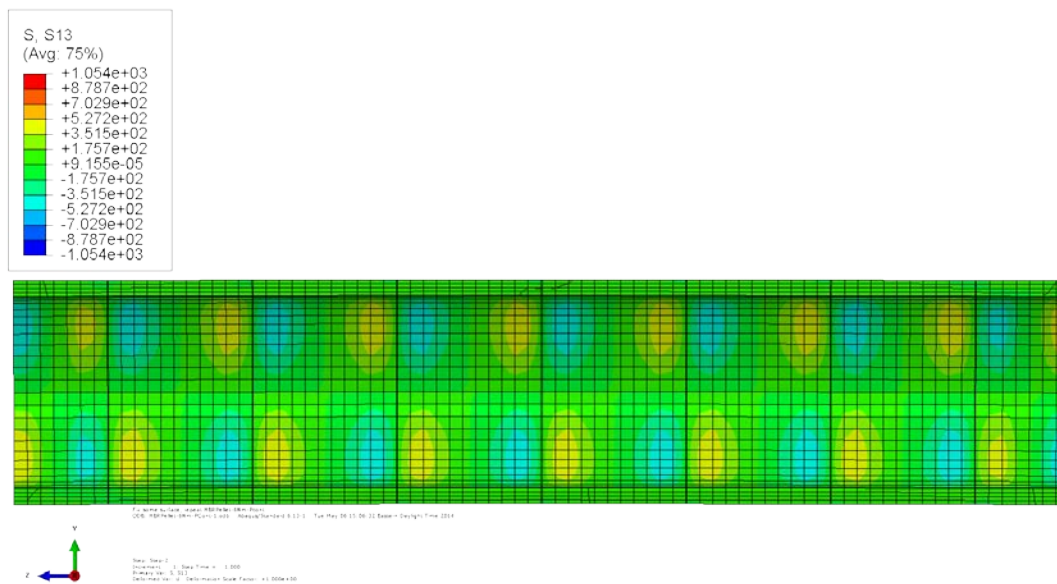
In Figure 6, the results of the perfect bond case show that the pellets carry significant bending moment resistance; the maximum stress resides on the pellets, and there is no yielding at either the pellets or the clad. It is also interesting to note that the von Mises stress distribution in debonded pellets appears to be quite different from the results of the bonded pellet-pellet interface case. For example, in Figure 6, a

dog-bone shape appears in a horizontal direction inside an HBR pellet as a result of von Mises stress distribution. However, in Figure 13, the dog-bone shape inside an HBR pellet is vertically oriented. The third discrepancy lies in the induced curvature. In the debonding case, the curvature is 0.16 m^{-1} , double that of the perfect bond case shown in Figure 6.

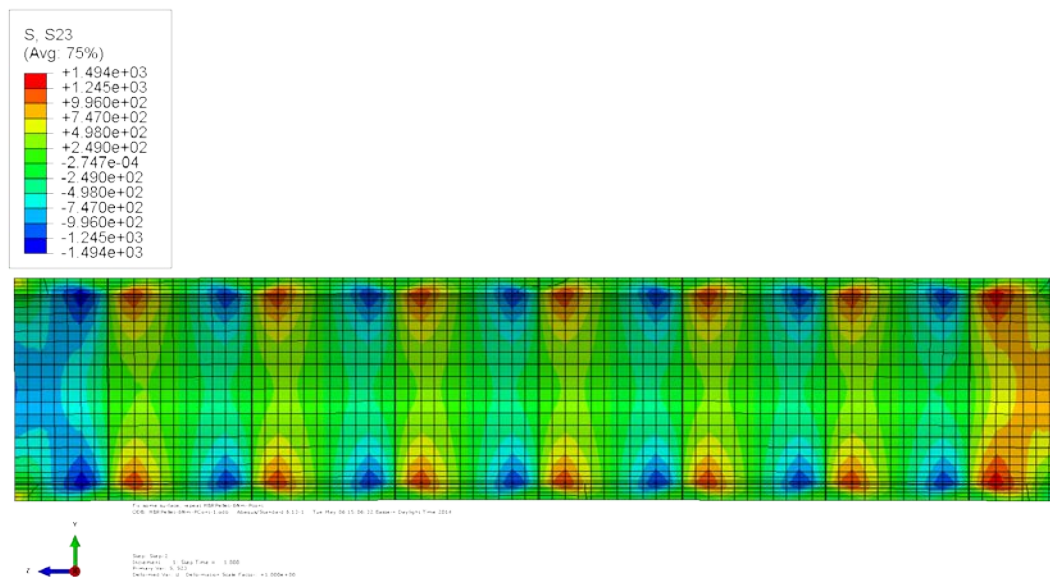
In Figure 14, the difference from the results in Figure 7 for the perfect bond case is apparent. With the pellet-pellet interfaces debonded, the shear stresses surge near the pellet-pellet interface debonding region inside the cladding. The reason might be an increase in shear stress due to a composite material mismatch at the debonded pellet-pellet interface boundary under bending flexural deformation. With good cohesive bonding at pellet-clad interfaces, the clad transfers some shear load at the debonding region. If there are small gaps at the pellet-pellet interfaces, the shear stress concentration occurs at both the top tension and bottom compression regions of the clad. Maximum stress levels are higher than in perfect bond cases; however, the shear stresses are still one order of magnitude lower than the normal stress in the same simulation case.



(a) Shear stress σ_{xy}



(b) Shear stress σ_{xz}



(c) Shear stress σ_{yz}

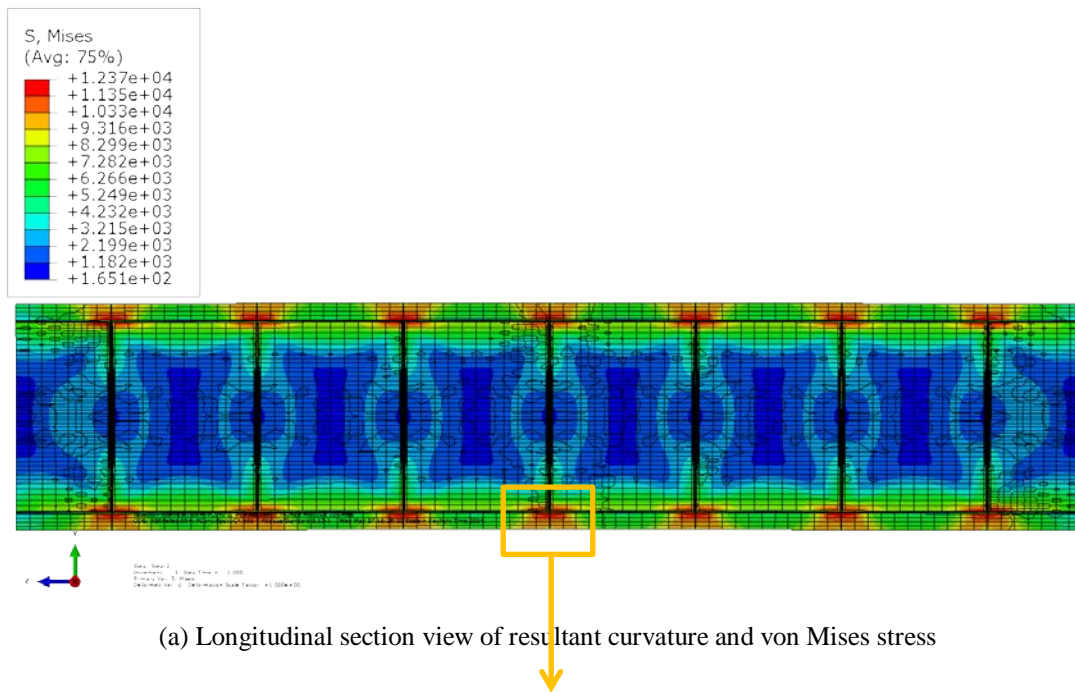
Figure 14. Shear stress distribution at the clad of the clad-epoxy-pellet section model of HBR pellets with debonded pellet-pellet interfaces with gaps and bonded pellet-clad interfaces using epoxy.

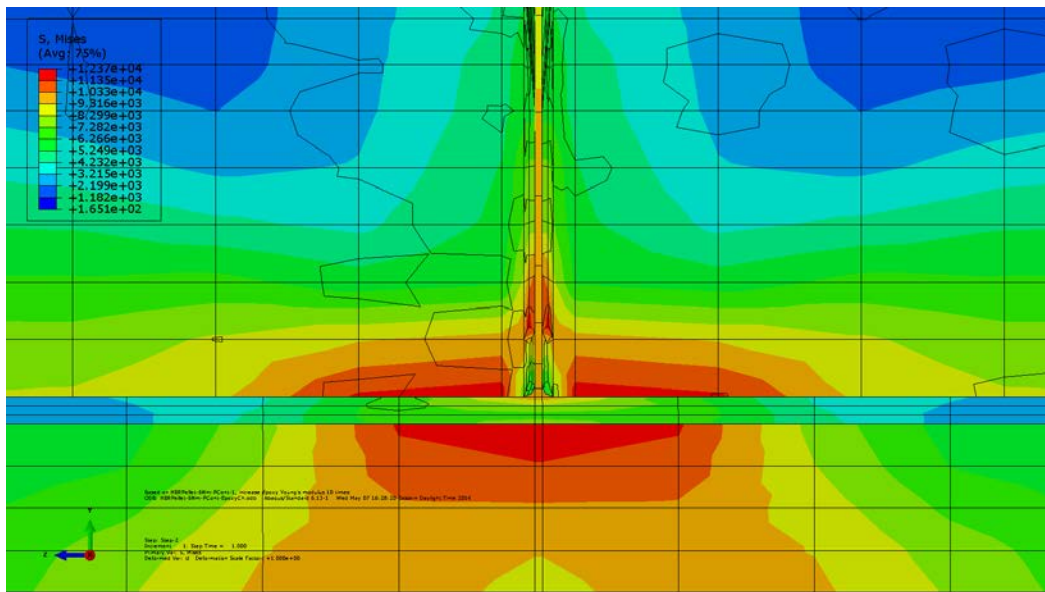
2.2.1.2 Interfacial Material with $10 \times$ Young's Modulus

The second case study of simulated pellet-pellet interfacial debonding was defined as having gaps at the pellet-pellet interfaces and a thin layer of cohesive bonding material at the pellet-clad interfaces. The cohesive bonding material is also tied to the adjacent surfaces, resulting in perfect cohesive bonding. Similar to the second case of the perfect bond study, the Young's modulus of the cohesive bonding

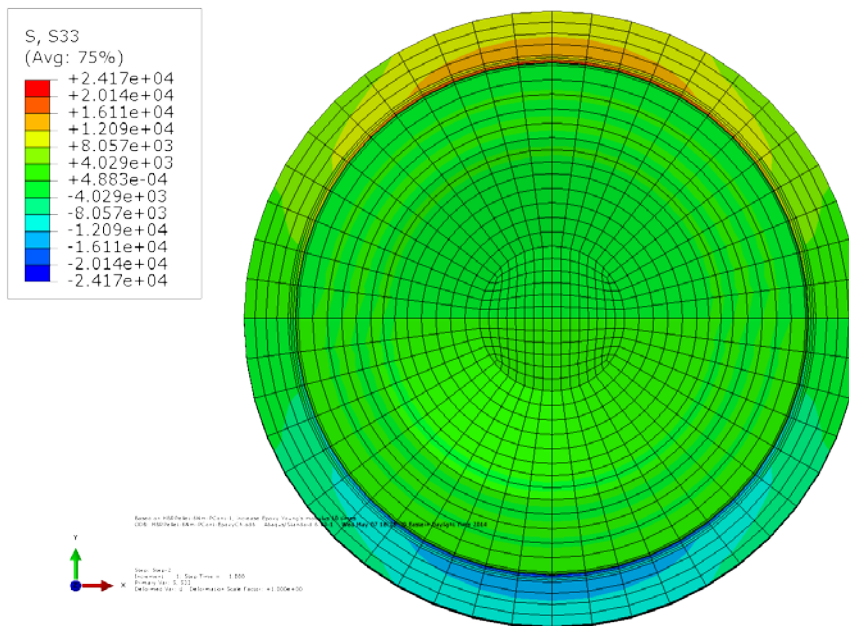
material at the pellet-clad interfaces was set to 10 times that of epoxy. Loading and boundary conditions were all the same as in the previous cases.

Figure 15 illustrates the simulation results for the pellet-pellet interfacial debonding condition, which shows a stress profile similar to that in Figure 13. However, stress concentrations are observed on both the pellets and the clad at pellet-pellet interfaces, as shown in Figure 15(b) in a detail view. The pellet-clad interaction tied by stiffer cohesive bonding causes stress concentrations on the pellets. The maximum stress on the Zr-4 clad occurs at the top and bottom portions of the pellet-pellet interface regions as a result of significant load shifting to the clad, whereas most of the clad has low stress because of the perfect pellet-clad bond. The HBR pellets and Zr-4 clad are all under yield stress. The cross section view of the resultant σ_{zz} shows that the maximum compressive stress fields reside in the cohesive bonding layer. The pellets have the same stress distribution depicted by the vertical dog-bone shape as in the previous case. The induced curvature of this pellet-pellet interface debonding in the stiffer cohesive bonding case is 0.118 m^{-1} , much smaller than that in the previous pellet-pellet interface debonding case. The big difference for this case compared with the debonded pellet-pellet interfaces with gaps is the stress concentration on the pellets as a result of stiffer cohesive bonding. Therefore, in this case, the HBR pellets would take more bending moment than those in the first simulation case.





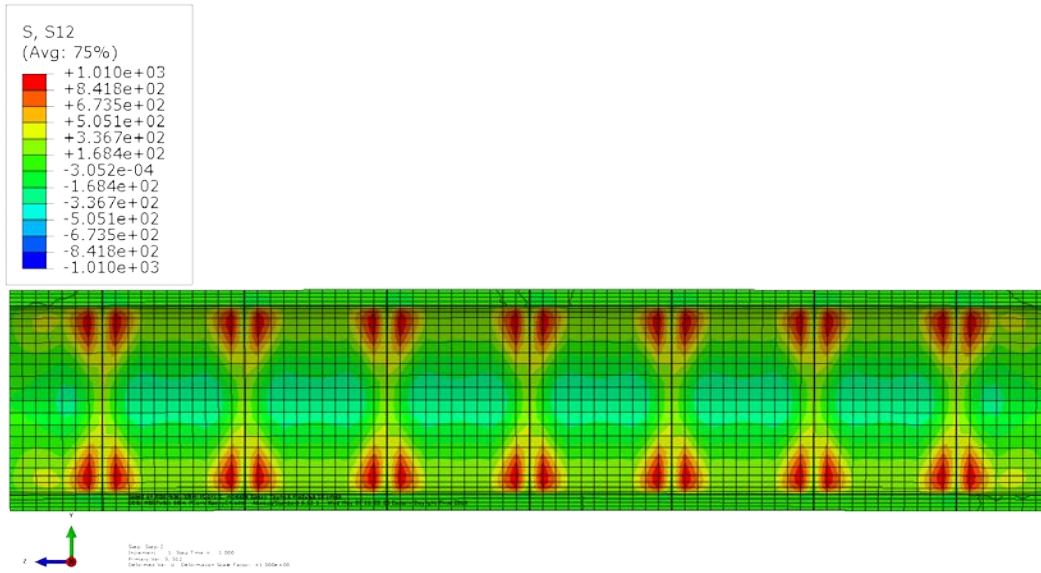
(b) Detail view



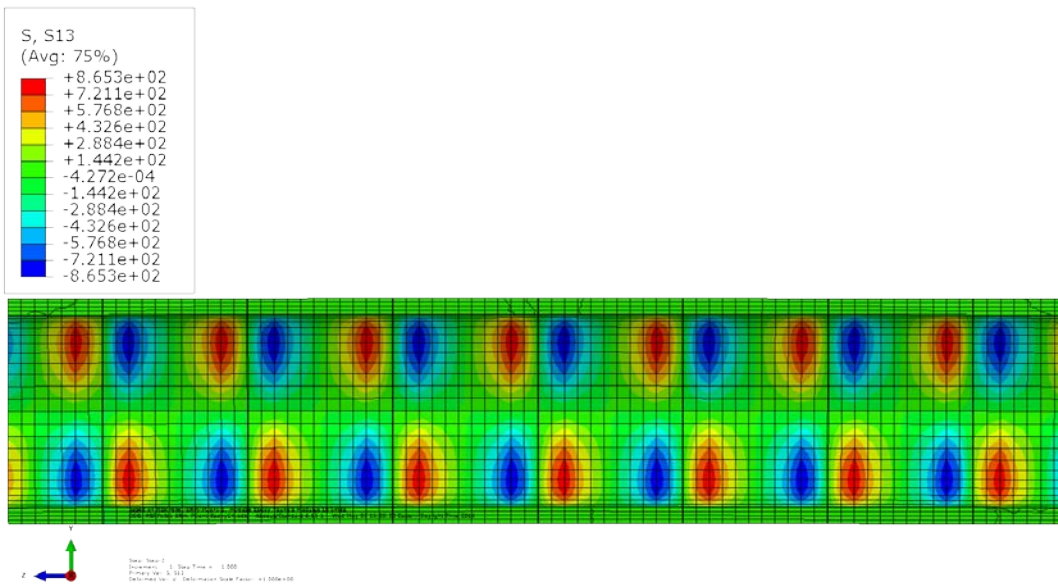
(c) Cross section view of σ_{zz} at a pellet-pellet interface

Figure 15. Normal stress distribution and curvature results for clad-epoxy-pellet section model of HBR pellets with debonded pellet-pellet interfaces with gaps, and bonded pellet-clad interfaces using a $10 \times$ Young's modulus material.

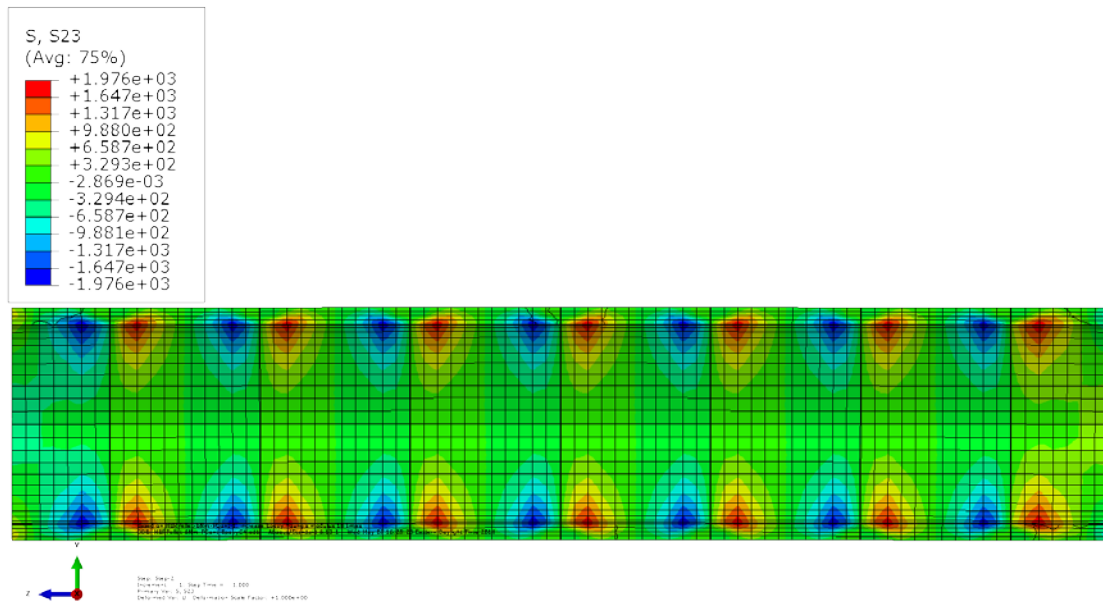
The results for shear stress distribution in Figure 16 show a similar pattern for the case in which epoxy is used as the cohesive bonding material. There are some changes in stress level, especially in the radial direction. For example, the maximum stress concentration in σ_{xy} is lower than the results in Figure 14, indicating that a stiffer interfacial material will increase the system stiffness and reduce the radial shear stress concentration under flexural deformation.



(a) Shear stress σ_{xy}



(b) Shear stress σ_{xz}



(c) Shear stress σ_{yz}

Figure 16. Shear stress distribution at the clad of clad-epoxy-pellet section model of HBR pellets with debonded pellet-pellet interfaces with gaps, and bonded pellet-clad interfaces using a $10 \times$ Young's modulus material.

2.2.2 Debonded Pellet-Pellet Interfaces without Gaps

Figure 17 illustrates the simulations of debond pellet-pellet interface and bond pellet-clad interface. There are no gaps at the pellet-pellet interfaces before bending loading is applied. Similar to the previous cases, a thin layer is applied and tied to the surfaces at the pellet-clad interfaces to simulate good cohesive bonding or radial compressive residual stress. Except for elimination of the gaps at the pellet-pellet interfaces, the geometry, materials, and loading and boundary conditions are all the same as in the previous simulations.

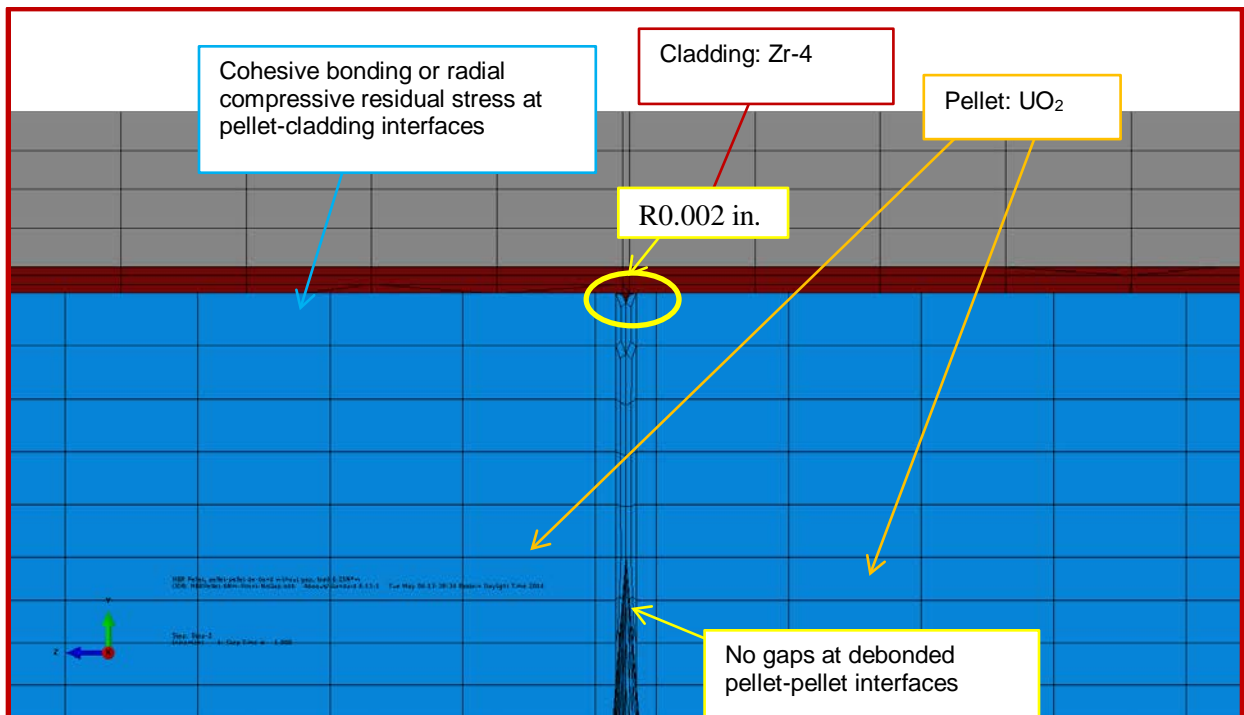
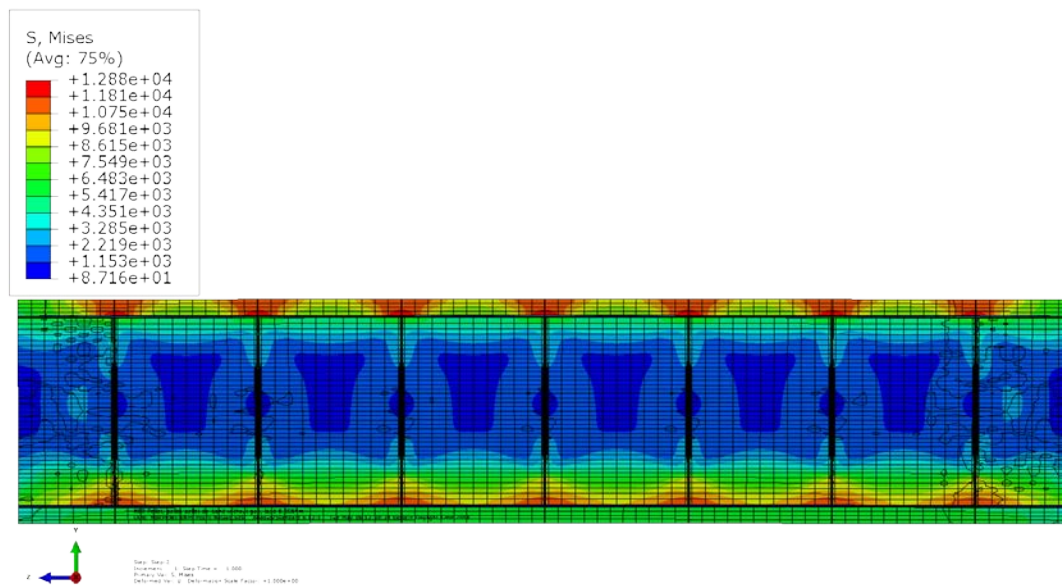


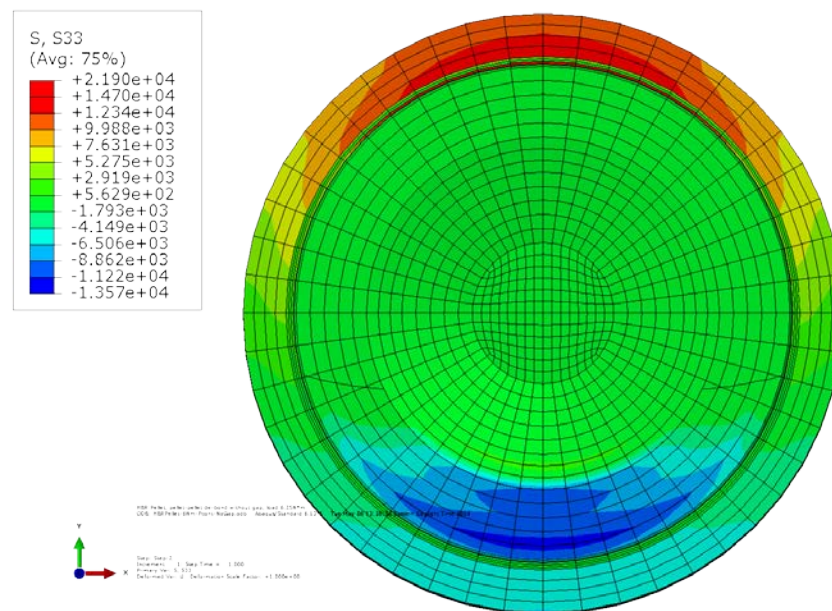
Figure 17. Detail from Figure 4 for the case of no gaps at debonded pellet-pellet interfaces.

2.2.2.1 Epoxy Used as Interfacial Material

For the third case in this section, the cohesive bonding material is an epoxy layer with the original Young's modulus. As illustrated in Figure 18, the normal stress distribution of this case appears to be different from that of the debonded pellet-pellet interface case with empty gaps shown in in Figure 13. The maximum stress occurs at the top of the clad at pellet-pellet interface regions; however, at the compression side, interface stress concentrations occur at the pellets instead of at the clad. This is because there are no gaps at the pellet-pellet-clad interface region. Thus, the contact pellets provide good internal support to the clad tubing structure. Furthermore, the pellets seem to carry a significant portion of the bending moment resistance via pellet-pellet interaction (pinching at pellet corners), which significantly mitigates the stress level of the clad at the bottom (compression) region. Because of the high yield strength of the pellet and clad materials, as well as the small bending load, the pellets and the clad are all under the linear elastic range at the maximum stress level. The pellet stress profiles do not show a clear dog-bone shape because of the asymmetric contact between the tension and compression sides at the debonded pellet-pellet interfaces. The resultant σ_{zz} profile without gaps at the pellet-pellet interface indicates that the pellets can carry more bending moment resistance than the pellets with gaps shown in Figure 13.



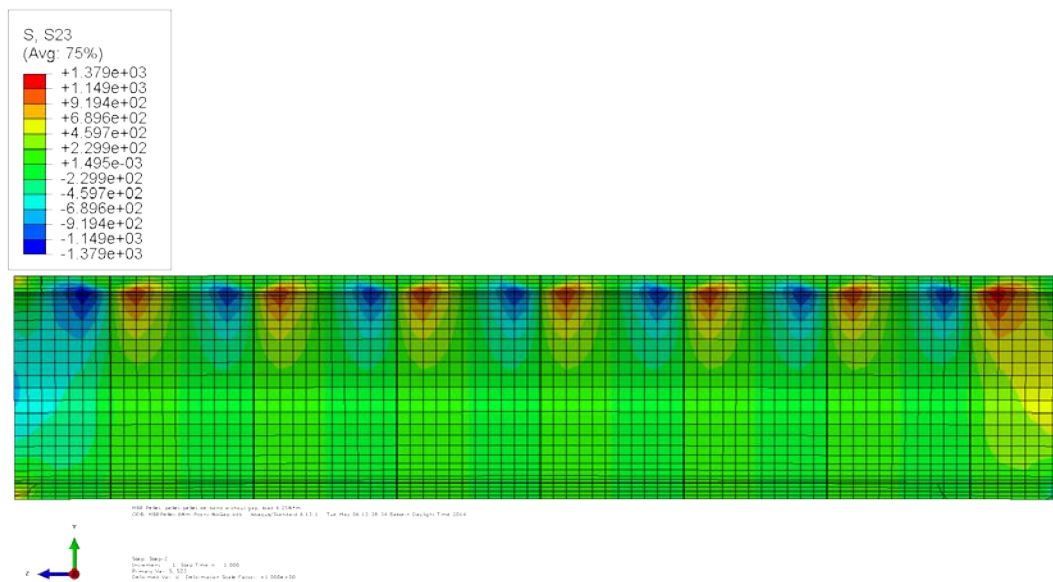
(a) Longitudinal section view of resultant curvature and von Mises stress



(b) Cross section view of σ_{zz} at a pellet-pellet interface

Figure 18. Normal stress distribution and curvature results for clad-epoxy-pellet section model of HBR pellets with debonded pellet-pellet interfaces without gaps, and bonded pellet-clad interfaces using epoxy.

Figure 19 shows the shear stress distribution at the clad for this case. The shear stress concentration occurs only at the top tension side, unlike in the case for pellet-pellet interface debonding with small gaps. The maximum stress concentration level is close to the results in Figure 14. At the bottom compression side, the shear stress level is low. The reason is the same as for the normal stress results: when the gaps are eliminated, pellet-to-pellet direct pinning helps lower the stress on the clad at the bottom region.



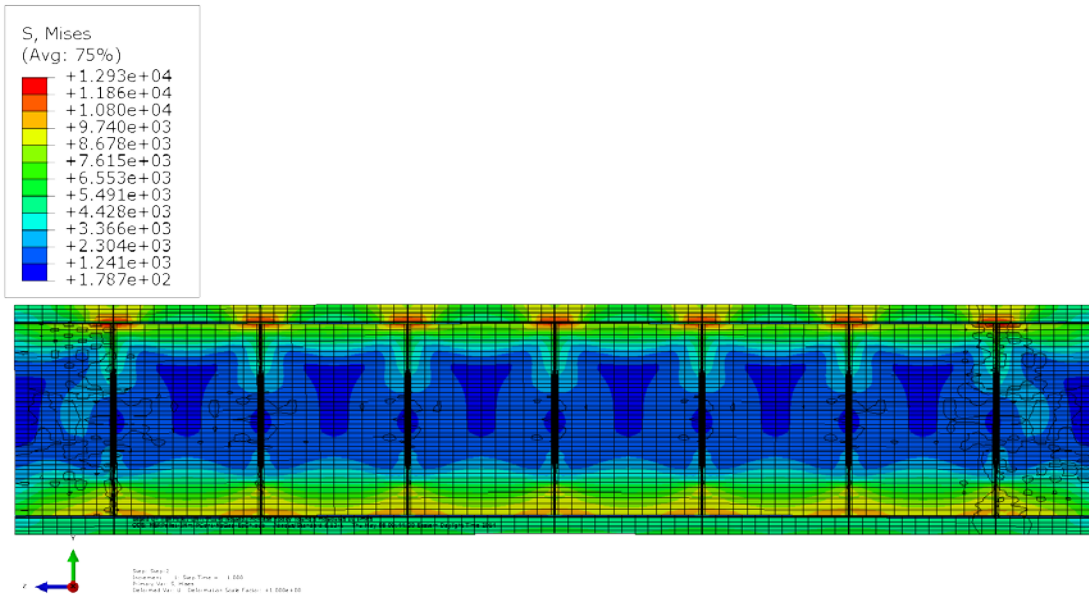
(c) Shear stress σ_{yz}

Figure 19. Shear stress distribution at the clad of the clad-epoxy-pellet section model of HBR pellets with debonded pellet-pellet interfaces without gaps, and bonded pellet-clad interfaces using epoxy.

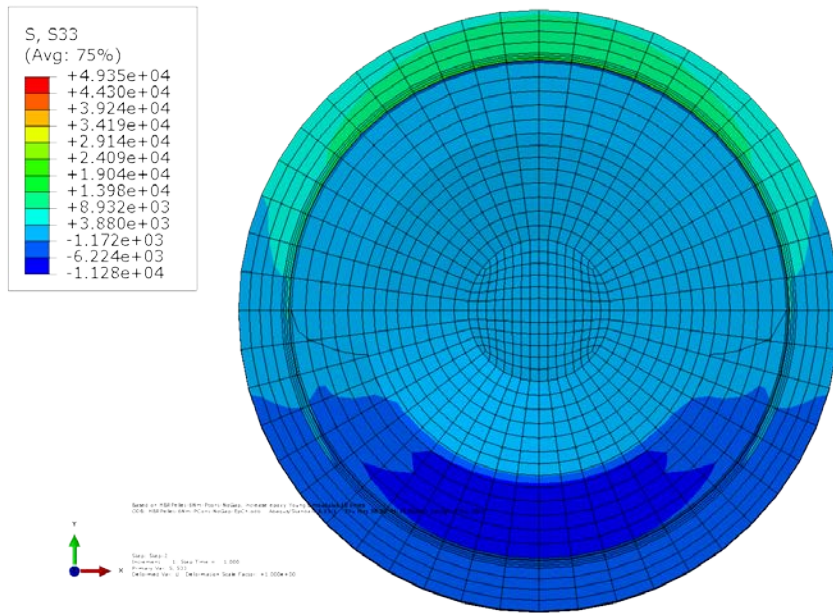
2.2.2.2 Interfacial Material with $10 \times$ Young's Modulus

The fourth case in this section is similar to the third case for debonded pellet-pellet interfaces without gaps between the interfaces. The difference is that the Young's modulus of the bonding material was set to 10 times that of epoxy, as in the second simulation case. Figure 20 shows the resulting normal stress distribution and curvature. The stress distribution generally is similar to that of the case illustrated in Figure 18. The maximum stress on the clad occurs at the top pellet-pellet interface regions; and at the compression side, the pellet pinching helps reduce the stress level at the bottom of the clad. However, stress concentrations occur both at the tops of the pellets (because of the stiffer cohesive bonding) and at the bottom pellet-pellet corners because of the direct contact between pellets. The maximum von Mises stress level is higher than that shown in Figure 18, but no material yields. The σ_{zz} results show a higher level stress concentration in the fuel rod system than that shown in Figure 18.

Figure 21 illustrates results for shear stress at the clad that are similar to the results in the third simulation case (Figure 19). There is no shear stress concentration at the bottom compression region, although the maximum shear stress levels are close to those in the second simulation case (Figure 16) because the same cohesive bonding material was used.

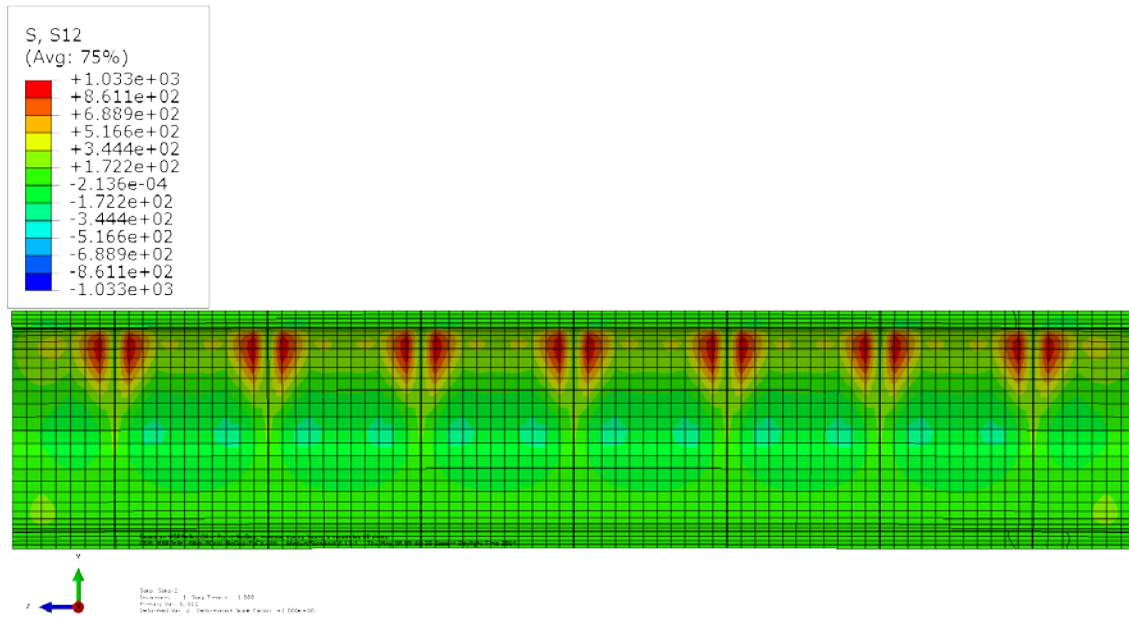


(a) Longitudinal section view of resultant curvature and von Mises stress

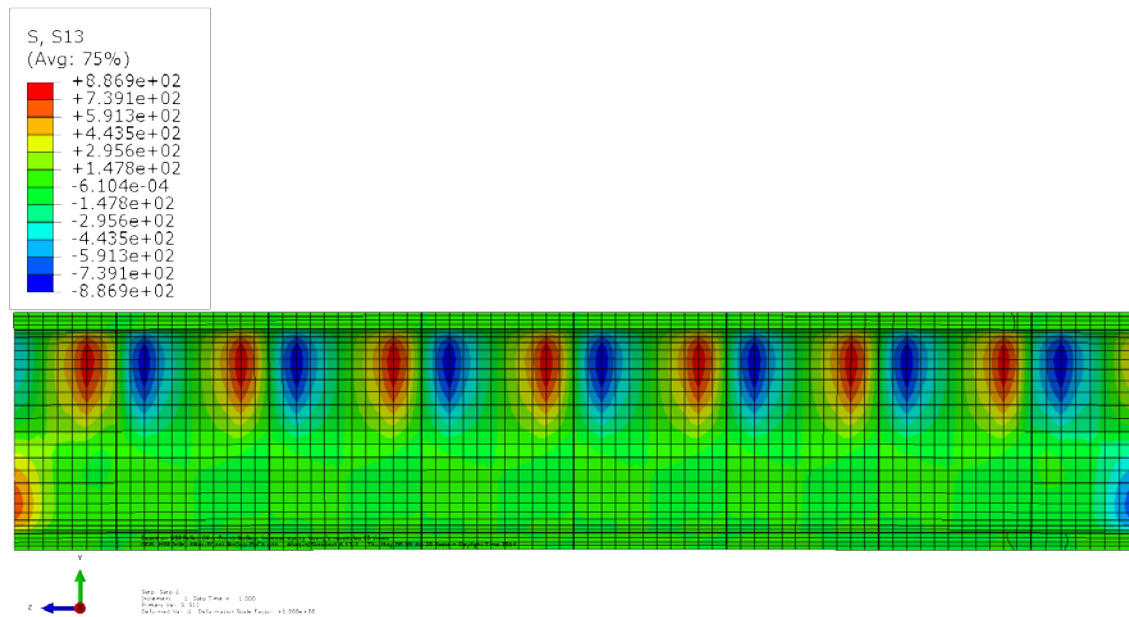


(b) Cross section view of resultant σ_{zz} at a pellet-pellet interface

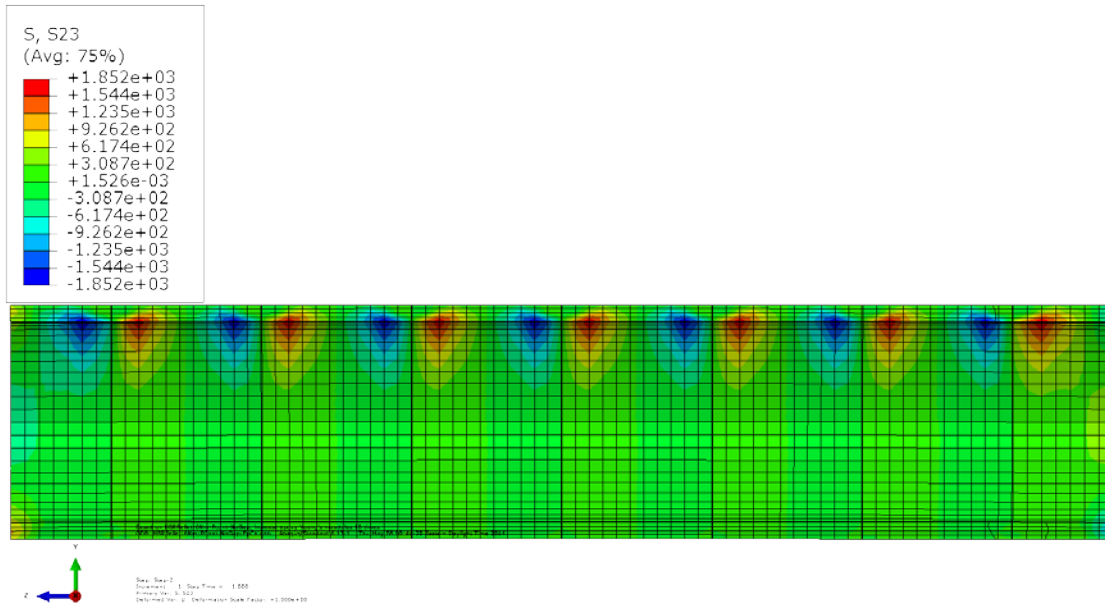
Figure 20. Normal stress distribution and curvature results for clad-epoxy-pellet section model of HBR pellets with debonded pellet-pellet interfaces without gaps, and bonded pellet-clad interfaces using a $10 \times$ Young's modulus material.



(a) Shear stress σ_{xy}



(b) Shear stress σ_{xz}



(c) Shear stress σ_{yz}

Figure 21. Shear stress distribution results at the clad of the clad-epoxy-pellet section model of HBR pellets with debonded pellet-pellet interfaces without gaps, and bonded pellet-clad interfaces using a $10 \times$ Young's modulus material.

Table 3 summarizes the estimate curvature, flexural rigidity, and components load-carrying capacity from the four FEA simulation cases discussed in this section. The same bending load, 6.25 N·m, was used in all of the FEA simulations. The curvature and the flexural rigidity listed in Table 3 indicate that for interface bonding simulation, the immediate consequence of debonding at the pellet-pellet interface is a significant increase in curvature, which results in a significant reduction in the estimated flexural rigidity. This phenomenon is primarily due to a shift in load-carrying capacity from the pellets to the clad.

Table 3. Comparison of curvature, flexural rigidity, and bending moment for the bonded pellet-clad and debonded pellet-pellet cases

	Curvature κ (1/m)	Flexural rigidity EI (N·m ²)	Clad bending moment M (N·m)	Pellet bending moment M (N·m)
Pellet-pellet interface with gap debonding; pellet-clad interface bonded with epoxy	0.160	39	5.73	0.52
Pellet-pellet interface with gap debonding, pellet-clad interface bonded with $10 \times$ Young's modulus material	0.118	53	4.90	1.35
Pellet-pellet interface without gap debonding, pellet-clad interface bonded with epoxy	0.119	53	3.99	2.26
Pellet-pellet interface without gap debonding, pellet-clad interface bonded with $10 \times$ Young's modulus material	0.097	65	3.52	2.73

The induced curvature of 0.160 m^{-1} for debonded pellet-pellet interfaces with gaps and a pellet-clad interface bonded with epoxy is twice the curvature value of 0.082 m^{-1} for the case of perfect bonding with epoxy in the gaps. The estimated flexural rigidity of $39 \text{ N}\cdot\text{m}^2$ for the case of a debonded pellet-pellet interface is a reduction of about 49% compared with of $77 \text{ N}\cdot\text{m}^2$ for perfect interfacial bonding.

Table 3 shows that there is a significant difference between curvature results for epoxy bonding at the pellet-clad interface and the results for a $10 \times$ Young's modulus bonding material. As the Young's modulus of the bonding material increases, the curvature decreases by 26% for a pellet-pellet interface with gaps and by 18% for a pellet-pellet interface without gaps. The flexural rigidity increases by the same percentages as the curvature decreases, indicating that the $10 \times$ Young's modulus material increases the stiffness of the composite system, and gaps at the pellet-pellet interfaces play a critical role in estimating the flexural rigidity of the HBR fuel rod. The induced curvature of 0.160 m^{-1} for the debonded pellet-pellet interfaces with empty gaps and a pellet-clad interface bonded with epoxy is 1.3 times that of the debonded pellet-pellet interfaces without gaps. The result is a 26% reduction in flexural rigidity, from $53 \text{ N}\cdot\text{m}^2$ for the case with no gaps to $39 \text{ N}\cdot\text{m}^2$ for the case with empty gaps. The pellet-clad interface bonded with the $10 \times$ Young's modulus material showed a similar when the gaps were eliminated. In Table 2, the perfectly bonded pellets carry more bending moment than the clad. Table 3 summarizes the estimate curvature, flexural rigidity, and components load-carrying capacity from the four FEA simulation cases discussed in this section. The same bending load, $6.25 \text{ N}\cdot\text{m}$, was used in all of the FEA simulations. The curvature and the flexural rigidity listed in Table 3 indicate that for interface bonding simulation, the immediate consequence of debonding at the pellet-pellet interface is a significant increase in curvature, which results in a significant reduction in the estimated flexural rigidity. This phenomenon is primarily due to a shift in load-carrying capacity from the pellets to the clad.

In Table 3, the data clearly show a significant shift in bending moment resistance from the pellets to the clad as a result of debonding at pellet-pellet interfaces. For all four simulation cases discussed in this section, the clad takes more of the bending moment than the pellets. In the fuel rod with the stiffer cohesive bonding material, the clad carries less bending load than in the rod with epoxy as the bonding material. When the pellets directly contact one another without gaps, the bending moment on the clad drops by around 30% compared with the pellets with empty gaps.

These results indicate that the gap-induced stress concentration and large deformations of the clad at the pellet-pellet interface region can lead to a significant reduction in the bending stiffness, i.e., flexural rigidity (EI), of the fuel rod system. If there are no gaps at the pellet-pellet interfaces, the pellets can carry a significant portion of the bending moment resistance via direct pellet-pellet contact (interaction) to mitigate the stress concentration and potential yielding at the clad.

2.3 Debonded Pellet-Clad and Pellet-Pellet Interfaces

Under flexural deformation, high shear stress will arise at the pellet-clad interfaces to compensate for the material mismatch and the flexural shear stress in the SNF system. Thus, under reversal bending loading during normal transportation, both cyclic normal stress and shear stress can further degrade the interface bonding at pellet-clad interfaces. In this section, debonded pellet-clad interfaces and debonded pellet-pellet interfaces are investigated using the clad-epoxy-pellet section model with eight HBR pellets.

2.3.1 Debonded Pellet-Clad Interfaces and Debonded Pellet-Pellet Interfaces with Empty Gaps

As illustrated in Figure 22, simulations of interfacial debonding at both pellet-clad and pellet-pellet interfaces initially focus on the case with empty gaps at debonded pellet-pellet interfaces and a thin layer at debonded pellet-clad interfaces. At pellet-clad interfaces, the outer pellet surfaces contact the inner surface of the thin layer, and the outer surface of the thin layer contacts the inner surface of the clad. Pellets have dips at both end surfaces with rounding of 0.002 in. A fuel rod consisting of Zr-4 clad and HBR pellet inserts is used to study the system response to the bending moment with debonded interfaces. Loading and boundary conditions are the same as that assumed in the previous cases, and the bending moment is assigned at 6.25 N·m.

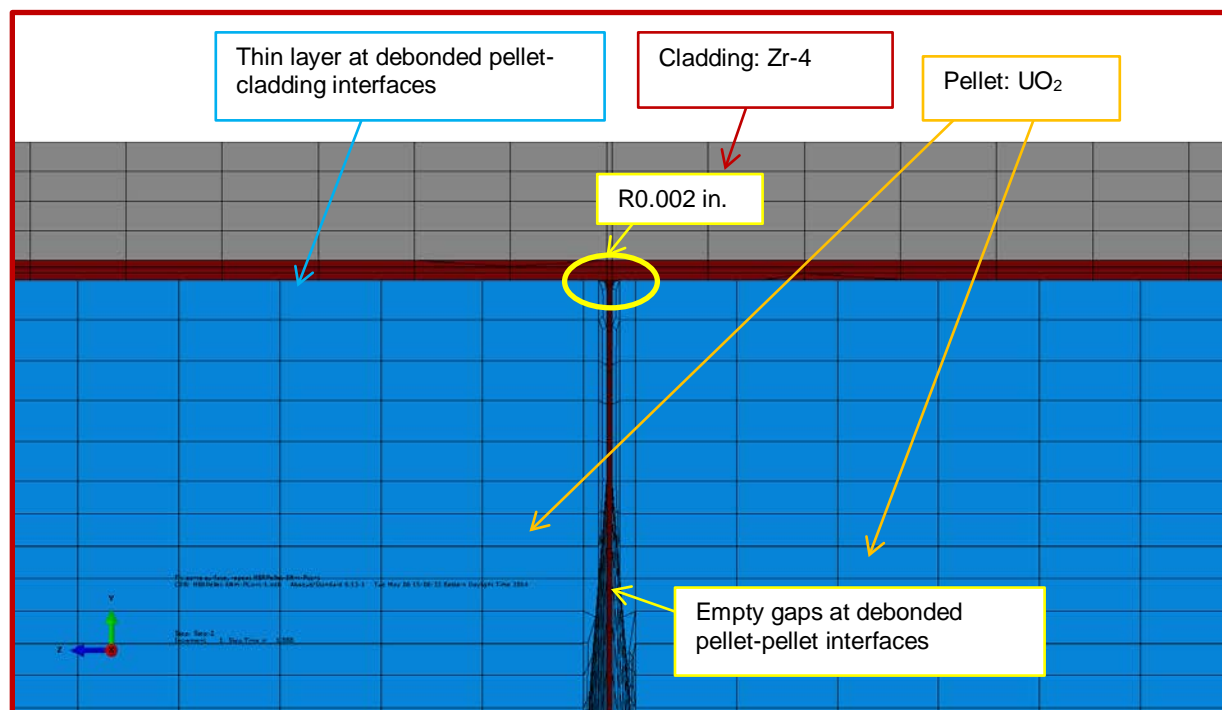
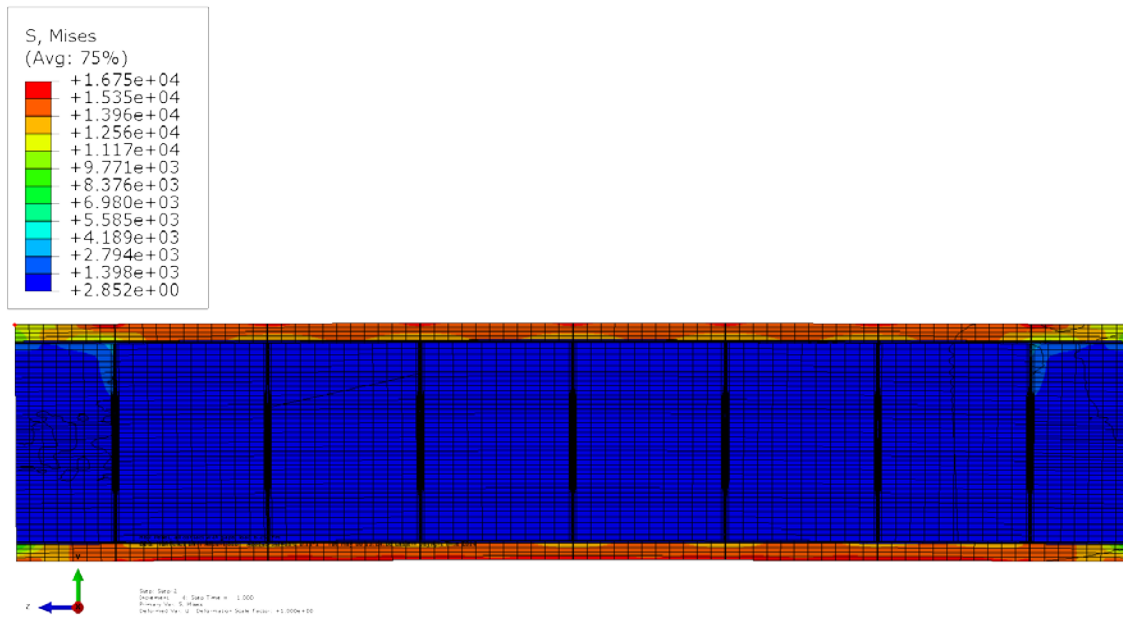


Figure 22. Detail area from Figure 4 for the cases of empty gaps at debonded pellet-pellet interfaces, and a thin layer filled at the debonded pellet-clad interfaces.

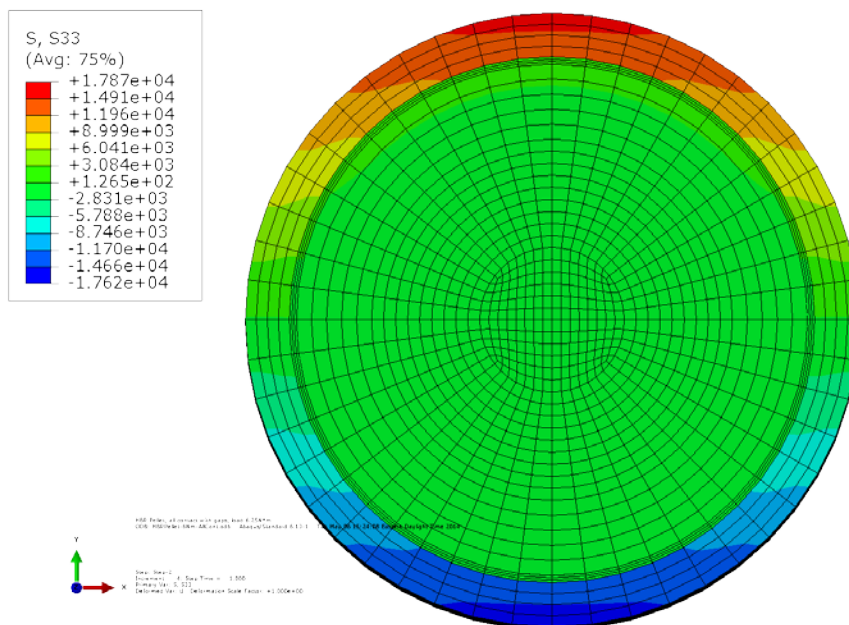
2.3.1.1 Epoxy Used as Interfacial Material

The first simulation began with a thin layer of epoxy. The resulting normal stress distribution shown in Figure 23 indicates that the clad reached maximum stress throughout the whole gauge section when interfacial debonding occurred at both pellet-clad and pellet-pellet interfaces. This result is in strong contrast to the results shown in Figure 13, in which the Zr-4 clad shows stress concentrations only locally at pellet-pellet interface regions. Because of the small bending load and the high material yield strength, the clad did not yield at the maximum stress. The pellets were all below the yielding stress, as well. The induced curvature of 0.218 m^{-1} is almost triple that of the perfect bond case. This suggests that, as a result of the interface debonding at both the pellet-clad and pellet-pellet interfaces, the pellets and the clad can contact (or pin) only at the pellet-pellet-clad interface region, and pellets cannot provide direct internal support to the clad. Therefore, the load-carrying capacity shifts significantly from the pellets to the clad at the entire gauge section. The results also indicate that the Zr-4 clad carries most of the bending moment

resistance. The bending deformation in the debonded pellet-clad region is likely to result in further pinning action at pellet-clad interfaces, which may also result in accelerated aging of the clad tubing.



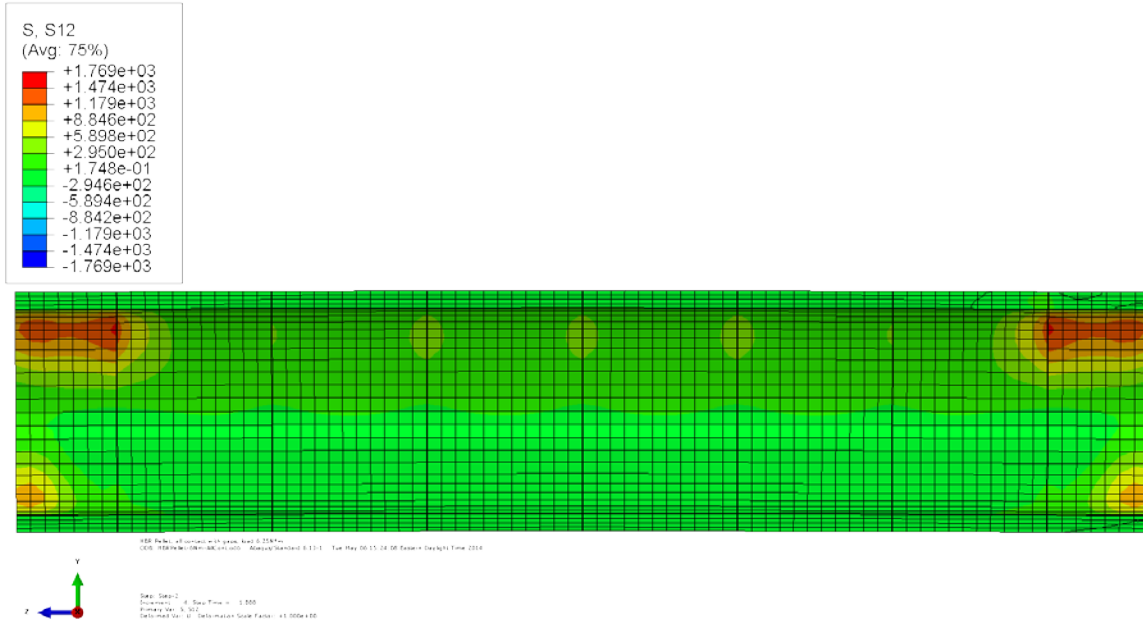
(a) Longitudinal section view of resultant curvature and von Mises stress



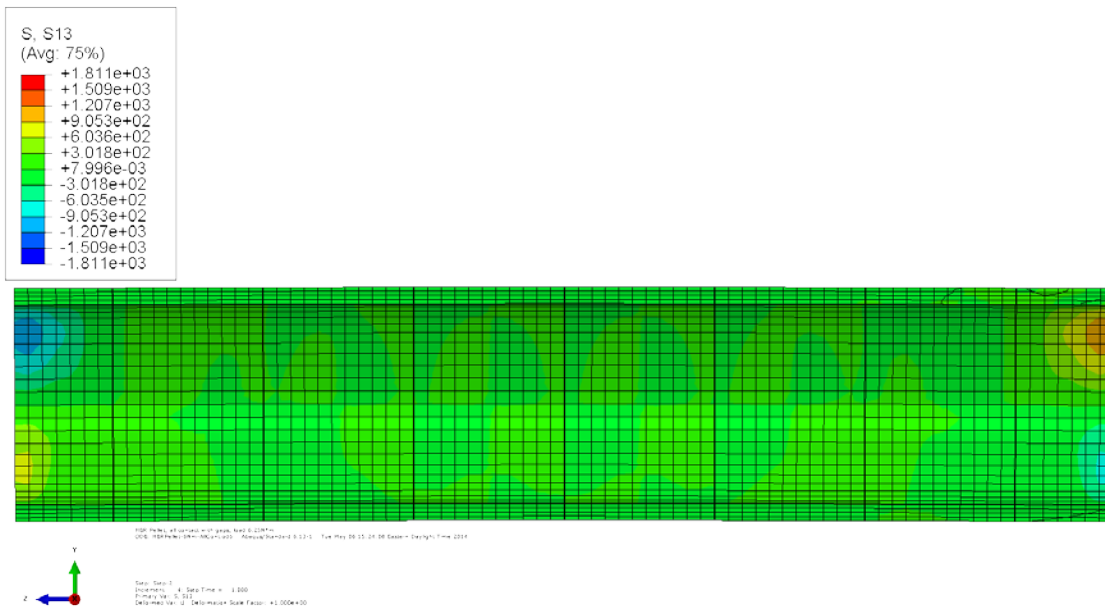
(b) Cross section view of σ_{zz} at a pellet-pellet interface

Figure 23. Normal stress distribution and curvature results for clad-epoxy-pellet section model of HBR pellets with empty gaps at debonded pellet-pellet interfaces, and an epoxy layer at debonded pellet-clad interfaces.

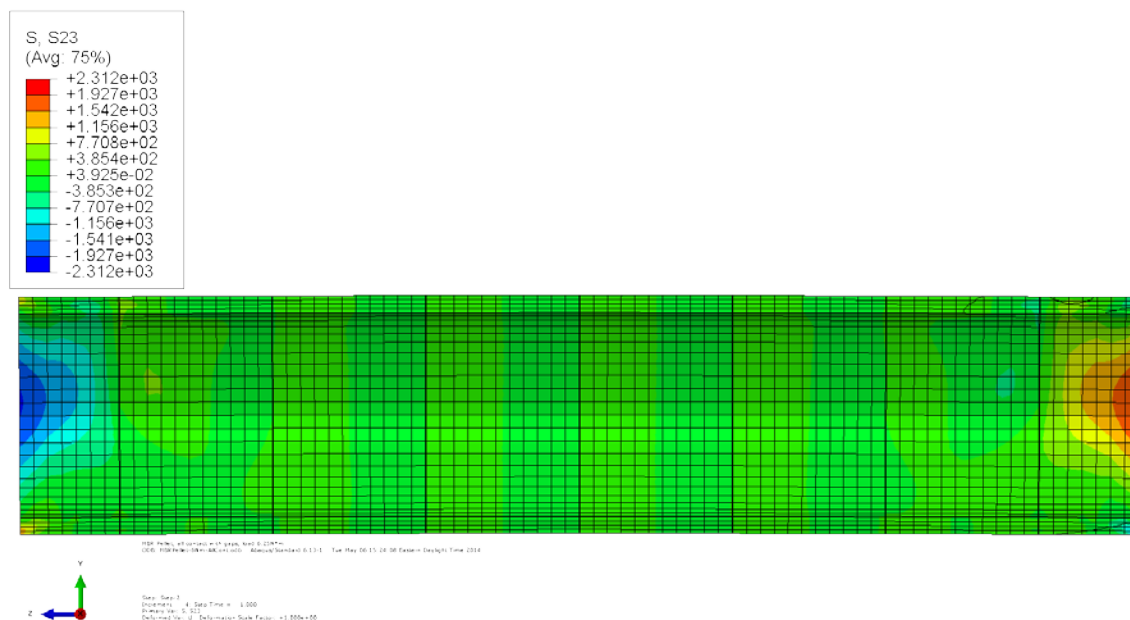
Figure 24 illustrates the shear stress results for this simulation case. The stress pattern appears to be similar to the perfect bond case. There are no shear stress surges inside the gauge section of the cladding as a result of further pellet-clad interface debonding. Because the pellets and the clad can make contact only at the interfaces, the clad cannot directly transfer the shear stress within the gauge section. However, there are some stress concentrations at the boundary as a result of component contact.



(a) Shear stress σ_{xy}



(b) Shear stress σ_{xz}



(c) Shear stress σ_{yz}

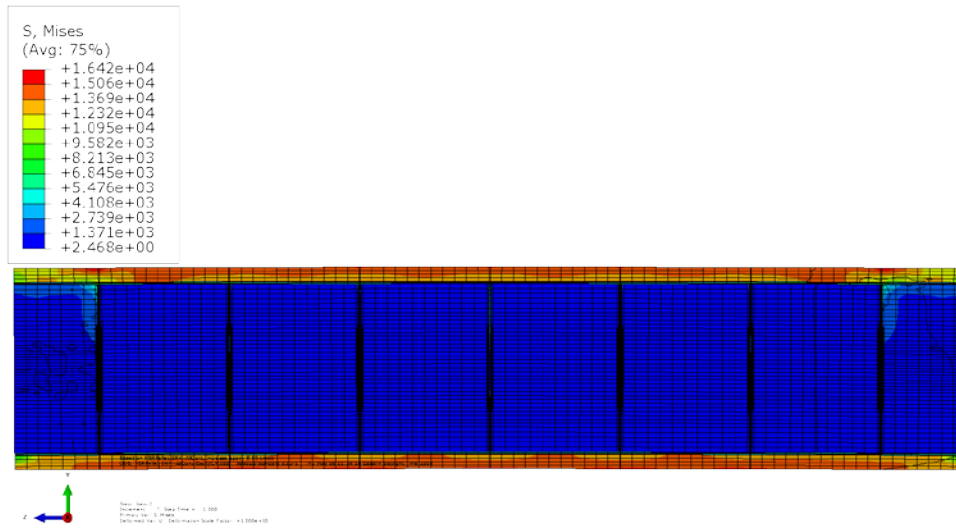
Figure 24. Shear stress distribution at the clad of the clad-epoxy-pellet section model of HBR pellets with empty gaps at debonded pellet-pellet interfaces, and an epoxy layer at debonded pellet-clad interfaces.

2.3.1.2 Interfacial Material with $10 \times$ Young's Modulus

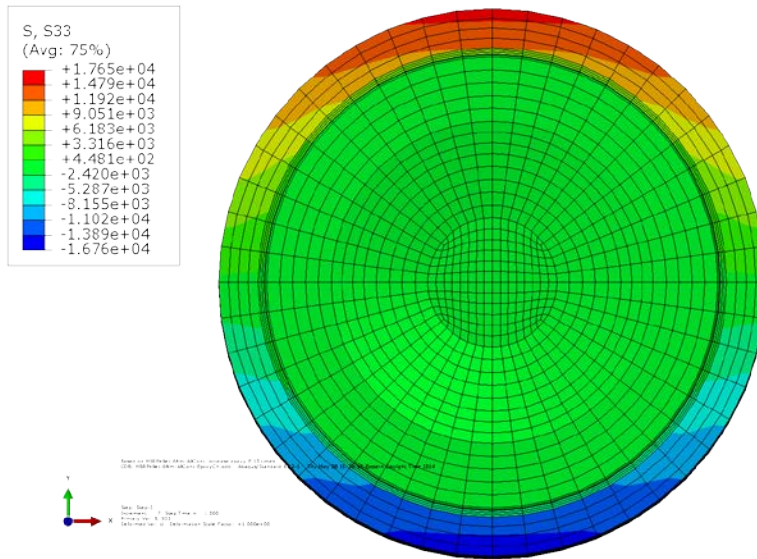
The second simulation case—interfacial debonding at both pellet-clad and pellet-pellet interfaces—used the same conditions as the first simulation except that the layer between the pellet and the clad had a Young's modulus 10 times that of epoxy.

Figure 25 shows normal stress distribution results very similar to those shown in Figure 23. The clad has reached maximum stress. The maximum stress level seen in the two figures is the same, which indicates that the property change in the interfacial material affects the bending response only slightly because of the interfacial debonding. Even though the stress concentration occurred over almost the entire gauge section, the maximum stress at the clad is still lower than the yielding strength. Therefore, the clad did not yield in this case.

The shear stress distributions in Figure 26 do not show a large change from the results of the first simulation case seen in Figure 24. There was no shear stress concentration inside the cladding. The stress levels are about the same as in Figure 24. That is because the pellets and the cladding contacted the bonding material as a result of the pellet-clad interfacial debonding. The interfacial material has a limited impact on the system's flexural response.

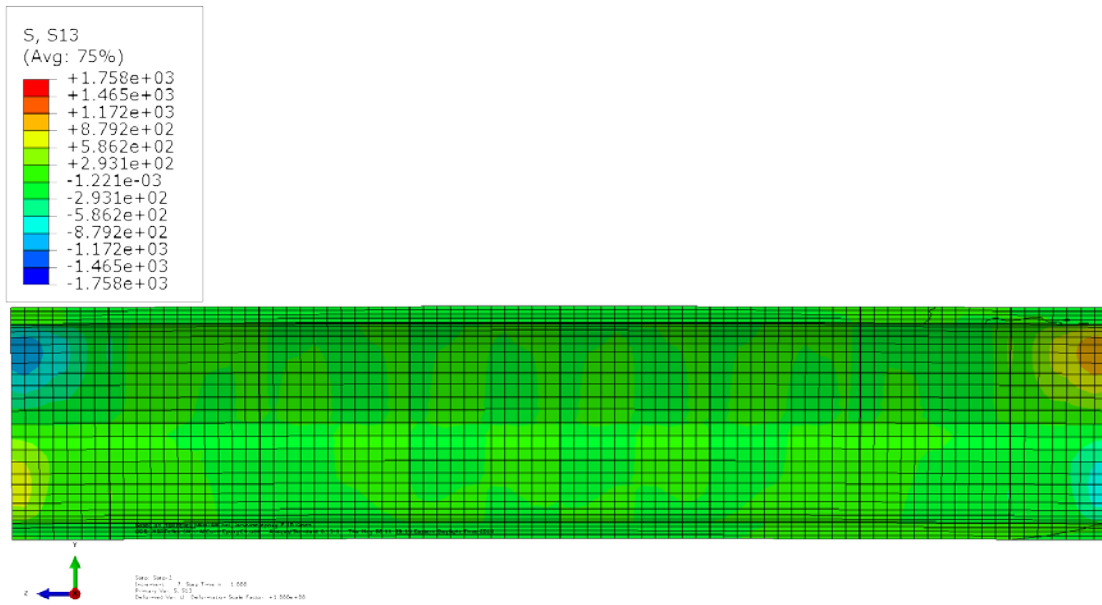
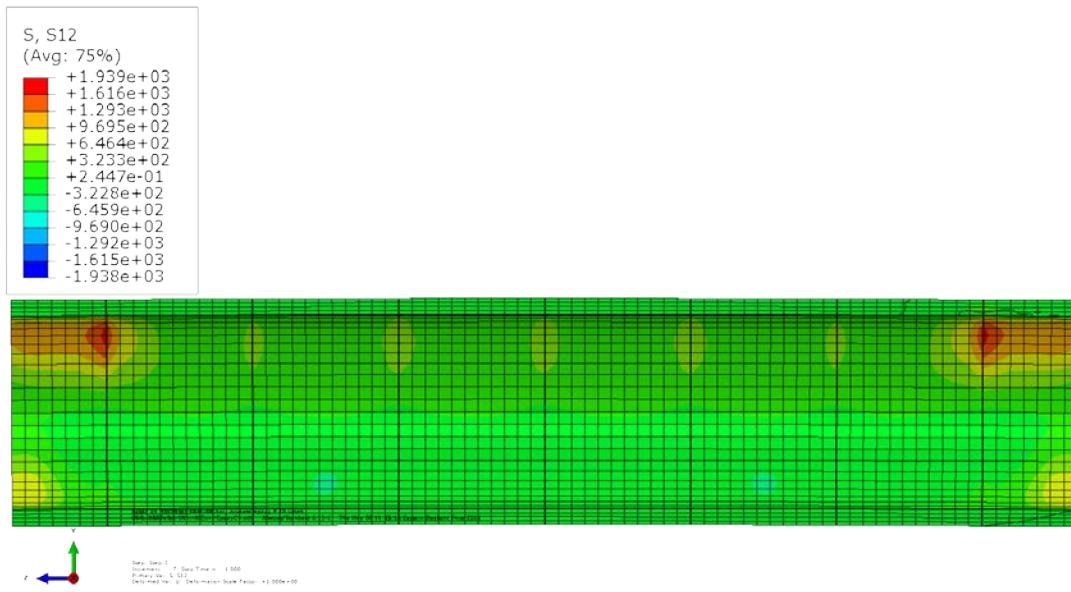


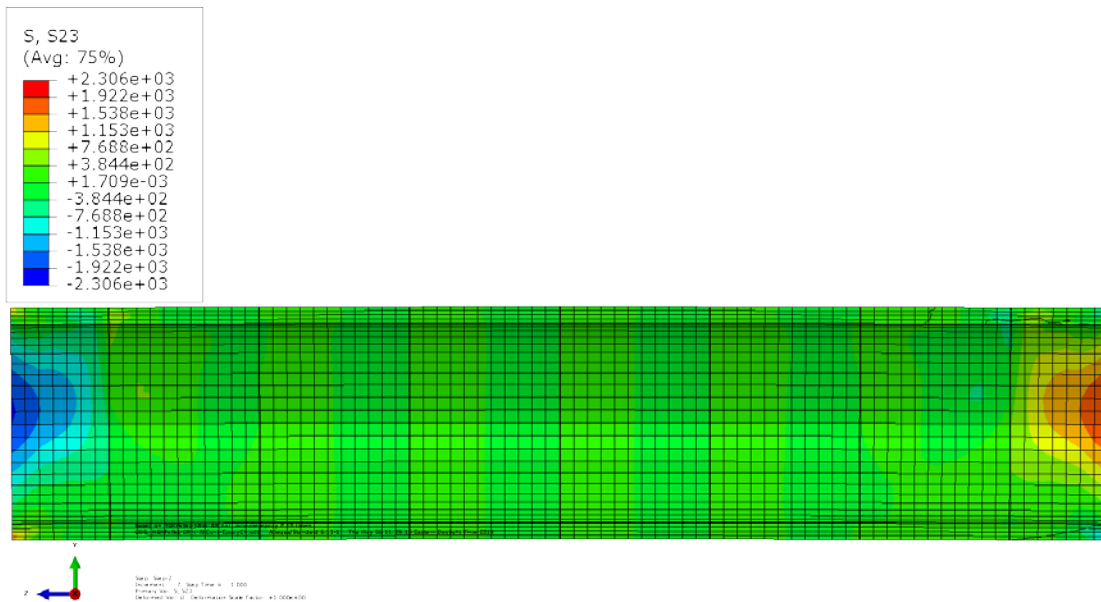
(a) Longitudinal section view of curvature and von Mises stress



(b) Cross section view of σ_{zz} at a pellet-pellet interface

Figure 25. Normal stress distribution and curvature results for clad-epoxy-pellet section model of HBR pellets with empty gaps at debonded pellet-pellet interfaces, and a layer with a $10 \times$ Young's modulus material at debonded pellet-clad interfaces.





(c) Shear stress σ_{yz}

Figure 26. Shear stress distribution at the clad of clad-epoxy-pellet section model of HBR pellets with empty gaps at debonded pellet-pellet interfaces, and a layer of $10 \times$ Young's modulus material at debonded pellet-clad interfaces.

2.3.2 Debonded Pellet-Clad Interfaces and Debonded Pellet-Pellet Interfaces without Gaps

The simulation cases for debonded pellet-pellet interfaces without gaps are shown in Figure 27, where a thin layer is filled at debonded pellet-clad interfaces, and the pellets are all in direct contact with one another without gaps at the pellet-pellet interfaces. The loading and boundary conditions and the material properties are the same as in the previous cases. In this case, there are still eight HBR pellets with rounding of 0.002 in.

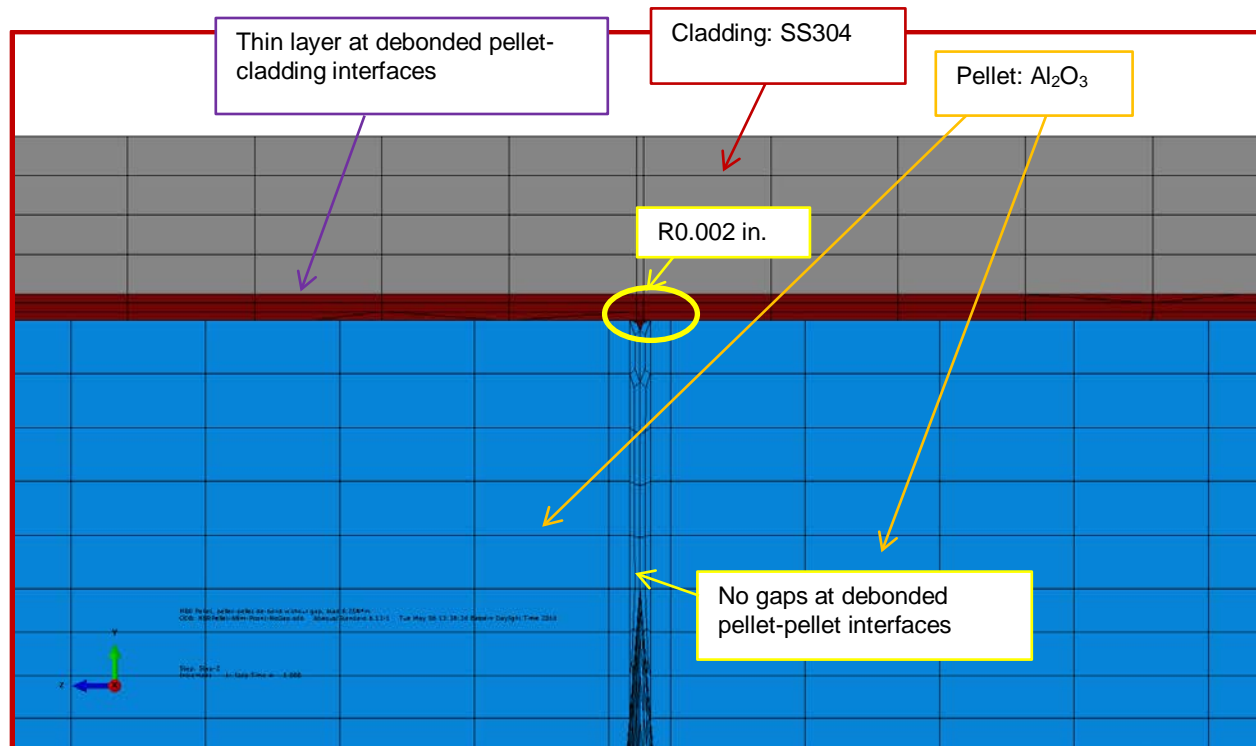
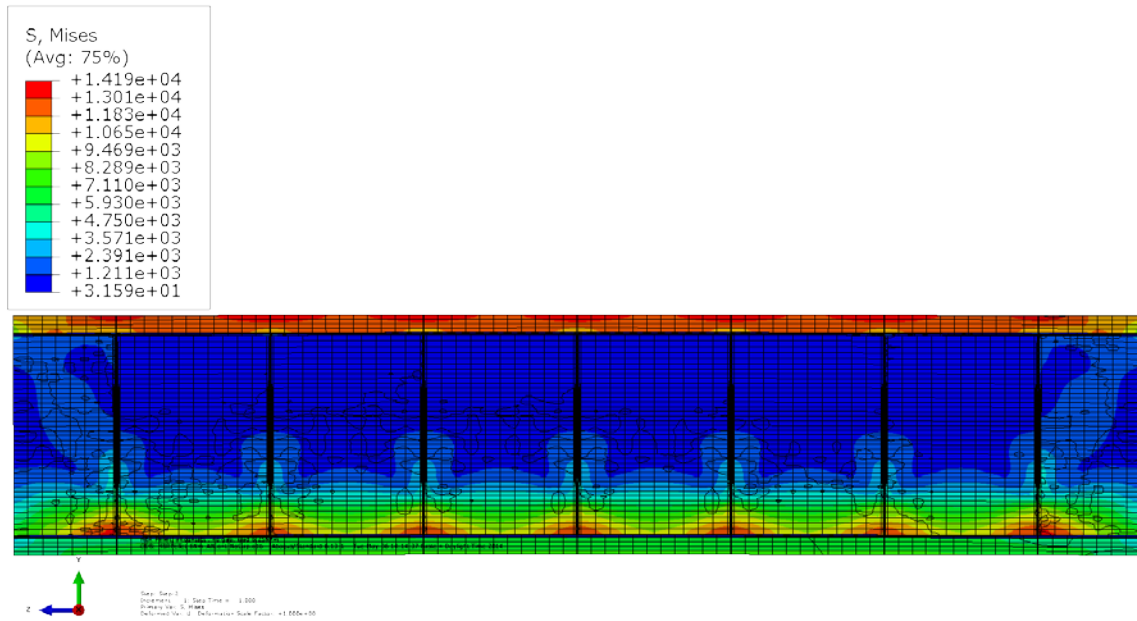


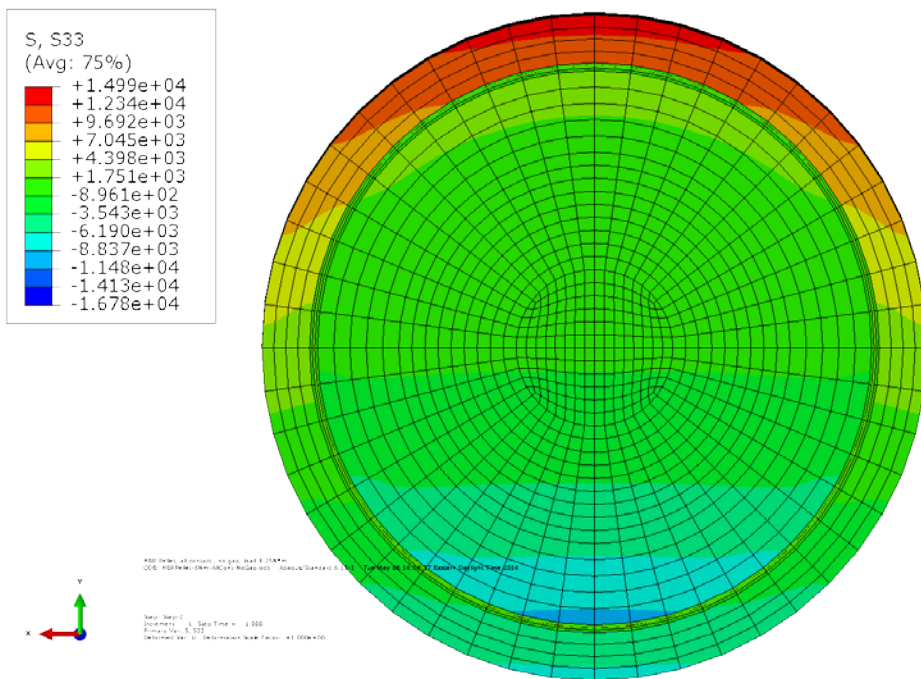
Figure 27. Detail area from Figure 4 for the case with no gaps at debonded pellet-pellet interfaces and a thin layer at debonded pellet-clad interfaces.

2.3.2.1 Epoxy Used as Interfacial Material

The third simulation case in this section used epoxy as the interfacial material filling the debonded pellet-clad interfaces and no gaps at debonded pellet-pellet interfaces. Figure 28 illustrates the HBR rod responses to the bending moment in this simulation. The longitudinal section view shows a stress concentration at the top (tension) region of the Zr-4 clad throughout the gauge section, but the rod did not yield. In the bottom (compression) region, the stress level is low at the clad. The maximum stress still occurred at the compression side of the pellet region where the pellets were pinned to one another. Figure 28 shows interfacial results similar to those observed in Figure 18 for the bonded pellet-clad interfaces and debonded pellet-pellet interfaces without gaps. The pellets carry a large portion of the bending moment resistance via the pinching pellet corners, and they reduce the stress intensity at the bottom (compression) portion of the clad. The major difference compared with the results shown in Figure 18 and Figure 28 is that there is an extensive stress concentration observed at the top region of the clad throughout the entire gauge section which is in contrast to the localized area observed at the interface region as depicted in Figure 18. The clad assumes most of the bending moment resistance because there is no direct mechanism for transferring the load from the pellet to the clad or vice versa due to the debonded pellet-clad interfaces.



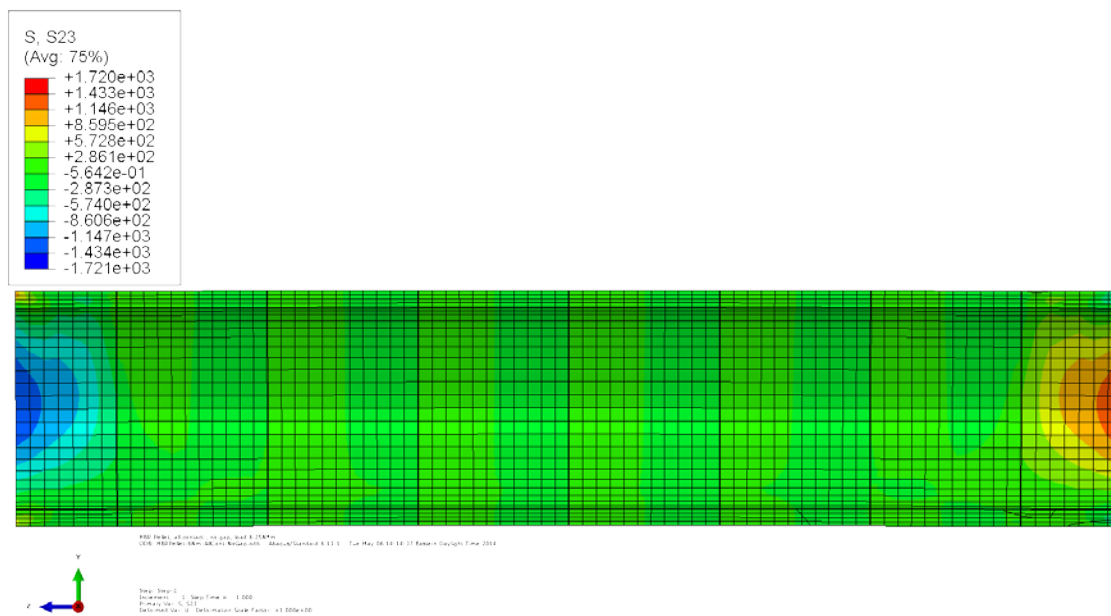
(a) Longitudinal section view of curvature and von Mises stress results



(b) Cross section view of the normal stress, σ_{zz} , results at a pellet-pellet interface

Figure 28. Normal stress distribution and curvature results for the clad-epoxy-pellet section model of HBR pellets without gaps at debonded pellet-pellet interfaces, and with an epoxy layer at debonded pellet-clad interfaces.

In Figure 29(a), the shear stress in radial direction σ_{xy} shows different stress levels at the top tension side and bottom compression side of the clad. Similar to the normal stress distribution, the shear stress at the



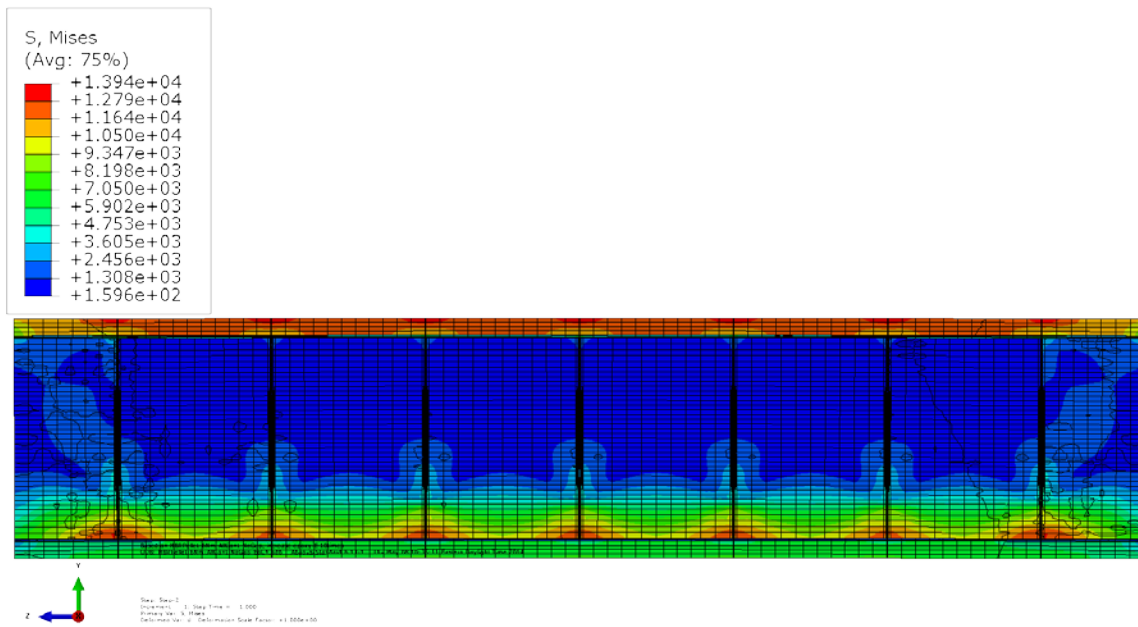
(c) Shear stress σ_{yz}

Figure 29. Shear stress distribution and curvature results for the clad-epoxy-pellet section model of HBR pellets without gaps at debonded pellet-pellet interfaces, and with an epoxy layer at debonded pellet-clad interfaces.

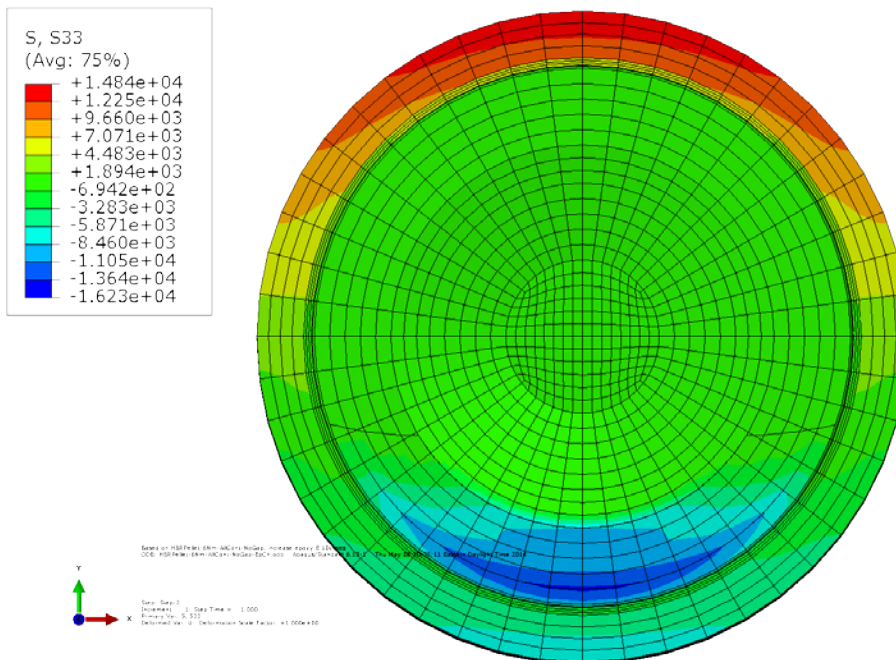
2.3.2.2 Interfacial Material at $10 \times$ Young's Modulus

The fourth simulation is similar to the third one (shown in Figure 27) except the thin layer at the pellet-clad interface used an interfacial material with a Young's modulus 10 times that of epoxy. Based on the normal stress results shown Figure 30, the change in properties in the interface material had little impact on the bending response due to interfacial debonding. The results are close to those seen in Figure 28. There is no significant difference between the shear stress results shown in Figure 31 and those shown in Figure 29.

The evaluated curvature and flexural rigidity results for the cases of debonding at pellet-clad and pellet-pellet interfaces are listed in Table 4. Generally, all interfacial debonding resulted in larger induced curvatures and smaller estimated flexural rigidities. Compared with the perfect bond case results in Table 2 for the all interfacial debonding cases with gaps, flexural rigidity was reduced by up to 66%. Compared with the results for debonded pellet-pellet interfaces listed in Table 3, flexural rigidity dropped (1) by 26–43% compared with the cases of pellets with gaps, depending on the interfacial material, and (2) by 19–31% compared with pellets without gaps. These results further validate the earlier hypothesis that interfacial bonding efficiency can significantly affect the flexural rigidity of the surrogate composite rod. However, the impact of the property change in the interfacial material is small enough to be ignored in these four cases because the interface layer cannot provide direct internal support to resist the bending moment due to interfacial debonding.

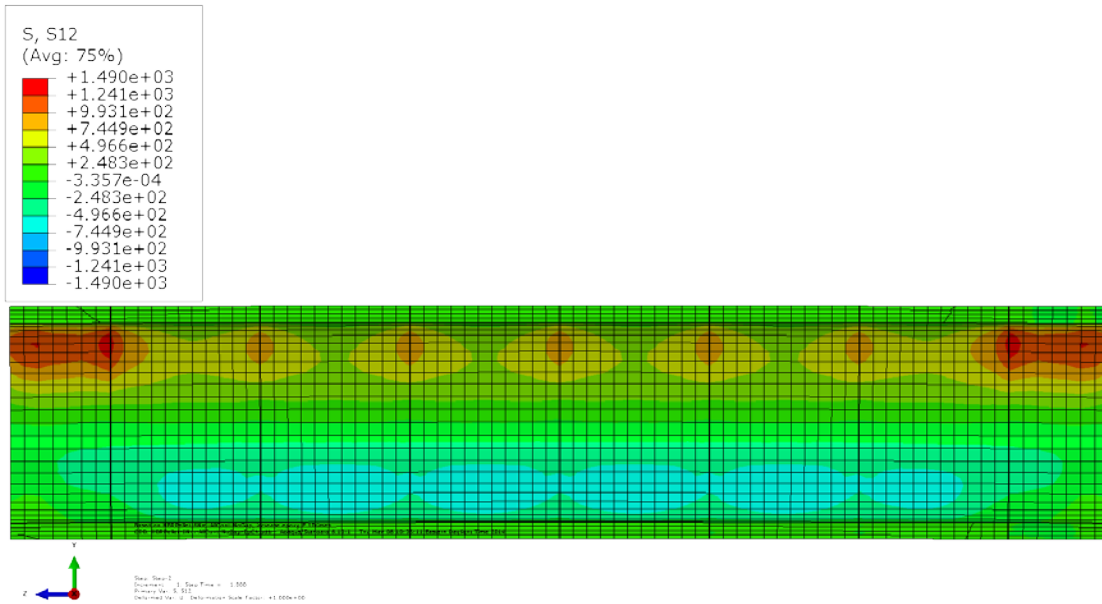


(a) Longitudinal section view of curvature and von Mises stress results

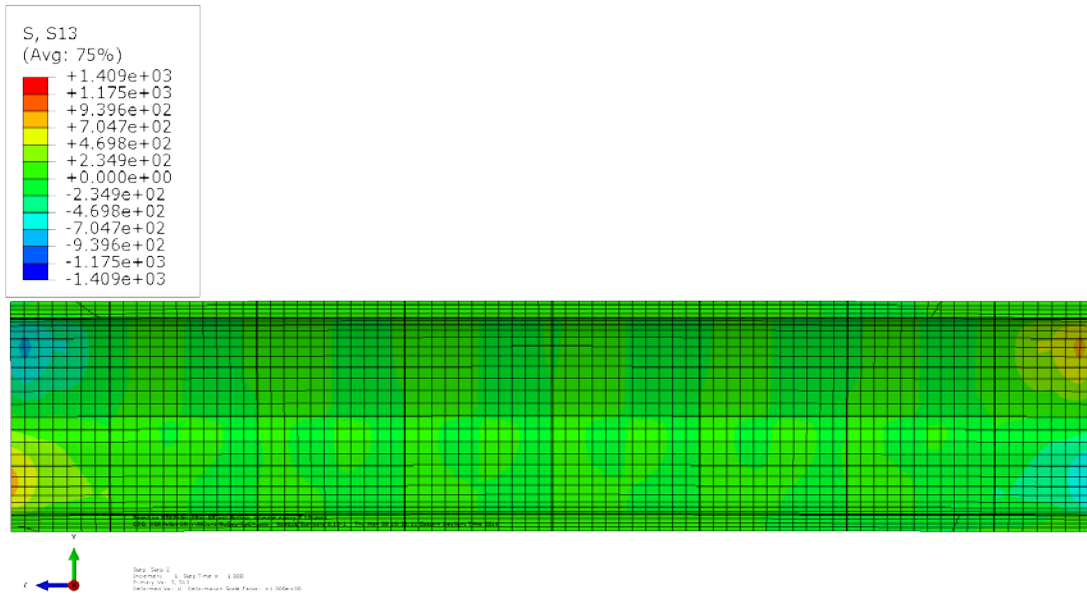


(b) Cross section view of normal stress, σ_{zz} , results at a pellet-pellet interface

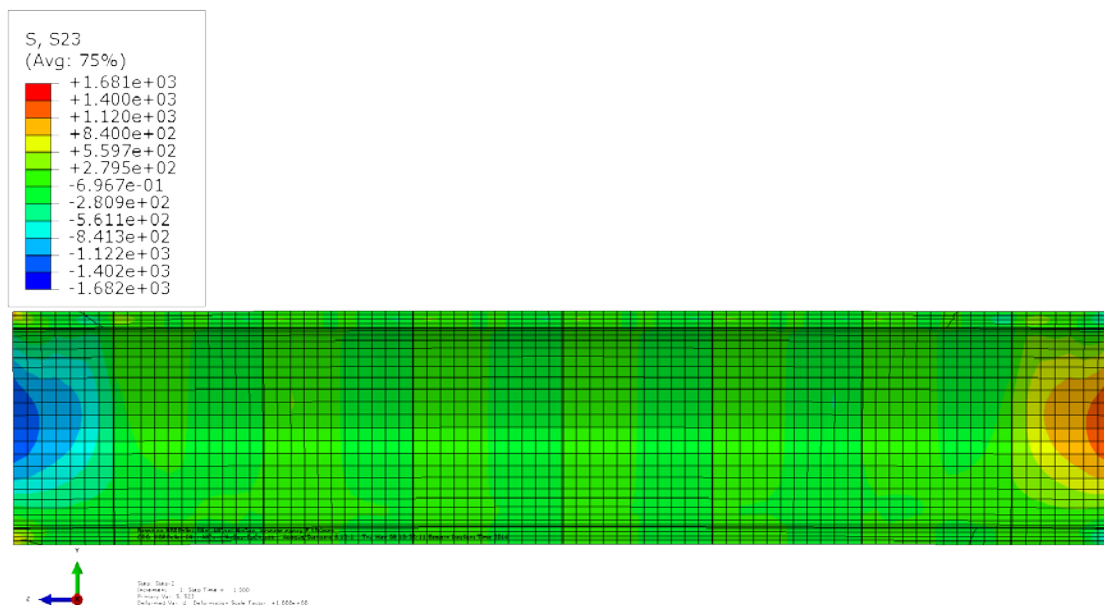
Figure 30. Normal stress distribution and curvature results for the clad-epoxy-pellet section model of HBR pellets without gaps at debonded pellet-pellet interfaces, and with a layer of $10 \times$ Young's modulus material at debonded pellet-clad interfaces.



(a) Shear stress σ_{xy}



(b) Shear stress σ_{xz}



(c) Shear stress σ_{yz}

Figure 31. Normal stress distribution and curvature of clad-epoxy-pellet section model of HBR pellets without gaps at debonded pellet-pellet interfaces, and with a layer of $10 \times$ Young’s modulus material at debonded pellet-clad interfaces.

Table 4. The curvature, flexural rigidity and bending moment comparison for debonded pellet-clad and pellet-pellet interfaces

	Curvature $\kappa(1/m)$	Flexural rigidity EI (N·m ²)	Clad bending moment M (N·m)	Pellet bending moment M (N·m)
Pellet-pellet interface with gap debonded; pellet-clad interface debonded with epoxy	0.218	29	6.23	0.02
Pellet-pellet interface with gap debonded; pellet-clad interface debonded with $10 \times$ Young’s modulus material	0.202	30	5.96	0.29
Pellet-pellet interface without gap debonded; pellet-clad interface debonded with epoxy	0.146	43	4.15	2.10
Pellet-pellet interface without gap debonded; pellet-clad interface debonded with $10 \times$ Young’s modulus material	0.140	45	3.98	2.27

The gaps play an important role in flexural rigidity estimation. In Table 4, the flexural rigidity of the case without gaps at pellet-pellet interfaces is 1.5 times of that of the case with gaps. Table 3 summarizes the estimate curvature, flexural rigidity, and components load-carrying capacity from the four FEA simulation cases discussed in this section. The same bending load, 6.25 N·m, was used in all of the FEA simulations. The curvature and the flexural rigidity listed in Table 3 indicate that for interface bonding simulation, the immediate consequence of debonding at the pellet-pellet interface is a significant increase

in curvature, which results in a significant reduction in the estimated flexural rigidity. This phenomenon is primarily due to a shift in load-carrying capacity from the pellets to the clad.

Table 3, the ratio of the flexural rigidity is 1.2 for the same comparison. The reason for the large increase in flexural rigidity is the direct pellet contact at the pellet-pellet interfaces at the compression side. The direct pellet-pellet contact interaction also provides a significant increase in bending moment resistance; it results in a much smaller curvature deformation, as shown in Table 4.

Table 4 shows that the bending moment significantly shifts from pellet to clad with all interface debonding, especially when there are gaps at pellet-pellet interfaces. When the pellets are in direct contact with one another, the pellets retake a large amount of the bending moment, which helps reduce the bending load on the clad.

2.4 Clad Curvature Estimation

The fuel rod bending curvature is derived from the clad deflection data. In CIRFT, there are three linear variable differential transformers (LVDTs) at two-inch gauge sections of the fuel rod to measure three points of deflections on the clad outside wall (Figure 32).

The curvature κ can be defined by the radius of circle R. Three deflection data points at the clad outside wall can be used to determine the radius of circle R in Figure 33, as follows:

$$\begin{cases} (U_{1y} - y)^2 + (U_{1z} - z)^2 = (U_{2y} - y)^2 + (U_{2z} - z)^2 = R^2 \\ (U_{1y} - y)^2 + (U_{1z} - z)^2 = (U_{3y} - y)^2 + (U_{3z} - z)^2 = R^2 \end{cases} \quad (2)$$

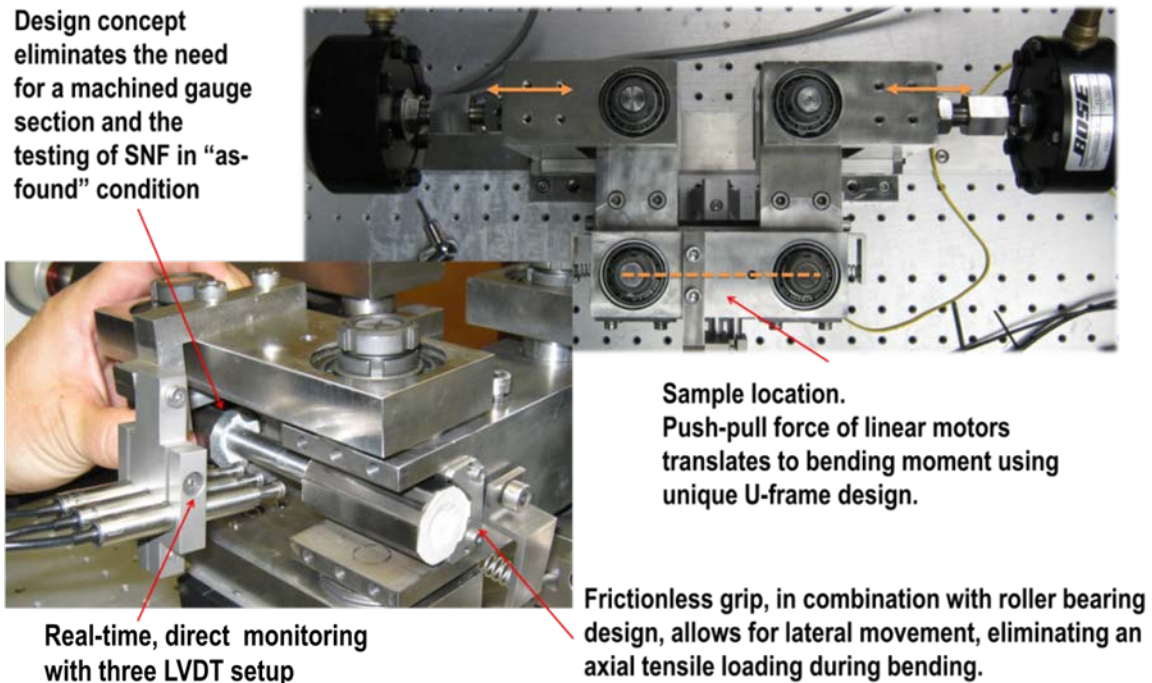


Figure 32. CIRFT system with horizontal U-frame test setup integrated to Bose dual LM2 TB.

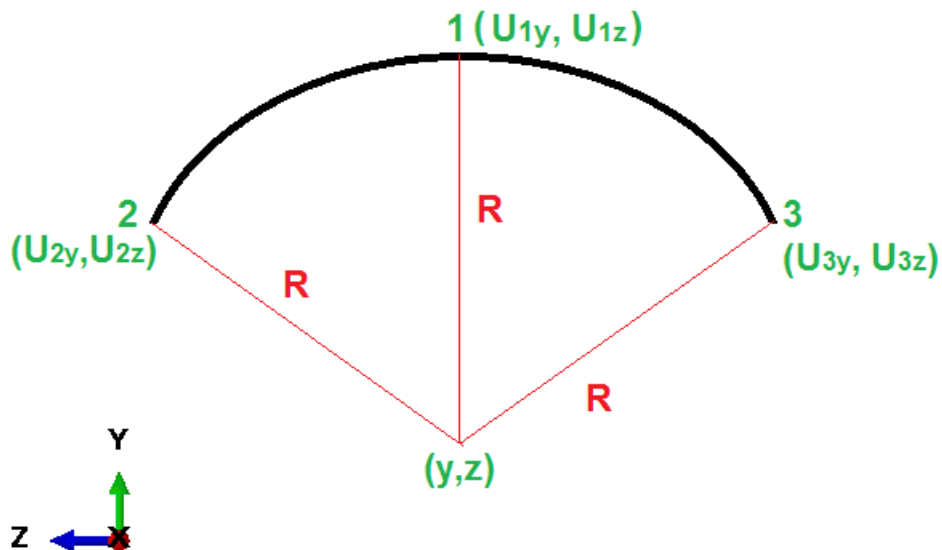


Figure 33. Sketch for curvature calculation.

Solving Eq. (2), the center coordinate of curvature (y, z) can be obtained as

$$\begin{cases} y = \frac{B2 \cdot C1 - B1 \cdot C2}{B2 \cdot A1 - B1 \cdot A2} \\ z = \frac{A2 \cdot C1 - A1 \cdot C2}{A2 \cdot B1 - A1 \cdot B2} \end{cases} \quad (3)$$

$$\text{Where } \begin{cases} A1 = 2 * U_{2y} - 2 * U_{1y} \\ A1 = 2 * U_{3y} - 2 * U_{1y} \\ B1 = 2 * U_{2z} - 2 * U_{1z} \\ B2 = 2 * U_{3z} - 2 * U_{1z} \\ C1 = U_{2y}^2 + U_{2z}^2 - U_{1y}^2 - U_{1z}^2 \\ C2 = U_{3y}^2 + U_{3z}^2 - U_{1y}^2 - U_{1z}^2 \end{cases}$$

So the radius of circle R is

$$R = \sqrt{(U_{1y} - y)^2 + (U_{1z} - z)^2} = \sqrt{(U_{2y} - y)^2 + (U_{2z} - z)^2} = \sqrt{(U_{3y} - y)^2 + (U_{3z} - z)^2} \quad (4)$$

The curvature κ can be determined as

$$\kappa = \frac{1}{R} \quad (5)$$

The following sections discuss the investigation of the curvature estimation using the clad deflection data. The global two-inch gauge section and the localized area where the testing probe cannot focus are analyzed to determine how they are different.

2.4.1 Epoxy Used as Interfacial Material

In this section, the cases of (1) pellet-pellet interfacial debonding without gaps and (2) pellet-clad interfaces with good bonding are used as examples to study curvature estimation. In the first study category, the interface material at the pellet-clad interfaces uses epoxy. As seen in Figure 34, the normal stress σ_{zz} result for this simulation is distributed nonuniformly in the two-inch gauge section. As discussed in the previous section, at pellet-pellet interface debonded regions, the clad takes most of the bending moment, which results in stress concentration. The maximum stress in these regions is 14.7 ksi. At the middle of the pellet-clad bond region, the clad has relatively less stress, with an average level of 9.1 ksi. There is significant deviation in stress distribution.

Therefore, two sets of deflection data were chosen to estimate curvature: one from the two-inch gauge section, referred to as “global data,” and the other from a finite localized area, referred to as “local data.” The first two sets of induced deflection data were selected from the tension side of the clad under bending deformation in Figure 34. One set of the deformed coordinates (U_{1y} , U_{1z}), (U_{2y} , U_{2z}) and (U_{3y} , U_{3z}) from three points at the outside wall of the clad in the global two-inch section range were output to calculate the curvature by following Eqs. (2) through (5). The estimated curvature and resultant flexural rigidity are listed in Table 5 for comparison. The other set of data for curvature estimation were selected from the localized area, the detail area shown in Figure 34. This localized area is at the pellet-pellet interface debonded region. The three points are located at a finite distance, where the LVDT cannot be focused in the testing. These three deformed coordinates were output to estimate curvature and flexural rigidity.

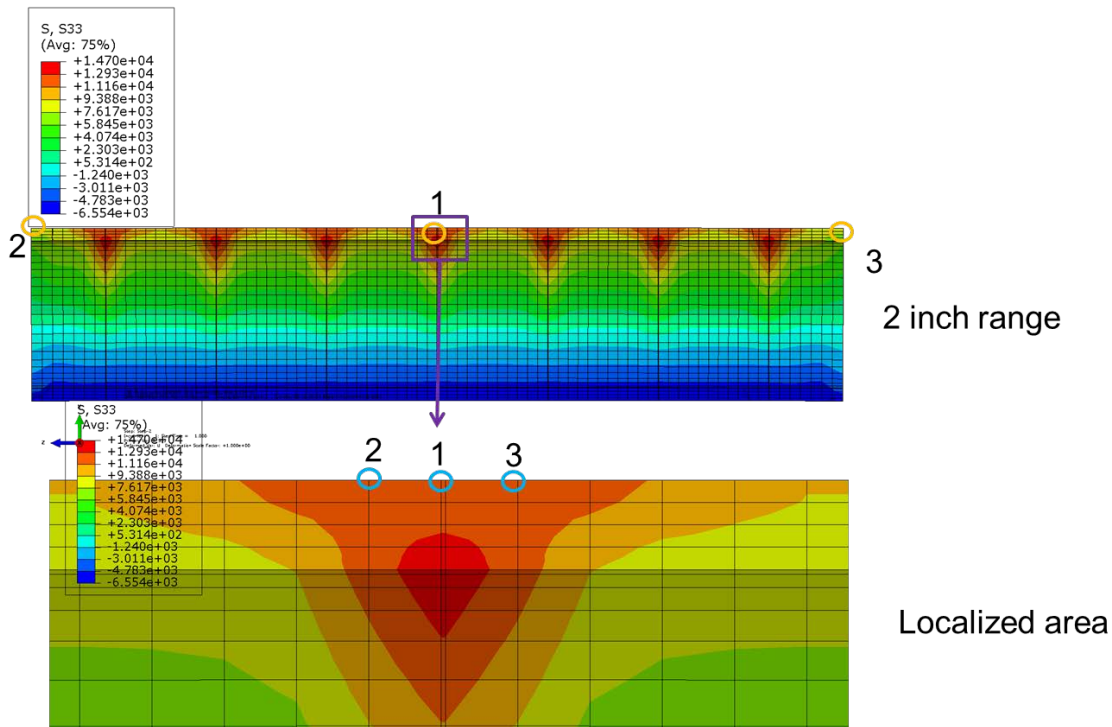


Figure 34. Curvature estimations from the deflection data at the tension side of the clad for case using epoxy as the interfacial material.

The summarized results in Table 5 show a large difference in curvature estimation and associated flexural rigidity when the three deflection data points are chosen from the relatively global and local areas. The data from the two-inch range results in a curvature only $\frac{1}{3}$ of that in the localized area at the pellet-pellet

interface debonded region. The result is due to a lack of pellet support at the debonded interfaces. Therefore, the flexural rigidity estimated from local tensile clad deflection data is approximately three times that estimated from the global data. When the study cannot be completed by testing because of instrumentation limitations, it is important to depend on the FEA simulation to investigate fuel rod behavior in detail, as shown in this example.

Table 5 Estimated curvature and flexural rigidity comparison from the tension side of the clad for case using epoxy as the interfacial material

	Curvature κ (1/m)	Flexural rigidity EI (N·m ²)
Two-inch range	0.118	52.825
Localized area	0.388	16.113

The previous discussion established that for debonded pellet-pellet interfaces and bonded pellet-clad interfaces, pellet-pellet direct pinning at the compression side helps significantly lower the stress at the compression side of the clad. Following the same approach, two sets of deflection data were drawn from the compression side of the clad to estimate curvature in the two-inch range, as well as from the localized area, as shown in Figure 35.

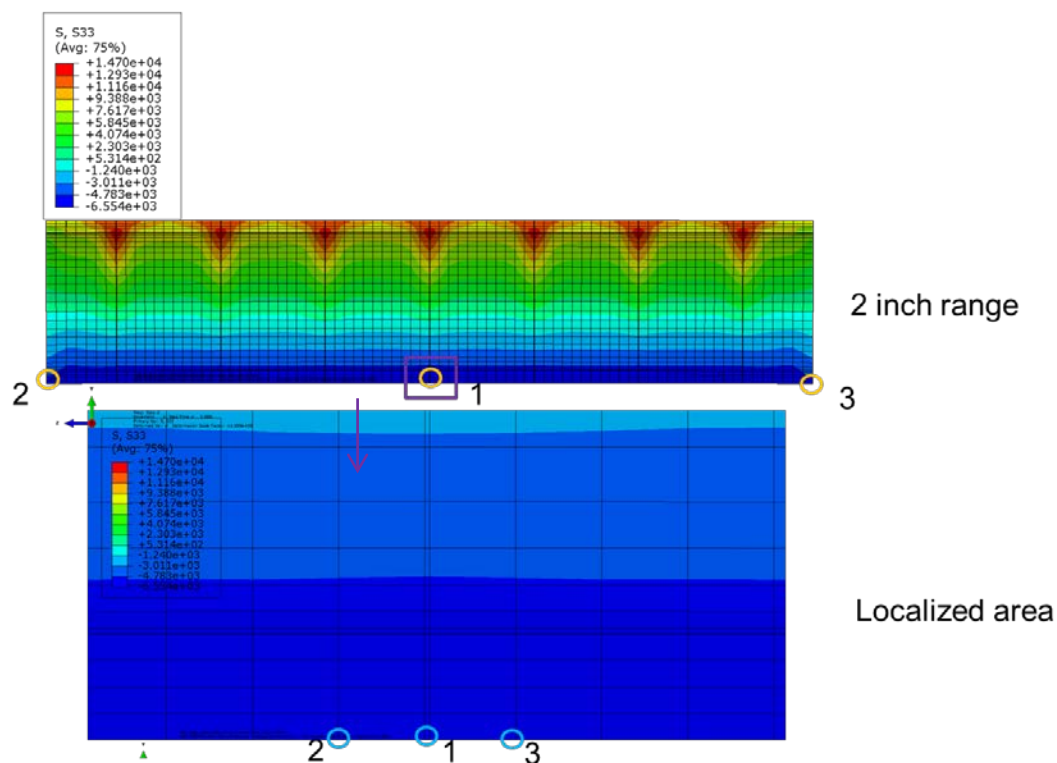


Figure 35. Curvature estimations from the deflection data at the compression side of the clad for the case using epoxy as the interface material.

The estimated curvature and flexural rigidity estimated from the deflection data at the compression side of the clad are compared in Table 6. The curvature estimated locally is still 39% higher than the curvature

estimated globally, which results in a 39% reduction in flexural rigidity. Compared with the estimation at the tension side in Table 5, the curvature and flexural rigidity estimated from deflection data in the global two-inch gauge section range are the same. That is because globally the nonuniform stress distribution averages out, although the curvature estimated in the localized area from the compression side is only half that estimated from the tension side. With pellet-pellet debonding at the clad compressive stress region, pellet-pellet pinning still provides support for resisting flexural deformation. Therefore, locally the flexural rigidity on the compression side is double that on the tension side.

Table 6 Estimated curvature and flexural rigidity comparison from the compression side of the clad for the case using epoxy as the interface material

	Curvature κ (1/m)	Flexural rigidity EI (N·m²)
Two-inch range	0.119	52.482
Localized area	0.195	32.077

2.4.2 Interfacial Material with a $10 \times$ Young's Modulus

The second study is also based on debonded pellet-pellet interfaces and well-bonded pellet-clad interfaces, but the interfacial layer is simulated as a $10 \times$ Young's modulus material to evaluate how a change in the properties of the interfacial material would impact the estimation of curvature and flexural rigidity.

The same procedure was followed that is outlined in Section 2.4.1. The first clad curvature estimation data were from the tension side (Figure 36). The stress distribution was still nonuniform. Table 7 shows the globally and locally estimated curvature and flexural rigidity as the interface material becomes stiffer. As a result of a lack of pellet support at the debonded interface, the local tensile clad curvature is approximately four times that of the global curvature. There is a larger difference between the results estimated from global and local deflection data. In the localized area, the curvature and flexural rigidity are close to the estimations in Table 5 for the case using epoxy as the interface material. The larger difference results mainly from the estimations in the global two-inch range. There is a 20% increase in flexural rigidity because of the $10 \times$ increase in the Young's modulus of the interfacial material. This result indicates that the interfacial material will have more impact in estimations of curvature and flexural rigidity globally than locally at the tension side of the clad.

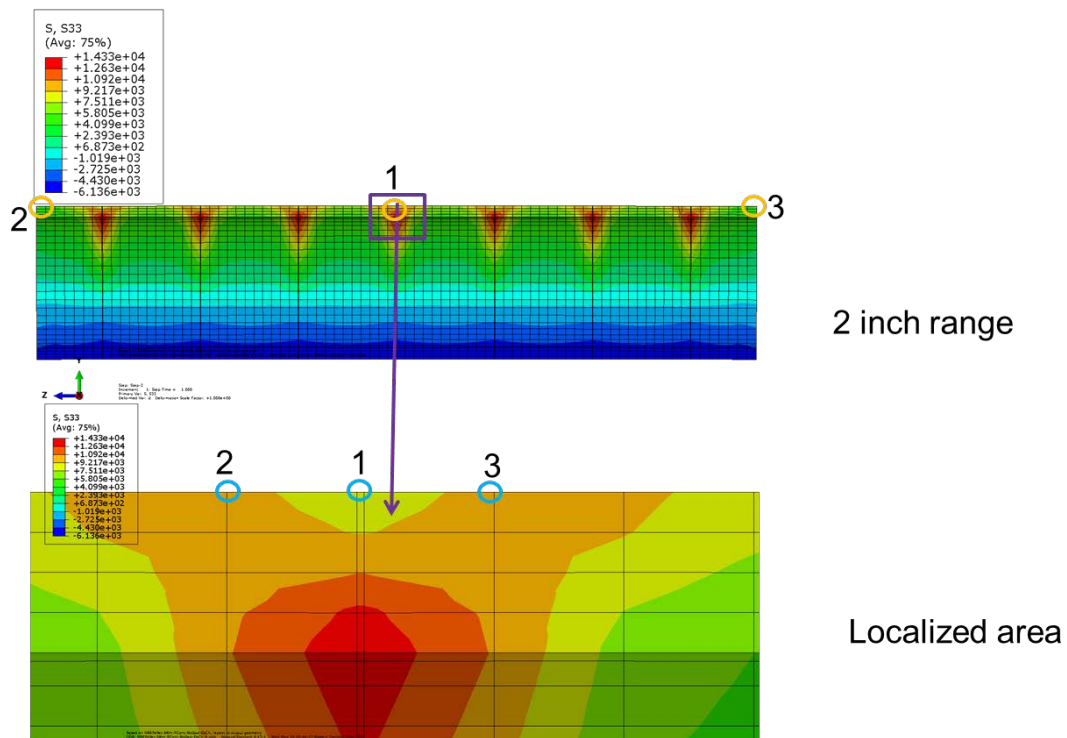


Figure 36. Curvature estimations from the deflection data at the tension side of the clad for the case using the $10 \times$ Young's modulus material.

Table 7. Estimated curvature and flexural rigidity comparison from the tension side of the clad for the interface material with a $10 \times$ Young's modulus

	Curvature κ (1/m)	Flexural rigidity EI (N·m ²)
Two-inch range	0.096	65.373
Localized area	0.369	16.949

The deflection data for the interface material with a $10 \times$ Young's modulus are also drawn from the compression side of the clad (see Figure 37). The estimated curvature and flexural rigidity are compared in Table 8.

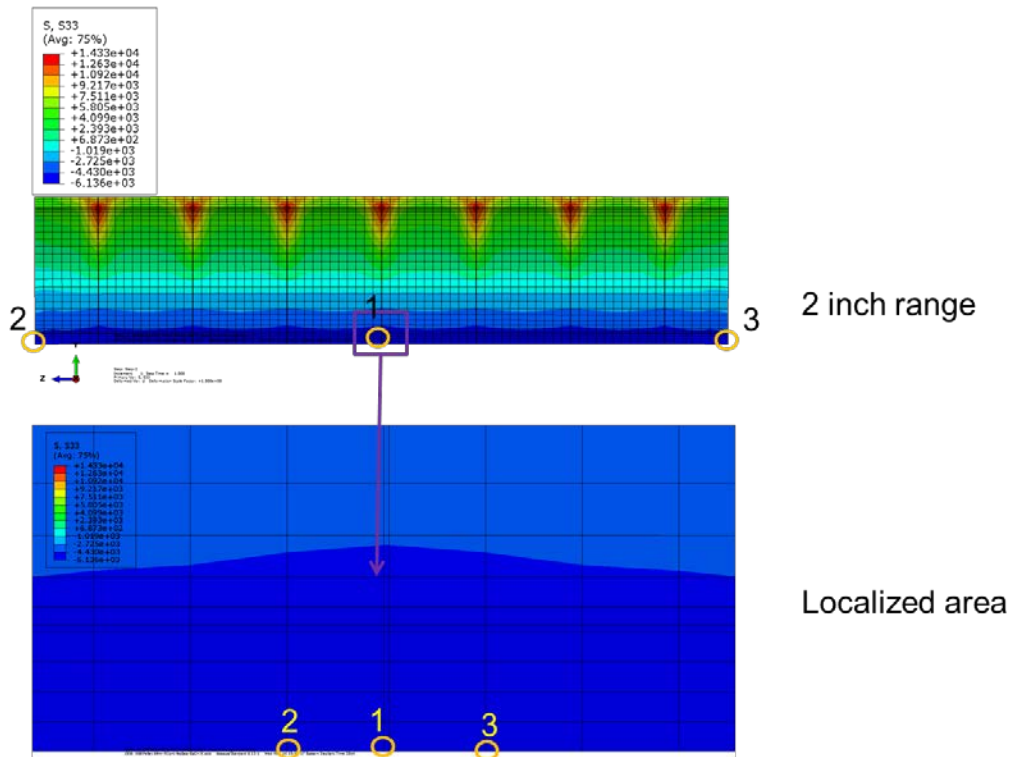


Figure 37. Curvature estimations from the deflection data at the compression side of the clad for the $10 \times$ Young's modulus material.

Table 8. Estimated curvature and flexural rigidity comparison from the compression side of the clad for the interface material with a $10 \times$ Young's modulus

	Curvature κ (1/m)	Flexural rigidity EI (N·m ²)
Two-inch range	0.097	64.687
Localized area	0.130	48.098

2.5 Clad Stress Investigation and Comparison

Since the stress distribution on the clad is nonuniform, clad stress was investigated in further detail to obtain a better understanding of the clad stress profile. In this study, epoxy was simulated as the interface material.

2.5.1 Clad Stress Estimation from Conventional Approach Based on Curvature and Flexural Strain

In Section 2.4, the clad curvature was estimated from clad deflection data. The clad stress can be further estimated using a conventional approach based on curvature and flexural strain and then compared with the stress profile obtained from FEA. Figure 38 illustrates the flexural strain evaluation of a uniform rod.

After flexural deformation, the length of the neutral surface remained the same. At the other sections, the flexural strain can be evaluated as follows:

$$\varepsilon = \kappa * y \quad (6)$$

Where

κ = curvature

y = distance from section surface to the rod neutral axis

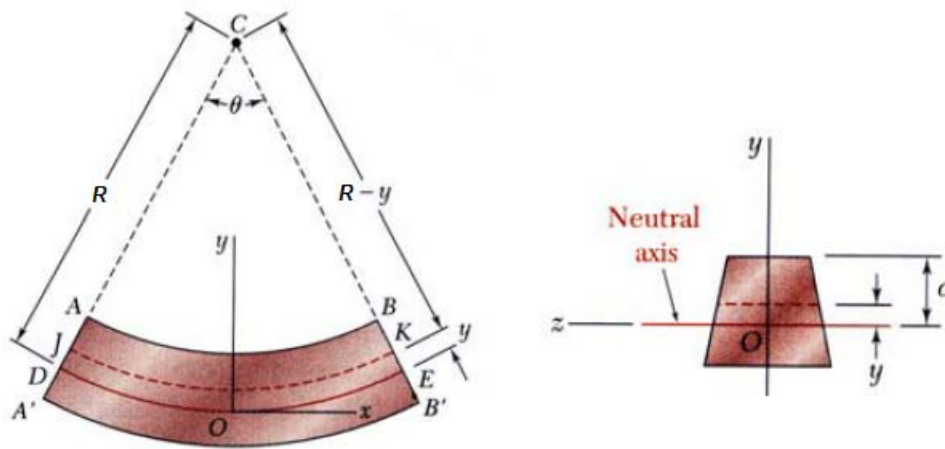


Figure 38. Flexural strain evaluation of a uniform rod.

For a single uniform rod, the neutral axis can be determined by section geometry and cannot change because it is based on geometric properties. However, for a composite fuel rod, the neutral axis will change because of the interface bonding condition and the shift in load-carrying capacity between the fuel pellets and the clad under flexural deformation, as shown in Figure 39 and Figure 40. In Figure 39, for the perfect interface bonding, the fuel pellets and the clad tie together to resist the bending moment, and the system responds symmetrically. Therefore, the neutral axis of the composite rod resides at the geometric center line. For the pellet-pellet interface that is debonding, as shown in Figure 40, the normal stress results show an apparent shift of the composite system neutral axis from the geometric center line. Based on the bending moment balance calculation, the composite system neutral axis shift Δ can be determined as follows:

$$F_{\text{tension}} = \sum A_i * \sigma_{zz} \quad (7)$$

$$y_0 = \sum A_i * \sigma_{zz} * y_i / F_{\text{tension}} \quad (8)$$

$$D = M / F_{\text{tension}} \quad (9)$$

$$\Delta = y_0 - D/2 \quad (10)$$

where

σ_{zz} = Resultant normal stress, S33 in Figure 40

A = Element area

y_i = Distance of individual force calculated from normal stress to geometry center

M = Bending load 6.25N*m

y_0 = Distance from tension force center to geometric center

D = Bending moment arm length

Δ = Composite system neutral axis shift

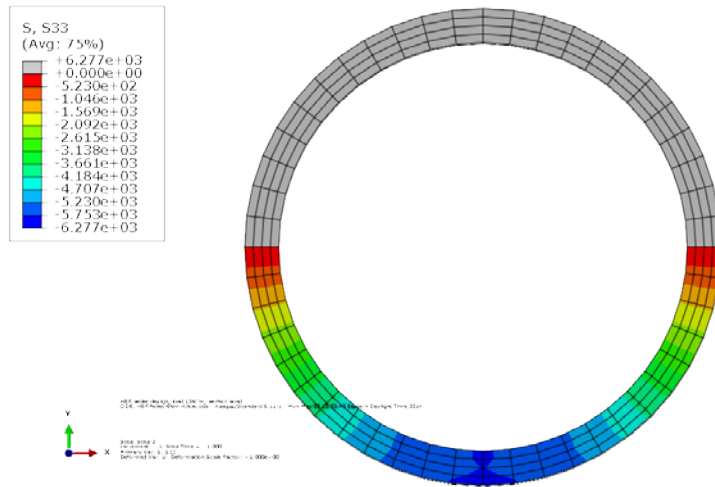


Figure 39. Clad neutral axis at geometric center line for perfect interface bonding.

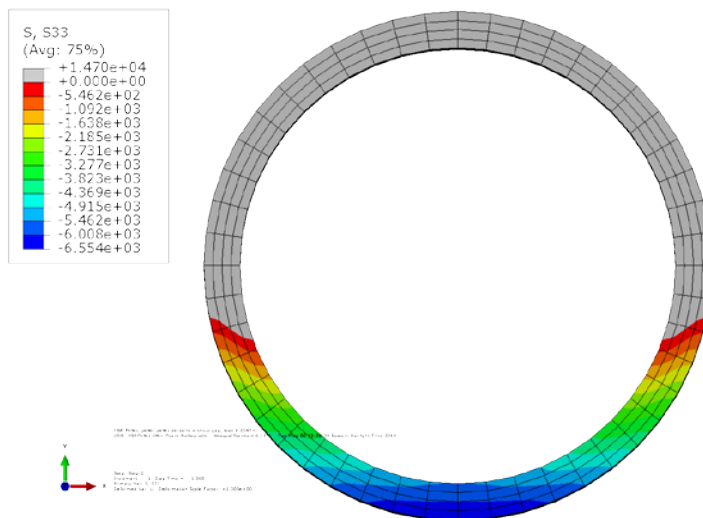


Figure 40. Clad neutral axis shifts from geometric center line for pellet-pellet interface debond and pellet-clad interface bond case.

Therefore, in the pellet-pellet debonding and pellet-clad bonded case, the fuel rod system neutral axis shifts down 0.039 inch from the geometric center based on the calculation. Applying Eq. (6), the flexural

strain of the clad’s outer surface can be estimated from the curvature data discussed in Section 2.4. For the perfect interface bonding, the distance from the clad’s outer surface to the composite neutral axis y is the clad radius, because the neutral axis lies at the geometric center line. For the pellet-pellet interface debonding case, y is the clad radius adjusted by the neutral axis shift of 0.039 inch. The normal stress of the clad can be further estimated from the strain and Young’s modulus, as follows:

$$\sigma_{zz} = \varepsilon * E \quad (11)$$

The Young’s modulus of the Zr-4 clad material is shown in Table 1. Table 9 summarizes the estimated curvature, strain, and stress for the two cases discussed in this section. The estimated stress lies right between the FEA stress result at the pellet-pellet interface and the stress not at the pellet-pellet interface. So the stress estimation–based induced curvature and estimated flexural strain shows fairly reasonable results. It can be considered as the average value of the nonuniform stress distribution.

Table 9. Estimated normal stress compared with FEA stress profile

	EI (N·m ²)	κ (1/m)	Estimated ε (m)	Estimated σ_{zz} (psi)	FEA at pellet-pellet interface σ_{zz} (psi)	FEA not at pellet-pellet interface σ_{zz} (psi)
Perfect bond	77	0.082	0.443E-3	5.842E+03	5.848E+3	5.686E+3
Pellet-pellet debond; pellet-clad bond	53	0.118	0.754E-3	9.950E+03	1.154E+4 (interior max stress 1.47E+4)	9.371E+3

2.5.2 Clad Stress Comparison between Different Interface Bonding Conditions

The FEA nonuniform normal stress and shear stress results for different interface bonding conditions with epoxy as the interface material are summarized in Table 10-Table 13 and are compared case by case at the tension side and the compression side of the clad. Table 10 shows the clad’s normal stress at the tension side. Because of nonuniform stress distribution, the normal stress at the pellet-pellet interface region and the stress for locations other than the pellet-pellet interface region are compared for several interface bonding conditions: perfect bonding, only pellet-pellet interface debonding, both pellet-pellet and pellet-clad interface debonding, and pellet-pellet interface with and without gaps.

Generally, at the tension side, the axial stress σ_{zz} is much higher than the lateral stress σ_{xx} and σ_{yy} as a result of bending. For the perfect bonding case, σ_{zz} is slightly different at the pellet-pellet interface region and for locations not at the pellet-pellet interface regions. With pellet-pellet interface debonding, the σ_{zz} is almost double that in the perfect bond case because of the significant bending moment shift from pellet to clad at the pellet-pellet interface region. At the pellet-pellet interface region, stress concentrations are higher than those not at the pellet-pellet interface region. Without gaps at the pellet-pellet interfaces, the levels of σ_{zz} are reduced because the pellets take a big portion of the bending load via pinning. With further debonding at the pellet-clad interfaces, the resulting axial stress σ_{zz} appears more uniform at the pellet-pellet interfaces and for regions other than the pellet-pellet interfaces. However, the lateral stress σ_{xx} and σ_{yy} vary at different locations of the clad. The levels of σ_{xx} and σ_{yy} at the pellet-pellet interface region are all higher than those not at the pellet-pellet interface region.

Table 10. Clad normal stress comparison at tension side for different interface bonding conditions

Tension side	At pellet-pellet interface region			Not at pellet-pellet interface region		
	σ_{xx} (psi)	σ_{yy} (psi)	σ_{zz} (psi)	σ_{xx} (psi)	σ_{yy} (psi)	σ_{zz} (psi)
Perfectly bonded	239.0	66.8	5.76E3	260.4	-5.2	5.37E3
Debonded pellet-pellet interfaces with gaps	2.05E3	381.1	1.33E4	1.18E3	10.2	9.63E3
Debonded pellet-pellet and pellet-clad interfaces with gaps	749.1	-190.9	1.46E4	46.8	2.5	1.46E4
Debonded pellet-pellet interfaces without gaps	1.96E3	435.0	1.25E4	1.37E3	-8.36	9.08E3
Debonded pellet-pellet and pellet-clad interfaces without gaps	1.60E3	-247.1	1.32E4	581.5	-18.4	1.32E4

At the compression side, as shown in Table 11, the normal stress results are similar to those at the tension side, except that the stresses are mostly for compression instead of tension. Especially for the perfectly bonded and debonded pellet-pellet interfaces with gaps, because of the symmetrical stress distribution, the stress levels are the same. The big stress level difference is evident in cases without gaps at the pellet-pellet interfaces. Because pellet pinching occurs at the compression side, the stress levels of σ_{zz} at the compression side are less than half those for the cases with gaps.

Table 11. Clad normal stress comparison at compression side for different interface bonding conditions

Compression side	At pellet-pellet interface region			Not at pellet-pellet interface region		
	σ_{xx} (psi)	σ_{yy} (psi)	σ_{zz} (psi)	σ_{xx} (psi)	σ_{yy} (psi)	σ_{zz} (psi)
Perfectly bonded	-239.0	-66.8	-5.76E3	-260.4	5.2	-5.37E3
Debonded pellet-pellet interfaces with gaps	-2.05E3	-381.1	-1.33E4	-1.18E3	-10.2	-9.63E3
Debonded pellet-pellet and pellet-clad interfaces with gaps	51.8	1.4	-1.47E4	561.7	-90.9	-1.47E4
Debonded pellet-pellet interfaces without gaps	-171.0	14.1	-6.0E3	-9.58	-9.97	-5.8E3
Debonded pellet-pellet and pellet-clad interfaces without gaps	747.5	-24.3	-6.22E3	1.15E3	-96.2	-6.24E3

Similar to the normal stress, the shear stress results at the tension side and at the compression side are compared in Table 12 and Table 13. In general, σ_{yz} dominates σ_{xy} and σ_{xz} by several orders of magnitude. The σ_{xy} and σ_{xz} are small enough to be ignored, so σ_{yz} was the focus for the comparison. At the tension side, for perfect bonding, the clad transfers less shear stress than for the other bonding conditions. As a result of the symmetrical stress distribution for perfectly bonded and debonded pellet-pellet interfaces with gaps, the shear stress σ_{yz} results at the tension side are the same as those at the compression side. At the compression side, the σ_{yz} for the case without gaps at the pellet-pellet interfaces is much smaller than that at the tension side. The reason might be the same as that discussed for the normal stress comparison: pinching by pellets.

Table 12. Clad shear stress comparison at tension side for different interface bonding conditions.

Shear stress from clad Node No. 810 at pellet-pellet interface region, tension side	σ_{xy} (psi)	σ_{xz} (psi)	σ_{yz} (psi)
Perfectly bonded	-1.08E-03	2.40E-04	-22.01
Debonded pellet-pellet interfaces with gaps	-2.72E-04	2.96E-05	-95.13
Debonded pellet-pellet and pellet-clad interfaces with gaps	-2.10E-05	-2.43E-03	57.78
Debonded pellet-pellet interfaces without gaps	5.15E-05	-3.46E-04	-121.56
Debonded pellet-pellet and pellet-clad interfaces without gaps	2.19E-05	-9.44E-05	59.67

Table 13. Clad shear stress comparison at compression side for different interface bonding conditions

Shear stress from clad node no. 816 at pellet-pellet interface region, compression side	σ_{xy} (psi)	σ_{xz} (psi)	σ_{yz} (psi)
Perfectly bonded	-3.91E-04	3.31E-04	-22.01
Debonded pellet-pellet interfaces with gaps	-3.63E-05	-3.25E-05	-95.13
Debonded pellet-pellet and pellet-clad interfaces with gaps	-1.27E-05	-2.21E-03	2.73
Debonded pellet-pellet interfaces without gaps	8.43E-04	-3.00E-04	5.04
Debonded pellet-pellet and pellet-clad interfaces without gaps	-1.34E-04	2.37E-04	13.25

3. CONCLUSION

Based on FEA simulation results and further verification from high burnup HBR rod bending test results, the localized system (stress-curvature) biases and uncertainties associated with CIRFT global response on the SNF rod system performance can be quantified and summarized as discussed below.

First, with good interface bonding and without fuel pellet and clad fracturing, the pellets in the HBR rod will carry more bending moment resistance than the clad under normal transportation vibration. The maximum stress resides in the pellets, and the stresses at the clad and pellet are both below the yield condition; therefore, the system is in a linear elastic state under the target bending loads. When the Young's modulus of the interface material is increased to 10 times that of epoxy, the fuel rod system stiffness increases. There is no shear stress surge inside the Zr-4 cladding.

Upon fuel pellet failure, including debonding at the pellet-pellet interfaces, the load carrying capacity shifts from the fuel pellets to the clad. The clad starts to carry most of the bending moment at the pellet-pellet interface region, resulting in localized stress concentrations in the clad. However, under the target bending moment, the clad does not yield. With good cohesion bonding at the pellet-clad interfaces, the pellets can continue to support the clad and carry a sufficient portion of the bending moment resistance; therefore, most of the clad at the gauge section remains in the linear elastic range. A shear stress surge occurs inside the cladding at the pellet-pellet interface regions. The flexural rigidity increases at $10 \times$ Young's modulus material, indicating that the stiffness of the HBR rod system increases.

When further debonding occurs at the pellet-clad interfaces, the embedded pellets can no longer provide effective structural support to the clad and assist load transfer within the HBR rod system. Thus most of the load-carrying capacity shifts to the clad throughout the entire gauge section. The shift leads to maximum stress concentrations in the clad in the entire gauge section instead of at localized pellet-pellet interface regions. For this case, the impact of the property change in the interface material is very limited. The clad does not yield because of the high material yield strength and the low bending load. There is no resulting shear stress concentration inside the clad for interface debonding.

When the pellets contact and pinch one another, they seem to take over a significant portion of the bending load resistance, especially where there are no gaps at the pellet-pellet interfaces. This pellet pinning action clearly mitigates and avoids stress concentration and potential yielding at the compression side of the clad.

All of the simulation cases are summarized in Table 14. The main parameter flexural rigidity EI is compared case by case. As the Young's modulus of the interface material increases to 10 times that of epoxy, the fuel rod system becomes stiffer. The flexural rigidity increases by up to 26% for the pellet-pellet interface debonding with gaps. When all the interfaces are debonding, the interface material has very limited impact on the flexural rigidity, an impact that is small enough to be ignored. The immediate consequence of interface debonding is a shift in the load-carrying capacity from the fuel to the clad, as well as a reduction in flexural rigidity. For example, the flexural rigidity is $77 \text{ N}\cdot\text{m}^2$ when the pellets are perfectly bonded with epoxy. In the case with gaps at the pellet-pellet interfaces, when there is debonding at the pellet-pellet interfaces alone, the flexural rigidity drops by 49% to $39 \text{ N}\cdot\text{m}^2$. In the case without gaps, it drops by 31%, to $53 \text{ N}\cdot\text{m}^2$. Further debonding at the pellet-clad interfaces causes the flexural rigidity to drop further, by 26% and 19%, respectively, for the cases with gaps and without gaps. Overall, for cases with gaps and without gaps, flexural rigidity drops by about 62% and 44%, respectively, between the perfect bond and the debond cases at all interfaces. The changes in flexural rigidity are similar for different bonding conditions for the two types of interfacial material.

Table 14. The flexural rigidity comparison between the different bonding and debonding cases

Interface bonding conditions	Flexural rigidity EI ($N \cdot m^2$)	Increase from epoxy to stiffer interface material (%)	Reduction from perfect bond (%)	Reduction from only pellet-pellet debond to further pellet-clad debond (%)	Increase from with gaps to without gaps (%)
Perfect bond with epoxy	77				
Perfect bond with $10 \times$ Young's modulus material	87	11			
Pellet-pellet interface with gap debond, pellet-clad interface bonded with epoxy	39		49		
Pellet-pellet interface with gap debond, pellet-clad interface bonded with $10 \times$ Young's modulus material	53	26	39		
Pellet-pellet interface without gap debond, pellet-clad interface bonded with epoxy	53		31		26
Pellet-pellet interface without gap debond, pellet-clad interface bonded with $10 \times$ Young's modulus material	65	18	25		18
Pellet-pellet interface with gap debond, pellet-clad interface debonded with epoxy	29		62	26	
Pellet-pellet interface with gap debond, pellet-clad interface debonded with $10 \times$ Young's modulus material	30	3	66	43	
Pellet-pellet interface without gap debond, pellet-clad interface debonded with epoxy	43		44	19	33
Pellet-pellet interface without gap debond, pellet-clad interface debonded with $10 \times$ Young's modulus material	45	4	48	31	33

Flexural rigidity is reduced more by debonding at pellet-pellet interfaces than by debonding at pellet-clad interfaces. Table 14 shows a flexural rigidity that is about 30% higher for the fuel rod without gaps, indicating a significant increase in system stiffness over the case with gaps. Therefore, the gaps at the interfaces of the fuel rod system have a significant impact on system reliability, especially at pellet-pellet interfaces. The flexural rigidity and bending moment resistance capacity of the fuel rod are highly dependent on interface bonding efficiency at pellet-clad and pellet-pellet interfaces. This discovery was validated by ORNL reversal bending fatigue test results performed on the fuel rod with HBR pellet inserts.

The estimates for curvature and the associated flexural rigidity vary widely between three deflection data points chosen from a relatively global area and a local area. Because of a lack of pellet support at the debonded interface, the local tensile clad curvature is ~3 to 4 times that of the global curvature at the tension side of the clad. At the compression side of the clad, the curvature and flexural rigidity estimated from the deflection data in the global two inch gauge section range are the same. However, the curvature estimated in a localized area from the compression side is ~ 1/3 to 1/2 that estimated from the tension side. With pellet-pellet debonding at the clad's compressive stress region, pellet-pellet pinning continues to provide good support to resist flexural deformation. Locally, the flexural rigidity estimated from the local compression side is double or triple that estimated from the local tension side.

The clad stress investigation reveals that the fuel rod system neutral axis shifts with interfacial debonding. The stress estimation based on induced curvature and flexural strain adjusted by the neutral axis shifting shows fairly reasonable results. The comparison between clad stress at the pellet-pellet interface region and away from the interface region shows a nonuniform stress distribution. The normal change in clad stress for different interface bonding conditions, especially a change in axial stress σ_{zz} , reveals a similar trend in the change in curvature. σ_{yz} dominates in the shear stress results. For the case without gaps at pellet-pellet interfaces, the σ_{yz} at the compression side is much smaller than that at the tension side as a result of pellet-pellet pinching.

4. REFERENCES

1. US Department of Energy, Used Fuel Disposition Campaign, *Used Nuclear Fuel Loading and Structural Performance Under Normal Conditions of Transport—Modeling, Simulation and Experimental Integration RD&D Plan*, FCRD-UFD-2013-000135, April 1, 2013.
2. B. Bevard, R. Howard, J.-A.J. Wang, Y. Yan, H. Wang, and H. Jiang, *FY 2014 Status Report: Vibration Testing of High Burnup Clad Fuel*, ORNL/LTR-2014/105, Oak Ridge National Laboratory, Oak Ridge, Tennessee, 2014.
3. J.-A.J. Wang, H. Jiang, and H. Wang, *Using Surrogate Rods to Investigate the Impact of Interface Bonding Efficiency on Spent Nuclear Fuel Vibration Integrity*, ORNL/LTR-2014/257, Oak Ridge National Laboratory, Oak Ridge, Tennessee, 2014.
4. H. Jiang, J. J. A. Wang, and H. Wang, “Potential Impact of Interfacial Bonding Efficiency on Used Nuclear Fuel Vibration Integrity during Normal Transportation,” *Proceedings of the ASME 2014 Pressure Vessels and Piping Conference*, PVP2014-29117, Anaheim, California, July 2014.
5. J.-A.J. Wang, H. Wang, Y. Yan, R. Howard, and B. Bevard, *High Burn-up Spent Fuel Vibration Integrity Study Progress Letter Report (Out-of-Cell Fatigue Testing Development—Task 2.1)*, ORNL/TM-2010/288, Oak Ridge National Laboratory, Oak Ridge, Tennessee, 2011.
6. J.-A.J. Wang, H. Wang, T. Tan, H. Jiang, T. Cox, and Y. Yan, *Progress Letter Report on U-frame Test Setup and Bending Fatigue Test for Vibration Integrity Study (Out-of-Cell Fatigue Testing Development—Task 2.2)*, ORNL/TM-2011/531, Oak Ridge National Laboratory, Oak Ridge, Tennessee, 2012.
7. H. Wang, J.-A.J. Wang, T. Tan, H. Jiang, T. Cox, R. Howard, B. Bevard, and M. Flanagan,
8. “Development of U-Frame Bending System for Studying the Vibration Integrity of Spent Nuclear Fuel,” *Journal of Nuclear Material* 440, 201–13, 2013.

This page intentionally left blank.